ornl

OAK
RIDGE
NATIONAL
LABORATORY

UNION
CARBIDE

NUREG/CR-1724
ORNL/NUREG/TM-404
CSNI-45

Proceedings of the CSNI Specialists Meeting on Nuclear Aerosols in Reactor Safety

Prepared for the U.S. Nuclear Regulatory Commission
Office of Nuclear Regulatory Research
Under Interagency Agreements DOE 40-551-75 and 40-552-75

OPERATED BY
UNION CARBIDE CORPORATION
FOR THE UNITED STATES
DEPARTMENT OF ENERGY

Printed in the United States of America. Available from
National Technical Information Service
U.S. Department of Commerce
5285 Port Royal Road, Springfield, Virginia 22161

Available from

GPO Sales Program
Division of Technical Information and Document Control
U.S. Nuclear Regulatory Commission
Washington, D.C. 20555

NUREG/CR-1724
ORNL/NUREG/TM-404
CSNI-45
Category Dist. R7

Contract No. W-7405-eng-26

Engineering Technology Division

PROCEEDINGS OF THE CSNI SPECIALISTS MEETING ON NUCLEAR AEROSOLS IN REACTOR SAFETY

April 15-17, 1980

Gatlinburg, Tennessee

Compiled by

T. S. Kress

Manuscript Completed – Sept. 29, 1980

Date Published – October 1980

Prepared for the
U.S. Nuclear Regulatory Commission
Office of Nuclear Regulatory Research
Under Interagency Agreements DOE 40-551-75 and 40-552-75

Fin No. B-0121

Prepared by the
OAK RIDGE NATIONAL LABORATORY
Oak Ridge, Tennessee 37830
operated by
UNION CARBIDE CORPORATION
for the
DEPARTMENT OF ENERGY

The Organization for Economic Cooperation and Development (OECD) was set up under a Convention signed in Paris on 14th December 1960, which provides that the OECD shall promote policies designed:

- to achieve the highest sustainable economic growth and employment and a rising standard of living in Member countries, while maintaining financial stability, and thus to contribute to the development of the world economy;

- to contribute to sound economic expansion in Member as well as non-member countries in the process of economic development;

- to contribute to the expansion of world trade on a multilateral, non-discriminatory basis in accordance with international obligations.

The Members of OECD are Australia, Austria, Belgium, Canada, Denmark, Finland, France, the Federal Republic of Germany, Greece, Iceland, Ireland, Italy, Japan, Luxembourg, the Netherlands, New Zealand, Norway, Portugal, Spain, Sweden, Switzerland, Turkey, the United Kingdom and the United States.

The OECD Nuclear Energy Agency (NEA) was established on 20th April 1972, replacing OECD's European Nuclear Energy Agency (ENEA) on the adhesion of Japan as a full Member.

NEA now groups all the European Member countries of OECD and Australia, Canada, Japan and the United States. The Commission of the European Communities takes part in the work of the Agency.

The objectives of NEA remain substantially those of ENEA, namely the orderly development of the uses of nulcear energy for peaceful purposes. This is achieved by:

- assessing the future role of nuclear energy as a contributor to economic progress, and encouraging cooperation between governments towards its optimum development;

- encouraging harmonization of governments' regulatory policies and practices in the nuclear field, with particular reference to health and safety, radioactive waste management and nuclear third party liability and insurance;

- forecasts of uranium resources, production and demand;

- operation of common services and encouragement of co-operation in the field of nuclear energy information;

- sponsorship of research and development undertakings jointly organized and operated by OECD countries.

In these tasks, NEA works in close collaboration with the International Atomic Energy Agency, with which it has concluded a Cooperation Agreement, as well as with other international organizations in the nuclear field.

The Committee on the Safety of Nuclear Installations (CSNI) is an international committee made up of scientists and engineers who have responsibilities for nuclear safety research and the nuclear licensing process. The Committee was set up in 1973 to develop and coordinate the Nuclear Energy Agency's work in nuclear safety matters, replacing the former Committee on Reactor Safety Technology (CREST) with its more limited scope.

The Committee's purpose is to organize international cooperation in nuclear safety. This is done essentially by:

(i) exchanging information about progress in safety research and regulatory matters in the different countries, and maintaining banks of specific data; these arrangements are of immediate benefit to the countries concerned;

(ii) setting up working groups or task forces and arranging specialist meetings, in order to implement cooperation on specific subjects, and establishing international projects; the output of the study groups and meetings goes to enrich the data base available to national licensing authorities and to the scientific community at large. If it reveals substantial gaps in knowledge or differences between national practices, the Committee may recommend that a unified approach be adopted to the problems involved. The aim here is to minimize differences and to achieve an international consensus wherever possible.

The technical areas at present covered by these activities are as follows: particular aspects of safety research relative to water reactors, fast reactors and high temperature gas-cooled reactors; probabilistic assessment and reliability analysis, especially with regard to rare events; siting research as concerns protection against external impacts; fuel cycle safety research; the safety of nuclear ships; various safety aspects of steel components in nuclear installations; licensing of nuclear installations and a number of specific exchanges of information.

The Committee has set up a Subcommittee on Licensing which examines a variety of nuclear regulatory problems, provides a forum for the free discussion of licensing questions and reviews the regulatory impact of the conclusions reached by CSNI.

ACKNOWLEDGEMENT

The experts group on nuclear aerosols in reactor safety would like to express their appreciation to the delegates and participants from the various member countries for their contributions in making the Specialists Meeting a successful, high quality, technical conference. Especially appreciated are the contributions of the conference chairman, Dr. W. O. Schikarski - Kernsforschungszentrun Karlsruhe, Federal Republic of Germany, M. Silberberg - U. S. Nuclear Regulatory Commission, and J. P. Olivier - Secretariat of the Nuclear Safety Division, OECD Nuclear Energy Agency.

Special thanks are offered to Ms. Kathy Rosenbalm of the ORNL Engineering Technology Division and to Ms. Norma Callaham - Technical Conference Coordinator for ORNL, whose contributions toward conducting and arranging the conference were immense.

CONTENTS

Page

Aerosol Processes

Measurement Techniques

Page

Page

Mathematical and Computer Modelling

Comparison of Codes and Experiments

Page

Application

FOREWORD

T. S. Kress

In 1978 the CSNI established a group of experts on nuclear aerosols in reactor safety and directed the group to prepare a state-of-the-art report on the subject. The report, issued in June 1979 as CSNI/SOAR-1 - Nuclear Aerosols, summarized the state of knowledge of nuclear aerosols and identified areas where limited information was available, areas where substantial progress had been made, and unresolved areas with recommendations for additional research. After completion of the SOAR-1 report, the experts group saw the need for an international technical conference to build on the findings of the report, to provide an update to the state of the art, and to promote additional information exchange among specialists working with nuclear aerosols. Consequently, the CSNI agreed to sponsor the Specialists Meeting on Nuclear Aerosols in Reactor Safety which was subsequently held at Gatlinburg, Tennessee, April 15-17, 1980, co-hosted by the Oak Ridge National Laboratory and the U.S. Nuclear Regulatory Commission.

The technical program, as recorded by these proceedings, included opening addresses, a panel discussion on "nuclear aerosol measurement," a panel discussion on "what remains to be done," six invited review papers, and 33 papers from six different countries grouped into the following topical areas:

(1) *aerosol source terms (nuclear aerosol formation and characterization, nucleation and condensation, size and composition of primary particles, aerosol source terms for postulated accidents);*

(2) *aerosol processes (correction factors, growth and interaction rates, removal rates);*

(3) *measurement techniques (focused on assessing limits of accuracy and implications for code validation for accident consequence analysis);*

(4) *mathematical and computer modelling;*

(5) *comparison of codes and experiments; and*

(6) *applications (focused on application of aerosol technology to reactor design, sensitivity of results, and implications for radiological consequence assessment for hypothetical accidents).*

Opening Address

Presented by: W. O. Schikarski
Kernforschungszentrun Karlsruhe (KFK)
Laboratorium für Aerosolphysik und
Filtertechnik (LAF)

Distinguished participants!

Ladies and Gentlemen!

As the Chairman of this CSNI-meeting on nuclear aerosols in reactor safety, I have the honour to open this conference and welcome you all in Gatlinburg. I hope that this conference which is the first with a larger international participation will play an important role in the promotion of knowledge on the safety and on environmental impact by nuclear power stations.

We all know that nuclear aerosols are of great significance in the understanding of both the environmental impact during normal operation and in the case of accidents in nuclear installations. Since it may not be clear to everyone in the audience, we can define the term "nuclear aerosols" as follows:

"Nuclear aerosols are airborne particles of solid or liquid nature which may be formed by various processes occurring in nuclear installations, which are usually composed of a variety of chemical elements and radionuclides and which pose a certain health risk in case of release into the environment."

Therefore, nuclear aerosols are not simply identical with radioactive aerosols which might be formed by natural processes also. It is also useful to characterize nuclear aerosols in comparison to environmental aerosols. Environmental aerosols, found in industrial, urban or rural areas, are composed of particular elements and appear mostly in relatively small concentration. By contrast nuclear aerosols are usually formed under strange (or extreme) conditions like high temperature, high pressure or high humidity. They also prefer to be formed with high concentrations. Consequently, their general behavior should be different and strongly depending on the environmental conditions under which they are formed, under which their transport is governed and their removal takes place. Also their chemical composition differs greatly from environmental aerosols.

Nuclear aerosol science is a young but not a new science. It is the privilege of the chairman of such a meeting of the international community of nuclear aerosol experts to take the opportunity to look back to the very beginning of nuclear aerosol science.

It was in the early 60's, when nuclear aerosols became a factor in reactor safety. Although the beginning of research on environmental aerosols can be dated back much earlier, yet the interest in nuclear aerosols rose sharply with the first licensing procedures for nuclear power plants. In particular, the licensing procedure for the Southwest Experimental Fast Oxide Reactor, which was an American-German undertaking and took place in 1964 and 1965, raised several nuclear aerosol problems concerning the LMFBR for the first time. I recall a lot of interesting discussions at that time with a number of friends who are today here in the audience, discussions which took place either at Atomics International in San Diego, or at General Electric in San Jośe or at Atomic Energy Commission Headquarters in Washington, D.C.:

What is the amount of Plutonium which can become airborne in a large core melt accident? What is the aerosol concentration as function of time after that accident in the containment? What properties should a containment system have to sustain such an aerosol release?
It was an easy calculation to show that the assumption of an airborne Plutonium aerosol concentration behaving like a noble gas led to unacceptable radiation dose values in the environment.

When I came back from my stay with General Electric in San Jośe to Germany (it was 1966), very soon we started a nuclear aerosol research group to tackle all these problems. Other groups, in the United States, Holland, Japan likewise stepped into the field and we took the opportunity of the International Radiation Protection Conference in Paris in 1969 to have shortly after at the Nuclear Research Center Karlsruhe the first International Specialist Meeting on nuclear aerosols. In the introduction to that meeting I presented experimental results on aerosol mass concentration decay curves from 10 experiments carried out up to 1969 at Atomics International at Brookhaven National Laboratory, at Reactor Centrum Nederland, and at Nuclear Research Center Karlsruhe, curves which I like to present

(with your permission) here today again, and I like to quote the corresponding remarks:

"The ten curves show a fairly disappointing situation. There is essentially no agreement between the experimental results of different laboratories, if one disregards the fact that all measure a decrease of mass concentration. The slope and shape of the time functions differ considerably."

Let me also read some of the recommendations given at the end of that first Specialist Meeting on nuclear aerosols, Ref. (1):

The following recommendations for future work were given:

- experiments should be carried out using adequate instruments to evaluate the weight of the different fundamental processes influencing the aerosol
- experiments with high initial mass concentration on the order of 1 g/m^3 and above should be carried out
- methods of generating high mass concentration aerosols and the influence of these various methods on the particle size distribution immediately after formation and on the long term should be studied
- experiments in larger vessels as well as in vessels with different surface/volume ratios (volume of 50 m^3 and above, height of 5 m and above) should be carried out with particular attention given to an investigation of the effect of varying vessel height on the time dependence of the aerosol mass concentration
- mixed aerosols composed of sodium and fuel particles should be studied with particular emphasis placed on an investigation of the effect of the Na/fuel ratio
- additional theoretical work is required on methods for treating the coagulation and settling of chains
- both theoretical and experimental work is needed on methods to account for particle impaction on surfaces in the event of large convection currents which will undoubtedly exist in a real accident

- additional experimental work is needed to develop suitable simulants for PuO_2, for use in large-scale tests. Comparison tests between the behavior of these simulants and PuO_2 aerosols are needed

I believe that much progress has been made since that early meeting about 10 years ago, both in solving problems asked in that time and in posing better (more specific and more accurate) questions to the final point we are looking for. I hope that this conference will show to what extent nuclear aerosol behavior has been understood and I am looking forward to all the presentations in our meeting program.

For those of you having entered the field of nuclear aerosol science recently, I may indicate the state-of-the-art-report of the CSNI group of experts on nuclear aerosols, which was issued a year ago under the chairmanship of Mr. Mel Silberberg, who will speak to us in a few moments. This report, indeed, contains most of the scientific results obtained in the recent years and, therefore, is very much recommended for reading.

But let me come back from history to today.
What are the present topics in nuclear aerosol science? This, of course, has to be considered in close relation to the objectives of our meeting here in Gatlinburg.

As in the past days, nuclear aerosol research work is strongly connected to licensing procedures. Licensing people contemplate more on accidents than on normal operation. This means:

(1) Nuclear aerosol behavior under accident conditions is still the focal point

Because the discussion on accident scenarios has progressed very rapidly in the recent years, not only the design basis accidents but also hypothetical accidents now under consideration. This means:

(2) Not only nuclear aerosol behavior in LMFBR's (where the DBA is a core-disruptive accident) must be studied, but also in LWR's or HTGR's.

Furthermore, nuclear aerosol behavior has been studied thoroughly in small-scale, laboratory-type experiments. These experiments carried out in vessels

of only a few cubic-meters cannot be easily extrapolated to large containments. This means:

(3) We need a number of experiments on aerosol behavior in sufficiently large vessels like CSTF, FAUNA and others.

Many of the recent experiments have been carried out without knowing the exact accuracy of the measurement techniques. This means:

(4) Well-instrumented experiments should be carried out with sufficiently calibrated measurement techniques.

Aerosol modelling is well advanced. A number of aerosol behavior codes like PARDISEKO, HAARM, ABC, Aerosim, NAUA, etc. are available. Since these codes deal with a complex system of differential equations, aerosol coefficients, correction factors, etc., the reliability of the input data is in question. This means:

(5) The improvement of the aerosol codes should include an as-good-as-possible assessment of the input data. Some of the important aerosol coefficients (i.e. form factors) should be measured independently.

Let me close this list of current topics by saying that a number of papers to be presented during this conference will deal with these questions and will give first or eventually final answers.

Last, but not least, I like to say a few words on the objectives of the meeting we are beginning today. It is the first meeting bringing together all international groups working in nuclear aerosols research or interested in nuclear aerosols from the standpoint of the regulator or the designer of nuclear power plants. In looking on the amount of problems to be solved, international cooperation is of great significance. But not only international cooperation in the sense of exchange of data, results and opinion is necessary. We also need international agreement on the three questions:

- What problems have been solved?
- Which problems should be solved in the near future? and
- What problems might become important in the long range?

I hope that this meeting will contribute significantly to these questions.

Finally, I thank the Committee on the Safety of Nuclear Installations of OECD for sponsoring this conference and providing organizational and other help in the preparation of the meeting.

I thank also the CSNI-expert group on nuclear aerosols who acted as the program committee to this conference. Finally, I like to thank the Nuclear Regulatory Commission of the United States and the Oak Ridge National Laboratory who co-sponsored the meeting and provided the necessary local arrangements.

I wish you a nice stay in Gatlinburg and all of us a successful meeting.

Reference

1) W. O. Schikarski, compiler, "The Behavior of Nuclear Aerosols in Closed Systems," Specialists Meeting in Karlsruhe on November 11 and 12, 1969, KFK-1206 (June 1970).

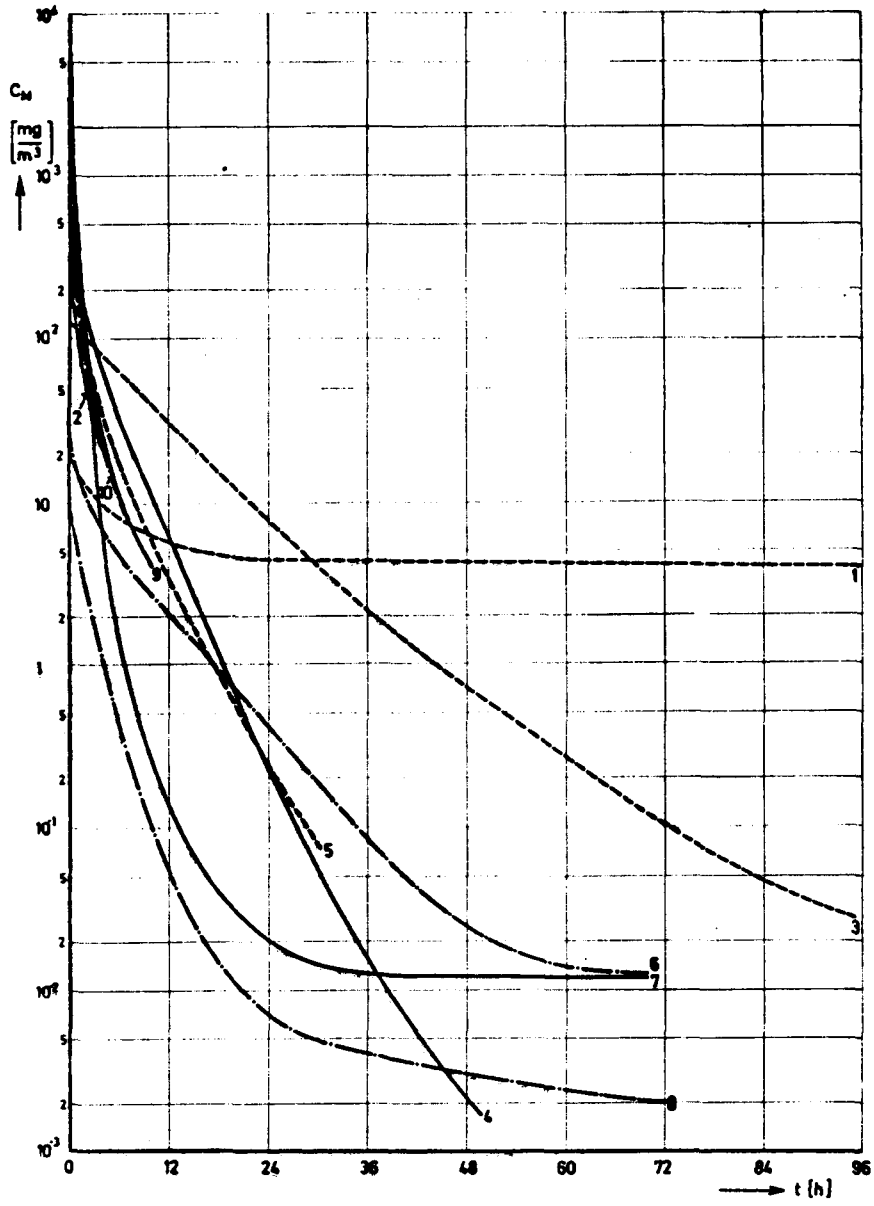

Comparison of experimental results on aerosol mass concentration C_M VS time

AEROSOL TECHNOLOGY - MEETING PERSPECTIVES AND THE FUTURE

M. Silberberg
U. S. Nuclear Regulatory Commission
Washington, D. C., U.S.A.

I would like to welcome you to Gatlinburg and to this CSNI Specialists Meeting on behalf of the U. S. Nuclear Regulatory Commission; and a special welcome to our visitors from abroad who have traveled far. We trust that you will have an enjoyable stay, one which is rewarding and meaningful to your work.

I would like to offer a few comments before we move to the first session of what promises to be an excellent technical meeting: First, I would like to acknowledge some people, second, say a few words about the future role and impact of aerosol technology in the United States and finally, place the meeting in perspective as to goals. What do we want to get out of this meeting?

I would like to personally thank and commend the Chairman of the meeting, Dr. Bob Schikarski, FRG, and his program committee for an excellent job in the organization and for the technical content of this meeting.

On behalf of the U.S. NRC and CSNI, I want to thank Dr. Tom Kress and his people at ORNL for their special efforts as hosts and for the arrangements and details that must be done in preparation for a meeting such as this. It is quite a demanding job to tackle, in addition to being the manager of a major program. We appreciate these efforts.

I would also like to take this opportunity to note again that the basis for this meeting was the CSNI-State-of-the-Art Report No. 1 published last fall by the OECD.

This report is noteworthy in many respects:

- It represents the first state-of-the art report published for a CSNI activity. It was truly a pioneering effort which led the way for a new series of reports from CSNI expert groups.
- The group of experts on nuclear aerosols made a significant achievement, not only because of their outstanding technical qualifications and contributions, but because of their fine spirit of cooperation and teamwork.

- Finally, regarding the report, I would like to acknowledge the excellent support of the Nuclear Energy Agency of OECD, the sponsors of the CSNI Experts Group, represented by Jean Pierre Olivier, our group secretary, for their excellent support.

When we look at the state-of-the-art report and the papers that will be presented here we find that aerosol technology, at least the behavior of aerosols in confined spaces, has not only come a long way in terms of resolving an important fast reactor safety issue, but in providing quantitative assessment tools for safety design or safety review. This situation has come about because of the continued pursuit and efforts of aerosol researchers and the users who are represented here and in attendance today. I believe we are probably much further ahead in aerosols than in any other area of fast reactor safety research. You all deserve credit for this. Nuclear aerosol transport analysis is an accepted tool in the United States for safety assessment in LMFBRs. While we have made excellent progress in aerosol transport behavior, we are not as fortunate with regard to quantitative source terms for LWRs or LMFBRs accidents.

As we approach refinements in aerosol behavior, we find that our ability to perform radiological consequence assessments are no better than, and are truly limited by, our state-of-knowledge of accident source terms. If we believe that the source terms are lower than we are currently assuming, we must provide convincing data.

In the United States, we are now starting to consider the consequences of degraded core cooling and core melt accidents in terms of siting and the possible need for the addition of mitigation features, and plans to conduct rulemaking in this area will soon be announced. We will need to sharpen our analyses in this regime of LWR accident analysis. It is very clear that we must now place more emphasis on applying our LMFBR aerosol technology to the LWR. I wish to note that the Federal Republic of Germany is making good progress in this regard. Fortunately, we have a good technical foundation and, even more important, good people to do it.

Finally, a few comments on the next 3 days: As noted in the call for this meeting, we must focus on new information or conclusions since SOAR No. 1 and try to obtain a clear picture of what work remains in this field and why it is important. To accomplish our meeting objectives, we need a good dialogue between the aerosol researchers and the users - both the

designers and the regulators - so that we might try to reach a consensus on what needs to be done. We should focus on the importance of work needed in the context of:

- Quantitative goals in a framework of risk assessment, and related sensitivity of uncertainties,
- Goals for different applications such as air cleaning systems design,
- Verification criteria for codes including the uncertainties in measurements.

AEROSOL SOURCE CONSIDERATIONS FOR LMFBR CORE DISRUPTIVE ACCIDENTS

A. B. Reynolds
The University of Virginia
Charlottesville, VA 22901

T. S. Kress
Oak Ridge National Laboratory
Oak Ridge, TN 37830

ABSTRACT

Factors that influence the radioactive source term in LMFBR Core Disruptive Accidents (CDA) are reviewed. Three groups of radioactive sources--actinides, sodium, and fission products--are discussed. Potential accident scenarios, including energetic and core-melt CDA's, are reviewed. Mechanisms for release and transport of radionuclides and aerosol formation are discussed at various phases of the scenarios, and programs contributing information on these mechanisms are briefly reviewed. Transport of aerosols between cells and aerosol behavior are not included in this review.

I. INTRODUCTION

As participants at this conference are well aware, the problem of specifying a radioactive source in the Reactor Containment Building (RCB) following a core disruptive accident in a LMFBR is a complex one. The fact that until recently source terms have to a great extent been assumed rather than calculated mechanistically is in itself evidence of the difficult nature of the analysis.

In this paper we are concerned with the production of fission products and actinides in the reactor core and the processes that influence the transport of these radioactive materials to the Reactor Containment Building. We will review some of the mechanisms for release and transport and some of the work in progress aimed at quantifying these mechanisms. Some of the transport to the RCB involves aerosol processes that will be the subject of the afternoon session. Hence we will not include these processes in our review.

Release and transport phenomena have not been quantified to the extent required for us in this review paper to provide numerical estimates of the source term in the RCB for particular LMFBR designs. Enough information was developed during the decade of the 1970's, however, to enable LMFBR designers to make considerably more realistic upper bound estimates for the source term at the end of the decade than was possible at the beginning. This is important because wherever adequate knowledge of release and transport mechanisms is lacking, there will be pressure to add engineered safeguards that can aggravate what is already a serious capital cost disadvantage for the LMFBR relative to the LWR. Simultaneously there will be pressure in the 1980's to reduce the capital cost of LMFBR's. Thus, in countries with serious LMFBR programs, there will be no shortage of tasks in the coming decade for those involved in radiation release and transport.

We shall begin this review with a description of fission product and actinide sources in the core. Next we will describe potential accident scenarios since the source term is so strongly dependent on the particular accident, and we will discuss phenomena in each scenario as they relate to the source term. We will be concerned only with core disruptive accidents in this review.

Earlier reviews have been made by participants in this conference, including a 1972 review by J. Gieseke, et al, [1], a 1976 review by W. Schikarski [2], and a major state-of-the art report on nuclear aerosols in 1979 from a Group of Experts of the OECD Nuclear Energy Agency's Committee on the Safety of Nuclear Installations (CSNI), with M. Silberberg as Group Chairman [3]. Recent French progress was reported in Reference 4. Major programs on aerosol source term are underway at several national laboratories in the U.S., at Cadarache in France, at Karlsruhe in Germany, and installations in the United Kingdom and Japan and elsewhere. Examples of U.S. DOE sponsored work at General Electric and Rockwell International are given in Reference 5-7. Existing analyses are being used and new ones are

being developed for application to specific fast reactor projects around the world. A perspective summary of aerosol safety questions for LMFBR's was reported by Abbey and Silberberg at the International meeting on Fast Reactor Safety Technology last year in Seattle [8]. All of the progress in this field cannot be reviewed in this paper and we regret the omission of important work with which we are not immediately familiar. We hope that this meeting will fill some of the gaps that we may leave out.

Space and time do not permit a review here of the computer systems available and under development for the transport of aerosols to the RCB. Aerosol behavior codes will be discussed throughout the meeting. Cell-to-cell transfer codes including or similar to CACECO [9] will also be discussed in later papers. We will discuss phenomena, such as material interactions, that form the starting point for CACECO-types transport codes. Two examples of the use of CACECO to study aerosol production and transport and containment evaluation for a number of core-melt and disruptive LMFBR accidents are reported in References 10 and 11.

II. ACTINIDES, SODIUM, AND FISSION PRODUCTS

One feature of the source term that can be accurately calculated for a particular LMFBR design is the production rate of each important group of radioactive sources, in particular the actinides, the fission products and the sodium activity. A group that is less important includes activation and corrosion products.

2.1 Actinides

Actinide inventories vary between designs and fuel cycle parameters. To provide typical order of magnitude values for the actinide inventories, approximate results are given for an average discharge burnup of 100 MWd/kg at the end of the equilibrium cycle in Table I. Typical plutonium isotopic compositions in the core are: ^{239}Pu, 0.68; ^{240}Pu, 0.22; ^{241}Pu, 0.07; and ^{242}Pu, 0.03.

TABLE I

TYPICAL ACTINIDE CORE INVENTORIES
AT END OF EQUILIBRIUM CYCLE

(Power = 1000 MWe; Average Discharge Burnup = 100 MWd/kg; Three-batch Loading; Average Burnup at End of Equilibrium Cycle = 67 Mwd/kg)

Actinide	Mass in Core (kg)
U	15 000
Np	10
Pu	3 200
Am	30
Cm	2
Fission Products	1 400
Total	19 600

2.2. Sodium Activity

Values are available for sodium activation during normal operation. The calculated ^{24}Na specific activity in the CRBR primary sodium (a loop design) is 30 Ci/kg (based on a primary system sodium inventory of 6.4×10^5 kg) [12]. The calculated ^{22}Na specific activity for CRBR after 30 years of operation is 3.5 mCi/kg. [12] For an early (1968) 1000 MWe General Electric pool design [13], the calculated ^{24}Na activity was 18 Ci/kg (based on a primary system sodium inventory of 1.3×10^6kg).

2.3. Fission Products

Fission product distributions for fission in ^{235}U and ^{239}Pu are compared in Fig. 1.

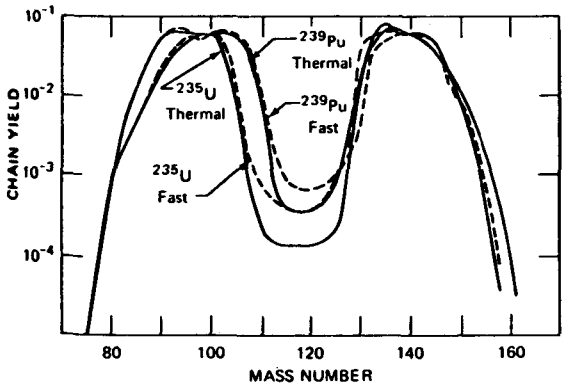

Figure 1. Fission yield spectra of U^{235} and Pu^{239}.

Note that fission products of mass numbers 105 to 110 are far more numerous (10 to 100 times more) from plutonium fission than from ^{235}U fission, although the difference between a Pu-fueled LMFBR and a ^{235}U-fueled LWR is partially offset by the fact that a significant fraction of the fissions in a LWR occur in plutonium. Important fission product elements with these mass numbers include the noble metals ruthenium, rhodium, and palladium. Also higher yields occur in the LMFBR than in the LWR for mass numbers around 120 which includes the elements silver, cadmium, and indium, although the absolute yields for these elements are low for both reactor types. Smaller fractional differences occur in the important mass number range around 90(Rb, Sr, Y); and large fractional differences, though small yields, occur for mass numbers above 150 (Pm, Sm, Eu, Gd).

Fission products are often grouped according to their volatilities or whether they exist predominantly as oxides. We have listed the principal fission products in Table II, following volatility groups similar to

TABLE II

FISSION PRODUCT CHARACTERISTICS[a]

Volatility Class	Element Symbol	Element Atomic Number	Element Family	% Condensed at 2500 K[b]	% Condensed at 4000 K[c]	Steady State Location	Principal Condensed State[d]	Principal Vapor State[d]	Normal Boiling Point of Principal Vapor Components[g] (K)	Vapor Pressure at 4000K[h] (Pa)
High	Kr	26	Noble Gas	0.0	0.0	Matrix, Bubbles	-	Kr		
	Xe	54	Noble Gas	0.0	0.0	Matrix, Bubbles	-	Xe		
	Br	35	Halogen	0.0	0.0	Matrix, Bubbles	-	Br, Br_2	331.8	8.3×10^4
	I	53	Halogen	0.0	0.0	Matrix, Bubbles	-	I, I_2	457.4	6.51×10^5
	Rb	37	Alkali Metal	49.7	52.8	Matrix	Rb, Rb_2O, RbO_2	Rb, RbO_2	961.0	4.2×10^5
	Cs	55	Alkali Metal	50.4	50.5	Matrix	Cs, Cs_2O, CsO_2	Cs, Cs_2, CsO, Cs_2O	951.4	4.26×10^6
	As	33	-	0.0	0.0	Matrix, Bubbles	-	As, AsO, As_2	886[e]	negligible
	Se	34	-	76.3	25.6	Matrix	Se, SeO_2	Se, Se_2, SeO	957.9	1.66×10^5
	Ag	47	Transition	99.1	69.8	Matrix	Ag, Ag_2O	Ag	2485.0	1.68×10^5
	Cd	48	Transition	20.6	9.9	Matrix	Cd, CdO	Cd	1038.0	5.87×10^5
	In	49	-	98.4	66.1	Matrix	In, In_2O_3	In	2353.0[f]	1.17×10^4
	Sn	50	-	99.6	89.6	Matrix	Sn, SnO, SnO_2	SnO, Sn	1353.0[f]	3.72×10^4
	Sb	51	-	98.5	67.3	Matrix	Sb, Sb_2O_3	Sb, Sb_2, SbO	2023.0	4.16×10^4
	Te	52	-	87.9	61.6	Matrix	Te, TeO_2	Te, Te_2	1663.0	-
Medium	Sr	38	Alkali Earth	100.0	100.0	Matrix	SrO	Sr, SrO	~3273.0	3.25×10^2
	Ba	56	Alkali Earth	100.0	99.9	Matrix	BaO	BaO	2273.0	2.66×10^3
	Mo	42	Transition	100.0	99.9	Matrix, Inclusions	MoO_2, MoO_3, Mo	MoO_3, MoO_2	1428.0[e]	1.33×10^4
	Tc	43	Transition	100.0	99.9	Inclusions	Tc, TcO_2	TcO_2, TcO, Tc	4000.0	3.37×10^3
	Ru	44	Noble Metal	100.0	99.2	Inclusions	Ru	Ru, RuO, RuO_2	4173.0	8.68×10^4
	Rh	45	Noble Metal	100.0	99.8	Inclusions	Rh, Rh_2O, RhO	Rh, RhO	4000.0	3.13×10^3
	Pd	46	Noble Metal	100.0	97.1	Matrix, Inclusions	Pd, PdO	Pd	3413.0	2.03×10^5
Low	Y	39	Transition	100.0	99.4	Solution in Matrix	Y_2O_3	YO	-	6.46×10^3
	Zr	40	Transition	100.0	100.0	Solution in Matrix	ZrO_2	ZrO_2, ZrO	~5273.0	7.46×10^1
	Nb	41	Transition	100.0	100.0	Solution in Matrix	NbO_2, NbO, Nb	NbO, NbO_2	-	1.38×10^2
	La	57	Rare Earth	100.0	99.9	Solution in Matrix	La_2O_3	LaO	-	1.36×10^4
	Ce	58	Rare Earth	100.0	99.8	Solution in Matrix	Ce_2O_3, CeO_2	CeO	-	1.21×10^4
	Pr	59	Rare Earth	100.0	99.8	Solution in Matrix	Pr_2O_3, PrO_2	PrO	-	4.56×10^3
	Nd	60	Rare Earth	100.0	97.8	Solution in Matrix	Nd_2O_3	NdO	-	1.71×10^5
	Pm	61	Rare Earth	100.0	100.0	Solution in Matrix	Pm_2O_3	PmO	-	9.77×10^1
	Sm	62	Rare Earth	100.0	98.9	Solution in Matrix	Sm_2O_3	SmO	-	2.39×10^4
	Eu	63	Rare Earth	100.0	84.6	Solution in Matrix	Eu_2O_3	EuO, Eu	-	5.34×10^4
	Gd	64	Rare Earth	100.0	99.7	Solution in Matrix	Gd_2O_3	GdO	-	6.13×10^2

a. Compiled by C.E. Apperson, based predominantly on Ref. 15.
b. Oxygen partial pressure = 2.3 Pa.
c. Oxygen partial pressure = 29.3 kPa.
d. Listed in order of predominance.
e. Sublimation Temperature
f. Decomposition Temperature
g. UO_2-PuO_2 normal (1 atmosphere)boiling point $\simeq$3040 K.
h. UO_2-PuO_2 vapor pressure at 4000 K = 4.86×10^5 Pa.

those suggested by Albrecht, Matschoss, and Wild [14]*. Also listed are the location in the fuel and the principal elemental or oxide forms. The fission products that are typically oxides have values of free energy of formation lower (more negative) than the oxygen potential for UO_2-PuO_2 fuel. Molybdenum is a mixture of metal and oxide because its free energy of formation is in the same range as the fuel oxygen potential. Fission products listed in the matrix tend to exist as interstitials rather than in the fuel lattice; those listed as solution in matrix tend to substitute directly in the fuel lattice. Inclusions tend to separate from the fuel into clusters of tens of micrometres in size, particularly in the columnar grain region.

III. ACCIDENT SCENARIOS

Our principal concern with regard to a radioactive source term is from a core disruptive accident (CDA), i.e. one for which fuel melts and the normal coolant flow is disrupted. In an LMFBR, a core disruptive accident can occur only if both the primary and secondary control systems fail to scram. If scram occurs, the source term is limited to local failures.

For purposes of organization, we divide CDA's into two classifications: (1) Energetic CDA's and (2) Core-melt CDA's. An energetic CDA involves hydrodynamic disassembly of the core, with subsequent mechanical work on the sodium above the core that might breach the vessel cover and, hence, the primary system. Core-melt CDA's involve melting of the fuel without disassembly. The primary system may or may not be breached, depending on whether fuel melts through the vessel or reactor tank, or the IHX, or, in a loop system, a primary coolant pipe. An energetic CDA also leaves molten fuel in the core area following the disassembly and expansion phase; hence, the core-melt CDA phenomena are also present in the energetic CDA.

An attempt has been made to list in Figure 2 the phenomena associated with both types of CDA that influence the source term. Many of these phenomena were considered in the CRBR analysis. In addition an attempt is being made by R. J. Williams in the United Kingdom to define fault trees for core disruptive accidents for the calculation of source terms, although we are not aware of publicly available results of this work. Fault tree analysis to define potential LMFBR accident scenarios is also being conducted at Sandia [16] and elsewhere in the U.S.

---

*Another grouping that is often quoted is due to Baker, et al, [15] in which the groups are: I. Nonvolatile, oxide forming (Sr, Ba, Y, Zr, La, Ce, Pr, Nd, Pm, Sm, Eu, Gd); II. Other nonvolatile (Nb, Mo, Tc, Ru, Rh, Pd); III. Volatile, soluble in sodium (Br, I, Rb, Cs, As, Se, Ag, Cd, In, Sn, Sb, Te); and IV. Noble Gases (Kr, Xe).

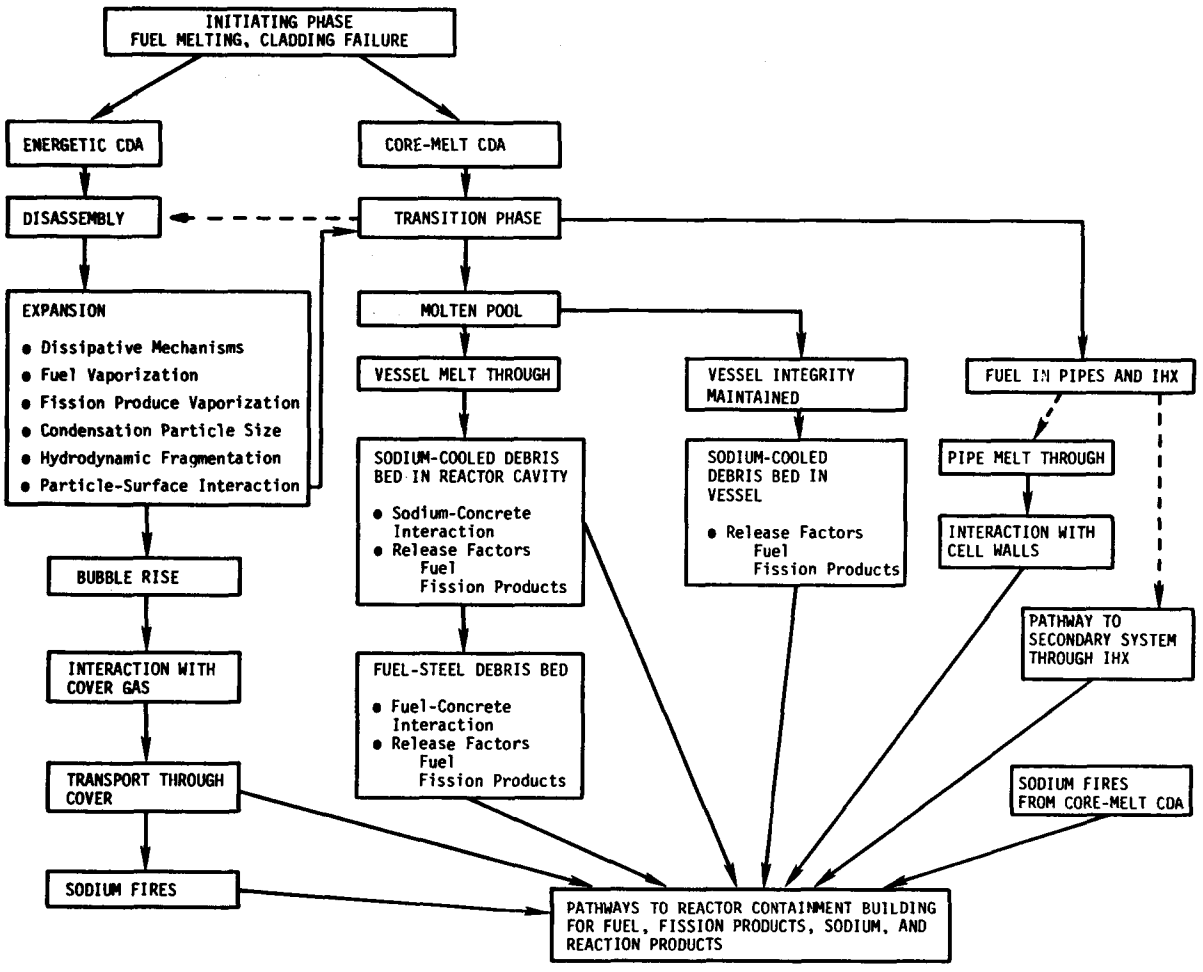

Figure 2. LMFBR Core Disruptive Accident Flow Charts

IV. ENERGETIC CDA

The question of how much mechanical energy the primary system must be able to contain in an energetic CDA has not been answered in the U.S. The cutoff in licensing activity for CRBR left the question suspended, with NRC suggesting 1200 MJ and the CRBR project proposing not more than 600 MJ. Recent application of the SIMMER code under development by the USNRC at LASL indicates that dissipative mechanisms likely exist that will reduce this work energy far below either value [17]. We have not attempted to assess the situation in Europe and Japan where progress on defining licensing requirements exceeds that in the U.S.

These questions do influence how we should divide our resources on source term research and development. At present we must continue to consider both an accident that results in the sudden breach of the primary system from mechanical work and the slower breach by molten fuel. Someday, in a reactor safety study for LMFBR's of the WASH-1400 type made for LWR's, if there is any probability of an energetic CDA leading to breach of the vessel cover, it will require analysis, and we had better develop the tools to do this.

The stages in an energetic CDA shown along the left side of Fig. 2 are described below as they relate to the source term.

3.1 Initiating Phase

In a transient overpower or transient under cooling accident without scram, cladding would fail and fuel would begin to melt in several seconds. Fission product gases from the fission gas plenum can be released during this phase. Correlations are available for the fraction of fission product gas released during normal operation [18]. Most is released from the columnar and equiaxed fuel, but much is retained by the unrestructured fuel. Fission gas from unrestructured fuel can be assumed to be released when the fuel melts. The halogens and arsenic would be released at this time in addition to the noble gases Xe and Kr.

Release of the fission products in the high volatility class in Table II other than the noble gases, halogens, and arsenic at the initiation of fuel melting is less clear. The "percent condensed" values in Table II between 2500 K and 4000 K (the fuel melting point is ~3040 K) indicates some but not all of these fission products are vaporized upon melting in an atmosphere with some oxygen partial pressure, despite the fact that the normal boiling point of the principal vapor components is always below the fuel melting point. The fission products in the medium volatility class appear to remain in the condensed phase, hence remain with the fuel.

Considerable data is available on fission product diffusion and

relocation during normal operation, e.g. Reference 19. Movement of the metallic inclusions, just prior to cladding failure has also been investigated [20].

3.2 Disassembly

During disassembly further melting occurs and more fission gas is released. The volatile fission products which are not gaseous at normal fuel operating temperatures begin to vaporize during disassembly. Little fuel and fission products actually vaporize until expansion occurs after disassembly because there is so little void space in the core. (The void space is primarily the space occupied by the sodium before it is expelled from the core.)

3.3 Expansion

• Understanding the Expansion Process

After disassembly, fuel expands into the void space above the core left by vaporized sodium and then into the sodium pool. Uncertainties in the fuel expansion stage are still great and this strongly influences the source term. Early calculations assumed isentropic expansion of fuel. Recent SIMMER calculations show that, if above-core structures are not displaced, potential dissipative phenomena reduce the work energy of the expansion dramatically [17]. These include self-mixing of the fuel in the early stage of the expansion, hydrodynamic effects due to pressure gradients between the core and the sodium pool caused by frictional flow, and heat transfer to structures. Also included are coolant entrainment and mixing of fuel with sodium, which leads to energy loss from the fuel but also to fragmentation and vaporization of some sodium. As indicated in Reference 17, however, if the above-core structures are forced out of position by excessively high core pressures, the damage potential rises significantly.

An important experiment in the U.S. in the area of fuel expansion is the 1/7 CRBR mockup test at Purdue University [21] using water as a simulant expanding fluid. While the primary objective of the experiment is the study of mechanical work effects, the results are of importance to radiation transport in defining bubble expansion processes. Early results indicate considerable heat transfer, entrainment, and hydrodynamic dissipation mechanisms resulting from vortices around structures above the fuel assemblies.

Information with regard to entrainment and two-phase expansion has been obtained from experiments at Stanford Research Institute and from the EXCOBULLE program at Grenoble. In these programs water was used for the two-phase fluid. Non-equilibrium effects have been demonstrated by the SRI tests [22]. Heat transfer and entrainment mechanisms were postulated to describe the EXCOBULLE results [23, 4].

The EXCOBULLE tests can be calculated with both the EXCOBUL [23] and the BAINS [4] models.

Programs on expansion with actual LMFBR materials are carried out both in-pile [as at TREAT (ANL), ACRR (Sandia), and CABRI (Cadarache)] and out-of-pile as in the FAST program at ORNL [21] and the CARAVELLE program at Cadarache [4].

The major program in the U.S. with reactor materials with the specific objective of aerosol transport from the core to the cover gas is the ORNL FAST program [24]. In the FAST tests UO_2 fuel is partially vaporized by capacitor discharge under sodium and allowed to expand. The objective is to study dissipative mechanisms that will affect the transport of fuel to the cover gas. Tests already performed under water and future plans for tests under sodium will be described in a later paper in this session [25].

Possible chemical reactions involving fuel, sodium, and structural materials in the bubble in an energetic CDA are analyzed in Reference 26.

· Fuel Vaporization

A potential source of small aerosol fuel particles is condensation of vaporized fuel. Hence the degree of fuel vaporization in the expanding fuel is of interest. An early calculation for the fraction of fuel vaporized during the expansion phase based on isentropic expansion and no self-mixing of fuel gave results of the order of 5% of the core for expansion to the available volume and 8% for expansion to the atmosphere [27]. These values were reduced considerably if early self-mixing of the fuel was assumed. The assumed isentropic expansion process is centainly too conservative, however. Results from the SIMMER analysis, together with experimental results from experiments like those at Purdue and SRI, will undoubtedly reduce the calculated fuel vaporization in an energetic CDA. Adiabatic free expansion in argon can give larger % though overall average may not be much more.

· Fission Product Vaporization

Fission products in the high volatility group of Table II can be assumed to vaporize completely during the expansion process from all the fuel that melts in an energetic CDA.

The fate of the fission products in the medium and non-volatile groups is unclear. They will not necessarily vaporize, and instead may remain in the fuel liquid phase. Information bearing on this behavior is given in Table II in which the vapor pressures of the predominant vapor species of these fission products at 4000 K are listed and compared with fuel vapor pressure. Values are taken from the work of Baker, et al, [15]; 4000 K is a reasonably characteristic value of the fuel temperature

during the expansion process. From Table II one notes that most of the fission product oxides are less volatile than UO_2-PuO_2; hence they may tend to remain with the molten fuel droplets. In the CRBR analysis (Appendix F, PSAR) of the structural Design Basis Accident, a fission product/fuel vapor bubble was assumed to be released instantly to the reactor cover gas, and the vapor bubble was assumed to contain ∿8% of the core plutonium and solid fission product inventory and 100% of the noble gases, halogens, and volatile fission products [12].

• Condensation

Submicron primary aerosol particles of fuel and fission products can result from condensation. In the ORNL condenser discharge vaporization of UO_2 pellets in argon, a distribution of UO_2 particles was measured in the range of 10^{-3} to 10^{-1} μm in diameter. This distribution has been calculated successfully by Chen [28] assuming gas dynamics expansion of the UO_2 which compresses the surrounding argon, followed by homogeneous nucleation of the vapor and then droplet growth by condensation. The time scale is of the order of 10 μs.

It is difficult to argue that a similar process can occur in the bubble expansion phase of a LMFBR energetic CDA. The expansion in a CDA would be slower, would be two phase so that condensation would more likely occur on existing droplets and surfaces rather than by homogeneous nucleation. However, fog formation from homogeneous nucleation may occur near cold surfaces above the core that might produce small primary particles [29]. Also if a bubble containing some fuel vapor could reach the argon cover gas, slower mixing with argon might cause homogeneous condensation of small droplets. Submicrometre particles from the slow condensation of UO_2 vapor in a cold gas have been measured at Batelle Columbus [30]. Also expansion of fuel vapor through channels in the cover may result in condensed particles (see Section 3.6).

Condensation of fuel and sodium vapor can also occur on the cold surface of the bubble. This process is retarded if inert gases such as fission gas are present. Most models for calculating this condensation are patterned after the model of Theofanous and Fauske [31].

• Hydrodynamic Fragmentation

As fuel moves upward from the core into a two-phase bubble, the liquid may fragment due to hydrodynamic forces (e.g. inertial and surface tension). These processes have been studied by Pilch and Erdman [32] and by Buttery [33], among others. The particles so produced are generally larger than a micrometre in diameter. Relatively little is

known regarding particle sizes from flashing, a process that is expected to occur according to SIMMER analyses, though the particle sizes are likely to be similar to those from other hydrodynamic fragmentation processes.

- Particle-Surface Interaction

Another phenomenon involved in bubble behavior during expansion is loss of fuel or fission product aerosol from the bubble to the surrounding pool of sodium due to contact with the bubble surface. Particle interaction with bubble surfaces is being studied experimentally at Cadarache [34] but we have not seen their results.

- Entrainment

Particles of sodium could be entrained into the bubble by several mechanisms, including Taylor instabilities [35] Kelvin-Helmholtz instabilities, and perhaps large vortex motion that cannot be specifically characterized by either instability. Such entrainment would influence the dynamics and energy partition of the bubble, which might influence the chance of breach of the cover, and influence the sodium aerosol that might escape from the primary system.

3.4 Bubble Rise

Rise of stable bubbles is well understood, beginning with the pioneering work of Davies and Taylor [36] and including recent work at Cadarache [37]. A stable bubble becomes capped, or lenticular shaped (spherical on top, flat on the bottom), and rises with a known velocity. It is unclear, however, whether a bubble could ever become a stable bubble detached from the vessel internal structure in an energetic CDA that can then rise to the surface. The two-phase bubbles produced in the SRI and Purdue experiments oscillate and chug as they are fed from the bottom. Bubbles produced in EXCOBULLE and FAST rise only if the cover gas pressure is well below atmospheric. Bubble rise in oscillating bubbles in EXCOBULLE was analyzed in Reference 38.

Perhaps a bubble that contains large amounts of inert fission gas could remain as a bubble after condensation and oscillation have ceased and could then rise as a stable bubble. Also a fission gas bubble resulting from cladding failure in many pins but without an energetic disassembly might rise to the pool surface.

Convection currents in stable rising bubbles were analyzed by Rose [39]. Analyses of convection currents and aerosol trajectories for a LMFBR bubble have been presented by Porrachia [40] and Kress and Ozisik [41]. In Reference 4 it is concluded that small particles would be transported into the cover gas, based on the PLEXICAP experiments. Analysis of heat and mass transfer has been further extended by Tobias [42].

3.5 Aerosol Transport into the Cover Gas

Studies are underway at Cadarache and ORNL to study aerosols transported to the cover gas. Aerosol collection techniques have been developed in the PLEXICAP program at Cadarache [43].

In the FAST program at ORNL, collectors have been developed to collect aerosols that survive to the cover gas, but thus far aerosols were found in the cover gas only when the pressure in the FAST vessel was reduced enough to allow the bubble to rise.

Floating of aerosols on sodium surfaces has been studied at Cadarache. Calculations with the IMPACT model indicate that UO_2 particles smaller than 2.6 mm will float on sodium [4].

Another interesting and unique aspect of Cadarache's PLEXICAP program was an experimental and analytical investigation of the hydrodynamics involved when a stable bubble broke through the liquid surface into the cover gas region [44].

3.6 Transport Through the Cover

Channels in the reactor cover might be opened by the impact of the sodium on the cover, thus allowing flow of core materials and sodium through the cover. Initially pure radioactive sodium might emerge. Later fission product gas, sodium contaminated by fission products, and two-phase fuel and fission products might emerge.

Material transport through the cover has held a high priority in the French safety programs, and a study of breach of the cover and sodium transport through the cover were primary objectives of the CARAVELLE experiments at Cadarache [4]. In these tests, a source containing a thermite charge ($Mg + Fe_2O_3$) and 1.4 ℓ water is placed in a tank filled with ~900 ℓ water. Initial pressures of 7 MPa are generated, a bubble radius of the order of 300 mm grows in 12 to 20 ms, and water impacts the cover with ~10 MPa dynamic pressure. Flow through two openings of 30 mm diameter and 180 mm length is observed. Only ~0.1 kg of water flowed through the two holes during the water hammer phase, but several kilograms flowed out later after separation of a gas-liquid emulsion.

An early calculation of particle sizes from hydrodynamic fragmentation during fuel and/or sodium transport through openings in the cover was made by Buttery [33]. He analyzed choked flow driven either by high pressure fuel vapor or sodium vapor in the cover gas region. Since that investigation, further analyses of these processes have been made by Pilch and Erdman [45]. It appears that primary particle sizes below 1 μm from hydrodynamic fragmentation are unlikely. In ongoing fault tree analyses by Williams of the U.K., choked flow of perfect gas through

breaches in the cover provides a source of aerosol.

If fuel or fission-product vapors do manage to escape through the cover, even as two-phase mixtures, the vapors might condense into submicrometre primary particles during the expansion into the region above the cover.

3.7 Sodium Fires

Sodium emerging from the cover can burn if oxygen is available, either in the region just above the cover or, if oxygen is unavailable there, in the Reactor Containment Building if the sodium escapes into the RCB. Some aspects of aerosol release from burning sodium will be discussed in Section IV, and analytical models of aerosol transport from sodium fires will be discussed at length in other sessions of this conference.

IV. CORE-MELT CDA

We now shift our attention to the processes that contribute to the source term in a core-melt CDA. (As noted earlier, core-melt phenomena are also present in an energetic CDA).

4.1 Initiating and Transition Phases

The initiating phase for the core-melt CDA may be similar to that of the energetic CDA. The plant protection system fails to scram so that fuel and cladding melt. However, the core then moves to a transition stage rather than experiencing disassembly and eventually forms a subcritical molten pool.

The noble gases would rise to the cover gas. Halogens and arsenic would escape from the fuel and would react with or be dissolved in the sodium. Other fission products in the high volatility class in Table II would be released as discussed in Section 3.1, and these released fission products would also remain in the sodium.

4.2 Potential Scenarios after the Transition Phase

After a subcritical molten pool is formed, the accident can move in several directions, as indicated in Fig. 2.

A core retention device in the reactor vessel or reactor tank may successfully keep the molten fuel from melting through the vessel or tank. In that case the fission product and fuel source may be contained in the primary system. Release of fission products and fuel from a sodium pool would provide a source term, however, if leakage paths from the primary system were present.

Without a core retention device, the fuel would melt through the vessel and fall into the reactor cavity. Release from a sodium pool would occur until sodium boiled away. The molten fuel and steel would then penetrate into the concrete below the reactor cavity or remain on a core retention device in the reactor cavity.

Some fuel may also move with the sodium into the pipes (in a loop system) and into the Intermediate Heat Exchanger (IHX), where its fate must be followed further.

4.3 Release from a Sodium Pool

Retention factors for fuel and several fission products for a hot sodium pool have been measured in the NALA program at Karlsruhe [46]. Retention factors for fuel and several fission products for a hot sodium pool have been measured in the NALA program at Karlsruhe. Retention factor is the ratio $(m_x/m_{Na})_{pool} / (m_x/m_{Na})_{released}$,

where m is mass and x refers to the fuel or fission product. Values have been reported for UO_2, Cs, NaI, and SrO. Retention factors are high for UO_2 (order of 1000), low for Cs (order of 0.1) and intermediate for NaI (order of 3) and SrO (order of 20). The sodium release rate is strongly dependent on pool temperature, gas flow rate at the pool surface, and temperature gradient above the pool. Between 780 K and 1165 K, the release rate increased by four orders of magnitude, roughly proportional to the sodium vapor pressure. Typical numbers for sodium release rates at low surface gas flow rate and T(gas) = T(pool) are 0.3 $kg/m^2 \cdot h$ at 800 K sodium temperature and 85 $kg/m^2 \cdot h$ at the sodium boiling temperature.

Further experiments are underway in the NALA program involving larger scale and more realistic LMFBR conditions. We are fortunate in being able to hear a further update on this especially impressive work in the last paper of this session [47].

Another phenomena in sodium pools concerns aerosols from boiling sodium pools. During the boiling process some fuel and fission products are carried over as aerosols in sodium droplets.

The literature on fission product behavior and chemistry in sodium is extensive and will not be reviewed here. Useful early reviews of this subject were reported by Castleman [48]. Even as early as 1968, Castleman and Tang reported theroretical analyses of fission product vaporization from sodium [49], while Pollock, Silberberg, and Koontz presented experimental measurements of the vaporization of cesium and NaI from sodium [50].

4.4 Sodium Interaction with Concrete

Sodium spilling from the reactor vessel into the reactor cavity (or from a pipe into a component cell) would fall onto a steel liner which lines the concrete walls. As long as the liner maintains its integrity, the sodium interaction with the concrete will be thermal. Heating of the concrete by the sodium will drive off both water vapor (e.g. Reference 51), and, if limestone aggregates are present, CO_2 gas from dissociation of $CaCO_3$. These gases must be vented to prevent damage to the liners.

If liners fail and sodium contacts concrete, a slow chemical reaction occurs in which hydrogen gas is generated. Sodium concrete chemical reactions and penetration rates were reported in two papers at the Seattle meeting [52, 53]. Calculational methods were reported in Reference 54.

4.5 Core Debris Interactions in the Reactor Cavity

In considering release of fuel and fission product aerosols from a core debris bed, consideration must first be given to the material on which the core debris falls. It may fall directly on the concrete liner and, after sodium evaporation, melt the liner and interact with concrete. On the other hand, the reactor design may include a core retention concept below the vessel. Sacrificial beds, crucibles, and trays are all being considered.

Without core retention systems, fuel would penetrate into the concrete. The rate of penetration is still being determined, for example in experimental programs at Sandia and ANL in the U.S. Analysis codes such as USINT (Sandia) and GROWS (ANL) are being developed to describe this penetration. Water vapor and CO_2 not released earlier by sodium heating would be released by further heating of the concrete. Oxidation of steel in the debris bed by these gases could generate H_2 and CO. Transport of these gases upward through the debris bed may sparge fission products and some fuel from the debris bed, thus providing another source of aerosols.

Sacrificial beds which have been considered for core retention include ThO_2, depleted UO_2, besalt, basaltic concrete, graphite, magnesium oxide, borax and other sodium borates, high alumina cement, and firebrick. Borax, basaltic concrete, firebrick, and alumina cement tend to emit either gas or aerosols upon contact with molten materials. Penetration by molten materials is especially slow in MgO, and little gases or aerosols evolve from the MgO itself during peneration. Recent experimental data on the interaction of core debris with these materials were reported at the Seattle meeting [55, 56].

An interesting phenomenon was reported by Peckover, et al, who

found that steel and oxide fuel in a molten pool could separate; and oxide fission products miscible in oxide fuel would stay with the fuel while metal fission products not miscible with fuel but miscible in molten steel would migrate to the metallic phase [57].

4.6 Gas and Aerosol Leakage Through Concrete

While this review does not cover analytical models for aerosol transport between cells, an interesting experiment regarding aerosol transport through concrete walls was reported at the Seattle meeting. Relatively larger leak rates of air through concrete than previously used data were measured at Petten [58]. Also leakage rates of particles in the 0.5 μm to 2.0 μm range through cracks in concrete ranging from 0 to 0.25 mm thickness were measured.

4.7 Aerosols from Sodium Fires

As indicated on Figure 2, sodium fires can occur in either energetic or core-melt CDA's. Data on the chemical composition and particle size of sodium aerosols produced in sodium fires were reported by five organizations at the Seattle meeting. Spray fire data was reported by HEDL [59], pool fire data by Karlsruhe [60] (in their FAUNA Facility), and both spray and pool fire data by Rockwell International [61] by ORNL [62], and by CEN Cadarache [63]. Reference 59 reported that most of the reaction products were Na_2O_2 and (due to the presence of water vapor) NaOH. Initial aerosol particle sizes were not reported, however, after about 10^3 seconds after the end of sodium spraying, the aerosols had agglomerated to a size in excess of 20 μm. Minimum sizes were of the order of 1 μm. In Reference 60 initial particle sizes were 0.5 μm diameter; the particle diameter during and shortly after the fire was 2 to 3 μm; it then decreased to 0.7 μm after 24 hours. The aerosol was entirely Na_2O_2. Reference 61 reported particle sizes from pool fires in the 5 to 120 μm range, with the mass of sodium in the form of Na_2O. In Reference 62 the aerodynamic diameters of the agglomerating sodium oxide particles produced in the pool fires grew to values as large as 4 μm. For the spray fires, aerodynamic mass mean diameters of the agglomerating aerosols increased rapidly from the source size to ∿7 μm and then decreased over 10 hours to about 1.5 to 2.0 μm.

Release of fuel and fission products in sodium fires must also be considered in sodium fires. Chatfield reported plutonium release fractions of 3×10^{-5} from burning sodium containing PuO_2 [64]. In tests at Atomic International Division of Rockwell International in 1975, plutonium release fractions were measured from 1×10^{-6} to 3.6×10^{-5}, with an average value of 1.1×10^{-5} for PuO_2 in sodium (as 10 to 223 parts per million of PuO_2 or $Na_4 PuO_4$) [65]. Sodium plutonate release fractions were several orders of magnitude below PuO_2.

REFERENCES

1. J.A. Gieseke, R.C. Behn, R.L. Ritzman, and J.M. Genco, "Aerosol Source Term for Fast Reactor Safety Analysis," Batelle Columbus Laboratories (August 1972).

2. W.O. Schikarski, "On the State of the Art in Aerosol Modelling for LMFBR Safety Analysis," Proceedings Int. Mtg. on Fast Reactor Safety and Related Physics, Vol. IV, pp. 1970-1914, Chicago IL (1976).

3. M. Silberberg, Chairman, "Nuclear Aerosols in Reactor Safety," A State-of-the-Art Report by a Group of Experts of the OECD NEA Committee on the Safety of Nuclear Installations (June 1979).

4. J.P.Breton, A. Lapicoré, A. Porrachia, M. Natta, M. Amblard, and G. Berthoud, "Expansion of a Vapor Bubble and Aerosols Transfer," Proceedings Int. Mtg. on Fast Reactor Safety Technology, Vol. III, p. 1445-1454, Seattle, WA (1979).

5. K.H. Chen, et al, "GE LOA-3 Tasks Annual Report, Sept. 1978-Aug. 1979," GEFR-00481, General Electric Company (August 1979).

6. T.C. Huang, et al, "Attenuation of Radiological Consequences Resulting from Postulated LOA-4 Scenarios," GEFR-00480, General Electric Company (August 1979).

7. "Annual Technical Progress Report, Reactor Safety-Accident Debris Behavior, FY 1978," ESG-DOE-13254, Rockwell International (Atomic International Div.) (December 1978).

8. F. Abbey and M. Silberberg, "Resolving Aerosol Safety Questions for LMFBR's--An International Consensus," Proc. Int. Mtg. on Fast Reactor Safety Technology, Vol. II, pp. 884-891, Seattle, WA (1979).

9. R.D. Peak and D.D. Stepnewski, "Computational Features of the CACECO Containment Analysis Code," TANSAO 21-274, Hanford Engineering Development Laboratory (1975). Also R.D. Peak, "User's Guide to CACECO Containment Analysis Code," HEDL-TME 79-22 (1979).

10. J. K. Long, A. R. Marchese, T. P. Speis, R. D. Gasser, and W. T. Pratt, "Radiological and Containment Analysis for a Postulated Fast Reactor Melt-Through Accident with Containment Venting," Proc. Int. Mtg. on Fast Reactor Safety Technology, Vol. III, pp. 1251-1260, Seattle, WA (1979).

11. S.E. Seeman and G.R. Armstrong, "Comparison of Containment Systems for Large Sodium-Cooled Breeder Reactors," HEDL-TME 78-35, Hanford Engineering Development Laboratory (April 1978).

12. Preliminary Safety Analysis Report, Clinch River Breeder Reactor (1974).

13. LMFBR Follow-On Study, Task II Re ort, "Conceptual Plant Design, System Descriptions, and Costs for a 1000 MWe Sodium-Cooled Fast Reactor," GEAP-5678, General Electric Co., p. 134 (1968).

14. H. Albrecht, V. Matschoss, and H. Wild, "Release of Fission and Activation Products During Light Water Reactor Core Meltdown," Nucl. Eng. and Des., Vol. 46, pp. 559-565 (1979).

15. L. Baker, Jr., J.D. Gabor, T.R. Johnson, R.M. Singer, E.S. Sowa, and R.P. Stein, "Postaccident Heat Removal Technology," ANL/RAS 74-12, Argonne National Laboratory (July 1974).

16. Advanced Reactor Safety Research Quarterly Report, April-June 1979, NUREG/CR-0984, SAND79-1597, Sandia Laboratories, pp. 219-223 (1979).

17. C.R. Bell, J.E. Boudreau, J.H. Scott, and L.L. Smith, "Advances in the Mechanistic Assessment of Postdisassembly Energetics," Proceedings Int. Mtg. on Fast Reactor Safety Technology, Vol. I, pp. 207-218, Seattle, WA (1979).

18. D.S. Dutt, D.C. Bullington, R.B. Baker, and L.A. Pember, "A Correlated Fission Gas Release Model for Fast Reactor Fuels," Trans. Am. Nucl. Soc., Vol. 15, pp. 198-199 (1972).

19. D. R. Olander, Fundamental Aspects of Nuclear Reactor Fuel Elements, Chapter 12, Technical Information Center, ERDA (1976).

20. P. Sasa, A. Cronenberg, and M. Stevenson, "The Contribution of Metallic Fission Product Inclusions to Axial Fuel Motion Potential," Proceedings Int. Mtg. on Fast Reactor Safety Technology, Vol. 1, pp. 130-138 (1979).

21. M. Saito and T.G. Theofanous, "The Termination Phase of Core Disruptive Accidents in LMFBR's," Proceedings Int. Mtg. on Fast Reactor Safety Technology, Vol. III, pp. 1425-1434 (1979).

22. R.J. Tobin and D.J. Cagliostro, "Nonequilibrium Phenomena in Flashing Water Used as an HCDA Source Simulant," Technical Report No. 8, SRI International (November 1979).

23. M. Amblard, G. Berthoud, J. Carre, A. B. Reynolds, and G. Sims, "Expansion and Collapse of Large Two-Phase Bubbles," Advances in Heat and Mass Transfer at Air-Water Interfaces, S. Sengupta, Editor, pp. 31-54, ASME (1978).

24. A.L. Wright, A.M. Smith, and T.S. Kress, "Fuel Aerosol Simulant Test (FAST) Plan," ORNL/NUREG/TM-129, Oak Ridge National Laboratory (1972).

25. A.L. Wright, T.S. Kress, A.M. Smith, "ORNL Experiments to Characterize Fuel Release from the Reactor Primary Containment in Seven LMFBR Accidents," CSNI Specialist Meeting on Nuclear Aerosols in Reactor Safety, Gatlinburg, TN. (1980).

26. W.A. Zanotelli and G.D. Miller, "The Possible Mechanisms for the Formation of the Observed and Expected Compounds During a HCDA," NUREG/CR-1134, MLM-2637, Mound Facility, Miamisburg, OH, (1979).

27. A.B. Reynolds, C.A. Erdman, and M. Kirbiyik, "Fuel Vapor Generation in LMFBR Core Disruptive Accidents," Nucl. Tech., Vol. 26, pp. 165-171 (1975).

28. K. Chen and A.B. Reynolds, University of Virginia, to be published (1980).

29. M. Epstein and D.H. Cho, "Fog Formation in Hypothetical LMFBR Accidents," Trans. Am. Nucl. Soc., 21, p. 324 (1975).

30. J.A. Gieseke, K.W. Lee, H. Jordan, and L.D. Reed, "Aerosol Measurements and Modeling for Fast Reactor Safety, Annual Report for FY 1978," NUREG/CR-0676, BMI-2021, Batelle Columbus Laboratories, pp. 26-31 (1979).

31. T.G. Theofanous and H.K. Fauske, "The Effect of Noncondensables on the Rate of Sodium Vapor Condensation from a Single-Rising HCDA Bubble," Nucl. Tech., Vol 19, p. 132 (1973).

32. M.Pilch and C.A. Erdman, "Particle Size Distribution from Multiple Hydrodynamic Fragmentation Events," Proceedings Int. Mtg. on Fast Reactor Safety Technology, Vol , pp. 239-248 (1979).

33. N.E. Buttery, "Possible Aerosol Formation Mechanisms Following LMFBR Whole Core Accidents," RD/B/N3497 (Rev), Berkeley Nuclear Laboratories (January 1976).

34. A Lapicoré, "Transfert de la Contamination dans l'accident de fusion du coeur d'un reacteur rapide," S.E.S.T.R. No. 18, C.E.N. Cadarache (July 1976).

35. M. Corradini, W.M. Rohsenow, and N.E. Todreas, "Effects of Sodium Entrainment and Heat Transfer with UO_2 Vapor During an HCDA," Trans. Am. Nucl. Soc., Vol 30, pp. 456-457 (1978).

36. R.M. Davies and G.I. Taylor, "The Mechanics of Large Bubbles Rising through Extended Liquids and through Liquids in Tubes," Proc. Roy. Soc., A 200, p. 375 (1960).

37. Lapicoré, Porrachia, Berna, and Cognet, "Generation and Rise of a Bubble in a Liquid," Communication presented at Congress Euromech 98, Eindhoven (November 1977).

38. A.B.Reynolds and D.R. Bradley, "Axial Motion of Large Two-Phase Bubbles," Proceedings Int. Mtg. on Fast Reactor Safety Technology, Vol. IV, pp. 1838-1847 (1979).

39. P.L. Rose, "Circulation in a Spherical-Cap Bubble," Report for the Chemical Engineering Tripos, University of Cambridge (1961).

40. A. Porrachia, "Etude du champ des vitesse du gaz dans une bulle en forme de calotte spherique, code CABU I," S.E.S.T.R. No. 12 (June 1979).

41. M.N. Ozisik and T.S. Kress, "Effects of Internal Circulation Velocity and Non-Condensable Gas on Vapor Condensation from a Rising Bubble," Nucl. Sci. and Eng., Vol. 66,, pp. 367-405 (1978).

42. M. L. Tobias, "Analysis of Heat and Mass Transfer Processes of a UO_2 Bubble in Sodium," Proceedings Int. Mtg. on Fast Reactor Safety Technology, Vol IV, pp. 1830-1837 (1979).

43. P. Le Feyer, A. Lapicoré, and G. Bertin-Maghit, "Relage et rendement de l'appareillage collecteur de particules du dispositif d'essai PLEXICAP," SESTR No. 78/265, C.E.N. Cadarache (December 1978).

44. Porrachia and Genetay, "Etude de l'eclatement de la bulle de gaz a la surface d'un liquide," S.E.S.T.R. No. 22, C.E.N. Cadarache (December 1976).

45. M. Pilch, C.A. Erdman, et al, "Bubble Behavior in LMFBR Core Disruptive Accidents, Annual Report July 1976-September 1977," NUREG/CR-0002, UVA/529106, Univ. of Va., pp. 3-44 (1977).

46. W. Schütz,"Fuel and Fission Product Release and Transport from Hot Sodium Pools,". Proc. Int. Mt. on Fast Reactor Safety Technology, Vol III, pp. 1455-1464, Seattle, WA (1979).

47. H. Santer and W. Schütz, "Aerosol Release from a Hot Sodium Pool and Behavior in Sodium Vapor Atmosphere," CSNI Specialist Meeting in Nuclear Aerosols in Reactor Safety, Gatlinburg, TN (1980).

48. A. W. Castleman, Jr., "LMFBR Safety. I. Fission-Product Behavior in Sodium," Nuclear Safety, Vol 11, pp. 327-390 (1970).

49. A. W. Castleman, Jr., and I. N. Tang, "Fission Product Vaporization from Sodium Systems," Proc. Int. Conf. on Sodium Technology and Large Fast Reactor Design, ANL-7520, Part 1, pp. 540-548 (1968).

50. B.D. Pollock, M. Silberberg, and R. L. Koontz, "Vaporization of Fission Products from Sodium," Proc. Int. Conf. on Sodium Technology and Large Fast Reactor Design, ANL-7520, Part 1, pp. 549-554.

51. J.D. McCormack, A.K. Postma, and J.A. Schur, "Water Evolution from Heated Concrete," HEDL-TME 78-87, Hanford Engineering Development Laboratory (February 1979).

52. R.P. Colburn, L.D. Muhlestein, J.A. Hassberger, and A.M. Mahncke, "Sodium Concrete Reactions,"Proceedings Int. Mtg. on Fast Reactor Safety Technology, Vol IV, pp. 2093-2102, Seattle, WA (1979).

53. R.U. Acton, R.A. Sallach, J.E. Smaardyk, and L.A. Kent, "Sodium Interaction with Concrete and Firebrick," Proc. Int. Mtg. on Fast Reactor Safety Technology, Vol IV, pp. 2122-2133, Seattle, WA (1979).

54. R. L. Knight and J.V. Beck, "Model and Computer Codes for Energy and Mass Transport in Decomposing Concrete and Related Materials," Proc. Int. Mtg. on Fast Reactor Safety Technology, Vol IV, pp. 2113-2121, Seattle WA (1979).

55. D. A. Powers, "A Survey of Melt Interactions with Core Retention Materials," Proc. Int. Mtg. on Fast Reactor Safety Technology, Vol I, pp. 379-388, Seattle, WA (1979).

56. M. Dallè Donne, S. Dorner, G. Fieg, G. Schumacher, and H. Werle, "Development Work for Fast Reactor Core-Catchers on the Basis of Sodium Borates," Proc. Int. Mtg. on Fast Reactor Safety Technology, Vol I, pp. 400-411, Seattle, WA (1979).

57. R.S. Peckover, T.A. Dullforce, and B.D. Turland, "Models of Core Melt Behavior after a Postulated Reactor Vessel Melt-Through," Proc. Int. Mtg. on Fast Reactor Safety Technology, Vol IV, pp. 2150-2159, Seattle, WA (1979).

58. J.F. van de Vate, W.F. van Leeuwen, A. Plomp, and H.C.D. Smit, "Aerodynamic Properties of Aerosols and Their Leakage through Concrete Containment Structures," Proc. Int. Mtg. on Fast Reactor Safety Technology, Vol II, pp. 804-813, Seattle, WA (1979).

59. J.D. McCormack, R.K. Hilliard, A.K. Postma and R.K. Owen, "Aerosol Behavior During Sodium Spray Fires and Comparison with Computer Codes," Proc. Int. Mtg. on Fast Reactor Safety Technology, Vol II, pp. 823-831, Seattle, WA (1979).

60. A. Alexas, W. Cherdron, S. Jordan, W. Lindner, and W. Schikarski, "Sodium Fire Aerosol Experimental and Analytical Results--Large Scale Tests in FAUNA," Proc. Int. Mtg. on Fast Reactor Safety Technology, Vol II, pp. 874-883, Seattle, WA (1979).

61. R.P. Johnson, C. Guderjahn, H.A. Morewitz, C.T. Nelson, and J. Otter, "Atmospheric Fallout of Sodium Combustion Aerosols," Proc. Int. Mtg. on Fast Reactor Safety Technology, Vol II, pp. 814-822, Seattle, WA (1979).

62. R.E. Adams, J.T. Han, T.S. Kress, and L.F. Parsley, Jr., "Behavior of Sodium Oxide and Uranium Oxide Aerosols in a Large Vessel," Proc. Int. Mtg. on Fast Reactor Safety Technology, Vol II, pp. 832-841, Seattle, WA (1979).

63. J.C. Malet, G. Duverger de Cuy, C. Casselman, J. Charpenal, M. Natte, and C. Devillers, "Sodium Fires-Progress Achieved in Research and Experimental Results," Proc. Int. Mtg. on Fast Reactor Safety Technology, Vol III, pp. 1192-1200, Seattle, WA (1979).

64. E. J. Chatfield, J. Fuel Material, Vol 32, p. 228 (1969).

65. "Characterization of Sodium Fires and Fission Products, Oct-Dec 1975 Progress Report," Rockwell International, Atomics International Division (1976).

LWR SOURCE TERMS FOR LOSS-OF-COOLANT AND CORE MELT ACCIDENTS*

A. P. Malinauskas and R. A. Lorenz
Oak Ridge National Laboratory
Oak Ridge, Tennessee, U.S.A.

and

H. Albrecht and H. Wild
Kernforschungszentrum Karlsruhe
Karlsruhe, Federal Republic of Germany

ABSTRACT

Fission product source terms for loss-of-coolant and core meltdown accidents in light water reactors are reviewed. The results presented in the Reactor Safety Study are summarized, and modifications of these results, due to more recent experimental studies, are described.

*This research was sponsored in part by the Office of Nuclear Reactor Regulation, U. S. Nuclear Regulatory Commission, under Interagency Agreement 40-544-75 with the U. S. Department of Energy under contract W-7405-eng-26 with the Union Carbide Corporation, and in part by Projekt Nukleare Sicherheit.

INTRODUCTION

It is axiomatic that the severity of a nuclear reactor accident is determined by the extent of radioactivity release which results. The main focus of site safety analyses is thus on fission product release and transport. Such analyses generally proceed by dividing the nuclear complex into a series of regions, or compartments, whose boundaries are usually defined by physical barriers, and then determining theoretically the behavior of the fission products within these regions subject to the chemical and thermalhydraulic conditions which are assumed to prevail. Such considerations can be reduced to the description of three processes: (1) the introduction of fission product species into a particular region (the "source terms" for that region); (2) attenuation mechanisms which modify the source terms in the compartment; and (3) transport across the barrier between this and the next adjacent compartment (the source terms for the adjacent region).

It is thus clear that the expression source terms has many possible meanings. In this review we apply the term to those quantities of fission products which escape from the fuel-cladding region and enter the primary coolant circuit.

This application is perhaps the most simple to describe; even so, it turns out to be an extremely complex function of the time/temperature history of the fuel-cladding system during an accident, since many mechanisms for release are involved. Depending on the particular fission product species, these release mechanisms range from simple gaseous expansion processes at low temperatures to evaporation-condensation processes (aerosol formation) over molten fuel. Because of these complexities, it is convenient to subdivide the time/temperature sequence of an accident into more or less discrete phases over which specific release mechanisms dominate.

Four such phases were defined for a core meltdown accident in the Reactor Safety Study [1]. These are the periods of (1) gap release, (2) meltdown release, (3) vaporization release, and (4) oxidation release. The fourth period involves exposure of the irradiated fuel to air; although some of the experimental data which we summarize in this report can provide further clarification of the processes involved in this phase, we dismiss it from further consideration.

The approach employed in the Reactor Safety Study for the specification of the fission-product source terms simplifies the problem considerably, even though some loss of uniformity results. In addition, the methodology applies equally well to boiling-water reactors (BWR) and pressurized water reactors (PWR), except that the duration of each phase varies both with regard to reactor type and accident sequence.

FISSION PRODUCT SPECIES

In principle, reactor safety analyses require source terms for each of the radiotoxic or otherwise significant species which are potentially releasable into the biosphere. Fortunately, however, it is possible to combine these species into groups having similar chemical behavior. Although differences in behavior and transport characteristics within the groups do exist, due to differences in mass, molecular size, and especially the decay characteristics of their precursors, such factors ordinarily give rise only to second-order effects for the long-lived isotopes. Precursor half-life may have a significant effect on the behavior of short-lived species, but this aspect will not be considered further. Indeed, we henceforth confine our considerations in a strict sense to long-lived fission products; the extension to short-lived species is generally straightforward, but is an unnecessary complication for purposes of this review.

It is customary to group the fission products as shown in Table I [1,2], where the various classes are listed in approximately decreasing order of volatility. Note also that in several important cases the chemical form of a particular species may undergo change as the fission product is released into a new chemical environment. Fission product iodine is an especially good example. This fission product is released from a defected fuel rod as CsI, and would thus enter liquid water coolant as iodide ion. In an oxidizing atmosphere, iodide can be oxidized to molecular iodine, and this species, in turn, can react to some degree with organic materials to yield organic iodides. In this manner fission product iodine can have decidedly different characteristics in the various regions of the reactor-biosphere system.

FISSION PRODUCT SOURCE TERMS

In this section we first summarize the approach and results which were utilized in the Reactor Safety Study [1] and then indicate how these have been modified as the result of more recent studies.

The Reactor Safety Study

As indicated previously, the approach employed in the Reactor Safety Study involved the subdivision of a "generic" core meltdown accident sequence into a series of phases, each being characterized by a dominant mode of fission product release. The first of these, which spans the approximate temperature range 700-2000°C, involves the release of fission products that are located in and on the surfaces of the interconnected voids within the fuel rod. These quantities of the fission products are designated as the "gap inventories."

Gap Inventories

The gap inventories are developed during the course of irradiation by two processes: (1) direct introduction by knockout or recoil from fission events near the fuel surfaces, and (2) diffusion from within the UO_2 matrix. Considerable study has been made of the manner in which the gap inventories of the noble gases within a fuel rod change with power history, since this can have a significant effect on the thermal characteristics of the rod. As a consequence, several computer codes have been developed to predict gap inventories of the noble gases [1,3-5], and a standard model for fission gas release is currently being formulated [6].

Considerations of fission products other than the noble gases are less detailed; in the Reactor Safety Study, distinctions between the noble gases and the remaining fission products, in terms of mechanisms for transport through the UO_2 matrix, were largely ignored. Thus variations in gap inventories among the various fission products were indicated to be due solely to differences in the diffusion coefficients characteristic of the transport process. (Since the corresponding diffusion coefficient values were generally derived from release experiments, differences in transport mechanisms were partially taken into account in an indirect manner.)

Gap inventory results, averaged over the entire core of a PWR prior to a core meltdown accident, are presented in Table II. (The differences in values between the three groups of contributors to the Reactor Safety Study are due to variations in the input parameters and calculation methods for both temperature profiles and fission product releases.)

Gap Release

Except for the noble gases, the gap inventories of all other fission products are present either as a condensed phase, or as vapor in equilibrium with a condensed phase. Hence, cladding rupture, which occurs over the temperature range from about 780-1100°C, will not release these species by simple gaseous expansion as for the noble gases. Rather, other thermodynamic and kinetic factors control their release. These factors were taken into account in the Reactor Safety Study by designating "escape fractions" for each fission product group. These escape fractions, which are also presented in Table II, are arbitrarily selected fractions of the gap inventory which are released during the gap release interval.

Meltdown Release

This phase is initiated with the formation of molten fuel, which probably first appears at the centers of individual pellets, and terminates when the molten mass just penetrates the reactor pressure vessel. Since thermal analyses of this phase of a core meltdown accident yield only generalized data on core temperature profiles and melt behavior, this and

the sparse data base for fission product release from molten fuel did not justify a mechanistic approach in the Reactor Safety Study. Accordingly, the core melt release fraction of fission product x as a function of time t, RCFx(t), was taken to be simply proportional to the fraction of core that was molten in that time period, FCM(t):

$$RCFx(t) = [RFx][FCM(t)], \quad (1)$$

where the constants of proportionality, RFx, are the fission-product release fractions. Values of these fractions are presented in Table III [1]. These results were largely developed on intuitive arguments which were based, in turn, on thermodynamics considerations and observations of release characteristics that were made on a very small number of experiments. Accordingly, uncertainties in the release fraction values were indicated by likely ranges of these values; these ranges are likewise presented in Table III.

Vaporization Release

After the molten mass has penetrated the pressure vessel, it falls into the reactor cavity. Vaporization release which occurs during this period is augmented by the sparging action of gaseous products that result from decomposition of the concrete. This sparging action, which is assumed to provide the dominant mode of release, is assumed to decrease exponentially with time, so that the vaporization loss fraction VLFx(t) for fission product x at time t of this phase of the core meltdown is given by [1]:

$$VLFx(t) = (VLFx)_T [1 - \exp(-0.693\ t/\tau)], \quad (2)$$

where $(VLFs)_T$ is the limiting value of the vaporization loss fraction and τ is the characteristic release half-time. In principle, τ has a characteristic value for each fission product species; in the Reactor Safety Study, however, τ was taken to be 30 min for all species [1]. In addition, Eq. (2) was assumed to apply to the first three half-times (i.e., 90 min); the limiting value was then assumed to be attained over the fourth half-time interval. Values of the corresponding release limits for each of the fission product groups are presented in Table IV [1]. Note that these fractions, as well as those described earlier, refer to the respective fission product inventories at the initial point of the particular release phase.

All of the release values indicated in the previous discussion are cited without regard to physical form. It is clear, however, that in both the meltdown release phase and in the vaporization release phase the molten fuel from which release occurs is at the highest temperature within the system. As a result, many of the fission products which vaporize from the melt are rapidly quenched, so that such releases are undoubtedly characterized by a dense smoke. Moreover, the sparging action in the vaporization release phase will yield a mist as well. Such smokes and

mists have two opposing effects. On the one hand, these aerosols have a scavenging effect by virtue of their high surface area, so that agglomeration and subsequent deposition reduce airborne fission product concentrations. On the other hand, these mechanisms provide an additional transport mode which is especially significant for otherwise nonvolatile fission product species.

Recent Experimental Studies

As had been indicated earlier, the data base available at the time of the Reactor Safety Study was generally sparse. In many cases release values were inferred from thermodynamics estimates or from semi-quantitative experimental observations. Since then, additional studies have been made which not only augment the data base, but also permit more realistic estimates of the release values. The results of these studies are presented in this section.

Gap Inventories

Input data for the codes employed in the Reactor Safety Study largely evolved from anneal tests with irradiated UO_2 specimens. Since then, considerable data have been obtained concerning noble gas gap inventories from post-irradiation examination of commercial fuel rods and specially prepared fuel rods. These data have been used to guide the development of more refined computer codes [3-5] than those employed in the Reactor Safety Study. Thus far these newer codes have been restricted in application to the noble gases, so they give no indication of gap inventories of other fission product species.

As can be seen from comparison of the three sets of gap inventory values which are presented in Table II, disagreement exists regarding the relative inventories of the noble gases, halogens, and alkali metals. A special procedure has since been developed to measure the gap inventories of these species directly [7,8]. Although only two such determinations have been made thus far, the results, as presented in Table V, indicate equal fractional inventories of the long-lived isotopes of the three types of fission product species.

Gap Releases

The main focus of the Reactor Safety Study was on the core meltdown accident; consequently, the treatment is deficient in accurately describing fission product releases in reactor accidents less severe than a core meltdown. More recent studies [9,10] have provided a more detailed mathematical description of release over the temperature range 500-1200°C, and additional experimental work [12,13] has further elaborated on release phenomena to about 1600°C.

The more recent approach describes release over the temperature range 500-1200°C as the result of two processes—burst release and diffusional

release. Burst release, which may be regarded as virtually instantaneous, refers to the sweeping action of the fill and fission product gases in the fuel rod as they are vented at the time of cladding failure. Release of the noble gases is thus by simple gaseous expansion, but that for species which are in equilibrium with a condensed phase is due to both thermodynamic and kinetic factors. For cesium and iodine species, the mass of the fission product released at rod rupture M_B, in g, was shown to be correlated by the semi-empirically derived expression [9-11].

$$M_B = \alpha V_B (M_o/A)^a e^{-(C/T)}, \tag{3}$$

where V_B is the volume of plenum gas vented (in cm^3) at 0°C and system pressure, M_o is the gap inventory of the fission product, (g), A is the internal area (cm^2) associated with M_o, and T is the temperature (K) at the rupture location. The parameters α, a, and C are adjustable constants which have the values indicated in Table VI. Note that Eq. (3) is applicable over the approximate temperature range 700-1000°C (i.e., about the range over which cladding rupture is expected to occur).

Once burst release has ceased, additional release occurs through the partial evaporation of condensed species which are located on the interconnected void surfaces, and the subsequent diffusion of these species to the point of clad rupture. For cesium and iodine species, this diffusional process could be described over the temperature range 500-1200°C by the semi-empirical expression [9-11]

$$M_D = M_o[1-e^{-(R_o t/M_o)}], \tag{4}$$

where M_D is the mass of fission product released by diffusion (g) over the time interval t (h), and R_o is the initial rate of release (g/h), which is given by

$$R_o = \delta(W/P)(M_o/A)^a(e^{-\gamma/T}), \tag{5}$$

where W is the width of the radial gap through which diffusion occurs in μm, P is the system pressure, (MPa), and the parameters δ, a, and γ γ have the values indicated in Table VI.

A comparison of release values for cesium and iodine species as calculated from Eqs. (3)-(5) with corresponding experimental results is presented graphically in Fig. 1. Excellent agreement (within a factor of 3) exists over six orders of magnitude in terms of mass released. It should be noted, however, that Eqs. (3)-(5) have been developed for application over relatively short time intervals, for which only a small fraction of the gap inventory is released.

Except for the occasional appearance of elemental antimony and ruthenium species (the latter in tests in air rather than steam),

releases of other fission product species were not detected in the experiments on which the data presented in Fig. 1 are based [7]. These same experiments also indicated the ejection of approximately 0.02% of the UO_2 fuel, as dust particles, during rod rupture. Analysis clearly indicated the particles to be irradiated UO_2, and although particles ranging about 10 μm and between 140-210 μm could be identified, it was not possible to determine a detailed size distribution [7].

The experimental studies of fission product release from irradiated commercial fuel over the temperature range 1200-1600°C have yet to yield a mathematical model for a description of the release behavior, but an additional release mechanism was observed. A manifestation of the new mechanism is shown by the data presented in Fig. 2. In this figure are plotted the amounts of krypton, iodine, and cesium that were observed to be released (or were calculated to be released) by diffusion alone over a 10-min period as a function of temperature. The sharp increase around 1350°C is believed to result from the coalescence of blind voids, or bubbles, which supplies both additional inventories and transport paths for release. Such a mechanism is in principle taken into account in the more recent computer codes that have been developed for noble gas releases [4], but an attempt to describe the experimental results with the computation program has not yet been made.

Above 1200°C, diffusional release from the matrix also begins to be a significant release mechanism, but this too should be within the capabilities of existing computer codes.

Meltdown Release

As the fuel, and consequently the core structural material, undergoes meltdown, vaporization-condensation mechanisms become the dominant release modes. Thus much of the recent studies of release under core meltdown conditions have been concerned principally with aerosol formation and characterization [14-17]. As the data presented in Table VII indicate, fission products comprise only a small fraction of the mass of material released from the molten composite.

Most of the recent core meltdown experiments have utilized simulated irradiated fuel containing appropriate quantities of structural materials (Corium A) [19] and have been performed in an air atmosphere. Rates of release of selected fission product species are presented as a function of temperature in Figs. 3 and 4; corresponding releases of the structural materials are listed in Table VIII [17].

Two significant results of these experiments [14-17] have been the observed dependence of fission product release on pressure, and the observation that the most probable size of the aerosol particles which were formed in air at temperatures in the range 1800-2700°C is less than 0.5 μm. The studies also suggest a possible distribution of the fission products among particle size; species of lower volatility appear to be concentrated in larger-sized particles, whereas higher concentrations of the more volatile species are observed on the smaller-sized particles.

Vaporization Release

Recent studies to further clarify vaporization release have thus far been concerned primarily with the core-concrete interactions which serve as the driving forces for radioactivity release. These interactions are violent; tests with 200 kg of molten steel and corium on concrete indicate the formation of a dense, brown aerosol which is accompanied by splashing, flames, and rapid gas evolution [20,21]. The size distribution of the aerosol was found to be multimodal, with mean particle diameters in the range 1-3 μm [11].

CONCLUDING REMARKS

The considerations of fission product source terms in the Reactor Safety Study represent the first serious attempt to develop these source terms in a realistic and unified manner. However, the data base underlying these considerations was sparse, and the study served to highlight this deficiency. As a result, new reactor safety research programs were initiated in several countries, the most notable programs being those in France, Germany, Japan, and the United States.

Although considerable progress has been made to supplement the fission product release data base, and these data have guided theoretical approaches, many areas of uncertainty remain. In this review, we have indicated how the more recent studies have served to clarify release mechanisms which were considered in the Reactor Safety Study. At this point we wish to indicate briefly where the treatments remain deficient.

Computational programs that have been developed to account for noble gas behavior in irradiated fuel rods have been shown to yield reasonable agreement [23] with experiments which were designed specifically to characterize noble gas releases [24]. In principle, rather accurate estimates of noble gas gap inventories appear to be possible. However, except for two measurements of gap inventories of cesium and iodine, studies of gap inventories of species other than the noble gases are largely nonexistent.

Releases of long-lived cesium and iodine species are perhaps adequately characterized up to 1200°C; from 1200°C to melting, however, both the data base and the theoretical treatments are lacking. Moreover, the experiments that have been conducted over the temperature range 700-1600°C indicate a release of noble gas fission products beyond the gap inventories [7,8,13]. The computation programs for noble gas behavior should focus on these results, as well as the results of studies of noble gas releases during rapid transients [25], both for purposes of code validation and code refinement.

Much of the work to date has concentrated on long-lived isotopes. Additional theoretical studies are necessary to extend the treatments to short-lived species, and to aid in the analysis of in-pile data that are presently being obtained in such facilities as BOUFFON in France [26], JMTR OWL-1 in Japan [27], and PBF in the United States [28].

The studies of fission product and structural materials release from the molten state, which have involved experiments in air, need to be extended to include steam atmospheres. Lastly, the investigations of core-concrete interactions, which have concentrated on the ablation characteristics of the concrete, need now focus on fission product release phenomena.

REFERENCES

1. Reactor Safety Study, Appendix VII, WASH-1400, NUREG 75/014 (October 1975).

2. Parker, G. W. and Barton, C. J., in The Technology of Nuclear Reactor Safety, Vol. 2, T. J. Thompson and J. G. Beckerly, eds., The MIT Press, Cambridge, Massachusetts, 1973.

3. Dearien, J. A., et al., FRAP-S3: A Computer Code for the Steady State Analysis of Oxide Fuel Rods - Volume 1, TFBP-TR-164 (October 1977).

4. Rest, J., GRASS-SST: A Comprehensive, Mechanistic Model for the Prediction of Fission-Gas Behavior in UO_2-Base Fuels During Steady-State and Transient Conditions, NUREG/CR-0202, ANL-78-53 (June 1978).

5. Mason, R. E., "Fission Gas Release (FGASRL)" in MATPRO-Version 11 (Revision 1). A Handbook of Materials Properties for Use in the Analysis of Light-Water Reactor Fuel Rod Behavior, NUREG/CR-0497, TREE-1280, Rev. 1 (February 1980).

6. Noble, L. D., Ritzman, R. M., and Lorenz, R. A., "ANS 5.4 Fission Gas Release Model. III. Low Temperature Release," Proc. ANS Topical Meeting on Light Water Reactor Fuel Performance, Portland, Oregon, April 29-May 3, 1979 (August 1979).

7. Lorenz, R. A., et al., Fission Product Release from Highly Irradiated Fuel, NUREG/CR-0722, ORNL/NUREG/TM-287 (February 1980).

8. Lorenz, R. A., et al., Fission Product Release from BWR Fuel Under LOCA Conditions, NUREG/CR-0000, ORNL/NUREG/TM-388 (in press).

9. Lorenz, R. A., Collins, J. L., and Malinauskas, A. P., Fission Product Source Terms for the LWR Loss-of-Coolant Accident: Summary Report, NUREG/CR-0091, ORNL/NUREG/TM-206 (June 1978).

10. Malinauskas, A. P., Lorenz, R. A., and Collins, J. L., Trans. Amer. Nucl. Soc. 32, 651 (1979).

11. Lorenz, R. A., Collins, J. L., and Malinauskas, A. P., Nuclear Technology 46, 404 (1979).

12. Malinauskas, A. P., Lorenz, R. A., and Collins, J. L., "Fission Product Release from Defected LWR Fuel Rods," Seventh Water Reactor Safety Research Information Meeting, Gaithersburg, MD, November 5-9, 1979.

13. Lorenz, R. A., et al., Fission Product Release from Highly Irradiated Fuel Heated to 1300-1600°C in Steam, NUREG/CR-1386, ORNL/NUREG/TM-346 (in press).

14. Albrecht, H., et al., Versuche zur Erfassung und Begrenzung der Freisetzung von Spalt-und Aktivierungsprodukten beim Kernschmelzen, KFK-2500, 429 (1977).

15. Albrecht, H., Matschoss, V., Nolte, K., and Wild, H., Untersuchung der Freisetzung von Spalt-und Aktivierungsprodukten beim Kernschmelzen, KFK-2600, 429 (1978); KFK-2700, 4300-19 (1978); KFK-2750, 4300-24 (1979).

16. Albrecht, H., Matschoss, V., and Wild, H., Nuclear Technology 46, 559 (1979).

17. Albrecht, H., Matschoss, V., and Wild, H., "Experimental Investigation of Fission and Activation Product Release from LWR Fuel Rods at Temperatures Ranging from 1500°C to 2800°C," IAEA Specialists Meeting on the Behavior of Defected Zirconium Alloy Clad Ceramic Fuel in Water-Cooled Reactors, Chalk River, Canada, September 17-20, 1979.

18. Bell, M. I., ORIGEN - The ORNL Isotope Generation and Depletion Code, ORNL-4628 (1973).

19. Peehs, M. and Mollwitz, K., Untersuchung der Metallurgischen und Chemischen Wechselwirkung Swischen Kernschmelze und Reaktorbehälterwand, BMFT RS 74 a (1976).

20. Perinic, D., et al., Betontiegelversuche mit Thermitschmelzen, KFK-2572 (1979).

21. Powers, D. A., Sustained Molten Steel/Concrete Interaction Tests, NUREG/CR-1066, SAND 77-1423 (June 1978).

22. Powers, D. A. and Muir, J. P., "Melt/Concrete Interactions: The Sandia Experimental Program, Model Development and Code Comparison Test," Seventh Water Reactor Safety Research Information Meeting, Gaithersburg, MD, November 5-9, 1979.

23. Pewitt, E. G. and Kyger, J. A., Light Water Reactor Safety Research Program: Quarterly Progress Report, April-June 1979, pp. 11-20, NUREG/CR-1164, ANL-79-81 (November 1979).

24. Zimmerman, H., "Investigation of Swelling in Mixed Oxides," Proc. Workshop on Fission Gas Behavior in Nuclear Fuels, EUR 6600 En, Karlsruhe, Germany, October 26-27, 1978.

25. Sachs, R. G. and Kyger, J. A., Light Water Reactor Safety Research Program: Quarterly Progress Report, July-September 1977, pp. 34-40, ANL-78-3 (January 1978).

26. Chenebault, P., Kurka, G., and Vivier, M., Release of Fission Products from a Rod Containing a Manufacturing Defect, DMB No. DF 60/75 (October 1975).

27. Ishiwatari, N., private communication to A. P. Malinauskas, May 1976.

28. Osetek, D. J. and King, J. J., "Measurement of Fission Product Release During LWR Fuel Failure," IAEA Specialists Meeting on the Behavior of Defected Zirconium Alloy Clad Ceramic Fuel in Water-Cooled Reactors, Chalk River, Canada, September 17-20, 1979.

Table I. Characteristics of Important Fission Product Elements

Group	Element	Probable Dominant Form Released
Noble Gases	Kr, Xe	Gaseous element
Halogens	Br, I	Alkali metal halide or element
Alkali Metals	Rb, Cs	Element
Tellurium	Te, Se, Sb	Element
Alkaline Earths	Sr, Ba	Element or oxide
Noble Metals	Mo, Tc, Ru, Rh, Pd	Element or oxide
Refractory Oxides	Y, Zr, Nb, La, Ce, Pr, Nd, Np, Pu, etc.	Oxide

Table II. Gap Inventories and Escape Fractions of Long-Lived Fission Products

Fission Product	Gap Inventory[a]			Escape fraction
	ANC[b]	BCL[c]	ORNL[d]	
Kr, Xe	0.06	0.10	0.08	1
Br, I	0.06	0.10	0.14	1/3
Rb, Cs	0.20	0.05	0.21	1/3
Te, Se, Sb	0.10 (estimate)			10^{-3}
Sr, Ba	4×10^{-6}	0.02	0.02	10^{-4}
Others	-	-	-	0

[a] Expressed as fraction of total inventory.

[b] H. L. McMurry and E. F. Aber, Appendix B, Ref. 1.

[c] R. L. Ritzman, Appendix A, Ref. 1.

[d] G. W. Parker, Appendix C, Ref. 1.

Table III. Fission Product Release Fractions for Release from Molten Fuel

Fission Product	Release Fraction	Range
Noble Gases	0.9	0.5 - 1
Halogens	0.9	0.5 - 1
Alkali Metals	0.8	0.4 - 0.9
Tellurium Group	0.15	0.05 - 0.25
Alkaline Earths	0.1	0.02 - 0.20
Noble Metals	0.03	0.01 - 0.10
Refractory Oxides	0.003	0.0001 - 0.01

Table IV. Limiting Values of the Vaporization Loss Fraction

Fission Product	$(VLFx)_T$
Noble Gases	1
Halogens	1
Alkali Metals	1
Tellurium Group	1
Alkaline Earths	0.01
Noble Metals	0.05
Refractory Oxides	0.01

Table V. Measured Fission Product Gap Inventories

Fuel Rod	Gap Inventory as Percent of Total Inventory		
	Noble gases	Cs	I
H. B. Robinson PWR	0.26	0.30	0.30
Peach Bottom BWR	11.4	12.4	12.1

Table VI. Burst and Diffusional Release Parameters for Cesium and Iodine Species

Parameter	Cesium	Iodine
α, $(g/cm^3)\cdot(g/cm^2)^{-a}$	3.49	0.163
a	0.8	0.8
C, K^{-1}	7.42×10^3	3.77×10^3
δ, $(g\cdot MPa/\mu m\cdot h)\cdot(g/cm^2)^{-a}$	1.90×10^3	1.22×10^2
γ, K^{-1}	1.98×10^4	1.48×10^4

Table VII. Activity and Mass Release During Core Meltdown

	Inventory[a]		Release[b]	
	Activity (10^8 Ci)	Mass (kg)	Activity (10^6 Ci)	Mass (kg)
Fission Products				
Noble Gases	3.4	299	306	270
Halogens	8.2	32	734	30
Alkali Metals	0.2	158	12	125
Tellurium Group	2.2	33	32	5
Alkaline Earths	3.7	116	37	10
Noble Metals	5.6	424	17	10
Refractory Oxides	29.3	1252	9	5
Structural Materials				
Cd	[c]	150	[d]	75
In, Mn, Ag, Sn		2950		300
Cr, Fe, Ni, Co		28,200		280
Zr, V		136,300		410

[a]Calculated for a 3200-MW(t) PWR with an average burnup of 17,600 MWd/tU. Fission product activities were calculated with the ORIGEN code [18], but isotopes with half-lives less than 1 h were ignored.

[b]Fission product releases according to Ref. 1; structural materials release according to Ref. 17.

[c]Less than 10% of total activity.

[d]Less than 1% of activity released.

Table VIII. Release Rates for the Elements of the Cladding and Structural Materials (from Experiments in Air, 0.2 MPa)

T(°C)	Release Rates (% per min)						
	Cr	Mn	Fe	Co	Sb	Sn	Zr
2350	0.055	0.96	0.024	0.023	1.05	0.74	0.003
2750	7.69	80.5	4.01	2.10	29.1	23.4	0.04

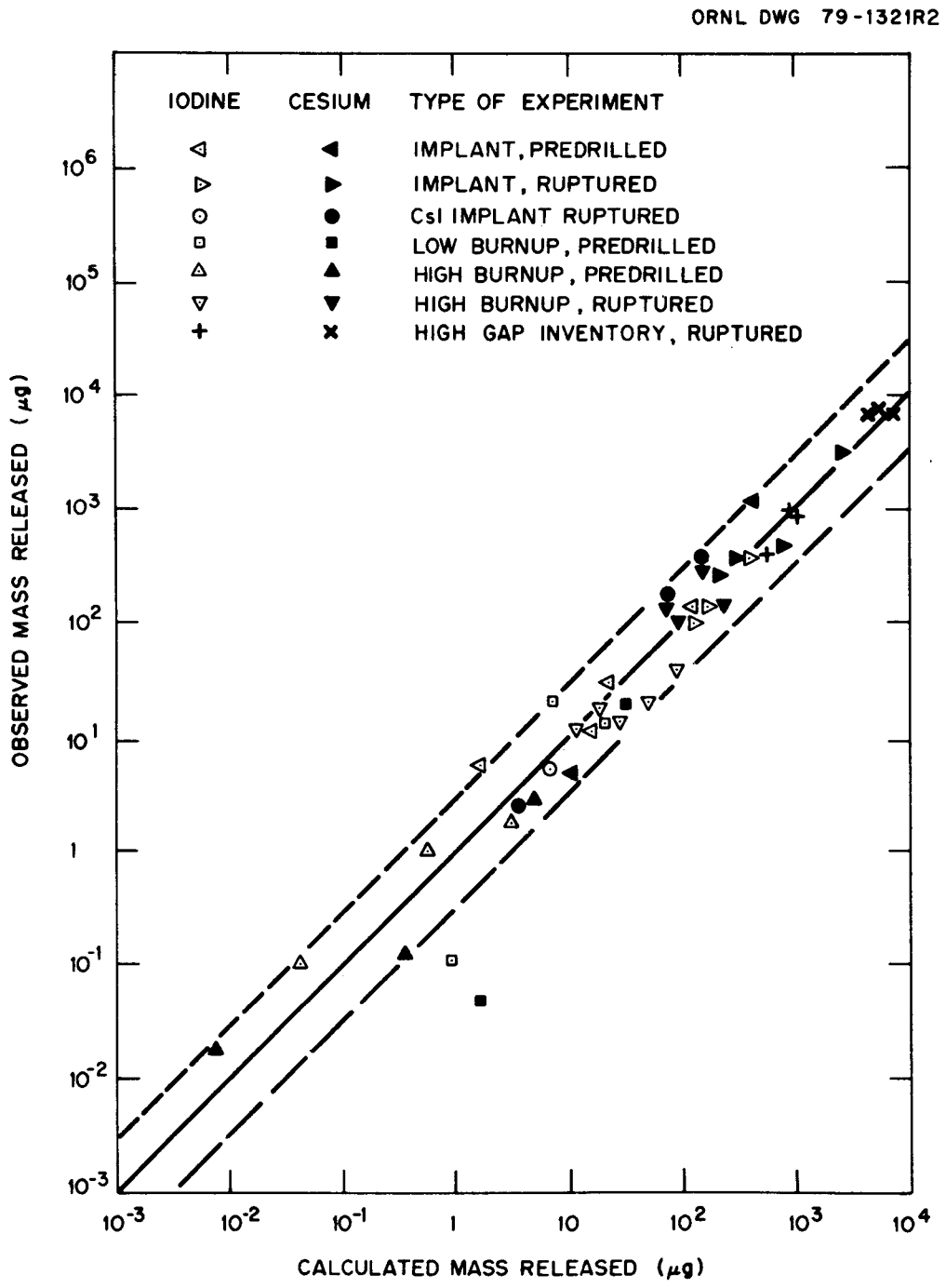

Fig. 1. Comparison of measured cesium and iodine releases and calculated values. Data points identified by ◁, ▷, and ○ are from tests with simulants, □ represents results with an irradiated capsule, △ and ▽ denote results with irradiated commercial PWR fuel, and + represents irradiated BWR fuel. "Ruptured" tests yield burst and diffusional release results, whereas "Predrilled" tests yield only diffusional release data. The dashed lines denote factor of three error limits.

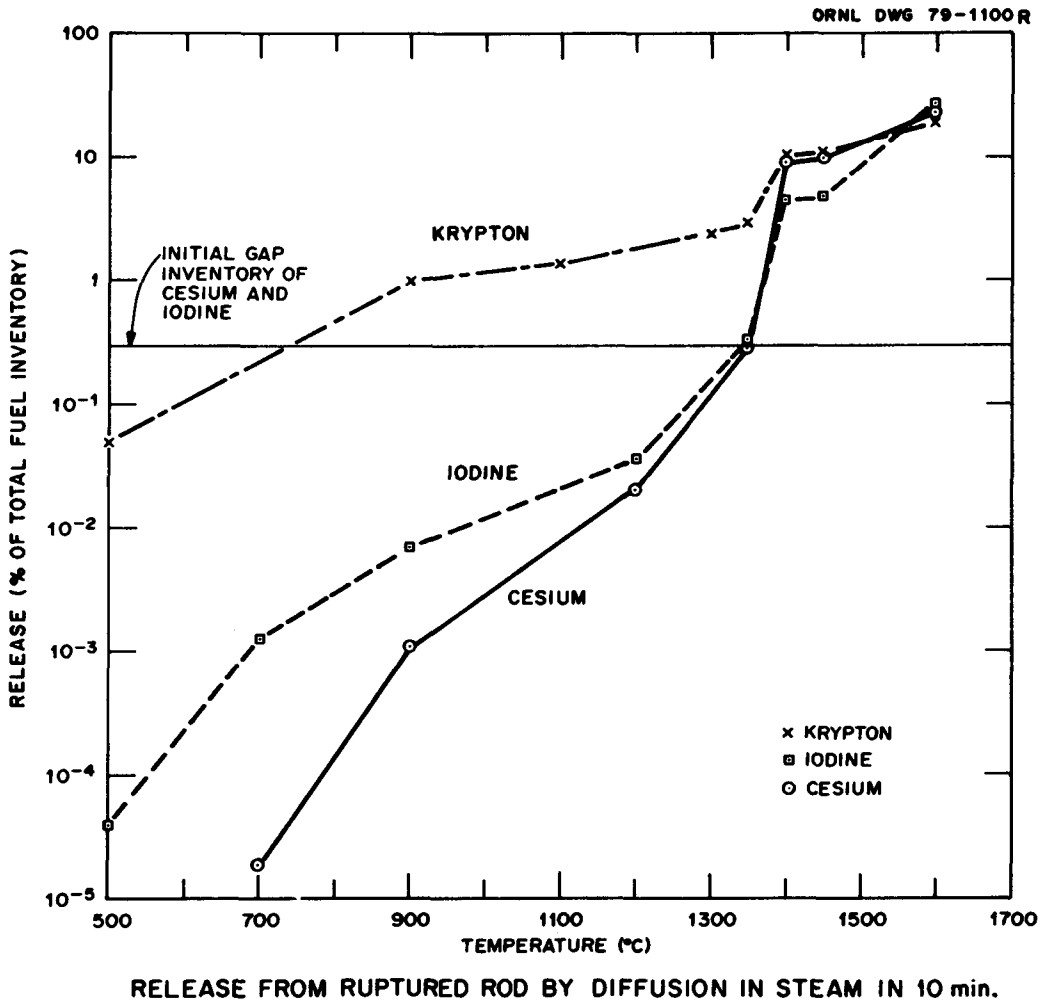

Fig. 2. Diffusional release of krypton, iodine, and cesium over a 10-min period as a function of temperature for irradiated PWR fuel. Krypton releases are in addition to the indicated gap inventory (horizontal line).

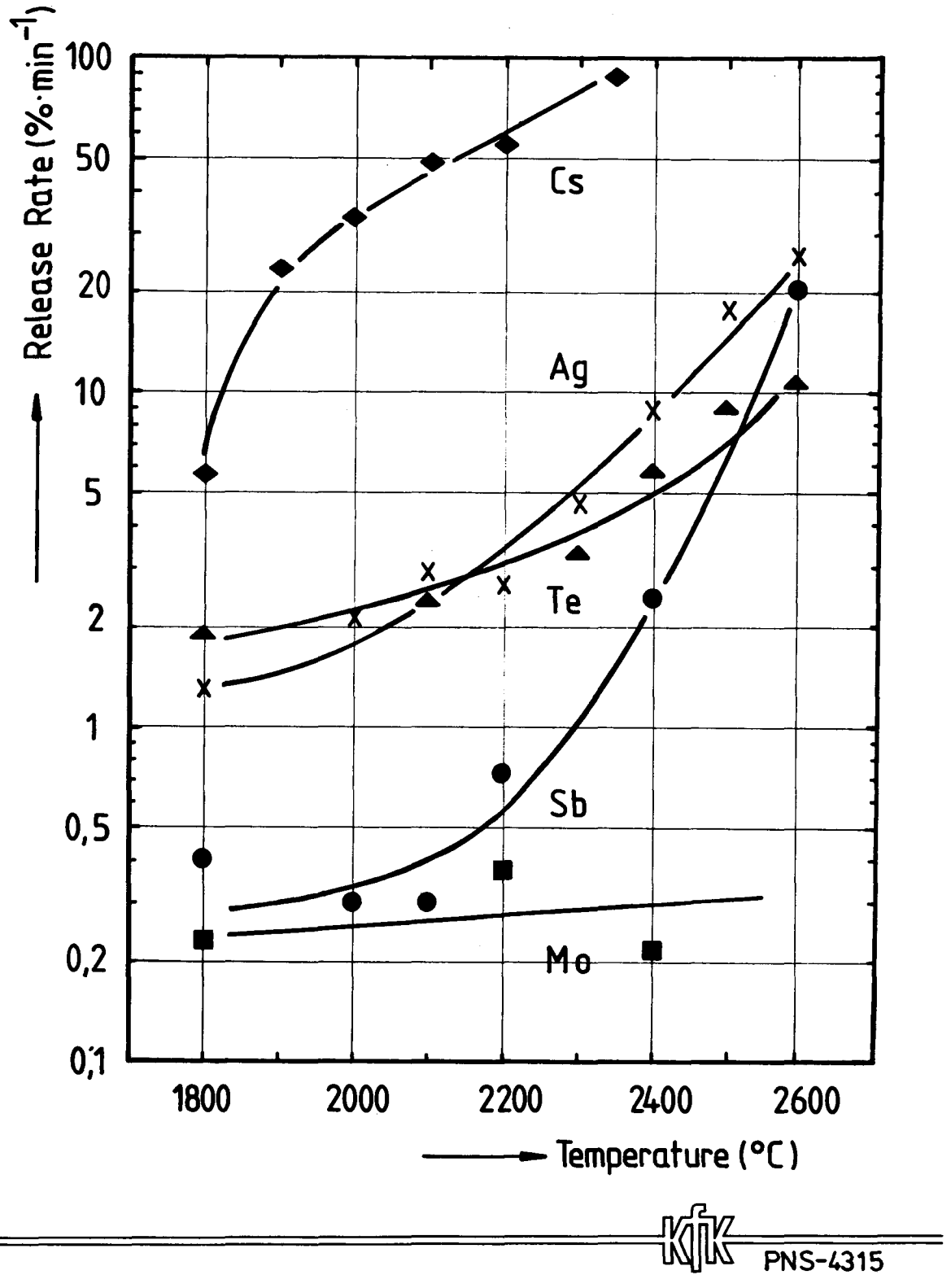

Fig. 3. Release rates of selected fission product species from corium mixtures in air. Moderately volatile species.

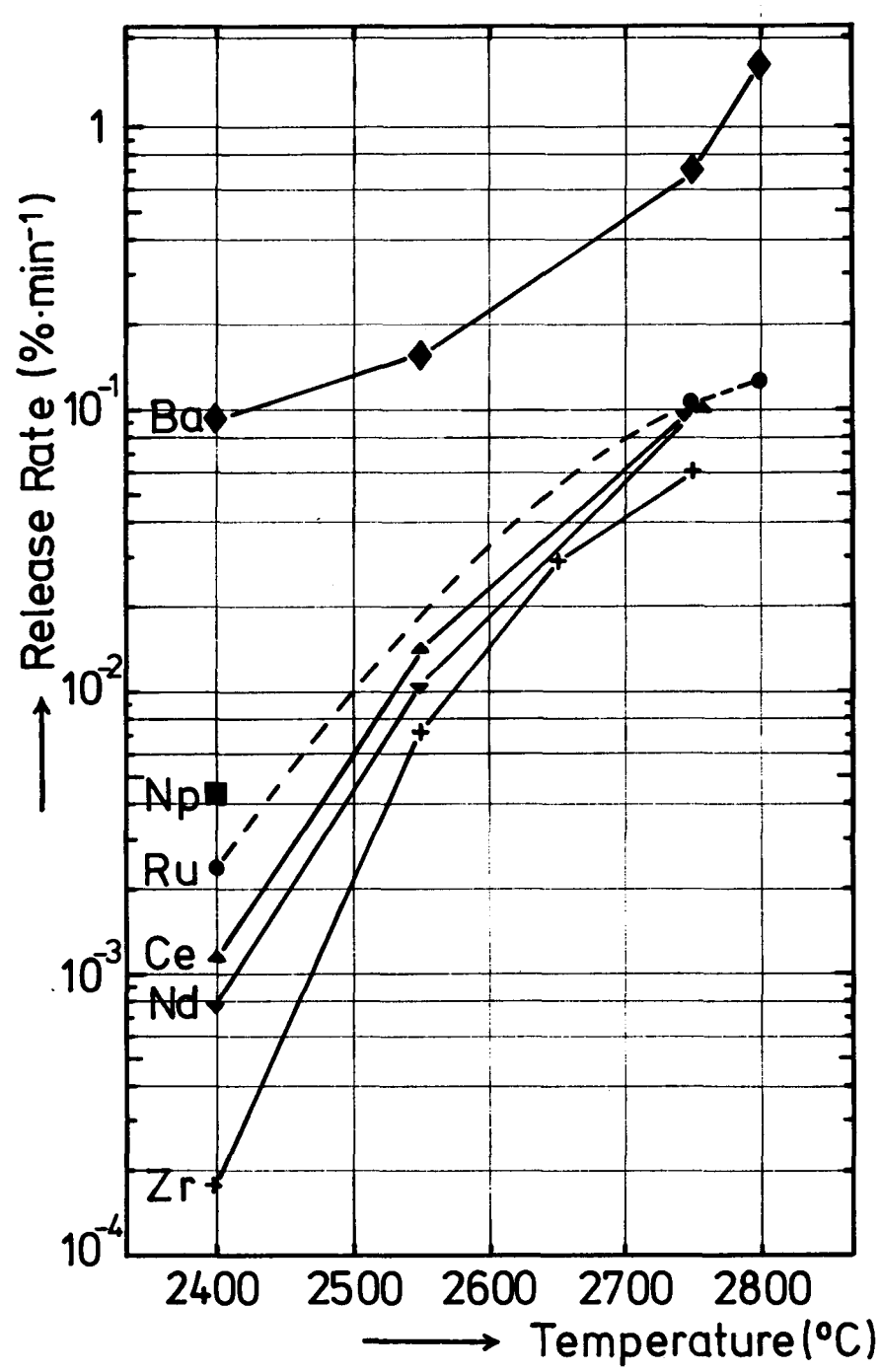

PNS-4315

Fission Product Release Rates in Air (2bar)

Fig. 4. Release rates of selected fission product species from corium mixtures in air. Relatively nonvolatile species.

AN APPROACH TO THE NUCLEAR AEROSOL SOURCE TERM ASSESSMENT IN AN HCDA OF LMFBR

T. Tachino, Y. Hasegawa, T. Sawada
Mitsubishi Atomic Power Industries, Inc.
Omiya, Saitama, Japan

K. Yamaguchi, N. Mitsutsuka, K. Mochizuki
Power Reactor and Nuclear Fuel Development Corp.
Akasaka, Minato, Tokyo, Japan

ABSTRACT

A calculational model was developed for estimating the amount of fragmented fuel particles released from the closure head of reactor vessel following a fuel coolant interaction in an HCDA of LMFBR. Sample calculations were performed to determine the relative importance of the various complex physical processes involved in this phenomena. The followings became clear through this investigation: i) the dimension, shape of bubbles and the contents of noncondensable gas have much influence on the vapor condensation rate. ii) the effect of the mass of the smallest diameter particles is predominant among others for aerosol release. In order to verify the behavior of bubbles, experimental studies are under way. Underwater experiments have been completed and the changes in the shape and velocity of the bubbles rising in a pool were investigated. A small scale sodium test will be started in the near future.

1. Introduction

In doing assessment of LMFBR accidents, determination of the aerosol source terms under hypothetical core disruptive accident (HCDA) is of particular importance for their radiological consequences.

Both analytical and experimental efforts are in progress in Japan to investigate transport phenomena of fuel particles in an HCDA. As for the analytical effort, FTAC-II, a code for estimating the transport of the relatively large ($\geq$10μm) fuel particles resulting from a fuel-coolant interaction(FCI) up to the secondary containment in an HCDA, is developed. This code employs an improved model originally starting from the Kennedy-Reynolds model [1]. It includes the effects of the presence of noncondensable gas in the bubble and the effects of convective motion both inside and outside of the bubble [2], [3]. Parametric calculations are carried out to determine the relative importance of the transport mechanisms such as thermodynamics, condensation, etc.

As for the experimental work, HCDA bubble behavior simulant tests are under way at Oarai Engineering Center of PNC. The changes in the shape and velocity of the bubbles rising in a pool were investigated using the argon bubbles in water. Some spherical-cap shaped bubbles were observed and their motions are being analyzed. A large scale as well as small scale in-sodium tests are planned. The design of small scale sodium test facility has been completed and the experiments will be started in the near future.

2. Analytical Model

2.1 Outline of Phenomena

If FCI is to occur, the sodium vapor bubble expand rapidly following a high pressure generation in the reactor vessel due to energy transfer from fuel to residual sodium in core. The core barrel and middle part of the reactor vessel could be deformed by the shock wave. The coolant slug being propelled by the vapor bubble strikes the shielding plug and could deform the top of the reactor vessel raising the shielding plug slightly. The fuel transport analysis starts in consistent with reactor containment response analysis at the moment the deformation of the top of the reactor vessel is completed. During this process, the cover gas might be released from the reactor vessel. Outline of phenomena treated in the analysis are as follows:

i) The sodium vapor bubbles, containing fuel particles generated in the FCI, rise in the sodium pool and a part of fuel particles may fall out during bubble rise. Condensation of the vapor takes place due to heat transfer between inside and outside of the bubble. During this period, liquid sodium is ejected through the plug gaps changing the external constraints of vapor bubbles.

ii) Upon reaching and covering the bottom surface of the plug, the vapor bubbles expel the liquid sodium still remaining in the plug gaps. When all the liquid sodium in the plug gaps is flushed out, the release of the vapor containing fuel particles begins. The fallout of fuel particles and condensation of vapor under the plug may also take place.

2.2 Analytical Model

1) Bubble Model

The behavior of spherical or spherical-cap shaped multiple bubbles is analytically formulated. The bubbles are composed of fuel particles, sodium vapor and noncondensable gas. The virial equation of state [4] is used for sodium vapor and ideal gas laws for noncondensable gas.

2) Fallout of Fuel Particles during Bubble Rise

Upward motion of bubbles in the sodium pool is evaluated by solving an equation of motion while considering the viscosity of sodium pool. Treatment of the motion of fuel particles is similar to that of Kennedy-Reynolds model [1] except that the Wilke's equation [5] is used for the coefficient of viscosity of vapor-gas mixture considering the existence of noncondensable gas. Fallout of fuel particles is evaluated from the relative motion of bubbles and fuel particles.

3) Bubble Condensation

Condensation of sodium vapor is evaluated by solving the transient mass diffusion equation in bubble space in conjunction with the problem of transient heat conduction and convection in surrounding pool according to Kress model [3]. In addition to Kress model, this approach includes the following improvements.

i) Heat transfer from fuel particles to vapor and radiation heat transfer from vapor to the surrounding sodium pool and structures are included.

ii) Time dependent molar concentration, temperature, pressure and density within the bubble are incorporated.

One-dimensional system shown in Figure 1 is intended to illustrate the temperature and concentration fields as functions of time and space.

The differential equations which describe the temperature field in the liquid phase and the concentration of noncondensable gas on the vapor-gas mixture side are given by

$$\frac{\partial x_i}{\partial t} = -\left(\frac{D}{x_{is}} \cdot \frac{\partial x_i}{\partial y}\Big|_{y=0}\right) \cdot \frac{\partial x_i}{\partial y} + \frac{\partial}{\partial y}\left[D^*(y)\frac{\partial x_i}{\partial y}\right] \quad , \quad (1)$$

$$\frac{\partial T_\ell}{\partial t} = \frac{\partial \alpha^*(Z)}{\partial Z}\frac{\partial T_\ell}{\partial Z} + \alpha^*(Z)\frac{\partial^2 T_\ell}{\partial Z^2} \quad , \quad (2)$$

where the turbulent diffusivity of heat and mass are defined by Cebeci's mixing length model [6]. The heat transfer equation at the interface is

$$-K_{\ell}\frac{\partial T_{\ell}}{\partial Z}\Big|_{Z=0} = H_v\frac{dW_{cond}}{dt} + \frac{dQ_{B\ell}}{t} \quad . \quad (3)$$

In addition, the temperature at the interface should satisfy the requirement

$$P_v(1 - X_{is}) = P_v^*(T_s) \quad . \quad (4)$$

The quantity of vapor condensation depends on the sodium vapor flux at the boundary and is given by

$$\frac{dW_{cond}}{dt} = -M_v.A_B\frac{C_B(t)D}{X_{is}} \cdot \frac{\partial X_i}{\partial y}\Big|_{y=0} \quad . \quad (5)$$

The changes in volume and specific volume of the gas in the bubble are calculated from fallout of fuel particles and the release of liquid sodium. The changes of mole concentration and density with time are calculated from condensation of sodium vapor and specific volume change of gases. The temperature change with time is obtained by solving the equations of heat transfer, volume change and enthalpy change simultaneously.

4) Bubble Behavior under the Plug and Release of Fuel Particles

When the top end of the bubble reaches the plug bottom, the bubble muffles there. The fuel particles are assumed to be dispersed uniformly under the plug space when the bubble covers the plug. After all liquid sodium in the plug gap paths is expelled, the release of gas containing fuel particles is initiated. Condensation of sodium vapor, heat transfer and fallout of fuel particles are evaluated in the same way as during bubble rise period, except that escape of sodium vapor containing fuel particles is considered in addition. It is assumed that the concentration of fuel particles in escaping mixture is equal to the average concentration of the entire bubble space under the plug. Thus the total quantity of fuel particles released from the reactor vessel is calculated until the pressure of vapor bubble decreases below the atmospheric pressure.

3. Sample Calculation

Preliminary calculations have been carried out to estimate the effect of bubble volume on the behavior of single bubble rising in an infinite sodium pool. Calculational conditions are as follows:

$T_B = 1360°K$, $u_{v\infty} = 0$, $X_{i\infty} = 0.01$, $W_{fo} = 0$, $T_{\ell\infty} = 1000°K$,

$V_B = 200, 300, 1000\ell$

Calculated results for vapor pressure and condensation rate versus time are plotted in Figures 2, 3 respectively. The followings became clear through these sample calculations: The smaller the initial volume, the faster the condensation rate and the decrease of vapor pressure. The spherical-cap shaped bubble condenses faster than the spherical bubble for the same volume. The dimension and the shape of bubbles have important effects on the behavior of rising bubbles due to the area of heat and mass transfer per unit mass of vapor.

Much uncertainty exists concerning the transport phenomena of fuel particles in an HCDA such as thermodynamics, bubble shape and numbers, size distribution of fuel particles, etc. Each of these parameters have been examined to access the relative significance of each uncertainty under typical HCDA conditions of a prototype LMFBR. In these survey calculations, noncondensable gas in bubble are ignored and the sodium vapor condensation is evaluated by solving the equation of state of saturated sodium vapor assuming the condensation heat transfer coefficient. Also a calculation has been performed to evaluate the effect of noncondensable gas on the condensation process for a vapor bubble containing 5 mole % Xenon.

Table I shows the analytical conditions for these calculations. The most pessimistic particle-size distribution is used which is obtained from many experiments. The particle distribution is divided into 11 sizes with 12% of the mass having a diameter of 10μm and 10, 14, 9, 7, 10, 6, 10, 8, 10 and 4% of the mass having diameters of 30, 70, 120, 170, 245, 350, 550, 850, 1450 and 2500μm respectively. The results are summarized in Table II. Bubble pressure and fraction of residual fuel particles versus time are shown in Figures 4, 5 respectively.

On of the conspicuous phenomena obtained from the parametric survey is that the fuel particle diameter is the most influential factor among others. For example, the amount of fuel particles released from the reactor vessel is governed by the total mass of the smallest diameter particles, while the particles of larger diameter groups shows lesser contributions to the aerosol release. In the case that the HCDA bubble breaks up to numerous-small bubbles they should collapse and vanish before reaching to the plug bottom surface when noncondensable gas are not contained. In the case that noncondensable gas is contained in the bubble, the amount of condensation evaluated is one order or so less than the case ignoring noncondensable gas, although the amount of fuel particles released from head seal are predicted to increase slightly.

4. HCDA Bubble Behavior Simulant Test

The parametrical survey using FTAC-II code within the framework of reasonably treatable conditions brought about the important suggestions in planning the experimental work. Based on the results, a definite plan of HCDA bubble behavior simulant test was programmed. The whole plan is divided into three phases, i.e. (1) the buoyant movement test in a large water

pool of room temperature, (2) the condensation test in hot water tank, (3) in-sodium simulant test. The purposes and the methods of these experiments are as follows:

1) Buoyant Movement Test

The purpose of this phase is to examine the change of bubble shape during the buoyant movement, and to obtain informations of the bubble motion. A large gas bubble is produced at the bottom of the test vessel by sticking a needle into a balloon preliminarily filled with gas. When the diameter of inner wall is not sufficiently large compared with the bubble diameter, the bubble behavior will differ from that in free circumstances. The resistance of counterchanging liquid may force the bubble to alter its shape from sphere to spherical-cap or toroidal ring. The upper structure that will still exist after the HCDA may split the flowing bubble into a cluster of small bubbles. The information of these phenomena will be clarified mainly through the optical techniques. The experimental parameters are the initial bubble volume, the bubble pressure and the sizes of structures.

2) Condensation Test

The condensation process of vapor and non condensable gas mixture is optically observed using the hot water tank. The bubble is produced by two methods i.e. by using the balloon and by rupturing the vaporizer unit in the pool. The latter one is feasible under sodium conditions. Consequently, the experiment in water with vaporizer unit have a status of preparatory study on the bubble behavior in sodium pool. The experimental parameters are the initial bubble volumes, the initial pressure differences between bubble and cover gas, the liquid subcoolings, and the noncondensable gas concentrations. Besides the photographs, transient data of bubble volumes, liquid and cover gas pressures, bubble collapsing times and so on are being analyzed.

3) In-Sodium Simulant Test

Small scale and large scale in-sodium comprehensive tests are planned. The design of the small scale sodium test facility has been completed as shown in Figure 6 and the experiments will be started in the near future. Three vaporizer units are inserted triangularly in the test vessel. Preliminarily charged sodium in the vaporizer is heated up instantaneously to yield the high pressure super-heated sodium vapor. Small amount of noncondensable gas is also stored in it. When the vapor and gas mixture exceeds a certain pressure level, a large bubble appears in sodium pool by rupturing the disk of the vaporizer. The experimental conditions and the data being analyzed are similar to those mentioned above.

5. Discussion and Conclusion

A computer code FTAC-II is developed for analyzing the fuel particle ($\geq$10μm) transport phenomena in an HCDA of LMFBR. In FTAC-II, fragmented fuel particles from FCI are suspended in a sodium vapor bubbles and carried to the outside of the reactor vessel.

The code is developed to assess the following points:

1) The behavior of multiple bubbles in spherical or spherical-cap shape is formulated.
2) Internal circulation effect on the sodium vapor condensation is considered by solving the transient heat and mass transfer equation of turbulent flow, according to Kress method [3].
3) The effect of noncondensable gas on the bubble pressure and viscosity is taken into account.
4) In addition to the heat transfer between bubbles and surrounding sodium, heat transfer between the bubbles and the fuel particles is considered.

Various complex physical processes are involved concerning the fuel and vapor transport after the accident such as thermodynamics, condensation, etc. In order to evaluate the magnitude of these effects, parametric survey calculations have been performed. The results may be summarized as follows:

- Dimension and shape of bubbles have important effects on the behavior of rising bubbles.
- As to the contribution to aerosol release, the effect of the mass of the smallest diameter particles is predominant among others.
- The effect of noncondensable gas on the vapor condensation is significant.

In this study, a calculational model has been developed for estimating the transport of fragmented fuel particles resulting from FCI to the secondary containment in an HCDA of LMFBR, although the sub-micron size aerosols are not treated in this model. However, in the event of HCDA in LMFBR, the bubble which contains fuel vapor and recondensed sub-micron size fuel particles may be produced. Further investigation is necessary for the transport of fuel vapor and recondensed fuel particles ($<$1um). In this case, radiation heat transfer has an important effect on the condensation process and the mechanism of these phenomena has yet to be sufficiently clarified. It largely depends upon future multilateral studies.

In order to verify the bubble behavior, an HCDA bubble behavior simulant tests are under way at Oarai Engineering Center of PNC. The whole plan is divided into three phases, i.e. (1) the buoyant movement test in a large water pool of room temperature, (2) the condensation test in hot water tank, (3) in-sodium simulant test. Underwater experiments (1), (2) have been completed. The chages in the shape and velocity of the bubbles rising in a pool were investigated using the argon bubbles in water. Spherical-cap shaped bubbles were observed and their motions are being analyzed. In in-sodium simulant test (3), the design of small scale sodium test facility has been completed and the experiments will be started in the near future.

The compensative three steps of test program aims at clarifying the basic problems that must be examined at first. Two important problems are left unsolved, i.e. (1) the scale effect of bubble sizes and structures, (2) the initial conditions of bubble formations. These subjects are now under discussion in designing the next large scale in-sodium test vessel.

Nomenclature

A_B = cross sectional area of bubble
C_B = total molar concentration of vapor-gas mixture
D = molecular diffusivity of mass
$D^*(y)$ = turbulent diffusivity of mass
H_v = latent heat of condensation of vapor
K_ℓ = thermal conductivity of liuiqd
M_v = molecular weight of vapor
$Q_{B\ell}$ = radiation heat transfer from vapor to liquid
T_B = bulk temperature of vapor
T_ℓ = liquid temperature
T_s = interface temperature
$T_{\ell\infty}$ = bulk temperature of liquid
$u_{v\infty}$ = internal circulation velocity of vapor-gas mixture
$u_{\ell\infty}$ = flow velocity of liquid over the bubble surface
V_B = volume of bubble
W_{cond} = mass of vapor condensation
W_{fo} = total mass of initial fuel particles
X = coordinate along the flat plate
Y = coordinate in the vapor phase
Z = coordinate in the liquid phase
$\alpha^*(Z)$ = turbulent diffusivity of heat
X_i = molar fraction of noncondensable gas
X_{is}, $X_{i\infty}$ = molar fraction of noncondensable gas at interface and bulk stream, respectively.

References

[1] Kennedy, M. F. and Reynolds, A. B.: "Methods for Calculating Vapor and Fuel Transport to the Secondary Containment in an LMFBR Accident", Nucl. Technol., Vol. 20, pp. 149-160 (1973).

[2] Theofanous, T. G. and Fauske, H. K.: "The Effect of Noncondensables on the Rate of Sodium Vapor Condensation from a Single-Rising HCDA Bubble", Nucl. Technol., Vol. 19, pp. 132-139 (1973).

[3] Özisik, M. N. and Kress. T.S.: "Effects of Internal Circulation Velocity and Noncondensable Gas on Vapor Condensation from a Rising Bubble", Nucl. Sci. Engng., Vol. 66, pp. 397-405 (1978).

[4] Golden, G. H. and Tokar, J. V.: "Thermophysical Properties of Sodium", ANL-7323, (1976).

[5] Wilke, C. R., J. Chem. Phys., Vol. 18, p. 517 (1950).

[6] Jones, W. P. and Renz, U.: "Condensation from Turbulent Stream onto a Vertical Surface", Int. J. Heat Mass Transfer, Vol. 17, pp. 1019-1027 (1974).

Table I Analytical Conditions for Survey Calculations

	Case 1	Case 2	Case 3	Case 4	Case 5	Case 6
Initial molar fraction of noncondensable gas	0	0	0	0	0	Xenon 5 mole %
Shape of bubble	spherical	spherical	spherical -cap	spherical	spherical	spherical
Number(and initial radius) of bubbles	1 (244cm)	100 (52.5cm)	1 (244cm)	1 (244cm)	1 (244cm)	1 (244cm)
Condensation heat transfer coefficient (BTU/h·ft^2·°F)	10,800	10,800	10,800	200	10,800	*
Coefficient of viscosity of bubble gas μ_B (g/cm·sec)	4.133×10^{-4}	4.133×10^{-4}	4.133×10^{-4}	4.133×10^{-4}	8.266×10^{-4}	**

Note) Other conditions are as follows:

$T_{\ell\infty}$ = 800°K, Sectional area of plug gap = 0.2m^2,
Heat transfer from sodium vapor to structures is not considered.

* Condensation rate is evaluated by the sodium vapor transport to bubble boundary.
** Calculated from Wilke's equation.

Table II Summary of Results for Survey Calculations

		Case 1	Case 2	Case 3	Case 4	Case 5	Case 6
Time of arrival of bubble at plug bottom surface(sec)		1.54	-	1.55	1.54	1.54	1.54
Bubble pressure when bubble reaches plug bottom surface (atm)		10.4	-	5.37	19.2	10.9	24.2
Quantity of condensation of sodium vapor during bubble rise (Kg)		23.7	150.6	89.3	-86.8	17.8	3.3
Time when bubble release starts (sec)		13.9	-	19.7	10.5	13.6	9.5
Time when bubble pressure reduces below atmospheric pressure (sec)		15.6	0.686	21.2	12.3	15.3	11.2
Total fuel mass remaining in bubble when bubble reaches plug bottom surface (Kg)		747.3	-	495.6	777.0	863.9	789.2
Total fuel mass remaining in bubble when bubble release starts		224.1	-	198.6	279.5	331.0	322.7
Leakage of fuel particles to outside of reactor vessel (Kg)	10μ:	187.7	-	163.2	199.6	201.8	211.8
	30μ:	9.3	-	-	48.2	90.0	79.3
	Total	197.0	-	163.2	247.8	291.8	291.1

Note) Initial mass of fuel particles in bubble is 2,000Kg.

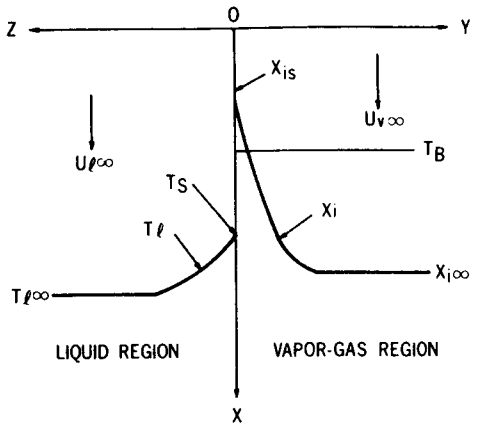

Figure 1. Transient profile of the temperature and concentration fields.

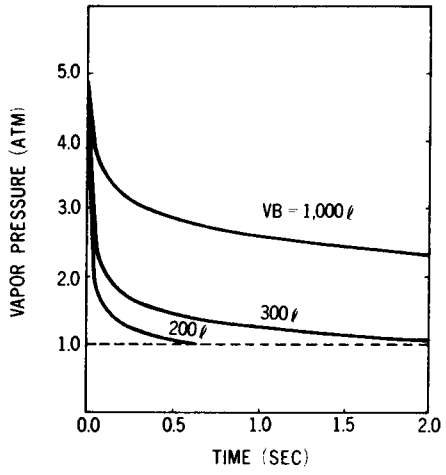

Figure 2. Effect of bubble volume on vapor pressure versus time.

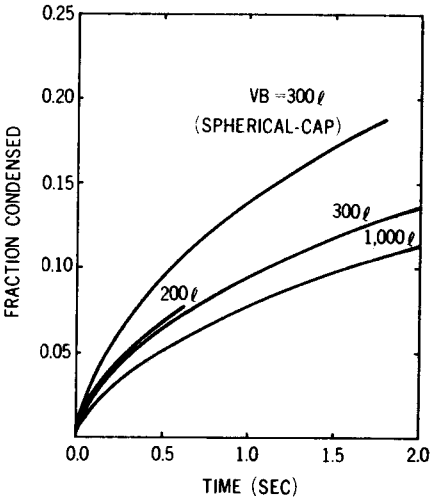

Figure 3. Effect of bubble volume on franction of sodium vapor condensed versus time.

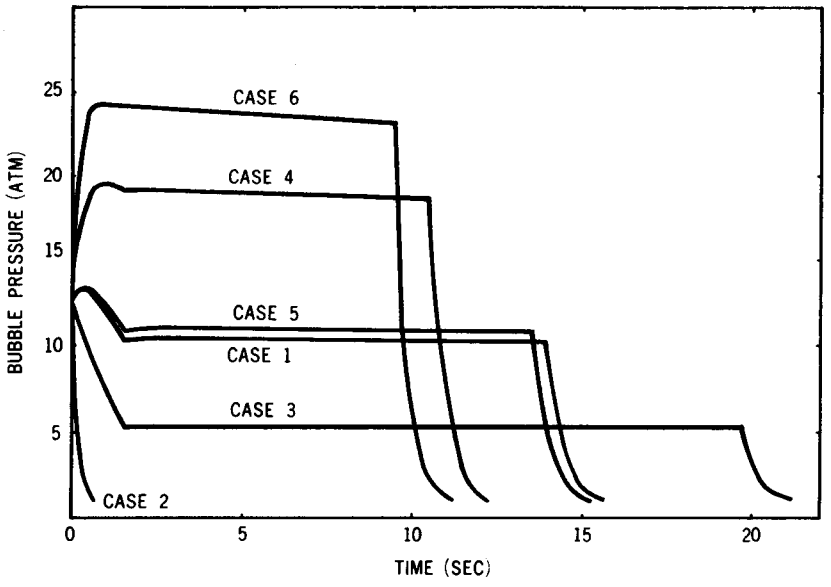

Figure 4. Bubble pressure versus time.

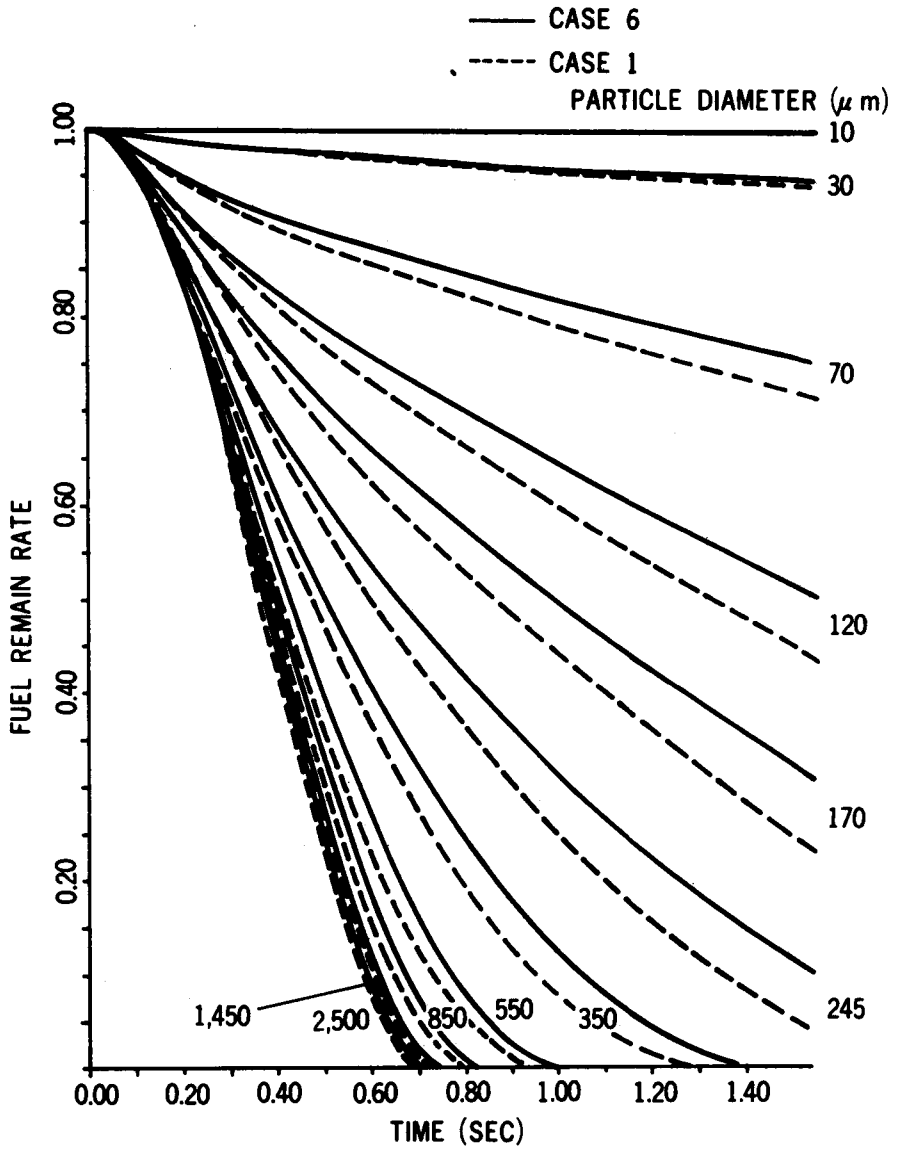

Figure 5. Time history of fuel remain rate.

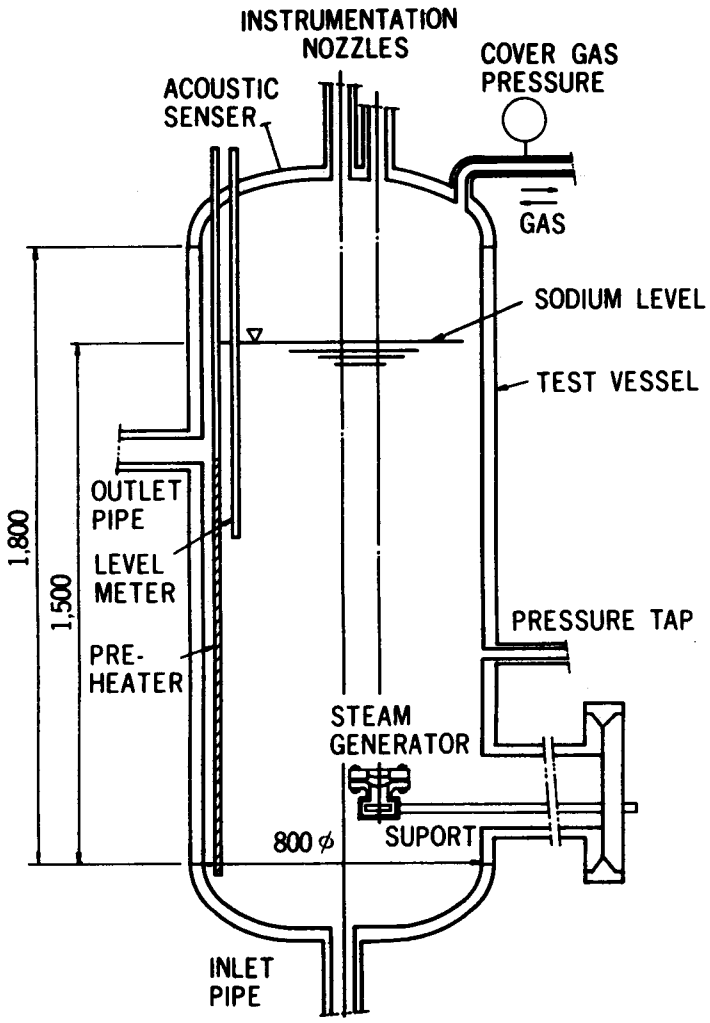

Figure 6. Experimental apparatus of HCDA bubble simulant test.

ORNL EXPERIMENTS TO CHARACTERIZE FUEL RELEASE FROM THE REACTOR PRIMARY CONTAINMENT IN SEVERE LMFBR ACCIDENTS*

A. L. Wright

T. S. Kress A. M. Smith

OAK RIDGE NATIONAL LABORATORY
Oak Ridge, Tennessee 37830

*Research sponsored by the Office of Nuclear Regulatory Research, Nuclear Regulatory Commission under Interagency Agreement 40-551-75 with the U.S. Department of Energy under contract W-7405-eng-26 with the Union Carbide Corporation.

ORNL EXPERIMENTS TO CHARACTERIZE FUEL RELEASE FROM THE REACTOR PRIMARY CONTAINMENT IN SEVERE LMFBR ACCIDENTS

A. L. Wright

T. S. Kress A. M. Smith

Oak Ridge National Laboratory

Oak Ridge, Tennessee 37830, USA

ABSTRACT

This paper presents results from aerosol source term experiments performed in the ORNL Aerosol Release and Transport (ART) Program sponsored by the U.S. NRC. The tests described were performed to provide information on fuel release from an LMFBR primary containment as a result of a hypothetical core-disruptive accident (HCDA). The release path investigated in these tests assumes that a fuel/sodium bubble is formed after disassembly that transports fuel and fission products through the sodium coolant and cover gas to be released into the reactor secondary containment. Due to the excellent heat transfer characteristics of the sodium, there is potential for large attenuation of the maximum release.

In LMFBR hypothetical accidents, the fuel is estimated to reach high energy states, up to and greater than 3500 J/g at core disassembly. A technique designated capacitor discharge vaporization (CDV) was developed at ORNL that uses electrical energy to place ∿20 grams of uranium dioxide pellets into these high energy states. These fuel samples then "disassemble" in different surrounding environments. Two series of tests are discussed: a) vaporizations in an argon gas environment; and b) vaporizations under a water pool. Vaporizations in a sodium pool will eventually be performed.

In the first series of tests, uranium dioxide samples disassembled and underwent essentially free expansions in an argon-filled vessel. A free expansion was expected to produce maximum vapor and result in an "upper limit" aerosol source. In these tests, up to 6 grams of fuel vapor - which rapidly converted to an aerosol - was formed. Vapor yields produced for high energy inputs were less than adiabatic free expansion maximums determined from preliminary calculations. However, the calculated values depend on knowledge of the fuel energy distribution before expansion. This distribution is not accurately known due to the lack of accurate fuel electrical and thermal properties at high temperatures. Additional work continues to improve the fuel energy state calculations. Measurements of the fuel aerosol primary particle size distributions were also made. The size distributions might be representative of aerosols produced by fuel vapor released directly into the secondary containment, though the aerosol may also partially consist of small droplets produced by fragmentation.

Under-water experiments were performed in the Fuel Aerosol Simulant Test (FAST) vessel which is .61 m in diameter and 1.83 m high. Water levels above the fuel sample were 1.12 m, with a .254 m argon cover gas space above the water. Xenon gas (to simulate non-condensable fission products) was included within the fuel sample containers. Results from tests performed at varied argon and xenon gas pressures and varied water temperatures indicate that rapid bubble condensation prevents the transport of the vapor bubble to the surface, except when the water temperature is initially near the boiling point. These results require cautious interpretation in terms of LMFBR aerosol source attenuation for two reasons: (1) water may not be an appropriate simulant for sodium, and (2) bubbles produced are smaller than those expected to be formed in LMFBR accidents and, so, would be more likely to rapidly condense.

In summary, results from the argon gas and under-water vaporization tests provide evidence that considerable reductions in the aerosol source that could be released to the secondary containment in LMFBR HCDAs are possible. To verify these observations, uncertainties in the estimates of fuel energy states after capacitor discharge must be determined, under-sodium tests must be performed, and the results evaluated and compared to those from under-water tests. Careful scaling of the results from these tests to larger-scale accident conditions must also be performed.

INTRODUCTION

Safety analyses prepared as a part of the licensing process for Liquid Metal Fast Breeder Reactors (LMFBRs) must provide estimates of the radiological consequences - that is, determine the aerosol "source term" - for hypothetical core disruptive accidents (HCDAs). In such accidents, some of the reactor fuel is assumed to reach highly energetic states (fuel temperatures of the order of 6000 K) and to then "disassemble" and produce a fuel/sodium vapor bubble that can transport fuel and fission products through the liquid sodium and cover gas to be released into the reactor secondary containment.

Important issues that need to be addressed to permit estimates of the fuel release via this route from the reactor primary containment in HCDAs are the following:

1. In calculating the "initial" contents of the fuel bubble produced - after the fuel expands to the surrounding system pressure - the expansion is assumed to occur such that the maximum amount of vapor is produced (by an adiabatic expansion). Two issues related to this initial vapor source are: a) whether less than the adiabatic vapor source limit can be assumed; or b) whether during fuel expansion aerosol-sized droplets (by fragmentation) are formed, that could be transported up in the bubble and so add to the initial aerosol source more fuel than assumed by adiabatic expansion.

2. It has been estimated that the fuel/sodium bubble produced would have an $\sim$2 second residence time within the sodium of the primary containment. In this time, there is potential for condensation of the bubble - due to radiation heat loss from the vapor, condensation at the vapor-sodium interface or onto droplets entrained in the bubble, condensation on structure in the bubble path, or fuel condensation due to cooling of fuel vapor by mixing with sodium vapor. The important condensation mechanisms and the likely amount of condensation must be determined. After the fuel has condensed, however, it may convert to an aerosol that could be carried through the coolant by the fission product gases that are present in the bubble or by uncondensed vapors.

This paper presents results from aerosol source term experiments performed in the ORNL Aerosol Release and Transport (ART) Program sponsored by the U.S. NRC. A technique designated capacitor discharge vaporization (CDV) was developed at ORNL[1] to heat portions of uranium dioxide fuel simulant samples to the high energy states (up to and greater than 3500 J/g) that could be produced at core disassembly in HCDAs. These fuel samples are then allowed to "disassemble" in different surrounding environments. Two series of the tests are discussed in this paper: a) vaporizations in an argon gas environment; and b) vaporizations under a water pool. Vaporizations in a sodium pool

will eventually be performed; however, in this paper the relation of the water test results to sodium tests will be discussed.

DESCRIPTION OF CDV TECHNIQUE AND TEST FACILITY

A schematic of the fuel samples used in the capacitor discharge experiments is shown in Figure 1. Each sample consists of a stack of UO_2 pellets, weighing ∿20 grams and about .1 m in length, that is surrounded by about 30 grams of UO_2 microspheres (microsphere diameters are ∿350 μm). The pellets and microspheres are contained in a quartz tube.

Sample heating by the CDV technique is performed in two stages, preheat and capacitor discharge. Heating of the fuel to high temperatures requires rapid heating rates of the order of 10^6 Watts/gram. This is not possible when the fuel samples are at room temperature, where their electrical resistance is ∿10^6 ohms. However, UO_2 has a highly negative dependence of resistivity with temperature-proportional to T^{-5}. Samples are preheated at various levels of constant power until a final level of ∿2000 Watts is reached where a substantial fraction of the pellet mass is expected to be molten. The presence of the microspheres permits pellet melting without melting of the quartz tube. At this point, the sample resistance is typically ∿0.5 ohms. A two-second "down time" between preheat and capacitor discharge is used; this results in a more uniform temperature distribution through the pellets at the start of capacitor discharge. The capacitor discharge phase typically lasts for 2-5 ms, during which energy input rates to the fuel are at ∿10 MW levels. Energy input to the fuel occurs until the internal fuel pressure bursts the quartz tube. Capacitor discharge voltage and current data are recorded to permit the amount of energy input to the fuel sample to be determined.

The fuel sample schematic shown in Figure 1 indicates that a steel tube (.13 mm wall thickness) surrounds the quartz tube; for tests discussed here that were performed in an argon gas environment, this steel tube was not present. For the under-water, and later under-sodium, tests, the presence of the steel tube permits energy input to the fuel without shunting to the surrounding liquid. In the gap between the steel and quartz tubes (this gap has a volume of ∿10^{-5} m^3) xenon gas is inserted. Xenon is used to simulate non-condensable fission products that could be in HCDA fuel bubbles. The amount of xenon present is one of the variables in the under-water and under-sodium tests.

Figure 2 is a simplified illustration of the facility in which the tests are performed. The capacitor system consists of six "banks," each containing ten capacitors. Each capacitor can store 3 kJ of energy at 2500 Volts, so the total capacitor energy storage capability is 180 kJ.

The tests in an argon gas environment were performed in the Containment Research Installation-III (CRI-III) vessel. This vessel has a .56 m^3 volume,

and is equipped with aerosol sampling equipment to permit measurement of the airborne aerosol concentration vs time (by filter sampling) and determination of the size distribution of the primary aerosol particles (by collecting samples on photomicrograph grids and viewing these under an electron microscope). High-speed movies (at 10,000 frames/sec) are taken of fuel heating, sample rupture, and fuel expansion.

Under-water (and later under-sodium) tests are performed in the Fuel Aerosol Simulant Test (FAST) vessel. This is a .46 m^3 vessel that is 1.83 m high and .61 m in diameter, roughly 1/10 the linear dimensions of the primary containment for the proposed Clinch River Breeder Reactor. The vessel is instrumented to permit measurement of the pressure transients produced due to bubble expansion and collapse, and also to make measurements of the properties of aerosols transported to the argon cover gas above the liquid. High-speed movies are taken during the water tests, and an acoustic detection system will be used to track the bubbles formed in under-sodium tests.

ARGON GAS FUEL VAPORIZATION EXPERIMENTS

Fuel vaporization experiments were performed in an argon gas environment (in the CRI-III vessel) because it was expected that after sample rupture, the fuel would undergo an essentially free expansion in the argon gas environment.

After the fuel vapor is produced, it rapidly cools, due to mixing with argon gas, and forms an aerosol. Measurements are made of the mass of airborne material in the argon gas as a function of time; extrapolation to zero time permits the initial airborne mass to be estimated. This measured airborne mass can be compared to the amount of fuel calculated to have vaporized, in an assumed free expansion after capacitor discharge occurs.

More than 50 capacitor discharge experiments have been performed at various levels of preheat and for different capacitor bank charging configurations. In these tests, the argon gas pressure in the test vessel was ∿.101 MPa. Results from three of these tests, all having the same preheat level before capacitor discharge and spanning the range of energy inputs, are summarized in Table I.

Table I

CDV Energy Inputs and Measured Aerosol Yields for Selected CDV Tests Having 2200 Watt Final Preheat (In Each Test, the Pellet Mass Was ∿22 Grams and the Microsphere Mass Was ∿36 Grams)

Test	CDV Energy Input (kJ)	Measured Aerosol Yield (grams)
CDV 22	8.0	.54
CDV 17	29.7	1.67
CDV 51	43.9	6.82

In a previously published report,[2] aerosol yields from a number of tests were compared with yield calculations from models for the electrical preheat, capacitor discharge, and the subsequent fuel expansion. These calculations used a temperature distribution calculated for preheat as input to the capacitor discharge calculation, and assumed an adiabatic fuel expansion, after capacitor discharge, to the surrounding argon gas pressure. For low CDV energy inputs (like that in CDV 22) the calculated yields were less than those measured. However, for higher energy inputs (like those in CDV 17 and 51) calculated vapor yields were a few times the measured aerosol yields.

However, two effects were not included in these preliminary calculations that could considerably change the results. These are:

1. An apparent increase in the electrical resistivity of UO_2 as it is heated through melt - this information comes from recent CRI-III experiments;[3]

2. The influence of the cooling of the fuel sample during the two-second time period between preheat and capacitor discharge.

In a recent series of CRI-III tests (done in argon gas) the preheat level before capacitor discharge was set well below that expected to produce fuel melt. A typical set of capacitor discharge voltage and current data from these tests is shown in Figure 3. The abrupt decrease in current (corresponding to an $\sim$25% resistance increase) at 2.9 ms is not observed in tests in which the pellets are melted prior to capacitor discharge during preheat. An increased UO_2 resistivity at temperatures greater than melt would lead to more energy being deposited to the microspheres (and less to the pellets) than previously expected; this would reduce the calculated vapor yield.

Results of parametric calculations for the influence of a resistivity increase by a factor of 2 through melt (MR = 2 corresponds to this, MR = 1 corresponds to no change) and also for the two-second cooling period between preheat and CDV are shown in Figure 4. These results indicate a) that the cooling of the sample between preheat and CDV must be included in vapor yield calculations, and b) yields calculated assuming a resistance increase through melt are, for a given energy input, considerably less than calculated without the melt resistance change. These results strongly suggest that the UO_2 electrical properties at high temperatures need to be accurately determined to allow confidence in the comparisons of measured and calculated vapor yields from CRI-III argon gas experiments.

Figure 5 shows the cummulative primary aerosol size distribution from three CRI-III tests. As shown, the aerosol was log-normally distributed; this distribution was found to be relatively insensitive to the CDV input energy for each test. This may be similar to the primary aerosol distribution that would be produced when fuel vapor is released from an HCDA bubble to the reactor cover gas and secondary containment. It is not certain, however, that these particles do not come from a combination of aerosol nucleation and liquid fragmentation when UO_2 liquid is dispersed after capacitor discharge.

A series of tests performed in cooperation with Sandia Laboratories personnel[4] may help to answer this question; in these tests, the debris produced immediately (less than 3 ms) after capacitor discharge is sampled in a vacuum environment. The size distribution of dispersed droplets can be determined and will be compared to primary aerosol size distributions.

UNDER-WATER FUEL VAPORIZATION TESTS

Nearly thirty under-water tests have been performed in the FAST facility within the past year. As outlined in Table II, these tests have been performed over a wide range of system pressures and temperatures, and also with

Table II

Test Parameters Varied In FAST Water Tests Performed To Date (All Tests Performed With Water Height Above Test Sample = 1.12 m)

Test Parameter	Values Used
System (Water Pressure = P_w	P_w = .025 MPa, .101 MPa, 2.02 MPa
System (Water) Temperature = T_w	T_w = 298 K, 363 K
Xenon Gas Pressure In Test Sample = P_x	P_x = .101, 505 MPa for P_w = .101 MPa
	P_x = .505 MPa for P_w = .025 MPa
	P_x = 2.02 MPa for P_w = 2.02 MPa

large variations in the pressure of the xenon gas in the 10^{-5} m^3 volume in the test sample. These test conditions were varied for the following reasons:

1. Variation of system pressure should cause the amount of fuel vapor produced in the bubble to vary, and so should influence bubble size and bubble dynamics;

2. Variation of system temperature should cause the amount of water vaporized to vary. If a large amount of water vapor is formed, it may carry condensed fuel aerosol through the water to the cover gas;

3. One analysis for UO_2 condensation, neglecting radiation heat loss, in HCDA-sized (~3 m diam) bubbles indicates[5] that fission product gases in the bubbles can greatly reduce the fuel condensation rate. Variation of the xenon gas pressure may provide insight as to whether this is the important condensation mechanism, or if radiation heat transfer dominates. The xenon also provides a medium for transport of condensed fuel through the coolant.

All of the tests discussed in this paper were performed under the same preheat conditions and had CDV energy inputs in the 30-40 kJ range. Therefore, we can assume all fuel samples had roughly the same energy content when bubble expansion began. In addition, all tests were performed with the liquid height above the test sample set at 1.12 m.

The major measurements made were of the pressure transients due to bubble expansion and collapse and of the amount of aerosol transported to the cover gas; visual results, from high-speed movies, were also produced. Pressure measurements were made using a Kaman Sciences transducer mounted 23 cm from the test sample. A typical pressure record is shown in Figure 6. The early-time pressure pulse is due to the initial sample rupture, while the later pulses occur due to the collapse and re-expansion of the bubble. We will call the time between the first and second pulses, T_p, the period between bubble formation and the first bubble collapse.

Values of the bubble period, T_p, as a function of test conditions are presented in Table III. As expected, increasing the system pressure causes the bubble period, T_p, to decrease. Two other results that are interesting to note are:

1. Increasing the xenon gas level for a fixed system pressure had very little effect on the initial bubble period. This could mean that the presence of the inert gas has little influence on bubble condensation during the time T_p;

2. Increasing the system (water) temperature to near its boiling point resulted in a substantial increase in T_p (from 55 to 80 ms). This is a good indication that a significant amount of water was vaporized during the time T_p.

For all tests except those performed at high water temperatures, no fuel vapor or aerosol was transported to the argon cover gas region (based on mass

Table III

Measured Initial Bubble Periods T_p For Various Test Conditions (For 1.12 m Water Height)

Test Conditions	Initial Bubble Period T_p (ms)
$P_w = P_x = 2.02$ MPa $T_w = 298$ K	∿4
$P_w = P_x = .101$ MPa $T_w = 298$ K	∿50
$P_w = .101$ MPa $P_x = .505$ MPa $T_w = 298$ K	∿55
$P_w = .101$ MPa $P_x = .505$ MPa $T_w = 363$ K	∿80
$P_w = .025$ MPa $P_x = .505$ MPa $T_w = 298$ K	∿180

measurements made in the gas space). Visual evaluation of the high-speed films for all tests indicates that there was an aerosol in the bubble within 100 to 200 ms of the start of bubble formation. This is an indication that in the water tests done at low water temperatures, there is no bubble rise phase - all condensation occurs in the early expansion and contraction phase.

In the water tests with water temperatures of ∿360 K, however, measurements in the cover gas indicate that ∿.1 gram of fuel is transported through the water. Assuming that the bubble contains roughly 2 grams of fuel vapor initially (based on argon gas test results), this means that ∿5% of the initial source seemed to be transported to the cover gas in these tests. The likely mechanism for this transport is a water vapor bubble produced by cooling of the hot fuel vapor and liquid in the bubble.

The water experiments were done as a prelude to performing sodium tests, mainly to permit visual observation of the formation and dynamics of fuel vapor bubbles. Interpretation of the condensation results (i.e. total condensation in 100-200 ms) in terms of LMFBR source term prediction should be done cautiously at this time for two reasons: water is not necessarily a good simulant for sodium, and the bubbles formed in these tests are considerably smaller than those possible in HCDA's.

The main reason that water is not a good simulant for sodium is that the thermal conductivity of water is much less than that of sodium. Based on results obtained in the under-water tests, one might expect that bubbles will collapse even more rapidly in sodium. This is certainly possible, but, since the potential for water vaporization is large, it is also possible that water vapor is being produced in the bubble. This water vapor could mix with much hotter UO_2 vapor and cause very rapid UO_2 condensation. This mixing-condensation mechanism may not be present in sodium tests.

Because bubbles produced in FAST tests are much smaller than those possible in HCDAs, rapid condensation in water or sodium tests may not mean rapid condensation in HCDAs. HCDA bubbles may be as large as 1.5 m in radius and are expected to have a roughly 2-second rise time. In contrast, bubbles produced in the FAST water tests seem to have radii as large as .1 m. This means that the surface-to-volume ratio for FAST bubbles may be 15 times that for HCDA bubbles. The condensation that occurs in the FAST tests is likely to be more rapid as a result of the large bubble surface-to-volume ratios.

SUMMARY

In summary, the following points can be made:

1. Fuel vaporization tests have been performed in an argon gas environment. The purpose of these was to compare the assumption of an adiabatic fuel expansion after capacitor discharge with the quantities of fuel aerosol

airborne in the experiments. Such a comparison would tend to indicate the margin available in using this assumption to establish maximum aerosol source due to an HCDA and will serve as a base line to establish the attenuation potential due to the bubble contact with sodium in later experiments. The comparison with the adiabatic assumption is very promising but not yet definitive primarily due to lack of knowledge of UO_2 properties (particularly electrical resistivity) at high temperatures. Measurements have been made of the primary aerosol size distribution produced in the argon tests. It is not yet clear that the airborne particles are produced by aerosol nucleation due to mixing of fuel vapor with argon gas, by fragmentation of liquid drops to small sizes, or by some combination of the two.

2. Under-water fuel vaporizations have been performed for a variety of test conditions. Rapid bubble condensation has been observed to occur in these tests, in roughly 100 to 200 ms after capacitor discharge. When the water was heated to near its boiling point aerosol was transported through the water to the argon cover gas above it. This is the only condition so far in which transport of fuel to the cover gas has occurred; it is likely that the fuel was transported in a water vapor bubble produced in these tests. This result implies that if significant sodium vaporization occurs in an HCDA (for instance, when sodium near the core is close to its boiling point) the possibility exists for fuel transport through the coolant in a sodium vapor bubble. However, water is not a good simulant for sodium, so the water test results should be evaluated with caution. In addition, the fact that the FAST tests are small scale implies that rapid bubble condensation could occur, and the results for under-water and under-sodium tests should be carefully interpreted and scaled.

ACKNOWLEDGEMENTS

This research is sponsored by the Office of Nuclear Regulatory Research, Nuclear Regulatory Commission, under Interagency Agreement DOE 40-551-75 with the U. S. Department of Energy under Contract No. W-7405-eng-26 with the Union Carbide Corporation Nuclear Division.

The authors wish to acknowledge the efforts of J. M. Rochelle (of the Instrumentation and Controls Division at ORNL) and H. E. Robertson in performing the experiments described in this paper.

REFERENCES

1. M. J. Kelly, G. W. Parker and J. M. Rochelle, "Development of the Capacitor Discharge Vaporization Technique to Produce Aerosols Formed Under Conditions Postulated for Hypothetical Core-Disruptive Accidents," ORNL/NUREG/TM-160, Oak Ridge National Laboratory (July 1978).

2. A. L. Wright, et al, "Effect of Energy Density on Aerosol Yield and Primary Particle Sizes Produced by the Capacitor Discharge Vaporization (CDV) of UO_2," ORNL/NUREG/TM-163, Oak Ridge National Laboratory (October 1978).

3. A. L. Wright, T. S. Kress, A. M. Smith and J. M. Rochelle, "Determination of UO_2 Electrical Conductivity Change When Heated Through Melt," to be presented at 1980 ANS Annual Meeting, June 8-13, 1980 in Las Vegas, Nevada.

4. T. S. Kress and J. T. Han, "LMFBR Aerosol Release and Transport Program Quarterly Progress Report for January-March 1979, ORNL/NUREG/TM-329, Oak Ridge National Laboratory (August 1979).

5. T. G. Theofaneous and H. K. Fauske, "The Effect of Noncondensables on the Rate of Sodium Vapor Condensation From A Single-Rising HCDA Bubble," *Nuclear Technology*, 19, 132 (1973).

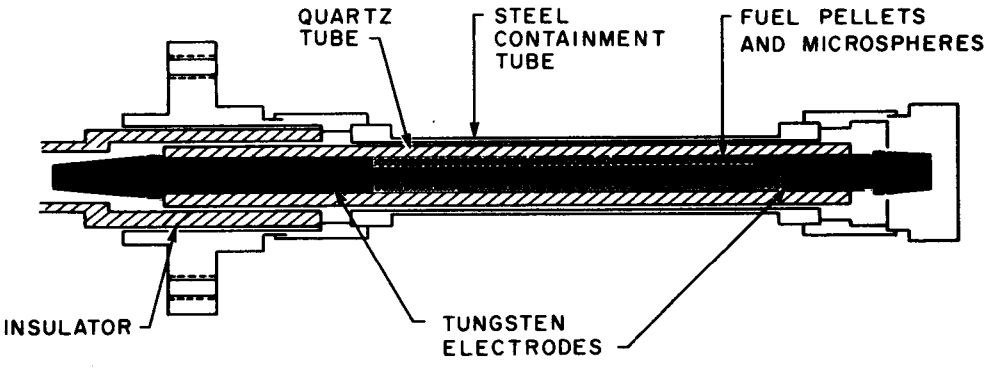

Fig. 1. Schematic of Test Sample Used In Capacitor Discharge Experiments; Sample Mounted Horizontally In Test Vessel As Shown. Steel Containment Tube Present In Under-Water Tests, Not In Argon Tests Discussed In This Report

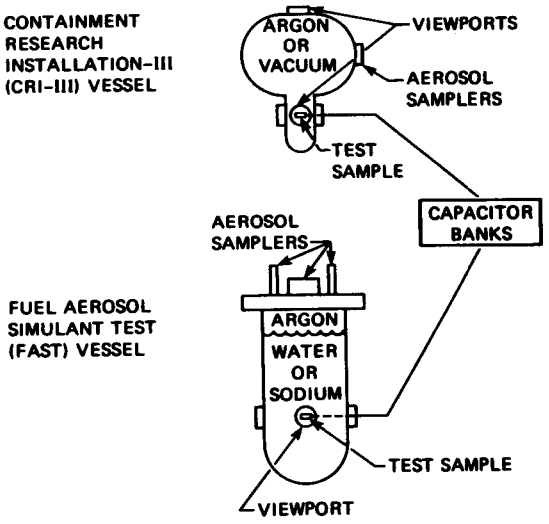

Fig. 2. Test Facility For Capacitor Discharge Fuel Vaporization Experiments

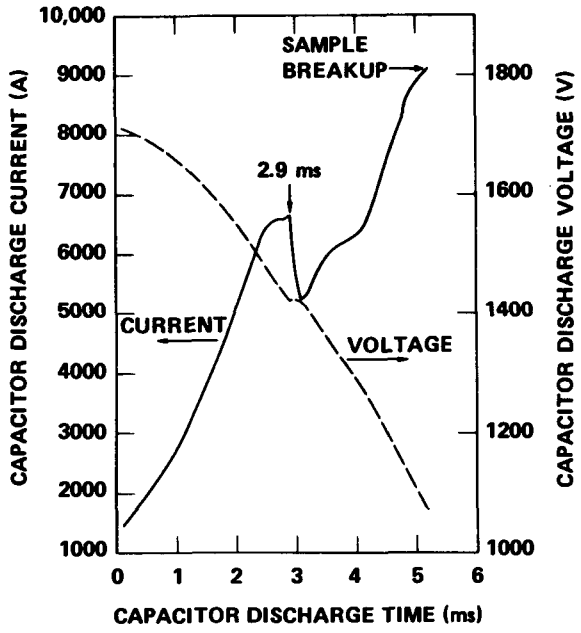

Fig. 3. CDV Voltage And Current Data From CDV 83, Test Where Preheat Level Used Did Not Produce Fuel Melt. Drop In Current At ∿2.9 ms Attributed To Increase In UO_2 Electrical Resistivity When Fuel Is Heated Through Melt.

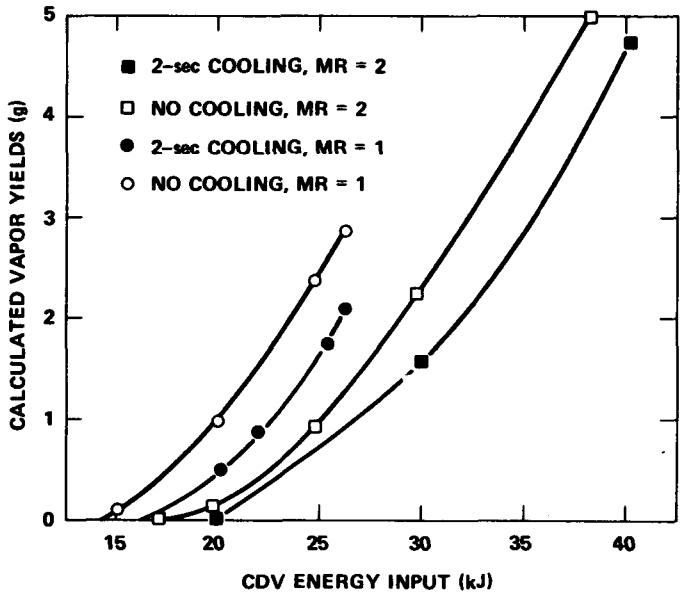

Fig. 4. Parametric Calculations For Vapor Yield vs CDV Energy Input. Initial Condition For Each Case Was Calculated Temperature Distribution After Preheat With Pellet Center Temperature = 3100 K, Slightly Below Fuel Melt. MR = Assumed Change In UO_2 Electrical Resistivity That Occurs As Fuel Is Heated Through Melt. "2 Second Cooling" Refers To Time Between Preheat and CDV, When Sample Is Not Being Heated.

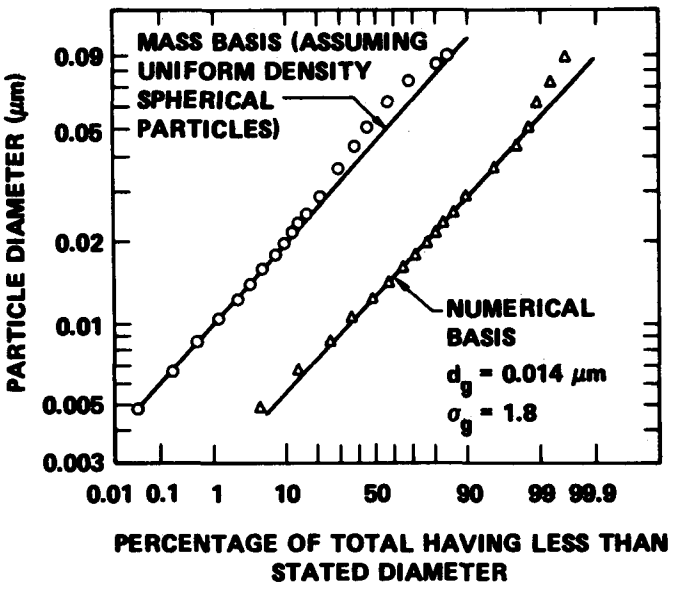

Fig. 5. Cumulative Primary Particle Size Distribution Data From Three CRI-III Argon Tests; 5330 Particles

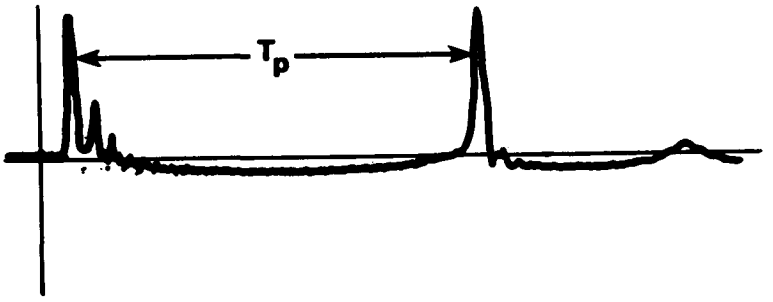

Fig. 6. Typical FAST Under-Water Test Pressure vs Time Data (from FAST 22). Pressure Pulses Shown Occurred At 0.9, 58.3, and 86.8 ms After Sample Breakup And Had Magnitudes Of 1.45, 1.40, and 0.23 MPa, Respectively. Pressure Was Measured ∿23 cm From Test Sample. Time Between First Two Pulses Is Time Noted As T_p In Text.

A TIME-RESOLVING SAMPLER TO DETERMINE INITIAL FUEL AEROSOLS UNDER CDA CONDITIONS

R. M. Elrick
Sandia National Laboratories
Albuquerque, New Mexico, USA

ABSTRACT

Using close-in, time-resolved sampling of fuel debris, high speed photography and photometric measurement of fuel temperatures the kinetic and thermal states of the disrupting UO_2 fuel were defined as it was neutronically heated to vapor by a 5 ms FWHM pulse of 2380 KJ/kg. From these data it was possible to obtain a fuel energy-temperature relation to the melt and debris kinetics in the form of particle distributions in velocity and size for particles from >10 μm to <3 nm in size. Several calculations and comparisons were made to establish the reliability of the sampling and analysis techniques.

Introduction

In order to assess the threat to public safety in the unlikely event of a breach of containment following a core disruptive accident it is important to know the physical characteristics and transport behavior of the aerosols produced under conditions similar to those hypothesized for the accidents.

The purpose of the study at Sandia was to measure the characteristics of debris produced from bare UO_2 fuel heated neutronically to vapor under CDA conditions. The measured debris characteristics are time dependent distributions in particle size and particle velocity obtained from the observed size, location and number of debris particles collected in a rotating wheel sampler. From these two distributions additional characteristics such as particle number density, momentum and pressure were calculated. In these experiments the fuel breakup produced particles from tens of μm to less than 3 nm in size and with velocities from less than 3×10^3 cm/sec to greater than 3×10^5 cm/sec.

To more completely define the breakup event the energy or thermal state of the fuel in both space and time must also be known. This was accomplished by calculating fuel temperature from surface radiance measurements made on the fuel using calibrated photographic film.

It is also of considerable importance to compare aerosols produced in out-of-pile experiments with those produced in-pile under similar heating conditions. A comparison study of this kind would begin to establish limits of interest on particle size and density. In a cooperative effort with ORNL, under their NRC sponsored Aerosol Release and Transport Program aerosols produced by resistively heating UO_2 pellets to vapor at ORNL are being compared with those that were produced in the Annular Core Pulse Reactor at Sandia. The same methods that were used in-pile for sampling fuel debris and for measuring fuel temperature have been used for the ORNL experiments. This paper covers the results of the first two in-pile aerosol experiments to measure fuel debris characteristics and define the thermal state of the fuel.

Experimental

A schematic of the aluminum experiment canister is shown in Figure 1. The fuel pin was a single piece of fresh, bare, 20% enriched UO_2, 6.35 cm long and 0.49 cm in diameter. The pin was mounted horizontally at the midplane of the reactor core and had the same diameter and about one-half the length of the pellet stack of depleted UO_2 fuel used in the ART studies at ORNL. The 6 cm diameter sampling wheel rotating at 6 ms/revolution was positioned 2 cm above the pin at its midpoint for sampling a representative portion of fuel debris. An aperture in the bottom of the wheel cover allowed fuel particles to enter one of 30 pie-shaped channels designed around the wheel.

Two 45° front surface mirrors in the canister allowed backlighting of the fuel with a 300 W lamp and viewing it through a quartz window in the top of the canister. The fuel support block could be positioned for viewing the fuel from either the end or the side. The fuel was viewed through a Questar telescope by a Fastax framing camera, both located outside the reactor, 10 m from the fuel. Photographic resolution was better than 10 line-pairs/mm. Photography established a timescale for sampling and gave a visual record of the disrupting fuel as it was driven to the liquid-vapor phase by a 5 ms full width at half maximum neutron pulse of 2380 KJ/kg. A 1-KW level fiducial mark from the reactor pulse and timing marks placed on the film synchronized the photographic and neutronic events. Sampling and neutronic events were synchronized by displaying on a continuously recording oscillograph the neutron pulse signal and a voltage generated for each rotation of the sampling wheel.

Photography showed that within a period of several milliseconds the fuel heated with an increasing brightness, melted and liquid drops were dispersed energetically and uniformly from the bare fuel at initial velocities up to several m/s. Within a fraction of a millisecond after the particles appeared, a vapor front was seen to move outward at a velocity of 50 m/s. Vapor filled the field of view, condensed on the optics and eventually obscured the action.

Fuel Temperature Measurements

Fuel temperatures were calculated from fuel radiance measurements and an emissivity value of 0.87[1] for UO_2 in the temperature range of interest (~2100 K to 3140 K) and assuming radiation was emitted from the fuel proportional to Planck's Radiation Law. Fuel surface radiance was obtained from photographic film by measuring the density of the processed film and relating the density to known radiance values. This relation between density and radiance was established from film response to a series of relative radiance levels using a flash lamp with a neutral density step wedge. Absolute values for this relation were established by photographing the filament of a standard lamp of known spectal radiance through the optics of the experiment and measuring the resulting film density. Stated uncertainty in temperature is 3 percent but recent calibration work indicates it may be less than this.

Radial temperature profiles were estimated from temperatures measured on the surface of the fuel and in the neighborhood of the fuel centerline in two successive but similar runs. Centerline temperature was estimated by viewing the pin from an end in which a deep hole had been drilled along the centerline. Average fuel temperatures were calculated from these profiles. In all cases the fuel was hotter on the surface with the ratio of surface to centerline temperature ranging from 1.08 to 1.13 over the temperature range of interest. Surface heating of the pin was very uniform with a temperature variation at any one time of less than 50 K.

Deposited Energy as Fuel Temperature Relation

The total thermal energy absorbed in the UO_2 fuel due to fission of U^{235} was estimated from fission product inventories made on a series of dosimetry runs. The time variation of this absorbed energy was determined from the time integral of the pulse of neutrons delivered by the reactor. The relationship between the specific fission energy deposited in the fuel and the average fuel temperature is shown in Figure 2. Uncertainties of 5% in the average energy and 3% in the average temperature are shown as error bars. The data lie less than 10% above published[2] enthalpy-temperature data for UO_2. After the experimental data were corrected for heat losses, the two sets of data effectively agreed to within experimental uncertainty.[3] Therefore, within the level of accuracy, the relation between energy and temperature is adequately described by equilibrium specific heat values for UO_2.

Fuel Debris Sampling

Of several more conventional methods available for particle sampling a small rotating wheel placed near the fuel was chosen for several reasons. 1) It could be used to sample debris for both in-pile and out-of-pile experiments. 2) By locating the sampler close to the fuel, debris particles were collected before they had time to significantly interact among themselves or with the canister. 3) A large sampling area was exposed which reduced damage to the fragile collection surfaces by the hot energetic debris and also decreased the possibility of particle buildup on the surfaces. 4) Rotation of the sampler during collection time-resolved particle collection, making it possible to relate particle characteristics to the energy state of the fuel and allowed particle velocities to be unfolded from the location of particles collected in each sampling channel.

Particles collected in the sampling wheel appeared to have velocities directed normal to the fuel axis as observed in the side and end views of the disrupting pin. By properly positioning the sampling wheel with respect to the fuel, particles entered the aperture with directed velocities along the wheel radius when viewed as in Figure 3. As the wheel rotates, these particles are collected on the top and bottom channel surfaces. By angling the top surface into the particle flow the fastest particles will begin to collect at larger wheel radii while slower particles will collect at smaller radii. Sufficiently slow particles will not collect on the top surface but will be swept onto the bottom surface with the slowest ones collecting closest to the flap that closes the lower part of the channel. Thus by separating particles on collection surfaces by virtue of their velocity, it is possible to unfold a velocity distribution for particles, knowing their position of collection in a channel.

Surfaces in each channel were designed to be removed for direct viewing in either an optical microscope or a transmission

or scanning electron microscope for size, shape and number count as a function of their position in a channel. All channel surfaces were covered with 25 m thick beryllium-copper sheet etched through with a pattern of holes. The sheet was covered with a film of collodion and evaporated carbon. After particles were sampled, pieces of the etched sheet were cut out and viewed directly in a microscope. Unfold equations[4] based on wheel geometry relate the position of collected particles to their velocity and the number of particles collected on a channel area are related to the number incident on the wheel. Since the collection time per channel was obtained from the width of the channel opening and the rotational speed of the wheel, particle flux per velocity interval as a function of particle velocity could be obtained as a function of time for all sampled debris. A velocity distribution from one of the channels is shown in Figure 4 where the particles measured ranged in velocity from 10^3 cm/sec to 3×10^5 cm/sec. In a similar manner particle flux per size interval as a function of particle size was obtained by summing particles with the same size instead of the same velocity for each channel analyzed.

Particle number density was calculated from particle flux divided by the velocity of the particles. Particle mass density was obtained by multiplying the number density by the mass of each particle. Particle momentum was obtained from the product of particle mass and particle velocity. Vapor-like particles are those less than 2 nm to 3 nm, the resolving limit of the transmission microscope used. These particles were deposited on the collection surface in an unresolved structure and the number of particles was estimated from the average thickness of the deposit. Maintaining a canister pressure of 13 Pa (0.1 Torr) or less allowed the vapor-like particles to reach the sampling wheel.

In addition to the directed velocity, particles would be expected to have thermal motion which would add a velocity component to the directed velocity and cause the particles to diffuse with time. The diffusion process added particles to the collection surface and therefore reduced the number of particles that would be collected downstream. To estimate the effect of diffusion a third side of each collection channel was positioned parallel to the directed particle velocity. Collection on this surface was due solely to particle diffusion as indicated in Figure 5 for vapor-like particles. On the semilog graph particle density was plotted as a function of distance from the channel entrance. The curve is concave up instead of linear because the particles had a range of velocities. A mean particle size of 2 nm was obtained from the slope of the curve using reasonable experiment parameters. This indicated some agglomeration of the initial vapor (~0.5 nm in size) probably took place. Particle flux calculated from the ordinate intercept of the curve is in order of magnitude agreement with the particle flux calculated from the unfolding technique described previously after correcting for particle diffusion.

Several other calculations demonstrated the reliablity of the sampling and analysis. Velocity data for the vapor-like particles of Figure 4 were compared in Figure 6 with the Boltzmann velocity distribution of UO_2 molecules at a temperature of 3760 K. The agreement between the two curves is reasonable and the peak value of the experimental curve gives a mean Boltzmann temperature of 3270 K. (The two curves were normalized to the same maximum ordinate value.)

A second check on the reliablity of the technique was that the total mass of fuel collected in the wheel should equal the mass of fuel directed toward the sampling wheel, calculated from the wheel and fuel pin geometry. The calculated mass in the wheel (using the bulk density of UO_2) was about 25 percent greater than the amount directed toward the wheel. Of the total amount collected (Figure 7), about 30 percent was less than 2 nm to 3 nm in size and 60 percent was larger than 1 μm in size.

A third calculation related particle momentum to the effective pressure generated by the fuel. This estimate of the rate of momentum change per unit area of the fuel gave peak pressure values between 10 MPa and 100 MPa. This order of magnitude value is in agreement with effective vapor pressure measurements obtained by other invesigators[5] using electron beams and lasers to vaporize the fuel. Especially during early times of collection, a significant portion of the calculated pressure was due to liquid particles in the one to ten micrometer size range. Some of these results are summarized in Figure 8. The energy pulse is synchronized with the sampling channels - each channel is shown as a dash in the broken line. Pressure values calculated for several of the channels are shown as well as the percent of pressure due to vapor.

Summary

This study has demonstrated that with the sampling and photographic techniques described it is possible to measure not only the debris characteristics of bare UO_2 heated neutronically to vapor but also the corresponding thermal and energy state of the fuel.

Fuel temperatures and radial temperature profiles were measured to melt. The fission energy as a function of temperature agreed with published enthalpy vs. temperature data for UO_2 within experimental error after corrections were made for heat loss from the fuel. Fuel debris distributions in particle size and velocity as a function of time were obtained. A reasonable level of confidence was established in the particle sampling and analysis based on the results of a series of comparison calculations: 1. The calculated mass of particles collected in the wheel agreed within 25% with the mass of fuel directed at the wheel. 2. The pressure exerted by the debris was in order of magnitude agreement with published effective vapor pressure measurements. 3. An analysis of particle diffusion produced a reasonable size for the vapor-like particles as well as a value for particle flux that was in order-

of-magnitude agreement with the flux obtained from the general unfolding technique that was described. 4. The velocity distribution of vapor-like particles was shown to be in reasonable agreement with Boltzmann's velocity distribution.

Some of the difficulties encountered with the sampler were: 1) the bigger particles did not stick to a dry surface, 2) thermal diffusion of particles complicated the unfolding process, 3) no sensitivity study has been made to optimize accuracy as a function of particle count vs. channel position, and 4) much analysis is required to unfold particle distributions.

In spite of these difficulties, this type of particle sampler seems uniquely suited for pulsed power experiments with energy states into the liquid and vapor.

ACKNOWLEDGMENT

This work was supported by the United States Nuclear Regulatory Commission.

REFERENCES

1. M. BOBER and H. U. KAROW, "Measurements of Spectral Emissivity of UO_2 Above the Melting Point", Seventh Symposium of Thermophysical Properties, National Bureau of Standards, Washington, DC, 1977.

2. "Properties for LMFBR Safety Analysis", ANL-CEN-RSD-76-1, Supplement 1, April, 1976.

3. E. BERGERON and J. ODOM, "Equation-of-State, Advanced Reactor Safety Research Quarterly Report, July-Sept., 1978, SAND78-2020, Sandia Laboratories, Albuquerque, NM, Sept. 1979.

4. R. M. ELRICK, "A First Study of Aerosols Produced by Neutronic Heating of Fresh UO_2 Fuel", SAND80-1166, Sandia National Laboratories, Albuquerque, NM, to be published.

5. D. A. BENSON, "Application of Pulsed Electron Beam Vaporization to Studies of UO_2", SAND77-0429, Sandia Laboratories, Albuquerque, NM, June 1977.

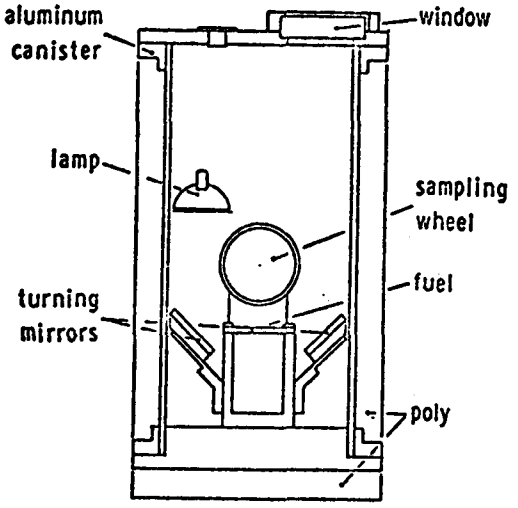

Figure 1. Schematic of the Experiment Canister

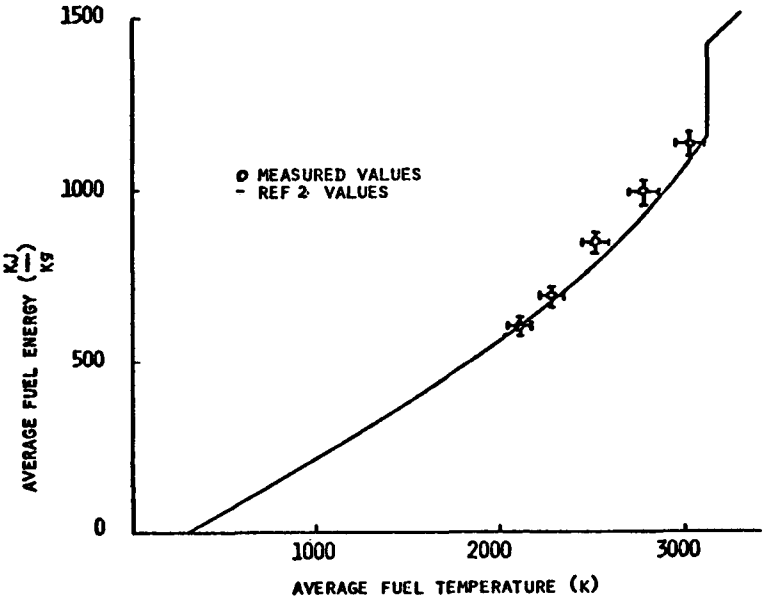

Figure 2. Measured values of energy-temperature (not corrected for heat loss) compared with published enthalpy-temperature data.

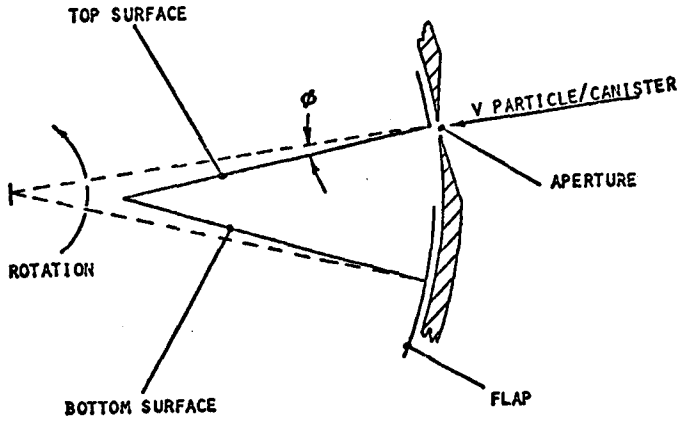

Figure 3. Schematic of one of thirty channels in the sampling wheel (not to scale)

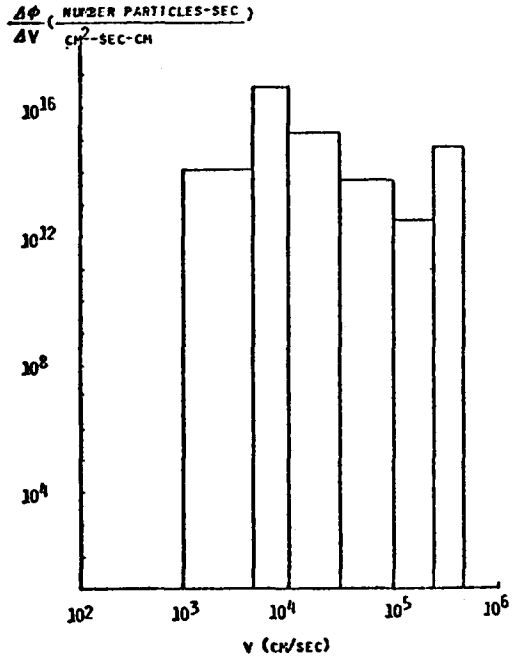

Figure 4. Velocity distribution for particles collected in one of the sampling channels.

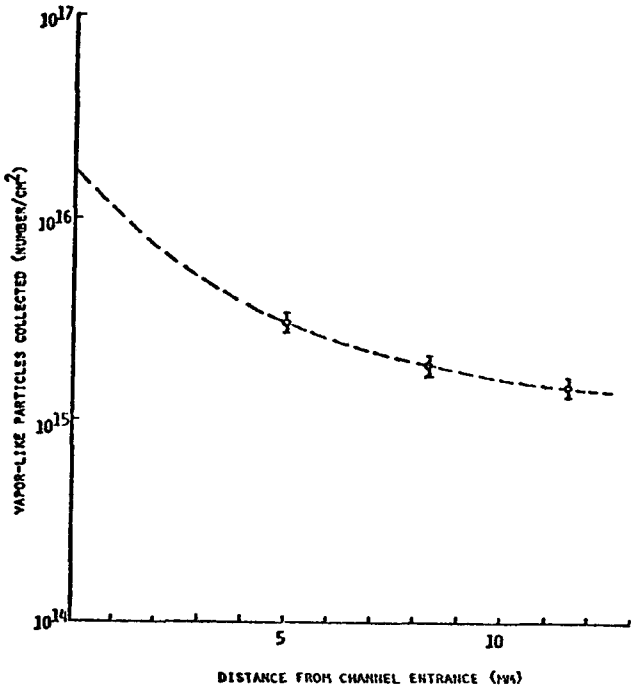

Figure 5. Density of vapor-like particles deposited on the channel surface designed to collect by diffusion.

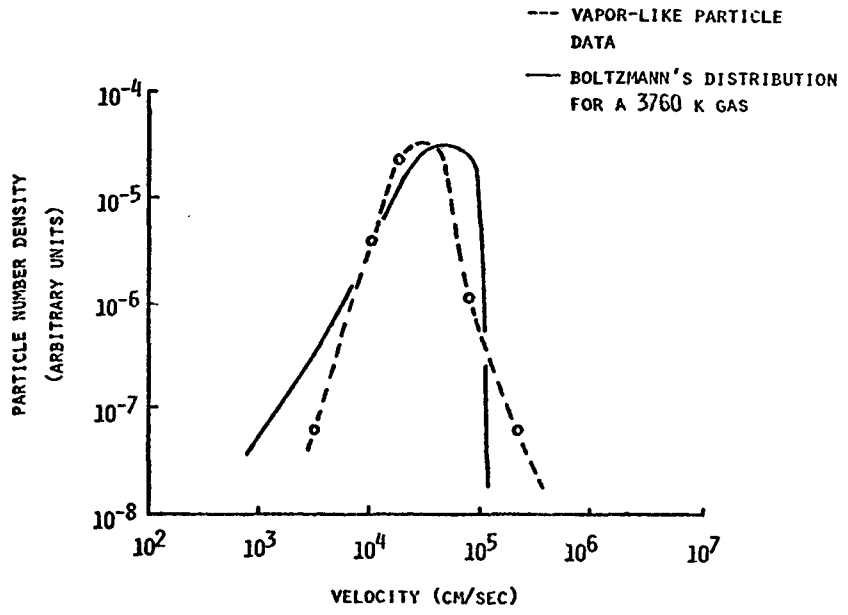

Figure 6. Velocity distribution of vapor-like particles compared with Boltzmann velocity distribution

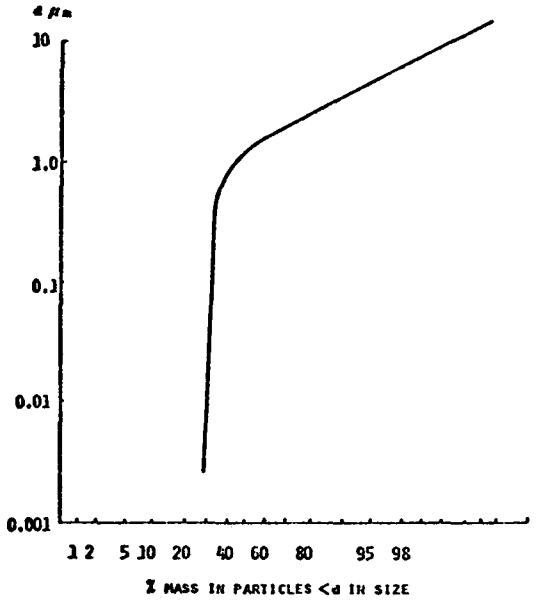

Figure 7. Total particle size distribution

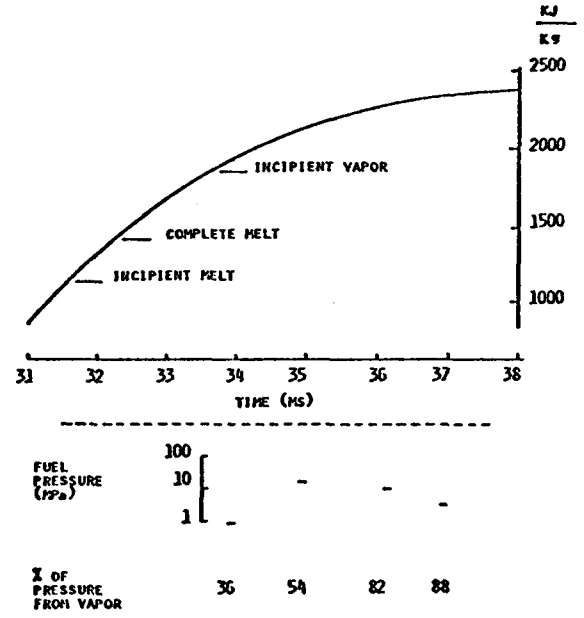

Figure 8. Fuel pressure calculated from measured momentum of fuel debris synchronized with the energy pulse.

AEROSOL RELEASE FROM A HOT SODIUM POOL AND BEHAVIOR IN SODIUM VAPOR ATMOSPHERE

H. Sauter and W. Schütz
Laboratory for Aerosol Physics and Filter Technology
Kernforschungszentrum Karlsruhe, FRG

ABSTRACT

For source term assessment, it is necessary to study the sodium retention capability for fuel and fission products, the release rate, the release mechanism, sodium evaporation into an inert gas atmosphere, aerosol formation and properties, and the aerosol behavior in the containment atmosphere. Experiments on these subjects are carried out in the KfK-NALA program, mainly related to the German SNR-300 core catcher problem. Results from small scale experiments with 100 g Na (NALA I) and from technical scale experiments with 1 kg Na in a heated 2.2 m^3 vessel (NALA II) are presented. UO_2, Cs, NaJ and SrO were used as contamination substances.

In case of the NALA I experiments, the released aerosols were transported by an inert carrier gas (forced convection) into cold traps and filters, either at isothermal conditions or with an open vessel in a glovebox. Besides the determination of retention factors, special emphasis was placed on the understanding of the release mechanisms. In the present paper, we focus on the UO_2 particle behavior (pool surface enrichment, size distribution in the surface layer and in the released sodium).

The NALA II experiments were carried out with a 400°C to 700°C sodium pool evaporating at natural convection into an 130°C argon atmosphere. First results on uranium, iodine and strontiom retention factors are presented, as well as the time behavior of the sodium aerosol mass concentration and the particle size. The mass concentration is compared to PARDISEKO code predictions. Finally, our results on the sodium evaporation rate are given and compared to the sodium vapor pressure.

INTRODUCTION

Radiological HCDA source term assessment studies are of great importance in nuclear reactor safety research. The 'primary source term', which is directly related to the core disassembly phase and limited to a relatively short time, is followed by a 'secondary source term' originating from a variety of long term aerosol sources like in case of LMFBRs evaporating pools, sodium fires or sodium reactions with concrete. In the inner containment, hot sodium pools are the main aerosol sources.

In the German LMFBR project, the core catcher is an important nuclear safety device. As a consequence of a core disruptive accident with tank failure, major quantities of sodium, fuel, and fission products will be released as gas, vapor or aerosol from the core catcher sodium pool into the inert gas containment atmosphere due to mechanical, chemical, or evaporation processes. For source term assessment, it is necessary to study the sodium retention capability for fuel and fission products, the release rate, the release mechanism, sodium evaporation, aerosol formation and properties, and the aerosol behavior in the containment atmosphere. Experiments on this subject are carried out in the KfK-NALA program. It is mainly related to the core catcher problem, but the results may also, in a more general view, be applied to any contaminated hot sodium pool, evaporating into an inert gas atmosphere. The fuel debris is simulated by UO_2 particles of various sizes. For the case of fission products, the investigations were concentrated on Cs, J, and Sr.

One of the main results of an experiment is the 'retention factor', defined as $RF = (X/Na)_{pool} : (X/Na)_{released}$, where X symbolizes the U, Cs, J, Sr masses. Large RF values correspond to a high sodium retention capability for the specific substances. In this presentation, however, we want to treat the RF values only as byproducts and concentrate ourselves on the information on aerosol behavior, i.e. the behavior of UO_2 and Na particles, which we have gained from our experiments until now.

NALA I EXPERIMENTS: EXPERIMENTAL SETUP, PARAMETERS, RESULTS, AND DISCUSSION

Our small scale experiments, performed with about 100 g of sodium, are named NALA I. Two experimental setups have been used. The first one, with a stainless steel vessel (7 cm diameter, 10 cm height) placed in an oven at pool temperatures between 400°C and 900°C, has already been described at the 1979 Seattle conference /1/. The sodium was contaminated with UO_2 powder of various mean particle sizes, UO_2 pellets, Cs metallic, NaJ powder and SrO powder. The released aerosols were transported by a variable inert gas stream at isothermal conditions into cold traps and a filter. After washing and titration, the sodium release rate and the fuel and fission product traces were determined. The main intention was to measure RF as a function of pool temperature, but also as a function of other parameters like UO_2 particle size, convection at the pool surface, and concentration in the pool. Typical RF values are 1000 (U), 20 (Sr), and 3 (J), almost independent of pool temperature. For Cs, a strong enrichment was found in the aerosol. Our results may be explained by assuming that Cs and J are released as vapor and UO_2 and SrO as particles due to mechanical processes.

The second experimental setup is shown in Fig. 1: It consists of an open stainless steel vessel (7 cm diameter, 10 cm height) in a glovebox with N_2 atmosphere, a funnel, cold traps, filters, and a pump to generate a carrier gas stream. Typically, pool temperatures of about 500°C are achieved. The aerosols are released into the glovebox N_2 atmosphere (50°C), sucked through the funnel and trapped in cold traps and filters. Although the pool temperatures are relatively low, this second setup has the advantage of a strong temperature gradient above the pool (like in case of a real LMFBR accident) and no interference between carrier gas and pool surface.

An important finding of our experiments is the uranium, iodine and strontium enrichment at the sodium pool surface. Although the contamination substances have a significantly larger specific gravity than sodium, small particles may stay at the pool surface due to the surface tension forces. This has been shown in almost all of our experiments after analyzing the sodium pool layer by layer. So, in a somewhat idealized picture, a contaminated pool may not be described as a homogenous mixture, but as a system with surface contamination, bottom contamination and some mixing due to the internal convection. We also realized that surface concentration and released concentration are usually of the same order of magnitude.

To understand the release mechanism, we studied relations between the surface enrichment and the release rate. For the UO_2 case, where sodium has been contaminated with UO_2 powder of a well known size distribution (average particle diameter 20 µm), we tried to gain some information on the size distribution of the released UO_2 and of the UO_2 at the pool surface. A filtration method has been used. Samples of the neutralized solutions from surface layer and released sodium were passed through filters of defined porosity (Schleicher und Schüll Selectron-type filters with average porosities of 0.2, 1, 5 and 12 µm) and re-analyzed on uranium traces by a fluorometric method. Although this filtration procedure is not absolutely accurate for particle size classification, it may at least be used to answer the following three questions:

- Is UO_2 released from the pool as molecules (e.g. due to evaporation or uranate reaction) or as particles?

- Is the primary distribution similar to the released distribution?

- Is the surface distribution similar to the released distribution?

In Fig. 2 a typical result of our investigations is shown.* We found that a significant amount of UO_2 traces was retained by the filters. A clear similarity was observed for the surface layer and the released sodium, and we may conclude that the surface UO_2 distribution and the released UO_2 distribution are nearly the same. In comparison to the primary distribution, there is a significant shift to smaller particles. In general, our results show strong evidence for the following statements:

- Small UO_2 particles may stay at the sodium pool surface due to surface tension forces.

- The surface enrichment is an important link in the release mechanism.

- The release of small particles from a non-boiling liquid is possible and may be classified as mechanical release.

- UO_2 is released from a hot sodium pool mainly as small particles and not as molecules.

---

*The regarded experiment was performed with 102 g Na and 2.0 g UO_2 powder. After the experiment, 22 µg of uranium were found in the released sodium and 221 µg in the pool surface layer. The retention factor was 800.

- The UO_2 particle size distribution found in the surface layer and in the released sodium are nearly the same, but they differ significantly from the primary distribution; there is a shift to smaller particles.

The investigation of the behavior of small particles in liquids, their enrichment at the surface and their interference between the liquid and the gas phase seems to be an interesting field. Additional research work will be necessary to fully understand the particle release mechanism and, hence, an important part of the secondary source term. To our knowledge, there is no theoretical work yet available in this particular field.

Other important data to characterize the source term are the sodium release rate and the initial sodium droplet particle size. The release rate will be discussed later. For particle size determination, we replaced cold trap and filter by an Andersen impactor. This way, a determination of the size distribution less than 1 second after its generation was possible. We found a lognormal distribution with a 50% value (aerodynamic mass median diameter) of 0.6 µm, and $\sigma_g = (d\ (84\%) / d\ (16\%))^{1/2} = 1.1$. These data have been used later on as input parameters for PARDISEKO /2/ calculations.

NALA II EXPERIMENTS: EXPERIMENTAL FACILITY, PARAMETERS, RESULTS, AND DISCUSSION

The SNR 300 core catcher is equipped with a floor cooling device to remove the post accidental decay heat and to prevent sodium pool boiling. According to /3/, the maximum estimated sodium pool temperature will not exceed 700°C, and the average inner containment atmosphere temperature above the pool will be around 150°C. For the presently performed NALA II experiments these temperature values are used as boundary conditions. We have pool temperatures from 400°C to 700°C, inert gas temperatures of 130°C, natural convection and admixtures of UO_2, NaJ and SrO in the pool. We determine fuel and fission product release rates and retention factors, sodium release rates, aerosol mass concentrations, aerosol particle size distributions and deposition behavior. In addition, our data are used for comparison with computer code calculations, especially regarding sodium evaporation and aerosol mass concentration versus time.

A scheme of the facility is shown in Fig. 3. The main components are a 2.2 m^3 heated vessel, a sodium pot of 26 cm inner diameter with external heating devices (acethylene burner) to be flanged to the vessel bottom, inert gas supply, survey instrumentation, and aerosol measurement instrumentation. Presently, the aerosol instrumentation consists of washing

bottles, filters and an automatic, continuously measuring device for sodium mass concentration measurements. An Andersen impactor is used for size distribution measurements, and a Stöber centrifuge will be added in the near future. We will also add an electrostatic precipitator for electron miscroscope observations.

Five experiments were carried out until now. The main parameters and results are summarized in Tab. I. Sodium amounts of the order of 1 kg were used with fuel and fission product admixtures of 1 g or 10 g, and we studied the release into a 130°C argon atmosphere. Our iodine results are in good agreement with NALA I. The SrO release is lower, probably since we have natural instead of forced convection. The series of UO_2 experiments began with 200 µm primary particles. A very small release has been observed, which may be expressed in a retention factor of the order of 10^4. More experiments with smaller primary particles will follow.

In Fig. 4, temperature, sodium aerosol mass concentration and aerodynamic mass median diameter versus time from experiment No. 5 are presented. The corresponding diagrams for exp. 1 to 4 are similar. The duration of external pool heating is indicated. On the T(t) diagram, sodium melting and freezing may clearly be seen. The dip in the T plateau is due to a short burner failure. The aerosol mass concentration was measured by washing bottles. To avoid errors due to Na deposition between sampling port and washing bottles (which is still one of our major experimental problems), the total piping was removed after each measurement and its sodium content determined. Although heated pipes were used, corrections up to 50% occurred. After the pool heating phase, a sharp drop in the mass concentration is observed, before an exponential decrease takes over. Our Andersen impactor measurements show lognormal size distributions with d (50%) rising from initial values less than 1 µm to final values of about 2 µm which remain fairly stable. The termination of pool heating and, thus, aerosol formation, has no strong effect on the size distribution; we observe only a very weak decrease. All distributions are relatively wide, with $\sigma = (d(84\%) / d(16\%))^{1/2}$ of the order of 1.

Usually, the time dependence of the aerosol mass concentration is compared to code predictions, like, e.g., from the PARDISEKO IIIb /2/ code. In Fig. 5, a comparison between our experimental results and a first PARDISEKO calculation is shown. An initial mass distribution with d(50%) = 0.6 µm and σ = 1.1 (see chapter NALA I) and shape factors of 1 were used as input parameters. The code overpredicts the experimental results by almost a factor of 3. A major part of this discrepancy may be due to the lack of a condensation term in the code.

For LMFBR source term considerations, the sodium evaporation rate is one of the most important quantities, especially at natural convection and large temperature gradient above the pool. In our case, each experiment provides a value of the evaporation rate since the full amount of evaporating sodium is either trapped (NALA I) or deposited on the vessel walls (NALA II). In Fig. 6, our values for the specific sodium evaporation rate $\dot{m}$ from NALA I glovebox experiments and NALA II experiments are shown in comparison with the sodium vapor pressure p. A good proportionality between $\dot{m}$ and p was found, which may be expressed by the approximation

$$\dot{m}\ [\mathrm{kg\ Na\ /\ m^2 \cdot h}] \approx 0.1 \cdot p\ [\mathrm{mm\ Hg}]$$

In our laboratory scale experiments with forced convection at isothermal conditions /1/, the same relation was measured at a gas flow rate of 10 l/min.

REFERENCES

/1/ W. Schütz, Fuel and Fission Product Release and Transport from Hot Sodium Pools, Int. Meeting on Fast Reactor Safety Technology, Seattle / Wash., Aug. 1979

/2/ H. Bunz, PARDISEKO IIIb: Ein Computerprogramm zur Berechnung des Aerosolverhaltens in geschlossenen Behältern, KfK-2903, Kernforschungszentrum Karlsruhe, 1980

/3/ Private Communication from INTERATOM Company, Bensberg / Germany

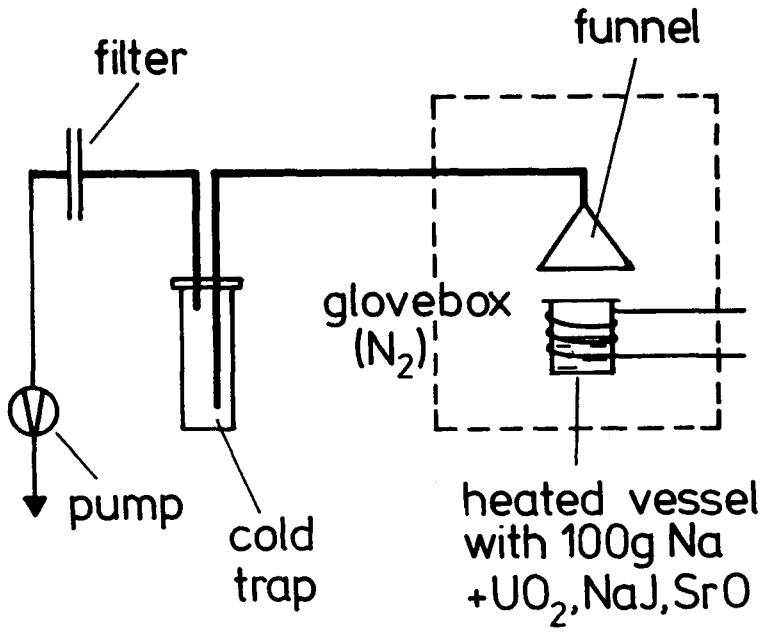

Fig. 1 The NALA I setup with open sodium vessel (7 cm diameter, 10 cm height) in a glovebox

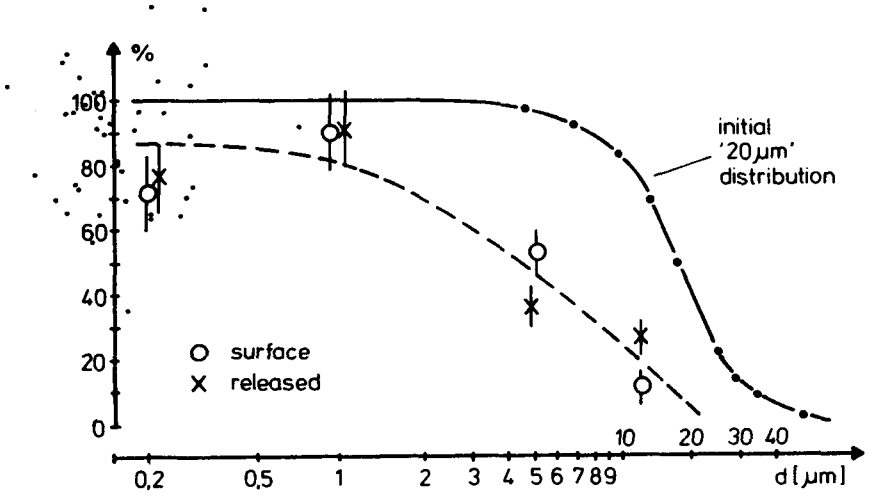

Fig. 2 Comparison of initial UO_2 particle size distribution (determined by sieving analysis) with distribution at sodium pool surface and released distribution (determined by filtration using filters of defined pore size).

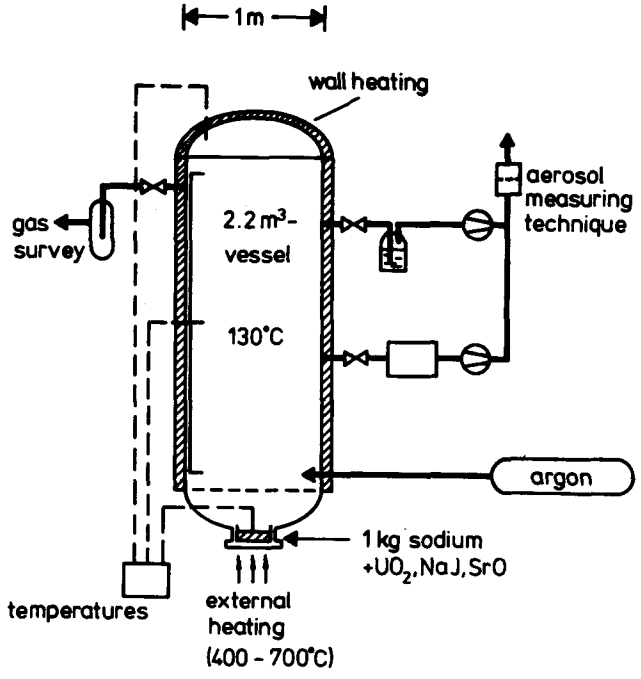

Fig. 3 Diagram of the NALA II facility

Experiment No.	1	2	3	4	5
Na [g]	258	1100	1315	1322	1146
NaJ [g]	1.00	1.06	1.00	10.0	----
SrO [g]	----	2.05	1.00	10.0	----
UO_2 [g]	----	----	----	----	10.87
particle size [µm]	----	----	----	----	180-225
average pool temp. [°C]	562	630	475	494	564
average gas temp. [°C]	130	130	130	130	135
t pool heating [min]	45	42	168	175	101
Na released [g]	82.8	125.6	22.8	44.9	113.9
RF (J)	3.97	2.97	1.11	12.1	----
RF (Sr)	----	> 50	> 4	370	----
RF (U)	----	----	----	----	10^4
Na release rate [kg $m^{-2}h^{-1}$]	2.94	4.30	0.236	0.338	1.656

Tab. I NALA II - experiments: Parameters and results

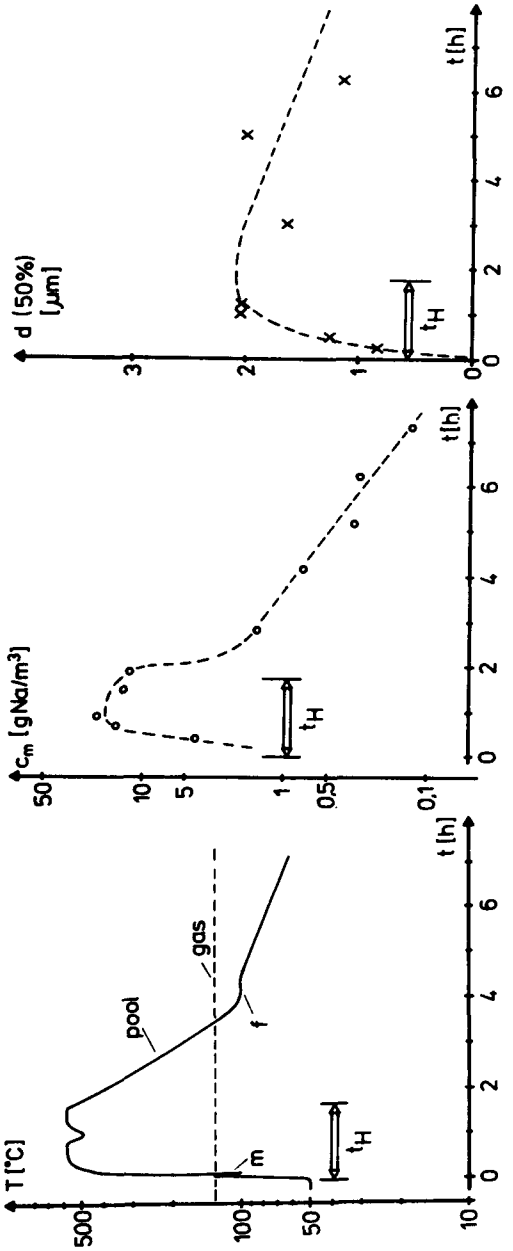

Fig. 4 Temperature, sodium aerosol mass concentration and mean particle size from NALA II experiment No. 5

t_H = time of external pool heating

m = sodium melting

f = sodium freezing

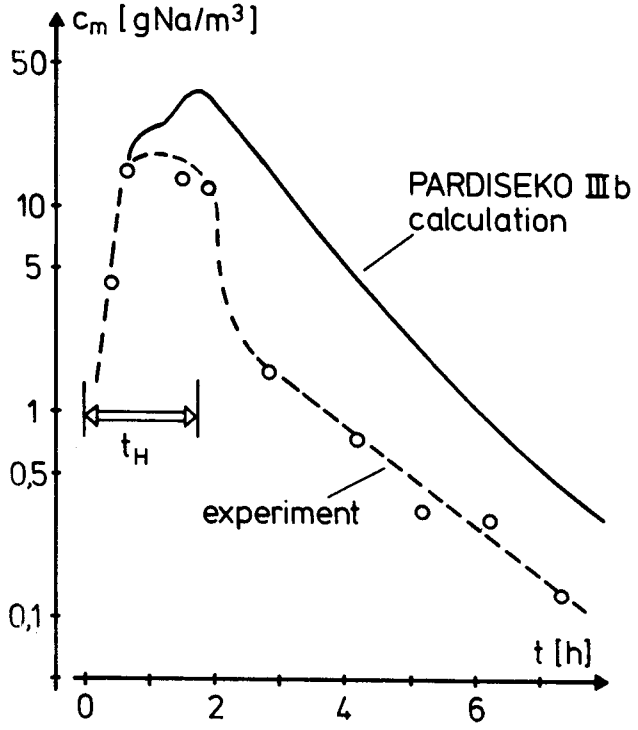

Fig. 5 Sodium aerosol mass concentration: Comparison of experiment (NALA II,No 5) and PARDISEKO IIIb calculation. Input parameters see text.

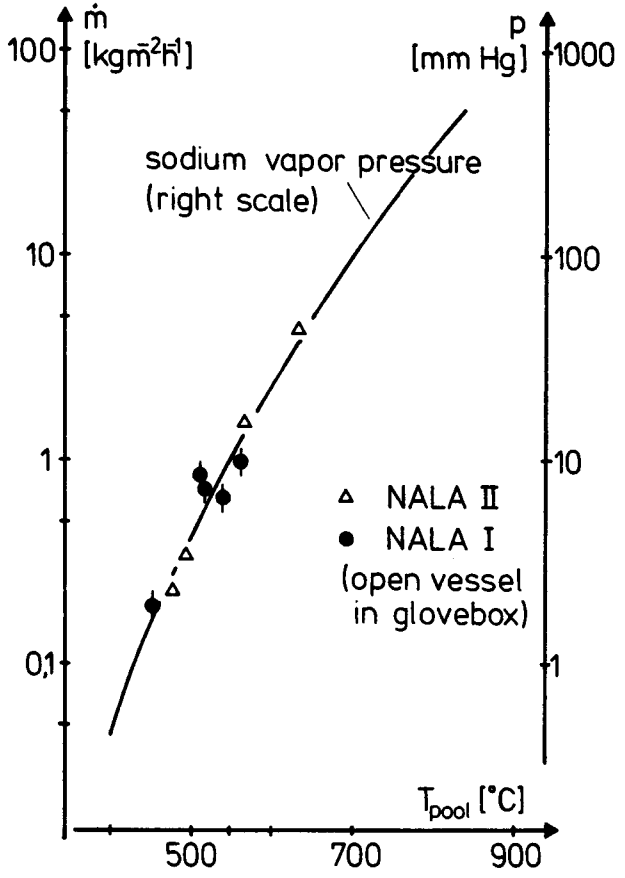

Fig. 6 Sodium evaporation rates from NALA I glovebox and NALA II experiments in comparison with sodium vapor pressure

PHYSICAL RATE PROCESSES IN CONFINED AEROSOLS

W. Stöber and G. Zebel
Fraunhofer-Institut für Toxikologie und Aerosolforschung
Münster, Federal Republic of Germany

ABSTRACT

Radioactive aerosols may come into existence as a result of a severe nuclear reactor accident. To assess the radiation hazard and to develop aerosol suppression systems, a detailed knowledge of the physical rate processes of a confined nuclear aerosol is necessary. For this reason, a theoretical model of the behavior is needed. The physical properties of the aerosol are mainly changed by Brownian and gravitational coagulation, sedimentation, diffusion and thermophoresis. There are still some open questions with regard to the influence of turbulent flow in the reactor containment and the condensation of different materials on the aerosol particles.

The non-sphericity of the coagulate particles has to be taken into account by modifying the mobility and the collision cross-section of the aggregates. For the evaluation of the plate-out mechanisms by diffusion and thermophoresis, assumptions about the boundary layer thickness have to be made.

The mathematical equations of these physical processes are given and their expected influence on the size and mass distribution as well as on the aerosol decay is discussed.

1. Introduction

As pointed out by Jordan et al. (1), a typical Light Metal Fast Breeder Reactor (LMFBR) of about 1000 megawatts operates with a fuel inventory of some 23 tons. If merely 1 % of this material evaporates in case of a nuclear accident, there will be some 230 kilograms of metal vapor distributed throughout the free space inside the containment. With a realistic assumption of about 10^5 cubic meters for the containment volume, a vapor concentration in excess of 2 grams per cubic meter is then a conservative estimate. This enormous concentration of vaporized metal would almost instantaneously condense to an extremely dense aerosol.

By comparison, a very dense fog contains little more than 1 gram per cubic meter of water in droplet form. However, while aqueous fog may be a rather stable system by mass transfer between the water droplets and the water vapor phase, a condensation aerosol from metal vapors cannot equilibrate with a vapor phase, except for very high temperatures. Thus, the dense metal condensation aerosol is inherently unstable and will age and change by physical contact processes like particle collisions. These processes are called coagulation. Coagulation changes the initial size and shape distribution of the aerosol particles. This, in turn, will influence the decay rate by which the aerosol will be lost to the containment walls due to sedimentation, diffusion, thermophoresis and other processes.

This paper will not deal with the kinetics of vapor condensation far away from thermal equilibrium. Instead, it may suffice here to note that the conditions for condensation in a hypothetical reactor accident will probably be such that an abundance of condensation nuclei is available. This will almost instantaneously produce a primary aerosol of rather small, possibly rather uniform particles. Exploding wire techniques, which most likely produce similar aerosols, give primary particle sizes near 0.03 to 0.04 μm. Kops et al. (2) found lognormal size distributions with a geometric standard deviation of 1.8. Thus, very few primary particles will exceed sizes of 0.15 μm, and at a concentration of some 2 grams per cubic meter, there should be a number concentration in excess of 4×10^9 primary particles per cubic centimeter. This is of the same order of magnitude as found for cigarette smoke leaving the tip of a cigarette during a puff drawn by a smoker.

Assuming now that an initial aerosol of this kind is present, an assessment of its future fate can be made by applying the physical laws that rule the changes of particle size distribution and number concentration. In the following chapters, this assessment will be made by considering first the various forms of coagulation of the aerosol without regard to the effects of the container walls. The wall influence and the pertinent plate-out mechanisms will be treated briefly in a subsequent chapter.

2. Aerosol Size Distribution Changes by Particle Coagulation

If wall losses may be neglected, then it can be assumed that the total mass concentration of the aerosol is conserved during coagulation, while the aerosol number concentration is decreasing if coagulates are counted as single airborne particles.

Coagulation occurs because the particles of an aerosol are in motion relative to each other. This happens for a number of reasons like Brownian motion, interacting electrical and mass forces, or other external force fields. As a consequence, random collisions will take place which, with a certain collision efficiency, will lead to a permanent aggregation of the collision partners. Counting such aggregates as new particles, this process of coagulation evidently reduces the number of particles and increases their sizes.

In mathematical terms, the equation

$$\frac{d}{dt} N_{ik} = K\ (v_i, v_k)\ n(v_k, t) \tag{1}$$

defines at some point in time t a coagulation rate at which per unit time particles of volume v_k collide with and stick to a particle of volume v_i. Consequently, this coagulation rate indicates the rate at which particles of volume v_k disappear in favor of the buildup of a particle exceeding the volume v_i. This buildup rate is proportional to the number concentration n of the particles of volume v_k at the time t under consideration. The proportionality factor K is called the coagulation kernel. In general, it is not a constant but still dependent upon the size of the collision partners, which fact will be discussed in a later section.

While Eq. (1) considers the number concentration of particles of various volume v_k with regard to collisions with one particle of a particular volume v_i, all the particles of various volume v_i must be accounted for if the net effect of all particles in a coagulating aerosol is to be represented. The integration over all the different particle volumes v_i and their number concentrations yields the integrodifferential equation

$$\frac{\partial n(v,t)}{\partial t} = \frac{1}{2} \int_0^v K(v', v - v')\ n(v', t)\ n(v - v', t)\ dv' - n(v,t) \int_0^\infty K(v, v')\ n(v', t)\ dv' \tag{2}$$

for the coagulation rate of an aerosol.

The physical significance of this equation is apparent: the first integral expresses the fact that particles of volume v can only be created by collisions between particles of sizes v' and v - v'. The factor $\frac{1}{2}$ takes care of the fact that every possible combination of v' and v - v' occurs twice in the integration. The second integral accounts simply for the fact that any coagulation involving a particle of volume v causes its disappearance from this size group.

The fundamental Eq. (2) was first derived in 1928 by Müller (3) and later corrected by Goldman (4). It has an important mathematical disadvantage: the integrands consist of the product of two variable concentrations and, thus, form non-linear expressions.

There have been numerous attempts to develop a suitable simplification. The most recent and intense effort was made by Tolfo (5) who utilizes a simple model proposed by Sutugin and Fuchs in 1970 (6). Besides his careful mathematical derivation, Tolfo also tested the quality of his approximation. It is instructive to look into the physical content of his final equations:

For practical reasons, Tolfo used a finite number p (p = 1,2 ...i) of size classes instead of a continuous size distribution:

$$\frac{dN_i}{dt} = -\sum_{j>i} K_{ij} N_i N_j - \frac{1}{2} K_{ii} N_i^2 \qquad (3)$$

$$\frac{dm_i}{dt} = \sum_{j<i} K_{ij} N_j m_j + \frac{1}{2} K_{ii} N_i m_i \qquad (4)$$

These expressions represent a system of 2 p simultaneous finite difference equations, where N_i is the number of particles in the p size groups i. The factor K_{ij} is the coagulation kernel or the frequency of effective collisions between particles of size classes i and j. Finally, m_i is the average mass of the particles in the size group i.

Then, Eq. (3) indicates that the decrease $\frac{dNi}{dt}$ of the number of particles of size class i is caused exclusively by effective collisions with particles of higher size classes. In case of collisions within the same size class the particle number will be halfed. Since the terms on the right side are all negative, the size classes can only decrease in particle numbers, which is in contrast to the exact coagulation equation.

In a similar way, Eq. (4) represents the increase of the average mass within a size group. This increase is exclusively related to effective collisions with smaller particles. In this case, by statistical assumption, one half of the collisions of the same size will remain in the original size class.

The apparent advantage of this system is the fact that a fixed set of p geometric size intervals may be used throughout the coagulation process. In contrast to this, the continuous Eq. (2) deals with individual particles and each effective collision creates a new size "class".

Figure 1 shows Tolfo's graphical comparison between the simplified and the exact model for the mass distribution of cloud droplets. For this demonstration, the coagulation was assumed to be caused by the differences in particle settling velocities. Apparently, sufficiently extended periods of coagulation do lead to considerable differences. Thus, the application of Tolfo's method has certain limitations and must be used with caution.

3. Coagulation Mechanisms

While the integration of the integro-differential equation for the coagulation rate is an inherent mathematical problem to be coped with, there remains the physical problem of formulating a proper expression for the coagulation kernel $K(v_1,v_2)$. Since coagulation is due to various physical effects, the derivation of a theoretical relationship depends, of course, on the coagulation mechanism under consideration.

3.1 Brownian Coagulation

The most obvious cause of coagulation for sufficiently small particles is Brownian motion. If particles are small enough to have reasonable residence time in the airborne state, then they may be treated like big molecules being subject to random diffusion processes. The continuum theory of diffusion in connection with Einstein's relation

$$D = BkT \tag{5}$$

between the diffusion coefficient D, the Boltzmann constant k, the absolute temperature T and the mechanical mobility B of a particle

$$B = \frac{C}{6\pi\eta r} \tag{6}$$

gives a basic expression for the coagulation kernel

$$K_o(r_1,r_2) = 4\pi\,(r_1+r_2)\,(B_1+B_2)\,kT \tag{7}$$

The zero index of K denotes that the continuum model of diffusion is the basis for this derivation. The factor C appearing in the mobility equation (6) is the so-called slip correction factor which increases from unity with decreasing particle radius r and adjusts the viscosity coefficient η of the air. The dimensionless characteristic parameter in this case is the Knudsen number

$$Kn = \frac{\lambda}{r} \tag{8}$$

which is the ratio between the mean free molecular path length λ of air and the particle radius r. Under normal brometric pressure, the slip cor-

rection will cause an additional increase of the mobility for particles below a few microns in diameter.

An estimate of K_o can easily be obtained from aerodynamic data. Under normal barometric pressure and room temperature, uniform particles of sizes r above one micron, for which the slip correction factor C may be assumed to be equal to one, give a value of $K_o(r,r) = 5.9 \times 10^{10}$ cm^3/sec.

According to Eq. (1), it will then take 4.7×10^5 particles per cm^3 to have one of them experience one collision by diffusion in one hour. Obviously, coagulation is insignificant at that point.

Besides the numerical value for K_o, an interesting general effect is predicted by the relation between r_1 and r_2 in Eq. (7): it indicates that the coagulation rate between uniform particles is always lower than for particles of different size at a given number concentration. This so-called Wiegner effect (7) is explained by the fact that the Brownian motion is more pronounced for the smaller collision partner, while the bigger one represents the target. Then, a particle of a given size will hit a bigger target faster than one of the same size. Vice versa, it will be hit faster by smaller particles than by particles of the same size.

Using the coagulation constant K_o in the integro-differential equation adds to the difficulties of an approximate solution. The first attempt to calculate the time dependency of the aerosol size distribution in a system coagulating by Brownian motion was made by Zebel in 1958 (8). However, it appears that in many practical cases, it may be sufficient to make use of a simple approximation given by Smoluchowski more than 60 years ago (9). Smoluchowski considered only the initial phase of coagulation. In this case, the size increase of the coagulates may be neglected so that the simple differential equation

$$\frac{dn}{dt} = -\frac{1}{2} K_o n^2 \qquad (9)$$

is obtained.

It may be noted here that some authors integrate the factor $\frac{1}{2}$ into the coagulation kernel. In this case, K_o will have half the numerical value as has been discussed here.

Eq. (9) can easily be integrated to

$$n = \frac{n_o}{1 + t/\tau_p} \qquad (10)$$

With n_o being the initial concentration of a mono-disperse aerosol, there will be a half-life time

$$\tau_p = \frac{2}{K_o n_o} \qquad (11)$$

A typical value of τ_p for initial concentrations of 10^6 particles/cm^3 would be little less than one hour.

Surprisingly, this simple relation is a satisfactory approximation for the coagulation of many aerosols. It is probably explained by the fact that most collisions will primarily involve the initial sizes whereas the coagulation among bigger sizes as produced by the coagulation is much slower.

So far, Brownian motion was theoretically treated as a diffusion problem in the continuous medium air and molecular kinetics entered only by way of the empirical slip factor C. If the aerosol particles are sufficiently small. the continuum model is no longer applicable for collision partners whose size is at close range with the mean free molecular path length λ in the air. Apparently, with decreasing sizes below 0.1 μm and Knudsen numbers far in excess of unit value, the coagulation kernel must approach the collision frequency between the gas molecules, which is given by the kinetic gas theory as

$$K(r,r) = 4\sqrt{2}\,\pi\, r^2\, \bar{v} \tag{12}$$

where

$$\bar{v} = \sqrt{\frac{8kT}{\pi m}} \tag{13}$$

is the expression for the mean thermal velocity of the small particles of mass m. Apparently, an appropriate correction factor β must be established which can bridge the transitional range of Knudsen numbers in excess of a value around one:

$$K(r,r) = \beta\, K_o(r,r) \tag{14}$$

There are several theoretical approaches for such a correction factor β which transforms K_o into K. Most well known is a concept first suggested by Fuchs in 1934 (10) and described in his book (11). Borrowing from kinetic models on vapor condensation, a final distance δ of the order of the mean free path length λ_p of the particles in air is used as a characteristic parameter, which determines when the theoretical approach must switch from the continuum model to a kinetic treatment of the collision problem. This leads to an expression

$$\beta_F = \frac{1}{\frac{r}{r + \delta/2} + \frac{4\sqrt{2}}{Pe}} \tag{15}$$

where

$$Pe = \frac{2\,\bar{v}\,r}{D} = \frac{16\,r}{\pi\,\lambda_p} \tag{16}$$

is the Peclet number prorating the effects of convective and diffusive

particle transfer and given here in two equivalent expressions.

It is easy to verify that for $\lambda_p << r$, as in case of the continuum regime, $K = K_o$ is obtained, while for $\lambda_p >> r$, as is the case for free molecular motion, Eq. (12) will emerge as designed.

Recently, Davies (12) rejected this mathematical model on the grounds that it relates to an equilibrizing process of condensation and evaporation, which he thinks is not appropriate for a one-way process like coagulation. Instead of Equation (15), Davies suggests a similar correction factor

$$\beta_D = \frac{1}{1 + \frac{4\sqrt{2}}{Pe} e^{-9.03Pe}} \qquad (17)$$

The derivation, however, includes some arbitrary if empirical numerical elements and must be accepted with caution. The main difference between β_F and β_D is shown in Figure 2. Both correction factors produce the same K_o- value for small Knudsen numbers, i. e. for sufficiently large particles. However, with increasing Knudsen numbers, the Davies correction preserves the classical K_o- value close to a pronounced peak around $Kn \approx 18$ before it drops to the gas kinetics value at high Knudsen numbers. The Fuchs correction peaks shallower and below $Kn = 6$. At $Kn = 20$, the difference between Fuchs' and Davies' mathematical models is of an order of magnitude. Davies claims that experimental evidence favors his solution, but it seems that more experimental investigations are needed to settle this issue. Davies has privately mentioned (13) that new experimental results will indicate that the classical K_o- value may be valid up to Knudsen numbers around 40.

3.2 Turbulent Coagulation

While coagulation by Brownian motion is exclusively caused by the thermal energy which randomly moves the air molecules and the particles, there is another type of coagulation that occurs in case of convective turbulence of the air.

Two mechanisms are to be distinguished in this case. The more important one causes collision and coagulation of two particles because the particles move with different velocities due to the spatial inhomogeneity of the turbulent flow. The other, less important mechanism provides collisions of particles of different inertia when accelerations of the turbulent air cause relative particle motions. For simplicity, Saffmann and Turner (14) excluded the latter case and derived a kernel for turbulent coagulation as

$$K_T(r_1, r_2) = 1.30 (r_1 + r_2) \sqrt{\varepsilon_o / \nu} \qquad (18)$$

under the condition

$$r^3 \sqrt{\varepsilon_o} \ll 2.5 \cdot 10^{-10} \frac{cm^4}{sec^{3/2}} \tag{19}$$

Under the root of these equations, ε_o represents the energy dissipation of the turbulent flow and ν is the kinematic viscosity of the air. Okuyama and coworkers (15) compared this equation with a more general expression in turbulent flow through cylindrical tubes. They found that as long as the parameter of Eq. (19) remains well below the numerical value given, the simple Eq. (18) gives an accurate description of the coagulation. The simplifying assumption of no inertial effects seems to be justified in this regime. However, for higher values of $r^3\sqrt{\varepsilon_o}$, Eq. (18) is no longer valid.

A particular difficulty for confined aerosols lies in the determination of the value of the energy dissipation ε_o. So far, approximations and measurements exist for tube flow only. If the heat convection is not too violent and if no special devices like fans create strong vortices, it appears that turbulent coagulation may be neglected compared to Brownian coagulation. Okuyama and coworkers showed this in their most recent experimental study (16). Apparently, gentle mixing by a fan had no influence on the coagulation process. It merely provided a homogeneous particle concentration throughout the chamber.

3.3 Gravitational Coagulation

While turbulent coagulation depends on the motion of the air and will be absent in still air, there will be gravitational coagulation whenever the aerosol particles are of sufficient size. The collisions in this case are due to different settling velocities of the particles. Therefore, gravitational coagulation is related to the aerodynamic size of the particles. The coagulation kernel is found as

$$K_S(r_1,r_2) = \pi (r_1 + r_2)^2 \varepsilon_{12} |v_{s1} - v_{s2}| \tag{20}$$

In this equation, v_{si} designates the settling velocity of a particle of radius r_i and ε_{12} represents a coefficient of capture. If the difference of the settling velocities is substantial, for instance, $v_{s1} >> v_{s2}$, and if the Stokes number

$$St = \frac{\tau v}{2 r} \tag{21}$$

with the relaxation time

$$\tau = mB \tag{22}$$

exceeds a value of 0.1, then Langmuir's expression (17)

$$\varepsilon = \frac{St^2}{(St + 0.125)^2} \tag{23}$$

may be used.

This equation does not account for the interception by the finite size of the particles. In 1974, Long (18) derived theoretical values for the kernel K_S of droplets by polynomial approximation. He gave two equations with different numerical scaling factors for sizes below and above 50 µm :

$$\begin{aligned} K_S &= 9.44 \cdot 10^9 \ (v_1^2 + v_2^2) \qquad r_1 < 50 \ \mu m \\ K_S &= 5.78 \cdot 10^3 \ (v_1^2 + v_2^2) \qquad r_2 > 50 \ \mu m \end{aligned} \tag{24}$$

3.4 Gradient Coagulation

In the absence of turbulence, another cause for coagulation in moving air may be of influence. If shear flow occurs in laminar flow, it may cause coagulation as soon as the velocity gradient across the flow is strong enough. Gradient coagulation was considered by Smoluchowski (19) who derived a coagulation kernel in this case as

$$K_G(r_1,r_2) = \frac{4}{3} \frac{\partial v}{\partial x} (r_1 + r_2)^3 \tag{25}$$

The derivation neglects the distortion of the streamlines by the approaching collision partners and it is most likely that the real K_G- value will be considerably lower.

For particles of uniform size, there is a simple expression for the ratio between gradient coagulation and Brownian coagulation. It can be given as

$$\frac{K_G}{K_B} = \frac{2 \frac{\partial v}{\partial x} r^2}{3 \pi D} \tag{26}$$

Thus, for a constant velocity gradient, the gradient coagulation increases with the square of the particle size. If the gradient is of the order of 100 sec^{-1}, the corresponding coagulation of particles of sizes of some microns may equal or exceed the coagulation by Brownian motion. Gradients of this order of magnitude may well exist in laminar boundary layers in tube flow.

3.5 Acoustic Coagulation

A review of the coagulation mechanisms would be incomplete, if the possibility of acoustic coagulation would not be mentioned. There have been many practical attempts to utilize acoustic oscillations to produce particle collisions. In the U.S., for instance, the Army and the Navy made expensive efforts during World War II to devise acoustic systems capable of precipitating fog on military air fields. However, in view of the limited practical success, most of these activities subsided when the war was over, with the possible exception of the efforts in the USSR. The war time experiences can be summarized as follows:

I. An effective acoustic coagulation requires strong sonic fields above 0.1 Watt/cm^2 corresponding to 150 dB.

II. The particle number concentration of the aerosol must be very high so that the mean distance between the particles is small. A light fog does not comply with this requirement.

III. If audible sound promises the most favorable results, then protective measures for the human ear are required.

IV. In most cases, acoustic coagulation is only an auxiliary method in conjunction with other aerosol removal techniques, e.g. filtration.

In recent years, the latter statement seemed to be subject to revision. After high-energy sirens with an acoustic efficiency of 40 to 60 % have become commercially available, acoustic coagulation may be the method of choice in many industrial fields, for instance, in dust precipitation in gas turbine power plants. The high-energy siren method has also been considered for the suppression of a sodium combustion aerosol in a hypothetical LMFBR accident (20,21).

Early theoretical approaches considered the so-called orthokinetic coagulation to be the most effective mechanism in acoustic agglomeration. The term denotes a collision of particles of different size due to their different degree of participation in the sonic vibration of the air. The ratio γ_p of the oscillation amplitude X_p of a particle to the amplitude X_g of the gas vibration is given by

$$\gamma_p = \frac{X_p}{X_g} = (1 + \omega^2\tau^2)^{-1/2} \qquad (27)$$

which equation neglects the inertia of the vibrating gas. The relaxation time τ of the particle introduces the particle size parameters {Eq.'s (6) and (22)} into Eq. (27), while ω is the circular frequency $2\pi f$ of the acoustic vibration. For a particle of unit density, a value of $\gamma_p \simeq 0.5$ will be found when the product $r^2 f$ attains a value of 20 $(\mu m)^2$ kHz. This requires a sound frequency of 20 kHz for particles of 1 μm radius or 5 kHz for particles of 2 μm radius. Then, for an optimum collision efficiency, the other collision partner should be either very much smaller so that

$\gamma_p \approx 1$ or very much bigger so that this particle would not participate in the gas vibration ($\gamma_p = 0$). Obviously, acoustic coagulation should be ineffective for mono-disperse aerosols. Furthermore, since the amplitudes X_G are proportional to the root of the sonic energy density, so should the acoustic coagulation efficiencies.

However, most of these hypotheses do not bear out experimentally. For instance, the dependency on the frequency f is less pronounced than anticipated. Furthermore, the experimentally observed acoustic coagulation of mono-disperse aerosols indicates that there are agglomeration mechanisms besides the orthokinetic coagulation mode.

In the formal equation for the kernel of acoustic coagulation

$$K_A = \pi \varepsilon (r_1 + r_2)^2 (X_{p2} - X_{p1}) f \qquad (28)$$

the collection efficiency $\varepsilon = \varepsilon(U_{rel})$ is dependent upon the relative velocity U_{rel} between the collision partners. In 1977, Shaw and his associates (22) developed a theoretical expression for this relationship. They also described experiments designed to check their theoretical derivation by using quasi-mono-disperse aerosols with a geometric standard deviation σ_g between 1.25 and 1.4 for particle radii in the range from 0.085 to 1.0 µm. Except for one siren experiment at 10 kHz, all experiments were run with loudspeakers of 1 to 3 kHz sound frequency. There was agreement with the theory for the quasi-mono-disperse aerosols and it was confirmed that audible sound would be important for the acoustic coagulation of bigger particles ($r > 0.5$ µm) while frequency changes in this range had no serious impact. From the practical point of view in industrial applications, it will be then advantageous to use low frequency sound waves because the attenuation losses will be less than for higher frequencies. In addition, the acoustic energy yield is better for the generation of low-frequency sound.

The energy consumption of the sound generator is an important parameter in acoustic coagulation. Consumption can be reduced if stationary rather than migrant waves are generated. In 1979, Rajendran et al. (22) explored this in experiments with ammonium chloride aerosols ($r_g = 0.65$ µm; $\sigma_g = 1.5$) at very high mass concentrations of 1.6 g/m^3 and frequencies between 635 and 1070 Hz. Flow-through systems and stationary systems were compared and it was found that the flow-through system reduced the acoustic turbulence, thus causing a reduction in agglomeration as well. To compensate this effect, a higher acoustic intensity than in the stationary system was required. To date, no theoretical approach has been developed for these phenomena.

4. Coagulation Kernel and Nonspherical Particles

A common simplification for all the coagulation kernels considered here is the assumption that the particles are and remain spherical. In practice, this would only be correct for droplets which on collision coalesce to bigger ones.

As the coagulation kernel for Brownian motion shows, the particle dimensions appear generally in two terms. In one term, they simply occur as the sum of the radii of the collision partners. This compounded size represents, in fact, the distance between the collision partners at the moment of contact. In other words, this term gives the radius of the effective collision cross section. It is, at least, the sum of the radii r_{vi} of the two volume equivalent spheres. But in reality, the actual value can be considerably bigger. It can be a complicated, orientation-dependent variable for irregularly shaped collision partners. In these cases, empirical collision shape factors f_c are used as corrections of a nominal cross section which is usually defined by the sum of the two volume equivalent radii

$$(r_1 + r_2) = f_c\ (r_{v1} + r_{v2}) \qquad (29)$$

For elongated and flaky collision partners, the collision shape factor f_c will be the result of an orientation-averaging process, while for isometric aggregates and particles, the factor f_c is closer related to the fluffiness of the particle configuration.

The other term in the coagulation kernel involving the dimensions of the collision partners consists of the sum of the mobilities of the particles. In this case, it is an established practice for Eq.(6) to use the volume equivalent particle radius r_v for non-spherical particles in connection with a dynamic shape factor κ which provides for the correct mobility of non-spherical particles (23).

The shape factor κ can be calculated for a number of isometric and ellipsoidal particles (24). For irregularly shaped particles it must be approximated or has to be determined experimentally. A variety of investigations for this purpose have appeared in the literature in recent years (25). Cartwright (26) and later Davies (27) have postulated that all irregular particles could be related to either prolate or oblate spheroids. For isometric aggregates, it has been shown that the dynamic shape factors may simply relate to the packing density of the aggregates (24). In view of this, it may be concluded that for isometric configurations, where the collision shape factor f_c relates to the fluffiness of the aggregates, the factor f_c should be identical with the dynamic shape factor κ, if the colliding aggregates have the same packing density. However, it may be noted that empirical experience with mathematical models for numerical calculations on confined aerosols does suggest that isometric shapes are not the prevailing types of configuration in coagulation aggregates. The model of Jordan et al. (28) gave best results for differing values of f_c

and κ. The authors used $f_c = 8.2$ and $\kappa = 3.5$ for their most representative calculations. According to Davies (25), these values would indicate elongated spheroidal shapes with axial ratios in excess of 50:1.

5. Plate-out Mechanisms

So far, no consideration was given to the fact, that the aerosol systems investigated were confined to a given volume so that the mass concentration could be assumed to remain constant. In reality, however, the aerosol system will gradually lose particles by their collision with and adhesion to the confining walls. The mechanisms providing these collisions will be discussed now.

At the outset, it is worthwhile to recall the well-known fact that, as pointed out by Fuchs (29), a temperature difference of the order of $0.01^{o}C$ in a container of linear dimensions around one meter will readily provide for convective mixing of aerosol particles up to sizes of 10 µm. Then, for all practical purposes, it is a safe assumption that aerosols inside a containment with a volume exceeding the order of cubic meters are always dispersed homogeneously by convection.

However, this homogeneity cannot be maintained in the immediate vicinity adjacent to the containment walls, because convection will diminish near the walls and an appreciable air flow component normal to the wall does no longer exist in this region. Therefore, the aerosol particles can penetrate such boundary layer only by virtue of their mobility, which will lead to their propagation due to forces of gravitational, diffusional, thermophoretic, diffusiophoretic, photophoretic and electrophoretic origin.

The driving forces for these deposition processes originate either from external influences like gravitation, light flux and electrical fields or they are generated within the boundary layer due to a gradient in temperature, or in aerosol component concentration.

The particles will then penetrate through the boundary layer with a certain velocity which, in general, depends upon the size of the particles. In case of a mono-disperse aerosol, this penetration to the wall will result in an exponential decay of the aerosol concentration in the containment. The exponent is directly proportional to the deposition rate and inversely proportional to a characteristic containment dimension, in general the ratio of the volume to the deposition surface.

5.1 Sedimentation

One of the most important plate-out mechanisms is, of course, gravitational settling. Fortunately, the theoretical aspects of this process are simple. For the size range of concern, the settling velocity can be derived from Stokes' law. By the terms utilized earlier in this paper, the sedimentation

velocity v_s is the product of the mechanical mobility and the weight of the particle. This is simply represented by

$$v_s = g\tau \tag{30}$$

the product of the gravitation g and the relaxation time τ of the particle, the latter being the product of the particle mass and its mobility in accordance with Eq. (22).

In spite of the increasing mobility with decreasing particle size, the settling velocity diminishes roughly with the square of the particle size and is generally insignificant for particles below 0.2 μm in radius.

5.2 Diffusional Deposition

In the size range below 0.5 μm, diffusion of the particles through the boundary layer will become increasingly dominant. The relation

$$j = - D \frac{\partial n}{\partial x} \tag{31}$$

gives the general equation for a diffusional flux j of particles with a diffusion constant D and a concentration gradient $\partial n/\partial x$. Assumed that all particles will stick to the wall after contacting it, then, within the boundary layer of thickness δ_v, there should be a concentration gradient diminishing from the homogeneous bulk concentration n to zero. A linear approximation gives then the gradient

$$\frac{\partial n}{\partial x} \simeq \frac{n}{\delta_v} \tag{32}$$

and since the flux j is simply the product of the particle concentration n and the diffusional velocity v_D towards the wall, the final result is

$$v_D = - \frac{D}{\delta_v} = - \frac{BkT}{\delta_v} \tag{33}$$

This equation shows that the diffusional deposition will increase with the particle mobility, which increases stronger than inversely to the particle size. Obviously, this type of deposition increases also with a diminishing boundary layer thickness δ_v. In the theory of boundary layer flow, it is shown that δ_v is not completely independent of the particle size for certain turbulent flow conditions, but in practice, δ_v is an empirical adjustment parameter, for which various experimental values have been quoted (30,31). Recent experience favors values of the order of several millimeters (32,33). A systematic study by van de Vate (34) yielded an empirical relationship

$$\delta_v = 4.6\ D^{0.265} \tag{34}$$

which is close to theoretical aspects requiring an influence by the fourth root of the particle diffusion coefficient (35).

5.3 Thermophoretic Deposition

It is next to impossible to establish truly isothermal conditions in large vessels. Therefore, heat flux to the containment walls by a temperature gradient across the boundary layer is a most common phenomenon in contained aerosols. As a consequence, the aerosol particles will be subject to thermophoresis. They move along the temperature gradient ∇T towards the colder surfaces, a process which is made use of, for instance, in thermal precipitators.

Thermophoresis has been studied theoretically by various authors like Einstein (36), Epstein (37), Derjaguin (38) and others (39). For very small and for very large particles, it appears that the thermophoretic motion is independent of the particle size, while for Knudsen numbers between 0.06 and about 2.5, there is a dependence on particle size. Brock and coworkers (40,41) developed an expression for Knudsen numbers below 0.2 as

$$F_{th}(r) = - \frac{9\pi\eta^2 r}{\rho_g} \frac{1}{1 + 3\, c_m Kn} \frac{\frac{k_g}{k_s} + C_t Kn}{1 + 2\frac{k_g}{k_s} + 2\, C_t Kn} \frac{\nabla T}{T} \qquad (35)$$

This equation postulates that the thermophoretic force F_{th} and, thus, the thermophoretic velocity

$$v_{th} = B\, F_{th} \qquad (36)$$

depends upon the gas density ρ_g, and the thermal conductivities of the gas and the particles, k_g and k_s, respectively. Furthermore, there are two empirical constants c_m and C_t involved, which have been used to fit some, but not all existing experimental data.

Recently, Prodi et al. (42) checked the Brock equation with sodium chloride particles. Figure 3 shows their experimental results in comparison to theoretical approaches in terms of thermal velocity per temperature gradient $v_{th}/\nabla T$. Curve 1 represents their experimental findings, while Curve 2 is the relationship for high Knudsen numbers derived by Waldmann (39)

$$\frac{v_{th}}{\nabla T} = \frac{3\lambda\bar{v}}{(8 + \pi\alpha)T} \qquad (37)$$

where λ is the mean free path length of the air molecules and α the fraction of air molecules reflected by the particle. Curve 3 represents the Brock equation for sodium chloride aerosols ($k_s = 1.55 \times 10^{-2}$ cal/cm sec ^{o}K) and Curve 4 is an empirical relation given by Mercer (43). It becomes apparent that the theoretical approach may need some improvement in the range of Knudsen numbers around one.

In 1975, Annis and Mason (44) derived a formulae for the thermophoretic velocity which is supposed to be valid from very small to very high Knudsen numbers :

$$V_{th} = -\frac{1}{5}\,\frac{1}{1+\frac{\pi}{8}}\,\frac{1+(1+\frac{\pi}{8})\,\frac{\Lambda}{p}}{1+(0.9+\frac{\pi}{8})\,\frac{\Lambda}{p}}\,\frac{k_g}{p}\,\nabla T \qquad (38)$$

$$\Lambda = \frac{\eta}{r}\,(\frac{\pi kT}{2m_g})^{1/2} \qquad (39)$$

The dimensionless ratio of Λ to the air pressure p rather than the Knudsen number has been used as a characteristic parameter in this approach. A comparison with experimental data up to Kn $\simeq$ 3 gave reasonable agreement although constistently elevated theoretical values are obtained for small Knudsen numbers.

5.4 Other Deposition Mechanisms

In view of the importance of sedimentation, diffusion and thermophoresis of particles for the plate-out process of enclosed aerosols, it may be permitted to consider the other physical phenomena effecting particle deposition altogether in one common paragraph. Of the remaining mechanisms, electrophoretic deposition may become of special significance in experimental arrangements involving charged aerosols and appropriate electrical fields. Otherwise, electrophoresis is no significant cause for the wall losses of contained aerosols. The same holds for photophoretic and diffusiophoretic effects, the former requiring an external light source and the latter depending upon the presence of an additional gaseous component with a gradient in partial pressxre. Enclosed systems involving water vapor represent cases where diffusiophoresis may be of special interest, particularly if heat transfer and, thus, thermal gradients are involved as well. As continuous heat source inside the containment in connection with a condensable vapor component is probably the most effective experimental arrangement to cause a fast deposition of the aerosol onto the container walls. However, under normal conditions, the contributions to the wall deposition rate of confined aerosols by electrical fields, light flux and diffusiophoresis appear to be negligable.

6. Summary

The theoretical representation of the rate processes ruling the dynamic behavior of confined aerosol meets a number of ambiguities and difficulties.

The mathematical treatment of coagulation cumulates in a highly non-linear integro-differential equation which requires numerical and approximate approaches for individual solutions. For the most important coagulation mechanism, i.e. Brownian motion, there is disagreement in literature to the extent that the corresponding coagulation kernels may differ for small sizes by an order of magnitude. No profound theoretical or experimental explorations of the influence of non-sphericity of aerosol particles or of the formation of particle aggregates on the coagulation rate are reported in the literature.

In reality, the plate-out mechanisms are cases of deposition from a stirred fluid, because thermal convection is practically inavoidable. Stirred deposition of aerosols on the container walls is mathematically well-understood and the physics of sedimentation and diffusion cause no serious problems. However, the quantitive derivation of the thermophoretic forces is still a matter of controversy and solutions found in the literature include empirical elements. Further theoretical and experimental efforts for a more detailed elucidation of the dynamic behavior of aerosols are definitely needed.

7. References

1. H. Jordan, W. Schikarski and H. Wild
Paper VII SFRP/241 of 7th International Congress "Containment of Radioactivity and the Use of Nuclear Energy", Versailles, France, May 28 - 31, 1974

2. J. A. M. M. Kops, G. Dibbets, L. Hermans and J. F. van de Vate, J. Aerosol Sci. 6, 329 (1975)

3. H. Müller, Kolloidchem. Beih. 27, 223 (1928)

4. D. E. Goldman, unpublished

5. F. Tolfo, J. Aerosol Sci. 8, 9 (1977)

6. A. G. Sutugin and N. A. Fuchs, J. Aerosol Sci. 1, 287 (1970)

7. J. Pich, in: T. T. Mercer, P. E. Morrow and W. Stöber (edit's.), Assessment of Airborne Particles, Ch. C. Thomas, Publisher, Springfield, Ill., p. 5 ff. (1972)

8. G. Zebel, Kolloid-Zeitschr. 156, 102 (1958)

9. M. v. Smoluchowski, Phys. Z. 17, 557, 585 (1916)

10. N. A. Fuchs, Z. Phys. Chem. 171A, 199 (1934)

11. N. A. Fuchs, The Mechanics of Aerosols, Pergamon Press, Oxford, p. 291 ff (1964)

12. C. N. Davies, J. Aerosol Sci. 10, 151 (1979)

13. C. N. Davies, personal communication to G. Zebel

14. P. G. Saffmann and J. S. Turner, J. Fluid Mech. 1, 16 (1956)

15. K. Okuyama, Y. Kousaka and T. Yoshida, J. Aerosol Sci. 9, 399 (1978)

16. K. Okuyama, Y. Kousaka and M. Adachi, J. Aerosol Sci. 11, 11 (1980)

17. I. Langmuir, J. Meteorol. 5, 175 (1948)

18. A. B. Long, J. Atmosph. Sci. 31, 1040 (1974)

19. M. v. Smuluchowski, Z. physik. Chem. 92, 129 (1918)

20. D. T. Shaw, Recent Developments in Aerosol Science, Wiley & Sons, New York, p. 279 ff. (1978)

21. D. T. Shaw and K. W. Tu, J. Aerosol Sci. 10, 317 (1979)

22. N. Rajendran, J. Wegrzyn, M.-T. Cheng and D. T. Shaw, J. Aerosol Sci. 10, 329 (1979)

23. W. Stöber, J. Aerosol Sci. 2, 453 (1971)

24. W. Stöber, in: T. T. Mercer, P. E. Morrow and W. Stöber (edit's.), Assessment of Airborne Particles, Ch. C. Thomas, Publisher, Springfield, Ill., p. 249 ff. (1972)

25. C. N. Davies, J. Aerosol Sci. 10, 477 (1979)

26. J. Cartwright, Ann. Occup. Hyg. 5, 163 (1962)

27. C. N. Davies, Nature 201, 905 (1964)

28. H. Jordan, W. Schikarski and H. Wild, "Nukleare Aerosole im geschlossenen System, Gesellschaft für Kernforschung Karlsruhe, Report No. KFK 1989, Oktober 1974

29. N. A. Fuchs, The Mechanics of Aerosols, Pergamon Press, Oxford, p. 250 (1964)

30. M. A. Greenfield, R. L. Koontz and D. F. Hansknecht, J. Colloid Interf. Sci. 35, 102 (1971)

31. P. J. Nolan, Proc. Roy. Irish Acad. 47A, 25 (1941)

32. J. F. van de Vate, J. Colloid Interf. Sci. 41, 194 (1972)

33. S. J. Rooker and C. N. Davies, J. Aerosol Sci. 10, 139 (1979)

34. J. F. van de Vate, to be published

35. N. A. Fuchs, Mechanics of Aerosols, Pergamon Press, Oxford, p. 267 (1964)

36. A. Einstein, Z. f. Physik 27, 1 (1924)

37. P. S. Epstein, Z. f. Physik 54, 537 (1929)

38. B. Derjaguin and Y. Yalamov, Doklad. Akad. Nauk, USSR, Phys. Chem. 155, 886 (1964)

39. L. Waldmann, Z. Naturforsch. 14a, 589 (1959)

40. J. R. Brock, J. Colloid Sci. 17, 768 (1962)
23, 448 (1967)

41. S. Jacobsen and J. R. Brock, J. Colloid Sci. 20, 544 (1965)

42. F. Prodi, G. Santachiara and V. Prodi, J. Aerosol Sci. 10, 421 (1979)

43. T. T. Mercer, Aerosol Technology in Hazard Evaluation, Academic Press, New York, p. 164 (1973)

44. B. K. Annis and E. R. Mason, J. Aerosol Sci. 6, 105 (1975)

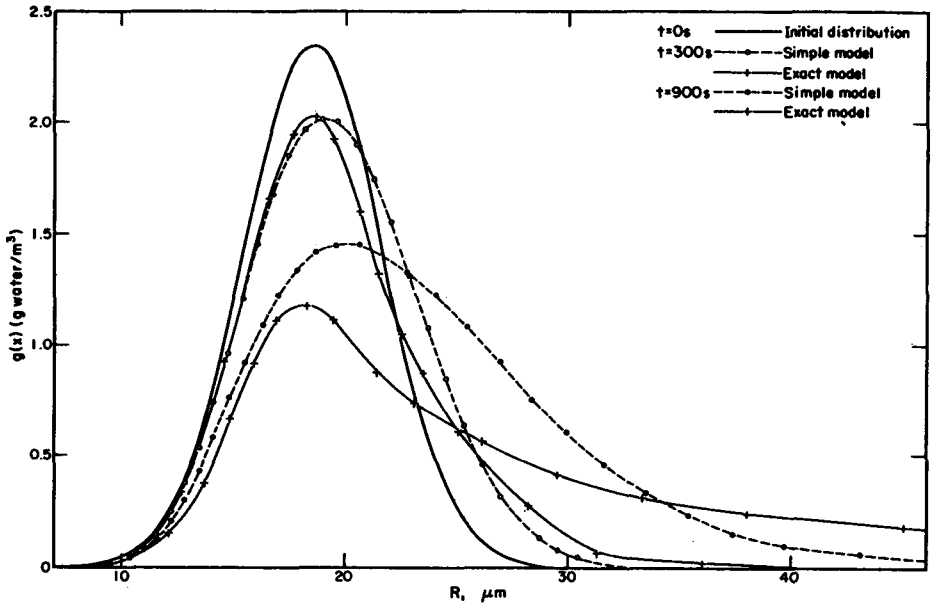

Figure 1 : Tolfo's comparison (5) between his simplified solutions for coagulation (in a maritime cloud) and the numerical solution of Eq. (2)

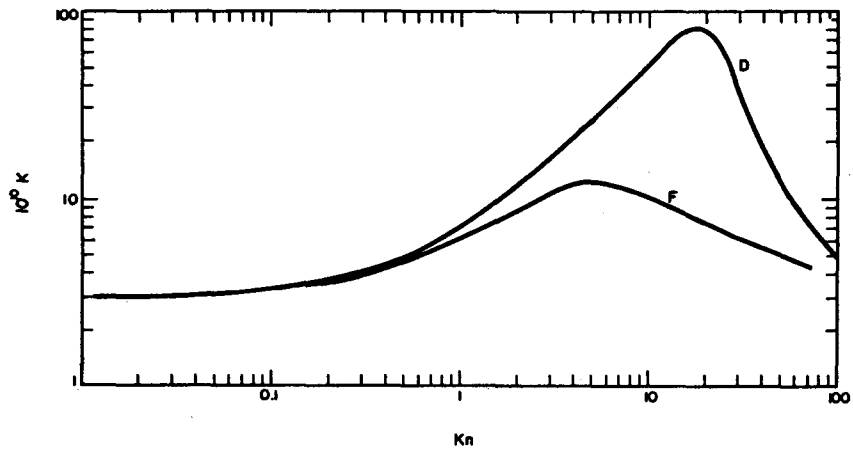

Figure 2 : Dependency of the coagulation kernel K upon the Knudsen number Kn according to the mathematical models by Fuchs (F) and Davies (D)

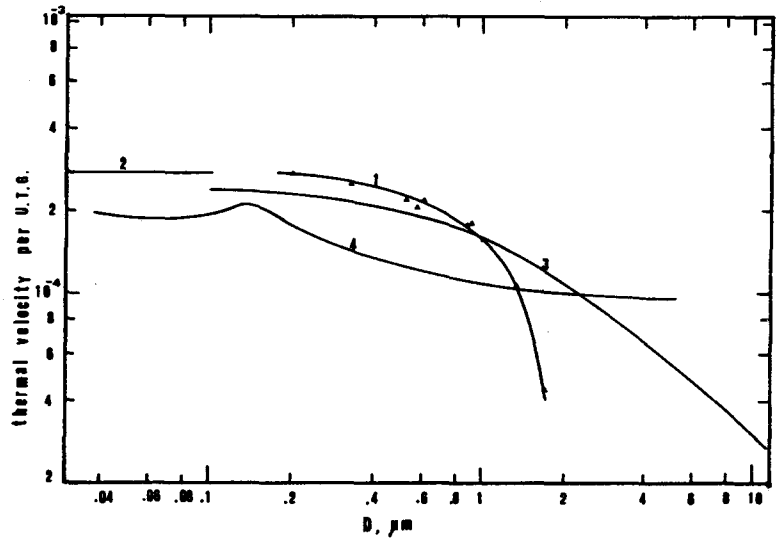

Figure 3 : Thermal velocities per unit temperature gradient as a function of particle diameter :
(1) measurements of Prodi et al.
(2) Waldmann's theory for high Knudsen numbers
(3) Brock's theory with thermal conductivity data for sodium chloride aerosols
(4) Mercer's interpretation of various empirical data

GRAVITATIONAL COLLISION EFFICIENCY OF LMFBR AEROSOLS

R. F. Tuttle and S. K. Loyalka
University of Missouri-Columbia
Nuclear Engineering Department
Columbia, Missouri 65211 USA

ABSTRACT

The development of an approach to obtain gravitational collision efficiencies for non-spherical post-HCDA LMFBR aerosols is discussed and the correct formulation of the gravitational collision kernel for non-spherical aerosols is presented. Using mass equivalent diameter as the defining length in the gravitational collision kernel, the aerodynamic shape factor, k, the density correction factor, α, and the gravitational collision shape factor, β, are used to correct the collision kernal for the case of collisions between aerosol agglomerates. A specific case of collisions between agglomerates modelled as oblate spheriods and spherical LMFBR aerosols has shown that the shape factor β needs to be investigated further if the growth in size of LMFBR aerosols due to the gravitational coagulation mechanism is to be modelled accurately. In this context, the HAARM-3 shape factors currently used to make corrections for non-spherical aerosols are briefly reviewed.

1. Introduction

In the event of a serious accident in an LMFBR, such as a Hypothetical Core Dissruptive Accident (HCDA), various materials, such as fuel, sodium, and core structural materials, may be released into the primary containment as a radioactive aerosol. Various aerosol behavior models have been developed to predict post-HCDA aerosol behavior in the containment structure [1]. These codes attempt to solve the aerosol rate equation, an integro-differential equation describing the rate of change of particle concentration due to various agglomeration and deposition mechanisms.

Since derivation of the aerosol rate equation has been adequately described in the literature [2], we do not review this derivation here. Typically, the aerosol particles are assumed to spherical in shape and the aerosol density distribution is calculated as a function of time. Particles grow in size due to collisions between different particles as predicted by the normalized collision kernel. This kernel contains three aerosol coagulation mechanisms, Brownian, gravitational and turbulent, which are assumed to be separative and additive. This allows each coagulation term to be determined separately. The validity of this assumption has not been established, but before any synergestic effects of one mechanism on another can be investigated, each of the three coagulation terms must itself be accurately defined.

Our research has been directed toward improving the analytical representation of the gravitational coagulation term. The gravitational coagulation term, $G(\eta,\xi)$, can be written as:

$$G(\eta,\xi) = \sigma_G(\eta,\xi)|V(\eta) - V(\xi)| \qquad (1)$$

where

η ~ volume of aerosol particle with terminal settling velocity of $V(\eta)$

ξ ~ volume of aerosol particle with terminal settling velocity of $V(\xi)$

$\sigma_G(\eta,\xi)$ ~ gravitational collision cross section between aerosol particles of size η and ξ undergoing gravitational motion.

Our previous work has been concentrated on developing accurate numerical formulations for the gravitational collision efficiency, ε, based on the assumption that all particles were spherical in shape. Most of our results have been published [3], but new data have become available and therefore it is appropriate to summarize our previous results. A general computer program called GCEFF was developed which allows the use of several different approximations to particle drag forces in the integration of the dynamical equation for two particle motions. It was found that

the gravitational collision efficiency is very dependent on the drag forces used in the integration of these equations. Drag forces used were the Stokes approximation, the Oseen approximation, Carrier-modified Oseen approximation and the superposition method with and without kinetic corrections to the Stokes velocity profiles. The Stokes and Oseen approximations to drag forces can lead to results for collisional efficiency that are different from each other by orders of magnitude. In this work it was also noted that the use of Oseen drag forces provide results that agree well with some atmospheric sciences data for large particles (radius $\geq$ 30μ). For smaller particles one would generally expect Stokes results to provide better agreement with experimental data, but we found that Stokes results differ from experimental data of Tu and Shaw [4] by about two orders of magnitude. The Oseen results showed at most one order of magnitude deviation for their data. Superposition results were several orders of magnitude low except when kinetic corrections were applied. The latter correction resulted in a significant improvement.

We have also recently completed some similitude experimental studies on gravitational collision efficiency for spherical particles. The detailed results are being presented elsewhere, but a major conclusion of this work has been that for particle radii > 10 μm, Carrier-modified Oseen drag forces leads to results for gravitational collision efficiency that provide reasonable agreement with the experimental data.

The simple expression used in the HAARM-3 Code is Fuch's interception approximation, which cannot correct for different density particles and shapes. Results from a sensitivity analysis of the HAARM-3 Code have shown that this model is sensitive to the gravitational collision efficiency, density correction term, and the two particle shape factors employed by the code. The influence of density is expected since we have shown that density can directly affect the collision efficiency. It is the purpose of this paper to describe our attempts at studying influence of non-spherical particles on the gravitational collision efficiency and the proper definition and determination of particle shape factors.

2. Equations of Aerosol Gravitational Coagulation

The gravitational collision cross section defined by Equation 1 can be written as:

$$G(\eta,\xi) = \sigma_G(r_{1,m},r_{2,m})|V(\eta) - V(\xi)| \tag{2}$$

$$= \pi(r_{1,m}+r_{2,m})^2\, \epsilon_n(r_{1,m},r_{2,m})|V(\eta) - V(\xi)| \tag{3}$$

where

$r_{1,m}$ = equivalent mass radius of aerosol particle of volume η

$r_{2,m}$ = equivalent mass radius of aerosol particle of volume ξ

$\epsilon_n(r_{1,m},r_{2,m})$ = non-spherical gravitational collision efficiency for particles η and ξ.

Mass equivalent radii are defined by the relationship:

$$r_{i,m} = (3\, m_i/4\pi\rho_i)^{1/3} \tag{4}$$

where m_i and ρ_i are the mass and material density of the ith particle. In the case of agglomerates, the actual agglomerate density, ρ_i', is related to the material density by:

$$\rho_i' = \alpha_i \rho_i \tag{5}$$

where α_i is called the density correction factor for the ith particle.

The terminal settling velocities, $V(\eta)$ and $V(\xi)$, of Equation 2 are related mathematically to the aerodynamic radii, $r_{i,a}$, by the formula:

$$V_{i,a} = \frac{2}{9} \frac{\rho_o}{\mu} \frac{r_{i,a}^2\, g}{\mu\, D(r_{i,a})} \tag{6}$$

where $V_{i,a}$ is the actual (measured) settling velocity, g is the gravitational constant, μ the fluid viscosity, $D(r_{i,a})$ is the corrected drag coefficient, and ρ_o is unit density.

The aerodynamic radius can be related back to the mass equivalent radius by means of Stokes settling velocity, $V_{i,s}$, which uses the volume equivalent radius, $r_{i,v}$, and the actual agglomerate density ρ_i', of the ith particle. Thus:

$$V_{i,s} = \frac{2}{9} \frac{\rho_i'\, r_{i,v}^2 g}{\mu\, D(r_{i,v})} \tag{7}$$

At this point the aerodynamic or dynamic shape factor, K_i, is defined as the ratio of the Stokes settling velocity to the aerodynamic (measured) settling velocity. Thus:

$$K_i = \frac{V_{i,s}}{V_{i,a}} = \frac{\rho_i'}{\rho_o} \left(\frac{r_{i,v}}{r_{i,a}}\right)^2 \frac{D(r_{i,a})}{D(r_{i,v})} \tag{8}$$

Referring to Equation 5, the volume equivalent radius of a sphere of the same volume as a non-spherical particle is related to the mass equivalent radius by:

$$r_{i,v} = \alpha_i^{1/3}\, r_{i,m} \tag{9}$$

Substituting Equations 8 and 9 into Equation 7 gives:

$$V_{i,a} = \frac{1}{K_i} \frac{2}{9} \frac{\alpha_i^{1/3}\, \rho_i\, r_{i,m}^2\, g}{\mu} \left(1 + C\, \lambda \frac{\alpha_i^{1/3}}{r_{i,m}}\right) \tag{10}$$

where the corrected drag coefficient, $D(r_{i,v})$, is approximated by the Cunningham correction factor, C, and the gas mean free path, λ, in the following expression:

$$D(r_{i,v}) = (1 + C \frac{\lambda}{r_{i,v}})^{-1} \tag{11}$$

Expression 3 can now be represented as:

$$G(\eta,\xi) = \pi(r_{1,m}+r_{2,m})^2 \, \varepsilon_n(r_{1,m},r_{2,m}) \cdot$$

$$\frac{2}{9}\frac{g}{\mu}\frac{\alpha_1^{1/3}\rho_1}{K_1} \left| r_{1,m}^2(1 + \frac{C\lambda\alpha_1^{1/3}}{r_{1,m}}) - \right.$$

$$\left. (\frac{\alpha_2}{\alpha_1})^{1/3}(\frac{\rho_2}{\rho_1})(\frac{K_1}{K_2}) \, r_{2,m}^2 \, (1 + \frac{C\lambda\alpha_2^{1/3}}{r_{2,m}}) \right| \tag{12}$$

This new expression has done little insofar as allowing the gravitational collision kernel to be evaluated since the non-spherical gravitation collision efficiency, ε_n, is still unknown. If one assumes that both particles of size η and ξ are spheres with radii $r_{1,m}$ and $r_{2,m}$ and that calculations give a maximum horizontal separation, y_{cs}, which determines a spherical gravitational collision efficiency, $\varepsilon_s(r_{1,m},r_{2,m})$, then ε_s is written as:

$$\varepsilon_s(r_{1,m}r_{2,m}) = (\frac{y_{cs}}{r_{1,m}+r_{2,m}})^2 \tag{13}$$

However, the nonspherical gravitational collision efficiency, ε_n, will in general differ from ε_s because the maximum horizontal separation will be influenced by the geometric projected area and hydrodynamic effects of the nonspherical particles. Equation 13 is thus written as:

$$\varepsilon_n(r_{1,m},r_{2,m}) = (\frac{y_{cn}}{r_{1,m}+r_{2,m}})^2 \tag{14}$$

From Equations 13 and 14, the gravitational collision shape factor, β, is defined:

$$\varepsilon_n(r_{1,m},r_{2,m}) = \beta \, \varepsilon_s(r_{1,m},r_{2,m}) \tag{15}$$

$$\beta = (\frac{y_{cn}}{y_{cs}})^2 \tag{16}$$

Expression 12 can now be evaluated by using our spherical collision efficiency results and a range of β values for different LMFBR aerosol particle shapes. Before discussing one method to calculate β values, the HAARM-3 expression for gravitational collision kernel will be reviewed.

Briefly, HAARM-3 expression is derived from Equation 12 by implicitly assuming:

$$\alpha_1 = \alpha_2 = \alpha$$
$$\rho_1 = \rho_2 = \rho \qquad (17)$$
$$k_1 = k_2 = k$$

These assumptions reduce Equation 12 to,

$$G(\eta,\varepsilon) = \varepsilon_n(r_{1,m},r_{2,m}) \frac{2\pi g\rho}{9\mu} [\alpha^{-1/3}(r_{1,m}+r_{2,m})^3|r_{1,m}-r_{2,m}| +$$
$$C\lambda(r_{1,m}+r_{2,m})^2|r_{1,m}-r_{2,m}| \frac{\alpha^{2/3}}{k} \qquad (18)$$

At this point HAARM-3 defines a dynamic shape factor, χ, as the square of the ratio of the volume equivalent diameter to the aerodynamic diameter (based on ρ' instead of ρ_o). Also a collision shape factor, γ, is defined as the ratio of the so called "collision diameter", d_c, to the volume equivalent diameter, d_v. It is not clear whether d_v is based on only one or both particles. The final HAARM-3 expression now becomes:

$$G(\eta,\xi) = \varepsilon_s(r_{1,m},r_{2,m}) \frac{2}{9} \frac{\pi g\rho}{\mu} [\alpha^{-1/3}(r_{1,m}+r_{2,m})^3|r_{1,m}-r_{2,m}| +$$
$$c\lambda(r_{1,m}+r_{2,m})^2|r_{1,m}-r_{2,m}|] \frac{\lambda^2}{\chi} \qquad (19)$$

It needs to be emphasized that all the shape factors except β are for individual particles. The assumptions made to derive Equation 18 are questionable and the introduction of χ and especially γ to Equation 18 lacks theoretical basis in view of their defining relationships and the final HAARM-3 expression. It appears that γ tries to represent the same quantity as β does but it is not clear how γ would be calculated or determined experimentally.

We plan to provide insights into the nature of β for irregularly shaped aerosols by first considering the case of oblate spheriods of different axis ratios. Besides providing a suitable coordinate system, an oblate spheriod of varying axis ratio will provide a general family of possible aerosol shapes by which the collision process can be studied. It is hoped that the methods developed in this research will provide the

basis needed to study more complex shapes.

Using oblate spheroidal coordinate systems (ξ,η,ϕ) described by Happel and Brenner [5], the Navier-Stokes equation can be written as:

$$E^2 G = \frac{\text{sech } \xi_o \text{ Re}}{2} \left[\frac{\cosh \xi \sin\eta}{\sinh^2\xi + \cos^2\eta}\right] J_{\xi,\eta}(\psi,F) \tag{20}$$

and

$$E^2\psi = G \text{ sech}^2 \xi_o \tag{21}$$

where J is the Jacobian, Re is the Reynolds number, ψ is the stream function, G and F are two modified vorticity functions of vorticity, ω, defined by:

$$G = \frac{\omega \cosh\xi \sin\eta}{\cosh\xi_o} \tag{22}$$

$$F = \frac{\omega \cosh \xi_o}{\cosh\xi \sin\eta} \tag{23}$$

and E^2 is an operator defined as:

$$E^2 = \frac{1}{\sinh^2\xi+\cos^2\eta} \left[\frac{\partial^2}{\partial\xi^2} - \tanh\xi \frac{\partial}{\partial\xi} + \frac{\partial^2}{\partial\eta^2} - \cot\eta \frac{\partial}{\partial\eta}\right] \tag{24}$$

The oblate spheroidal coordinates have the ranges:

$$0 \leq \xi \leq \infty, \quad 0 \leq \eta \leq \pi, \quad 0 \leq \phi < 2\pi \tag{25}$$

The solution to Equation 20 and 21 will be discussed in Section 3.

Derivation of the equations of motion for two interacting particles has been discussed in the literature [6,7]. We find it convenient to cast the equations in the form:

$$\frac{dU_1}{dt} = \frac{z^*}{Stk} \left(\frac{1}{1-o/\rho_1} - F_{1x}\right) \tag{26}$$

$$\frac{dV_1}{dt} = \frac{z^*}{Stk} \left(- F_{1y}\right) \tag{27}$$

$$\frac{dU_2}{dt} = \frac{z^*}{Stk} \left(\frac{1}{1-o/\rho_1} - \left(\frac{\rho_1}{\rho_2}\right) \left(\frac{1}{a^*}\right)^3 \text{AR } F_{2x}\right) \tag{28}$$

$$\frac{dV_2}{dt} = \frac{z^*}{Stk} \left(- (\rho_1/\rho_2) \left(\frac{1}{a^*}\right)^3 AR\ F_{2y}\right) \tag{29}$$

$$\frac{dy}{dt} = U_2 - U_1 \tag{30}$$

$$\frac{dy}{dt} = V_2 - V_1 \tag{31}$$

where:

U_i ~ nondimensional vertical velocity of ith particle, i = 1,2.

V_i ~ nondimensional horizontal velocity of ith particle, i = 1,2.

F_{iz} ~ nondimensional z-direction drag force of ith particle, i = 1,2.

F_{ip} ~ nondimensional -direction drag force of ith particle, i = 1,2.

ρ_i ~ density of the ith particle, i = 1,2.

ρ ~ density of the viscous fluid.

AR ~ axis ratio of oblate spheroid.

a^* ~ ratio of the radius of the sphere to the semi-major axis, a_1, of the oblate spheroid.

z^* ~ nondimensional parameter defined by

$$a^{*4}\left(\frac{\rho_2}{\rho_1}\right)^2 \left(\frac{1 - \rho/\rho_2}{1 - \rho/\rho_1}\right)$$

Stk ~ Stokes number defined by

$$\frac{U_{\infty 1}^2 a^{*4}}{g\ a_1} \left(\frac{\rho_2}{\rho_1}\right)^2 \frac{(1 - \rho/\rho_2)}{(1 - \rho/\rho_1)^2} .$$

Velocity was nondimensionalized with respect to the terminal settling velocity of the oblate spheroid, length with respect to the semi-major axis of the spheroid, and time with respect to both the velocity and

semi-major axis of the spheroid. Also, force terms are:

$$F^*_{ij} = K\, F_{ij},\ i = 1,2;\ j = z, \tag{32}$$

where

$$K = \frac{4}{3}\,\pi\, g a_1^3\, AR(\rho_1 - \rho) \tag{33}$$

When applying the superposition technique, force terms become:

$$\begin{aligned} F_{1x} &= U_1 - U_{2F} \\ F_{1y} &= V_1 - V_{2F} \\ F_{2x} &= U_2 - U_{1F} \\ F_{2y} &= V_2 - V_{1F} \end{aligned} \tag{34}$$

where U_{iF} and V_{iF} are velocities of the fluid due to the motion of the ith particle, i = 1,2.

Flow fields around the oblate spheroid and the sphere are converted to cylindrical coordinates by applying the transformation from oblate spheroidal to cylindrical coordinates. Similar transformations exist for the spherical case. However, in the limit as the axis rates approach one, the spheroid becomes a sphere. For this problem it was found that an axis ratio equal to 0.999 approximates the flow field for creeping motion around a sphere.

3. Method of Solution

A variety of numerical methods are available to solve the equations in Section 2. Currently there exists no analytical solution to Equations 20 and 21 and so it becomes necessary to solve them numerically. The approach being used involves a finite difference scheme [8].

The method currently being used to evaluate the partial derivatives in the transformations for velocity profiles involves cubic spline interpolating polynomials followed by differentiation of the interpolating polynomical for a particular interval. Two IMSL routines were selected but one had to be modified to handle the differentiation of the splines. End point conditions were chosen by applying forward and backward difference procedures. The indeterminant result at η=0 was easily calculated by applying L'Hospital rule to Gregory-Newton extrapolation formulas. This technique resulted in errors of less than

10^{-4} when compared with Oberbeck's solution as given by Happel and Brenner [5].

The solution to the set of six nondimensional equations (Equations 26-31) require that a numerical scheme be used. The solution of the six equations yields the aerosol particle trajectories and the particle-particle grazing collision condition can be determined from these trajectories. The integration schemes currently being applied are HPCG found in the IBM System/360 Scientific Subroutine Package and the IMSL routine called DGEAR. The HPCG program uses Hamming's predictor-corrector-modified method with a Runge-Kutta routine to start the integration. Because the six equations of aerosol particle motion exhibit the mathematical property of stiffness for small aerosol particles, the integration routine HPCG was replaced by DGEAR, a routine based on Gear's method [9].

4. Preliminary Results

To verify computer routines written to calculate ε_n, the results of the present research was compared to the work of atmospheric sciences and the experimental data. The theoretical results of Pitter [11] corresponding to the conditions:

$$\mu_{air} = 1.667 \times 10^{-4} \text{ P}$$

$$\rho_{air} = 9.267 \times 10^{-4} \text{ gm/cm}^3$$

$$\rho_{sphere} = 1.00 \text{ gm/cm}^3$$

$$\rho_{oblate} = 0.92 \text{ gm/cm}^3$$

were compared for oblate spheroids with a semi-major axis equal to 160μm and axis ratio of 0.05. Collision efficiencies with spherical particle radii equal 16.0, 17.0, 18.0 and 19.0 μm were found to agree with those of Pitter. We also verified the fact that water spheres of certain sizes were found which could not collide inside of some inner critical offset, y_{min}, where $y_{min} < y_{cn}$. The collision domain can be pictured as a circular annulus of radii y_{min} and y_{cn} instead of the typical flared cylinder.

Collision efficiencies ε_n for sodium particles simulated as oblate spheroid with semi-major axis lengths of 39, 66 and 120 μm with material density of 2.27 gm/cm^3 were calculated for collisions within spheroid sodium particles with radii 5, 10 and 15 μm. In all cases ε_n was found to be zero. This result is supported by the observations of Pitter and Pruppacher [12] who have reported that similar results were found for the rimming process between ice crystals and water drops. The latter authors show a minimum spheroid size exists below which an oblate

spheriod will not be able to collect any size water spheres. They place this minimum size between 147 and 160 μm for the semi-major axis (AR = 0.05). The field observations of Wilkins and Auer [13] and Ono [14] found that simple hexagonal plates of ice had to be larger than 150 μm radius in order to be able to collide with drops.

These results are important since a similar process may be taking place for sodium aerosol particles and thus the factor β in Equation 12 would have a significant influence on the gravitational collision kernel term.

We plan future computer experiments to better define β for other densities, axis ratios, and semi-major axis. Experimental verification of these results would also appear to be of considerable importance.

References

[1] Numerous aerosol behavior code have been reported. We list here several:

(a) Gieseke, J. A., K.W. Lee, and L.D. Reed, "HAARM-3 Users Manual," BMI-NUREG-1991 (1978).

(b) Jordan, H. and C. Sack, "A Computer Code for Determining the Behavior of Contained Nuclear Aerosols (PARDISEKO-III)," KFK2151 (1975).

(c) Lindaner, G.D. and A.J. Castleman, Jr., "The Importance of Gravitational Coagulation on the Settling of High Mass Density Aerosols," Nucl. Sci. Engr., 42, p. 58, (1970).

[2] The aerosol behavior equation has been discussed in several books:

(a) Fuchs, N., The Mechanics of Aerosols, Pergamon (1964).

(b) Hidy, G.M. and J.R. Brock, The Dynamics of Aerocolloidal Systems, Pergamon (1971).

(c) Pruppacher, J.R. and J.D. Klett, Microsphysics of Clouds and Precipitation, Reidel (1978).

(d) Friedlander, J., Smoke, Dust and Haze, Wiley-Interscience (1977).

[3] Pertmer, G.A. and S.K. Loyalka, "Gravitational Collision Frequency of Post Hypothetical Core Disruptive Accident Liquid-Metal Fast Breeder Reactor Aerosols: Spherical Particles," Nucl. Technol., 47, p. 70, (1980).

[4] Tu, K.W. and D.T. Shaw, "Experimental Determination of Interception Collection Efficiencies for Small Cloud Droplets," J. Colloid Interface Sci., 62, p. 40, (1977).

[5] Happel, J. and H. Brenner, Low Reynolds Number Hydrodynamics, Englewood, Cliffs, N.J., Prentice Hall, Inc., (1965).

[6] Shafrir, U. and M. Neiburger, "Collision Efficiencies of Two Spheres Falling in a Viscous Medium," J. Geophys. Res., 6, p. 4141, (1963).

[7] Shafrir, U. and T. Gal-Chen, "A Numerical Study of Collision Efficiencies and Coalescence Parameters for Droplet Pairs with Radii up to 300 Microns," J. Atmos. Sci., 31, p. 741, (1971).

[8] Pitter, R.L., H.R. Pruppacher, and A.E. Hamielec, "A Numerical Study of Viscous Flow Past A Thin Oblate Spheroid at Low and Intermediate Reynolds Numbers," J. Atmos. Sci., 30, p. 125, (1973).

[9] Gear, C.W., Numerical Initial Value Problems in Ordinary Differential Equations, Prentice-Hall (1971).

[10] Pertmer, G.A., "Gravitational Agglomeration of Post-HCDA LMFBR Aerosols," Ph.D. Dissertation, University of Missouri, Columbia, Missouri (1978).

[11] Pitter, R.L., "An Experimental and Numerical Investigation of the Evolution of Ice Particles In Atmospheric Clouds," Dissertation, UCLA (1973).

[12] Pitter, R.L. and H.R. Pruppacher, "A Numerical Investigation of Collision Efficiencies of Simple Ice Plates Colliding with Supercooled Water Drops," J. Atmos. Sci., 31, p. 551, (1974).

[13] Wilkins, R.L. and A.H. Auer, "Rimming Properties of Hexagonal Ice Crystals," Preprints, Conf. Cloud Physics, Fort Collins, Colo., American Meteor. Soc., p. 81, (1970).

[14] Ono, A., "The Shape and Rimming Properties of Ice Crystals in Natural Clouds," J. Atmos. Sci., 26, p. 138, (1969).

DETERMINATION OF SODIUM FIRE AEROSOL PROCESS COEFFICIENTS FROM FAUNA-EXPERIMENTS

W. Cherdron, S. Jordan
Laboratory for Aerosol Physics and Filter Technology
Kernforschungszentrum Karlsruhe, FRG

ABSTRACT

In the containment of the FAUNA facility large sodium fires were performed and the time dependent behavior of the aerosols during and after the fire was investigated.

One of the main objectives of three sodium fire experiments was to verify calculations with the aerosol code PARDISEKO IIIb.

In dynamic experiments the size of different aged sodium fire aerosols were measured by different methods. 10-30 seconds old aerosols were found to have a mass median diameter of about 0.9 µm with log-normal distribution. The median aerodynamic diameter and the mass equivalent diameter of aerosols were measured during the fire tests. χ was measured during different time of the test and found to be 1.1 at the beginning of the fire.

The course of the sodium mass concentration was recalculated with PARDISEKO for a 2 and a 12 m² sodium fire test. The coagulation shape factor f, which takes into account the nonsphericity of particles in the coagulation process, was determined by parameter fitting.

The course of the aerosol mass concentration during and after a 2 m² and a 12 m² sodium fire in the FAUNA containment was recalculated with PARDISEKO. Good agreement with experimental data was in particular found in the long term region.

INTRODUCTION

The behavior of sodium fire aerosols in large containments is of great importance for estimating the environmental impact of accidents in sodium cooled fast breeder reactors. Major spills of hot sodium may occur by leaking pipes or core disruptive accidents resulting in large amounts of sodium fire aerosols released into the containment.

In the containment of the FAUNA test facility [1] large sodium fire tests were performed and the time dependent behavior of the aerosols during and after the fire were investigated.

One of the main objectives of three sodium pool fire experiments was to verify the calculations with the PARDISEKO IIIb aerosol code [2] . Therefore, input data for the code were measured either during the sodium fire tests or in separate experiments.

PARDISEKO IIIb recalculates the course of the aerosol mass concentration during and after a sodium fire. The code takes into account the aerosol processes of coagulation, sedimentation, thermophoresis and diffusion and is based on the numerical solution of the resulting integral differential equation system.

The input parameters for the code can be subdivided into three groups

- Parameters for controlling the program.
- Containment specific data.
- Aerosol physical data.

Especially the aerosol data were determined during the FAUNA sodium fire tests but also in separate dynamic experiments.

Here the measurement of the geometric radius of primary particles including the standard deviation, the density of particle material and the concentration of particle numbers are of great importance for accurate calculations.

The PARDISEKO IIIb code system takes into account the mobility of non-spherical particles by the dynamic shape factor χ which can be determined from the ratio of the aerodynamic diameter and the mass equivalent diameter. Both diameters can be derived from measured aerosol data.

The coagulation shape factor f, which takes into account the non-sphericity of particles in the coagulation process, can be determined by parameter fitting and comparison of the calculated and measured decrease of aerosol concentration after a sodium fire in a containment.

EXPERIMENTS AND DISCUSSION

In an open gas loop consisting of a blower and a continuously and nearly constant burning spray fire, sodium particles of definite age were analyzed. The size distribution of 10 seconds old primary particles was measured with an aerosol centrifuge. The aerodynamic mass median diameter was found to be 0.89 µm. The distribution was definite log normal, the standard deviation $\sigma = 1.4$ can be seen from Fig. 1 [3] . From the electron microscope photographs (Fig. 2) of these particles it can be derived that the shape of the particles differs not too much from spheres. In nearly all simultaneous measurements of aerodynamic and the derived volumetric diameters the aerodynamic diameter was found to be equal to or greater than the volumetric diameter. This means that the particle density must be equal to the material density or smaller. The density of deposited particles was determined by a pycnometer to be 1.76 g/cm³ instead of the material density of 2.80 for Na_2O_2.

The dynamic shape factor was determined from the aerodynamic and volumetric diamter using formulae derived by [4] and [5] and was found to be 1.1.

PARDISEKO calculations were made with $\chi = 1.1$ and with a primary particle diameter $d_{50} = 0.89$ µm.

The course of the aerosol mass concentration during and after three sodium pool fires F1 - F3 was recalculated with PARDISEKO.

First some information on the pool fires themselves. Different quantities of hot sodium were released into differently sized burning pans (2 and 12 m²). In the reaction vessel (220 m³) the pressure and oxygen content were kept constant during experiment. The airborne reaction products were found to be 100% Na_2O_2. The reaction product in the pan was Na_2O_2 and Na_2O in a ratio of 40 : 60.

Test data and some major results have been compiled in Table 1.

The temperature gradients in the reaction vessel were measured with particular accuracy because of their importance for theoretical recalculations. Fig. 3 shows the course of the temperature profile with the time at different places of the vessel level in the reaction vessel for the experiments F1 and F3. The temperature gradient in the reaction vessel during the fire is higher for smaller burning areas in the center of the diameter (F1). The temperature gradients decrease substantially when the burning area covers nearly the whole cross-section of the reactor (F3). Therefore, for theoretical recalculations it seems necessary to take into account these temperature gradients. In the test F3 temperatures up to 650°C were measured 4 m above the burning pan. Sodium fire codes (SOFIRE II) underestimate these values substantially [6] . The course of the aerosol mass concentration during and after the sodium fire is of great importance for the layout of reactor safety components. Therefore, the sodium mass concentration was measured continuously with a high accuracy (± 5%) over several days after the fire. Fig. 4 shows the decreasing aerosol mass concentration with the time after tests F1, F2 and F3. The development of the concentration after test 1 and test 2 - using the same burning pan - was nearly identical. During the test 3 (12 m² burning pan) a higher concentration was measured. Immediately after the fire a faster decrease of concentration was observed than after test 1 and 2.

The course of airborne mass concentration was recalculated by the PARDISEKO IIIb code using the input data mentioned above (d_{50} = 0.89 µm, σ_g = 1.1). In the Fig. 5 the calculated aerosol mass concentration during and after F1 is shown for different f-values between 4 and 8, with and without gravitational coagulation. As can be seen, the calculations overestimate the course of mass concentration during the fire but the decrease of aerosol concentration after the fire is calculated fairly well. The influence of gravitational coagulation is low. In particular during the fire the code overestimates the concentration by a factor up to 3.

Excellent agreement between the calculation and measured curves can be reached by recalculations, starting with the calculation at the end of the fire, in our case after 2 hours, and using the particle diameter measured at that time.

Fig. 6 shows a PARDISEKO calculation for the experiment F3, using the same aerosol input data as in the previous figure. Here also the disagreement between both curves is greatest during the fire in the first two hours. Here the concentration is mainly determined by the particle release function of the aerosol source. The particle source term was determined from the measured overall sodium mass released into the vessel and the sodium remaining in the burning pan. The release function was adjusted to the sodium temperature during the fire. For FAUNA 3 the measured sodium mass released was extremely high (40%) which greatly influences the calculations.

For the release of high aerosol concentrations from particle sources it probably cannot be assumed that the aerosols are uniformly mixed in the whole vessel. There is probably a substantial concentration gradient between the source and the containment walls. Coagulation and sedimentation are probably much higher just above the pan than calculated. This reduces the aerosol mass released into the containment.

Fig. 7 represents the variation with the time of the mass median diameters calculated with PARDISEKO for the FAUNA 2 experiment, as compared with diameters measured either with the impactor or the centrifuge. Although both devices measure the aerodynamic diameter, there is a relative good agreement between measured and calculated values.

CONCLUSIONS

- The dynamic shape factor was determined for primary sodium fire particles by dynamic experiments and found to be $\chi = 1.1$.

- FAUNA-experiments can be recalculated with the PARDISEKO IIIb aerosol code using the shape factors $\chi = 1.1$ and $f = 4$. During the fire the code overestimates by a factor 4 the mass concentration for relatively small fires and by a factor 10 for large fires.

- For extremely high aerosol release rates, deposition processes near the source should be taken into account.

- The measured steep decrease of mass concentration for a period shortly after the fire might be caused by deposition processes from tubulences.

- The influence of gravitational coagulation on the calculated decrease in concentration is relatively small.

REFERENCES

[1] A. Alexas, W. Cherdron, S. Jordan, W. Lindner, W. Schikarski: Sodium Fire Aerosol Experimental and Analytical Results - Large Scale Tests in FAUNA, ANS/ENS Int. Meeting on Fast Reactor Safety Technology, Seattle, August 19-23, 1979

[2] H. Bunz: PARDISEKO IIIb - Ein Computerprogramm zur Berechnung des Aerosolverhaltens in geschlossenen Behältern, KfK-2903

[3] Ch. Hofmann, S. Jordan, W. Lindner: Reaktionen von Natriumbrand-aerosolen in der Atmosphäre, Jahrestagung der GAF, 26.-28.9.1978, Wien

[4] J.F. van de Vate et al.: Aerodynamic Properties of Aerosols and their Leakage through Concrete Containment Structures ANS/ENS Int. Meeting on Fast Reactor Safety Technology, Seattle, August 19-23, 1979

[5] W. Stöber, H. Flachsbart, D. Hochrainer: Der aerodynamische Durchmesser von Latexaggregaten und Asbestfasern, Staub-Reinhalt. Luft 30 (1970), 217-316

[6] A. Alexas: Entwicklung eines Rechencodes zur Beschreibung von Na-Spritz- und Flächenbränden
I: Die Codes SOFIRE II und NABRAND im Vergleich, KfK-2824

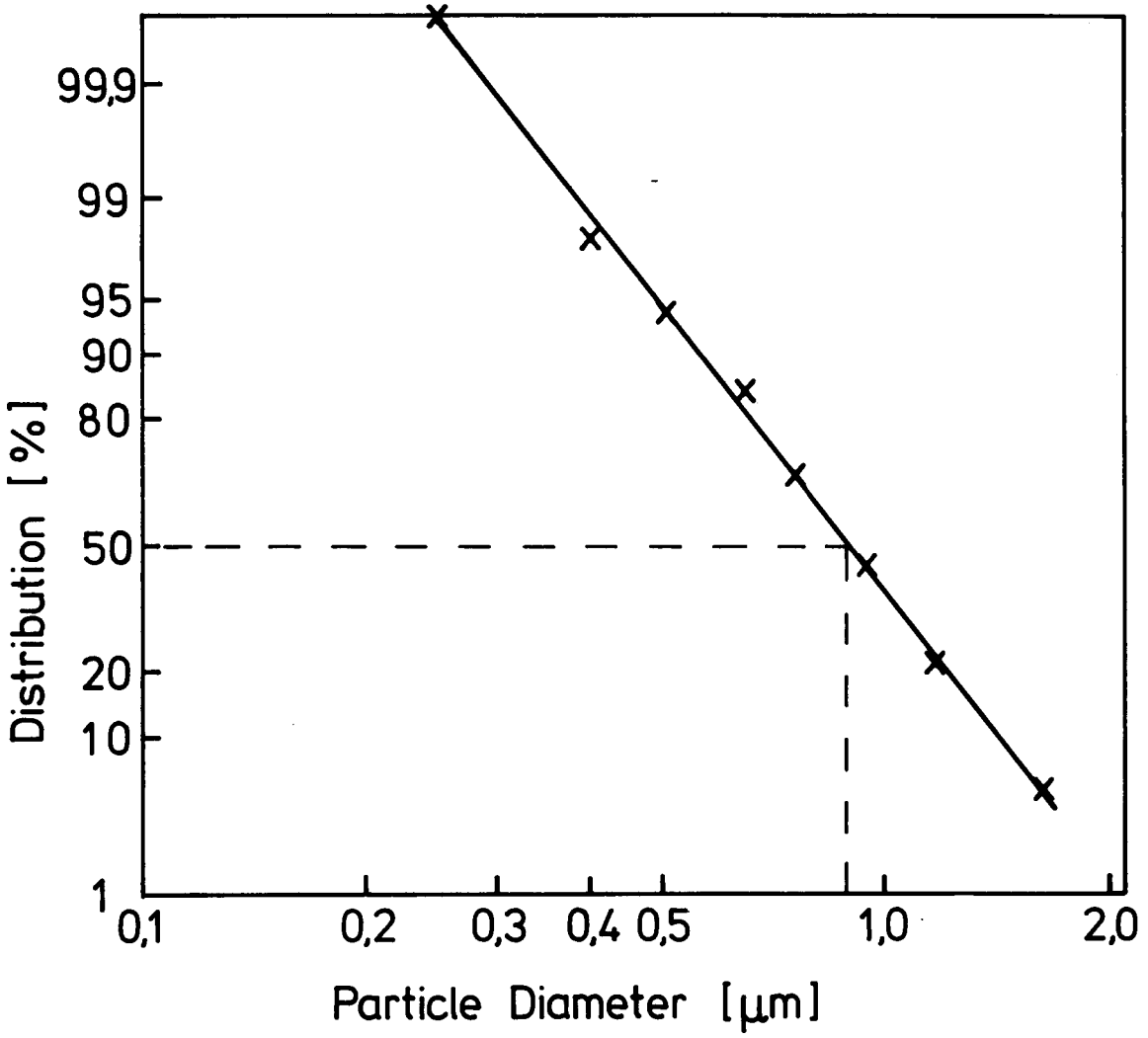

Fig. 1: Primary Sodium Fire Aerosol

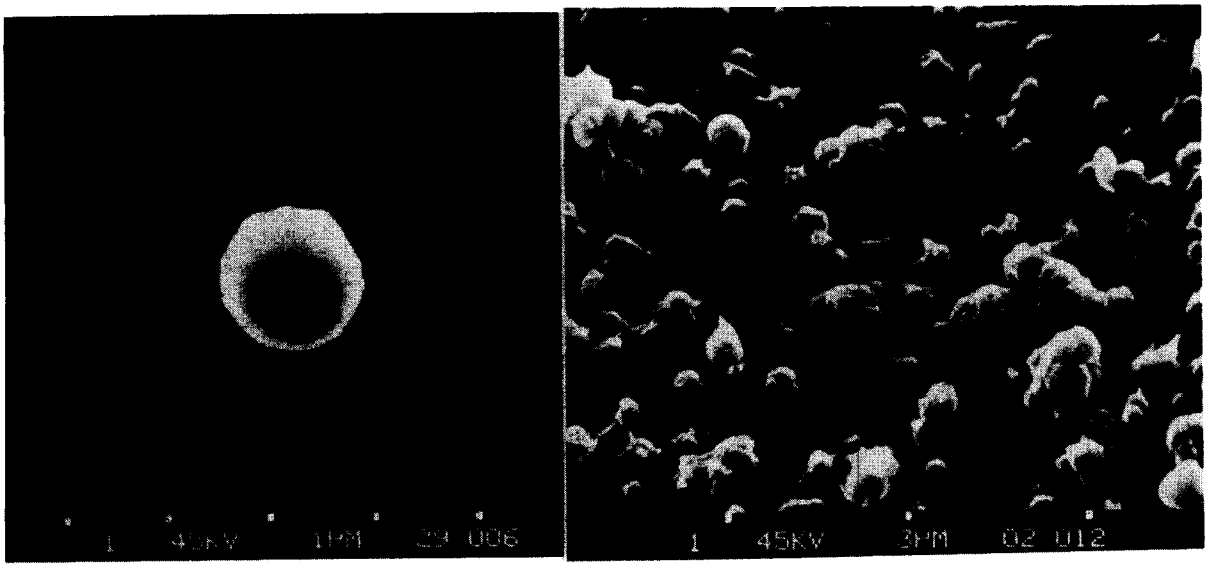

Fig. 2: Sodium Fire Particles

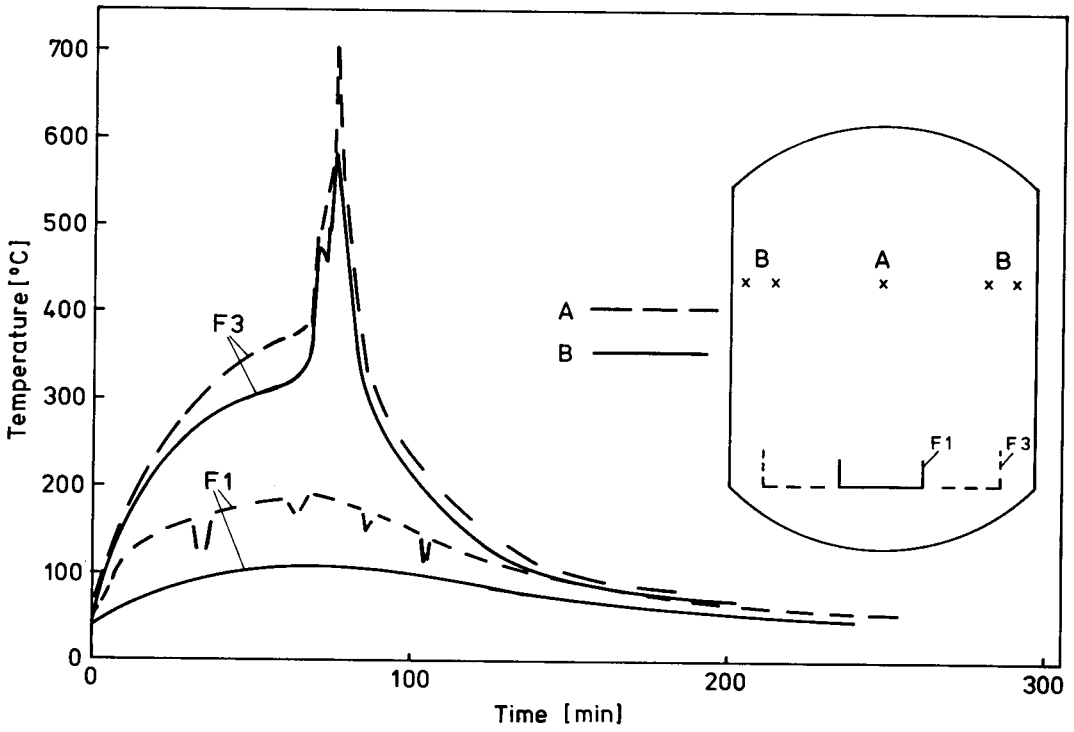

Fig. 3: Temperature in the FAUNA-Containment during Pool Fires

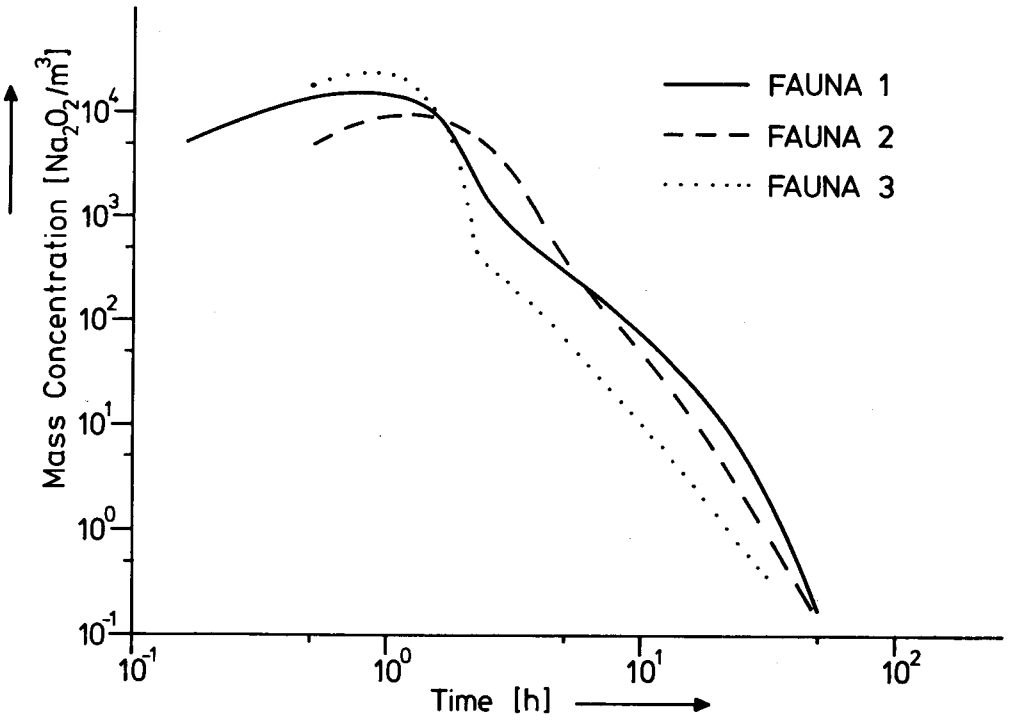

Fig. 4: Aerosol Mass Concentration after Sodium Pool Fires

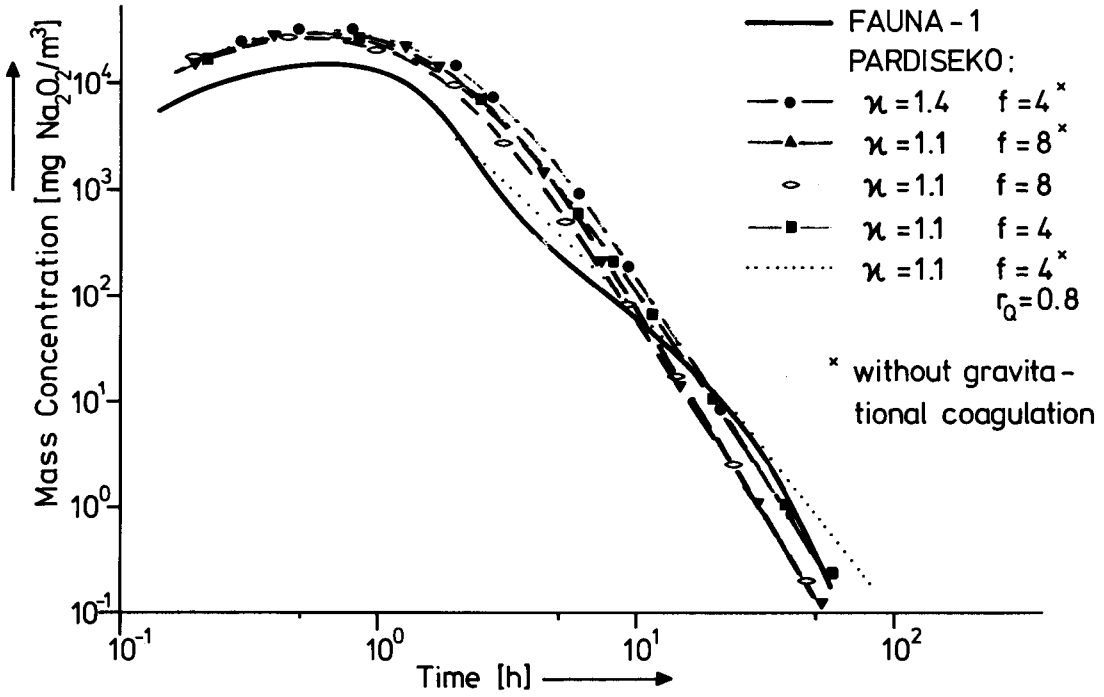

Fig. 5: PARDISEKO IIIb Recalculations of FAUNA-1 Experiment

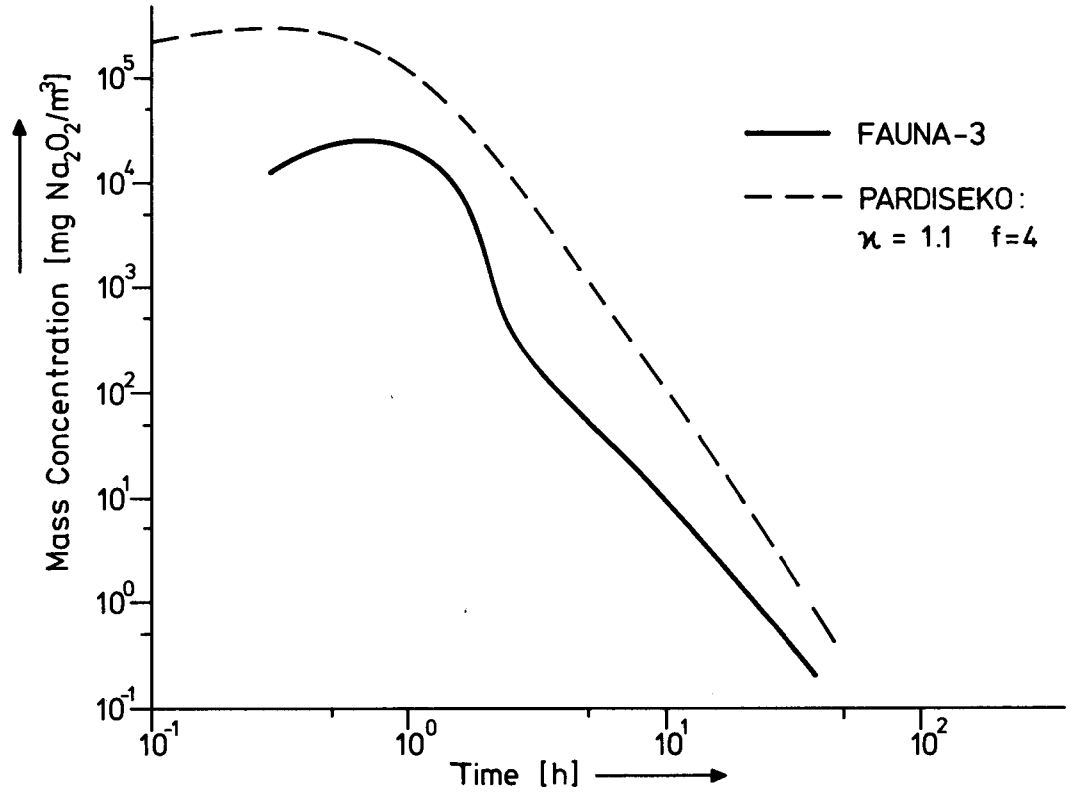

Fig. 6: PARDISEKO IIIb Recalculations of FAUNA-3 Experiment

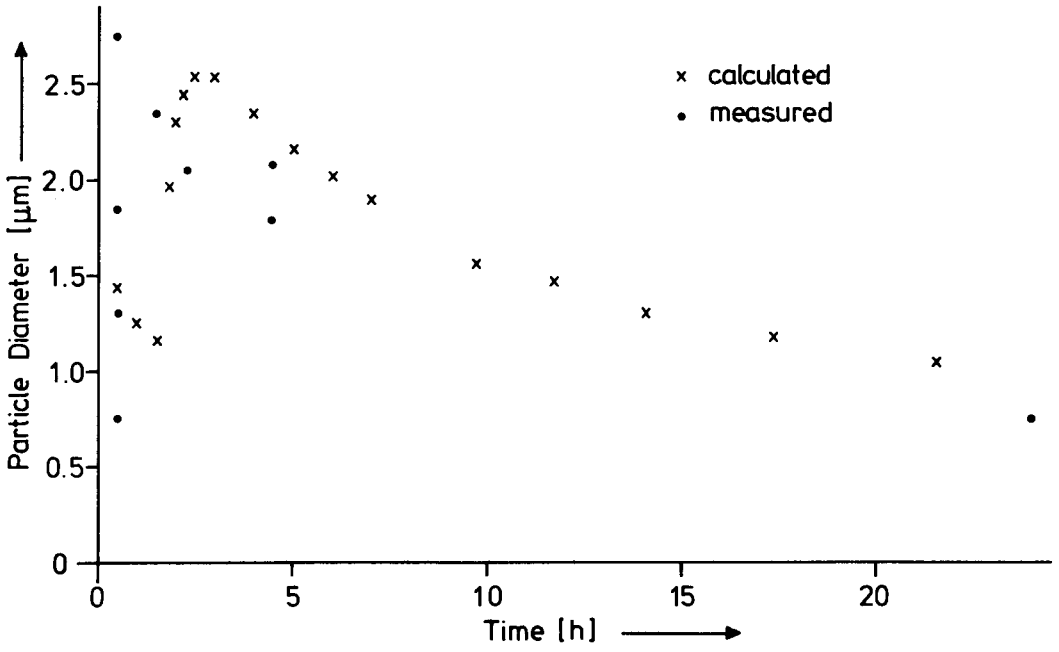

Fig. 7: Measured and Calculated Particle Diameters

Table I: Data and Results of Pool Fires

			FAUNA - Tests F 1	F 2	F 3
Data:					
Burning Area	:	m^2	2	2	12
Na - Quantity	:	kg	150	250	500
Na - Initial Temperature	:	°C	500	500	500
Results:					
Duration of Fire	:	min	110	210	80
Reacted Na	:	kg	110	170	460
Max - Na - Temperature	:	°C	620	620	700
Medium Gas-Temperature	:	°C	110	107	309
Na - Burning Rate :					
Min.			20	16	18
Med.		$kg/m^2/h$	29	25	33
Max.			84	40	94
Reaction Products	:	Na_2O_2/Na_2O		40 / 60	
Max. Aerosol - Mass Concentration	:	g/m^3	24	20	30

DIRECT MEASUREMENT OF THE COAGULATION SHAPE FACTOR OF AEROSOL PARTICLES

B. Rehn
Laboratory for Aerosol Physics and Filter Technology
Kernforschungszentrum Karlsruhe, FRG

ABSTRACT

In order to measure the coagulation shape factor of an aerosol, a vertical tube of 10 cm internal diameter and variable length was used. Two sampling nozzles, one at the bottom and one at the top of the tube, allowed to connect aerosol measuring instruments to the tube.

A platinum oxide generator was built which could produce more than 10^6 particles/cm³ in the size range $0.0178\ \mu \leq d \leq 0.0316\ \mu$. The carrier gas of constant flow rate passed upwards through the tube. Efforts have been made to avoid turbulent flow and to obtain a rectangular velocity profile across the tube.

An electrical aerosol size analyzer was used to measure the size distribution of the test aerosol both at the beginning and at the end of the tube corresponding to aerosol ages between t = 0 and t = 150 sec. Simultaneously, the measured size distribution for t = 0 sec was used as input data for theoretical calculations with the aerosol behavior code PARDISEKO IIIb. The coagulation shape factor was then derived by comparison between the calculated and the measured size distribution of the coagulated aerosol.

Due to the small size of the generated platinum oxide particles Fuchs' correction has been taken into account for the calculations, thus leading to coagulation shape factor of about 1.0. Without Fuchs' correction the obtained values are too low, in case in point only about 0.2.

INTRODUCTION

Coagulation is the most important interaction between aerosol particles in the containment of a LMFBR or LWR after an accident with core-disassembly.

Thus, all computer programs calculating the behavior of an aerosol as a function of time, have to include the calculation of coagulation.

In order to obtain a reasonably negligible deviation between experimental and mathematical results, the input data for the calculation have to be determined as exactly as possible. This is of particular importance in long-term calculations where uncertainties in the input data could lead to large errors.

Most of the input data can be determined with appropriate measuring instruments in a relatively simple way.

Difficulties arise, however, when the dissimilarity in shape of the particles is taken into account: most of the aerosol particles, including those generated during a hypothetical core disruptive accident, differ from the shape of a sphere.

Thus, shape factors are introduced in order to characterize the actual behavior of a non spherical particle by comparing it with the behavior of a spherical particle of a well defined diameter [1] .

In the past, measurements of the dynamic shape factor which is important in the field of particle mobility, have been carried out already. But until now there are no direct measurements available for the equally important coagulation shape factor.

EXPERIMENTAL APPARATUS AND METHOD

In order to measure the coagulation shape factor of an aerosol, a vertical tube with an internal diameter of 10 cm and variable length was used (Fig. 1). Two sampling nozzles, one at the top and one at the bottom of the tube, allowed to connect aerosol measuring instruments, such as the electrical aerosol analyzer, to the tube.

In the first part of the experimental program, platinum oxide was used as a simulation aerosol for uranium oxide because it is easier to handle. Experiments with UO_2 and mixed aerosols will be carried out in the near future.

In order to obtain a sufficiently high number of platinum oxide particles, a very efficient generator was built which could produce more than 10^6 particles/cm³ of a size ranging between $0.0178\ \mu \leq D \leq 0.0316\ \mu$.

The construction of this generator was relatively simple: a platinum wire with a length of 90 cm and a diameter of 0.5 mm was mounted in a cylindrical housing of an internal diameter of 10 cm and connected to a DC power supply. The current through the wire was kept constant at 12.5 A, the corresponding temperature of the wire was about 1200°C.

The flow of synthetical air through the generator was controlled by a needle valve and measured by a flowmeter. By diluting the generator airstream with different amounts of clean air in a buffer vessel, it was possible to influence the aerosol size distribution. The outlet of the buffer vessel was connected to the vertical coagulation tube so that the carrier gas passed upwards through the tube.

To avoid turbulent flow, two laminators have been installed at both ends of the tube. By use of a hot wire anemometer, the velocity profile across the tube has been measured and was found to be nearly rectangular.

Due to this result and the fact that the flow rate of the carrier gas was kept constant during the whole experiment, there was a direct proportionality between the age of the aerosol under observation and the distance between the two sampling nozzles at the bottom and the top of the tube. Effects such as diffusion or thermophoresis which might have a distruct influence on the particle size distribution, have been estimated to be negligible.

Wall losses due to thermophoresis, for example, could not occur because of only insignificantly different temperatures of the carrier gas and the inner wall of the tube.

Losses by diffusion, on the other hand, have been neglected since only the center portion of the flow in the coagulation tube was extracted and the thickness of the diffusion boundary layer never exceeded a few percent of the tube radius [2] .

The geometry of the tube together with the chosen flow rate of 16.5 l/min made it possible to measure size distributions during coagulation times of up to 150 seconds. An electrical aerosol size analyzer was used to measure the size distribution of the aerosol both at the beginning and at the end of the tube corresponding to aerosol ages of $t = 0$ and $t = t_1$ seconds. Because of the variable length of the tube, these measurements have been made for 6 different aerosol ages between 0 and 150 seconds.

Simultaneously, the measured size distribution for $t = 0$ sec was used as input data for theoretical calculations with the aerosol behavior code PARDISEKO IIIb [3]. Thus, it was possible to calculate the expected size distribution for the test aerosol of $t = t_1$ seconds of age and to compare the result with the measured distribution of the same aerosol age. The corresponding coagulation shape factor was derived from this comparison (Fig. 2).

RESULTS AND DISCUSSION

In the course of evalutation of the experimental results, at least three major difficulties arise:

i) The size distribution which is measured with the electrical aerosol analyzer is given as a step-function. Thus, this representation of the size distribution does not correspond with the size distribution existing in reality. Mathematical calculations of the behavior of particles which are estabilshed on the basis of a step function, must therefore necessarily be erroneous.

ii) The equations used in the aerosol behavior code PARDISEKO are based on the values of the mass equivalent radius. On the other hand, when the electrical aerosol analyzer is applied, the mobility equivalent radius is determined. The latter is not directly proportional to the mass equivalent radius because of the necessary application of the Cunningham slip correction.

iii) Due to their size, the generated platinum oxide particles are in the range of the transition regime between the free-molecule and the continuum regime. As there is no theory for this transition regime, equations based on empiric deduction have to be established, thus creating a few uncertainties.

These three problems have been solved in the following way:

i) The range of particle size which extends from 0.01 to 1.0 μ is divided by the electrical aerosol analyzer into 8 different classes. The possibilities offered by the PARDISEKO code are in no way fully exploited by the simple division in just 8 size classes. Thus, each size class has been subdivided into 10 arithmetic classes.

Of course, the total amount of particles contained in the 10 arithmetic classes must necessarily be the same as in the corresponding size class.

This condition can very easily be fulfilled in the case of a step-function as demonstrated in Fig. 3 (for the sake of clarity each size class has here been subdivided into only three arithmetic classes). In order to get closer to reality, i.e. to put the lower curve into a more continuous shape without thereby affecting the sum of particles, the sum function of the particle size distribution has been established. The number of particles per arithmetic class in thus indicated by the difference between two adjacent points of interpolation on the curve, as shown in Fig. 4.

ii) In the PARDISEKO code (as well as in most of the other aerosol behavior codes) only the mass equivalent radius is contained and not the mobility equivalent radius which is the only radius, however, to be determined by the electrical aerosol analyzer.

This problem of different radii appears in the calculation of the coagulation rate in the following formulae:

a) $$K\,(R_p,R'_p) = \frac{2kT}{3\eta} \cdot \frac{f_M}{\rho_M} \cdot \left(\frac{C(R_M)}{R_M} + \frac{C(R'_M)}{R'_M}\right) \cdot (R_M + R'_M)$$

b) $$K\,(R_p,R'_p) = \frac{2kT}{3\eta} \cdot \frac{f_M}{\rho_M} \cdot \left(\frac{C(R)}{R} + \frac{C(R')}{R'}\right) \cdot \left(R\,\frac{C(R_M)}{C(R)} + R'\,\frac{C(R'_M)}{C(R')}\right)$$

where

R_p, R'_p = radii of particles undergoing Brownian coagulation

R_M = mass equivalent radius

R = mobility equivalent radius

$C(R), C(R')$ = Cunningham slip correction

f_M = coagulation shape factor

χ_M = dynamic shape factor.

The correlation between the mass equivalent radius and the mobility equivalent radius is given by

$$\frac{R}{C(R)} = \chi_M \cdot \frac{R_M}{C(R_M)}$$

In earlier experiments, the dynamic shape factor of platinum oxide was determined as being 3.5. Thus, the diameters of particles measured with the electrical aerosol analyzer have been corrected for the calculation according to Fig. 5.

iii) The dynamic behavior of particles is determined by the ratio between the particle mean free path and the radius of the particle and thus by the Knudsen number.

For Knudsen numbers < 0.1 (continuum regime) the particle is subjected to other physical laws as for Knudsen numbers > 10 (molecule regime). For Knudsen numbers $0.1 \leq Kn \leq 10$ (transition regime) where most of the experimentally generated platinum oxide particles are to be located, an approximation formula was established by Fuchs [4] which was slightly modified by Walter [5] and Williams [6] :

$$K(R_p, R'_p) = K_o(R_p, R'_p) \cdot \frac{1}{1 + G_o}$$

$$\text{where } G_o = 4\,kT \left(\frac{B(R) + B(R')}{R + R'}\right) \cdot \sqrt{\frac{m \cdot m'}{m + m'} \cdot \frac{\pi}{8kT}}$$

$$\text{and} \quad m = \varrho \cdot \frac{4\pi}{3} \cdot R_M^3, \qquad m' = \varrho \cdot \frac{4\pi}{3} \cdot R_M'^3$$

$K_o(R_p, R'_p)$ = coagulation constant (Smoluchowski) [7]

$K(R_p, R'_p)$ = modified coagulation constant

R, R' = mobility equivalent radii of particles P and P'

R_M, R'_M = mass equivalent radii of particles P and P'

ϱ = density of particles P and P'

For the calculation of the coagulation shape factor Fuchs' correction (in the version of Walter and Williams) has been taken into account and the results obtained in this way have been compared with those obtained without the Fuchs' correction being taken into account.

Fig. 6 shows the size distribution of platinum oxide as a function of time, measured at the bottom (t = 0 sec) and at the top (t = 150 sec) of the coagulation tube.

As mentioned above, the coagulation shape factor was derived from the comparison between the measured size distribution of the coagulated aerosol and the calculated size distribution of the same aerosol.

Fig. 7, for example, shows this comparison for t = 150 sec and χ_M = 3.5. The calculation has been carried out without using Fuchs' correction and leads to an obviously too small coagulation shape factor of f_M = 0.2.

If Fuchs' correction is taken into account, however, the coagulation shape factor yields much higher values of about 1.0 (Fig. 8).

In order to demonstrate the influence of Fuchs' correction on the coagulation of small particles, an additional calculation has been carried out using the same input data as above but without the inclusion of Fuchs' correction. The resulting curve (also given in Fig. 8) differs significantly from the measured curve, thus indicating that Fuchs' correction should be taken into account for calculations of the coagulation of particles in the size range of the transition regime.

CONCLUSIONS

The coagulation shape factor of aerosol particles can be determined experimentally with the described apparatus. Due to the small size of the generated platinum oxide particles Fuchs' correction has to be taken into account for the calculation of the coagulation. In case of application of the correction formula the obtained coagulation shape factor yields the expected value. Without the Fuchs' correction the obtained values are obviously too low. The influence of Fuchs' formula on the coagulation rate can practically be neglected for particle radii r > 0.1 μ [6] because the importance of the correction formula decreases for the particles of increasing size which are, for example, generated in the course of a hypothetical core disruptive accident. Further experiments involving uranium oxide and mixed aerosols will be carried out in the near future as for the particle shapes then to be observed other values for the coagulation shape factor could be obtained.

REFERENCES

/1/ Nuclear Aerosols in Reactor Safety, Chapt. III, Nuclear Energy Agency, June 1979

/2/ Zebel, G.: Aerosol Science, Chapt. II, Academic Press, London - New York, 1966

/3/ Bunz, H.: "PARDISEKO IIIb - Ein Computerprogramm zur Berechnung des Aerosolverhaltens in geschlossenen Behältern", KFK-2903, November 79

/4/ Fuchs, N.A.: "The Mechanics of Aerosols", Pergamon Press, 1964

/5/ Walter, H.: "Coagulation and Size Distribution of Condensation Aerosols", Aerosol Science, Vol. 4, pp. 1-15 (1973)

/6/ Williams, R.J.: "Review of Aerosol Problems and the Theory of Aerosol Physics with Particular Reference to Sodium Cooled Fast Reactors", UK AEA, SRD82, 1978

/7/ von Smoluchowski, M.: Phys. Zeitschrift 17, pp. 557-585, 1916

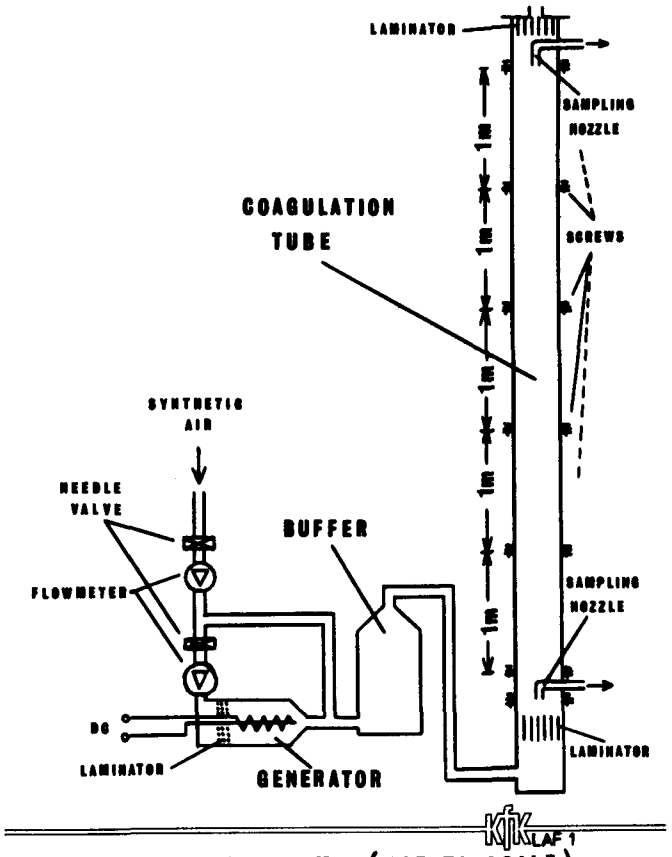

SCHEMATIC DIAGRAM (NOT TO SCALE) OF APPARATUS

Fig. 1

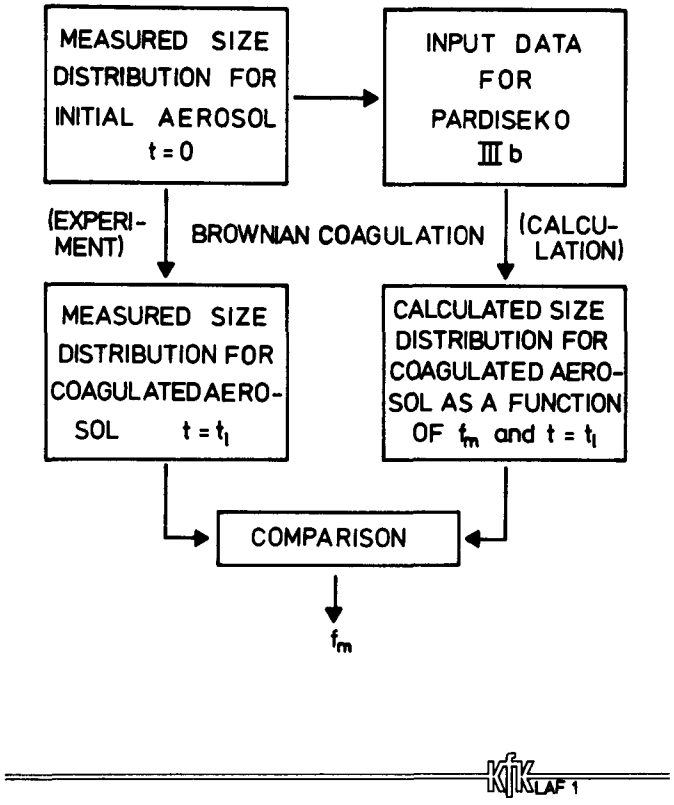

FLOW CHART FOR THE CALCULATION OF THE COAGULATION SHAPE FACTOR

Fig. 2

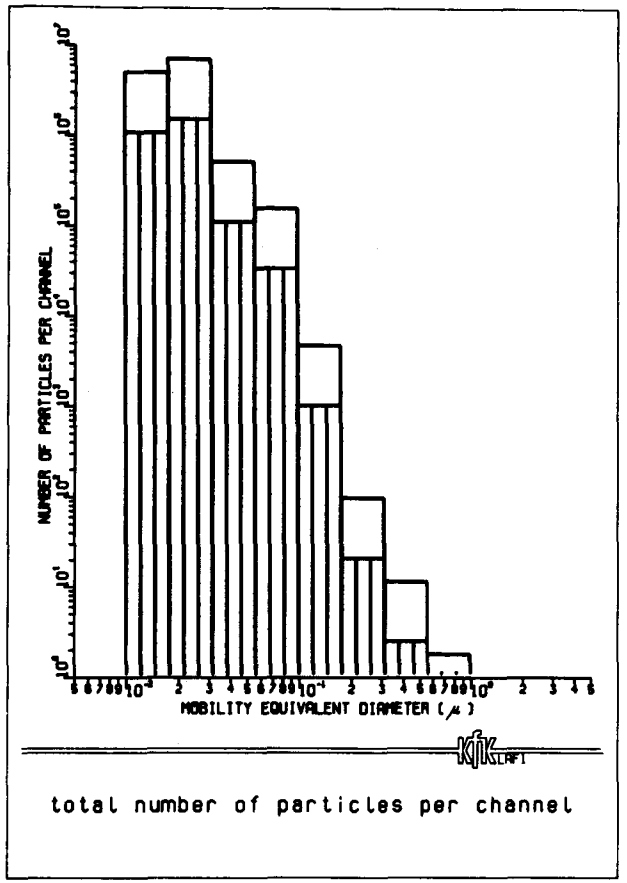

total number of particles per channel

Fig. 3

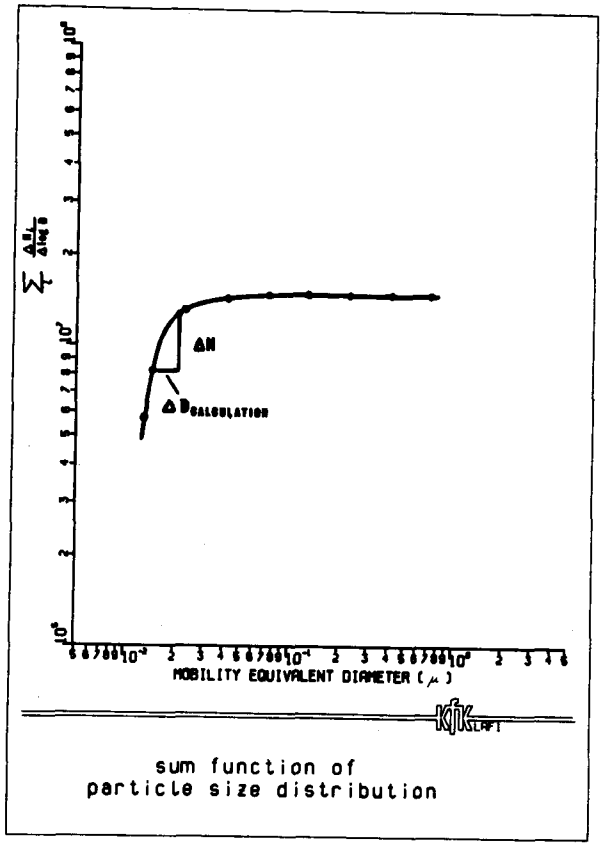

sum function of
particle size distribution

Fig. 4

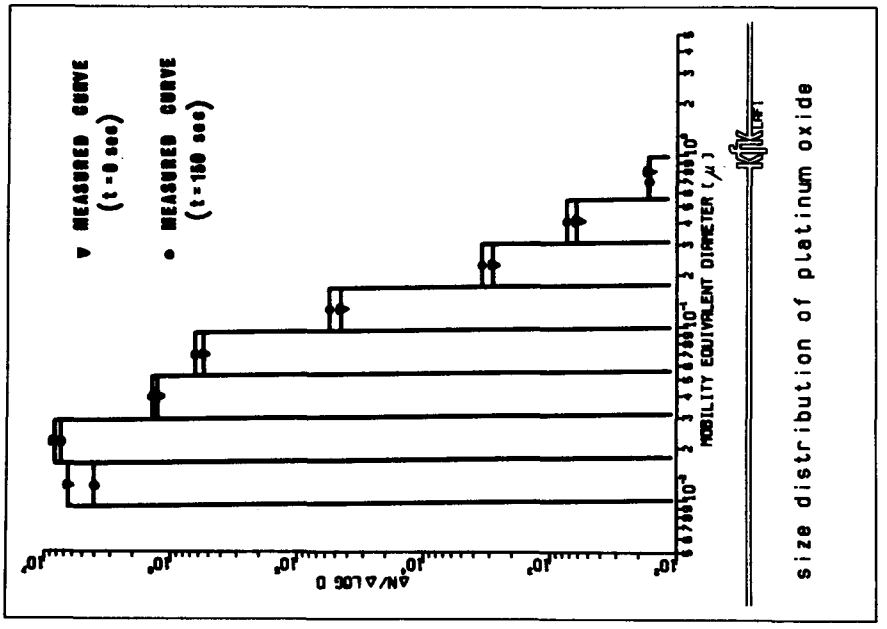
▼ MEASURED CURVE
(t = 0 sec)
• MEASURED CURVE
(t = 150 sec)
ΔN/ΔLOG D
MOBILITY EQUIVALENT DIAMETER (μ)
size distribution of platinum oxide

Fig. 6

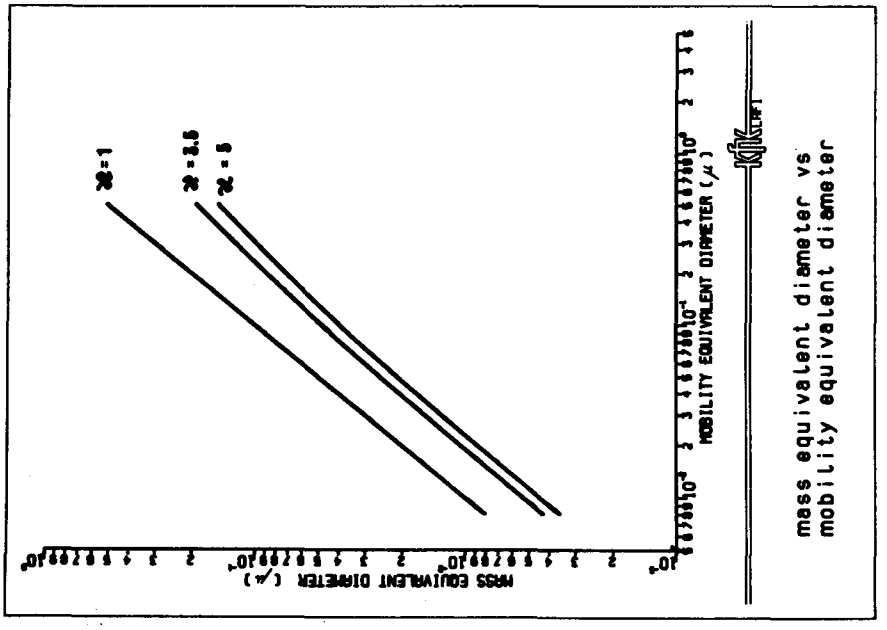
χ = 1
χ = 2.5
χ = 5
MASS EQUIVALENT DIAMETER (μ)
MOBILITY EQUIVALENT DIAMETER (μ)
mass equivalent diameter vs
mobility equivalent diameter

Fig. 5

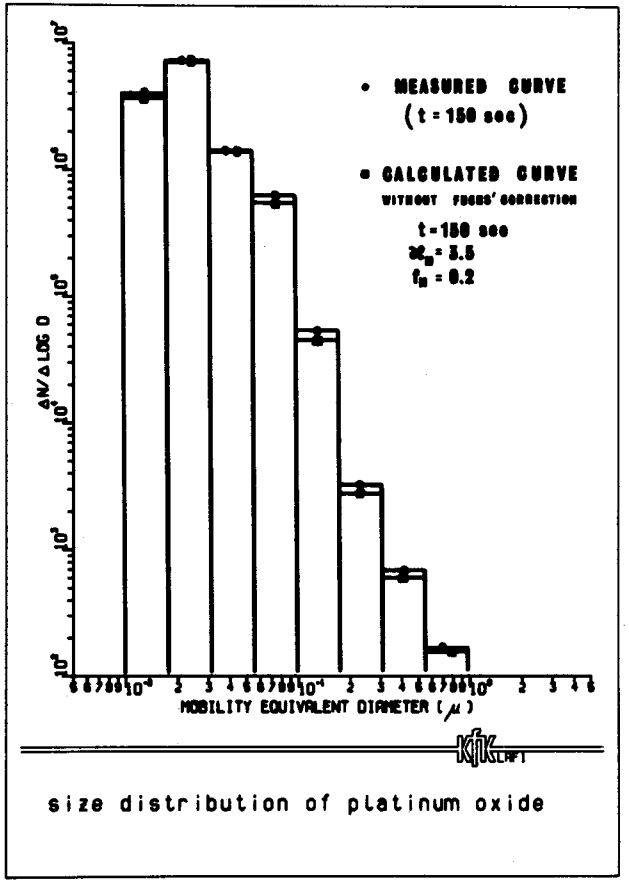

size distribution of platinum oxide

Fig. 7

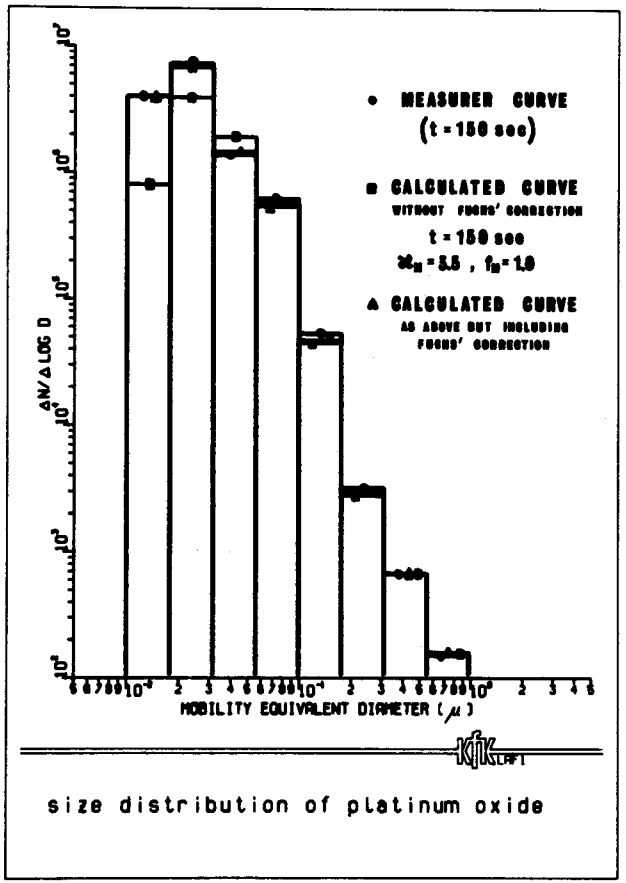

size distribution of platinum oxide

Fig. 8

MORPHOLOGY AND AERODYNAMICS OF SODIUM OXIDE AEROSOL AT LOW RELATIVE HUMIDITIES

J.F. van de Vate, W.F. van Leeuwen, A. Plomp and H.C.D. Smit
Netherlands Energy Research Foundation
Petten, The Netherlands

ABSTRACT

Experiments have been conducted in one of ECN's aerosol chambers using Exploding Wire produced sodium oxide aerosol under dry air conditions ($\lesssim$ 100 ppm H_2O). Electron microscope analysis of particles immediately after sampling revealed the typical appearance of metal oxide smoke particles, viz. aggregates of large numbers of solid primaries. The diameters of the primary particles were distributed lognormally with a geometric median diameter of 0.085 μm and a geometric standard deviation of 1.5. Spiral centrifuge analysis yielded dynamic shape factors κ between 2 and 4 for aggregates of aerodynamic diameters between 0.57 μm and 0.92 μm resp.. The relation between κ and the number of primaries per aggregate was found to fit nicely the ECN-model for such aggregates, which model has been validated previously experimentally with aerosols of Fe-oxide, Au, U_3O_8 and Cu-oxide. This model with the Na-oxide primaries input data leads to aerodynamic diameter values of about 1.5 μm for a 10 $g.m^{-3}$ aerosol after 15 minutes of dominant Brownian coagulation. This is in reasonable accordance with some experimental observations. Increased humidity or sampling artefacts will lead to compaction of the fluffy aggregates resulting in an increased aerodynamic diameter of about 4 μm or more.

Note added in proof

In contrast to the above given results on Exploding Wire produced sodium smoke, very recent ECN observations on a low-temperature, small ($\sim$ 0.2 g) Na-fire revealed the existence of larger primaries, very similar to Gieseke's results [11]. Due to this the applicability of the results of this study to pool fires becomes uncertain; likely, application to more vigorous fires is justified. These newer results could be taken into account only to a limited extent in this paper.

1. Introduction

Smokes of metals formed either by vaporization and subsequent condensation or by burning, are composed of aggregates if the aerosol material is solid at the ultimate aerosol temperature [1]. The sizes of the primaries are usually of the order of a few 0.01 μm. To this general rule only one exception is known, namely the generally held opinion that particles produced by sodium fires are spherical [2]. Therefore, a study of the morphology (and possible sampling artefacts) of sodium smoke particles was initiated. Further interest in the actual appearance of sodium smoke particles was due to the existence of an ECN model for the aerodynamics of chain-like aggregates ([3] and [4]). It was realized, however, that relative humidity (or better: the partial water vapour pressure) plays a key role in the morphology of sodium smoke particles, together with the type of sodium oxide (Na_2O_2 or Na_2O) formed by the fire. The reaction product NaOH will lead to wetting of the particles even under relatively dry conditions. Such wetted particles will immediately attain a spherical shape due to the surface tension of the liquid. Since Na_2O_2 is non-hygroscopic (if the powder is exposed to laboratory air, it remains dry for at least several hours) and Na_2O is deliquescent, it is obvious that the extent to which these oxides are formed in a fire is also of major importance for aerosol morphology. According to various observations ([5] through [9], particularly the French studies [8] and [9]) and thermochemistry [5], Na_2O_2 is the predominant compound formed by burning sodium in excess O_2 containing gases like air. Likely, at least in case of Na_2O_2, the rate of attack of the particles by water vapour is mainly reaction rate limited and not by diffusion in the gas phase. In case of H_2O absorption by NaOH or Na_2O also the H_2O transport in the particle itself will be rate limiting. Therefore, artefacts in morphology due to sampling can be prevented most efficiently by having as short as possible transportation times of the samples to the electron microscope (EM), better than using complicated transport equipment with low-humidity atmospheres.

2. Materials and Methods

In view of the importance of short transportation times samples taken directly on EM grids were analysed in the EM within one minute after sampling. Simple small-size ($\sim$ 15 mm^3) transport boxes were used. From the attack observed it could be concluded that centrifuge sampling gives least particle deterioration. Therefore, such samples were used for morphological observations. Aerodynamic diameter (d_a) classified sampling has been carried out also by means of the Stöber centrifuge. The mass equivalent diameter d_e as a function of d_a has been obtained from the mass and number of particles in a sample of certain d_a. Determinations of sodium mass and particle number were done by means of AAS and counting of electron micrographs, resp.. From sets of (d_e,d_a) data the dynamic shape factor κ was calculated using

$$\kappa = \frac{\rho}{\rho_0} \frac{d_e^2}{d_a^2} \frac{F(d_e)}{F(d_a)} \qquad (1)$$

where: $\rho_0 = 1\ g.cm^{-3}$, and ρ for sodium oxide was arbitrarily taken as

2.5 $g.cm^{-3}$; F(d) = slip correction factor of particle of diameter d.
Microstructure analysis (primaries size distribution) was performed with the aid of a semiautomatic particle size analyzer (digitizer/microcomputer).
Sodium smoke aerosols investigated, were produced in a 1 m^3 vessel containing HEPA-filtered air conditioned by means of soda lime and molecular sieve treatments. Relative humidities of 0.5 %, 5 % and 30 % were applied. CO_2 concentrations were below 10 ppm.
The Exploding Wire technique was used for aerosol production [10]. Wire masses of about 20 mg were aerosolized each experiment. Some criticism should be considered concerning the simulation of the aerosol formation in a sodium fire by the Exploding Wire technique. The similarity, however, observed earlier [10] of the microstructure of MgO aerosols formed by burning or exploding electrically a Mg-ribbon in air, proves the comparibility of the burning and the EW-technique. The appearance of crystalline MgO primaries proves that in both cases particle formation occurs after oxidation of vaporized metal atoms, which is also the likely route for sodium smoke formation in fires ([1], [6], [11]).

3. Morphology of sodium smoke particles

Figures 1, 2 and 3 depict electron micrographs of major parts of the aggregates sampled from atmospheres with relative humidities of 0.5 %, 5 % and 30 %, respectively. Clearly, at these relative humidities, in all cases non-spherical particles have been observed. Using palladium shadowing the three-dimensional character of the aggregates could be further visualized (fig. 4). Comparing the aggregates with their shadows often revealed differences, indicating the vuln r bility of the aggregates after being sampled. Also the collapsing is seen to occur during EM observation. Exposing the samples to the humidity of human breath destroys the aggregates, converting them into a droplet-like deposit (fig. 5) and indicating the expected affinity of the particle's material to water. The same picture is obtained in those cases where samples appeared in the EM to be taken unsuccessfully, indicating spurious attack by humidity during sampling or during the transport afterwards. Closer examination of high-magnification electron micrographs revealed various degrees of "foaming" which could indicate gas production (O_2) from local reaction of Na_2O_2 with water. This could reduce the density of the primaries considerably as supposed by Gieseke [11] who also found a reduced primaries density (average 0.88 $g.cm^{-3}$). In a few cases clusters of needles were present on the aggregates, which could be the reaction products with CO_2 or the formation of $Na_2O_2.8H_2O$ crystals (hexagonal).
Comparison of the figures 1 through 3 leads to the conclusion that with increasing humidity the microstructure becomes more attacked: small primaries have disappeared and the aggregates become more compact. It should not be excluded that these microstructure changes have occurred during the sample transport and that for not too large RHs the original microstructure of the airborne aggregates is similar to or even finer than the 0.5 % RH case. With increasing humidity the conversion of the non-hygroscopic Na_2O_2 to Na_2O or NaOH in the aerosol is enhanced, thereby making the sampled aggregates more susceptible to shape changes from water uptake.
Only the microstructures of the low-humidity aerosols were analyzed

because of the compacted and attacked structures at 5 % and 30 % relative humidities. The primaries size distributions of the 0.5 % RH smoke particles sampled at various degrees of aging and from various aerosol experiments were measured. The primaries distributions appeared to be perfectly lognormal (correlation coefficients $\gtrsim$ 0.996 for n = 100 - 200) with a geometric mean diameter d_{1g} of 0.085 μm and a geometric standard deviation σ_{1g} of 1.5. Gieseke et al. [11] claim to have measured d_{1g} = 0.45 μm and σ_{1g} = 1.47. There is no obvious explanation for these differing observations on d_{1g}. Gieseke's primaries could have been attacked during sample transport, which perhaps is indicated by his observation of a very low primaries density (0.88 $g.cm^{-3}$). However, also the sodium vapour concentrations could have been different at the points of time of oxide particle formation under the two experimental conditions. *)

4. Aerodynamic properties of sodium smoke particles

Mass aerodynamic diameter distributions observed were also nicely lognormal (correlation coefficients $\gtrsim$ 0.99 for n $\approx$ 10).
The geometric mean aerodynamic diameter $(d_a)_g$ goes through a shallow maximum with time going on: after 5; 25 and 50 hours $(d_a)_g$ amounts to 0.73 μm, 0.95 μm, and 0.83 μm, resp.. Fig. 6 shows that at higher RHs $(d_a)_g$ increases to values of 1.1 - 1.2 μm. The geometric standard deviation ranges from 1.3 to 1.4 irrespective of relative humidity or the aerosol age.
The ECN model for the aerodynamics of solid aggregates relates the dynamic shape factor κ to the number n of primaries per aggregate by

$$\frac{\kappa}{F(d_e)} = \frac{1}{R_1F_1(Kn)}\, n^{1/3} \qquad (2)$$

where $R_1F_1(Kn)$ is a factor primarily related to the size of the primaries ([3],[4]). This model has been validated with various aerosols ([3],[4]). $R_1F_1(Kn)$ amounts to about 3 for primaries of some 0.01 μm and to unity for larger primaries of some 0.1 μm. The measuring data on sodium smoke were analyzed in a similar way as in reference [4]. Table I summarizes the calculations. $\frac{\kappa}{F(d_e)}$ is found to be proportional to the cube root of the number of primaries per aggregate, viz.

$$\frac{\kappa}{F(d_e)} = 0.32\, n^{1/3} \qquad (3)$$

This further supports the ECN model. More importantly, it supports the above given morphological observations of solid aggregates of sodium smoke. The proportionality factor $\{R_1F_1(Kn)\}^{-1}$ obtained amounts to 0.32 ± 0.03 (n=9) which is equal to the value found for U_3O_8 and Cu-oxide, viz. 0.32 ± 0.02 (n=9). Fig. 7 visualizes this nice fit. This, however, is surprising since the sodium smoke primaries are several times larger. Therefore, a value more near unity was to be expected.

---

*) We believe at least the latter explanation to be correct: see "note added in proof" with this paper's abstract.

The above mentioned reduced effective density of the primaries is no explanation because it works in the opposite direction. Probably, in reality the airborne aggregates were composed of finer aggregates than observed in the EM. This requires a primary-particle size reduction to about 0.05 µm in order to obtain the proper proportionality constant from our basic experimental data.

5. Comparison with sodium fire experiments

It is worthwhile to extrapolate the above given results to large-scale experiments for the purpose of comparison. Usually, aerosol mass concentrations in sodium fire experiments (10 $g.m^{-3}$) are much higher than those in this study. Allowing the aerosol to coagulate for about 15 minutes, the number concentration will have dropped to 3×10^5 cm^{-3} (irrespective of a large initial concentration), thereby resulting in an average particle mass of 3×10^{-11} g assuming negligible deposition. If d_{lg} = 0.085 µm, σ_{lg} = 1.5 and ρ = 2.5 $g.cm^{-3}$ (see above), it follows that the particles are composed of almost 2×10^4 primaries. Using relation (3) one obtains an "average" dynamic shape factor $\bar{\kappa}$ of 8.9 and an aerodynamic diameter of 1.5 µm. When, contrary to this, Gieseke's results are taken ($d_{lg} \approx 0.5$ µm and $\sigma_{lg} \approx 1.5$) we find $\bar{\kappa} \approx 1.5$ and d_a = 3.7 µm.

Sodium pool fires [12] in the Nuclear Safety Pilot Plant at Oak Ridge produce peak aerosol concentrations of about 10 $g.m^{-3}$. During the first 20 - 30 minutes cascade-impactor measurements have yielded d_a-values of about 2 µm which agrees not too badly. Newer reports from ORNL [13], however, indicate that the aerodynamic diameter is much larger, viz. about 4 µm, which probably relates to experiments of higher peak concentrations (25 $g.m^{-3}$) at later points of time ($\sim$ 30 min). Calculations taking into account these different data yield an aerodynamic diameter only slightly larger: 2.1 µm, instead of the observed 4 µm. However, there is a striking fit of this d_a-value of 4 µm with the calculated d_a-value of 3.7 µm using Gieseke's microstructure data.

We could consider the effect of compaction of the aggregates either during sampling [4] or due to wetting (see above). The increase $f \left(= \frac{d_a'}{d_a} \right)$ of the aerodynamic diameter d_a' of the compact aggregate relative to the aerodynamic diameter d_a of the original aggregate, can be calculated [4] by means of

$$f = \sqrt{\kappa \frac{F(d_a)}{F(d_a')}} \qquad (4)$$

f equals 3.1 and 3.8 for the above given cases of 10 g m^{-3} and 25 $g.m^{-3}$, respectively. As a result, the "compacted" d_a' - values amount to 4.6 µm and 8 µm, resp., which shows a better comparison.

In conclusion, compaction prior to or during sampling can explain the observed larger aerodynamic diameters.

[1] Harvey, J., Disc. Faraday Soc. 30 (1960), 113.

[2] e.g. a) Hilliard, R.K., et al, Preliminary Results of CSTF Aerosol Behaviour Test AB-1, HEDL-SA-138 (1977).
b) Allen, M.D., et al, Health Physics 34 (1978), 539.

[3] Kops, J.A.M.M., The Aerodynamic Diameter and Specific Surface Area of Branched Chain-like Aggregates, ECN-5 (1976).

[4] Van de Vate, J.F., J. Aerosol Sci. 11 (1980), 67.

[5] Humphreys Jr., J.R., Sodium Air Reactions as they pertain to Reactor Safety and Containment, Proc. 2nd United Nations Intern. Conf. Peaceful Appl. Atom. En. paper 1893 (1958), p. 176.

[6] Casselman, C., Liquid Sodium Pool Fires. IWGFR/IAEA Specialist Meeting on Sodium Fires, Cadarache(France), November 20-24, 1978.

[7] Aerosol Release and Transport from LMFBR Fuel, Oak Ridge Nal. Lab. Quarterly Report, April-June, 1979.

[8] Colome, J., et al,"Confinement et filtration d'aerosols produit par un feu de Sodium", Proc. Int. Congress "Le Confinement de Radioactivité dems l'Utilisation de l'Energie Nucleaire", SFRP, Versailles (France), May 28-31, 1974, p. 437.

[9] Chalot, A. et al, Consequences thermiques d'un feu de Sodium, see ref. [8], p. 315.

[10] Van de Vate, J.F., The Safety of SNR-300 and the Aerosol Model; a Summary Report of RCN Aerosol Research 1967-1971, RCN-174 (1972)

[11] Gieske, J.A., and L.D. Reed, Aerodynamic and Thermophoretic Behaviour of coagulated Sodium Oxide Aerosols, in "Airborne Radioactivity, Selected Papers ANS Winter Meeting, Nov./Dec., 1977.

[12] Fontana, M.H., and T.S. Kress, Breeder Reactor Aerosol Release and Transport Program Quarterly Progress Report for April-June 1977, ORNL-NUREG/TM-142.

[13] Adam, R.E., et al, Behaviour of Sodium-oxide and Uranium-oxide Aerosols in a Large Vessel, Proc. Int. Meeting Fast Reactor Safety Technology, ENS/ANS, Seattle (Wash.), August 19-23, 1979.

Table I The relation between dynamic shape factor κ of sodium smoke particles and their microstructure

d_a (μm)	$\bar{m}$ (pg)	n	$F(d_e)$	κ	$\frac{\kappa}{F(d_e)} n^{-1/3}$
0.49	0.10	61	1.39	2.0	0.36
0.57	0.18	107	1.32	2.1	0.34
0.57	0.20	121	1.31	2.3	0.35
0.68	0.38	224	1.25	2.1	0.27
0.80	1.3	770	1.17	3.7	0.35
0.80	0.83	492	1.19	2.9	0.30
0.92	2.2	1290	1.14	4.0	0.32
0.92	2.3	1340	1.14	4.1	0.33
1.10	3.5	2070	1.12	3.9	0.27

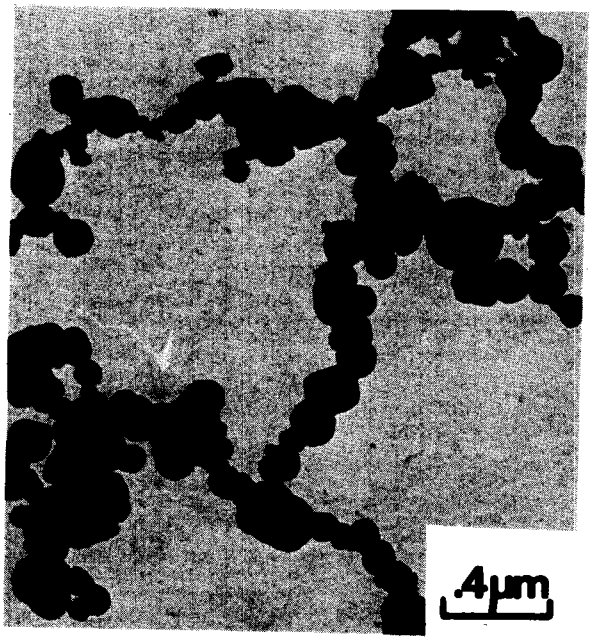

Fig. 1 RH = 0.5%

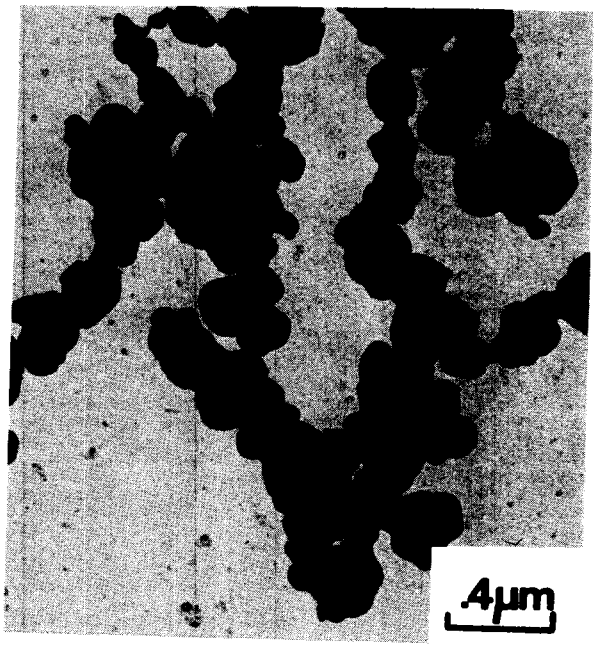

Fig. 2 RH = 5%

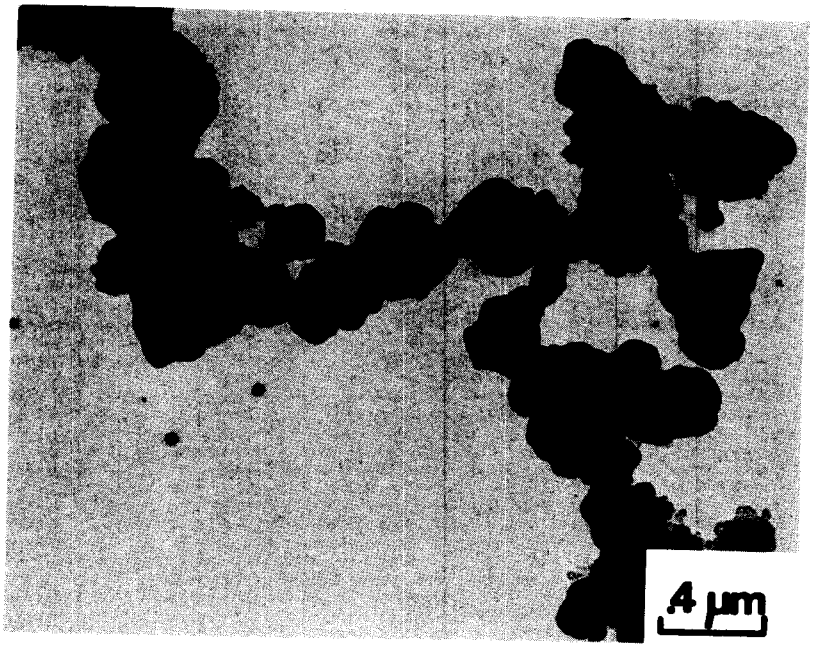

Fig. 3 RH = 30%

Figs. 1 - 3 Na-oxide particles at various relative humidities

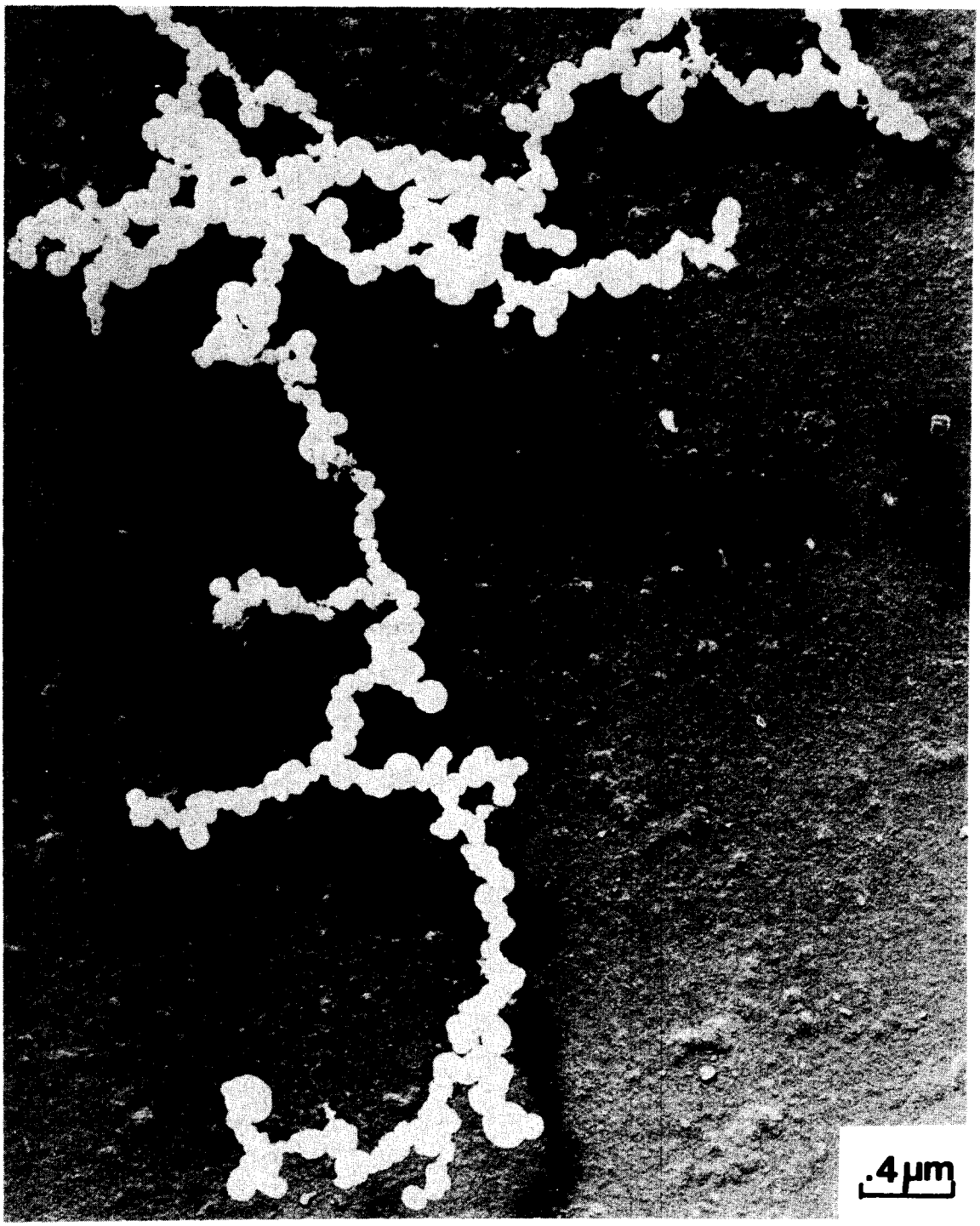

Fig. 4 **Palladium shadowed Na-oxide particle**

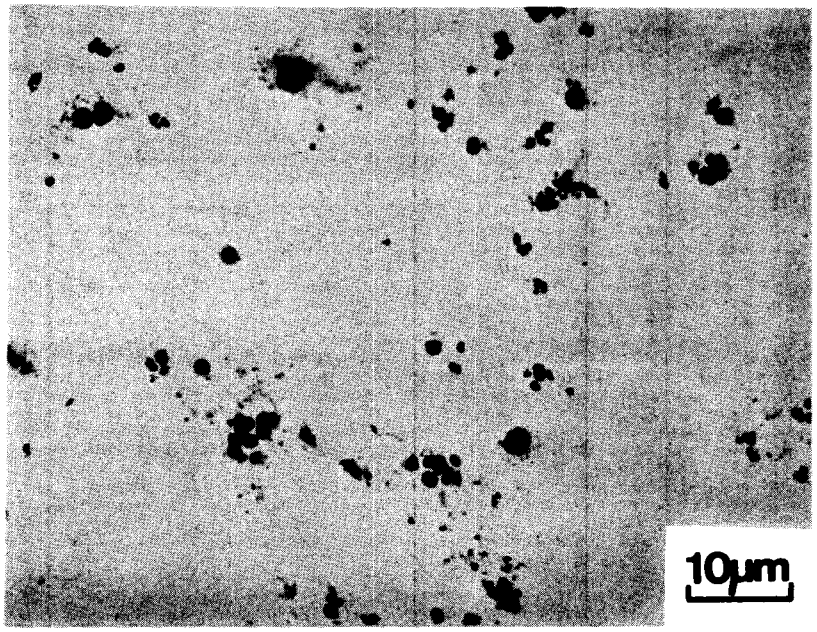

Fig. 5 **Na-oxide particles after exposure to humid air**

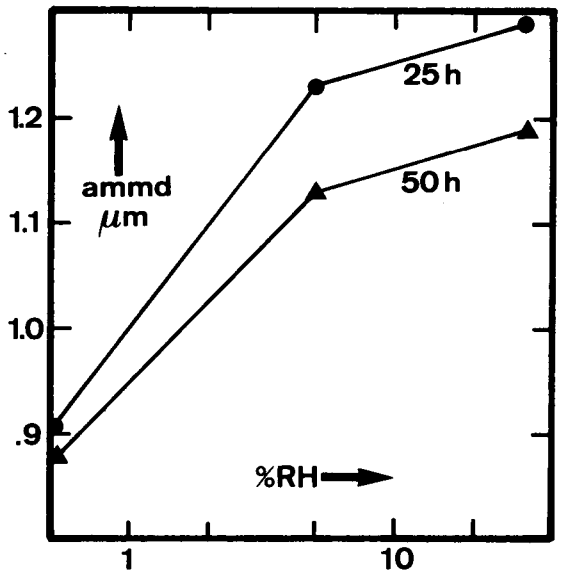

Fig. 6 Aerodynamic mass median diameter (ammd, in µm) as a function of RH, 25 hours and 50 hours after the Naoxide aerosol formation.

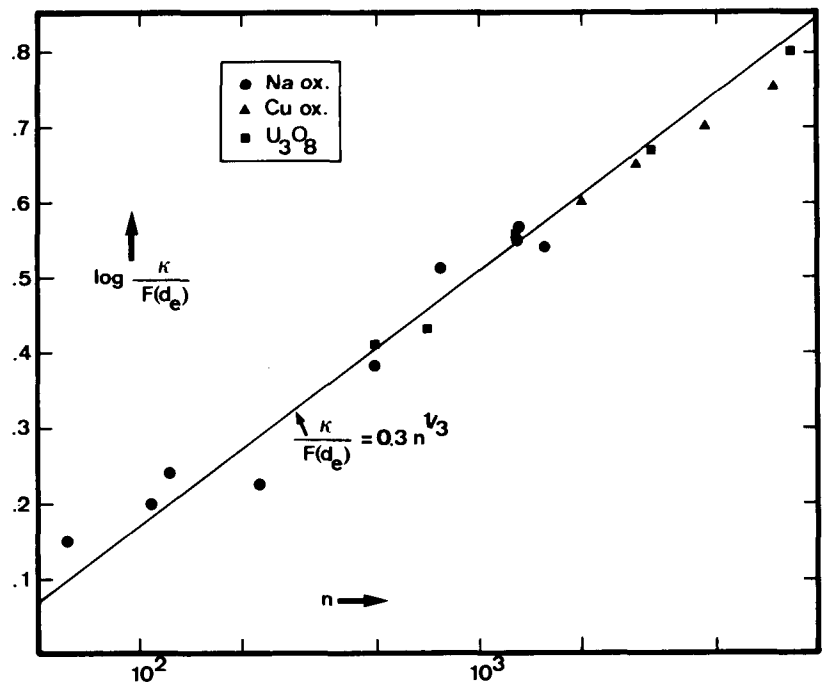

Fig. 7 $\frac{\kappa}{F(d_e)}$ **as a function of the number n of primaries per aggregate of sodium smoke, copper oxide and uranium oxide.**

THE BOUNDARY LAYER FOR DIFFUSIVE AEROSOL DEPOSITION ONTO WALLS

J.F. van de Vate
H.M. ten Brink
Netherlands Energy Research Foundation
Petten, The Netherlands

ABSTRACT

Important incoherence exists in literature on the effective thickness δ of the boundary layer across which aerosol particles are deposited by Brownian concentration diffusion onto walls. Values of 1 μm up to several centimeters are reported. The rate of deposition of particles smaller than 0.1 μm will be greatly influenced by diffusive transport through this boundary layer, the rate of which is inversely proportional to δ. Consequently, a reevaluation of the literature data in the light of new experimental information is worthwhile. New experimental data from ECN on stirred diffusive deposition in the size range from molecular up to 0.3 μm reveals that δ is proportional to D^n (D = diffusion coefficient of the particles) with n = 0.27. This agrees with Fuchs' theory giving $n \approx 0.25$. The conflicting literature data on δ (which are too small as a rule) are discussed. From the obtained relation it can be shown that non-stirred diffusive aerosol deposition is unrealistic. It is concluded that stirred diffusive deposition plays a minor role in removal of the aerosol mass from post accident nuclear atmospheres.

1. Introduction

Only part of hazardous aerosols formed inside safety enclosures is available for release to the environment due to the removal from the enclosure atmosphere by stirred deposition onto the walls. Basically, stirred deposition assumes the aerosol content of a containment to be well mixed apart from the boundary layer at the walls where aerosol deposition takes place. This means that the aerosol particles are transported to these boundary layers by thermal convective flows. The aerosol transport velocity across the boundary layer by some deposition process (settling, diffusion, thermophoresis, etc.) is negligible compared to the convective velocities inside the aerosol vessel. Consequently, stirred aerosol deposition can be considered as deposition from a homogeneous cloud source to the walls across the relatively thin boundary layer. The general equation describing the decay of the aerosol number concentration c_n is the following

$$\frac{dc_n}{dt} = - vS \frac{c_n}{V} \tag{1}$$

where: v = deposition velocity
S = wall surface area onto which deposition takes place
V = containment volume.

Small particles ($\lesssim$ few tenths of a μm) show considerable Brownian motion in air leading to concentration diffusion deposition through the boundary layer at the walls. According to Fick's law the rate of deposition per unit wall surface area equals $\frac{Dc_n}{\delta}$ (D = particle diffusion coefficient; δ = boundary layer thickness). Consequently, the velocity of diffusion deposition v_d is given by

$$v_d = \frac{D}{\delta} \tag{2}$$

which (substitution in (1)) yields

$$\frac{dc_n}{dt} = - \frac{DS}{\delta V} c_n = - \beta_d c_n \tag{3}$$

D can be calculated when particle size is known (or vice versa) using

$$D = \frac{kT}{3\pi\eta d} F(d) \tag{4}$$

where k = Boltzmann constant
T = Kelvin temperature
η = gas viscosity
d = particle diameter
F(d) = slip correction factor for particle of diameter d.

When dealing with monodisperse particles, β_d is independent of time and integration of (3) leads to an exponential decay of c_n with a decay constant equal to β_d.

2. The thickness of the boundary layer for diffusive deposition

The magnitude of the boundary layer thickness is a matter of concern since literature data on δ ranges from 5×10^{-4} mm [1] up to several mm [2]. According to Fuchs δ depends both on the intensity of convection and on D as well [1]. Assuming the convection to be the result of heat transfer, there will be only a weak dependence of the value of δ on different enclosure conditions, since δ is roughly inversely proportional to the square root of the natural convection velocity [3] which in turn is roughly proportional to the square root of the product of average wall length and the temperature difference related to the gas/wall heat transfer [4]. The relation between δ and D is explained by Fuchs [1] by eddies or turbulencies which carry the larger particles closer to the wall and in so doing partly compensate for the small value of D. As a result only for gas molecules the thickness of the diffusion boundary layer will be nearly equal to that of the laminair boundary layer. Fuchs obtains a $D^{\frac{1}{4}}$ dependence of δ where the exponent may be even smaller in reality. In conclusion, δ will be largely independent of both particle size, and containment size and conditions. Therefore, it is surprising to find in literature magnitudes of δ differing more than three orders. From the viewpoint of an experimentalist the lowest δ-values are the most suspicious because we may assume that small δ-values are the result of additional deposition processes, like thermophoresis or electrophoresis, whose contributions to aerosol deposition rates were not taken into account. Some literature data on δ are given in Table I. Those obtained for SO_2 [5], $CaCO_3$ [6], and "room particles" ([2] and [7] probably are coherent. However, the data obtained e.g. by Harrison [8], Kitani [9] and Greenfield [10] obviously are a separate category. We believe they are too small due to thermophoretic deposition ([9] and [10]) or due to electrophoresis [8].
In this stage it is worthwhile to analyze the four coherent (D, δ)-pairs given in Table I (references [2], [5], [6] and [7]). Power curve fitting yields

$$\delta = 4.1\ D^{0.254} \qquad (5)$$

with a correlation coefficient of 0.95 (n = 4). The exponent to D is found nearly equal to $\frac{1}{4}$ which is the relation between δ and D predicted by Fuchs ([1], see above).

3. Experimental determination of δ

Considering the rather meagre experimental data on δ available for the abovegiven analysis a few additional experiments have been performed. Use was made of particles with sizes ranging from 10^{-3} µm to about 0.3 µm. δ-values were determined for water molecules, nitric acid molecules, NaCl particles (0.06 µm) and a variety of singlet or multiplet polystyrene spheres (0.071 µm - 0.26 µm).
The rather straightforward experiments with water vapour were conducted in a 200 liter vessel filled with dry air. After introduction of a pool of water on the vessel floor, the humidity of the vessel atmosphere was measured. The observed rate of humidity increase was used for the calculation of δ, yielding a value of 3.5 cm.

The decay rate of HNO_3 vapour concentration was measured after its formation in a 1 m^3 smog irradiation chamber containing nitrous acid (HNO_2) in air. A specific measuring technique for HNO_3 was applied. The observed decay rate of 2.3 x 10^{-3} s^{-1} in the smog chamber (6.1 m^2 internal wall surface area) leads to a boundary layer thickness δ of 2.6 cm.

The decays of NaCl aerosols in a 1.2 m^3 cylindrical vessel were followed by means of a condensation nuclei counter. The aerosols produced by drying a nebulized NaCl-solution had a log-normal diameter distribution with a geometric mean of 0.06 µm and a geometric standard deviation of 1.7. The decay curves were analyzed with the aid of a model for combined coagulation and stirred deposition. The fit between model and experiment was within ± 10 %. Using the known D (1.7 x 10^{-5} $cm^2.s^{-1}$) of 0.06 µm diameter particles a δ-value of 0.26 cm was obtained.

The polystyrene sphere aerosols were produced directly in a 1 m^3 vessel by nebulizing an aqueous suspension and subsequent drying in the vessel atmosphere. The particles were not electrically neutralized. Number concentrations were obtained by counting of singlets, doublets, etc. individually from electron micrographs of samples taken electrostatically from a known aerosol volume. After an initial short period of vessel filling the number concentration appears to decay exponentially (fig.1). The decay constants from these curves were corrected for stirred gravitational settling using a decay constant

$$\beta_s = v_s \frac{S_f}{V} = \frac{\rho g}{18\,\eta} \frac{S_f}{V} d^2 F(d) \qquad (6)$$

where: v_s = Stokes' settling velocity
ρ = particle density (≃ 1.06 $g.cm^{-3}$)
S_f = floor surface area
V = vessel volume

Particle sizes of multiplets have been calculated using the "size factors" for multiplets from Stöber [10]. After this correction δ-values were calculated with the aid of (3).

Table II summarizes the experimentally obtained δ-values. In addition the last column gives the δ-values as can be calculated from (5) for the particles and molecules used. Obviously, there is good agreement between most of our experimental results and equation (5) which is based on the scarce literature data. Only the results for the five largest polystyrene spheres deviate more than 40 % from the calculated values. Probably, the same explanation for the observed too low δ-values is valid as for Harrison's results [8]: electrophoresis. The polystyrene particles carrying 10 - 100 charges (mainly positive) could be deposited on the steel walls of the vessel due to image charge formation.

In conclusion our experiments strongly support equation (5) which is based on Fuchs theory of the diffusive boundary layer and scarce literature data. Adding our data (excluding the results of the 5 largest particles) to these literature data a power curve fit yields

$$\delta = 4.8\, D^{0.274} \qquad (7)$$

with a correlation coefficient of 0.985 (n = 9).

4. Diffusive deposition from a stagnant atmosphere

4.1. Literature survey

There is an extensive theoretical literature on non-stirred diffusive deposition. Though sometimes stated explicitly, usually the models derived by these authors imply the occurrence of diffusive deposition from a stagnant atmosphere. It is assumed in the PARDISEKO-1 code [11]. Todorov [12] gives an extensive calculational model, arguing that this model "of a spherical space, with convection ignored, is of practical significance". Also Pollak [13] and Fürth [14] assume a stagnant atmosphere in their model for the calculation of diffusion coefficients of aerosol particles from aerosol decay curves. Goldberg [15] treats also the theory of aerosols that are simultaneously diffusing and settling from a stationary gas. Pich in two publications ([16] and [17]) claims to give a theoretical description of the behaviour of aerosol stored in vessels postulating the "gaseous medium is stagnant, especially there are no convection currents". Pich states his "method can be applied to containers of arbitrary shape". Even Fuchs [18] assumes in his discussion of rotating aerosol chambers that the aerosol is stagnant relative to the (rotating) walls of the system.

4.2. Application of the obtained results on δ

An aerosol enclosed in a vessel will be removed by the "stirred-deposition" mechanism when the deposition velocity is smaller than the velocity of the flow keeping the aerosol homogeneously distributed in the vessel space. Assuming these flows to be caused by natural convection (which is a very realistic assumption), this convection velocity v_c can be calculated from Prandtl's relation [4]

$$v_c = 0.5\ (g.\alpha.\Delta T.l)^{\frac{1}{2}} \qquad (8)$$

with α = coefficient of thermal expansion of the gas,
ΔT = average temperature difference causing the convection,
l = characteristic length of the vessel walls ($\approx V^{1/3}$).

When diffusive deposition is the rate determining removal mechanism, the (diffusive) deposition velocity v_d is given by (2). Putting $v_d = v_c$ and substitution of (7) one obtains the maximum diffusion coefficient D_{max} for which the "stirred-deposition" model would fail

$$D_{max}^{0.726} = 2.4\ (g.\alpha.\Delta T.l)^{\frac{1}{2}} \qquad (9)$$

For an extreme case of $\Delta T = 10^{-4}$ K (the average temperature difference between gas and walls will be usually much larger) and for $l \approx 1$ m, D_{max} amounts to 0.34 $cm^2.s^{-1}$. This means that stirred, non-stagnant, conditions in aerosol vessels are realistic even in the case of low-molecular gases ($D \approx 0.1$ $cm^2.s^{-1}$). Therefore, diffusive deposition is of the "stirred" typeusually and stagnant conditions will only occur when special precautions are taken to stabilize the vessel atmosphere like cooling the lower vessel part.

5. Nuclear aerosols

The stirred diffusive removal of a nuclear aerosol inside a safety containment is given by (2), (3) and (7), combination of which yields an exponential aerosol decay with a characteristic decay constant

$$\beta_d = 0.21\, D^{0.726}\, \frac{S}{V} \qquad (10)$$

It is worthwhile to compare this diffusive aerosol removal with that due to gravitational settling for the case of the Postulated Generalized Working Accident as defined for LMFBR by a group of experts of the NEA Committee on the Safety of Nuclear Installations [19]. The cylindrical containment has base dimensions of height = 50 m and diameter = 50 m which means S = 64,00 m^2, V = 98,000 m^3 and $\frac{S}{V} = 7\times10^{-2} m^{-1}$. The particle size can be assumed to be roughly 0.5 μm aerodynamic diameter in view of the calculations by the various computer codes as given in [19].
Consequently, (10) yields

$$\beta_d \approx 5 \times 10^{-9}\ s^{-1}$$

$(D\ (0.5\ \mu m) = 6.2 \times 10^{-7} cm^2.s^{-1})$

From (6) we obtain the decay constant for gravitational settling

$$\beta_s = 2 \times 10^{-7}\ s^{-1}$$

$(v_s(0.5\ \mu m) = 10^{-3}\ cm.s^{-1})$

From the difference of nearly two orders of magnitude between β_d and β_s we can conclude that stirred diffusive deposition is negligible compared to stirred gravitational removal. The value of 0.5 μm chosen for the aerodynamic diameter in the abovegiven calculation pertains to aerosol with a life of hours or more. In earlier stages the particle size is smaller and the aerosol number concentration correspondingly larger. In this period diffusive deposition could play an important role. However, the second order kinetics of coagulation makes coagulation overwhelming in the initial part of aerosol life compared to the deposition processes.

Literature

[1] Fuchs, N.A., The Mechanics of Aerosols, (Pergamon, Oxford, 1964), p.254.

[2] Nolan, P.J., Proc. Roy. Irish Acad. 47A (1941), 25.

[3] Davies, C.N., "Deposition from moving Aerosols" in Aerosol Science (ed. C.N. Davies, Academic, London, 1966).

[4] Prandtl, L., Fuhrer duch Stromungslehre (Braunschweig, 1949).

[5] Cox, R.A., and S.A. Penkett, Atm. Envir. 6 (1972), 365.

[6] Rooker, S.J., and C.N. Davies, J. Aerosol Sci. 10 (1979), 139

[7] Mercer, T.T., and M.I. Tillery, J. Coll. Interf. Sci. 37 (1971), 785.

[8] Harrison, A.W., J. Coll. Interf. Sci. 69 (1979), 563.

[9] Kitani, S., et al., J. Nucl. Sci. Techn. 10 (1973), 566.

[10] Stöber, W., Staub 30 (1970), 277.

[11] Keller, K., Theoretische Behandlung des Aerosolverhaltens im geschlossenen zylindrischen Behälter (Pardiseko I), KFK 1490 (1971).

[12] Todorov, I., and A. Sheludko, Kolloidnyi Zhurnal 19 (1957), 496.

[13] Pollak, L.W., et al., Geofis. Pura et Appl. 32 (1956), 177.

[14] Fürth, R., Geofis. Pura et Appl. 31 (1955), 80.

[15] Goldberg, I.S., et al., J. Aerosol Sci. 9 (1978), 209.

[16] Pich, J., Atm. Envir. 10 (1976), 131.

[17] Pich, J., Atm. Envir. 11 (1977), 989.

[18] Fuchs, N.A., Kolloidnyi Zhurnal 36 (1974), 1183.

[19] Nuclear Aerosols in Reactor Safety, a State-of-the-Art Report by a Group of Experts of the NEA Committee on the Safety of Nuclear Installations (OECD, Paris, 1979).

Table I Literature data on the boundary layer thickness δ for diffusion deposition of aerosols

"particles" in air	"particle" diameter (μm)	diffusion coefficient ($cm^2.s^{-1}$)	δ (cm)	investigator
SO_2	$(7 \times 10^{-4})^a$	0.10	2.5	Cox [5]
$CaCo_3$	0.01	5.2×10^{-4}	0.4	Rooker [6]
"room particles"	0.02	1.3×10^{-4}	0.6	Mercer [7]
"room particles"	0.07^a	1.2×10^{-5}	0.23	Nolan [2]
polystyrene spheres	0.23	1.8×10^{-6}	2.9×10^{-2}	Harrison [8]
,,	0.50	6.3×10^{-7}	0.87 x ,,	,,
,,	0.76	3.8 x ,,	0.68 x ,,	,,
,,	1.1	2.7 x ,,	0.44 x ,,	,,
,,	2.0	1.3 x ,,	0.06 x ,,	,,
NaO_x	1	3 x ,,	10^{-5}	Kitani [9]
,,	~ 2	10^{-7}	10^{-3}	Greenfield [10]

^{a} Calculated from D using Eq. (4).

Table II Experimental data on δ for various molecules and particles

"particles" in air	"particle" diameter (μm)	diffusion coefficient ($cm^2.s^{-1}$)	δ (experimental) (cm)	δ^b (calculated) (cm)
H_20	$(5x10^{-4})^a$	0.24	3.5	2.9
HNO_3	$(7x10^{-4})^a$	0.10	2.6	2.3
NaCl	0.06	$1.7x10^{-5}$	0.26	0.25
Polystyrene	0.071	$1.2x10^{-5}$	0.18	0.23
,,	0.085	$8.9x10^{-6}$	0.20	0.21
,,	0.107	$6.0x10^{-6}$	0.12	0.19
,,	0.127	$4.5x10^{-6}$	0.11	0.18
,,	0.137	$4.x10^{-6}$	0.11	0.17
,,	0.22	$1.9x10^{-6}$	0.08	0.14
,,	0.26	$1.5x10^{-6}$	0.10	0.14

^{a} Calculated from D using (4)

^{b} Calculated from D using (5)

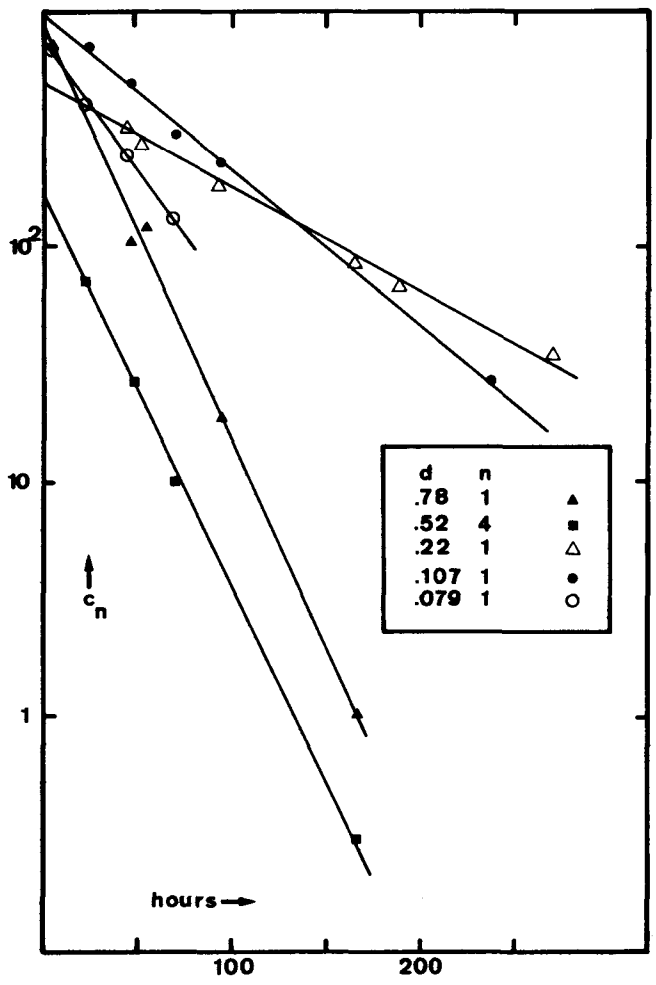

Fig. 1 Decay cures of monodisperse spheres in a 1 m^3 vessel (height = 2 m. c_n in cm^{-3}; t in hours; d in μm; n = number of spheres per particle.

MEASUREMENTS OF THE CONDENSATION OF STEAM ON DIFFERENT AEROSOLS UNDER LWR CORE MELT DOWN CONDITIONS

H. Bunz, W. Schöck
Laboratory for Aerosol Physics and Filter Technology
Project Nuclear Safety
Kernforschungszentrum Karlsruhe, FRG

ABSTRACT

Condensation of steam on aerosol particles has been demonstrated to be a very effective mechanism for the natural removal of particulate fission products from the containment atmosphere of an LWR during core meltdown accidents. The exact modeling of this process, however, was not possible to date because of missing data of condensation velocities of steam onto the non-spherical and non-uniform particles that are generated by core melting.

In the first phase of the experimental part of the NAUA research program the condensation of steam onto realistic aerosols was investigated. Condensational shape factors were evaluated which make the NAUA calculations agree with the experimental results. These shape factors are different for different aerosol materials. In this article a method is described which - by appropriate definition of the particle size with respect to condensation - reduces the condensational shape factor to unity in all cases of LWR accident aerosol behavior calculations.

INTRODUCTION

The necessity of determining the model parameters for steam condensation in a computer code, which describes the aerosol behavior in post-accident LWR containments, has been recognized in the very beginning of the development of the NAUA code [1].

As has been shown [2] steam condensation is the most effective process in the natural removal of particles from the containment atmosphere. Moreover, this process is very sensitive to the aerosol parameters size and shape and to the chemical composition of the particles. In order to keep the computer program operable the condensational shape factor concept was created, and an experimental program was conducted to measure these shape factors. The experimental activities have been concentrated on the measurement of steam condensation onto such aerosol particles which are representative for the aerosol in the LWR containment during core meltdown accidents.

An initial series of experiments with platinum oxide aerosols was conducted which was reported earlier [3]. The subsequent measurements with UO_2 aerosols yielded surprisingly different results. The interpretation of the differences finally led to a modified concept which equally well explains both measurement series and which finally leads to a single formulation of the condensation processes in the NAUA code.
The experiments and the new condensation concept will be discussed in the following.

EXPERIMENTAL METHODS

Even though the condensation of steam onto aerosols could be investigated in a bench scale experiment the test facility was constructed somewhat larger because also combined experiments with wall condensation and long term validation experiments have to be performed. Fig. 1 shows a schematic diagram of the facility. The 3.7 m^3 stainless steel vessel is thermostated up to 150 °C with an overall homogenity of better than 1.5° by two thermostating units. A steam generator and an adiabatic expansion mechanism are used to create the necessary supersaturations for the condensation experiments. The experiments which are reported in this article were all performed with the adiabatic expansion by means of the compensator bellows. This method creates a homogeneous supersaturation which is well defined with respect to magnitude and time dependence.

Different aerosol generators were used to supply the aerosol. UO_2-aerosols were generated in an arc vaporization generator, soluble salt aerosols were delivered by nebulizing solutions. The platinum oxide aerosols were generated inside the vessel using a standardized generator [4].

Besides the fast measurement of the thermodynamic variables during an expansion experiment the following aerosol parameters were measured:

- Aerosol sizes and concentration before the condensation by drawing nuclepore filter samples
- Time dependent size and concentration of the growing droplets during the condensation with a high time resolution using fast optical techniques

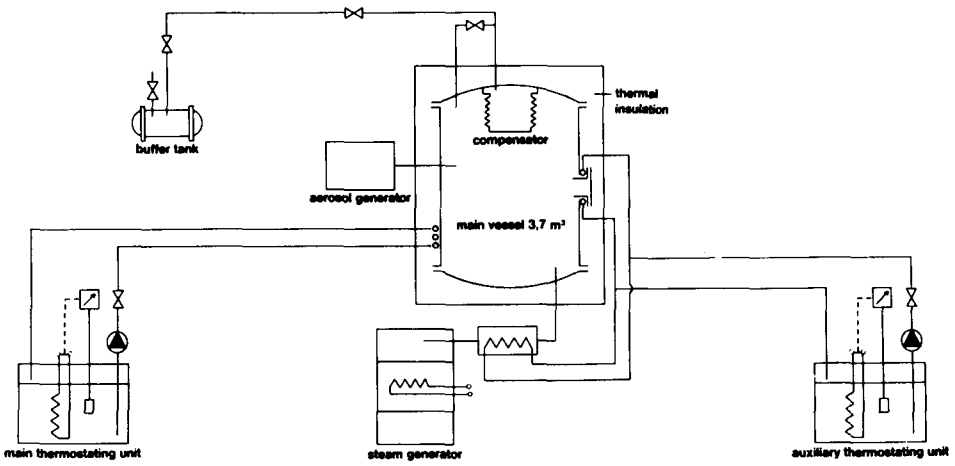

Fig. 1: Schematic diagram of the NAUA test facility

Since the optical droplet sizing constitutes the crucial part of the experimental procedure we shall explain it in some detail now.

The expansion of the volume lasts typically 10...18 sec. Compared to the velocity of other aerosol mechanisms this expansion rate predominates, all other proesses can be neglected during the condensation process. This also involves that this condensation process produces droplets of uniform size at all times, as long as the expansion goes on. Therefore, the measurement of the droplet size can be done at a particle collective rather than at single particles. An extinction measurement through the total vessel is used consequently.

Fig. 2 shows the dependence of the extinction coefficient α on the droplet diameter for water droplets. The characteristics of this function are the general d^2-dependence and the oscillations with a period of $\Delta d = 1.91\ \mu m$ when using He-Ne-lasers for illumination. The total transmitted intensity across the vessel is

$$I = I_o \cdot \exp - (K\ C_n\ \alpha) \tag{1}$$

where K is a geometrical constant and C_n is the concentration of the droplets. Taking

$$\alpha \sim d^2 \tag{2}$$

from Fig. 2 as an average dependence we have

$$I \simeq I_o \cdot \exp - (K' \cdot C_n \cdot d^2) \tag{3}$$

with another constant K'.

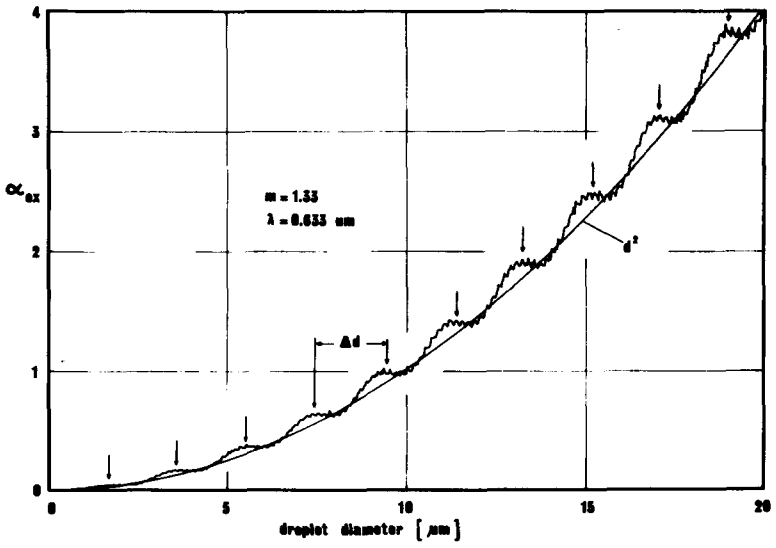

Fig. 2: Extinction coefficient for water droplets

For the evaluation of the measured data this equation is linearized in the form

$$\sqrt{\ln \frac{I_o}{I}} = b \cdot d \sim \sqrt{C_n} \cdot d \qquad (4)$$

Plotting experimental data in this form leads to a representation as in Fig. 3. The differences Δb betweeen the oscillations of Fig. 2 are now equidistant in the ordinate direction, the corresponding abszissa values correspond always to an increase in the droplet diameter of $\Delta d = 1.91$ µm.

Additionally, since $b \sim \sqrt{C_n}$, where the proportionality factor is merely geometrical, an initial calibration of b versus C_n can be used to evaluate the concentration C_n of the droplets from each measurement, too. Summarizing, concentration and time dependent size of the droplets can be simultaneously evaluated from the optical transmission measurement.

Finally the parameters of the 'dry' aerosol before condensation and the droplet data during condensation are input into NAUA calculations to evaluate the necessary correction factors for the condensation of steam onto the aerosol particles. In the NAUA code the condensation process is calculated with the modified Mason equation [2]

$$\frac{dd}{dt} = \frac{A}{d} \left(S - \exp\left(f_m \frac{B}{d}\right)\right) \qquad (5)$$

which gives the growth of droplet diameter d as a function of the supersaturation S and the thermodynamic variables A and B. f_m is the 'condensation shape factor' which corrects this idealized equation for the influences of

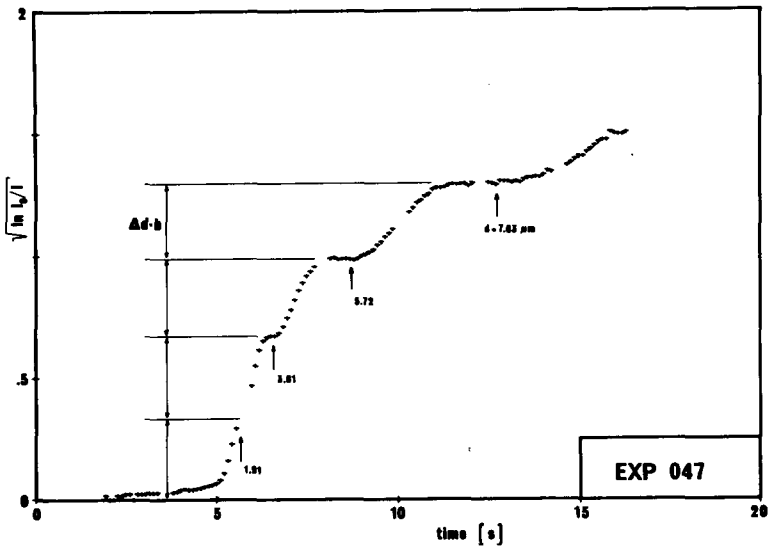

Fig. 3: Linearization of the transmission data

particle shape and composition of the realistic aerosol under investitation.

The purpose of our condensation experiments was to check the validity of this equation for condensation processes under LWR conditions and - if so - to determine the values of the shape factor f_m for the aerosol species which are present in the containment during core meltdown accidents.

RESULTS OF THE EXPERIMENTS

The first series of condensation experiments was conducted with platinum oxide aerosols. This aerosol has the same agglomerate shape as other metal oxide aerosols which are produced by vaporisation. The advantages of platinum oxide aerosol are that it is not radioactive and easily and reproducibly generated. As these experiments have been reported earlier [3] we will only recall the results. For four experiments Table I shows the mean mass equivalent diameter d_m and the concentration C_o of the dry aerosol before condensation. C_e is the measured droplet concentration after the condensation. It can be seen that the ratio C_e/C_o is rather low except for experiment 35 where the initial concentration C_o is low. From these data the shape factors f_m were calculated as defined in equation (5).

The f_m values of experiments 33 and 35 agree very well, because the aerosol was the same with a difference in age only. Equally experiments 39 and 40 were done with the same aerosol and yielded the same f_m. But the aerosol shapes in the latter two experiments were different from those in 33 and 35. So a noticeable difference in the f_m value exists between the two groups. The last column of Table I will be discussed below.

EXP	d_m µm	C_o	C_e	f_m	ϱ_{eff}
		10^3P/cm³			
33	.066	9.5	2.5	.62	2.9
35	.1	1.6	1.5	.60	2.7
39	.052	100.	8.	.67	1.6
40	.072	32.	6.	.66	1.6

Table I: Typical results of condensation experiments with PtO_x aerosols

The second part of the experimental program was to repeat these measurements with UO_2 aerosols. Table II gives some results. The particle size is now expressed by the mean geometrie diameter d_g. C_o and C_e are again the measured concentrations of the dry aerosol and of the droplets respectively. The efficiency of the particle-droplet conversion is now much higher than with the PtO_x aerosol. In fact, due to the large particle diameters the concensation process involves nearly all particles. This is of course a specific phenomenon of the experiment, it depends also on the expansion rate and on the particle concentration.

EXP	d_g µm	C_o	C_e	C_c
		10^3P/cm³		
101	.48	29.7	25.1	26.
102	.56	22.	17.5	21.
108	.80	13.	(13.)	12.7
109	.67	7.8	(8.)	7.7
116	.55	2.9	2.9	2.8

Table II: Typical results of condensation experiments with UO_2 aerosols

More important is the comparison with the calculated droplet concentrations C_c which are given in the last column of Table II. The agreement between C_c and C_e is excellent in four cases. The important result, however, is that $f_m = 1$ was used to calculate all values of C_c. Of course a better fit would have been obtained also for experiment 102 with another f_m value,

but the intention is to show that the simple assumption $f_m = 1$ fits the majority of the UO_2 experiments, also those not shown in Table II.

THE GENERALIZED CONDENSATION SHAPE FACTOR CONCEPT

An $f_m = 1$ was a very unexpected result because it contradicts the necessity of the shape factor concept itself. On the other hand shape factors with a value of 1 are highly welcome in aerosol modeling. So the question is now how to explain the value for the UO_2 aerosol and subsequently how to account for the different value in the PtO_x experiments.

The first problem is easily solved with the aid of Fig. 4 which shows a typical UO_2 aerosol sample photographed with a scanning electron microscope.

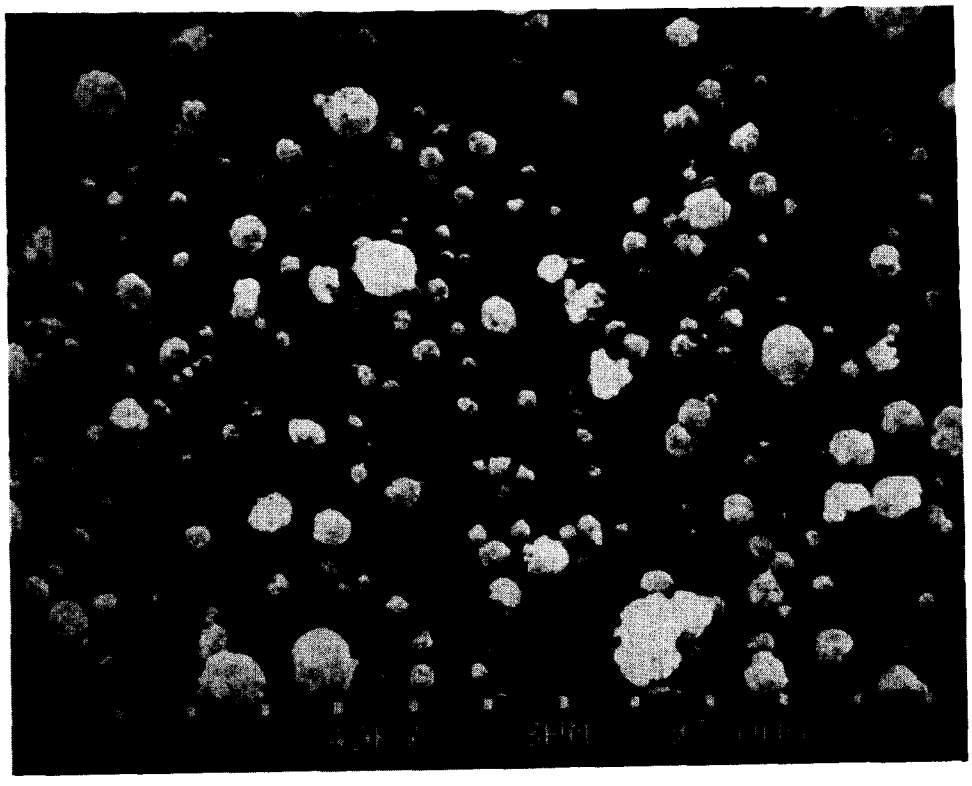

Fig. 4: Typical UO_2 aerosol sample from a NAUA experiment

The most important property with respect to our experiments and to LWR aerosol behavior calculations is the spherical shape of the particles, which has been found without exception in all our experiments. Closer investigation at higher resolution shows that the spheres consist of compacted and smoothed high order aggregates which are formed by condensation-evaporation processes that the particles have undergone. The particles collected directly at the output of the UO_2 aerosol generator show indeed the well

known chain like branched aggregate structure. In the steam saturated atmosphere of the NAUA facility (and of a reactor containment), however, random condensation may occur. When the so formed droplet evaporates and contracts the chains are compressed into spherical shape.

The spheres are only loosely compacted, the effective density was between 2.5 and 5 g/cm³ and agrees reasonably with the effective density of UO_2 powder which is approximately 3.9 g/cm³.

With this spherical shape of the particles and taking the geometrical diameter as a basis for the calculations, it is quite evident that the condensation shape factor must be $f_m = 1$. The particles can be considered as soaked with water as soon as the saturation approaches the value of $S = 1$. Then the Mason equation (5) is valid directly without corrections.

Concerning the PtO_x aerosol experiments the difference consists only in that the mass equivalent diameter has been used for the NAUA calculations yielding f_m values < 1. The question is whether the use of geometric diameters as the basis for calculations would lead to an $f_m = 1$ also. Unfortunately the geometric diameters of the PtO_x aerosol cannot be measured due to their small size. But as the geometric diameter and the mass equivalent diameter of spheres are connected via the effective density [1], we were able to do the following calculations. The diameters of the PtO_x aerosol were adjusted such that the experimental results could be calculated using a condensation shape factor $f_m = 1$. These adjusted diameters were taken as the geometric diameters of the PtO_x aerosol. The comparison with the mass equivalent diameters in Table I then led to the effective densities ρ_{eff} which are given in the last column of Table I.

As before an agreement cna be seen between experiments 33 and 35 as well as between experiments 39 and 40. The values of ρ_{eff} are comparable to the measured effective densities of PtO_x aerosols [5] and to those of the UO_2 aerosol.

These results lead to the conclusion that for the purpose of modeling condensation of steam onto particles during core meltdown accidents the best method is to use the geometric diameters of the particles and the unchanged Mason equation. Then the necessity to determine condensational shape factors does no longer exist. Instead a new problem is created: determining the effective density of the aerosol particles. This new problem, however, can be solved much easier experimentally as well as in the computation process.

Further it has to be pointed out that the spherical shape of the particles not only influences the modeling of condensation, but also leads to a changed treatment of the shape factor problem for the other aerosol processes. After a reliable determination of the effective densities of the aerosol it might be necessary to redefine the equations in the NAUA model.

We should emphasize again that this simple approach is valid only in LWRs where the steam saturated atmosphere guarantees the formation of spherical particles by continuous condensation and evaporation of steam onto the dry aerosol.

CONDENSATION ON SOLUBLE PARTICLES

For completeness the behavior of soluble particles has to be treated, too. The main difference compared to insoluble particles as UO_2 or PtO_x is that even in the undersaturated regime of the steam air mixtures soluble particles exist in the form of solution droplets already which are much larger than the corresponding 'dry' nuclei. So condensation due to supersaturation will involve much more particles as would be expected on the basis of their 'dry' diameter. This has been proved by an extensive series of condensation experiments with $Na\,NO_3$ aerosols.

Moreover, during our UO_2 experiments with rather low particle concentrations impurities of soluble particles always participated in the droplet formation process in spite of their relatively small size. So the C_e values in Table II were actually measured higher for experiments 108 and 109 (in brackets) and had to be corrected for the undesired effect of soluble aerosol particles. (The given C_e values are for UO_2 particles only).

For the application in an LWR core meltdown aerosol behavior model, however, it should be noticed that the fraction of soluble aerosol material is exceedingly small compared to the insoluble species. Only 6% of the total aerosol is constituted by fission products, among these a small fraction is in soluble chemical form.

Therefore, taking internal mixing of the particles for granted, the soluble fraction of a particle will not bind so much water that the particle grows significantly beyond its 'geometrical diameter' which will be used in computation. Soluble aerosol materials in core meltdown accidents may consequently be left out of special considerations regarding steam condensation phenomena.

CONCLUSIONS

Measurements of condensation of steam on aerosol particles have been performed under LWR post accident conditions in order to determine input data for the NAUA model. Platinum oxide, uranium dioxide and sodium nitrate have been used as aerosol materials. The generalized result from 122 tests is that after condensation-evaporation processes the particles are always compacted to spheres irrespective of their original shape. Since in an LWR containment local short lived condensation processes will contiuously occur the shape of the particles may be assumed as spherical throughout the whole computation.

The modeling of the condensation process is then possible using the unmodified Mason equation and the geometric diameter of the spherical particles as a size measure. Moreover, the spherical shape facilitates also the treatment of other aerosol processes. The determination of the effective density together with the geometrical diameters will then solve the shape factor problem for condensation, coagulation and mobility in LWR accident aerosol behavior modeling.

REFERENCES

[1] Nuclear Aerosols in Reactor Safety, CSNI/SOAR 1, OECD (1979)

[2] G. Haury, C. Sack, W. Schöck, in Project Nuclear Safety Semiannual Report 1976/1, pp 450-469, KFK 2375 (1976)

[3] H. Bunz, W. Schöck, The Behavior of Highly Concentrated Aerosols in a Condensing Steam Atmosphere. 6th Annual Meeting of the Gesellschaft für Aerosolforschung, Vienna, 26-28 September, 1978

[4] Generation of Test Aerosols - Platinum Oxide Generator, Guidelines of the Verein Deutscher Ingenieure, VDI 3491, Blatt 6 (1980)

[5] W. Muhr, W. Schöck, Generation of a Platinum Oxide Aerosol, 6th Annual Meeting of the Gesellschaft für Aerosolforschung, Vienna, 26-28 September, 1978

PREDICTION OF THE RATES OF CHEMICAL TRANSFORMATION OF SODIUM FIRE AEROSOLS

Douglas W. Cooper
Harvard School of Public Health
Boston, Massachusetts, U.S.A.

ABSTRACT

Sodium fires resulting from accidental releases of liquid sodium from a liquid metal fast breeder reactor (LMFBR) would produce aerosols consisting of oxides of sodium, which would tend to react with available water vapor and carbon dioxide. The hydroxide aerosol particles thus formed would be particularly corrosive and hazardous, likely exceeding the U.S. industrial hygiene threshold limit value of 2 mg/m^3. Reaction of the hydroxide with carbon dioxide to form the carbonate would make the aerosol substantially less hazardous chemically. We extend the analysis of Clough and Garland to study the rates of transformation of the oxides to hydroxide and the hydroxide to the carbonate, assuming that mass transfer is limiting. The cases studied here are gas-phase transport to solid or liquid particles and the transport within particles which are liquids, solids, or agglomerates. For sodium fire aerosols less than 10 μm in diameter, mass-transfer rates in air are sufficiently fast that the particles should be converted to the carbonate within seconds, except those particles which are solid or have a solid shell (and are larger than 1 μm). Such non-porous particles would be expected only if the aerosol passes through a liquid state during or after agglomeration, due to melting or the absorption of water.

INTRODUCTION

Interest in the development of Liquid Metal Fast Breeder Reactors (LMFBR's) has spurred the study of the reactions of molten sodium with air and with other gas mixtures that might be used in the reactor containment volume. Sodium and the compounds formed in sodium fires are quite reactive; the aerosols from a sodium fire can be hazardous chemically (as well as radioactively), as is indicated by the existence of a U.S. industrial hygiene standard for NaOH aerosols, (2 mg/m^3), a standard reviewed critically elsewhere [1,2].

In this paper, we continue our analysis of the kinetics of the transformations of sodium fire aerosols, building upon and extending the work of Clough and Garland [3]. We analyze the reactions between the oxides of sodium and water and between sodium hydroxide and carbon dioxide in terms of the mass transfer of the reagents, assuming that these reactions proceed more quickly than the mass transport of the reagents through the gas and through the particles. The chemical composition of the aerosols can be critical with regard to their toxicity and their aerodynamic behavior [1,2,3].

THEORY

Relevant Chemical Reactions

We analyze here the transport of reagents for the following aerosols: droplets (aqueous solutions) of sodium hyroxide and sodium carbonate, droplets of molten NaOH, solid particles of the oxides and the hydroxide, and their agglomerates.

Most of the relevant reactions of sodium with oxygen, water and carbon dioxide are summarized in Table I [4]. (In some circumstances, the carbonate/bicarbonate equilibrium will be important, too). The reactions we focus on are those emphasized by Clough and Garland [3], the formation of the hydroxide from the oxides:

$$Na_2O_2 + H_2O \rightarrow 2NaOH + \tfrac{1}{2}O_2 \qquad (1)$$

$$2NaO_2 + H_2O \rightarrow 2NaOH + 3/2\,O_2 \qquad (2)$$

and the formation of the carbonate from the hydroxide:

$$2NaOH + CO_2 \rightarrow Na_2CO_3 + H_2O. \qquad (3)$$

At low humidities (<35% RH), the sodium hydroxide will be a solid, but at higher relative humidities it will be a droplet, a slurry or an aqueous solution. As either solid or liquid, it can form the less alkaline carbonate. The hydroxide and carbonate in solution will precipitate, if saturated, to form a slurry that will become a solid, having various compositions depending upon the amounts of hydroxide and carbonate present. The carbonate solution will dry forming $Na_2CO_3 \cdot 10\,H_2O$, and perhaps other hydrates, unless the relative humidity is greater than 95% RH[3].

Table I. Relevant reactions of sodium and its compounds [4].[a]

In the presence of an excess of water:	
$Na + H_2O\ (l) \rightarrow NaOH + \frac{1}{2}H_2$	$\Delta H^\circ_{298} = -33.7$ kcal/mole[b]
$Na + H_2O\ (g) \rightarrow NaOH + \frac{1}{2}H_2$	$\Delta H^\circ_{298} = -45.7$ kcal/mole
$Na_2O + H_2O \rightarrow 2NaOH$	$\Delta H^\circ_{298} = -46.8$ kcal/mole
In the presence of an excess of sodium:	
$2Na + H_2O \rightarrow Na_2O + H_2$	
$Na + NaOH \rightarrow Na_2O + \frac{1}{2}H_2$	$\Delta H^\circ_{298} = 1.59$ kcal/mole
$Na + \frac{1}{2}H_2 \rightarrow NaH$	$\Delta H^\circ_{298} = -13.7$ kcal/mole
In absence of water vapor:	
$2Na + \frac{1}{2}O_2 \rightarrow Na_2O$	$\Delta H^\circ_{298} = -100.7$ kcal/mole
$2Na + O_2 \rightarrow Na_2O_2$	$\Delta H^\circ_{298} = -120.6$ kcal/mole
In presence of CO_2:	
$2Na + CO_2 + \frac{1}{2}O_2 \rightarrow Na_2CO_3$	$[\Delta H^\circ_{298} = -175.3$ kcal/mole$]$
$2NaOH + CO_2 \rightarrow Na_2CO_3 + H_2O$	$[\Delta H^\circ_{298} = -40.0$ kcal/mole$]$

[a] Based on summaries by Settig [5] and Reist [6].

[b] 1 cal = 4.18 joule.

In the vicinity of a sodium fire, it is unlikely the relative humidity will be high enough that the aerosol will be aqueous solution droplets. The moisture which represents 50 percent relative humidity at 25°C (77°F) represents about 28 percent relative humidity at 35°C (95°F) and about 17 percent relative humidity at 45°C (113°F), well below the NaOH transition humidity.

Some physical constants of the sodium compounds of interest are given in Table II [7]. Two notable facts are: 1. sodium carbonate decahydrate, a common form under atmospheric conditions, loses most of its water of hydration above 34°C, tending to become the monohydrate, with a weight loss of about 60 percent; 2. sodium hydroxide melts at 318°C, which means it may not be solid near the fire, depending on conductive and radiative heat transfer.

Interphase Mass Transfer

Although the burning of sodium can proceed in the gas phase as a molecular interaction between the sodium vapor (vaporized by the heat of combustion) and oxygen, the other reactions (conversion of the sodium oxides to hydroxides to carbonate) are expected to proceed at the particle surface and within it. Determining how long it takes to convert a particle

Table II. Some Physical Constants for Sodium Compounds [7].

Name	Formula	Molecular Weight	Specific Gravity	Melting Point (°C)	Boiling Point (°C)
carbonate	Na_2CO_3	106	2.53	851	
-decahydrate	$Na_2CO_3 \cdot 10H_2O$	286	1.44	(loses H_2O at 34°C)	
-monohydrate	$Na_2CO_3 \cdot H_2O$	124	2.25	(" " " 100°C)	
bicarbonate	$NaHCO_3$	84	2.16	(loses CO_2 at 270°C)	
hydroxide	NaOH	40	2.13	318	1390
monoxide	Na_2O	62	2.27	sublimes at 1275°C	
peroxide	Na_2O_2	78	2.80	decomposes at 460°C and 657°C	
-octohydrate	$Na_2O_2 \cdot 8H_2O$	222		decomposes at 30°C	
superoxide	NaO_2	55			

to a different chemical form is rather difficult, being an example of interphase mass transfer.

The rate at which chemical species A in the particle is converted to species AB by reaction with species B from the gas phase is determined by the rate at which A is transported to the particle surface, the rate at which A spreads through the particle, the rate of reaction of A and B, and the rates of transport diffusion of the reaction products through the particle and the gas.

Our discussion of this follows Welty et al. [8]. Figure 1 (after [8]) shows schematically the concentration (c_A), as a function of radial distance, of a species A during the transfer of that species from the gas to the particle. The concentration is assumed to reach that of the bulk of the gas within a distance δ_G and to reach the concentration of the interior of the particle within distance δ_L. For now, we assume the particle is a liquid droplet. (This analysis will not be appropriate for the very last stages of transformation, as the concentration at the interior of the particle becomes affected by the transformation.)

The flux of species A (having partial pressure p_A) will be given by [8]:

$$N_{A,G} = k_G(p_{A,G} - p_{A,i}) \tag{4}$$

for the flow through the gas "film," and, for transfer through the particle,by:

$$N_{A,L} = k_L(c_{A,i} - c_{A,L}), \tag{5}$$

and these two fluxes will be equal during the steady-state transfer of component A. The subscripts G, i, L refer to the gas, the interface, and the liquid. Generally, neither the partial pressure nor the concentration is known at the interface, so that the values p_A^* and c_A^* are used instead;

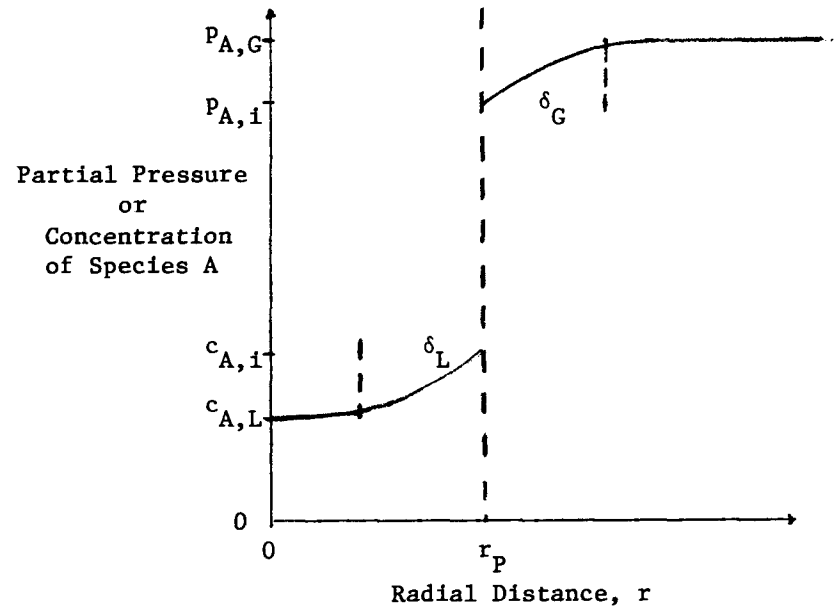

Figure 1. Schematic of relationships of gas partial pressure and liquid concentrations of species A during interphase mass transfer.

p_A^* is the partial pressure that would be in equilibrium with the concentration $c_{A,L}$ of the particle and c_A^* is the concentration that would be in equilibrium with the partial pressure of A in the gas phase, $p_{A,G}$. With this stipulation, the transfer can be described either in terms of an overall mass-transfer coefficient for the gas phase:

$$N_A = K_G(p_{A,G} - p_A^*) \tag{6}$$

or the particle phase:

$$N_A = K_L(c_{A,L}^* - c_{A,L}). \tag{7}$$

If the partial pressure and the concentration are related by

$$P_{A,i} = H\, c_{A,i}, \tag{8}$$

where for liquids H is the Henry's law constant, then the overall mass-transfer coefficients are related by:

$$1/K_G = 1/k_G + H/k_L \tag{9}$$

$$1/K_L = 1/k_L + 1/Hk_G \tag{10}$$

For a highly soluble gas (which is similar to one being consumed by a reaction), the liquid is not providing the resistance to mass transfer; rather, the transfer is gas-phase controlled. For gases (such as CO_2 in

water) of low solubility, H is so large that only the liquid phase resistance to transfer need be considered, and the transfer is liquid-phase controlled.

Gas-Phase Controlled Transfer

In this section, we assume that the transfer from the gas phase to the particle is the limiting step. We use mole fraction, y, rather than partial pressure, p, but they are related to the total pressure, P, by

$$y = p/P \tag{11}$$

for perfect gases.

The rate W (moles/s) at which the gas diffuses to the particle is given by

$$W = -k\pi d^2(y_i - y_b)/(1 - y_i), \tag{12}$$

in which k is a transfer coefficient, d is the particle diameter (m), and b and i refer to the bulk of the gas and the interface, the particle surface. This equation assumes that we have a steady-state flux, which occurs for times, particle diameters, and gas diffusivities(D*) such that:

$$t >> d^2/4D^* \tag{13}$$

in which t is time (s). For particles 20 μm in diameter and for CO_2 diffusing in air ($D^* = 0.15$ cm^2/s), steady state is reached for times greater than 10^{-5}s. (The diffusivities are somewhat different for water vapor and for oxygen in air.)

The relative motion between the particle and the gas in which it is suspended enhances mass transfer somewhat (the "ventilation factor" [10]), but this enhancement is less than 4 percent for a particle 20 μm in diameter, having unit specific gravity, and is negligible for particles this small. Then k becomes cD^*/d, where c is the carrier gas (air) concentration.

Assume $y_i << y_b$, which is consistent with reaction within the particle or with the dissolving of the gas into the particle, at least during the early stages of approach to equilibrium, then, in a continuum:

$$W = 2\pi cD^* y_b d. \tag{14}$$

The following empirical interpolation factor proposed by Fuchs and Sutugin [11] can be applied to this equation for diffusive flux, to extend its range to include particles smaller than the gas mean free path ($\lambda = 0.065$ μm for air at NTP):

$$[(1 + Kn)/(1 + 1.71\,Kn + 1.333\,Kn^2)] \tag{15}$$

where $Kn = 2\lambda/d$. This correction is 0.42 for $d = 0.1$ μm, 0.72 for $d = 0.3$ μm, and 0.91 for $d = 1.0$ μm.

Tables III and IV show, respectively, particle diameter, gas diffusion rate (equations (14),(15)) for particles of this diameter, number of moles of the sodium compound indicated, and the time it would take for enough of the gas phase species to diffuse to the particle to convert it to the chemical species indicated. The mole fractions assumed were 330 ppm for CO_2 and 1.0×10^{-2} for H_2O (thirty percent relative humidity at 25°C). For the transformation of the oxides to the hydroxide, we assumed that the diffusion of the water vapor to the particle, not the diffusion of the oxygen away from the particle, would be limiting.

Table III. Time Needed (Theoretically) for Gas-Phase-Controlled Diffusion of H_2O to Convert Solid Na_2O_2 Particles of the Indicated Diameters to NaOH Particles at 30 Percent Relative Humidity and 25°C.

Particle Diameter (μm)	H_2O Flux (Moles/s)	Particle Na_2O_2 (Moles)	Time Needed (s)
0.1	3.1×10^{-12}	1.9×10^{-17}	6×10^{-6}
0.3	1.6×10^{-11}	5.0×10^{-16}	3.1×10^{-5}
1.0	6.6×10^{-11}	1.9×10^{-14}	2.8×10^{-4}
3.0	2.2×10^{-10}	5.0×10^{-13}	2.3×10^{-3}
10.0	7.3×10^{-10}	1.9×10^{-11}	2.6×10^{-2}

Table IV. Time Needed (Theoretically) for Gas-Phase-Controlled Diffusion of CO_2 to Convert Solid NaOH Particles of the Indicated Diameters to Na_2CO_3.

Particle Diameter (μm)	CO_2 Flux (Moles/s)	Particle NaOH (Moles)	Time Needed (s)
0.1	0.6×10^{-13}	2.8×10^{-17}	2×10^{-4}
0.3	3.0×10^{-13}	7.5×10^{-16}	1.2×10^{-3}
1.0	1.3×10^{-12}	2.8×10^{-14}	1.1×10^{-2}
3.0	4.2×10^{-12}	7.5×10^{-13}	0.9
10.0	1.4×10^{-11}	2.8×10^{-11}	1.0

A sodium fire will raise the temperature in its vicinity and, unless there is a major failure of containment integrity, raise the pressure as well. The diffusivity at elevated temperatures and pressures (T_2,P_2) in comparison to that at standard temperature and pressure (T_1,P_1) is [8]:

$$\frac{D_2^*}{D_1^*} = \left(\frac{P_1}{P_2}\right)\left(\frac{T_2}{T_1}\right)^{3/2}\left[\frac{\Omega_D(T_2)}{\Omega_D(T_1)}\right] \qquad (16)$$

where $\Omega_D(T)$ is a very weak function of temperature. Sodium fire temperatures measured by Ettinger et al.[12] ranged from 390°C to 670°C; at 670°C equation (16) implies a 5.6 increase in the gas diffusivity and a $(943/298)^{\frac{1}{2}} = 1.8$ increase in the diffusive flux, taking into account the local expansion of the gas (thus decrease in its concentration), assuming the heating does not substantially increase the pressure in the vessel. The values in Tables III and IV can be adjusted easily to compensate for the dependence of diffusivity on temperature and pressure.

From Tables III and IV, it is evident that the transfer of water vapor to the oxide particles is about two orders of magnitude faster than the diffusion of carbon dioxide to the hydroxide particles, but that in both cases the gas-phase transfer is rapid enough to allow complete transformation in seconds and generally in much less than seconds.

The transformation of the sodium oxides to NaOH will result in the formation of droplets if the relative humidity is greater than 35% RH. These droplets will be larger than the dry NaOH particles assumed for Table IV, and the flux of CO_2 to their surfaces will be more rapid. To use Table IV for calculating the time for enough carbon dioxide to diffuse to the droplet to convert all the sodium hydroxide, one can determine the droplet diameter, d, from the dry particle diameter, d_o, using an expression we developed, patterned after that of Neiburger and Wurtele [13], which closely matches the values computed by Clough and Garland [3]:

$$d/d_o = 0.87/(1 - H)^{1/3} \quad \text{for } 0.35 < H < 0.99 \tag{17}$$

One can interpolate the carbon dioxide diffusion rate from Table IV and calculate the moles of Na present to be reacted with the CO_2. A final check must be made to compare the mole concentration of the sodium in the aerosol with the mole concentration of carbon dioxide in the air. At 100 mg/m^3 of NaOH there are about four times as many moles of CO_2 as there are moles of Na in the same volume, thus only about one-eighth of the available carbon dioxide will be consumed, and y_b will not be very different from 330 ppm, even when the reaction is finished and even assuming no carbon dioxide diffuses into the aerosol cloud from without. At higher concentrations of NaOH, depletion of CO_2 may become limiting.

Particle-Phase-Controlled Transfer

If diffusion through the particle phase is the rate-limiting step, then (ignoring the reaction) the concentration of A in the gas at the surface of the particle is essentially what it is in the bulk of the gas. The concentration in the particle material right at the surface(c_i) is that which would be in static equilibrium with the gas concentration. For liquids obeying Henry's law, c_i would be proportional to the concentration in the gas. For diffusion without reaction, the relation of the average concentration of A throughout the particle ($\overline{c}$) to that at the interface (c_i) is [14]:

$$(c_i - \overline{c})/c_i = f(t/t_d) \tag{18}$$

in which $t_d = d^2/4D_p^*$ is the characteristic time for diffusion and D_p^*

is the diffusion constant for diffusion through the material of which the particle is made. The function $f(t/t_d)$ is an infinite series of exponential functions; $f(t/t_d)$ falls to $\leq 1 \times 10^{-2}$ for $t/t_d \geq 0.4$, so that the particle would be at an average of 99 percent or more of the surface concentration for $t \geq 0.4\ t_d$.

The diffusivity of carbon dioxide in water (at 293°K) is 1.77×10^{-5} cm^2/s and that of sodium chloride is about 25% less than this, depending a bit on concentration [8]. Using a value of 1.8×10^{-5} cm^2/s for D_p^*, one obtains the following values for $d^2/4D^*$, the characteristic time for diffusion (for the particles as aqueous solutions):

$d_p(\mu m)$:	0.1	0.3	1.0	3.0	10.0
$t_d = d^2/4D_p^*(s)$:	1.4×10^{-6}	1.3×10^{-5}	1.4×10^{-4}	1.3×10^{-3}	1.4×10^{-2}

Diffusion throughout the droplets would occur in much less than seconds. However, the solubility of the gaseous species, despite this rapid achievement of concentration equilibrium, may not provide an adequate flux of reactant to achieve comparably swift chemical transformation.

Analysis of the interphase transport to the liquid metal droplets and, especially, to the solid particles, is hindered by a lack of information on the solubility and diffusivity of the gases in the metal and its compounds. For transport for which the particle phase is limiting, we are assuming that reagent is being transported from the gas phase very rapidly. Therefore, it seems reasonable to view the surface as a sink for the particle-phase reagent and to estimate the time which is characteristic of the diffusion of the sodium to the surface. The solution is an infinite series in $t/t_d = d^2/4D_p^*$. The concentration at the center of the sphere is one-tenth its original value at $t/t_d = 0.3$ and less than one-thousandth its original value at $t/t_d = 1$ [8]. We will use our limited information about the diffusion of Na to estimate t_d for these cases, assuming that the diffusion of the reaction product gases is as fast or faster.

For sodium metal as a liquid, it is difficult to find diffusivities for O_2 (or H_2O), but they can be expressed in the form [15]:

$$D_p^* = D_0^* \exp(-Q/RT) \qquad (19)$$

where $Q = 2.4 \times 10^3$ cal/mole, $R = 1.99$ cal/mole/°K and $D_0 = 1.1 \times 10^{-3} cm^2/s$. At 226°C (approximately the Na ignition point in air) $D_p^* = 1.0 \times 10^{-4} cm^2/s$, and at 98°C (the Na melting point) $D_p^* = 4.3 \times 10^{-5} cm^2/s$, values less than an order of magnitude different from the values for the aqueous solutions discussed above.

Sodium as a solid has a diffusivity which follows the same Arrhenius-type equation, with $D_0^* = .242$ cm^2/s and $Q = 10.45 \times 10^3$ cal/mole [15], giving $D_p^* = 6.6 \times 10^{-9} cm^2/s$ for the self diffusion of Na in solid Na. The diffusion of Na in the mineral "permutite" is $1.3 \times 10^{-8} cm^2/s$ and in "natrolite" ($Na_2O \cdot Al_2O_3 \cdot 3SiO_2 \cdot 2H_2O$), it is $1.5 \times 10^{-10} cm^2/s$ [16]. In estimating the characteristic diffusion time for a solid particle, we used $t_d = d^2/4D_p^* = d^2/10^{-8}(cm^2/s)$, giving the following characteristic diffusion times:

d_p(μm):	0.01	0.1	1.0	10
t_d(s) :	10^{-4}	10^{-2}	10^{0}	10^{2}

Each of these values is about 10^6 larger than for diffusion through a droplet (aqueous solution or molten liquid).

Effect of Reaction on Mass Transport

A previous analysis of the mass transfer limitations on transformation [3] assumed that the CO_2 had to reach an equilibrium concentration, given by its Henry's law solubility, in the droplet surface layer and then diffuse through the droplet. This led to estimates of $\sim 10^2$s seconds for 10 μm droplets. For a very rapid reaction, it is appropriate to assume that the concentration of the particle-phase reactant approaches zero at its surface and that diffusion of this reactant, with the characteristic diffusion times we have given above, is the rate-limiting step in the particle phase. The characteristic diffusion times become the estimates for the time for this step, and they are much shorter than those calculated previously [3], because the relevant concentration is that of the particle-phase material, not the gaseous species dissolved in the particle.

Mass Transfer Across a Solid Shell

At relative humidities above 35 percent, sodium hydroxide particles will be droplets. As they react with carbon dioxide to form the carbonate, the mixture will no longer in equilibrium with the humidity as a solution. The surface will tend to dry and form a carbonate shell, leaving a core of hydroxide. (See also reference 23.) Mass transfer of CO_2 through this shell will be proportional to the diffusivity of CO_2 through the solid (probably $10^{-9}cm^2/s$), without any acceleration due to reaction since the reaction in the solid will have already occurred. Our estimates for the time for diffusion through the solid particles without reaction indicate the order of magnitude for, say, the case in which half the particle volume is solid and half liquid. For particles one to ten micrometers in diameter, this implies times of 10^0 to 10^2 seconds. If one knew the molar concentration of dissolved CO_2 in the solid at the surface (c_1) and the diffusivity in the solid (D_p*), then the molar flux through a shell of thickness $d - d_1$ would be:

$$W \doteq \frac{2\pi c_1 D_p^* d_1 d}{d - d_1} \qquad (20)$$

and one could make the rough estimate of diffusion time much more nearly exact.

Mass Transfer Within Agglomerates

The aerosol of sodium fire products will be made up of agglomerates unless the humidity is high enough to form droplets or the temperature is high enough to keep the reaction products molten (see Table II).

The diffusivity within a porous solid is related to the diffusivity of the gas in air [19]:

$$D_e^* = (e/\tau)D^* \tag{21}$$

for continuum flow transfer, where e is the void fraction of the solid and τ is the tortuosity factor, generally 1.5 to 2 for unconsolidated solids [19]. For Knudsen transfer, the non-continuum case [19]:

$$D_K^* = \frac{8e^2}{3\tau S_g \rho_b}\sqrt{\frac{2RT}{\pi M}} \tag{22}$$

in which S_g is the total surface of the material per unit mass and ρ_b is the bulk (not particle material) density. In SI units, this equation becomes:

$$D_K^* = \frac{194e^2}{\tau S_g \rho_b}\sqrt{\frac{T}{M}} \tag{23}$$

The combined effective diffusivity is the harmonic mean of D_K^* and D_e^* (thus, the smaller of the two is controlling). Knudsen diffusion occurs where the pores are similar in size to the gas mean free path, λ(= 0.065 μm at STP), our case. Assuming that the particle is made up of N' primary particles of diameter d', its volume is

$$V_p = N'(\pi/6)(d')^3/(1 - e) \tag{24}$$

and its surface-to-mass ratio is

$$S_g = \frac{6}{d'}\frac{(1 - e)}{\rho_b} \tag{25}$$

and equation (23) becomes

$$D_K^* = \frac{194\ e^2 d'}{6\tau(1 - e)}\sqrt{\frac{T}{M}} \tag{26}$$

From a series of analyses of sodium fire aerosols (found to be sodium carbonate and perhaps its hydrates), Hinds et al.[17] measured an average particle density of ρ = 0.8 g/cm^3. (The mass median aerodynamic diameters averaged 1.8 μm with an average geometric standard deviation of 1.6.) This implies the following porosities for the indicated species: 45% (as $Na_2CO_3 \cdot 10\ H_2O$), 63% (as $Na_2CO_3 \cdot H_2O$), 68% (as Na_2CO_3). In a different set of tests,

the bulk density of sodium fire aerosol deposits was 0.33 g/cm^3 for particles which were found (by acetone immersion) to have a material density of 2.3 g/cm^3 [18], meaning that the deposit porosity was about 86%. This provides another estimate of the porosity of the individual particles: Tapping the graduated cylinder almost doubled the bulk density [18], bringing the porosity to 74%. Solid aerosol particles ($d \sim 1$ μm) normally form cakes with roughly 50% porosity; if this is true for the packing of the sodium fire aerosols in the graduated cylinder, it suggests the individual particles had porosities of about 50%. For $e = 0.5$, $d' = 1 \times 10^{-7}$m(0.1 μm), $\tau = 2$, $T = 300°K$, and $M = 44(CO_2)$, D_K^* becomes 2×10^{-6}m^2/s (0.02 cm^2/s, rather than 0.15 cm^2/s). This effective diffusivity, although low compared with the usual gas diffusivity, is still three orders of magnitude larger than that of the liquid species discussed here. The flux at the agglomerate surface is governed by equation (14), with D^* being replaced by D_K^*, giving times needed for transformation which are about ten times longer than those in Tables III and IV. This indicates rapid diffusion within the agglomerates, followed by diffusion within the primary solid particles, which we have seen to take about 10^{-2}s for primaries with diameters about 0.1 μm.

DISCUSSION: EXPERIMENTAL INVESTIGATIONS BY OTHERS

Murata et al. [20] vaporized sodium to form aerosols of 1 mg/m^3 concentration and then allowed them to react with oxygen in the presence of water vapor at several humidities and several concentrations of carbon dioxide. The dry particles were about 2 μm in mass median aerodynamic diameter with geometric standard deviations of 1.8 to 2.0. The mean residence time in the stirred reaction chamber was 1.4 minutes. Measurements were made of sodium content and of particle aerodynamic size distribution. For humidities below 40% RH, the particles remained dry. As the concentration of carbon dioxide in the chamber increased, the particles remained solid at increasingly high humidities. For atmospheric CO_2 levels, the transition to droplets was at humidities between 40 and 60% RH, suggesting the particles were predominantly sodium hydroxide, but at thirty times the carbon dioxide level the transition to droplets occurred at between 70 and 90% RH, suggesting the particles were predominantly in the carbonate form. The study qualitatively agreed with the work of Clough and Garland [3], but the relative amounts of carbonate and hydroxide were not identified for the various conditions, and the effect of humidity was confounded.

Zwicker et al. [21] used aerosols from controlled burning of sodium vapor to expose rats. The chemical form of the aerosol was ascertained by measuring pH while titrating with HCl. The aerosols were found to be primarily Na_2CO_3, having particle size distributions with mass median aerodynamic diameters between 0.5 and 1.5 μm and geometric standard deviations of about 3. The residence time was 18 seconds. The CO_2 exhalations of the animals may have contributed to the transformation of the aerosols to the carbonate form. In some instances a tenth or so of the aerosol was in the

form of bicarbonate, also less alkaline than the hydroxide. Aerosols containing some unreacted NaOH were formed by raising the humidity to 85% RH (thus increasing particle size and diluting the sodium compound) or by removing CO_2 (using Ascarite) from the air carrying the aerosol.

Hofmann et al. [22] made limited but informative tests involving aerosols generated by a sodium spray fire. The mass median aerodynamic diameter of the aerosols was 0.4 μm. The transition from oxide to hydroxide occurred within 10 seconds for these aerosols. They found that at 40% RH and at 70% RH, these aerosols had become predominantly (90% or more) sodium carbonate within 30 seconds. This work also supports the conclusions of Clough and Garland [3] and of Cooper et al. [1,2]. The following should be noted, however:
1. The reaction to form the carbonate was proceeding simultaneously with coagulation rather than after coagulation; thus the reaction was occurring for the primary particles, the small size of which favors rapid transformation, rather than for the agglomerates.
2. The hydroxide aerosols were probably liquid at both humidity levels.

Hilliard et al. [18] performed pool burning tests in the Containment Systems Test Facility at Hanford, and they found that the aerosol formed during the initial part of the burn was NaOH (from Na_2O_2 and the water vapor in the containment section), becoming about equally mixed with Na_2O_2 as the water vapor available was depleted. The amount of CO_2 available was limited. By the time the fires ended (60 minutes), the mass median aerodynamic diameters were 5 to about 12 μm, decreasing to about 3 μm in 24 hours. The particle sizes produced in this kind of simulated accident were, thus, substanially larger than those studied by Hofmann et al.[22].

CONCLUSIONS

The times (in seconds) characteristic of mass transport to the particles, under the assumptions indicated in the text above, are as follows:

mechanism	0.1 μm	1.0 μm	10 μm
diffusion within a reacting droplet	1×10^{-6}	1×10^{-4}	1×10^{-2}
gas-phase transport of H_2O	6×10^{-6}	3×10^{-4}	3×10^{-2}
diffusion of H_2O within a Na_2O_2 agglomerate	-	10^{-3}	10^{-1}
gas-phase transport of CO_2	2×10^{-4}	1×10^{-2}	1
diffusion of CO_2 within a NaOH agglomerate	-	10^{-1}	10^{1}
diffusion within a reacting solid particle	10^{-2}	10^{0}	10^{2}

Thus, for sodium fire aerosols in air, we expect the particles to become sodium carbonate within seconds. The reported persistence of NaOH at high humidities for times longer than 10 seconds[20,21,22] may be due to the formation of a shell of reacted solid (carbonate).

Further experimental work under controlled conditions and further modeling would be valuable in helping to predict the consequences of accidents involving technologies involving liquid sodium.

REFERENCES

1. Cooper, D.W., Underhill, D.W.,and Ellenbecker, M.J., "A Critical Review of Sodium Hydroxide Aerosol Toxicity," Prepared for the U.S. Nuclear Regulatory Commission, Contract AT(49-24)-0300, Report HSPH/EHS (NUREG)-880, Harvard School of Public Health, Boston, MA (December 1977).

2. Cooper, D.W., Underhill, D.W., and Ellenbecker, M.J., "A Critique of the U.S. Standard for Industrial Exposure to Sodium Hydroxide Aerosols," Am. Indus. Hyg. Assoc. J., Vol. 40, pp. 365-371, (1979).

3. Clough, W.S. and Garland, J.A., "The Behavior in the Atmosphere of the Aerosol From Sodium Fire," J. Nucl. Energy, Vol. 25, pp. 425-435 (1971).

4. Tadmor, Jacob, "Consequences of an Accidental Release of Sodium to the Environment from an LMFBR," Nuclear Safety, Vol. 14, No. 4, pp. 324-340, (1973).

5. Sittig, M., Sodium: Its Manufacture, Properties, and Uses, Reinhold, New York (1956).

6. Reist, P.C., "Review of the Probable Characteristics of Aerosols Resulting from Accidental Loss of Sodium Coolant," Report for U.S.A.E.C. on Contract AT(30-1)841, Harvard School of Public Health, Boston, MA (May 1969).

7. Weast, R.C., Handbook of Chemistry and Physics, Chemical Rubber Co., Cleveland, OH (1970).

8. Welty, J.R., Wicks, C.E., and Wilson, R.E., Fundamentals of Momentum, Heat, and Mass Transfer, 2nd Ed., John Wiley and Sons, New York (1976).

9. Fuchs, N.A., The Mechanics of Aerosols, The Macmillan Company, New York (1964).

10. Bird, R.B., Stewart, W.E., and Lightfoot, E.N., Transport Phenomena, John Wiley and Sons, New York (1960).

11. Friedlander, S.K., Smoke, Dust, and Haze, John Wiley and Sons, New York (1977).

12. Ettinger, H.J., Moss, W.D., and Busey, H., "Characteristics of the Aerosol Produced from Burning Sodium and Plutonium," Nuclear Sci. and Engng, Vol. 30, pp. 1-13, (1967).

13. Neiburger, M. and Wurtele, M.G., "On the Nature and Size of Particles in Haze, Fog, and Stratus of the Los Angeles Region," Chem. Rev., Vol. 44, pp. 321-335, (1949).

14. Perry, R.H. and Chilton, C.H., Chemical Engineers' Handbook, 5th Ed., McGraw-Hill, New York (1973).

15. Smithells, C.J., Metals Reference Book, 4th Ed., Plenum Press, New York (1967).

16. National Research Council, International Critical Tables, McGraw-Hill, New York (1926).

17. Hinds, W., Mallove, E., and First, M.W., "Density and Shape Factor of Sodium Aerosol," Report to U.S. ERDA, Contract No. E(11-1)-2803, Harvard School of Public Health, Boston, MA (April 1977).

18. Hilliard, H.K., McCormack, J.D., Hassberger, J.A., and Postma, A.K., "Sodium Oxide/Hydroxide Aerosol Properties and Behavior in a Large Vessel," HEDL-SA 1466, 15th DOE Nuclear Air Cleaning Conference (1978).

19. Sattersfield, C.N. and Sherwood, T.K., The Role of Diffusion in Catalysis, Addison-Wesley, Reading, MA (1963).

20. Murata, M., Naritomi, M., Yoshida, Y., and Kokubu, M., "Behavior of Sodium Aerosol in Atmosphere," J. Nucl. Sci. Technol., Vol. 11, No. 2, pp. 65-71, (1974).

21. Zwicker, G.M., Allen, M.D., and Stevens, D.L., "Toxicity of Aerosols of Sodium Reaction Products," J. Environ. Pathol. and Toxicol., Vol. 2, pp. 1139-1150 (1979).

22. Hofmann, C., Jordan, S., and Lindner, W., "Chemical Reactions of Sodium Fire Aerosols in the Free Atomsphere," (abstract) J. Aerosol Sci., Vol. 10, pp. 191-192, (1979).

23. Getler, J.L., Shelton, H.L., and Furlong, D.A., "Modeling the Spray Absorption Process for SO_2 Removal," J. Air Pollut. Control Assoc., Vol. 29, pp. 1270-1274, (1979).

SAMPLING TECHNIQUES AND ELECTRICAL MEASUREMENTS OF NUCLEAR AEROSOLS

COUNTING AND SIZING BY CONDENSATION NUCLEI COUNTER AND DIFFUSION BATTERIES

by Guy.J. Madelaine
Commissariat à l'Energie Atomique, Institut de Protection et de Sûreté Nucléaire
Département de Protection, Services Techniques de Protection
Service de Protection Technique, Laboratoire de Physique de l'Atmosphère
BP n°6, 92260 Fontenay-aux-Roses, France

Abstract

In a first part we examine sampling techniques and we insist on precaution to take to have the most representative sampling of the aerosol to be analysed.

The purpose of the second part of this paper is to review the basic principles of the various electrostatic measurement of aerosols. The latest knowledges about electrostatic measurement and sizing devices are discussed.

The third part concerns the utilisation of Condensation Nuclei Counter and diffusion batteries for detecting and sizing fine particles.

Workers in the field of atomic energy can be routinely exposed to weak concentration of radioactive aerosols, and, in the case of an accident, to higher concentrations entailing a serious risk.

It is imperative to know the properties and characteristics of these aerosols in order to set safety standards which can apply to the public and to workers in general, as well as previsions concerning the consequence of an accident. Such knowledge makes it possible, moreover, to define the behavior of the aerosols with time and after, to determine the best action to be taken in order to reduce the consequences as much as possible.

The most important quantities which condition aerosol dynamic behavior are concentration and size distribution, the latter being the most dominant factor of all particle properties. These two characteristics must be know in order to determine the behavior of aerosols released in the environment, the determination of purification and filtering systems, and the risk associated with aerosol inhalation.

The first part of this paper will deal with the sampling and collecting conditions, which are very important, as in most cases they determine the quality of the subsequent analysis.

In the second part, the methods based on the electric properties of aerosols will be examined in order to obtain indications concerning the concentration and the size distribution of the particles. The last part of this paper will treat the detection and measurement possibilities for submicronic particle size by means of condensation nuclei.counters associated or not with diffusion batteries.

I. Sampling and Collection

In order that the analyzed aerosol be representative of aerosols in the environment, the essential characteristics of total concentration, size distribution, and chemical nature must be preserved. The conservation of these parameters throughout the various sampling stages is the main problem when collecting and analyszing aerosols, and can be diagramed as follows (Figure 1) :

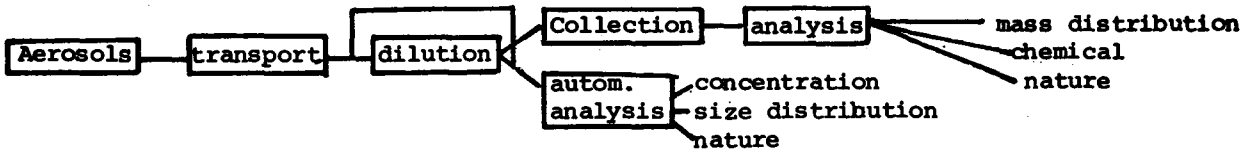

1) Actual sampling.

2) Transport with or without dilution depending on the aerosol concentration.

3) Actual analysis either automatic or in the lab after collection by the appropriate instrument.

I.1. Sampling

Sampling an aerosol through the opening of a pipe can be affected by :

- 1) particle characteristics : size, shape, and density.
- 2) suction rate and geometry of the sampling pipe.
- 3) gas motion around the opening which can be due to the suction alone or which can be complicated by local turbulence.

Taking into account the geometry of the collection tube opening, which should be as well-concived as possible, (rugosity, profile...), in calm air the optimal conditions leading to the most representative state possible for particles in suspension can be defined. The conditions should also take into account the choice of a collection pipe as a function of the suction rate ; the size and the density of the particles to be sampled. Davis (1) has defined the criteria for pipe capture. They depend upon :

- The inertia of the particle characterized by Stokes' number. $Stk = \frac{\tau U}{R} < 0.032$. τ being the relaxation time ($\tau = \frac{\rho D^2}{18\mu} C$) with ρ and D respectively the particle density and diameter, U et μ the average flow velocity and the dynamic viscosity of the air, R the radius of the pipe.

- The relative sedimentation velocity $V's = \frac{Vs}{U} < 0.04$ ($Vs = \tau g$). V's being be the terminal velocity and g gravity acceleration. These criteria are extremely limiting. Agarwal (2) be recalculation, has given the sampling efficiencies which are found in terms of Stockes number and of the relative sedimentation velocity. The results are shown in Figure 1. Thus, if the flow rate Q and the pipes radius are known, the sampling efficiency can be determined. For example, for a particle of unit density, a pipe radius of 1 cm, and flow rate of 50 l mn^{-1}, the theoretical sampling efficiency is 100 % up to 60 µm. It becomes 90 % for d = 70 µm.

If collection takes place in pipes where flow exists and as soon as particles larger than 5 µm are found, velocities must be sampled from the isokinetic meaning that the collection rate should be adjusted so that the linear velocity of the air in the collection orifice is equal to that of the air in the pipes. If the former exceeds the latter, some particles due to their inertia, will not be collected, and the concentration will be underestimated. In the opposite case, it will be overestimated.

If this is not the case, corrections should be made and expressed as a function of the respective velocities in the pipes and during collection as well as a function of Stockes number (Figure 2).

Very strict, detailed standards determine the numbrer and place for the sampling as a function of the pipe geometry so that the samples are representative of the concentration and of the real size distribution of the particles in the pipes.

1.2. Aerosol transport

The following question can now be asked : when an aerosol is transported in a pipe having a diameter D and a length L at a rate Q, what will be the fraction (F = N/NO) of the aerosol which passes through the pipe ? This fraction should be a maximum in order to obtain the best possible représentation.

The part collected will depend upon several parameters linked either to the flow rate (laminar or turbulent) or to forces which can act upon the particles (gravity, electricity, thermophoresis).

For laminar flow, that is for a flow rate having a Reynolds number of less than or equal to 1200, the principal deposit mechanisms are mainly Browian motion for particles smaller than 0.1 µm and sedimentation for particles larger than 1 µm. Using equation by Gormley and Kennedy (3) as well as Fuchs (4) make it possible to evaluate diffusion and sedimentation loss in a cylindrical pipe. Figure 3 and 4 show the penetration values as a function of particle diamter. The parameters are respectively $L/R^2\bar{U}$ and $3L/8R\bar{U}$ which for laminar flow leads to the value $\frac{Q}{R} < 20$. L is the length of the pipe, R its radius $\bar{U}$ and Q being respectively the average velocity and the sampling rate. Losses by diffusion apply only to particles smaller than 0.1 µm and by sedimentation to particles larger than 5 µm in diameter.

For turbulent flow corresponding to a Reynolds numbrer greater than 3000, the deposit mechanisms will be due to turbulent diffusion and eventually to sedimentation.

By using works by Sehmel (5) and more recently by Liu and Agarwal (6), the loss percentage by turbulent diffusion as a function of particle diameters can be found (Figure 5).

In conclusion, a certain number of recommandations can be made concerning the best collection and transport conditions for a particle cloud :

1) If the collectionline is verticale.

   - a turbulent flow should be used as it limits the Browian diffusion of fine particles if most of the aerosol is submicronic ;
   - a laminar flow should be used which avoids turbulence for larger particles if most of the aerosol is greater than a micron.

2) If the collectionline is horizontal,

   - a turubulent flow will be chosen in all cases in order to limit Browian diffusion on the one hand and to reduce sedimentation on the other.

Remarks

It should be noted that in the above, the important abnormalities which can be caused by the presence of obstacles, diaphrams, valves, etc., and which should be reduced to a minimum, were not taken into account.

If the presence of a curve becomes indispensable, its curve radius should be greater tan eight times the diameter of the pipe. In any case, the length of the collection line should be shortened as munch as possible.

The internal surface should be particularly well-cared for so that any rugosity capable of modifying the Reynolds number or increasing the captation parasite in addition to the particle should be avoided. The nature of the material should be adapted to the chemical nature of the aerosol under study. Special attention should be given to captation of aerosol be electrical image effect. This phenomenon can be reduced by using when possible grounded metallic materials instead of other materials such as plastics, rubber, or glass. If possible the aerosol should have a minimum electric charge by puting the particles into a Boltzmann equilibrium before introducing them into the collection line. Figure 6 (7).

Finally, the results given above correspond to particles of unit density. If, for example, this density is greater than a factor of 2 to 3, the minimal size of the captured particles can be greatly reduced.

1.3. Concentrated Aerosol

If the concentration is very high, which is usually the case for aerosols resulting from sodium combustion, the collection instrument should generally have a dilution device making it possible to treat the problem in an easier way.

This dilution can be dynamic, meaning that a mixture of clean air and the sample takes place constantly or it can be "pseudo static", that is, a known volume of contaminated gas is introduced into an vessel whose characteristics are known. If the aerosol is very concentrated, thus making great dilution necessary (> 1000), the first device in general calls for a prohibitively large instrument necessitating a very important gas flow.

If the dilution used is "pseudo static", the time spent in the dilution volume should be reduced as much as possible in order to avoid :

- losses by sedimentation which will vary as a function of the ratio t/H, H being the height of the enclosure used, t the time spent by the aerosol ;

- losses by diffusion as a function of the ration $\frac{S}{E}$ (surface and volume of the enclosure) and of the diffusion bounday layer ;

- modification of the aerosol size spectrum by aerosol coagulation. The aerosol size distribution will be radically modified in a relatively short time if the numerical concentration goes over 10^6 p.cm^{-3}. and will depend on the more or less important presence of fine particles. A rapid decrease of very fine particles (D $\sim$ 0,01 µm) will take place, although particles greater than a µm should not evolve too quickly.

1.4. Conclusion

This short review which is by no means exhaustive, shows the importance given to the definition of a collection device, even before defining an experimental procedure for measuring "in situ". If this device is poorly defined, important errors greater than those introduced by analysis itself can be incurred.

The most reasonable procedure, before beginning any series of experiments, is to calibrate not only the measurement device but also the entire collection structure as seen schematically in Figure 1. With a well-chosen aerosol calibrator, an assessment showing the losses and the aerosol size distribution modifications to be studied should be obtained.

II. Electrical Measurement of Aerosols

The high electric mobility of aerosols in an electric field makes it possible to collect, separate, and classify particles.

The rapid advances in electronics during the past few years have resulted in a number of electrostatic measurement techniques and instruments being brought into general use.

II.1. Basic principles of electric aerosol measurement

A charged particle suspended in a gas and having a charge q is examined. The application of an electric field $\vec{E}$ produces a force $\vec{F_e} = q\vec{E}$ on the particle. The particle then moves at a terminal velocity $\vec{V}_E$ due to $\vec{E}$, the friction force $\vec{F}_F$ being equal to $\vec{F}_e$. The velocity $\vec{V}_E$ can be combined geometrically with velocities due to other forces. Because by definition the dynamic mobility B, $\vec{V}_E = \vec{F}_e B$, measuring Ve q and E results in

$$B = \frac{\vec{V}}{q\vec{E}}$$

B is determined by particle force and size. However, if q is not known, only qB can be found experimentally.

In general, a measurement device based on the electric properties of aerosols can logically be classified into three main parts :

- aerosol charging ;
- precipitation or classification by electric mobility ;
- aerosol detection.

Two charge mechanisms which have given rise to measurement techniques are worth mentioning :

- electrification of particles which results from the contact of a particle with a surface ;
- charging by fixation of one charged particle with another. The charged particle may be an electron, a small ion, or another charged particle.

II.2. Contact electrification

The transfer of charge between particles and a probe via contact electrification can be used as the basis of a monitor for particulate matter. Important advantages of this type of device include the ability to make real time measurement (response time $\sim$ 10 sec) sensitivity over a wide range of concentration (0 - 10 g/m^3).

The development of this technique has been very slow because no quantitative theory has been found for this phenomenon especially concerning the insulating materials. Harper's theory (8) refers principally to the transfer of a charge between two bodies as the result of pure contact.

These instruments function on the following principle : an aerosol flux is directed around or through an insulated probe. The charge is transferred causing a shock between the particle and the probe. The result is a current which can be measured with an electrometer. Several instruments (Konitest, Ikor air quality monitor) use either a spherical or tubular metallic electrode.

The following has come out of studies done on the various instruments :

- The total charge collected correlates well with the masse determined by gravimetry.
- No perturbing effect from humidity is found below the dew point.
- The sensitivity is weak, even null, for very fine particles.
- The sensitivity varies on almost two orders of magnitude : 0.05 µc/g up to 3 µc/g depending on the conductivity of the material.
- The sensitivity depends on the probe surface conditions.

With some additional work, this technique could show good results after calibration for measuring the mass and the evolution of sodium aerosols.

More recently, Guichard (9) developed a new instrument in which the aerosol is first charged by passing it through a fluidized bed then measuring it with a second fluidized bed connected to an alectrometer.

II.3. Charging with small ions

The most widely used method for charging an aerosol before it is measured is to affix a charge carrier to it. In most cases, small ions obtained by a radioactive source or by a Coronna decharge are used with or without a superimposed electric field. The examination and discussion of the various aerosol charge theories would go beyond the scope of this paper, which is to discuss the three essential characteristics conditioning size distribution analysis of a particle cloud :

- The charged fraction which, given the theoretical laws, becomes pratically non-measurable for particles of less than 0.002 µm and 0.001 µm for charges which are unipolar and bipolar respectively. The corrections which should be made would limit the use of instruments for measuring particle size.

- The relationship between the electrical mobility K and particle size. Figure 7 shows the relationship existing (Whitby (10) between K and d for different limit charge laws. For the various existing instruments, the uppermost limit is on the order of a micrometer.

- The discrete nature of the electric charge which can cause measurement errors if no correction is made.

It can be seen that whatever the conception of the electric analyzer used, the size range which can be studied with these techniques falls pratically between 0.01 and 1 µm.

II.4. Measurement techniques

Electric measurements of the concentration alone necessitate detection methods only. On the other hand, if a size classification is to be obtained a separation device should preceed detection.

These instruments are based on the following general principle :

If the charges particles move with the gas in a laminar flow through a condenser in which an electric field is applied, the particle will move across the streamlines and may finally be deposited on the field generating condenser plates. The location of its deposition depends on :

- The electrical mobility of the particle.
- The electric field.
- The velocity distribution of the flow field.

Cylindrical condensers and parallel plates have been used for deposition. Both can give either cumulative or discrete samples depending on the kind of inlet system used.

II.4.1. Cumulative sampling

If the aerosol uniformly fills the whole entrance, all the particles with $k_e > k_1$ will be removed from the air and deposited on the condenser plate. The condenser acts as a selective filter. Observation of either the depositing or the escaping particle yields approximatively one bit of information per particle about its k_e value. By changing the operating conditions (mostly the electric field) we can obtain the distribution of the k_e values. If k is a monotonous function of size ; a size distribution in terms of Stockes' equivalent diameter can be derived.

Although this technique is very simple ; to obtain ΔI, and hence the number of particles falling within a given mobility range, requires that the current versus voltage curve be differentiated twice. This seriously limits its accuracy for size distribution measurement. This technique has mostly been used for measuring small and intermdiate ions of relatively high mobility.

II.4.2. Discrete sampling

If the aerosol enters the condenser in the former of a this sheet over, or surrounded by, clean air streams, scanning of the deposition locations yields directly the discrete distribution of k_e. Instruments of this type have beer. developped by Megaw and Wells (11) and in is miniature form by Pourprix (12).

The aerosol deposit can be analysed in many different ways ; by optical and electron microscopy, chemical analysis, or, if radioactive, by activity measurement. Its greatest disadvantage is the amount of labor necessary to evaluate the deposits on the plate in order to obtain size distribution data.

Like in cumulative sampling, a knowledge of the charge distribution (i.e. the conditional probability that a particle carries a charge q if its mobility is known to be k) is necessary though insufficient for finally arriving at the size distribution because the q versus k relation may be complicated.

II.5. Aerosol electric analyzer

This instrument makes it possible to measure the particle concentration as a function of their size for submicronic aerosols.

It is composed of three main parts : the aerosol charger, the mobility analyser and the current sensor.

The devices samples aerosols at the rate of four liters per minute.

The aerosol is first sampled into the charger where the particles become electrically charged. Figure 7 shows the relationship between k (electrical mobility) and the size. The mobility analyzer is a cylindrical condenser with clean air and aerosol flowing down the tube in a laminar stream. The charged aerosols are deflected by the voltage applied. For a given voltage on the center rod, particles above a certain mobility are precipitated. By changing the voltage and measuring the corresponding electrometer current, the mobility size distribution of the aerosol can be determined. The commercial instrument gives 10 equal geometrical intervals between 0.0032 to 1.0 µm but the practical threshold is 0.01 µm. Above these dimension results are not accurate. Figure 8 shows a size distribution of an aerosol produced during the combustion of 1 g of sodium.

It is possible with this type of instrument to obtain a necessary indication about an aerosol having a standard deviation of 1.4 for particles of 0.56 and 1.1 for particles on an order of several hundred µm. Resolution abnormalities exist due to the transition between singly and multiply charged particles. Using this type of measurement device is particularly adapted to studying submicronic aerosols, for instance, fuel aerosols or primary particles produced from sodium fire. Special attention should be given when measuring radioactive particles, as they could perturb the charge of the aerosol to be analyzed.

II.6. Electrical aerosol sampler

Many devices have been studied and produced for industrial use or in a more sophisticated form for sampling which will then be analyzed.

- The two main advantges of this kind of instrument are : its relatively good efficiency for fine particles and its low pressure drop.

- The disadvantages are : non-classification of particles as a function of their size and orientation under the influence of an electric field (chain aggregate).

III. Condensation Nuclei Counter

These optical instruments which detect aerosols are limited by light diffusion laws to around 0.3 μm. Below this size the light diffused is too weak to be differentiated from molecular diffusion and electronic background.

In order for the detection sensitivity to be increased an artifice which enlarges the fine particles by vapor condensation on their surface must be used. This produces droplets large enough to be detected by classical optical means.

III.1. Basic principle

If an aerosol whose radius is r suspended in a gas saturated by a vapor at a temperature T1 is examined ; or, if lowered, by adiabatic expansion or by cooling the mixture to a temperature value T2, vapor condensation will take place on the particle.

Each value of r can have critical saturation value necessary in order for a drop to develop around the nucleus whose radius is r.

By well calculating the sursaturation applied, particles larger than several tens of Angströms whose concentrations are from $1 \cdot 10^7$ p.cm^3 can be detected.

The main problem envolved with this type of instrument is its calibration. Until recently, the difficulty was to produce particles of less than 0.01 μm in known concentration thus making it impossible to carry out such work under satisfactory conditions. Recently results Figure 9 have been obtained in particular by Liu, Madelaine, and Metayer (13) showing a counting efficiency which decreases with particle size. The lowest detection limit is on the order of 0.006 μm.

These kinds of counters make it possible to measure the numeric concentration of a submicronic aerosol but do not make it possible to find particle size.

In order to obtain data on particle size distribution, a device capable of measuring size must be associated to the detector. The main device used in association with this type of detector is diffusion batteries.

IV. Diffusion Batteries

IV.1. Principles of operation

Each particle suspended in a gas exhibits Browian motion resulting from its mechanical interaction with the gas molecules. If this particle contacts a surface, it sticks to the surface and is thus removed from the airborne state since, upon physical contact, adhesive force dominante.

An aerosol passing through a cylindrical tube or parallel plate looses particles as they stick to the walls. This effect, very often unwanted, is used in diffusion batteries (DB) to gain information about the aerosol. The quantity of particles of identical diameter (monodispersed aerosols) which stick or penetrate through the DB can be calculated. The deposition and the penetration probabilities depend on :

- The properties of the aerosol (size, shape...).
- The properties of the gas : viscosity, flow characteristic (laminar flow).
- The properties of the DB : geometry and thermodynamic conditions. Hence two types of samples can be taken by DB'S.

A - The penetration measured for instance by a condensation nuclei counter.

B - The deposition in the DB as a function of the distance from the entrance, for instance, radioactive detection.

In both cases, the number concentrations, the total particle mass and their activities can be measured.

IV.2. Equivalent size measured

The diameter which can be determined is the size of a particle with the same diffusivity as the spheres with a diameter D. These diameters are called diffusion equivalent diameters Dd.

In order to establish the necessary penetration probability versus Dd curve either an empirical calibration with monodispersed aerosols or theoretical calculations can be used.

All the foregoing considerations apply only to an aerosol of identical particles. If, however, a polydispersed aerosol passes a DB, which in practice is the only interesting case if the DB's are used as sizing instruments, interpretation becomes complex. However, several methods have been studied and developed making it possible to either measure with batteries of different lenghts or to vary the flow through a given battery. After, by mathematical or graphic means, it is possible to find the size distribution of an aerosol.

Figure 11 shows an example of size distribution obtained in this way for an atmospheric aerosol compared to that obtained with an electrical aerosol analyzer.

For now, this is the only method in spite of its imperfections which makes it possible to determine the size of particles smaller than 0.01 μm. The disadvantage is that calibration in the lab is necessary. The theoretical calculation can, for the time being, be applied only to particles of simple geometry.

The results obtained concerning these ultrafine particles especially for fuel aerosols are only on a semiquantitative order.

Bibliography

[1] C.N. Davis
The entry of aerosols into sampling tubes and heads
Brit.J. Appl. Phy. Ser. 2 Vol 1, 1968

[2] J.K. Agarwal
Aerosol sampling and transport
PhD thesis University of Minnesota, 1975

[3] Gormely and Kennedy
Diffusion from a stream flowing through a cylindrical tube.
Proceeding Roy. Irish Acad., 1949, 52, 163

[4] N.A. Fuchs
Mechanic of aerosols
Pergamon Press, 1964

[5] G.A Sehmel
Aerosol deposition form turbulent airstreams in vertical conduits
BRM 578 PNL, Richland Washington, 1968

[6] B.T. Liu and S.K. Agarwal
Experimental observation of aerosol deposition in turbulent flow
J. of Aerosol Sciences, Vol 5, 1974

[7] J. Charuau
Thèse de Docteur de l'Université, en cours de publication

[8] W. Harper
Contact and frictional electrification
W.R. Harper Oxford, 1967

[9] Guichard
Nouveau procédé de mesure en continu de la concentration en poussières
GAF Bad Souen, 1973

[10] K.T. Whitby
Electrical Measurement of Aerosols. Fine particles
Acad. Press, 1975

[11] J.W. Megaw, and A.C. Wells
Electrical Mobility of submicron particles
Nature, 1968

[12] M. Pourprix
Un nouveau précipitateur electrostatique
Rapporr CEA 4553, 1974

[13] G. Madelaine, Y. Metayer
Note à paraitre dans J. of Aerosol Science

Sampling efficiency in function of
stockes number and relative settling velocity (ρ_p = 1 g/cm^3)

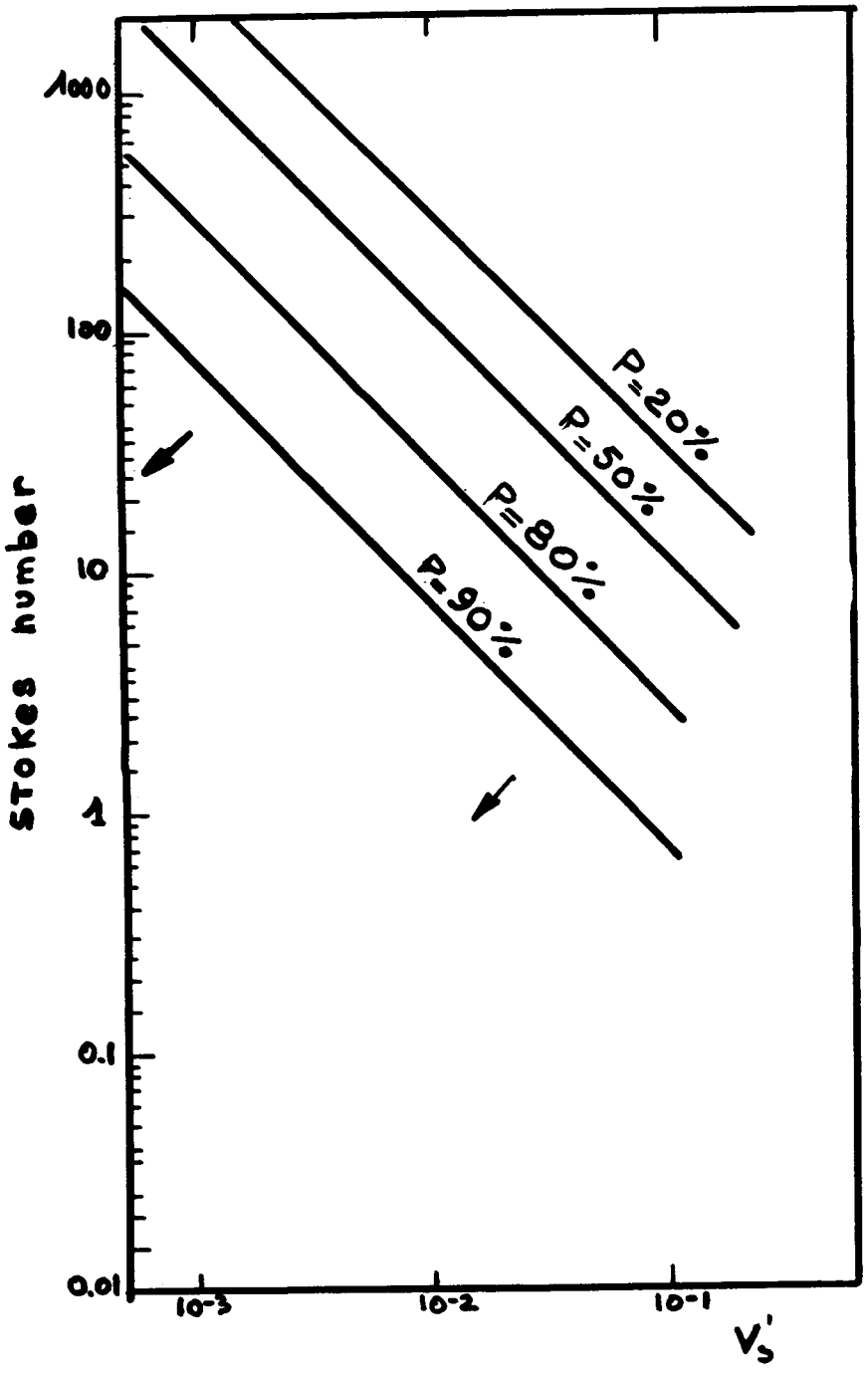

FIGURE 1

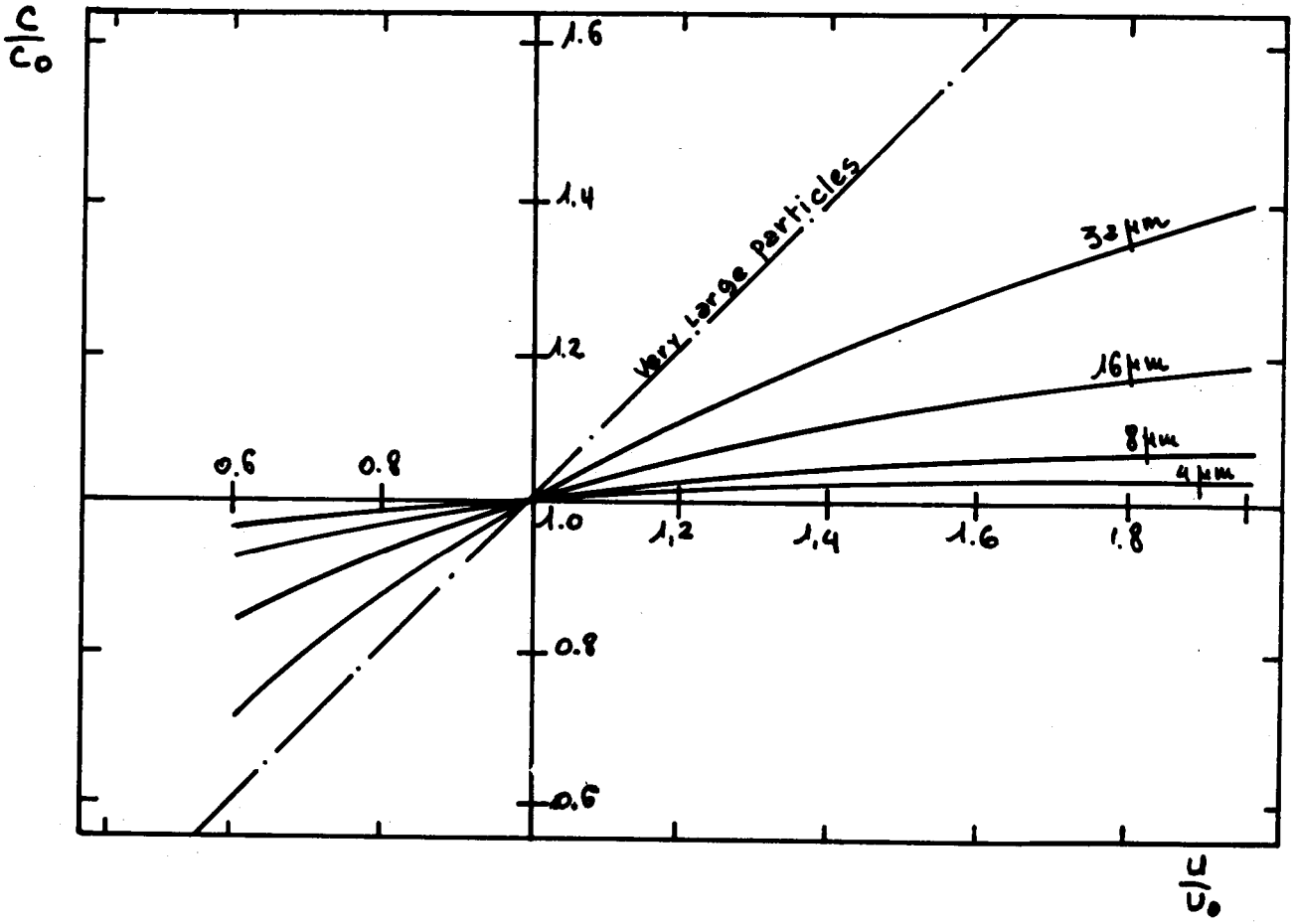
C/C0
1.6
1.4
1.2
1.0
0.8
0.6
0.6
0.8
1.0
1,2
1,4
1.6
1.8
Very Large Particles
32 µm
16 µm
8 µm
4 µm
U/U0

Figure 2

Penetration in a tube in function of particle size
(brownian diffusion and lammar flow)

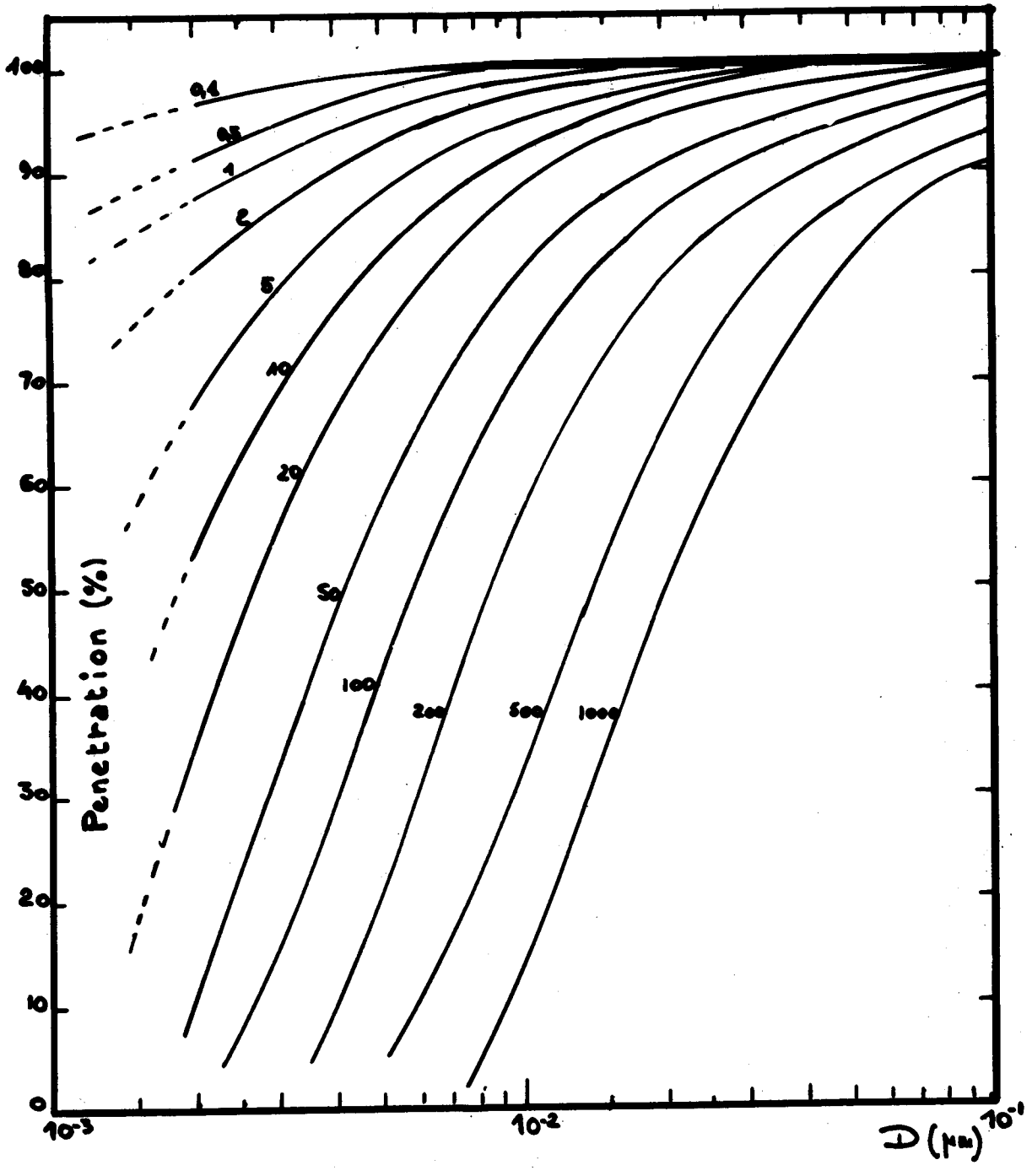

FIGURE 3

Penetration in a tube in function of particle size
(settling and laminar flow)

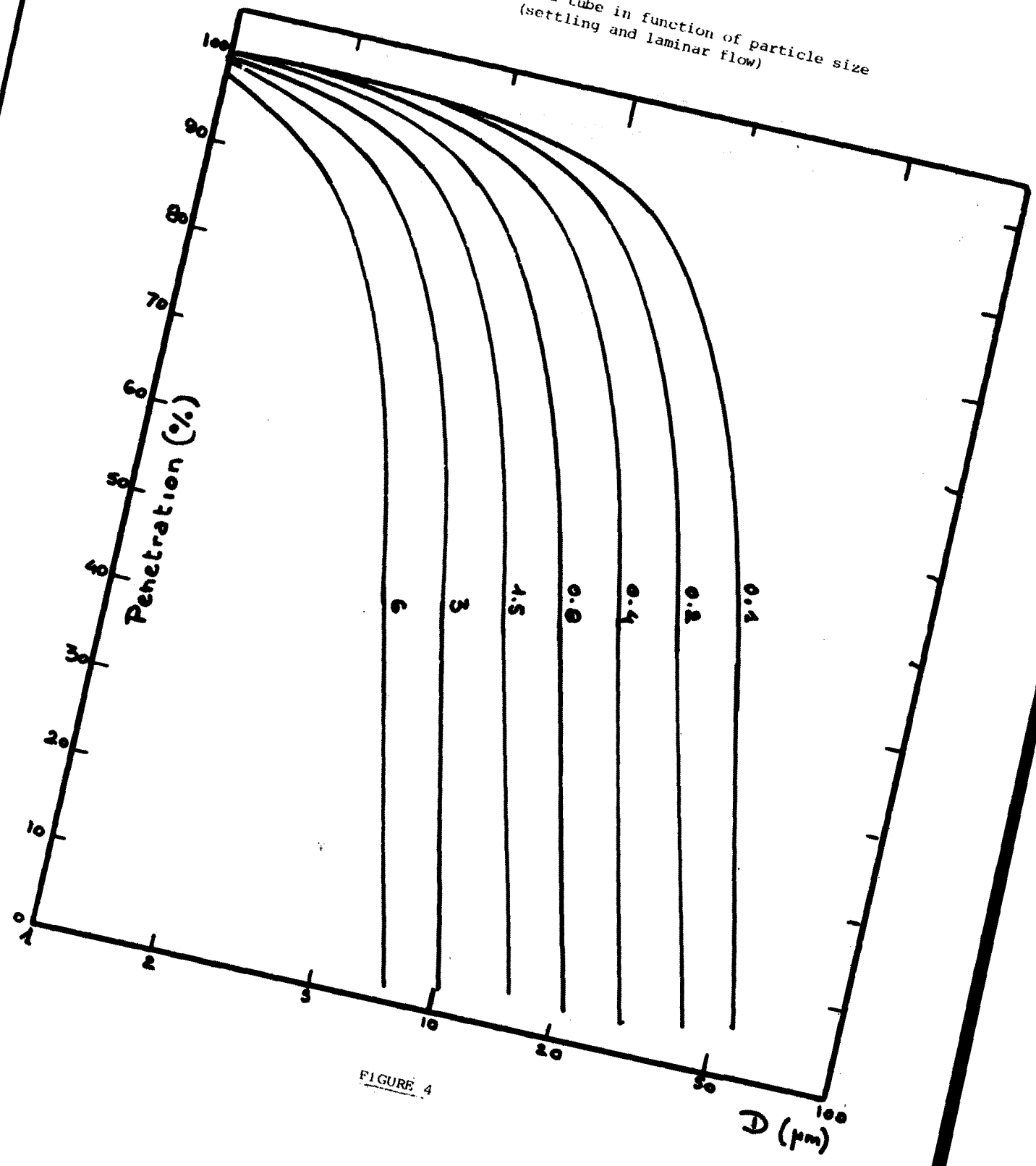

FIGURE 4

Penetration in a tube in function of particle size
(turbulent diffusion) R = 1 cm - Q = 50 l mn^{-1} - Re = 3268

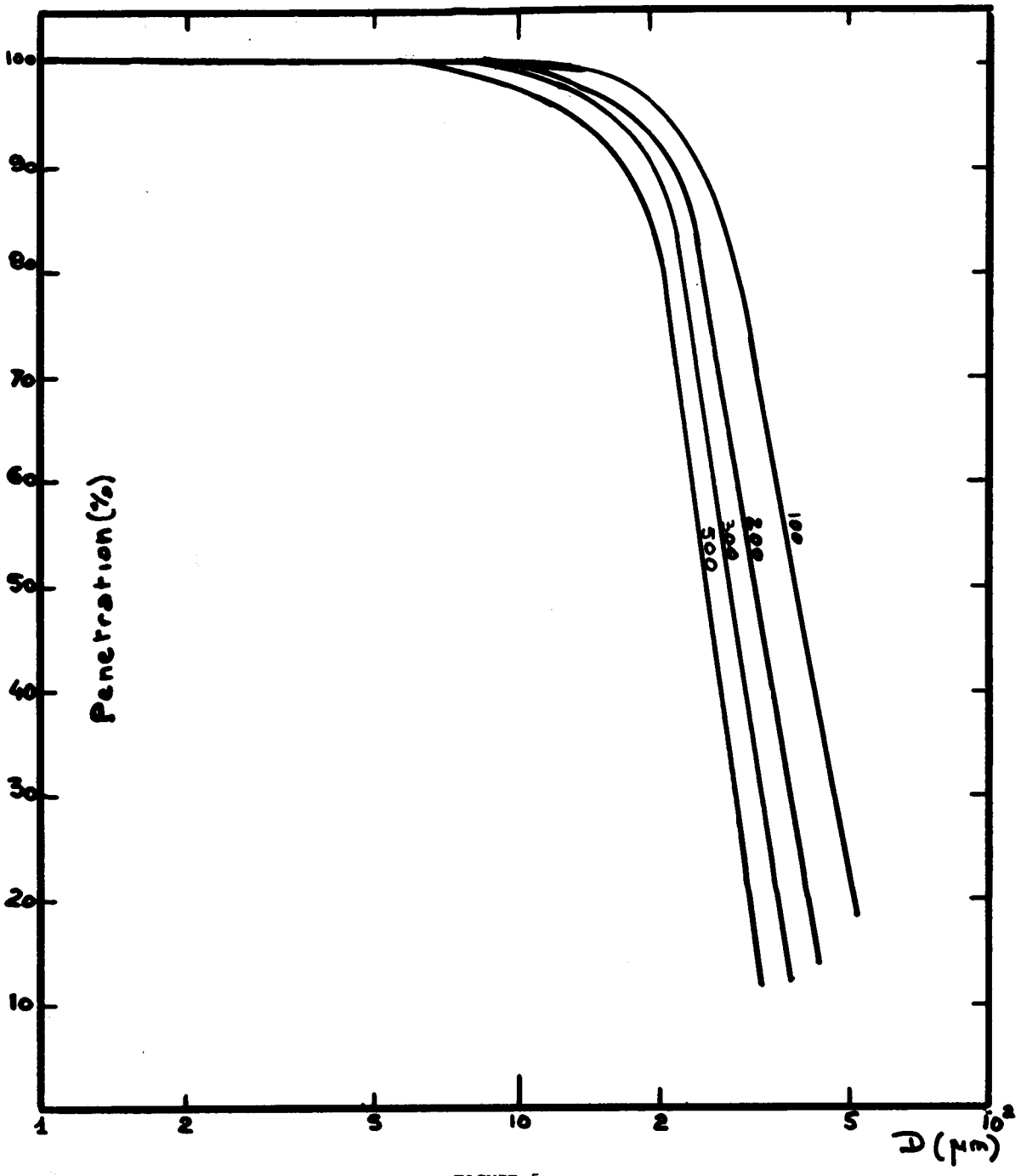

FIGURE 5

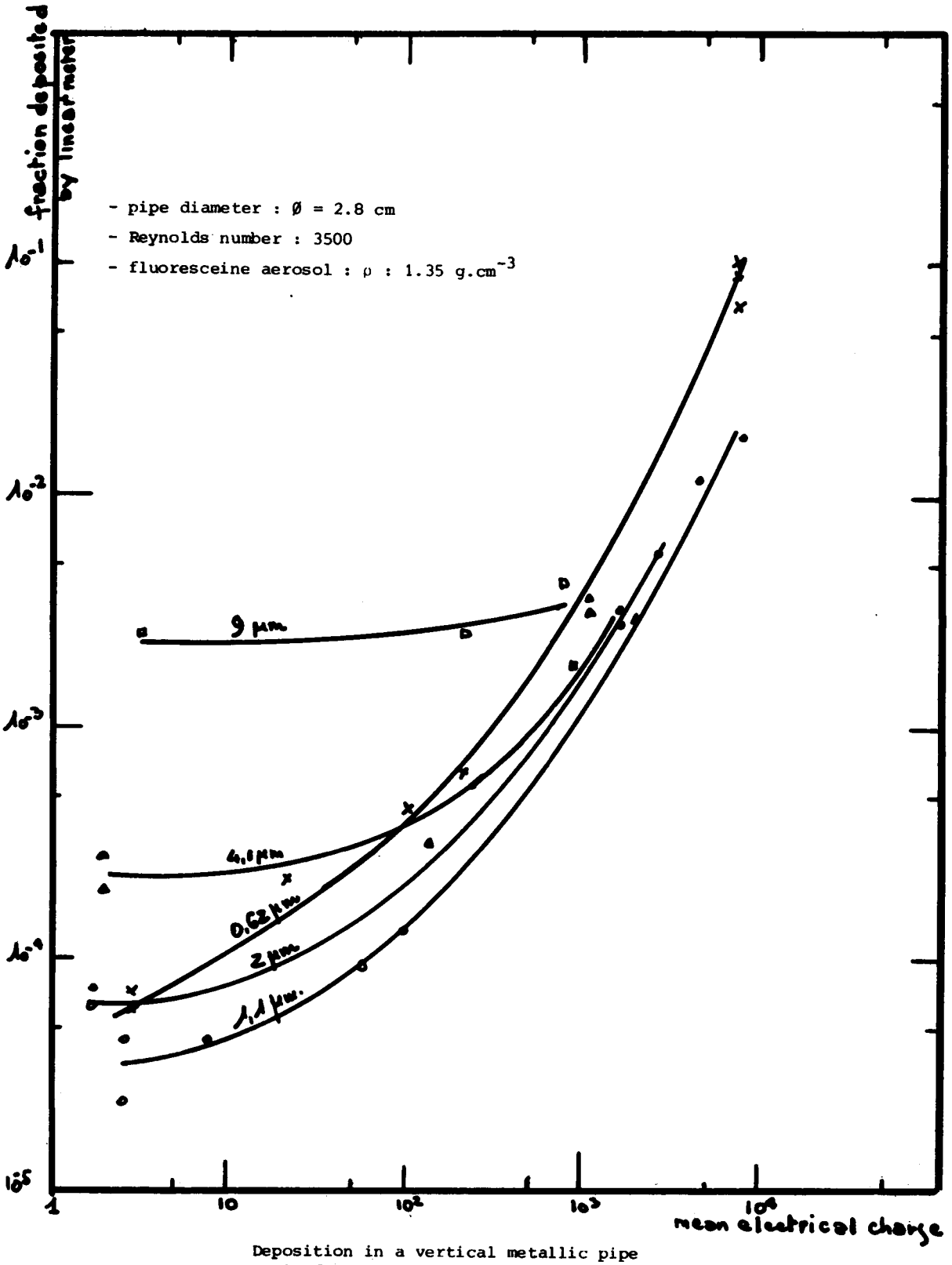

Deposition in a vertical metallic pipe
in fonction of electrical charge

Figure 6

Electrical mobility in function of particle size

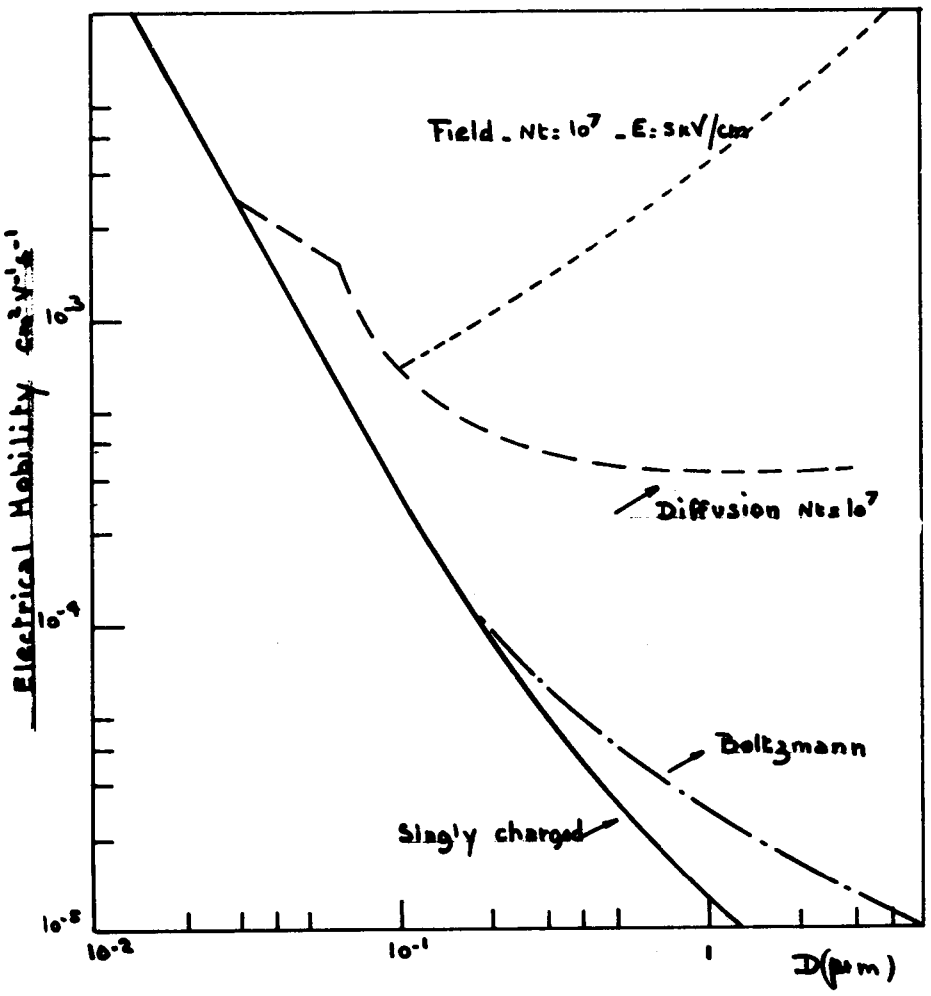

FIGURE 7

Size distribution of sodium aerosol (masse. 1920 mg/m^3)

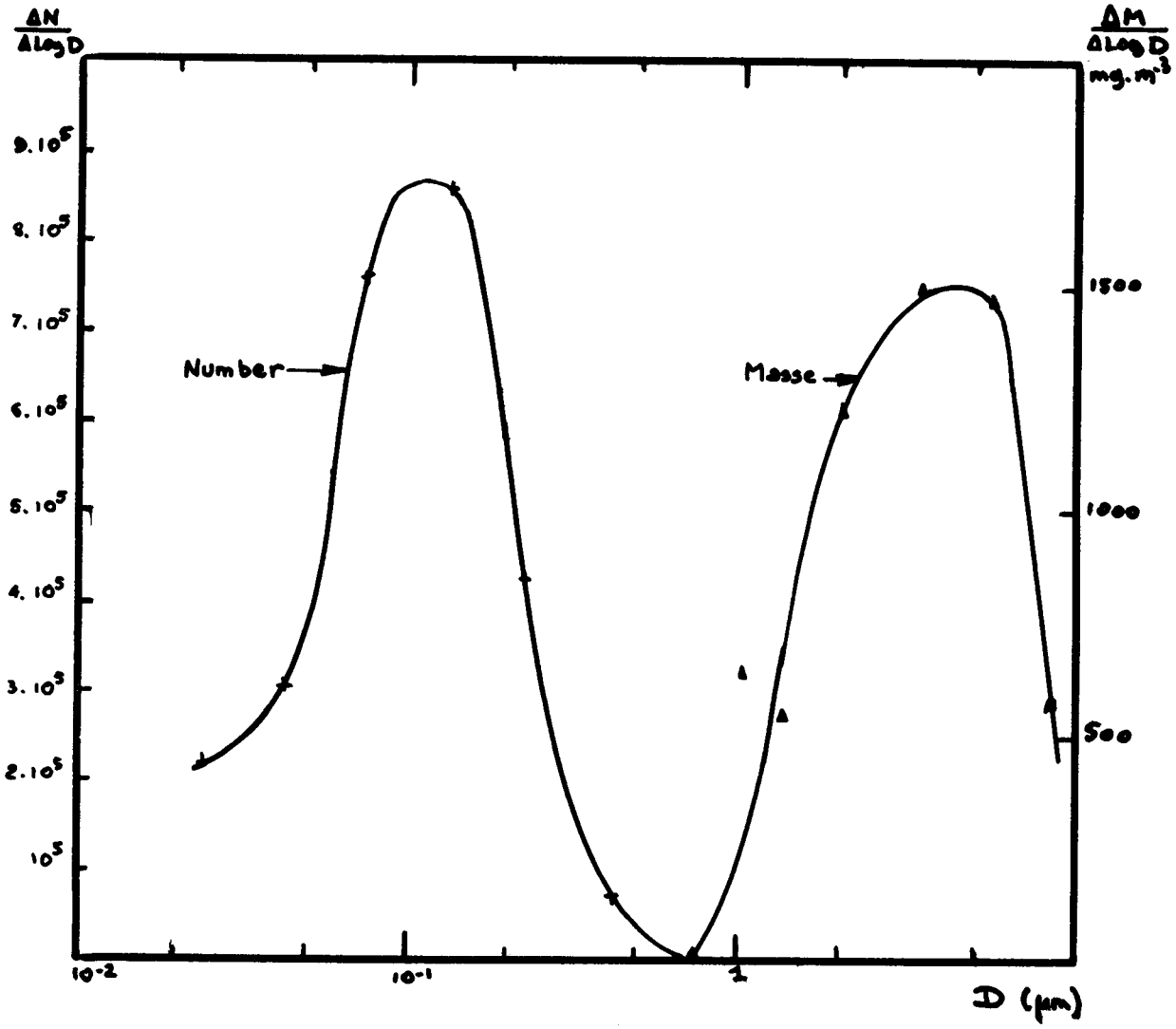

FIGURE 8

Calibration of condensation nuclei counter

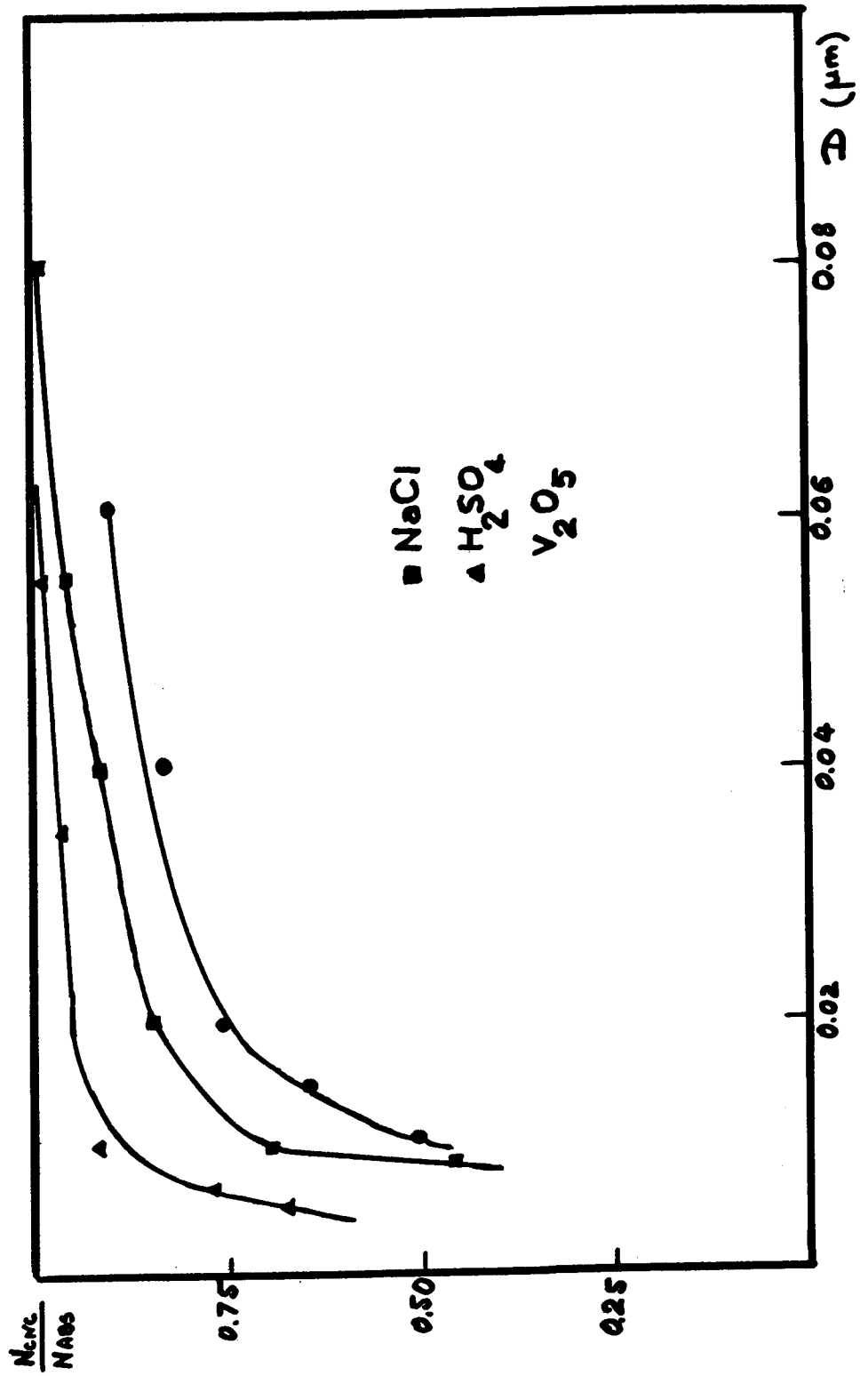

FIGURE 9

Size distribution of atmospheric aerosol obtained
by EAA and DBM

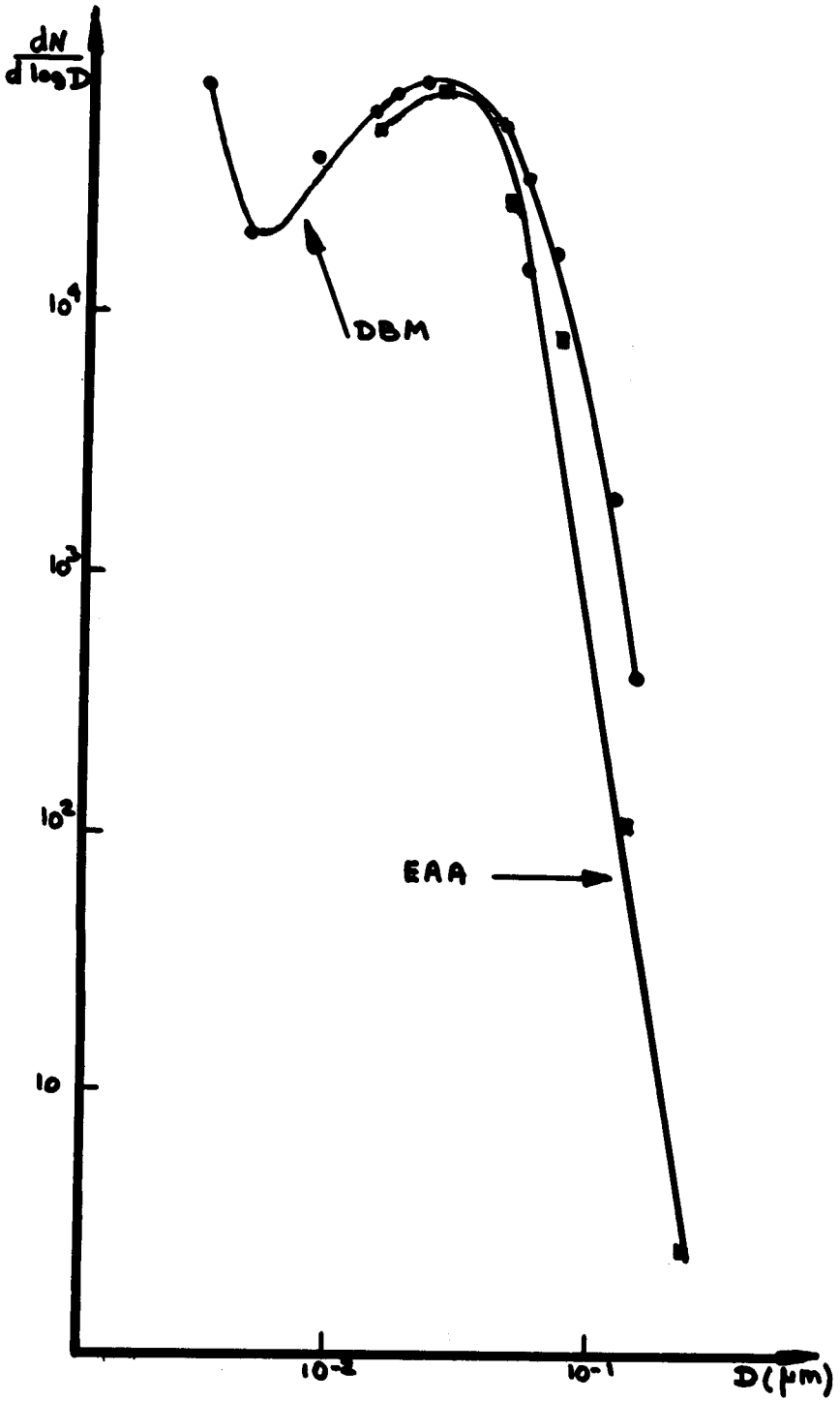

FIGURE 10

APPLICATION OF OPTICAL METHODS IN NUCLEAR AEROSOL MEASUREMENTS

W. Schock

Laboratory for Aerosol Physics and Filter Technology
Kernforschungszentrum Karlsruhe, FRG

ABSTRACT

Optical aerosol measurement techniques are used as light scattering devices in nuclear aerosol research. The underlying scattering theory, the Mie theory, is known since 1908. Nevertheless, a practical application of light scattering instruments has only recently become possible.

The use of light scattering techniques for particle measurement is manyfold, scattering, absorption and extinction methods can be applied to single particles or particle ensembles. The Mie theory gives excellent agreement with measured data as long as the underlying assuptions are met. The assumptions are that particles are spherical and that their complex refractive index is known. With nuclear aerosols this is true only for liquid sodium or water droplets, in which cases the use of in situ measuring optical particle spectrometers is highly recommended.
For nonspherical particles the Mie equations hold only approximately, the degree of the approximation varies with particle size. In these cases optical spectrometers can be recommended after careful calibration.

In all cases, however, the advantage of optical techniques is that in situ measurements can be done without influencing the aerosol and with high time resolution. These properties are extremely useful for measuring dynamic aerosol systems, or particles which cannot be sampled without changing their properties.

Some commercial and a variety of special laboratory prototype instruments exist capable of measuring particles sizes > 0.1 µm in the concentration range up to 10^5 P/cm³. Photometer type instruments have larger ranges but the interpretation of the meter reading is difficult in most cases.

INTRODUCTION

Up to now optical aerosol measuring techniques have not been used frequently in the field of nuclear aerosol instrumentation regardless of their many advantages of which four shall be mentioned as examples.

Optical techniques are on line. The reading is available at the moment of the measurement.

Optical techniques are in situ. This option is highly desirable in nuclear aerosol research when dynamic systems have to be measured.

Optical techniques are non-influencing. Particles are measured in the airborne state without influencing their properties.

Optical devices are not influenced by the aerosol. As the instrument does not touch the particles, the particles likewise do not touch the instrument. The problems with plugging, corrosion etc. are easily avoided.

Looking for disadvantages it is recognized immediately that optical techniques are expensive and require intensive maintenance.

This is, however, not specific for optical instrumentation. Most of the size resolving devices are equally expensive and need much care in operation.

The same is true for data evaluation which may raise problems for optical spectrometers as well as for other instruments.

The remaining possible explanation of the fact that optical aerosol measurement methods are scarcely applied to nuclear aerosols may be a prejudice against the first generation of dust counters which were, indeed, not very useful for nuclear aerosol research. The today's instrumentation, however, has been developed so far that they are very well suited to applications in the field of nuclear aerosol measurements. Yet in many cases these new instruments did not have the time to make their way into the nuclear aerosol scientists' laboratories.

In this article a survey of recent developments in optical measurement techniques will be given to show the capabilities of these methods with special emphasis on nuclear aerosol applications.

Prior to the discussion of types of instruments, an introduction to the principles of the optical particle measurement, the main relations, and the general scheme of data interpretation will be given.

THEORY OF LIGHT SCATTERING

The first general theory of light scattering by single particles was given in 1908 by G. Mie [1] . However, Mie's theory is exceedingly tiresome to evaluate, and thus the first break-through did not occur until today's computers became available [2] .

The final event, then was the experimental proof of the calculated calibration functions. This could be done in full extent since lasers became available as light sources in the last two decades [3,4]

Mie's scattering of light by a spherical particle means the simultaneous absorption, diffraction and refraction of an incident plane light wave [5] .

The observable scattered light intensity depends on
- the wavelength of the incident light
- the complex refractive index of the particle
- the particle diameter
- and the coordinates of the point of observation, which are commonly expressed in spherical coordinates as distance R, scattering angle ϑ and polarization angle. The two angles are measured against the electrical vector of the incident light wave.

Fig. 1 shows as an example the total scattered intensity I_{tot} for water droplets as a function of droplet diameter d in microns and scattering angle ϑ in degrees. I_{tot} is in arbitrary units, 'total scattered intensity' means that the incident light is unpolarized. The refractive index for water is m = 1.33, the wavelength of the incident light was taken as λ = 0.633 microns.

This, at the first glance confusing, diagram can serve to illustrate some of the most important properties of light scattering:

For small particles, d << λ, dipole scattering predominates. [6] The dependence of the scattered intensity on the diameter is $I \sim d^6$.

For large particles, d >> λ, the scattered intensity (in forward direction (small ϑ)) is proportional to the geometrically projected area of the particle; for spheres $I \sim d^2$ [7] . Superimposed to this d^2 dependence are oszillations due to interference of diffracted and refracted waves.

For large particles and large scattering angles the scattered intensity exhibits a very confusing behavior, this region cannot be recommended for easy application of light scattering for particle sizing. Nevertheless, instruments which operate in this region have been built, but special attention has to be paid to calibration and interpretation of data.

Many attempts have been made to smoothe the oszillations by integrating over scattering angles and/or wavelengths or by measuring ratios of intensities scattered at different angles. All these efforts failed, at least the first deep groove at non-zero ϑ angle never disappears. It is only possible to obtain more or less extended diameter ranges with non-oszillating calibration functions. Therefore, optical size spectrometers are mostly built for special applications and their application to a different problem requires special care.

Fig. 1 was calculated for water droplets which are non-absorbing. In Fig. 2 the total scattered intensity is shown for a refractive index of m = (1.33 - 0.33 i) which belongs to a fairly absorbing material.

As an immediate consequence all the oszillations due to refractive interferences have vanished. The forward scattering lobe is completely smooth. The remaining grooves are caused by diffraction.

In this case the direct forward scattering yields unambiguous calibration curves. And since the forward scattered intensity is roughly two orders of magnitude higher than the intensities at larger scattering angles ϑ, also observations which include the forward scattering give smooth calibration functions. Thus, e.g. extinction measurement and 4π-observation can be recommended.

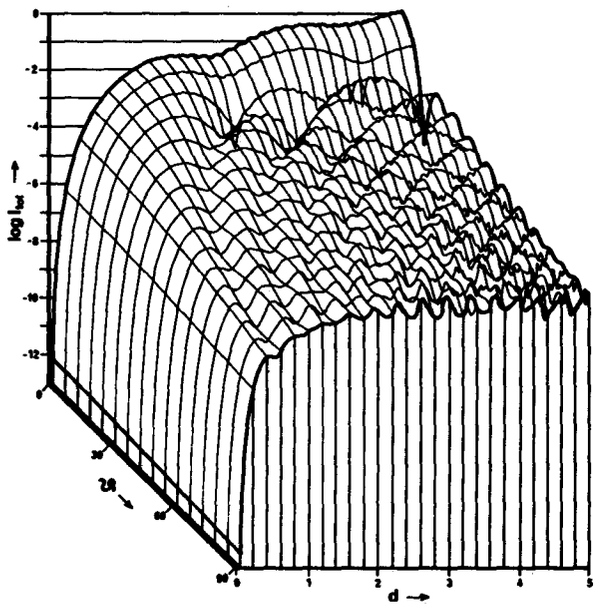

Fig. 1: Scattered Intensity of Water Droplets

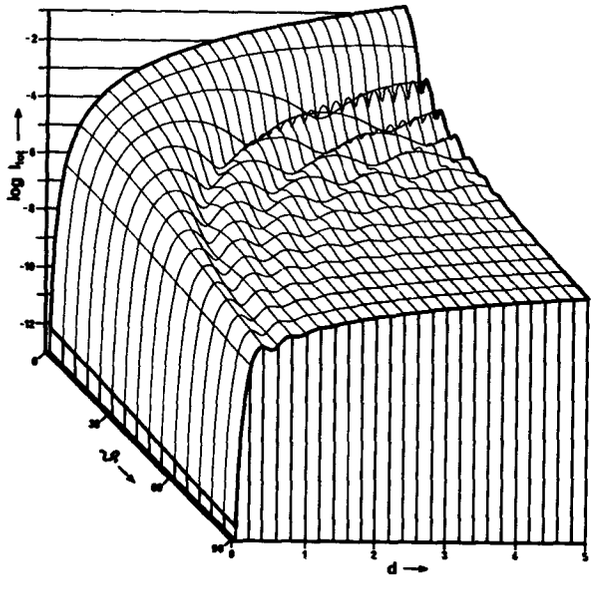

Fig. 2: Scattered Intensity of Absorbing Spheres

It should be emphasized again that these calculated diagrams can be verified experimentally in every detail if the conditions are fulfilled: spherical particle, known refractive index. This is one of the major advantages of light scattering devices: the underlying principle is understood in full extent and calibration functions can be pre-calculated with extreme precision.

RESOLUTION AND SENSITIVITY

The last question to theory would be about the size resolution and the sensitivity of the method.

Concerning size resolution it is immediately obvious that a response signal which is proportional to the 2nd ... 6th power of the measured quantity 'particle size' has an excellent inherent resolution. The limiting factor is, indeed, the quality of the optical system and the subsequent electronics. Devices with a size resolution of 2% can be built using some amount of care and experience [8] , 5 ... 10% are achievable without much efforts.

The real problem is related to size ranges. As can be seen the scattered signal ranges over many orders of magnitude, which are by far too much for a single linear size range. Logarithmic converters can be used but they degrade the signal considerably.

Concerning sensitivity, one has to consider real optical systems and integrate intensities over observation apertures. This means integration over the two spherical angles, giving an instrument related scattering cross section. Having this done one obtains a function of the instrument, the only remaining variable is the wavelength λ of the incident light.

The wavelength appears in constants and in the scattering cross section. At the lower end of the size range the cross section is proportional to the minus fourth power of the wavelength. The immediate consequence when trying to improve the sensitivity of a given optical system is to use shorter illumination wavelengths. This not only improves the cross section, but also the efficiency and signal/noise ratio of the optical detector will be much better.

It is also possible to calculate the sensitivity of an instrument absolutely [3] . The main dependence is on input light density, residence time of the particle in the sensing volume and the geometrical configuration of the device. We calculated the sensitivity for some instruments and found a rather good agreement with measured detection limits.

Asking for the lowest detectable energy of a scattered signal, the answer is clearly: 1 photon, and corresponds to particle diameters of 0.05 ... 0.2 µm depending on the instrument. 1 photon is a rather impractical quantity for aerosol particle sizing, because a scattered light pulse consisting on one photon has, of course, a vanishing size resolution. Nevertheless, these considerations are useful because they also work with 100 or 10.000 photons in a pulse, and because it follows from this that size resolution must vanish at the lower end of the size range.

Decreasing size resolution for very small particles is not an indication of bad alignment of the system, but a fundamental property of photon statistics.

However, since the scattered pulse increases with d^6 the size resolution improves with d^3 and the practical lower limit of the measuring range will not be very much greater than the absolute detection limit.

PHOTOMETERS

The discussion of instruments will be divided in two parts, photometers and size spectrometers, the difference being obvious and self explaining.

Photometers are aerosol measuring devices which deal with aerosol collectives. When measuring the light scattering of a collective of aerosol particles it can be deduced from the preceding discussion that the scattered signal will be depending on

- the optical properties of the particle material
- the size or rather the size distribution
- the number concentration of the particles

besides all the given properties of the apparatus.

Therefore, given a well defined aerosol material, the instrument output still depends on the size distribution and the particle concentration simultaneously.

Most photometers are used making assumptions on one of those two parameters, mostly size distribution. If e.g. the size distribution is kept constant, then the output of the instrument would be proportional to the concentration.

Concentration measurements, consequently, are the most widespread applications of photometers today. It should be noted that in this mode of operation the response signal is independent on the aerosol flow velocity through the sensing volume. This in one of the major advantages of the photometric technique. Photometers are commercially available in a great variety of models which are mostly constructed for industrial monitoring and environmental protection purposes. The measuring ranges are suited for nuclear aerosols. The reading is commonly in mass concentration calibrated for a 'standard dust'. Nuclear aerosol application requires, therefore, a new calibration.

As an example Fig. 3 shows a cross section of the optical system of a portable photometer which was designed for coal mining monitoring [9] .

The light source 1 is a Ga-As-diode which emits monochromatic light at 0.94 µm. The scattered light at an angle of 70° is detected with a silicon photodiode. A special feature of the instrument is the protection against stray signals by using optical filters and lock-in electronics.

This instrument was presented here because its performance has been extensively investigated. The details, however, cannot be discussed and should be referred to the original paper.

The general experience with photometers at KfK shows that they can be recommended as monitors during one single experiment. But they should not be used as absolute instruments when no other information about the aerosol system is available.

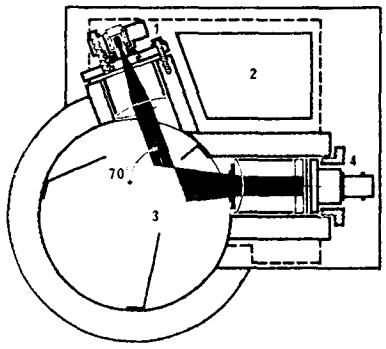

Fig. 3: Photometer optical system. Taken from [9] .

AEROSOL SIZE SPECTROMETERS

Spectrometers, by definition, are instruments that measure size spectra. This requires to keep optical properties of the aerosol constant, which is a condition that can be matched more frequently with nuclear aerosols. Optical spectrometry of aerosol particles means that single particles are sized one after the other. Consequently small enough sensing volumes have to be formed which contain only one particle at a time.

The sensing volume can be formed by the cross section of a narrow aerosol stream with the illuminating light beam. This technique yields very small sensing volumes which allow the measurement of particle sizes at concentrations up to 10^5 P/cm³. The size resolution of this type of instruments is very high, too.

Fig. 4 shows the optical system of an instrument which has, to my knowledge, the highest sensitivity of all present aerosol spectrometers [8] Illumination is with a Ar^+-laser of 2 W output power. The laser beam is focussed to the sensing volume with the lens L. The scattered light pulse is collected with a microscope optical system O and detected with the photomultiplier PM. Perpendicular to the plane of the drawing the aerosol inlet system is mounted, which is shown in Fig. 5 . The aerosol is conducted through the central tube, sheath air through the outer tube.

In the outlet nozzle system at the lower end the aerosol stream is narrowed to extremely small diameters, typically 40 µm. This method is known as aerodynamic focussing of the aerosol stream and permits the high particle concentrations of up to 10^5 P/cm³ to be handled without coincidences in the sensing volumes.

An additional possibility of the aerodynamic focussing system is to replace the sheath air by Helium and thus significantly reduce the background Rayleigh scattering of the gas molecules. The sensitivity is increased correspondingly, the quoted detection limit in [8] is 0.05 µm.

Instruments of this type still suffer from one disadvantage. They are not really in situ measuring, the aerosol is sucked through a capillary nozzle which may become plugged. Further the necessary pressure drop in the capillary causes droplets to evaporate. These instruments can, therefore, only be recommended for aerosols of solid and small particles. For this kind of aerosol they represent, indeed, the most advanced stage of optical aerosol sizing techniques.

For the measurement of coarser particles or droplets with high vapor pressure a type of spectrometer has to be used which shall be labeled 'in situ' spectrometer in this article. In these instruments both illumination and observation optics focus on a small sensing volume, particles outside that volume are either not illuminated or not 'seen'. The sensing volume can be located in a large duct or even in a vessel containing the aerosol, which yields a real in situ measurement without influencing the particles. Such spectrometers are mostly known as the Knollenberg type counter [10] . The Knollenberg counters use forward scattering which gives good sensitivity but low concentration ranges.

Higher concentration ranges at the expense of sensitivity can be achieved with a 3 x 90° configuration of illumination, observation and particle movement direction. An instrument of this type using a white light source [11] is commercially available, a special development with a laser light source [12] was published and is used at KfK for LWR aerosol investigations. Both instruments have a sensitivity limit of approximately 0.4 µm and a concentration range of up to 10^5 P/cm³. The size resolution of these in situ spectrometers is somewhat lower than that of the Fig. 4 type due to boundary effects of the sensing volume. However, computational routines for correcting these effects are available.

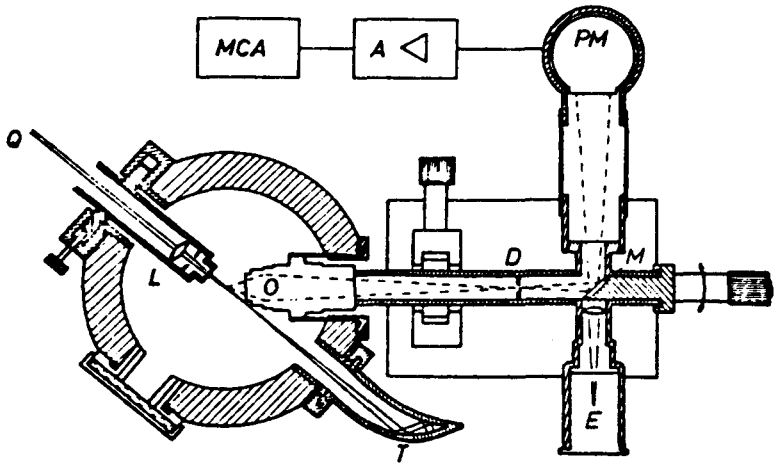

Fig. 4

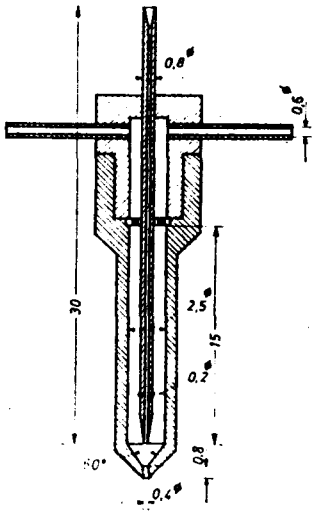

Fig. 5

Optical System and Aerosol Inlet of a Laser Aerosol Spectrometer. Taken from [8] .

OPTICAL MEASUREMENTS OF NON-SPHERICAL PARTICLES

As stated above the Mie theory is based on the assumption of spherical particles. A few solutions are known for ellipsoids and cylinders. Further analogue experiments for irregular particles using microwave techniques have been done [13] . All these shapes are mostly far from the shapes encountered in nuclear aerosol research. The question now arises about the feasability of measuring nuclear aerosols with optical techniques at all.

The question can be answered easily for two cases. For small particles, where dipole scattering predominates, the response is proportional to the square of the volume of the particle, irrespective of the particle shape. For large particles and in forward scattering the response signal is proportional to the projected area of the particle. These two theoretically derived relations have been experimentally validated by measuring aggregates of spherical particles [14,15] . The benefit for measuring nuclear aerosols is obvious.

The interval between 'small' and 'large' particles, which is roughly 0.5 ... 2 μm for red light, can be shifted by chosing different illumination wavelengths, because 'small' and 'large' is always compared to the wavelength of the incident light. In cases where this is not possible aerosol size spectra extending into this interval may be measured after experimental calibration of the instrument. Experimental calibration of an optical size spectrometer is recommended in all cases, even when a theoretically calculated calibration curve would do as well.

The calibration procedure also yields a valuable argument against the common objection that 'optical diameters' be useless for nuclear aerosol research. This objection is not very well established per se, because of two reasons. Firstly, the measurement of the so called optical diameters involves the calibration of the instrument with a standard aerosol, e.g. latices, which has properties that are so greatly different from those of nuclear aerosols that such a calibration is obviously worthless and should not be used. Secondly, when the optical spectrometer is calibrated by comparison to the reading of a reference method using the same aerosol of the 'nuclear' type, then the 'optical diameter' does not appear in the procedure, but the calibration is in terms of a more meaningful size parameter as e.g. mass equivalent diameters or mobility diameters, and this is exactly the same procedure that is used in calibrating all other aerosol size spectrometers.

So after proper selection of an optical aerosol measuring instrument which is applicable to the specific problem, and after reliable calibration preferably with an aerosol of the same type as that to be measured, optical aerosol measurement are correct. Moreover, the technique has many advantages which are not available with other methods as the on line and in situ capability.

CONCLUSIONS

Optical aerosol measurement techniques have only recently been developed to such a state that their application in nuclear aerosol research can be recommended. Especially size spectrometers became available which can measure aerosol particle sizes of aerosols with high particle concentration. The use

of lasers as light sources led to a sufficiently high sensitivity with respect to particle size.

The light scattering process can be calculated for spherical particles with extreme precision, and calibration curves of an instrument can be predicted. For non-spherical particles, as most nuclear aerosols are, the calibration can also be calculated except for an intermediate size regime. In this regime and for aerosols with unknown optical properties an experimental calibration has to be done, as for all other aerosol instrumentation, too. The calibration procedure should use a size parameter which is meaningful for nuclear aerosols, e.g. mass equivalent or mobility diameter.

Optical aerosol measuring methods have some unique advantages over other techniques. The most important are the in situ and non-influencing properties. Indeed, optical aerosol sizing is the only existing in situ method, and the simultaneous fact that sizing by light scattering does not affect the particles is also unique. Therefore, for some measuring problems optical techniques are the only feasible method, as for measuring size spectra of droplets.

All these facts lead to the conclusion that the non-usage of light scattering devices in nuclear aerosol research is only historical, and that after the new generation of instruments has become available their application is highly recommended.

REFERENCES

1 G. Mie, Ann. Phys. 25, 377 (1908)

2 J.R. Hodkinson, I. Greenleaves, J. Opt. Soc. Am. 53 (1963)

3 W. Schock, Meßbereichsgrenzen und Auflosungsvermogen bei optischen Partikelgrößenspektrometern, Kolloquium Aerosolmeßtechnik, IENT/RWTH, Aachen, 4.3.1975

4 W. Schöck, Fortschritte in der Laser-Aerosol-Spektrometrie, 38. Physikertagung, Nürnberg, 23.-27.9.1974

5 R.G. Newton, Scattering Theory of Waves and Particles, McGraw Hill (1966)

6 J.W. Rayleigh, Scientific Papers - Lord Rayleigh, Vol IV, 397 (1892-1901)

7 H.C. van de Hulst, Light Scattering by Small Particles, J. Wiley & Sons, New York (1957)

8 C. Roth, J. Gebhard, G. Heigwer, J. Coll. Sci 54, 265 (1976)

9 H. Breuer, et. al., Staub 33, 182 (1973)

10 R.G. Pinnick, H.J. Auvermann, J. Aerosol Sci. 10, 55 (1979)

11 F. Durst, H. Umhauer, Local Measurements of Particle Velocity ..., Proc. LDA Symposium, Copenhagen 1975

12 W. Schöck, Messung von Tröpfchengrößenspektren ..., 4th Annual Meeting of the Gesellschaft für Aerosolforschung, Bad Soden, 3.-6.11.1976

13 R. Zerull, Streufunktionen nicht-kugelförmiger Teilchen, 2nd Annual Meeting of the Gesellschaft für Aerosolforschung, Bad Soden, 16.-19.10.1974

14 C. Roth, J. Gebhard, Microscopica acta 81, 119 (1978)

15 R.G. Pinnick, J.M. Rosen, J. Aerosol Sci. 10, 533 (1979)

INERTIAL CLASSIFICATION OF AEROSOLS FOR SIZE MEASUREMENT

J. A. Gieseke
Battelle, Columbus Laboratories
Columbus, Ohio

G. W. Parker
Oak Ridge National Laboratory
Oak Ridge, Tennessee

ABSTRACT

Major inertial size classification techniques and devices have been reviewed. Principles of operation, advantages and limitations of each technique, precautions to be taken in design and operation of the devices are discussed with respect to their applications to nuclear aerosol analyses. Included in the review are sedimentation chambers, elutriators, cascade impactors, centrifuges and cyclones. Based on the comparison of various techniques, it has been concluded that spiral duct centrifuges and cascade impactors are suitable for measuring the aerosol size distribution for nuclear aerosol applications. It is also emphasized that because of the possible operational problems and the variations in performance resulting from sampling conditions, any inertial aerosol measurement device should be calibrated and evaluated under conditions as close as possible to the experimental conditions expected during their use.

INTRODUCTION

Inertial classification is probably the most widely used technique for measuring aerosol particle sizes and is almost exclusively the method chosen for those cases where aerosol composition must be measured as a function of size. Inertial classification provides for fractionation or separation of particles by aerodynamic size and in most cases provides for physical collection of the size fractions. Devices or techniques commonly designated as inertial classifiers include cascade impactors, elutriators, spectrometers, centrifuges, cyclones, and sedimentation cells. Each of these devices depends on the principle that particles with greater inertia will move more rapidly across flow streamlines than will particles with lesser inertia. Differences among the various techniques are largely related to the methods for providing high inertial conditions for the particles and in the nature of the gas flow relative to the collection surfaces.

The purpose of this review is to provide brief descriptions of some of the major inertial size classification techniques for aerosols, to identify their principles of operation, to note known problems and limitations of the techniques, and most importantly, to identify advantages and disadvantages of the various techniques for application to nuclear aerosol systems. For this final goal it has been assumed that major practical differences between nuclear aerosols and more commonly encountered aerosols (such as atmospheric dust) are the high concentrations, extensive agglomeration, and radioactivity associated with many nuclear aerosol systems.

Descriptions of Selected Inertial Techniques

Horizontal Sedimentation Chamber

A horizontal sedimentation cell is perhaps the simplest inertial classifier and consists of a horizontal flow channel through which the aerosol passes while gravitational forces cause particles to settle onto the floor of the channel. Typical of such a device is the Cassella M.R.E. instrument shown in Figure 1a. Larger particles deposit closer to the aerosol inlet while smaller particles settle more slowly in the vertical direction and are deposited farther along the channel. However, this sedimentation device is intended only to provide for sampling respirable dust fraction, which is the fraction penetrating the sedimentation chambers. Better size resolution could be provided by a design shown in Figure 1b where the aerosol initially forms a thin layer above a clean air stream. Horizontal sedimentation chambers are impractical for collecting small particles because of the long channels required. Only particles larger than a few microns can be conveniently classified in such devices.

Classification of particles from an aerosol layer is related to the settling velocity of particles, v_s, and the flow velocity along the channel, v. The distance along the channel, ℓ, at which a particle entering at height h would be expected to deposit is simply

$$\ell = \frac{vh}{v_s} \quad . \tag{1}$$

If sedimentation velocity is given by Stokes law as

$$v_s = \frac{d_e^2 \rho_p g C}{18\ \eta \chi} \tag{2}$$

where d_e = the mass equivalent diameter

C = slip correction factor

χ = a mobility correction factor which accounts for non spherical particle shape

η = the gas viscosity

ρ_p = the particle material density

g = acceleration of gravity

or as

$$v_s = \frac{d_a^2 g}{18\eta} \tag{3}$$

where d_a is the aerodynamic equivalent diameter (Note that with d_a, the material density is assumed to be 1 g/cm^3). The aerodynamic diameter can be related to deposition location as follows

$$d_a = \frac{18\eta v h}{g\ell} \tag{4}$$

It is to be noted that the spiral duct centrifuge and various spectrometers to be discussed later are basically sedimentation chambers in which gravity is replaced by a centrifugal force.

Vertical Elutriators

A verticle elutriator is a device in which an aerosol particle is separated from a vertically flowing stream when its sedimentation velocity exceeds that of the stream velocity. Smaller particles with lower setting velocities are carried upward with the stream and can subsequently be separated by size in vertical streams of lower velocity. The principle of a vertical elutriator is illustrated in Figure 2. The size separation provided by an elutriator stage is given by Equation (3) if the sedimentation velocity is replaced with the vertical gas stream velocity to provide the following relationship:

$$d_a = \sqrt{\frac{18\eta v}{g}} \tag{5}$$

where v is the vertical stream velocity in this case.

Vertical elutriators are practically limited to separating particles with diameters greater than about 10 microns. Successive size fractionations are made by returning the small penetrating particles and repeating the single stage separation with reduced gas velocity. These devices are sometimes used as a single separation stage to exclude large particles from a sample. For example, in sampling cotton fiber dust, a single stage elutriator allows only particles smaller than about 15 μm to be collected for assessment as inhalable dust.[1] In this mode of operation the vertical elutriator is used in a manner analogous to that of a Cassella M.R.E. sedimentation chamber noted previously.

Cascade Impactor

Cascade impactors consist of a series of jets impinging against impaction plates with each successive jet/plate combination (stage) being operated at a higher gas velocity. Larger particles with higher inertias are selectively removed from the lower velocity jets with successively smaller particles being collected in stages with higher velocities. The principle of cascade impactor operation is illustrated in Figure 3. Because of geometrical considerations, a distribution of particle sizes is collected at each stage. The exact fate of an individual particle is dependent on its location within the jet as it flows toward the impaction plate. The analyses of impaction efficiency are based on trajectory calculations for the particles as dependent on flow velocities, jet and impaction plate geometry, and particle size and density.

The efficiency of particle collection in any impaction stage is most dependent on the particle Stokes number which is defined for an impactor jet as

$$Stk = \frac{v_j d_e^2 \rho_p C}{9\eta d_j}$$

where v_j = jet velocity

d_j = jet diamter.

Changes in impaction stage geometry (jet diameter, w, jet-to-slide distance, s, jet throat length, t) and flow Reynolds number may affect the general shape of the efficiency curve as well as the general correspondence between Stokes number and efficiency.[2] Figure 4 illustrates the calculated effects of the ratio of s/w on collection efficiency.[3] Since most impactors have a fixed stage geometry and a fixed sampling flow rate, it is necessary in practice to know only the efficiency characteristics of each impaction stage. These are usually given as the "cut-off diameter" for each stage which is the particle size collected with an efficiency of 50 percent in the impaction stage. Because the collection efficiency is not a step function with particle size, it is sometimes important to consider the shape of the efficiency curve in analyzing particle size distributions. Methods to give statistical credence to size distributions obtained from impactor collections have been developed[4,5].

Aerosol Centrifuge

Aerosol centrifuges are sedimentation chambers in which the deposition channel, of a circular or spiral configuration, is rotated to provide a centrifugal force on aerosol particles contained in flow through the channel. The first such device was built by Sawyer and Walton[6] and called a Conifuge. The operation of this device is illustrated in Figure 5. Low sampling rates and flow instabilities led to the design of Stöber and Flachsbart[7] of a spiral duct spectrometer as shown in Figure 6. Modifications to this device were primarily either to decrease the length or to increase the height of the flow channel in attempts to improve flow stability.[8,9] Additional modifications led to creation of spectrometers with cylindrical channels or ducts as shown in Figure 7.

An analytical expression relating aerodynamic particle diameter with deposition distance along cylindrical ducts have been developed by Tillery[10], but for both this design and the spiral duct designs it is better to use experimental calibrations as specific sets of operating conditions. This is because secondary flows made analytical calibrations inaccurate. Calibration curves for spiral duct centrifuges are available in the literature[9]; however, it should be noted that such calibrations are usually obtained at very low sampling flow rates (low aerosol to clean air flow rate ratios) which give higher resolutions than one can expect in practical sampling situations.

Cyclones

Cyclones have long been used to remove large particles and allow penetrations of respirable dust for measurement in industrial hygiene applications. This has been particularly true in the small personal samplers carried or worn by workers in dusty environments. Six identical cyclones in parallel, each operating at a different flow rate, were used by Lippmann and Kydonieus[11] as a multistage sampler giving particle size selective collections.

The most common use of cyclones has traditionally been as an air cleaner to remove large particles. In such an application, the large particles impinge on the wall of the cyclone and settle downward along the wall for collection in a hopper. Obviously adhesion of the particles to the wall is undesirable in such a situation. In contrast, when a cyclone is used as a size selective sampler, the particles impinging against the wall must adhere because reentrainment would lead to less sharp size selectivity. That this occurs is partially the result of the particle sizes of interest and that fact that smaller sampling cyclones operate with laminar or mixed laminar/turbulent flows where large industrial cyclones have turbulent gas flow.

Theories for large gas cleaning cyclones are generally inapplicable to sampling cyclones. The efficiencies of cyclones are primarily dependent on Reynolds number for the flow and Stokes number for the particles. The efficiency predictions of Blachman and Lippman[12] seem to give the best correlation of sampling cyclone data[13]. Again, for practical purposes it is desirable to use efficiency calibrations based on experimental data obtained for the specific cyclones to be used in the sample collection since

small geometrical variations and outlet configurations can affect results. Even with accurate calibration, cyclones cannot be expected to give as definitive size distribution data as impactors because the efficiency curves for cyclones are broader than those typical of impactors.

Inertial Sampler Characteristics

There are specific advantages and disadvantages associated with each of the inertial particle classifiers described in the proceeding sections. Some of these characteristics will be discussed, particularly those which relate to size measurement of nuclear aerosols. As stated previously, the sampling problems of nuclear aerosols are caused by high airborne number and mass concentrations, and by the presence of large agglomerates.

The sedimentation chamber and vertical elutriator devices have the disadvantage that they are most applicable for particles larger than many of most interest. A sedimentation chamber does seem suitable for use as a first stage to precede some other method which is more applicable to smaller particle sizes. Careful flow control is necessary for such an application to be successful and if the aerosol residence time is sufficiently long, agglomeration growth of particles could occur within the sampler itself.

Cascade impactors suffer from problems with particle bounce from the impaction plate, losses of aerosol by deposition onto walls, and breakup of agglomerates.[14] The particle bounce or reentrainment problem is often solved by coating the impaction surface with an adhesive. The effects such procedures have on collection efficiency are shown in Figure 8.[15] The problem with such data is that the results are time dependent in terms of impaction surface coverage by deposited particles.

If an impaction stage is operated for an infinite time, it is obvious that the deposited particles would be piled quite high and no more net collection would occur. Under such long time sampling the efficiency may approach zero. For the other extreme, at initial conditions the surface is clean and any losses are strictly from particles bouncing. The point at which surface coverage begins to affect collection efficiency is probably at a mono layer of particles. With grease coatings it is possible that particles may "sink" below the surface of the grease film and for a time continue to leave a fresh surface exposed. The effects of high loadings on deposition surfaces have been noted by Knuth[16] who found both increases and decreases in impactor stage efficiencies as deposits began to build up.

Wall or interstage losses are unavoidable in an impactor, and can be handled best by choosing an impactor designed to minimize such losses and by either measuring these depositions along with those on the impaction plate or accounting for such losses through use of a prior calibration. Examples of interstage losses have been summarized for three impactor designs by Marple[3] and are shown in Figure 9.

The problem of breakup of agglomerates within impactors has not received much attention in the literature. Breakup can occur in high shear flow fields or on impact of agglomerate onto the impaction plate. Both effects were noted in a study of coal and quartz dusts by Davies et al.[14]

Reentrainment and wall losses are not problems in the centrifuge classifiers but entrace losses, secondary flows, instability of the particle-laden gas layer, and by-pass loss along the top and bottom edges of the ducts may lead to inaccuracies. Entrance losses may be significant for larger particles with about sixty percent of particles of 5 μm diameter being lost in the inlet under somewhat high-flow but fairly typical operating conditions.[17] Although a relationship between inlet losses and particle sizes is available from work by Oeseburg and Roos, these data are valid only at one set of flow conditions and good practice would suggest a calibration of each instrument at intended operating conditions if particles larger than about one micron in diameter are to be sampled.

Because of secondary flows, particle size is not resolved with foil length along the edges of the foil.[9,17] Furthermore, losses out the duct exhaust occurs from that portion of the flow near the edges of the foil. These losses have been measured and related to the mass deposited in the center of the foil as a function of particle size.[17] Edge and carry-through losses can exceed the amounts deposited in the center of the foil. However, such losses are specific to centrifuge design details and selected operating conditions, and therefore individual calibrations are desirable.

A final problem with duct centrifuges arises when the aerosol stream is sufficiently more dense than the clean air stream. As these streams experience the centrifugal forces, the aerosol stream is forced outward and through the clean air stream. If the aerosol stream is dense enough, it can become unstable and stream en masse through the clean air toward the deposition foil. In such a case the aerosol layer moves en masse rather than as individual particles thereby destroying the size separating capabilities of the process. It has been noted that if the aerosol layer has a density in excess of about 1.1 times the density of the clean air layer, this streaming effect occurs.[9] The limits for this problem to be significant are still being resolved; however, an aerosol density of about 1.05 times the clean air density is probably a reasonable upper limit.

Cyclones offer a useful alternative for cases where the aerosol concentration is high or when a large amount of material is to be collected. However, cyclones can be subject to the same problems of bounce and reentrainment as can occur with impactors. Further, cyclones do not usually provide as sharp a separation of sizes as impactors and careful data analysis is therefore required.

CONCLUSIONS

Inertial collections of size separated aerosol particles provide for the direct measurement of size distributions in terms of aerodynamic diameters. The present status of inertial techniques suggests that a spiral duct centrifuge is the preferred technique although cascade impactors can be recommended almost as strongly. However, any inertial technique is subject to some problems, and the magnitude of the problems depends on the specific application and the selected operating conditions. Any statement regarding collector performance is rarely completely valid for more than one set of operating conditions on one application. Because of the possible losses and errors which are highly variable, it is imperative that any device be calibrated and thoroughly evaluated under conditions as close as possible to the conditions expected during use of the device.

REFERENCES

1. Barr, H. S., R. H. Hocutt, and J. B. Smith, "Cotton Dust Controls in Yarn Manufacturing", Report on Contract No. HSM 99-72-44, NIOSH (March, 1974).

2. Marple, V. A., A Fundamental Study of Inertial Impactors, Ph.D. Dissertation, University of Minnesota, Particle Technology Laboratory Publication No. 144 (1970).

3. Marple, V. A., and K. Willeke, "Inertial Impactors", in Aerosol Measurement, Lundgren, D. A., et al., editors, University Presses of Florida, Gainesville (1979).

4. Raabe, O. G., and M. I. Tillery, "Analysis of Cascade Impactor Data by a Weighted Least-Squares Methods", Fission Product Inhalation Program Annual Report, Lovelace Foundation, Albuquerque, New Mexico (1968).

5. Fuchs, N. A., "Aerosol Impactors (A Review)", in Fundamentals of Aerosol Science, D. T. Shaw, editor, John Wiley and Sons, New York (1978).

6. Sawyer, K. F., and W. H. Walton, "The 'Conifuge': A size sampling device for airborne particles", J. Sci. Instrum. Vol. 27, p. 272, (1950).

7. Stöber, W., and H. Flachsbart, "Size Separating Precipitation of Aerosols in a Spinning Spiral Duct", Environ. Sci. Technol., Vol. 3, p. 1280, (1969).

8. Kotrappa, P., and M. E. Light, "Design and Performance of the Lovelace Aerosol Particle Separator", Rev. Sci. Instrum., Vol 43, p. 1106, (1972).

9. Stöber, W., "Design, Performance and Applications of Spiral Duct Aerosol Centrifuges", in Fine Particles, B.Y.H. Liu, editor, Academic Press, Inc., New York (1976).

10. Tillery, M. I., "Aerosol Centrifuges" in Aerosol Measurement, Lundgren, D. A., et al., editors, University Presses of Florida, Gainesville (1979).

11. Lippmann, M., and A. Kydonieus, "A Multi-Stage Aerosol Sampler for Extended Sampling Intervals", J. Amer. Industrial Hygiene Assoc., Vol. 31, p. 730, (1970).

12. Blachman, M. W., and M. Lippmann, "Performance Characteristics of the Multicyclone Aerosol Sampler", J. Amer. Industrial Hygiene Assoc. Vol. 35, p. 311, (1974).

13. Ayer, H. E., and J. M. Hochstrasser, "Cyclone Discussion", in Aerosol Measurement, Lundgren, D. A., et al., editors, University Presses of Florida, Gainesville (1979).

14. Davies, C. N., M. Aylward, and D. Leacey, "Impingement of Dust from Air Jets", Archives of Ind. Hyg. and Occup. Med., Vol. 4, p. 354, (1951).

15. Rao, A. K., An Experimental Study of Inertial Impactors, Ph.D. Dissertation, University of Minnesota, Particle Technology Laboratory, Publication No. 269 (1975).

16. Knuth, R. H., "Comments on Inertial Impactor Calibration and Use" in Aerosol Measurement, Lundgren, D. A., et al., editors, University Presses of Florida, Gainesville (1979).

17. Oeseburg, F., and R. Roos, "Properties of the Stöber Centrifugal Aerosol Spectrometer at a High Sampling Flow Rate: Calibration, Resolving Power and Correction Factors for Particle Losses", J. Aerosol Sci., Vol. 10, p. 539 (1979).

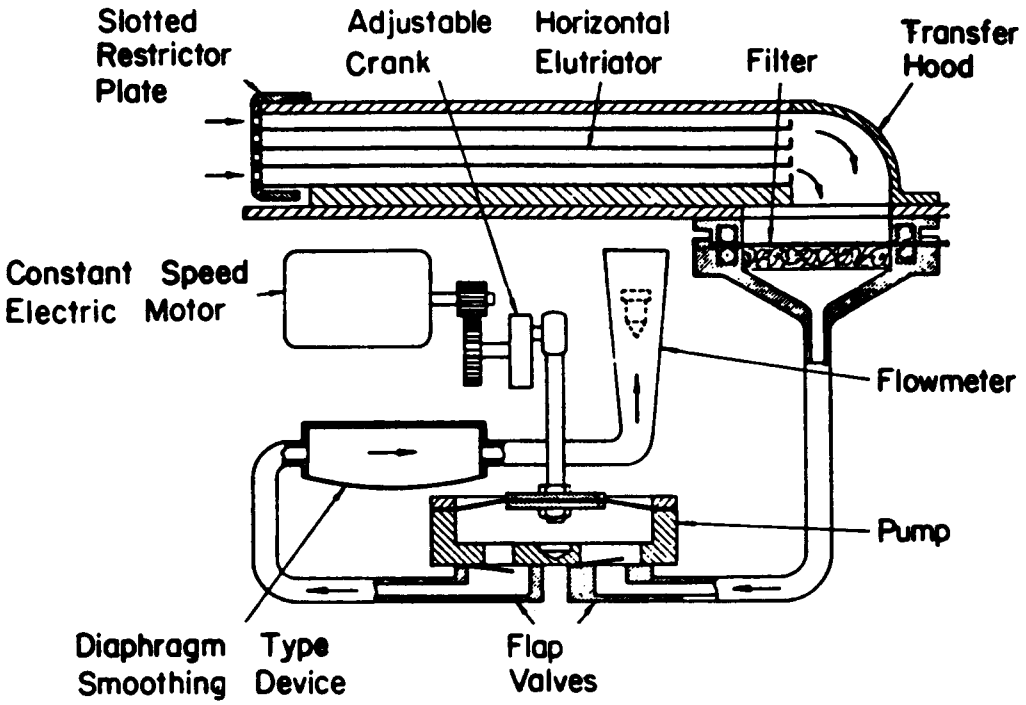

(a)

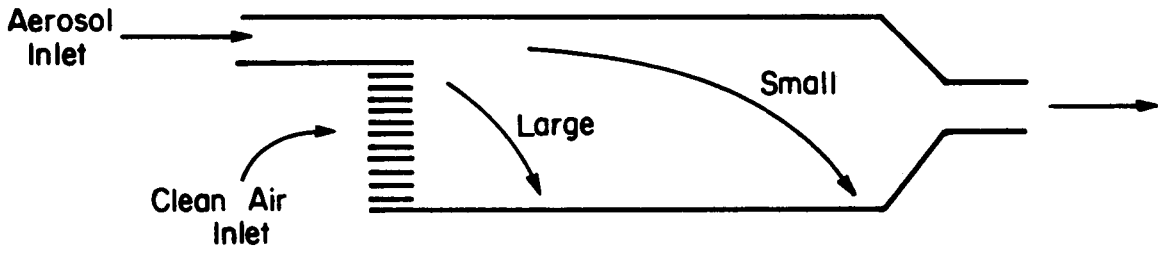

(b)

FIGURE 1. HORIZONTAL SEDIMENTATION CHAMBERS

(a) COMMERCIAL RESPIRABLE SIZE SELECTOR
(b) SEDIMENTATION SPECTROMETER

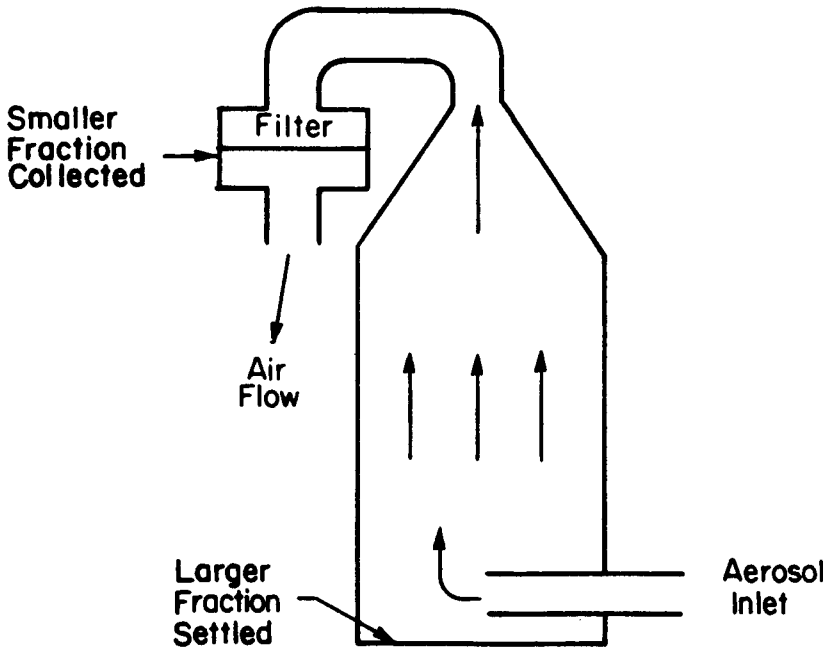

FIGURE 2. VERTICAL ELUTRIATOR

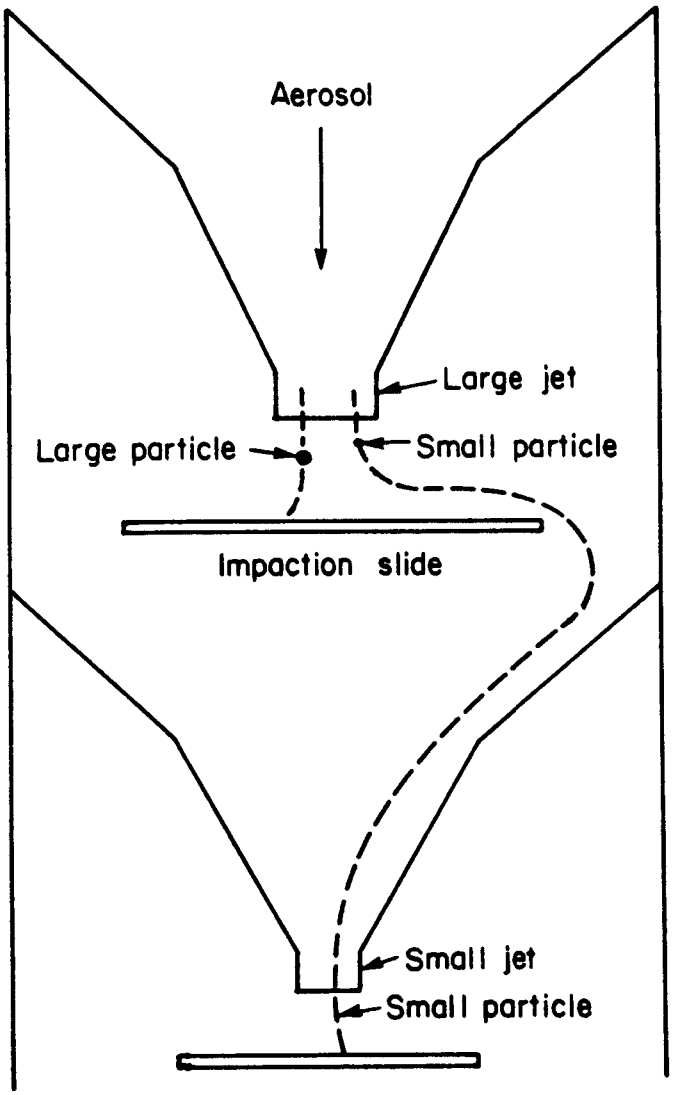

FIGURE 3. SCHEMATIC DIAGRAM SHOWING PRINCIPLE OF THE CASCADE IMPACTOR

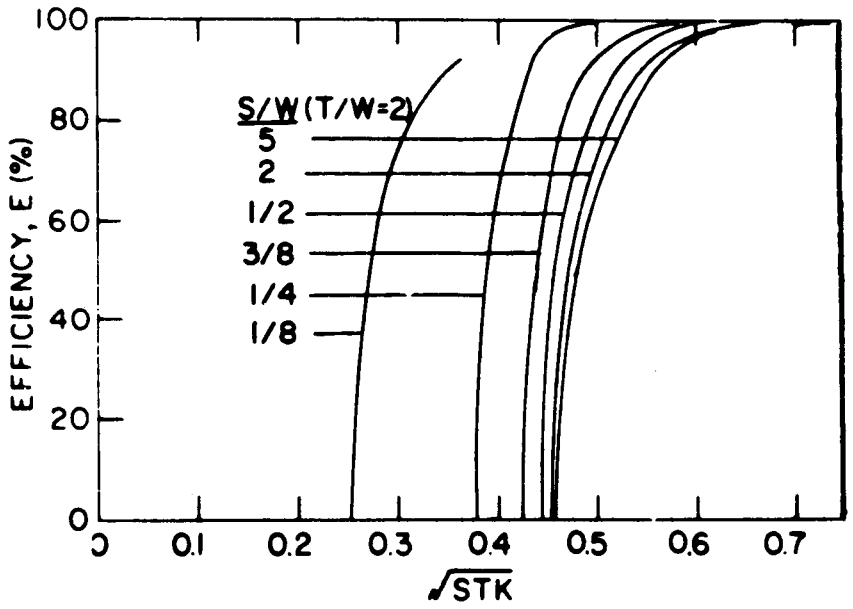

FIGURE 4. IMPACTOR EFFICIENCY SHOWING DEPENDENCE ON S/W

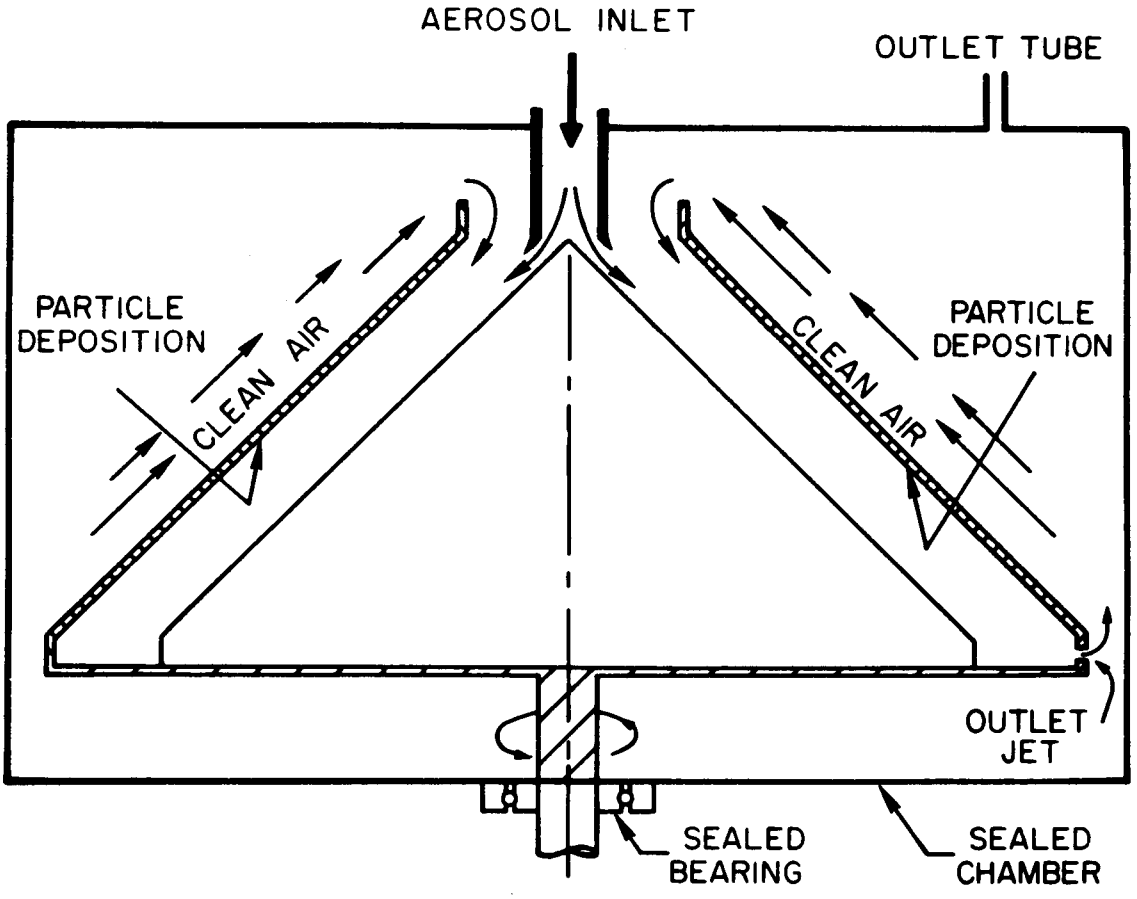

FIGURE 5. CONIFUGE

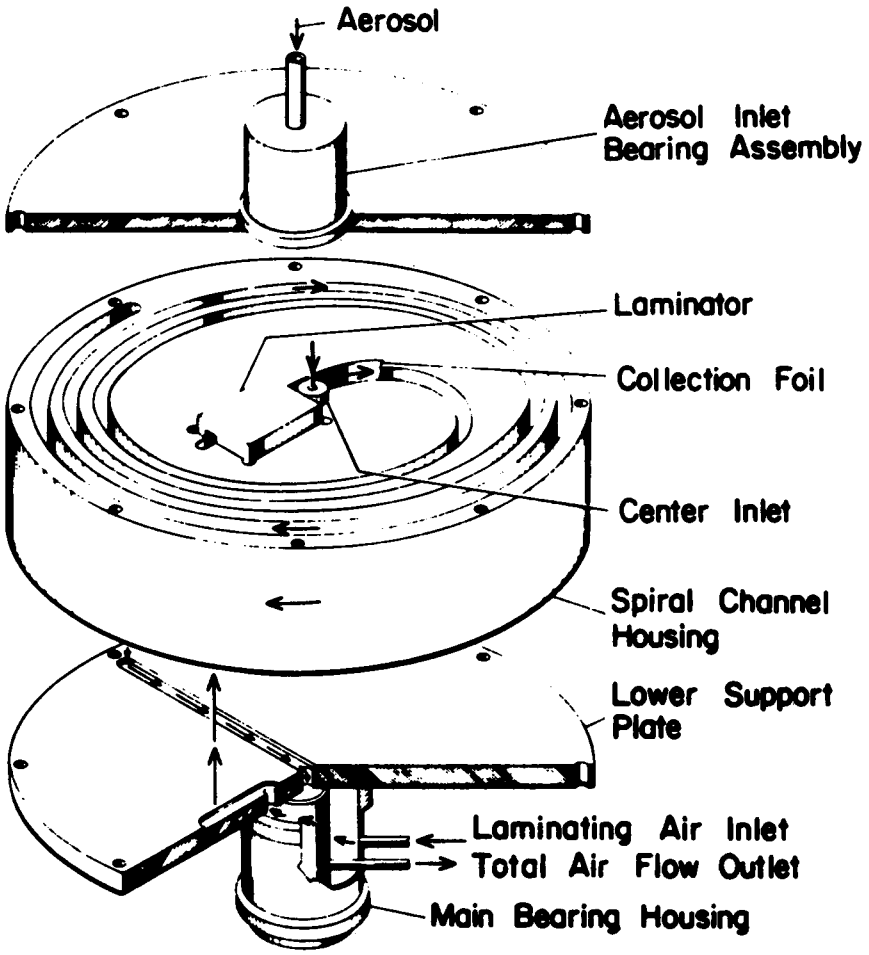

FIGURE 6. BLOWUP OF SPINNING, SPIRAL DUCT SPECTROMETER

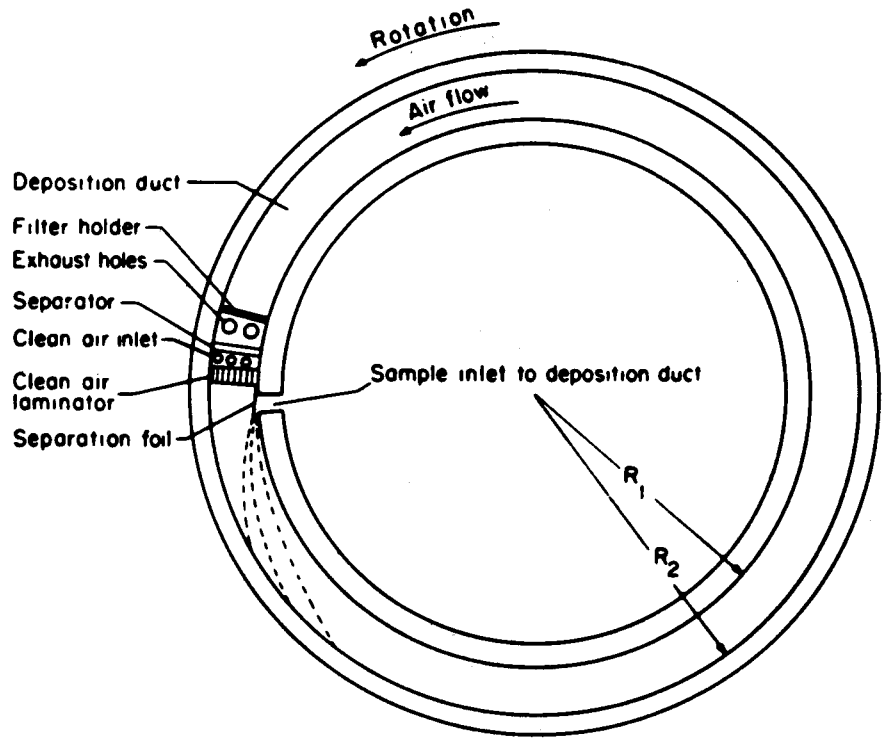

FIGURE 7. TOP VIEW OF CYLINDRICAL DUCT AEROSOL SPECTROMETER

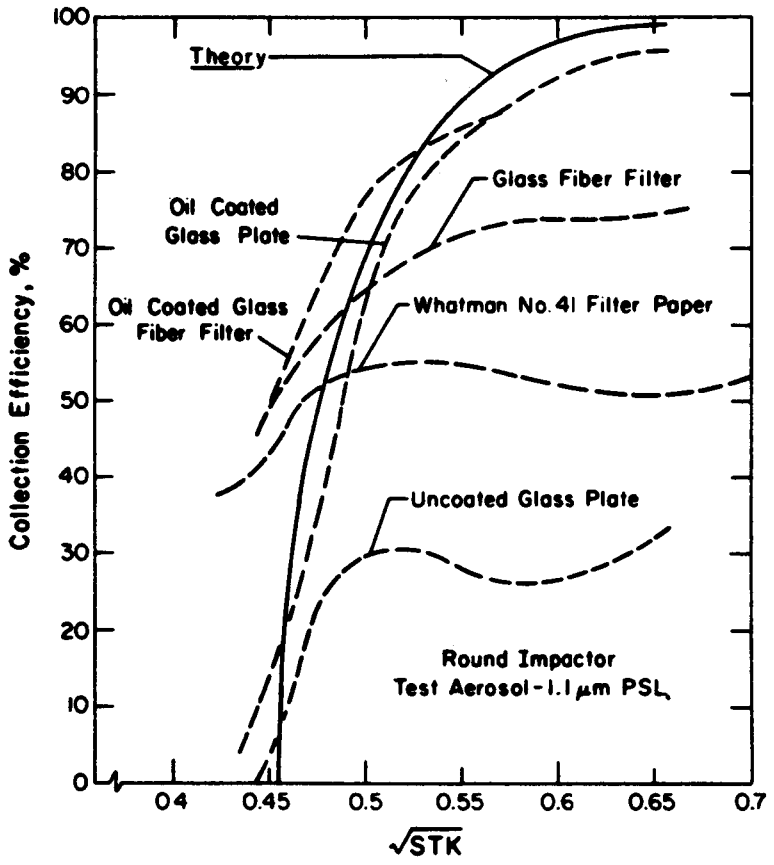

FIGURE 8. COLLECTION EFFICIENCY OF A TYPICAL SINGLE STAGE IMPACTOR FOR VARIOUS COLLECTION SURFACE MEDIA[3]

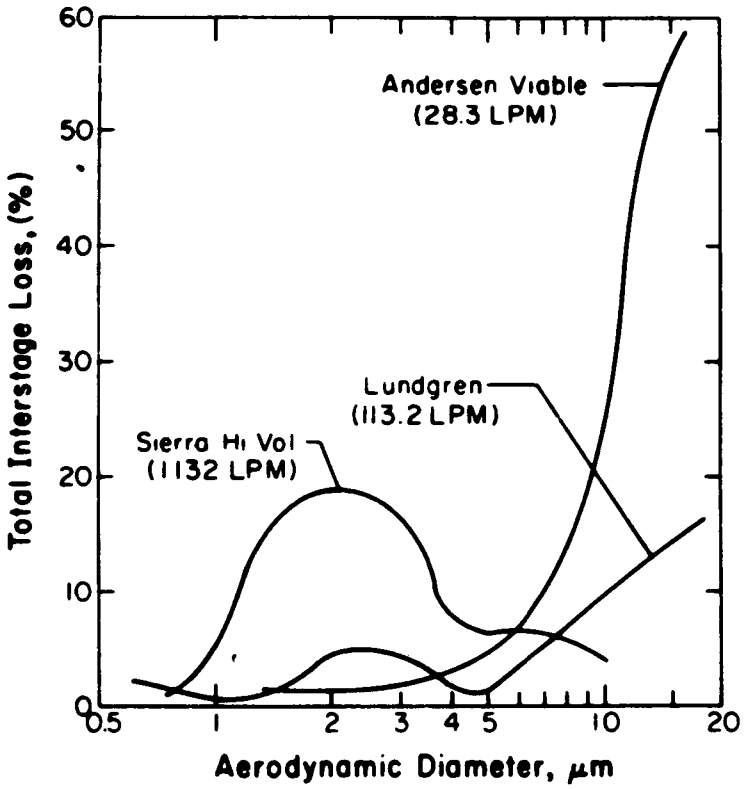

FIGURE 9. INTERSTAGE PARTICLE LOSSES FOR THE THREE IMPACTORS[3]

AEROSOL MEASUREMENT TECHNIQUES AND ACCURACY IN THE CSTF

J. D. McCormack and R. K. Hilliard
Hanford Engineering Development Laboratory
Operated by Westinghouse Hanford Company for
The U. S. Department of Energy under Contract EY-76-C-14-2170
Richland, Washington, U. S. A.

ABSTRACT

The Containment Systems Test Facility (CSTF) provides the capability of performing large-scale aerosol behavior experiments at a scale factor of approximately 0.5 in height for a typical reactor containment building. The containment height is 20.3 m, the volume is 850 m^3, the design pressure is 5 bar, and quantities of sodium up to 1250 kg can be sprayed or spilled for sodium combustion product aerosol sources. Instrumentation is provided for characterization of the aerosol and the containment atmosphere. This paper describes the aerosol sampling techniques and instruments used in the CSTF and discusses their accuracy and reproducibility.

INTRODUCTION

The Containment Systems Test Facility (CSTF) is a multi-purpose facility engaged in studies of sodium fire aerosols within a model reactor containment vessel and in the development of air cleaning systems for removing such aerosols from the vessel atmosphere. The accurate and reliable sampling of the aerosols is of great importance to these tests. Various sampling methods have been used in both flowing and static atmospheres, and it is the methods, their accuracy and precision which will be discussed in this paper.

DESCRIPTION OF THE CSTF

The main feature of the CSTF is the large sized model containment vessel. This insulated carbon steel vessel is 20.3 m high and 7.6 m in diameter. Either spray fires or pool fires can be used to generate the test sodium oxide/hydroxide aerosols. The fires are supplied by transfer of 600°C sodium from external tanks. Quantities up to 1250 kg can be released in times as short as 100 seconds for pool fires or extended to over 40 hour periods for small spray fires. Both the containment vessel and the air cleaning system are equipped with multiple sampling stations for aerosol concentration, aerosol size, atmosphere composition and temperature. These sampling systems are shown schematically in Figure 1, and details will be discussed in the subsequent sections.

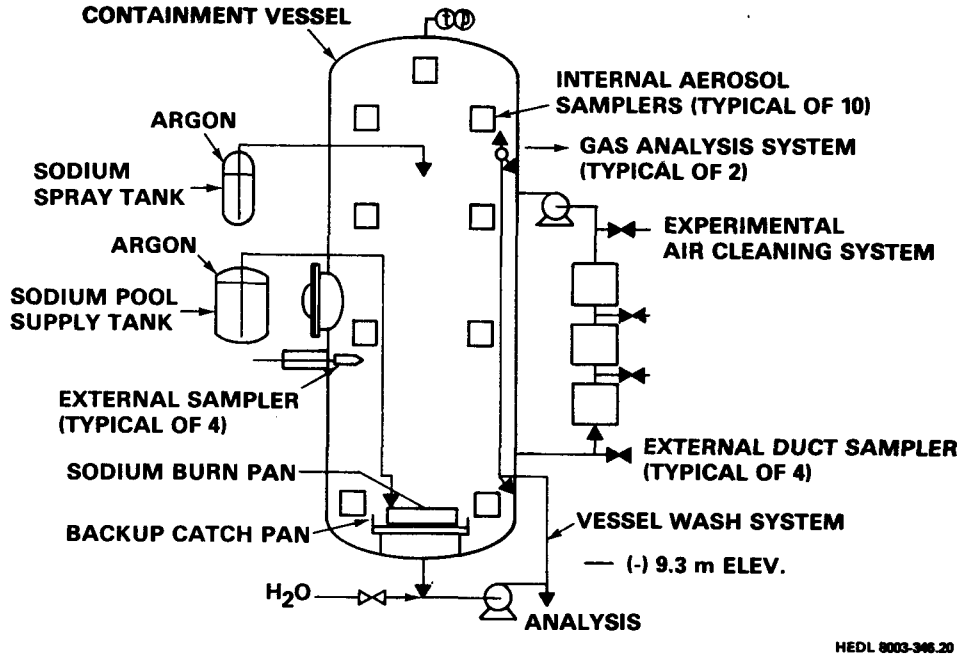

FIGURE 1. Schematic Diagram of CSTF Sampling Systems.

AEROSOL MASS CONCENTRATION MEASUREMENTS

External Through-The Wall Filter Samples

Airborne mass concentration of the containment vessel atmosphere is determined by filtering measured volumes of the atmosphere and analyzing the filters for sodium. An air lock arrangement, shown in Figure 2, permits the filter samples to be inserted into the containment atmosphere without using a sample delivery line. Four locations on the vessel wall are equipped with air locks to permit sampler insertion and withdrawal through a large ball valve. The filter holder is mounted on a push rod which slides through a gas seal.

These four stations are at various elevations and angular positions on the shell of the vessel and thus allow sampling for aerosol variations with height. Similar "thief" stations are located at the inlet and outlet ducts of the various air cleaning components. These stations use stainless steel holders* with 47-mm diameter filter papers. Filter media are fiberglass (Gelman* Type A/E) when the aerosol concentration is high. The fiberglass paper has a high loading capacity, which permits reasonably long sampling periods, but contains ~0.2 mg Na, which reduces the accuracy of low concentration samples. When the airborne concentration is low, a membrane filter with a very low sodium background level (Gelman Acropor 3000) is used.

* Manufactured by Gelman Instrument Co., Ann Arbor, MI 48106

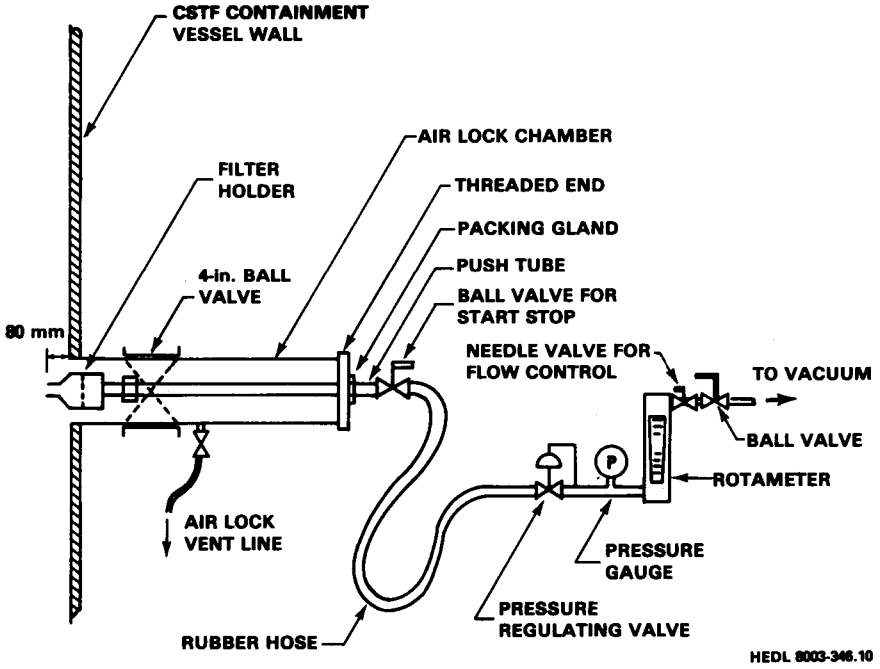

8004000-8

FIGURE 2. Through-The-Wall Sampling Station Used in CSTF Aerosol Tests.

Chemical Analysis

The filter media from the aerosol samplers are leached with demineralized water and analyzed for sodium by acid titrimetry or emission spectrometry. The two methods were compared and found to agree within 5%. Appropriate blank corrections are made to account for background sodium in the filter media and demineralized water.

The chemical forms of the suspended and deposited aerosol are analyzed by a combination of methods:

- X-ray diffraction for crystalline forms (Na_2O, NaOH, and hydrates).
- Sodium peroxide by reaction with iodide ions, giving free iodine which is then titrated with thiosulfate.
- Sodium carbonate by potentiometric acid titration or liberation of CO_2 with acid, measurement by gas chromatography.
- Sodium hydride and metallic sodium by measuring the quantity of H_2 released by gas chromatography when the sample is added to water.
- Total sodium content by emission spectrometry or by titration.

Of course, it is essential to minimize chemical changes due to sampling and handling. This is accomplished by collecting the aerosol on Teflon membrane filters, sealing the collecting sampler, and performing the analyses in an

argon atmosphere glove box where necessary.

Total aerosol mass is measured by weighing the filter paper before and after sampling. Again, an effort is made to protect the collected aerosol from exposure to ambient atmosphere. Weighing is performed to ±0.1 mg.

Isokinetic Considerations

The inlet to the filter holder is a 5-cm long pipe with a bore of 1.2 cm. This represents a reasonable compromise for sampling from both the quiescent containment atmosphere and the flowing duct streams. Sample flows vary from 47 cm^3/sec up to 470 cm^3/sec, depending on the expected aerosol concentration and the filter type. Because of the variable air flow rate in the duct, isokinetic sampling is not always achieved, and in some extreme cases the sample flow rate may be a factor of six low. This could lead to 50% enrichment in 5-μm diameter particles and approximately a 10% error in 3-μm diameter particles [1]. Sampling at these same rates from the relatively slow moving atmosphere in the containment vessel meets the criterion discussed by Dennis [1]. During sampling, the flow, metered by calibrated rotameters, is kept constant and any changes in pressure drop caused by deposited aerosol on the filter noted. The sample volume is then corrected to standard reference conditions (0°C, 760 mm Hg).

Reproducibility

The reproducibility of the method has been examined by taking replicate samples during times of nearly constant aerosol concentration. A series of typical measurements is presented in Table I. The precision of the

TABLE I

SAMPLING PRECISION - (a)

Test AC4 Sample	Time Min	mg Na	Net wt Gain mg	Wt Ratio Na/Total	Concentration, g/m^3 at STP	
					Na Basis	Total wt
T3-F22A	0	9.6	42.3	0.227	5.42	23.9
B	2	9.1	37.0	0.246	5.18	20.9
C	4	9.85	38.1	0.259	5.56	21.5
D	6	9.1	30.5	0.298	5.13	17.2
E	8	10.0	37.3	0.268	5.66	21.1
F	10	9.5	(b)	(b)	5.37	(b)
G	12	10.4	33.7	0.309	5.89	19.0
Mean		9.65	36.48	0.2678	5.459	20.60
σ		0.475	4.02	0.0311	0.2683	2.287
σ,%		4.92	11.0	11.6	4.91	11.1

(a) All samples are 0.0017 m^3 STP, taken 7.6 cm from the wall.
(b) No data.

series is about 5% for total sodium (±1 standard deviation) and 11% for total weight. The larger error for the total weight is due to variable moisture pick-up by the hygroscopic deposits during handling and weighing.

The effects of distance from the vessel wall was measured by taking samples at various distances up to 1.4 m from the wall. These data show that the concentration is nearly independent of distance from the vessel wall. The standard deviation of 5.88% was only slightly greater than that obtained in the series taken at the same distance from the wall, 4.92%.

Error Analysis

Errors in the calculation of the airborne mass concentration result from errors in the measured gas sample volume and the determination of the sodium or weight of the collected material. Assuming that the errors combine as the root mean square, the accuracy of the measurements are given in Table II. We estimate that the sample volume for our worst case conditions is known to ±12%. The error in analysis by titration is ±6% and by emission spectrometry is ±10%. Determination of the mass is ±22%. The somewhat larger estimated error for sodium by the emission method is because this method is used for low concentration samples and the sodium blanks on the filters become important. Typical sodium blanks for several sampling materials are given in Table III.

TABLE II

AEROSOL CONCENTRATION ACCURACY FOR SEVERAL METHODS

	Accuracy, Percent	
	Na Basis	Weight Basis
Sample Volume	12	12
Analysis	8	22
Total Error	14	25

TABLE III

TYPICAL FILTER MATERIAL BLANKS

Material	Sodium, mg
Gelman A/E fiber glass	0.20
Gelman Acropor 3000	0.011
Sierra impactor stage	0.014
Sierra backup filter	0.125
Andersen stage	0.23
Andersen backup filter	0.37

Sampling Through Tubes

Sampling directly from the containment atmosphere as described in the preceding section avoids the errors and uncertainty associated with sampling through lines. The aerosol material deposited in the CSTF 5-cm long filter holder inlet is washed and added to the filter for analysis so that there is no loss. It averages 5% of the total sample.

Direct sampling is not always possible. Sampling through lines is acceptable if the line is cleaned after each sample and the deposited material recovered for analysis. Otherwise, unknown line losses or gains may occur, resulting from gravity settling, diffusion and turbulent deposition to the tube walls. Even when the aerosol particle size is known, prediction of line loss can be inaccurate. As an example, several samples of the containment atmosphere in CSTF test AC5 were taken sequentially through various sizes of tubes.

Each tube consisted of a long straight entry section, a 90° elbow, a short length of tube and the standard CSTF sampling filter in series. After sampling, the tube was cut just upstream of the elbow and the sections were washed and analyzed for sodium. The data show greater line loss with greater length and diameter. The aerosol size was measured by a cascade impactor to be 3.3 μm aerodynamic mass median diameter (AMMD) with σ_g = 2.54. The calculated line deposition due to settling under laminar flow conditions in the straight inlet section are given in Table IV. The measured line loss is slightly greater than predicted. The difficulty of estimating line loss by simple calculation is obvious. The deposition in the 30-cm long section containing the elbow averaged 2.5%. This is lower per unit length than the inlet section, showing that an elbow at that location has minor effects for these sampling conditions. Corrections for line losses can only be made when the particle size distribution is known accurately.

TABLE IV

COMPARISON OF PREDICTED VS MEASURED LINE LOSS

Sample No.	Length m (a)	Line Loss, % Calculated[b]	Line Loss, % Measured
C	0.67	12.4	17.6[c]
B, E, J	1.67	24.6	33.5[c]
D	3.67	37.9	42.8

(a) Straight horizontal inlet tube, 10.9-mm ID.

(b) Settling in laminar flow for 3.3 μm AMMD, σ_g = 2.54 particles. See Reference [2], Equation 25.14.

(c) Mean.

In-Vessel Cluster Samplers

The four "thief" sample locations are supplemented in some tests by sample clusters hung at 10 locations within the CSTF atmosphere. Each cluster contains 12 filter holders, each with a separately controlled solenoid valve. Figure 3 shows a bottom view of a cluster retrieved from the containment vessel after test AB1.

The precision of the cluster sample method is lower than for the thief samples. The samples are exposed to the test atmosphere for the entire duration of the test. Diffusion and convection effects deposit material on the filters. As the concentration decreases at later times in a test, the standard deviation between clusters increases from about 8% to 40%.

Airborne concentrations determined by the two sampling methods during test AB2 are plotted in Figure 4. The concentrations agree within an error band of ±30%. The concentrations in Figure 4 are expressed in terms of containment conditions, hence a correction for each sample volume is necessary.

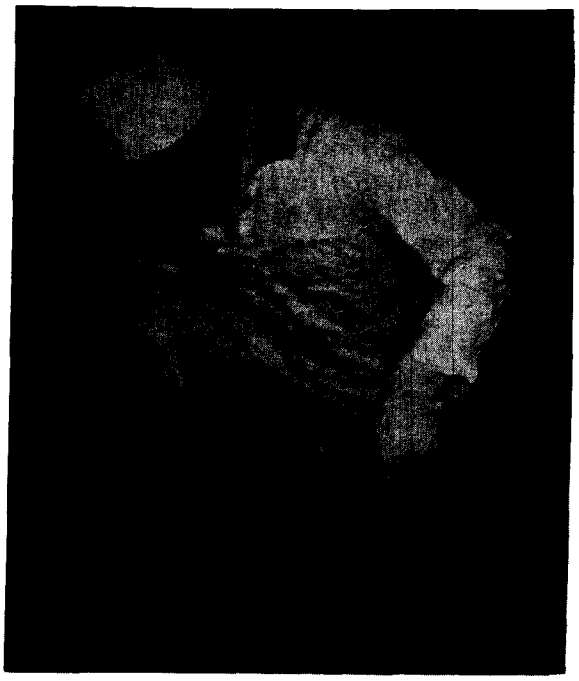

779932-9cn

FIGURE 3. Bottom View of an In-Vessel Cluster.

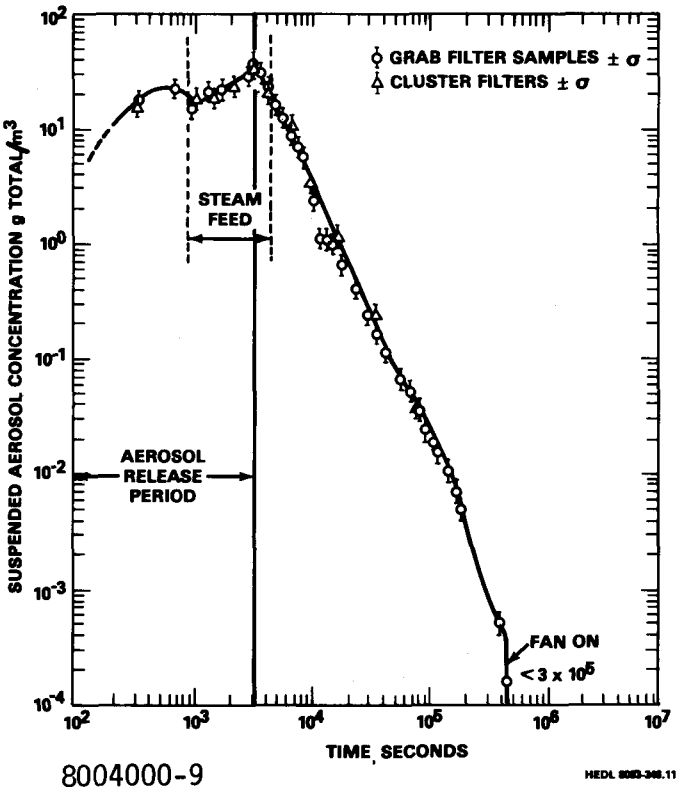

8004000-9

FIGURE 4. Suspended Mass Concentration, Test AB2.

Absolute containment pressure is recorded continuously to ±0.5%. Because of temperature variations within containment, temperature corrections are made using an average atmosphere temperature. This average is obtained at sample time using ten thermocouples distributed throughout the vessel volume. The accuracy of these couples is estimated to be ±0.8% of the absolute temperature, although the deviation of a location high or low in the vessel could be more. The atmosphere temperature in test AC5, for example, had a standard deviation of 9°C at the start of sodium spray, deminishing to 3°C after natural convention currents were established. The error in the correction to containment conditions is estimated to be less than 3%.

AEROSOL PARTICLE SIZE MEASUREMENT

Cascade Impactors

Two types of multi-jet impactors are used to help evaluate biases that might be associated with particular impactor designs. An 8-stage circular jet impactor (Andersen Mark III High Temperature Sampler*) and a 6-stage rectangular jet impactor (Sierra Model 226 Stack Sampler**) were used. Figures 5 and 6 are photographs of these impactors. The photographs show the stages individually covered with precut fiberglass paper. Samples taken with and

* Manufactured by Andersen 2000, Inc., Atlanta, GA.
** Manufactured by Sierra Instrument Company, Carmel Valley, CA

without the glass fiber collection surface agree very closely, hence the paper mat is used in all samples to minimize re-entrainment and to simplify deposit analysis.

The stage accumulations of sodium are obtained by washing each stage collection paper with water and analyzing the water by flame emission spectrometry. Suitable allowance is made for background sodium in the glass fiber paper. Losses to the impactor walls are ignored. The sample size is controlled so that the maximum deposit on any single stage is 5 mg as Na to minimize particle bounce and re-entrainment.

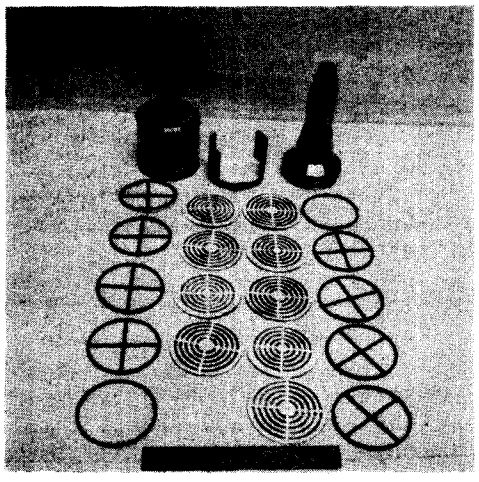

7893063-34

FIGURE 5. Circular Jet Impactor

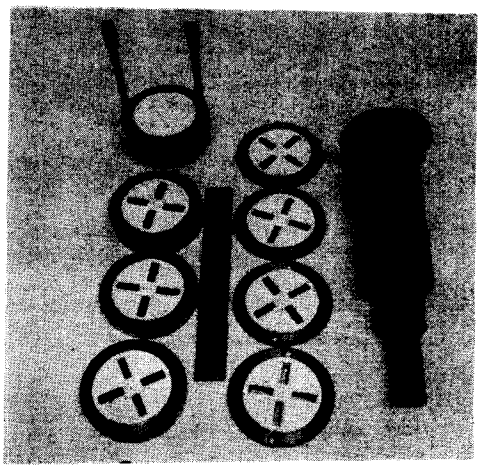

789063-32

FIGURE 6. Rectangular Jet Impactor

Equation (1) is used to determine d_{50} values at flow conditions different from those used to calibrate the impactor.

$$d_{50} = (d_{50})_{ref} \left[\frac{\mu}{\mu_{ref}} \cdot \frac{Q_{ref}}{Q} \right]^{0.5} \qquad (1)$$

Where:

D_{50} = Aerodynamic diameter at sampling conditions,
μ = Viscosity of gas at sampling conditions,
Q = Gas flow rate at sampling conditions, and
ref = Subscript indicating value of parameter under calibration or reference conditions.

Stage cut-off diameters for the two types of impactors used in the CSTF are listed in Table V.

The d_{50} values listed in Table V for the Andersen impactor are those recommended by the manufacturer. These values are in good agreement with

TABLE V

REFERENCE STAGE CUT-OFF DIAMETERS FOR CASCADE IMPACTORS USED IN THE CSTF

Andersen Mark III (a)		Sierra Model 226 (b)	
Stage	d_{50} μm	Stage	d_{50} μm
0	13.2	1	18.0
1	8.3	2	11.0
2	5.64	3	4.4
3	3.8	4	2.65
4	2.45	5	1.70
5	1.25	6	0.95
6	0.77		
7	0.52		

(a) Flow conditions: 14.1 actual liter/min at 21°C and 1 atmosphere pressure. Precut glass fiber mats.

(b) Flow conditions: 7.0 actual liters/min at 22°C and 1 atmosphere pressure. Precut glass fiber mats.

calibration data for the same instrument provided by Cushing, et al [3] using ammonium fluorescein and polystyrene latex spheres. The d_{50} values for the Sierra impactor are taken directly from Cushing, et al [3]. Particle size distributions are calculated by the method described by Mercer [4].

Desposition Coupons

Differential deposition rates are obtained by inserting stainless steel coupons (51-mm diam) into the vessel atmosphere through the wall ports. Aerosol deposited on the upper surfaces of the coupons is subsequently removed with water and analyzed for sodium content. Based on exposure time and airborne sodium concentration, a deposition velocity (gravity settling velocity) is calculated from Equation (2).

$$u_t = \frac{\text{Na deposition flux}}{\text{Na suspended mass concentration}} \qquad (2)$$

A settling diameter can be computed from the desposition velocity, u_t, and Stokes law, as indicated in equation (3).

$$d_s = \left[\frac{18\,\mu_f u_t}{g\rho_p}\right]^{0.5} \qquad (3)$$

Where:

d_s = mean settling diameter,
μ_f = fluid viscosity,
g = acceleration due to gravity, and
ρ_p = effective particle density.

In using equation (3), the particles are assumed to be spherical with unit density in order to compare with the similar assumption used for the cascade impactor data.

Using ±10% and ±15% for the average errors in the deposition flux and suspended concentration, respectively, the error for d_s is ±18%.

Gravity Settling Sampler

A gravity settling chamber was built to withdraw particles under low shear conditions. Large agglomerate particles can theoretically be fractured in the cascade impactors, and the horizontal elutriator used to help evaluate whether particle breakup in the impactors is significant.

The sampler consists of a vertical array of 16 rectangular flow channels, each of which is 2.49 mm high, 50.4 mm wide, and 203 mm long. The unit is backed up by a high efficiency filter so that the total mass of aerosol entering the sampler can be determined. The horizontal flow channels are formed from thin stainless steel sheets. After a sample is withdrawn, the sheets are cut into transverse segments and the deposit removed in a water wash. Particle size distribution is computed by iteration until the observed deposition profile fits one computed on the basis of laminar flow.

Calculation from Airborne Attenuation Rate

The mean aerodynamic settling diameters can be calculated from the airborne concentration curves by differentiating the curves at times when the source is zero and equating with the Stokes settling removal term. This neglects wall plateout, which is reasonable in view of the fact that in the CSTF 93% of the mass settles and only 7% plates. Thus,

$$\frac{dC}{dt} = \frac{u_t A_s C}{V} \qquad (4)$$

Where:

C = Time dependent suspended mass concentration,
u_t = Terminal settling velocity,
A_s = Horizontal surface area, and
V = Gas volume.

The settling velocity, u_t, is calculated by Equation (4) and the settling diameter calculated from Stoke's law (Equation 3).

Using ±15% and ±25% as the average errors in measuring C and dC/dt, respectively, the combined error in d_s by this method is ±29%.

Comparison of Methods

Particle size information obtained by the various methods discussed in the preceding sections can be compared if the data are all converted to the settling diameter, d_s. Cascade impactor data and computer code HAA-3B [4] output can be converted to d_s by Equation (5).

$$(d_s)_a = \text{AMMD} \exp(\ln^2 \sigma_g) \quad (5)$$

Where:

$(d_s)_a$ = aerodynamic settling mean diameter,

AMMD = aerodynamic mass median diameter,

σ_g = geometric standard deviation.

Figure 7 shows data from CSTF test AB2 made by Andersen cascade impactor, Sierra cascade impactor, deposition coupon, gravity settling sampler, and calculation from suspended concentration decay. Also shown is a HAA-3B [6] prediction. Particle diameters computed by the various measurement techniques agree quite well with each other and with HAA-3B predictions except for the early sample. In general, the measurements fall within a 20% error band. The fact that the cascade impactor data are in agreement with the other methods suggests that particle fracture and re-entrainment in the impactor stages is not significant for the sampling conditions used in the CSTF.

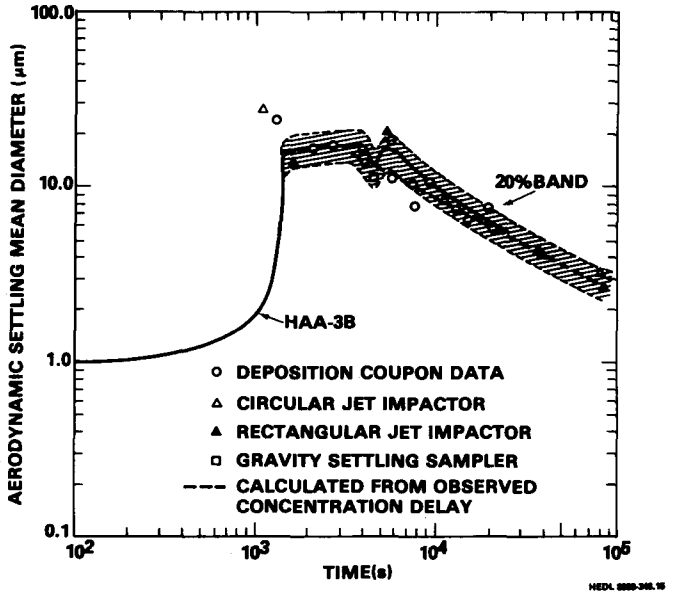

8004000-12

FIGURE 7. Comparison of Measured and Predicted Settling Mean Particle Diameters in Test AB2.

AEROSOL SOURCE RATE DETERMINATION

The aerosol source for CSTF experiments is generated from burning sodium in an air atmosphere by either a pool fire or a spray fire. For the pool fire, the duration of burning is controlled by closing a lid on the burn pan to terminate the fire while it is still burning vigorously. The average source rate is then determined by post-test washing of the

containment vessel surfaces to obtain the total released sodium mass and dividing this by burning time. The resulting accuracy is ±8% for the average source term, though the instantaneous rate could differ by ±20% from the mean. After the burn pan lid is closed, the source is known to be zero.

In tests where the aerosol is generated by a sodium spray fire, the sodium drops are small (on the order of 500-μm MMD) and the fall distances are sufficiently large to completely oxidize the sodium. An estimate of the fraction of sprayed sodium which is released as an aerosol is made by selective post-test washing of vessel areas. For short duration sprays (∿10 min), the aerosol generation rate is very nearly 100% of the spray rate. For longer duration sprays, crusting of the spray nozzle disturbs the spray pattern and causes some of the sodium to burn as a local pool fire, thus reducing the fraction aerosolized, in some cases to as low as 20% of the spray rate.

A factor affecting the source term is the absorption of the water vapor by the suspended particles to form $NaOH \cdot xH_2O$. This mechanism increases the suspended mass and changes the physical properties of the agglomerated particles. The importance of this effect will depend on the specific conditions of the test or plant accident [5].

MISCELLANEOUS MEASUREMENTS

Integral Settled Mass

The final distribution of aerosol within the vessel is of interest for aerosol code comparison. Settled mass is determined by use of ten deposition trays located throughout the vessel on the bottom head, deck and upper catwalk. These are removed at the end of the test and analyzed for total sodium content. This method of measuring average integral settling flux is accurate to ±5% for single locations, but considerable differences are found between locations. As an example, in test AC1, with a spray fire source, the mean of ten sampling locations was 0.267 g Na/cm^2 and the standard deviation was 0.137 g Na/cm^2. This large deviation is partially due to some of the samplers being located in shadowed regions.

Integral Wall Plated Mass

Aerosol deposits on vertical surfaces are determined by decontaminating measured areas of about 0.1 m^2. Selected locations are wiped with a series of three damp swabs. The deposits are very soluble, 99% of the sodium is removed by the first swab. The method is accurate to ±10% for any single location, but considerable differences are found between locations. For example, in test AC1, washes at four elevations averaged 0.00263 g Na/cm^2, with σ = 0.0018. This plating flux is approximately 1% of the deposition flux to upward facing horizontal surfaces.

Overall Material Balances

The quantity of sodium delivered to the vessel is measured by load cells on the sodium supply tanks to ±0.5% accuracy. At the end of each test the vessel is washed and steamed to recover deposited sodium. Any sodium in the

external air cleaning system is determined and an overall sodium balance is made. The fraction of the sodium aerosolized is determined by adding the amount in the air cleaning system to the deposited quantities. We estimate the overall material balances to be accurate within ±8%.

CONCLUSIONS

The sampling methods used in the CSTF are described and assessed for precision and accuracy. During a test approximately 1000 determinations are made from the samples taken. From an analysis of errors associated with the methods we conclude that:

1) Through-the-wall samplers can provide suspended mass concentration values accurate to 14% for sodium and 30% for total mass.

2) Remotely controlled in-vessel cluster samples are accurate at early times to 20% for sodium and 30% for total mass. At longer times, when concentrations are very low, these values increase to 40% and 50%, respectively.

3) Sampling through tubes can produce variable and unpredictable errors unless the tube is washed and analyzed after each sample.

4) Particle size distributions measured with two types of cascade impactors agree within 20% of sizes derived from settling measurements.

5) Source rate determinations during pool fire tests are accurate to 20%. Spray fire source rates are less well known, with errors ranging from 25% to 500%.

6) Integral settling flux determinations are accurate to 10%; similar determinations of integral plating on vertical walls are accurate to 20%.

7) Overall material balances at the end of CSTF tests are accurate to 8%.

REFERENCES

1. R. Dennis, "Handbook on Aerosols," TID-26608, 1976 (p. 96).

2. N. A. Fuchs, "The Mechanics of Aerosols," The MacMillan Co., New York, p. 112 (1964).

3. K. M. Cushing, et al, "Particulate Sizing Techniques for Control Device Evaluation: Cascade Impactor Calibrations," EPA-600/2-76-280, Southern Research Institute, Birmingham, Alabama, October, 1976.

4. T. T. Mercer, "The Interpretation of Cascade Impactor Data," Industrial Hygiene J., 26, 1965, pp. 236-241,

5. R. K. Hilliard, J. D. McCormack and A. K. Postma, "Aerosol Behavior During Sodium Pool Fires In A Large Vessel-CSTF Tests AB1 and AB2," HEDL-TME 79-28, June, 1979.

6. R. S. Hubner, et al., "HAA-3 User Report," AI-AEC-13088, Atomics International, March 30, 1973.

EXPERIENCE ON MEASUREMENT METHODS FOR SODIUM FIRE AEROSOLS

W. Cherdron, Ch. Hofmann, S. Jordan
Laboratory for Aerosol Physics and Filter Technology
Kernforschungszentrum Karlsruhe, FRG

ABSTRACT

In sodium cooled fast breeder reactors sodium fires may occur accidently by leaking pipes. One of the most important effects of sodium fires is the release of large amounts of aerosols. The knowledge of the physical and chemical properties of these aerosols is of great importance for the lay-out of filter systems, reactor components and for estimating the environmental impact of reactor accidents.

During sodium fire tests in the FAUNA containment different devices for measuring the aerosol mass concentration and size distribution were used A new developed automatically and continuously working sodium aerosol mass concentration analyzer will be explained and its output data compared with data from the other methods. The analyzer was found to be the most reliable and sensitive instrument.

During and after sodium fire the particle diameter was measured by an Andersen impactor, an aerosol centrifuge, a light scattering instrument, and by analysis of electron microscope photographs. The experience with these instruments is discussed. The measured data are compared and the errors in the measurements of aerosol size distribution derived.

The influence of inaccuracies in mass concentration and particle size measurements on code validation is discussed.

INTRODUCTION

In sodium cooled fast breeder reactors, sodium fires may occur accidently by leaking pipes. One of the most important effects of sodium fires is the release of large amounts of aerosols. The knowledge of the physical and chemical properties of these aerosols is of great importance for the layout of filter systems, reactor components and for estimating the environmental impact of reactor accidents.

Performance tests on reactor components and filter devices and validation of aerosol behavior codes call for the accurate measurement of aerosol properties. This includes measurements of aerosol mass concentrations as well as of aerosol size distributions.

During sodium fire tests in the 220 m^3 FAUNA containment different devices were used for measuring the aerosol mass concentrations and size distributions.

AEROSOL MASS CONCENTRATION

The aerosol mass concentration during and after the pool fires F1 - F3 was measured by four different methods: The reference method was based on a continuously operating Sodium Aerosol Measuring Monitor (SAMM). Moreover, the mass concentration was measured by washing out the aerosol in water, with at least two impingers in series, and by subsequent titration. Filter samples were taken from the reaction vessel at intervals for chemical analysis and for mass determination. Besides concentrations less than 0.1 g/m^3, the mass concentration was determined with a mass balance meter.

Under the continuous and the impinger methods the soluble aerosols are scrubbed into the liquid phase where the sodium content is analyzed either by a sodium electrode or by titration. Use of a sodium electrode requires that the aerosol is dissolved in water as completely as possible and brought to the electrode in the aqueous phase. For this purpose, a mixing cell was developed ensuring complete dissolution of the aerosol in water by sufficient stay time and mixing. The individual components of the system appear from Fig. 1.

The aerosol is dissolved in the mixing cell (1). The liquid phase is separated from the gas phase in the separator (2). The remaining gas is sucked through the impingers (4) via the vacuum pump (7) and subsequently its volume is measured with the gas meter (8). The liquid (water) in the impingers (4) serves as a control for incomplete dissolution of aerosols.

Subsequently, the solution is carried through the NH_3 diffusion bottle which is filled with concentrated NH_4OH. Here passive NH_3 diffusion takes place via a silicon tube in order to raise the pH of the solution to about 10-11 to eliminate the cross sensitivity of the sodium electrode to hydrogen ions. From here the solution flows via the sodium electrode (5) into a measuring cylinder where the volume can be recorded. The electrical potential of the solution is a measure of the sodium concentration.

During measurement of high aerosol concentrations cloggings occur upstream of the water entry. Therefore, the inlet cross section must be as large as possible. However, flushing is necessary from time to time.

In the tests performed in the FAUNA facility the long term measurement did not produce difficulties since the aerosol concentration quickly decreased to a value at which the instrument with a reduced water flow measured for more than 16 hours without maintenance.

Fig. 2 shows plots of sodium mass concentration in different ranges over more than 20 hours. A sodium mass concentration as low as 0.1 mg/m^3 can easily be measured, the error is smaller than $\pm$ 0.05 mg/m^3.

The filter samples can be analyzed either by weighing or by wet chemical titration with hydrochlorid acid. By wet-chemical analysis the sodium mass concentration is usually determined which should be converted into Na_2O_2 or Na_2CO_3 by calculation. The chemical composition of the aerosol must be known and determined from separate samples.

The determination of the weight of filter samples raises problems concerning chemical transformation during balancing. An inert atmosphere should be provided in the balance.

The micro-balance is a well-known aerosol instrument and it is not necessary to explain it here.

Fig. 3 shows the course of the airborne sodium concentration over a range of about 50 hours measured by different methods. There are no extreme deviations. Impinger, filter and SAMM-measurements agree very well. Only the values of the mass balance are higher in nearly all experiments at low concentrations compared to the SAMM-values. This might be caused by chemical conversion of Na_2O_2 particles into Na_2CO_3 due to leakages from outside into the vessel.

The course of sodium mass concentration can be measured with an accuracy of at least $\pm$ 10% during the experiment.

PARTICLE DIAMETER

The situation seems to be worse as regarding the determination of particles diameters.

As can be seen from Table 1, different methods had been used to measure the particle size distribution during and after the fire of FAUNA test 2. The instruments used were the Andersen 8-stage stack sampler, the Stöber centrifuge and a light scattering system. The Andersen sampler as well as the centrifuge are well known instruments in particle sizing which need no further explanation here. The light scattering instrument was the HC 15 particle size analyzer, manufactured by Gertsch. This instrument uses a white light source, focused on the measuring volume. The intensity of the light, scattered in the direction of 90 degrees towards the optical axis, is proportional to the size of the particle.

All instruments were calibrated with Latex-particles. In Table 1 diameters are comparable which were measured at the same time during the course of the experiment. In this and in other FAUNA experiments median diameters D_{ae} measured with impactor and centrifuge agree within an error of about $\pm$ 30%. The volume equivalent diameters D_{ev} were calculated from mass concentration and number concentration. These two diameters are necessary to calculate the dynamic shape factor using the formula

$$\chi = \frac{D_{ev}^2 \cdot C(D_{ev}) \cdot \rho}{D_{ae}^2 \cdot C(D_{ae}) \cdot \rho_o}$$

with

$$\rho_o = 1 \text{ g/cm}^3$$

and with the Cunningham correction C(D), related to the diameter D_{ev} and D_{ae}, written as

$$C = 1 + \frac{12.64}{76 \cdot D} + \frac{4.02}{76 \cdot D} \cdot e^{-0.1095 \cdot 76 \cdot D}$$

These formulas are used to show in Fig. 4 the functional connection between the dynamic shape factor and different values of D_{ae} and D_{ev}. The calculations are made with $\varrho / \varrho_o = 1$, this means that equal particle sizes D_{ev} and D_{ae} lead to $\chi = 1$.

It is obvious that in the region of the steep gradient of χ and for a given diameter D_{ev} the diameter D_{ae} must be measured very precisely to get a satisfactory accuracy of χ

The sensitivity of χ , expressed as the percentage deviation of χ , related to (percentage) errors in the measurement of the diameter D_{ae} for given diameters D_{ev}, is shown in Fig. 5. The dynamic shape factor χ is greatly influenced even by relatively small errors in the diameter D_{ae}. For example, the aerodynamic diameter D_{ae} of a particle with a volume-equivilent diameter D_{ev} of .5 µm is measured 20% too small. This error leads to a dynamic shape factor which is 47% too high. This shows, that the particle diameters must be measured extremely accurate to receive reasonable results for the dynamic shape factor.

CONCLUSIONS

- The sodium aerosol mass concentration in a closed containment during and after a sodium fire can be measured with an accuracy of at least $\pm$ 10%.
- Measurements of the aerodynamic diameter with impactor and centrifuge agree within $\pm$ 30%.
- An error in the measurement of the particle diameter may cause a significantly larger error in the dynamic shape factor.

Time [h]	Mass Concentration [g Na_2O_2/cm^3]	Number Concentration [P/cm^3]	Calculated Diameter $\gamma = 2.805$ [µm]	Measured Diameter [µm]	Method
0.5	$4.58 \cdot 10^{-6}$	$2.8 \cdot 10^{5}$	2.26	2.75	Impactor
2.3	$6.1 \cdot 10^{-6}$	$2.5 \cdot 10^{5}$	2.57	2.05	Centrifuge
"	"	"	"	3.70	Impactor
"	"	"	"	0.52	Light scattering
4.5	$4.29 \cdot 10^{-7}$	$3.0 \cdot 10^{4}$	2.16	1.80	Centrifuge
"	"	"	"	2.08	Impactor
27.0	$3.39 \cdot 10^{-9}$	$3.0 \cdot 10^{3}$	0.93	0.70	Centrifuge

Table 1 Sodium aerosol properties

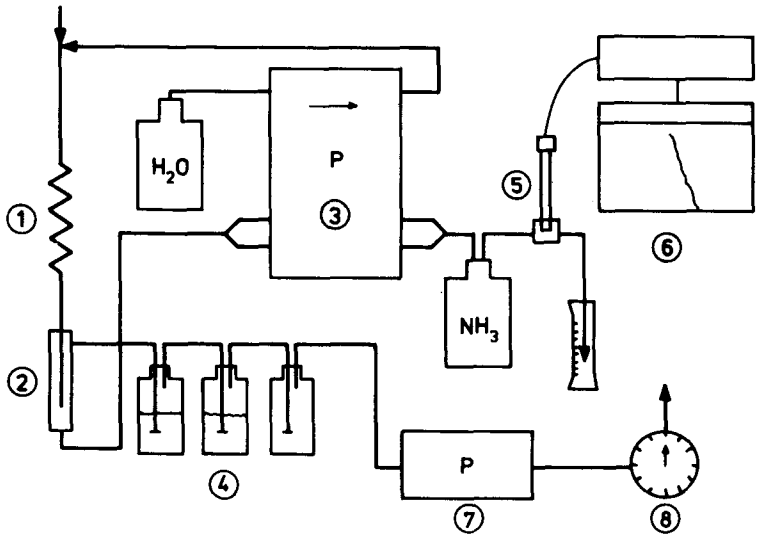

① Mixing cell
② Liquid seperator
③ Fluid pump
④ Impingers
⑤ Sodium Electrode
⑥ pH/mV meter and plotter
⑦ Vacuum pump
⑧ Gas meter

Fig. 1 Components of the sodium aerosol mass meter (SAMM)

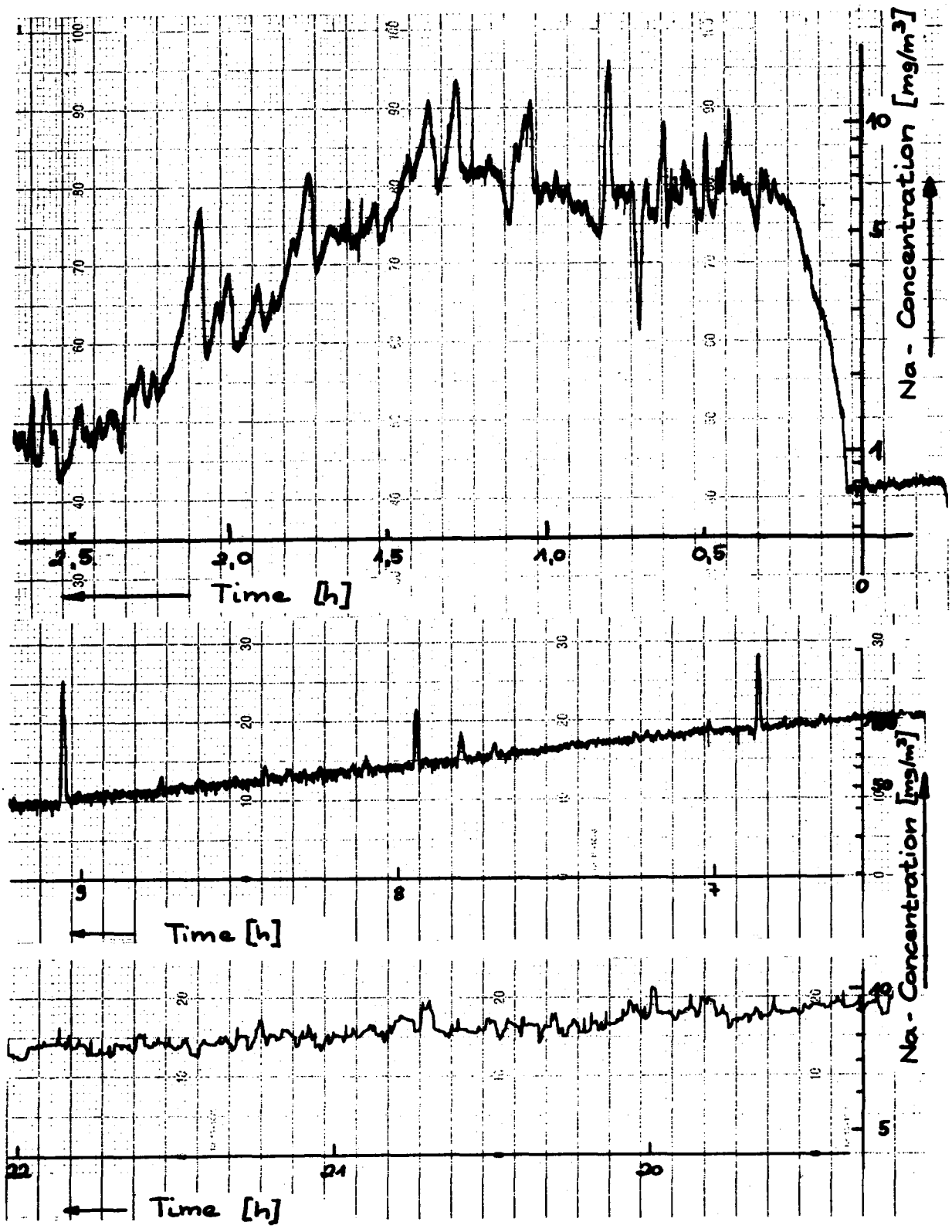

Fig. 2 Output of SAMM using different ranges of sensitivity

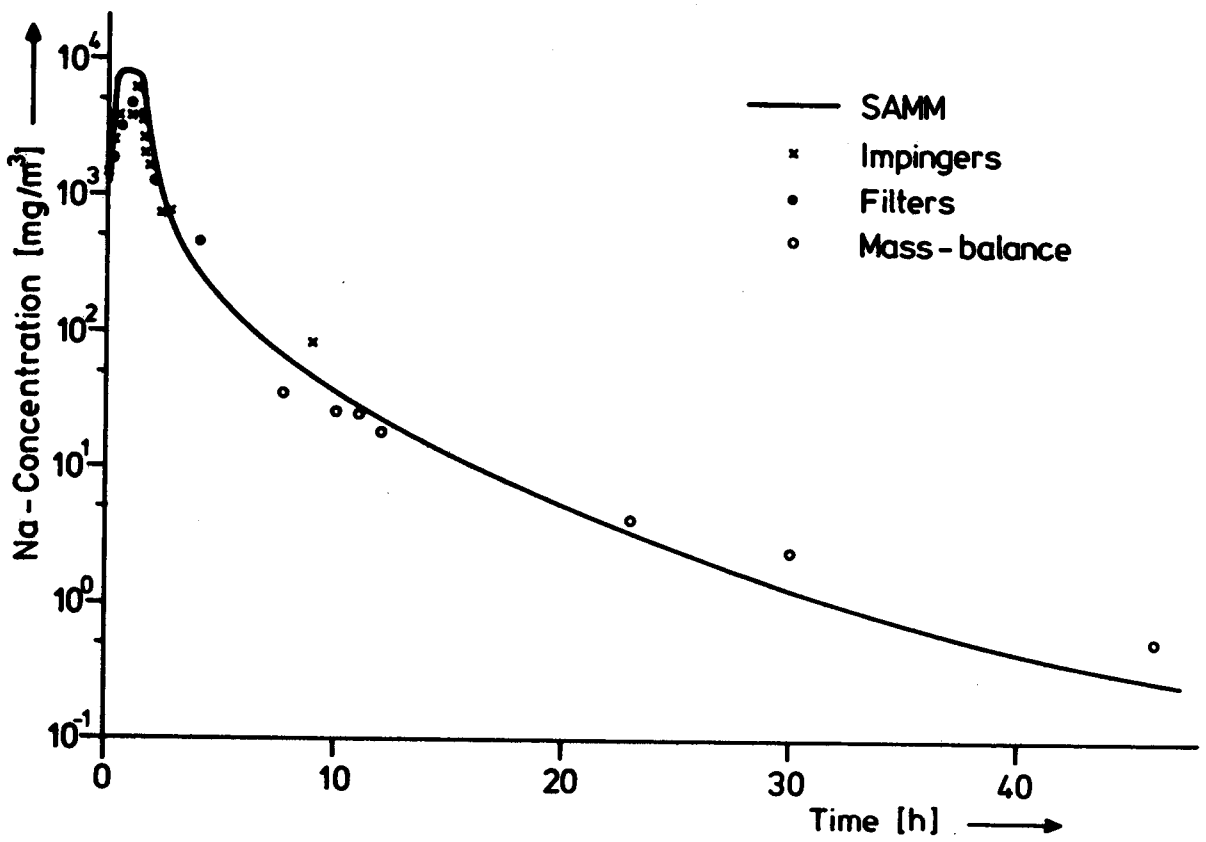

Fig. 3 Airborne sodium concentration measurement using different instruments

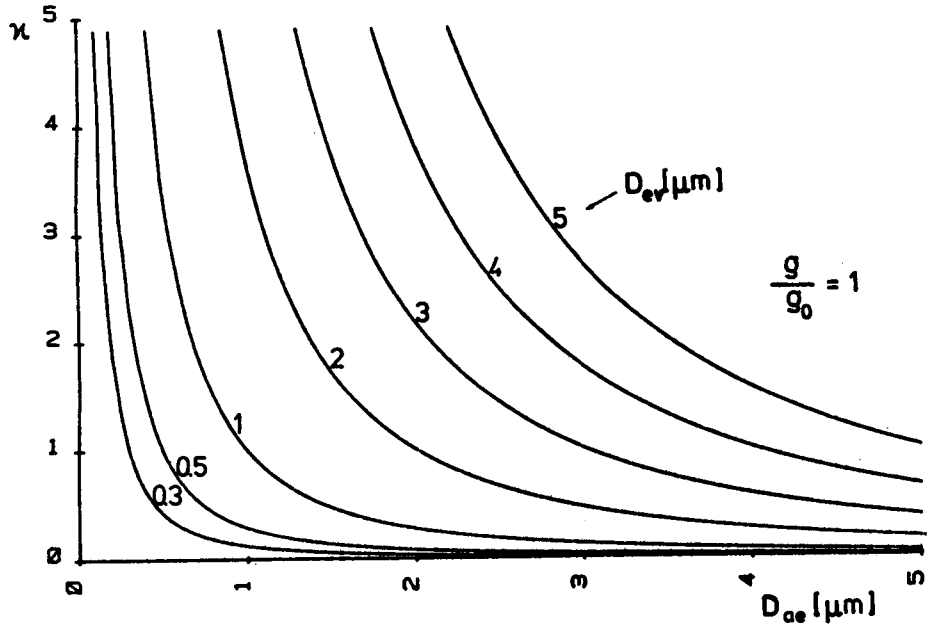

Fig. 4 Calculation of the dynamic shape factor using different diameters

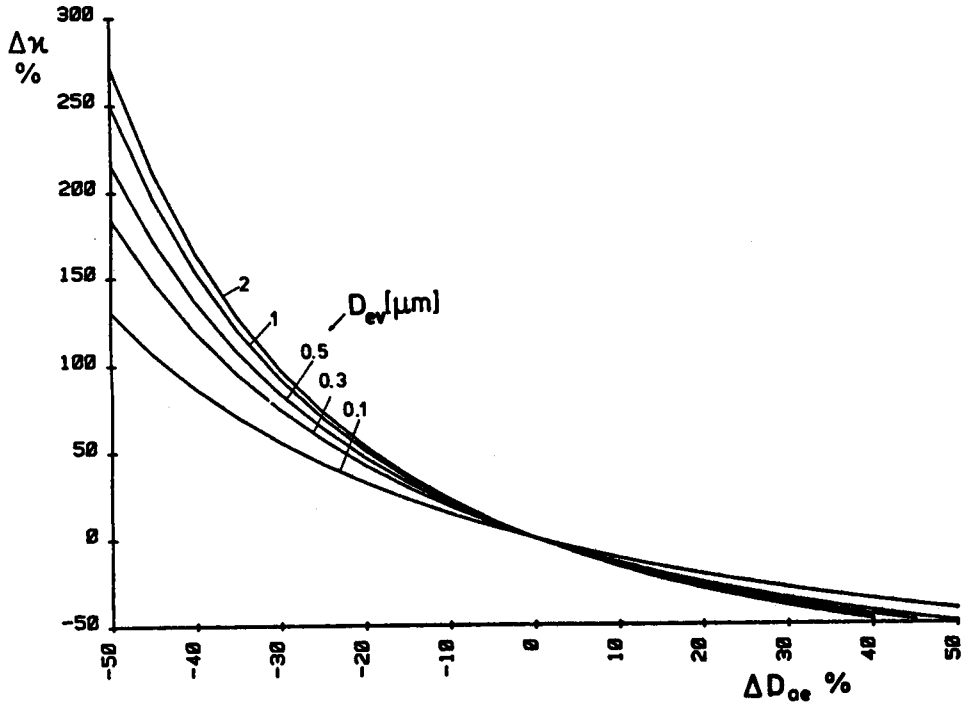

Fig. 5 Sensitivity of the dynamic shape factor χ

MEASURING TECHNIQUES FOR NUCLEAR AEROSOL EXPERIMENTS

Carl T. Nelson and R. P. Johnson
Rockwell International
Canoga Park, California 91304, USA

ABSTRACT

The various sampling techniques which are currently in use at Atomics International Division, Energy Systems Group of Rockwell International, to characterize the aerosols produced from sodium fires and the vaporization of UO_2 are discussed as well as the expected capabilities and accuracy of these techniques under test conditions. By using a variety of sampling techniques in which the aerosol concentration, wall plating, and fallout histories are obtained for each test, a mass balance of the released aerosols can be obtained. Examination of the mass balance will usually indicate the validity and accurancy of the data.

MEASURING TECHNIQUES FOR NUCLEAR AEROSOL EXPERIMENTS

Most of the sampling techniques which exist today measure the particles of the respirable size range in environments of low concentration. The sizing of these particles is obtained by diverse methods or instruments, each of which can be calibrated from aerosols of known size and density. The preferred method of characterizing aerosols under test conditions is to use a variety of techniques which are known to be suitable for the aerosol in question and compare the results. Single measurements are of little value even if sampling techniques and sampling conditions are compatible.

Assuming the boundary conditions used in the theoretical analysis and the sampler design conform reasonably well, the theoretical analyzing technique can predict the sampler characteristics with relatively good accuracy.[1] In addition, the application and accuracy of the various laboratory instruments such as the microscope, X-ray spectrometer, and flame photometer which are used as aids in various analytical measurements are fairly well known and will not be discussed.[2]

The purpose of this paper is to discuss aerosol measurement techniques currently used at Atomics International Division, Energy Systems Group of Rockwell International (AI/ESG), and the expected accuracy of those techniques. The types of aerosols investigated are those which are expected to be produced by hypothetical LMFBR accidents. In such accidents, a combination of aerosols of sodium oxide and fuel materials are produced.

Considerable effort has been directed toward the design, development, and fabrication of sampling devices needed for high-temperature, high-airborne concentration, and high-pressure environments. Efforts to date have included design and fabrication of aerosol samplers: (a) nonclogging fallout deposition samplers (turntables and weighing devices), (b) a manual sampling system for obtaining spot aerosol concentration and impactor samples within the experiment containment at any time throughout the tests, and (c) wall plating deposition samplers for measuring deposition vs time for various heights.

Figure 1 shows the deposits on the floor as a function of time for a typical test as an average fallout measured by a turntable fallout collection device and a linear voltage differential transformer (LVDT) fallout weighing device. Air concentrations were measured by filter techniques at several heights, and the average value at the sampling station is shown vs time. The wall data is the average value from the several wall samplers.

By taking the average value of many samples and obtaining a mass balance of the released aerosol vs time, the sampling techniques described are expected to have few potential errors. By carefully examining the mass balance data, any anomaly due to faulty sampling techniques, instrumentation defects, or analysis inaccuracies are easily detected.

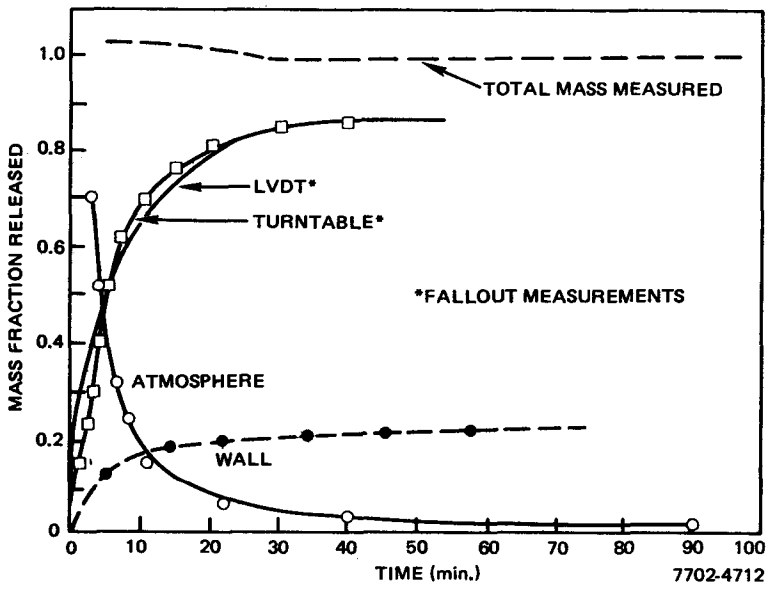

Figure 1. Mass Distribution on Floor or Walls and in Atmosphere vs Time

Impactors used for size classification are frequently subject to errors when sampling in high-concentration aerosols, as both inlet plugging and overloading can occur in a relatively short period. Proper operation of impactors requires that the aerosol stream pass through the stages at a constant flow rate. When sampling for short periods, such as two or three seconds, constant flow rates are difficult to establish. In addition, a large portion of the sampled aerosol may be captured between the impactor stages at termination of the flow. To provide the constant flow of gas, a purge line was added to the impactor, as shown in Figure 2.

During operation, the gas velocity through the impactor was established using the clean purge gas which blocked the aerosol flow (Figure 2a). By use of a valve in the purge gas line, the purge gas can be shut off so that aerosol laden gas enters the impactor (Figure 2b). In this manner, by momentarily closing the purge gas valve the aerosol can be sampled without significant change in gas velocity. In addition, the inlet is swept clean prior to sampling. Although calibration of the impactors was not attempted under these conditions, the accuracy of measurement is expected to be adequate. During each test, several impactor samples were taken to determine particle size history. Reproducibility of the data obtained under these circumstances suggests that the correct sampling techniques were used.

In the tests where UO_2 aerosol was produced by an arc-melt furnace, the air elutriation method was selected to measure particle size distribution. Air elutriation is the process by which a gas stream of constant velocity carries aerosol particles slowly through a narrow channel in which fallout

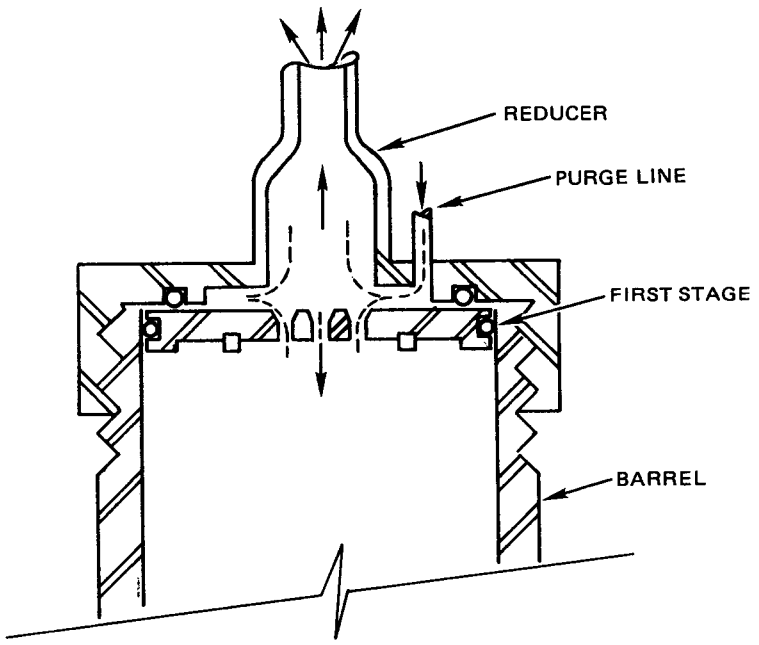

a. With Purge Flow — Aerosol Blocked

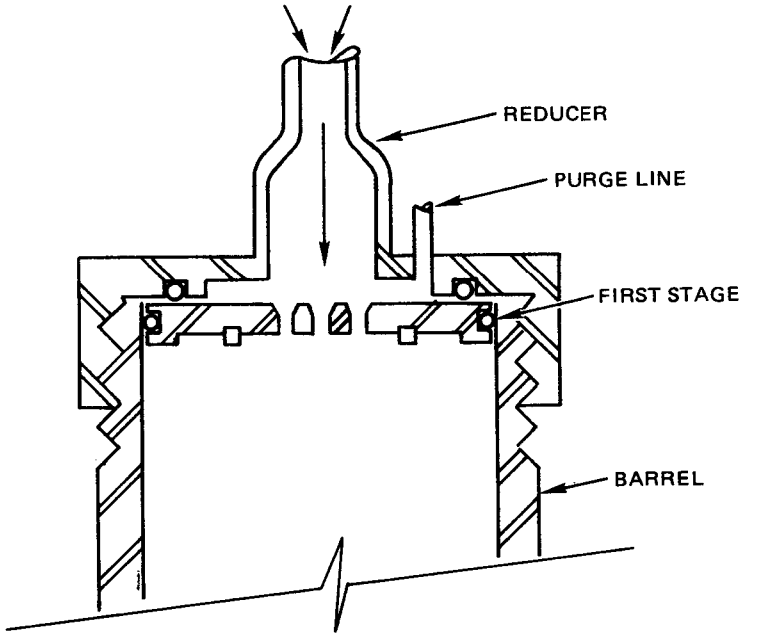

b. No Purge Flow

Figure 2. Modified Impactor

particles are collected.[3] [4] The heavier particles fall out closer to the entrance, while the smaller particles are carried downstream, as shown in Figure 3.

The elutriator has the advantage of separating the airborne particles from the cloud while the particles are in the original state of dispersion. By proper selection of the flow channel design and flow rate, the desired cutoff diameter can be chosen, e.g., the elutriator can be designed as a first-stage collector in which the unrespirable particles are removed. The respirable size particles which pass through the elutriator can be collected by an impactor and filter downstream.

A plot of the reciprocal diameter as a function of distance along the elutriator for molybdenum disulfide particles is presented in Figure 4. A density of 1.15 is assumed. When the mass distribution is required, the relative amounts of fallout collected along the channel are measured.

The elutriator has not been compared with other instruments in the environment produced by the arc melter. To determine the cutoff diameters for the various size particles collected in the elutriator, the particles were examined for size with a microscope. However, the use of a microscope can produce errors, especially for nonspherical particles, since the projected area diameter may vary from the average diameter.

In elutriation sampling at large flow rates, reentrainment occurs. By reducing the flow rate, the problem is minimized. Other uncertainties exist, but usually these can also be minimized by proper design and application so that the data obtained are within the desired limits of accuracy for code validation.

REFERENCES

1. Lippmann, M., "Respirable Dust Sampling," American Industrial Hygiene Association Journal 31, 138-159, (1970).

2. Malizza, H., Analysis of Airborne Particles by Physical Methods, CRC Press, Inc., Florida (1978).

3. Mercer, T. T., Aerosol Technology in Hazard Evaluation, Academic Press, New York and London (1973).

4. Particle Size Analysis in Estimating the Significance of Airborne Contamination, Technical Report Series No. 179, Chapter 4, International Atomic Energy Agency, Vienna (1978).

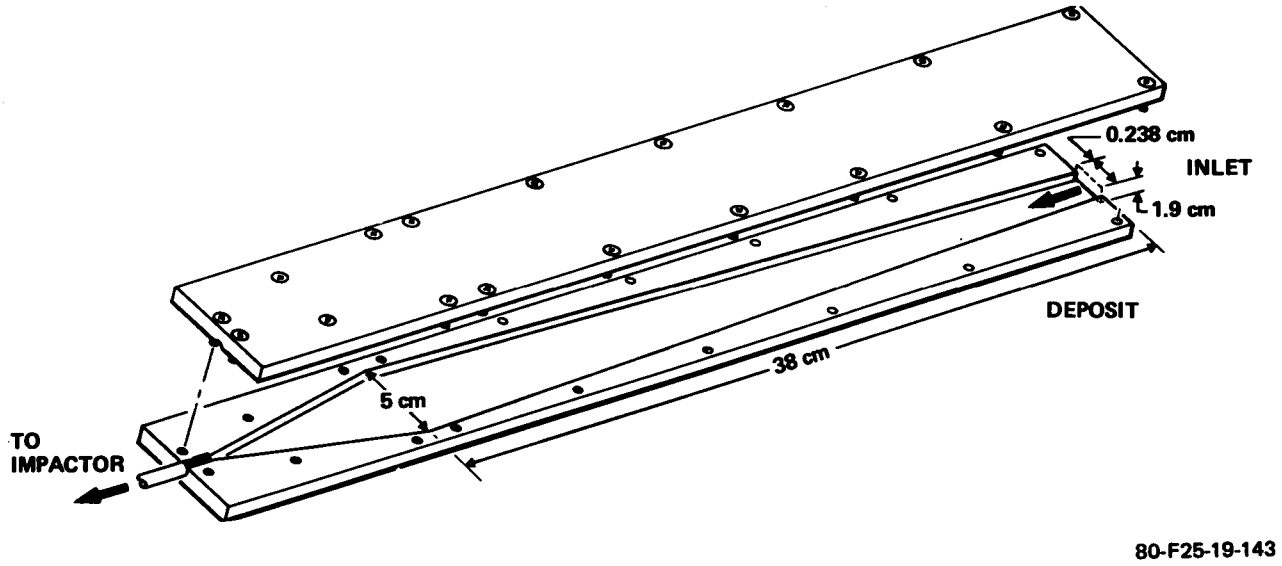

Figure 3. Elutriator

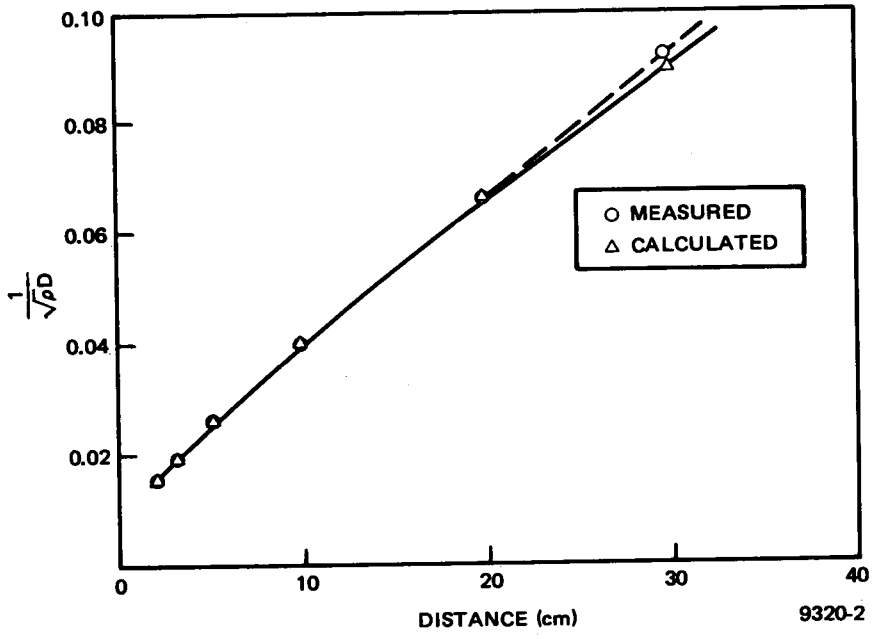

Figure 4. Recipical Aerodynamic Diameter As a Function of Distance Along the Elutriator

EXPERIMENTAL TECHNIQUES FOR THE CHARACTERIZATION OF NUCLEAR AEROSOLS*

G. W. Parker
Oak Ridge National Laboratory
P.O. Box X
Oak Ridge, Tennessee

To be published in Proceedings of CSNI Specialist Meeting on Nuclear Aerosols in Reactor Safety, held in Gatlinburg, Tennessee, April 15-17, 1980

---

*Research sponsored by Office of Nuclear Regulatory Research, U.S. Nuclear Regulatory Commission under Interagency Agreements 44-551-75 and 40-552-75 with the U.S. Department of Energy under contract W-7405-eng-26 with the Union Carbide Corporation.

EXPERIMENTAL TECHNIQUES FOR THE CHARACTERIZATION OF NUCLEAR AEROSOLS*

G. W. Parker
Oak Ridge National Laboratory
Oak Ridge, Tennessee

ABSTRACT

Nuclear reactor fuel aerosols differ in many respects from environmental aerosols, and the differences limit the applicability of many measurement techniques which have been developed for atmospheric aerosol characterizations.

Direct application of the various inertial multistage cascade impactors provides the simplest approach to aerosol size determination; however, the accuracy of these measurements can deviate by 50%. The best measurements for this type of aerosol are now being made with the long-duct (Stöber) spiral aerosol centrifuge, primarily because of its freedom from chain-agglomerate fragmentation problems and its ease of precise calibration. Particle diameters obtained by this method usually exceed those from the impactors; they are supported in credibility by much lower standard deviation values and a better agreement with settling diameters. Reproducibility with the centrifuge is unequalled by any other technique, and an accuracy of 5% can be achieved if care is exercised to obtain the highest resolution.

---

*Research sponsored by Office of Nuclear Regulatory Research, U.S. Nuclear Regulatory Commission under Interagency Agreements 44-551-75 and 40-552-75 with the U.S. Department of Energy under contract W-7405-eng-26 with the Union Carbide Corporation.

I. INTRODUCTION

The behavior of vaporized mixed-oxide fuel aerosols postulated to result from fast reactor core-disruptive accidents is intensely evaluated in fast reactor safety analysis, containment design, and site-selection licensing procedure.

In this program, several uranium oxide aerosols produced by vapor condensation of the superheated uranium oxides have been produced by various methods and have been intercompared with respect to particle morphology, number concentration, deposition behavior, surface area, oxygen content, and diffusion, sedimentation, and agglomeration rates. Within a relatively narrow range, the agglomerated aggregate particles are almost identical when examined for initial shape, size distribution, and effective density. However, primary particles in those aerosols produced by the most rapid heating methods, followed by nearly instantaneous cooling, are smaller and generally spherical. Those produced by slower processes in combination with delayed cooling give rise to a large proportion of crystalline particles which result in more tightly bound agglomerates. Deposition behavior of the chain agglomerates is not significantly affected by this difference.

Sodium peroxide and mixed oxide aerosols show similar deposition rates, but the sodium appears to form tight-cluster aggregates instead of chains.

II. EQUIPMENT AND FACILITY DESIGN

The Containment Research Installation (CRI-II) is a 4.52-m^3 stainless steel vessel with cylindrical walls, a dished flanged head, and a conical botton (Fig. 1). It was originally designed, constructed, and operated in the 1960s for use in safety studies of the Light-Water Reactor type in support of the National Reactor Testing Station--loss-of fluid test (NRTS-LOFT) program and was reactivated in 1974 by the Nuclear Regulatory Commission for the liquid-metal fast breeder reactor--reactor safety research (LMFBR-RSR) program. It is housed in a semi-enclosed, specially shielded and ventilated area in the radiochemical hot laboratory at Oak Ridge National Laboratory (ORNL). It is presently equipped with three unique fuel aerosol generators designed for attaining high concentrations of UO_2, U_3O_8, or Na_2O_x mixed aerosols. One of the UO_2 generators, a 100-kW dc electric arc, cold-hearth furnace in which molten UO_2 is literally boiled off as vapor, is capable of vaporizing about 50 g of UO_2 per minute. The second generator employs a 40-kW dc plasma arc to ignite a mixture of powdered uranium metal and oxygen and produces even higher concentrations of vapor-condensation U_3O_8. The sodium aerosol is produced by burning a finely divided spray of hot liquid metal in the third generator. Concentrations of dry Na_2O_2 aerosol of up to about 50 g/m^3 have been routinely produced. Higher concentrations of Na_2O_2 aerosol are more difficult to prepare since the increased combustion heat contributes to an enhanced thermophoretic wall deposition. Simultaneous operation of both a uranium oxide generator and the sodium spray burner is normally the preferred procedure for preparing a mixed oxide. A short alternate delay of either generator would probably yield a somewhat different aggregate particle.

where

M = mass of an agglomerate (μg)

C = aerosol concentration ($\mu g/cm^3$)

N = nuclei count/cm^3;

and

$$P_n = \frac{6M}{\pi d^3 \rho}$$

where

P_n = number of primary particles/agglomerate

d = diameter of primary particle (cm)

ρ = density of primary particle (g/cm^3).

An example is given in Table V, in which the calculation has been made for a typical run with each of the present aerosols. Using the full-oxide bulk density (10.9 for UO_2) and (8.3 for U_3O_3), values of more than 10,000 particles per agglomerate are calculated for the CDV aerosol (Fig. 20a) about 450 for the arc-furnace aerosol (Fig. 20b) and 250 to 600 for the plasma torch aerosol. Transmission electron microscope (TEM) photomicrographs and individual optical counting with a size comparator agree with these calculations. For the plasma torch aerosol, a typical photograph of agglomerates (Fig. 20c) shows many aggregates with this approximate number of primary particles.

Photomicrographic Morphology of Mixed-Oxide Aerosols

Several earlier attempts to photograph primary particles of sodium peroxide on microscope grids generally gave unsatisfactory results, because atmospheric moisture destroyed the original features of the spherical sodium compound aggregates. Since introducing the concept of first depositing a protective organic polymer coating over the particles before collecting on grids, we have been able to produce relatively well defined particle photographs by both the scanning electron microscope (SEM) and TEM techniques. Figure 21 shows typical TEM photographs at different magnifications. Small chain-like aggregates are U_3O_8, and the large popcorn-ball-like spheres are sodium peroxide. They appear to be coagglomerated as is indicated by the constant symmetrical size distributions in Fig. 15. In the larger magnifications the sodium seems to encapsulate large numbers of U_3O_8 primary particles.

VI. SUMMARY AND CONCLUSIONS

A variety of characterization techniques are necessary to obtain an adequate description of closed-vessel nuclear aerosol morphology and

deposition behavior. The controlling characteristic, that which limits the settling rate, is the aerodynamic particle size, and this determination is of special importance. Composition of the aggregate particles can be almost completely established by combining electron microphotography, chemical analysis, number count, and aerodynamic size.

Size distribution measurements on concentrated aerosols, ≤ 50 g/m^3, have been performed on both uranium oxide (UO_2 and U_3O_8) chain agglomerates and on spray-fired sodium oxide (Na_2O_2) cluster aggregates, and on mixtures generated simultaneously. In general, the aggregate size distributions measured during most of the duration of the deposition (settling and plateout) period indicate that at the same aerosol mass concentration, almost the same aerodynamic size distribution will be observed for each over a self-preserving size interval; the settling rate of all such aerosols is essentially the same.

Reproducibility (within a few percent) by the Stöber centrifuge is always better than by the impactors. A calibration check for the centrifuge, before and after a measurement using monodisperse latex microspheres and requiring only about 30 min, will apparently guarantee an accuracy of about 5% in aerodynamic diameter. The full range of size distributions using several impactors will approach 30%.

VII. REFERENCES

1. Schikarski, W., The Karlsruhe Research Program on Nuclear Aerosol and Its Relation to the Plutonium Hazard of Fast Sodium Reactors, KFK-798 (July 1968).
2. Parker, G. W., Buchholz, H., and Martin, W. J., "Radioactive Aerosol Size Classification Experience with a Low Pressure Cascade Impactor," Proceedings of the Tenth AEC Air Cleaning Conference, Aug. 28, 1968, pp. 263-311, CONF-680821.
3. Stöber, W., "Design, Performance, and Application of Spiral Duct Aerosol Centrifuges," in Fine Particles, B. Y. Liu, ed., pp. 351-397, Academic Press, New York, 1976.
4. Tillery, M., "Aerosol Centrifuges," in Aerosol Measurement, D. A. Lundgren et al., eds., pp. 3-28, University Presses of Florida, Gainesville (1979).
5. Talley, D., Raabe, O. G., and Mewhinney, J. A., "Lovelace Aerosol Particle Separator Design Modifications," in Aerosol Measurement, D. A. Lundgren et al., eds., pp. 29-35, University Presses of Florida, Gainesville (1979).
6. Moss, O. R., Ettinger, H. J., Coulter, J. R., "Aerosol Density Measurements Using a Modified Spiral Centrifuge Aerosol Spectrometer," Environ. Sci. Technol., Vol., 6, p. 614 (1972).
7. Moss, O. R., "Comments on Centrifuges," in Aerosol Measurement, D. A. Lundgren et al., eds., pp. 24-28, University Presses of Florida, Gainesville, (1979).

Table I. Calibration data for inertial impactors

Stage No.	Cutoff diameters (D_{50} μm) Andersen Mk-II (8 ℓ/min)	Andersen Mk-III (8 ℓ/min)	Sierra-2110 (7 ℓ/min)	Low pressure (8 ℓ/min)
1	10.7	17.1	18	
2	6.8	11.0	11	
3	4.7	7.5	4.4	1.2
4	3.3	5.0	2.65	0.5
5	2.1	3.2	1.7	0.2
6	1.1	1.6	0.95	0.05
7	0.7	1.0	0.53	
8	0.4	0.7		

Table II. Size measurement of U_3O_8 for Run PT-31

Sizing instrument	Time (min)	Graphic values D_{50} (μm)	Graphic values GSD[a] (σ)	Calculated values D_{50} (μm)	Calculated values GSD[a] (σ)
Andersen Mk-III and preseparator	24	2.72	1.6	2.62	1.6
Andersen Mk-II and preseparator	29	3.32	1.7	3.02	1.7
Spiral centrifuge, 3000 rpm	73	2.92	1.4	2.97	1.4
Andersen Mk-III, no preseparator	87	2.72	1.5	2.71	1.5
Andersen Mk-II, no preseparator	92	3.16	1.7	3.04	1.6
Spiral centrifuge, 3000 rpm	111	2.94	1.4	2.85	1.4
Spiral centrifuge, 3000 rpm	161	2.92	1.4	2.87	1.4
Andersen Mk-III, no preseparator	265	2.27	1.5	2.22	1.5
Andersen Mk-II, no preseparator	268	2.66	1.5	2.58	1.5

[a]Geometric standard deviation.

Table III. Size distribution measurements for mixed oxide Run PT-28

Instrument	Time (min)	Uranium D_{50} (μm)	Uranium GSD[a] (σ)	Sodium D_{50} (μm)	Sodium GSD[a] (σ)
Spiral centrifuge, 3000 rpm	19	5.10	1.52	4.21	1.60
Impactor No. 1, new stages[b]	22	3.43	1.84	3.86	2.27
Impactor No. 2, new stages	61	3.46	1.82	3.86	2.20
Impactor No. 3, old stages	107	3.07	1.69	3.02	1.84
Spiral centrifuge, 3000 rpm	203	4.81	1.46	3.83	1.53
Impactor No. 4, new stages	231	3.46	1.82	3.54	2.08
Spiral centrifuge, 3000 rpm	256	4.40	1.46	3.42	1.53
Impactor No. 5, old stages	287	2.63	1.66	2.56	1.86
Impactor No. 8, old stages	352	2.70	1.70	2.90	1.86

[a]Geometric standard deviation.

[b]Andersen Mark-II impactor.

Table IV. Mixed-oxide aerosol size measurements for Run PT-33

Instrument	Time (min)	volume (ℓ)	Diameter[a] Sodium (μm)	Diameter[a] Uranium (μm)	Standard deviations[a] Sodium (σ)	Standard deviations[a] Uranium (σ)
Centrifuge, 3000 rpm	10	2	2.64	2.46	1.84	1.6
Andersen impactor[b]	16	7.99	3.19	2.8	2.2	1.97
Centrifuge, 2000 rpm	36	3.98	2.66	2.51	1.66	1.63
Andersen impactor	67	23.81	2.64	2.83	2.01	1.92
Centrifuge, 3000 rpm	89	14.8	2.46	2.41	1.57	1.52
Andersen impactor	137	78.56	2.8	2.59	1.95	1.93
Centrifuge, 2000 rpm	166	21.71	2.46	2.46	1.54	1.54
Centrifuge, 3000 rpm	253	28.7	2.2	2.2	1.43	1.43
Centrifuge, 2000 rpm	346	28.4	2.36	2.27	1.43	1.49
Andersen impactor	361	263.3	2.53	2.46	1.8	1.75

[a]Determined by graphing.

[b]Andersen Mark-II impactor.

Table V. Number of primary particles per agglomerate

Time (min)	Type of aerosol: Capacitor discharge UO_2 CDV-16	Plasma torch U_3O_8 PT-20	Arc furnace UO_2 AF-10
20	6,600	1,882	280
40	12,400	3,103	440
60	10,300	3,311	500
80	9,200	3,065	530
100	8,900	2,671	550
150		1,774	580
200		1,292	510
250		1,064	570
300		957	510

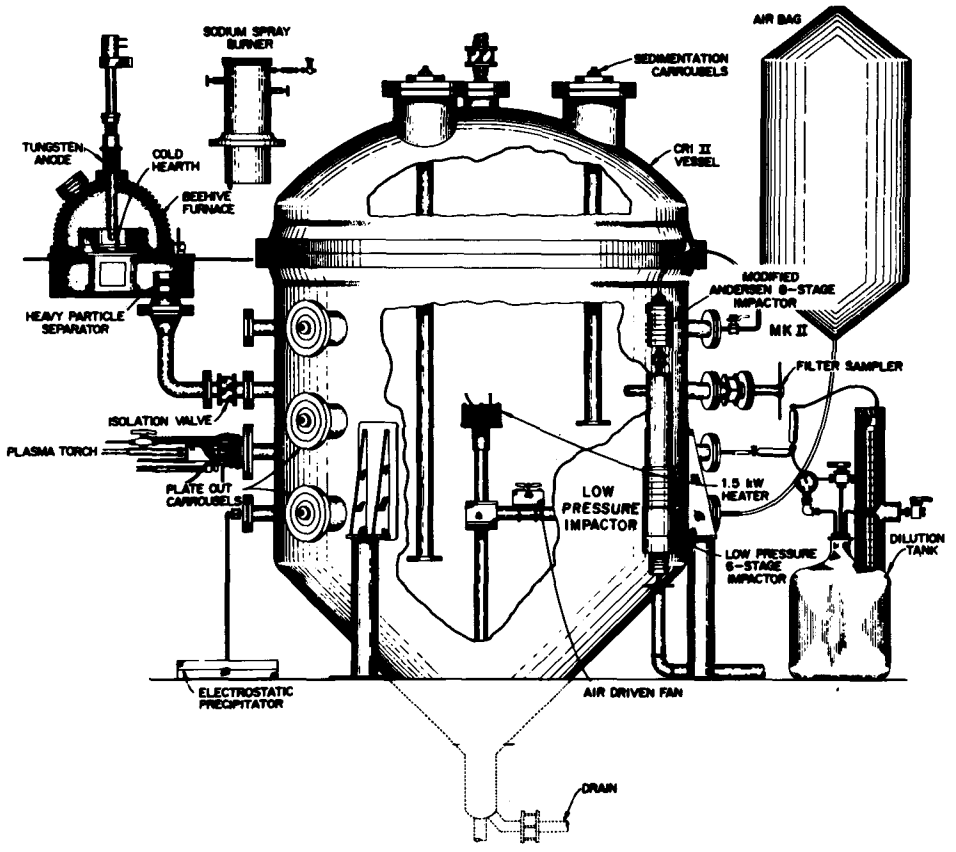

Fig. 1. Schematic of containment aerosol test vessel (CRI-II) with generators and instrumentation.

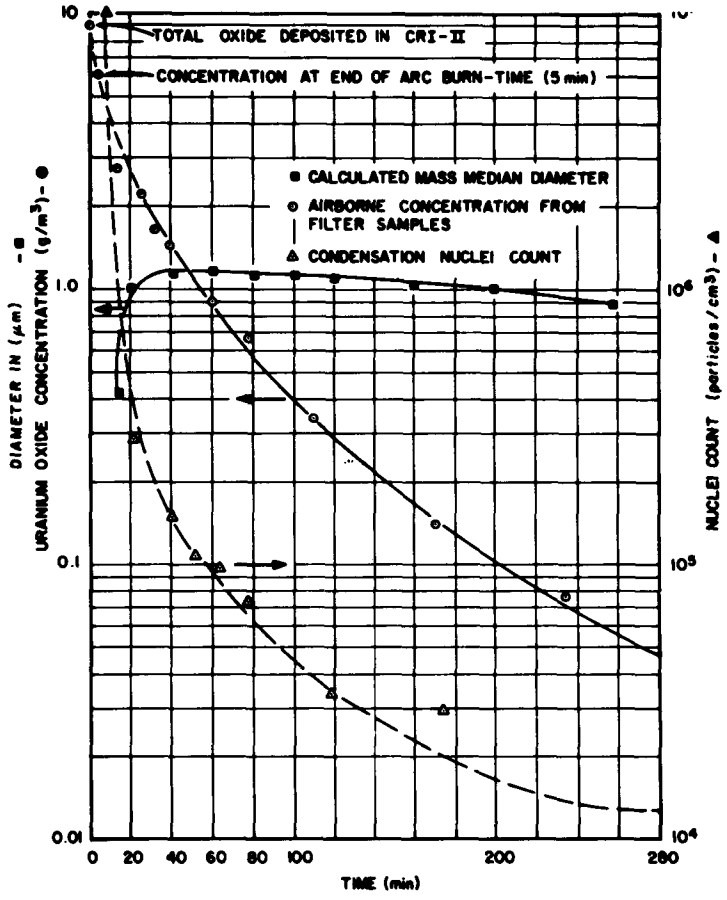

Fig. 2. Airborne arc-furnace aerosol (UO_2) deposition and particle count data.

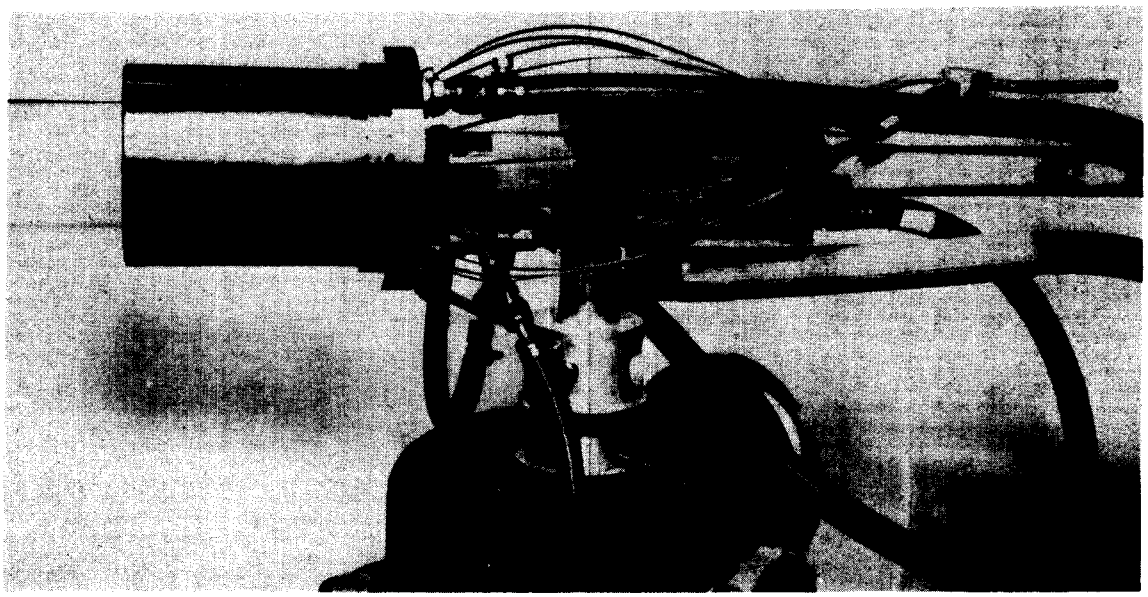

Fig. 3. Metal-oxygen plasma torch U_3O_8 aerosol generator.

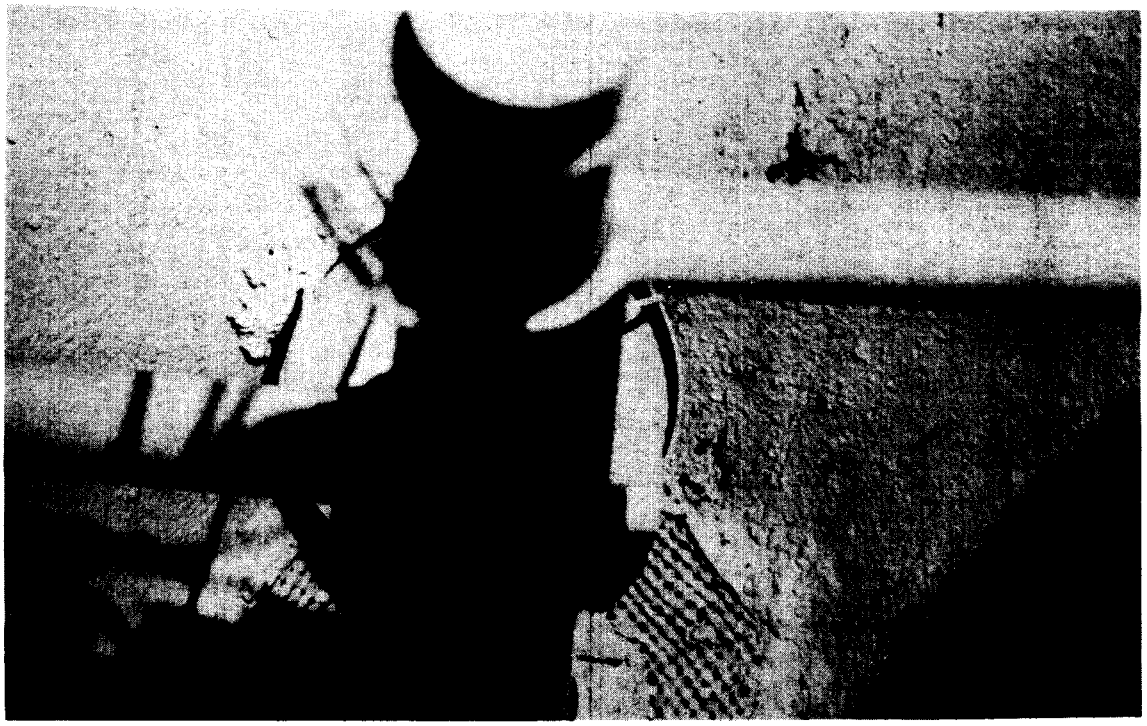

Fig. 4. View into CRI-II vessel after sodium-aerosol spray test.

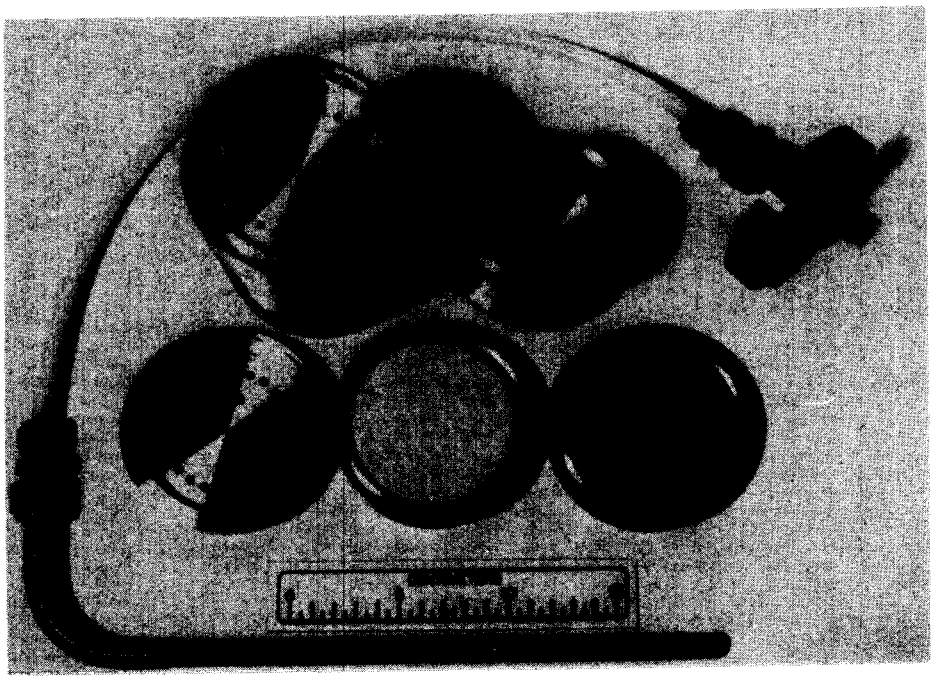

Fig. 5. Andersen Mark-II impactor (modified) with preseparator and sample probe.

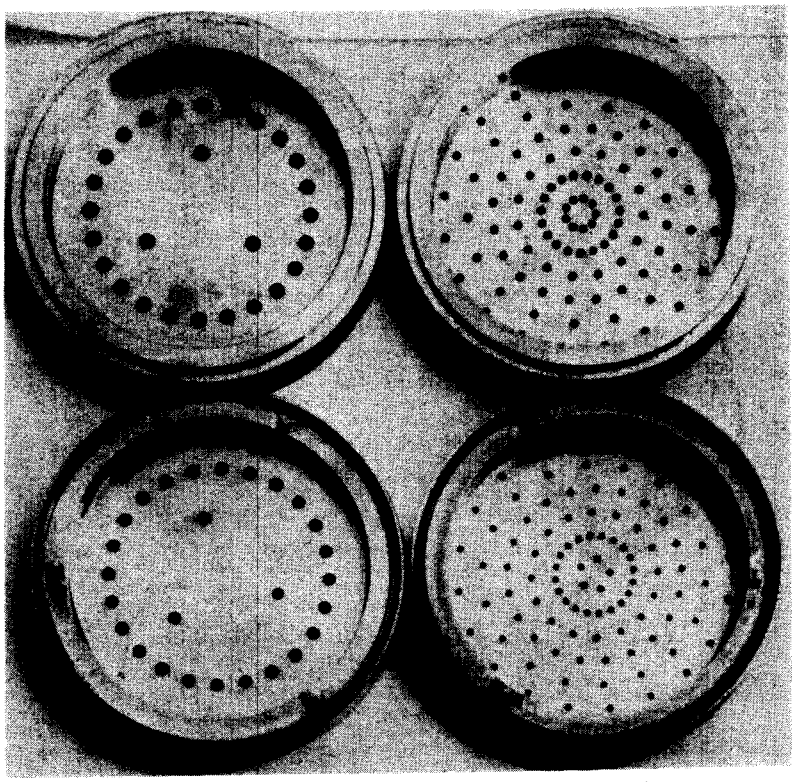

Fig. 6. Andersen Mark-II first and second stages; old and new design.

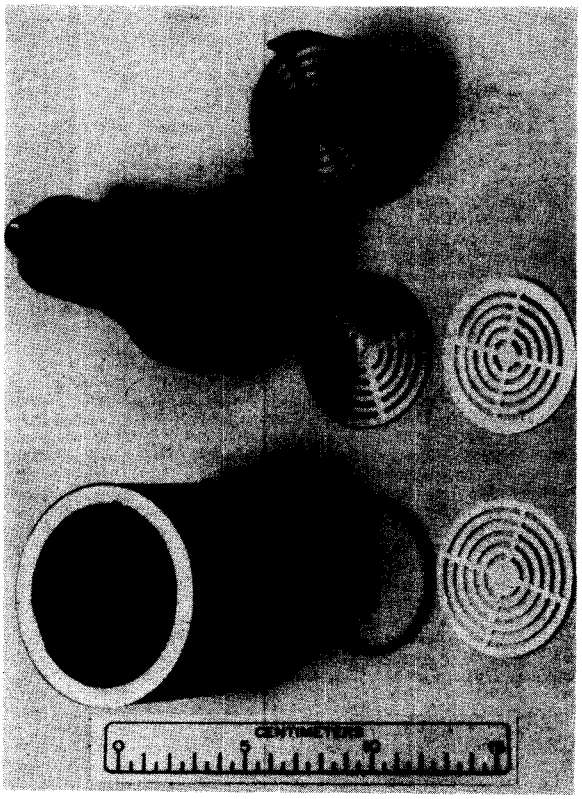

Fig. 7. Andersen Mark-III impactor (stack sampler) and fiberglass collector inserts.

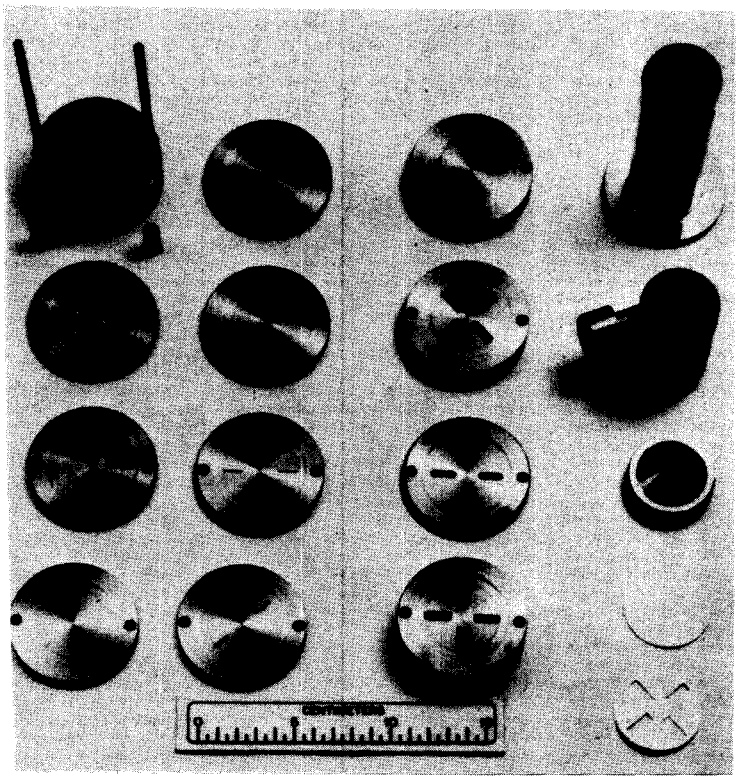

Fig. 8. Sierra rectangular slit impactor (Model 2110) and fiberglass collector inserts.

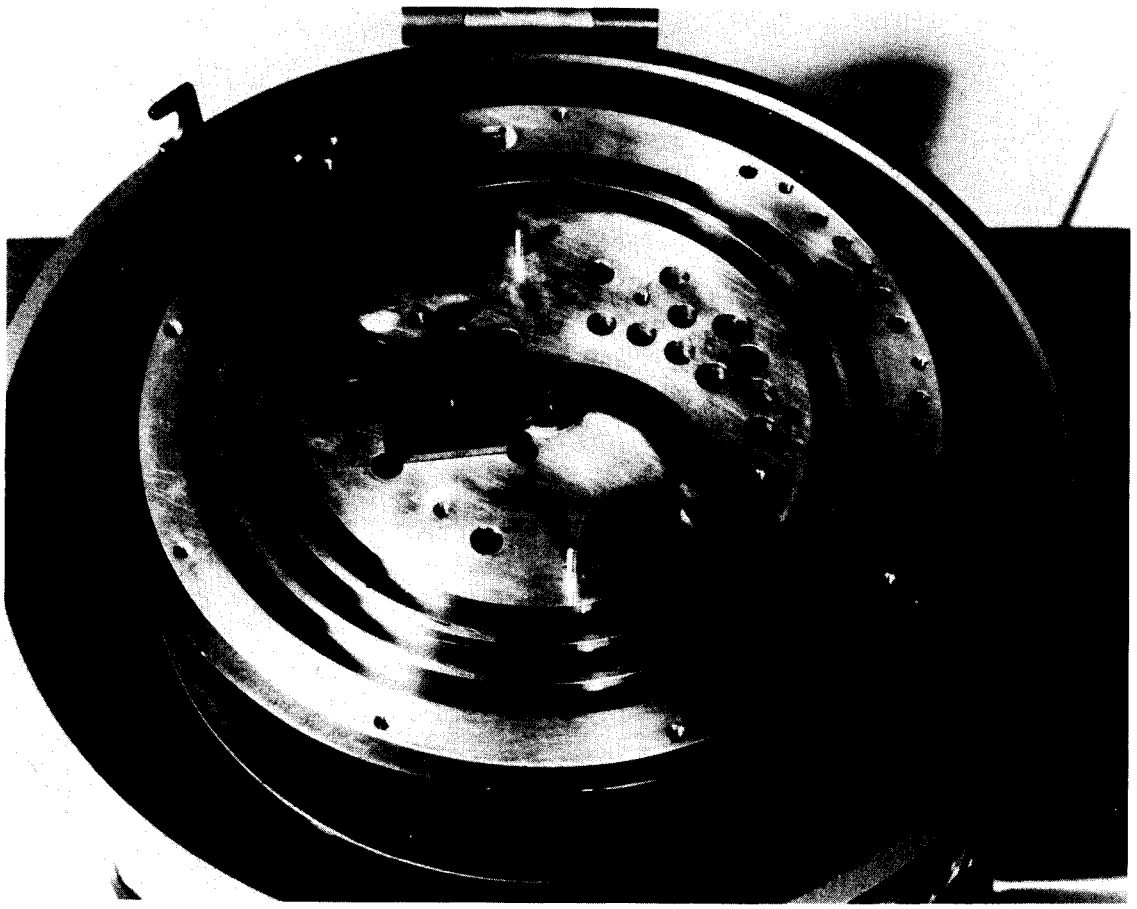

Fig. 9. LASL-Stöber long-duct spiral centrifuge rotor and inlet fixtures.

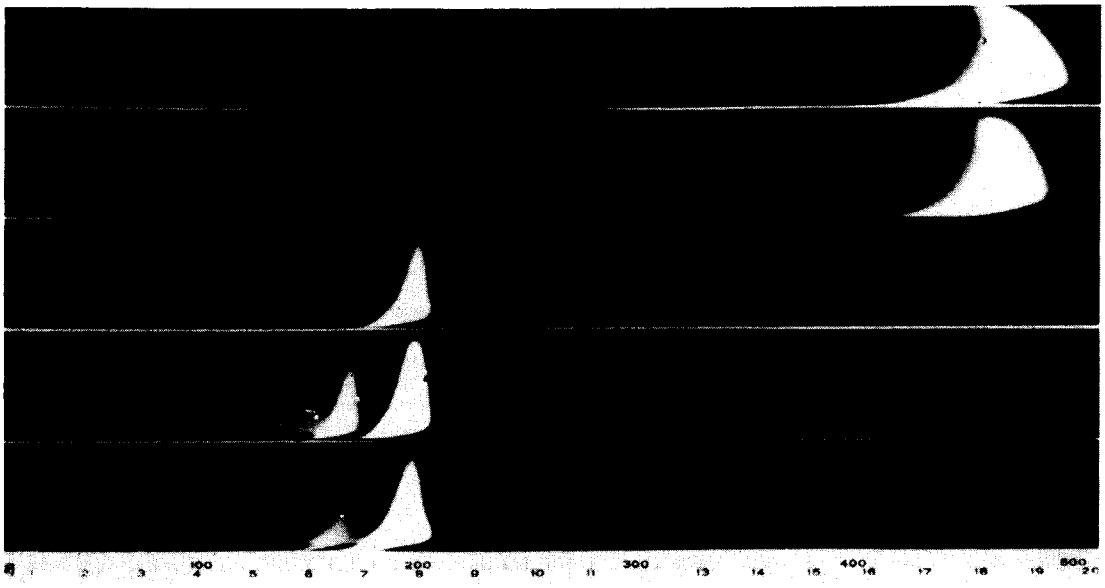

Fig. 10. First polystyrene latex (PSL) calibration foils for 0.5 and 1.1 PSL microspheres with TEM grids in place.

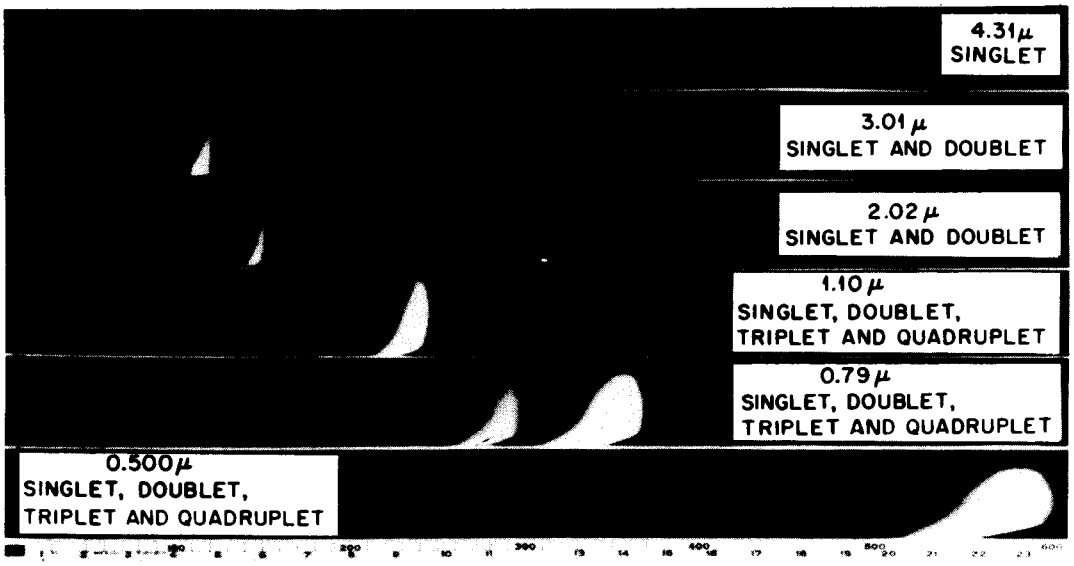

Fig. 11. Photograph of deposits of PSL microspheres on collector strips used in recalibration of LASL-Stöber centrifuge.

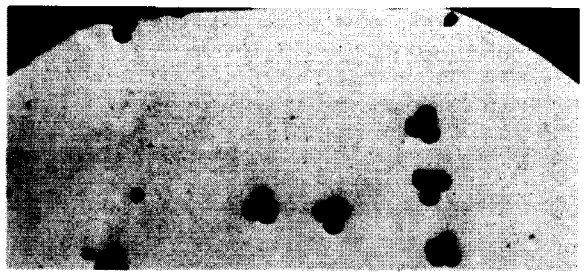

CLUSTER QUADRUPLETS

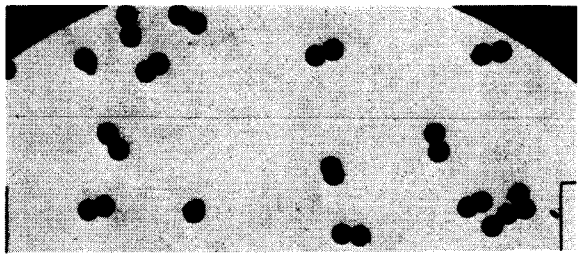

DOUBLETS

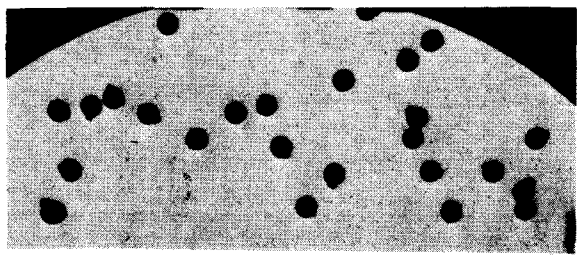

SINGLETS

Fig. 12. Typical TEM photographs of 0.5-μm centrifuge-separated singlet and cluster microspheres.

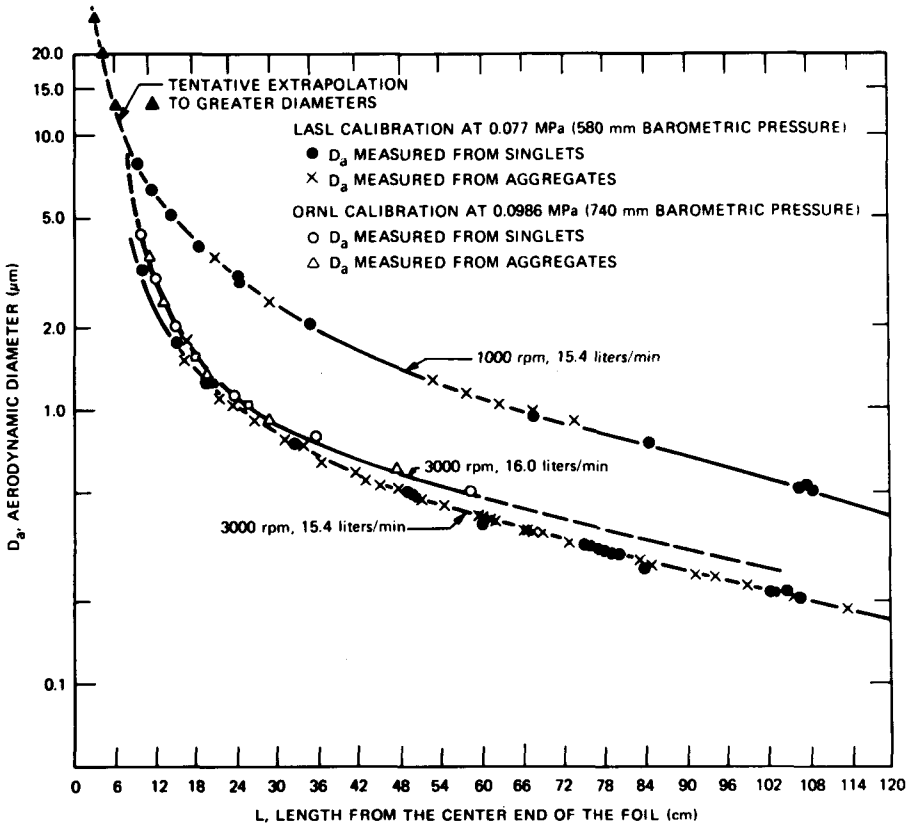

Fig. 13. Comparison of original LASL calibration curves at low atmospheric pressure and ORNL calibration at higher pressure.

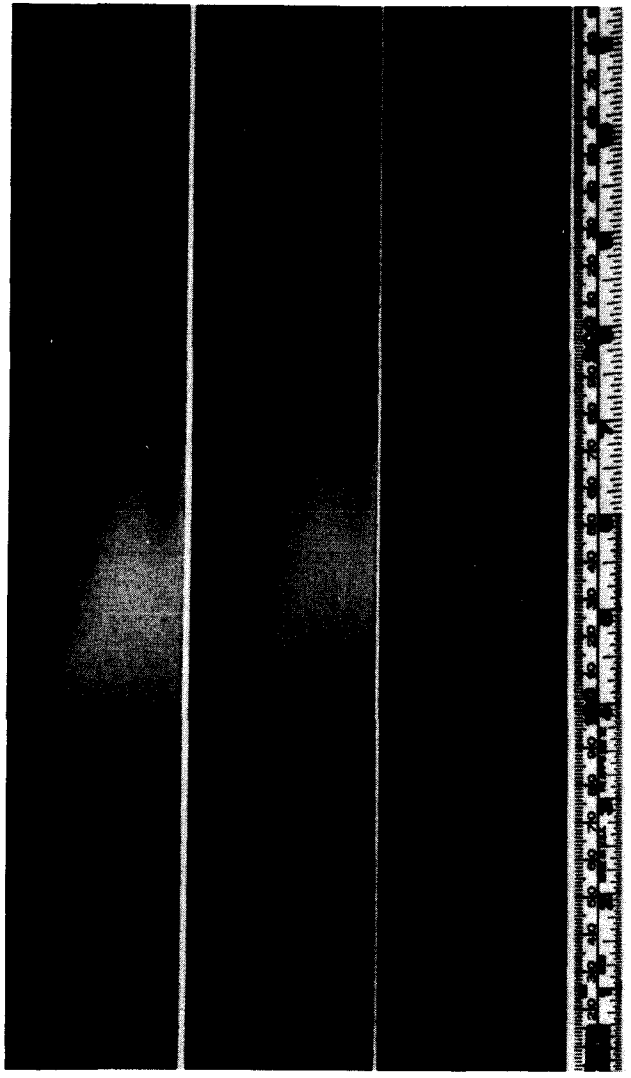

Fig. 14. Appearance of centrifuge collector foils for mixed-oxide run 28 at different time intervals.

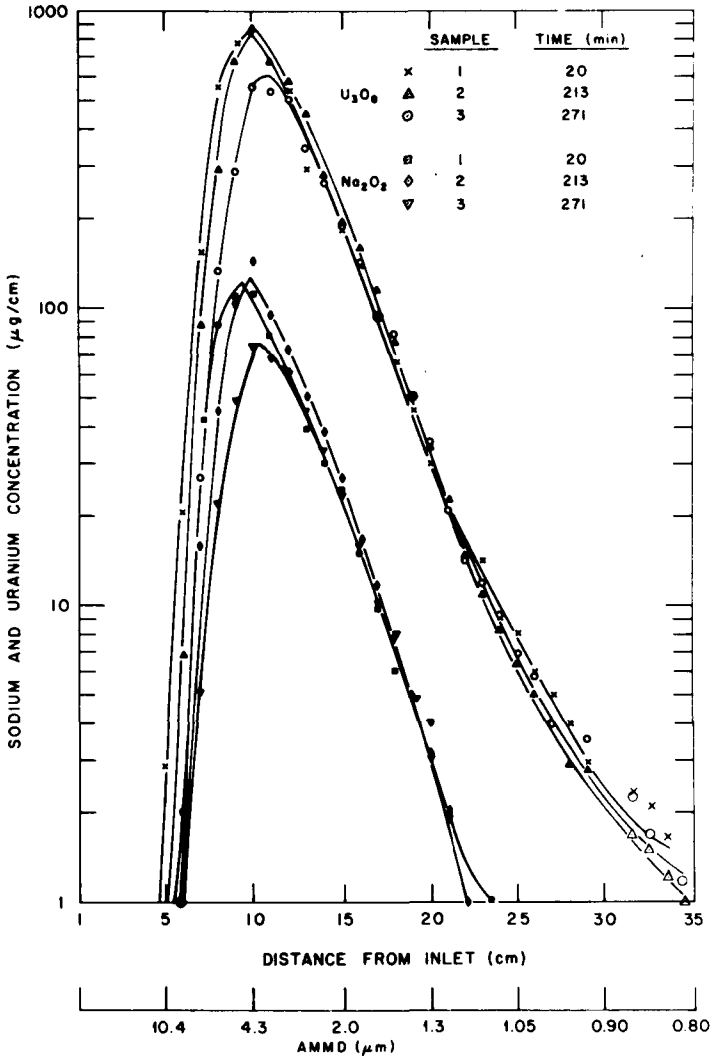

Fig. 15. Spiral centrifuge data for uranium and sodium concentrations and size distributions for mixed-oxide run 28.

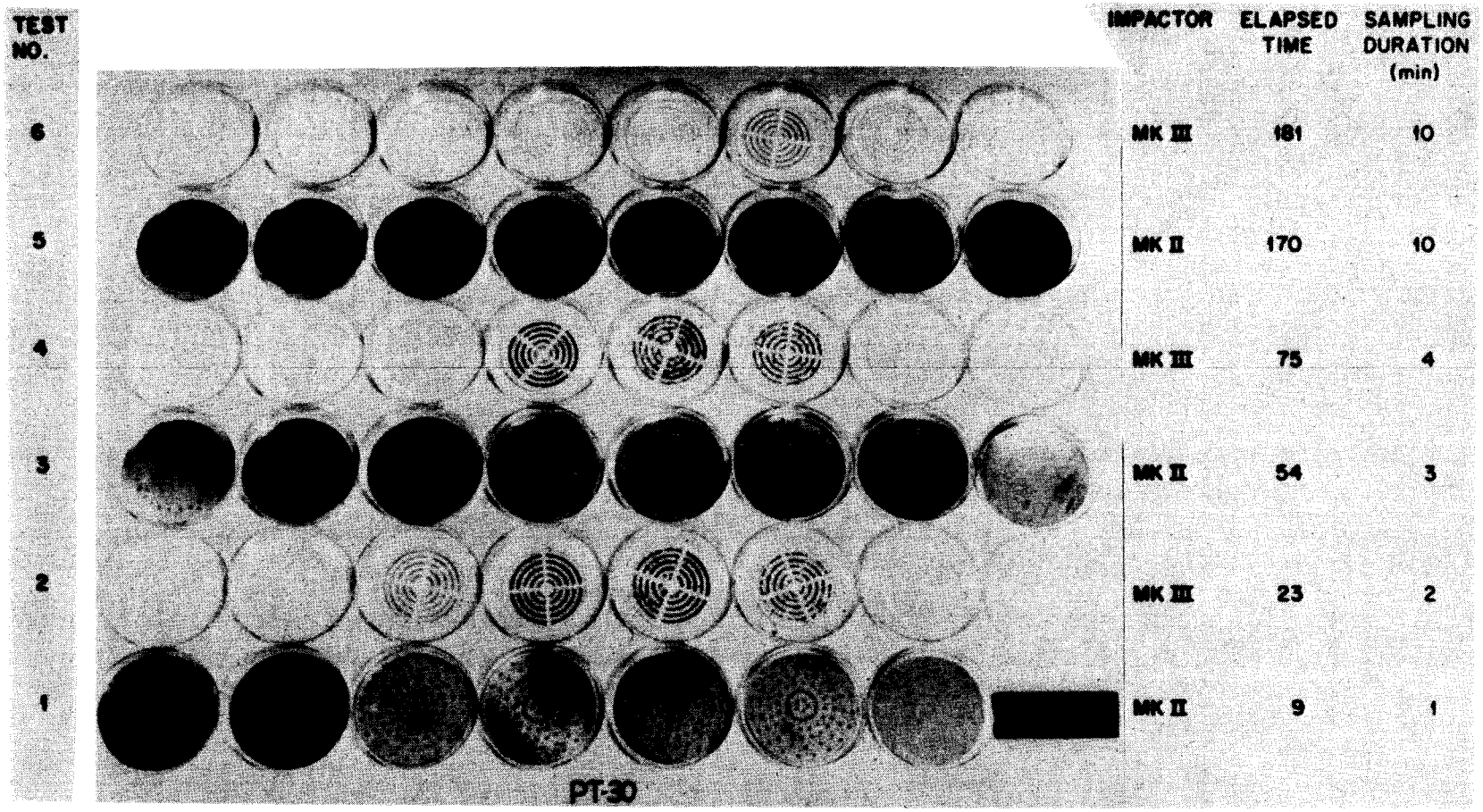

Fig. 16. Typical set of collector plates from Anderson Mark-II impactors for U_3O_8, run 30.

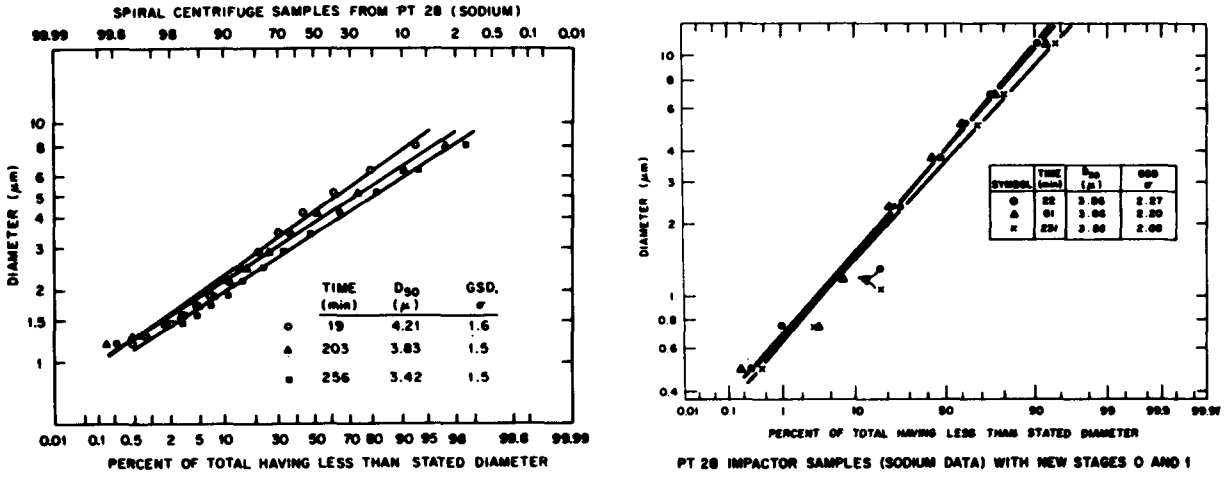

Fig. 17. Comparisons of size distributions obtained for sodium aerosol by the centrifuge with that by the Andersen Mark-II impactor.

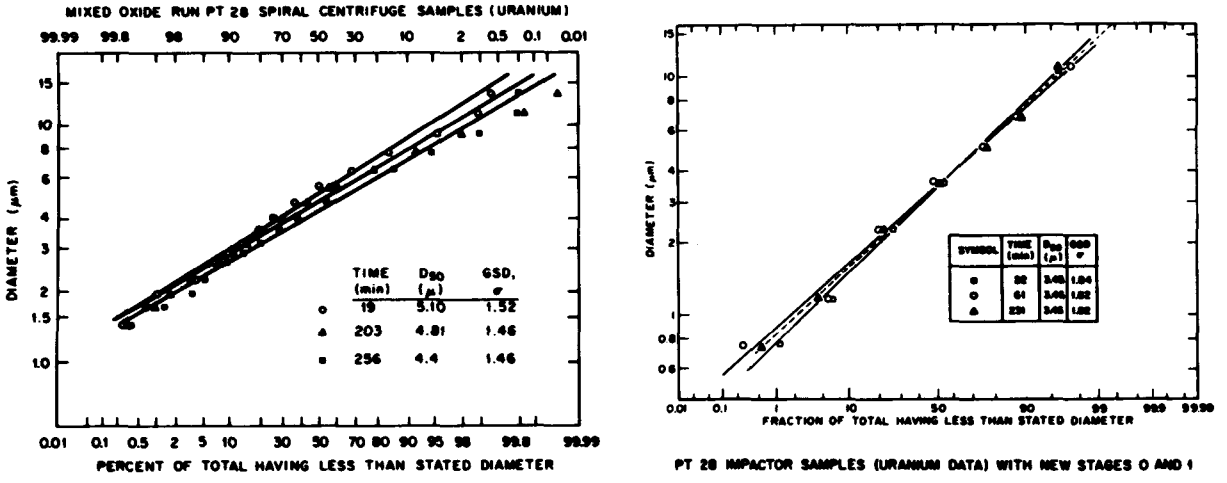

Fig. 18. Comparisons of size distributions obtained for uranium aerosol by the centrifuge with that by the Andersen Mark-II impactor.

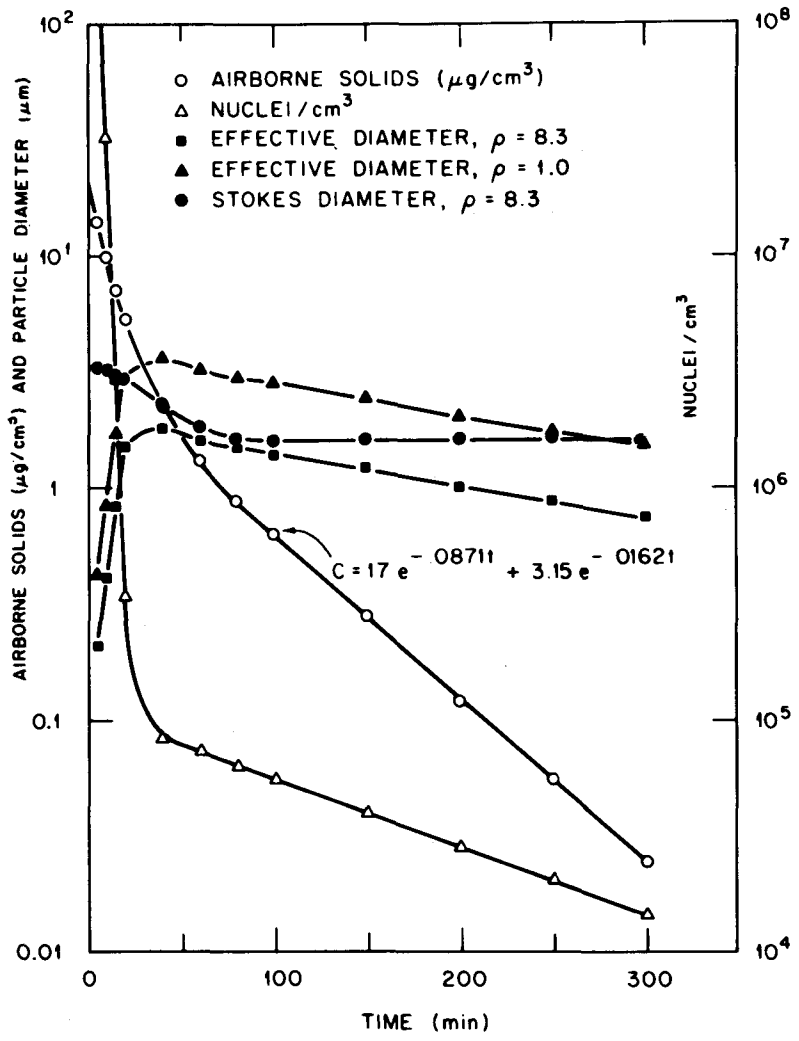

Fig. 19. Particle sizes calculated from number concentration and airborne mass for U_3O_8 run 22.

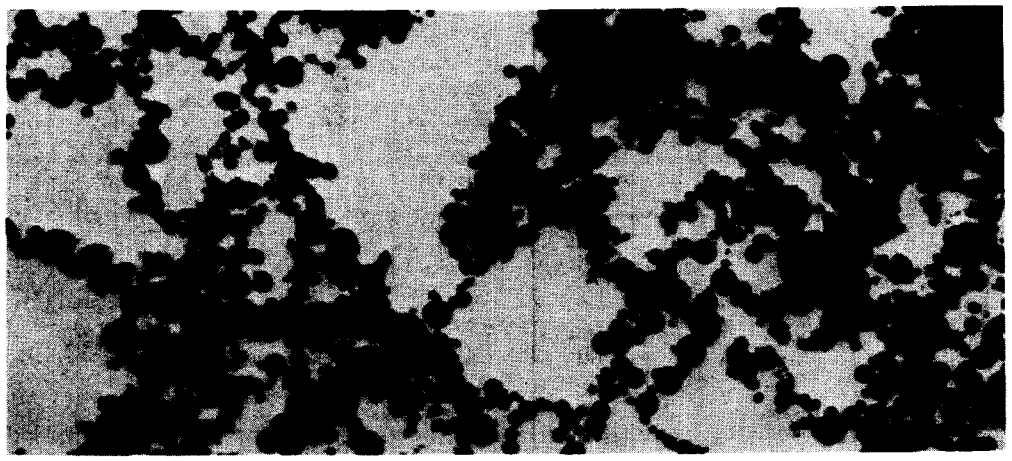

(*a*)

(*b*)

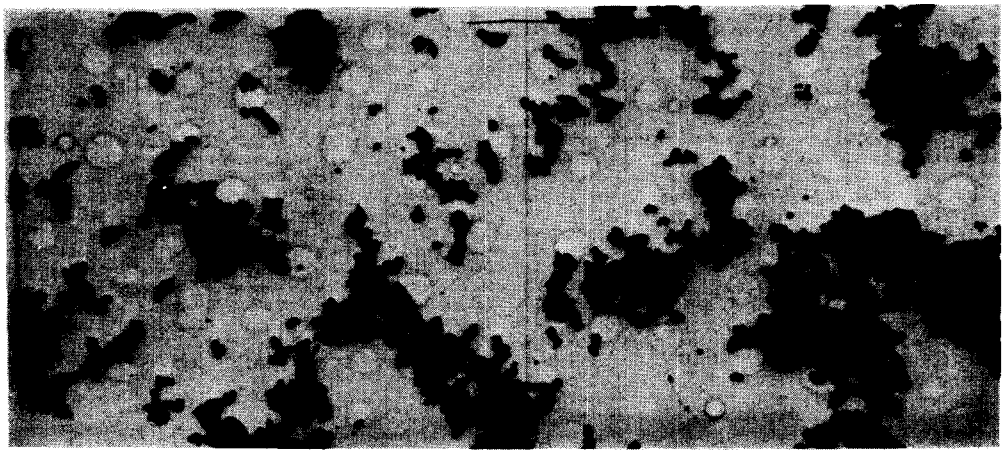

(*c*)

Fig. 20. Characteristic uranium oxide chain agglomerate particles. (*a*) CDV UO_2 aerosol at high magnification; (*b*) arc furnace UO_2 aerosol at high magnification; (*c*) PT U_3O_8 aerosol agglomerates at low magnification.

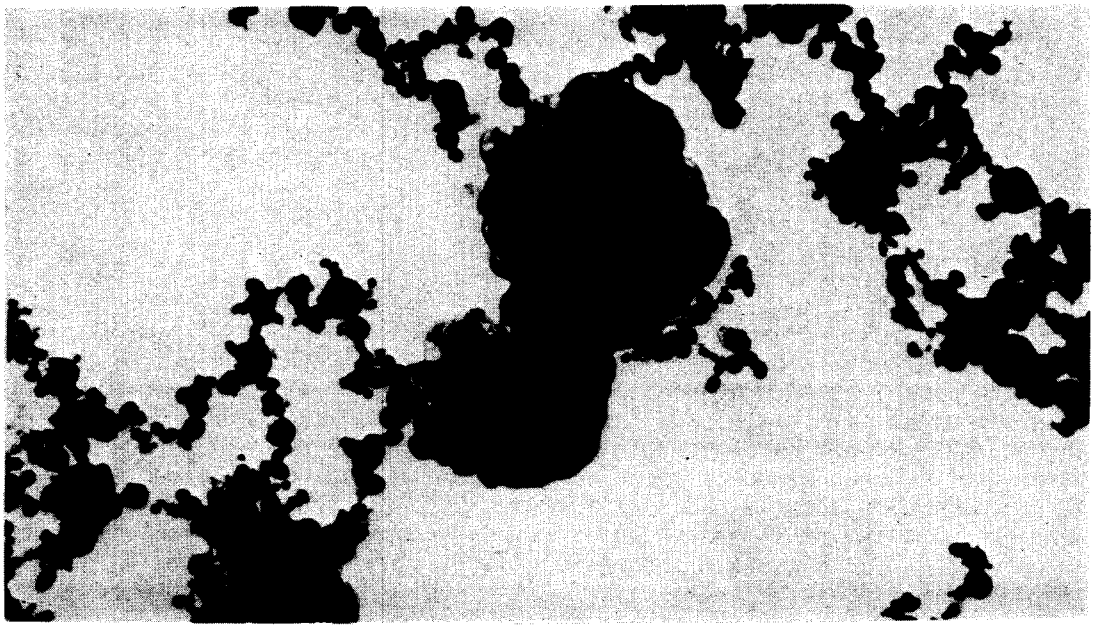

(*a*)

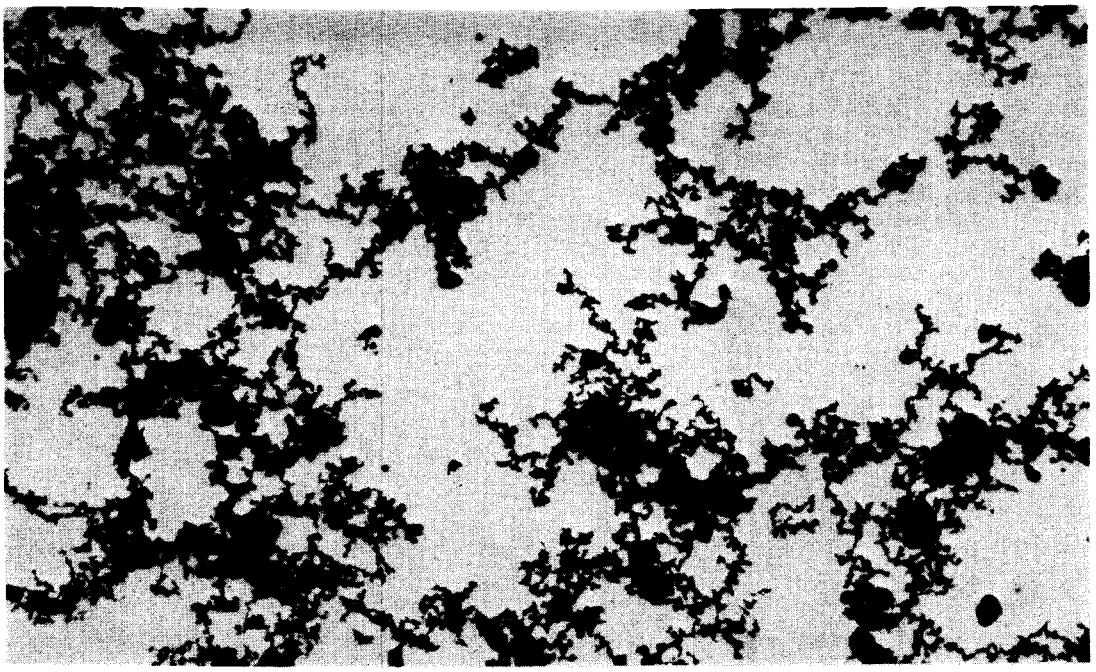

(*b*)

Fig. 21. Photomicrographs showing Na_2O_2 cluster aggregrates on U_3O_8 chain agglomerates. (*a*) PT-33 mixed oxides at high magnification; (*b*) PT-33 mixed oxides at low magnification.

A COMPARATIVE INSTRUMENTAL STUDY ON THE SIZE CHARACTERISTICS OF YTTRIUM OXIDE AGGREGATE AEROSOLS*

G. M. Kanapilly, Y. S. Cheng, R. H. Gray and H. C. Yeh
Inhalation Toxicology Research Institute, Lovelace Biomedical and Environmental Research Institute
Albuquerque, NM, U.S.A.

ABSTRACT

Condensation aerosols formed from supersaturated metal oxide vapors are often highly irregularly-shaped aggregates. These irregularly-shaped aerosols cover a wide spectrum of size ranges and are likely to be important aerosols associated with hypothetical nuclear events in which nuclear materials are vaporized. Instrumental methods commonly used for measuring particle size parameters utilize specific aerosol properties and all instruments have size limitations. This report presents the results of a comparative instrumental size characterization study on small Y_2O_3 aggregate aerosols. The instruments used were (1) a TSI model 3030 electrical aerosol analyzer (EAA), (2) a TSI model 3040 wire mesh diffusion battery (DB), (3) a Stöber aerosol centrifuge (SAC) and (4) a high resolution transmission electron microscope (TEM). The relative reliabilities of the instruments are discussed. The aerosols used in this study were produced by controlled vapor condensation methods. Radiolabeled aerosols, $^{90}Y_2O_3$ and "monodisperse" aerosols obtained by using an electrostatic classifier were also used. The electrical aerosol analyzer provided somewhat larger geometric standard deviations than the other instruments. The nominal diameters of the electrically classified Y_2O_3 aggregate aerosols were different from those measured by other methods. The sizes measured using the EAA, DB, centrifuge and TEM generally agreed with each other. Stereo electron micrographs revealed that these aggregate aerosols were three-dimensional structures. The dynamic shape factors of these aerosols were about 2.

*Research performed under U. S. Department of Energy Contract Number DE-AC04-76EV01013.

Introduction

Condensation aerosols formed from supersaturated metal oxide vapors are likely to be important aerosols associated with hypothetical nuclear events in which nuclear materials are vaporized (1,2,3,4). Depending on the physicochemical properties of the vapors, rapid cooling or chemical transformation may yield supersaturated vapors which initiate nucleation, condensation and aerosol growth processes (4,5,6). These supersaturated vapors form ultrafine primary particles or condense on pre-existing primary particles (5). The primary particles existing in high number concentrations rapidly coagulate. Refractory materials such as the oxides of actinide, lanthanide and transition metal oxides sinter only at high temperatures and, therefore, the coagulated condensation aerosols of these refractory materials exist as irregularly shaped aggregate particles.

Aerosol properties such as the diffusion coefficient, electrical charging characteristics, shape factor and density of these aggregate aerosols are neither known nor are they readily predictable. Instrumental methods commonly used for measuring particle size parameters utilize the above mentioned aerosol properties. These instruments are calibrated with aerosols of known physical properties, usually spherical aerosols of known density. Thus, the applicability of these instruments for the size characterization of aggregate aerosols cannot be readily assumed. Furthermore, the principles of operation, useful size range and measured size parameters are often different for these instruments (Table I). Thus, intercomparison and integrated use of particle sizes measured in different instruments is not readily done. For these reasons, a comparative instrumental study of the size parameters of irregularly-shaped aggregate Y_2O_3 aerosols was conducted to evaluate the applicability of these instruments for the size characterization of these aggregate aerosols. Results of these studies and a critical assessment of four instrumental methods for size characterization of the aggregate aerosol are reported.

Materials and Methods

Aerosol Size Measurements

The electrical aerosol size analyzer (EAA) (7) used in this study was a TSI Model 3030 (Thermosystem, Inc., St. Paul, MN). The reduction of EAA data was done according to a modified data reduction method (8). A screen-type diffusion battery (DB) (9), TSI Model 3040, was used in this study. Penetration of aerosols was determined either by collecting the $^{90}Y_2O_3$ aerosols on filters and beta counting or by using a Faraday cup. The Faraday cup was used to monitor the aerosol concentrations by measuring the electric current associated with the charged particles (10). The Stöber aerosol centrifuge (SAC) (11) used in this study was calibrated with monodisperse polystyrene latex aerosols (Dow Chemical Company, Midland, MI) and with fused montmorillonite clay aerosols (12) in conjunction with the transmission electron microscopic (TEM) technique. A Hitachi HU-11C transmission electron microscope was used to obtain electron micrographs of aerosols collected on Formvar carbon-coated 200 mesh copper grids. Both polydisperse aerosols and the electrically classified aerosols

were collected on TEM grids by a point-to-plane electrostatic precipitator (13). Aerodynamically classified aerosol samples were also collected on a TEM grid placed on the collection foil of the SAC. Stereo electron micrographs were obtained by taking micrographs of identical aerosol fields at 0° and at 10° angles. The primary particle diameters, D_p, were determined from the electron micrographs by using a calibrated magnifier. The volume equivalent diameter, D_e, of an aggregate aerosol was calculated by assuming log normal distribution of primary particle sizes and then using the relationship,

$$D_e = n^{1/3} D_p \exp [1.5 \ln^2 \sigma_g]$$

where n is the number of primary particles per aggregate and σ_g is the geometric standard deviation of the primary particle size distribution. The number of primary particles per aggregate was determined by examining the stereo micrographic pairs under a stereo viewer and counting the number of particles per aggregate. These values of D_e were used to determine the size distributions of aggregate aerosols by TEM method. Size classified aerosols were obtained by using a TSI Model 3071 electrostatic classifier (Thermo System Inc., St. Paul, MN).

Generation of the Y_2O_3 Aggregate Aerosols

Aggregate Y_2O_3 aerosols were produced by vaporizing an organic chelate of Yttrium with subseqeunt thermal degradation of the vapor at 1100°C (6). The organic chelate was a diketone, 2,2,6,6-tetramethyl-3,5-heptandione (THD). The yttrium chelate (Y-THD) was vaporized between 150 to 280°C. Details of the preparation and use of the Y-THD were described elsewhere (6).

A schematic of the aerosol generation and sampling system is shown in Figure 1. Low temperature (160-180°C) vaporization of Y-THD was done in a sample boat with 200 cc of N_2/min used as a vapor carrier. Carrier air was used in sufficient quantities (2 to 3 l per minute) for carrying the vapor and aerosol across the furnace while also providing sufficient oxygen for oxidizing the Y-THD into Y_2O_3. Aerosol size distributions were determined simultaneously on the same aerosol by the different instrumental methods. Both the SAC and DB analysis required relatively longer periods, 30 to 60 minutes. During this period, multiple EAA and point-to-plane electrostatic precipitator samples for TEM were obtained to verify the stability of the size characteristics of the aerosol. Radioactive ^{90}Y was used in some DB and SAC size characterization studies. A gas proportional counter (Wide Beta II, Beckman) was used to count the low level beta activities.

Results

The electron micrographs (Fig. 2) represent some typical Y_2O_3 aggregate aerosols studied. Stereo micrographs (Figs. 2A) illustrate the relatively small aggregates of the polydisperse aerosols. In most cases, the primary particle size distributions were narrow, with σ_g as low as 1.2. The aerodynamic diameter of the aerodynamically monodisperse aerosols (Fig. 2B) was 0.1 μm. The electrically classified aerosols (Fig. 2C) had count median diameters (CMD) of 0.21 μm.

A comparison of the size distribution of a polydisperse Y_2O_3 aggregate aerosol determined by four different aerosol sizing methods is presented in Figure 3.

The CMD and the geometric standard deviation (σ_g) of the aerosol measured in the EAA were 0.046 μm and 1.77 respectively. The CMD and σ_g measured by the TEM method were 0.050 and 1.36, respectively. According to the DB measurements, the mass median diameter (MMD) and σ_g were 0.092 and 1.2, respectively. The activity median aerodynamic median diameter (AMAD) and σ_g as measured in the SAC were 0.10 and 1.11, respectively. The size distribution of an electrically classified Y_2O_3 aggregate aerosol of CMD equivalent to 0.103 μm was determined in the EAA, DB and the SAC (Fig. 4). The EAA provided a CMD of 0.085 μm and a σ_g of 1.37. According to the DB, the MMD was 0.102 μm and the σ_g was 1.2; the corresponding calculated CMD was .092 μm. The AMAD and σ_g measured in the centrifuge were 0.090 μm and 1.17, respectively.

The CMD measured using the EAA, DB and TEM of electrically classified spherical particles are shown in Figure 5. These aerosols were separated from polydisperse aerosols of silver chloride and fused clay particles (10). The nominal diameters from the electrical classifier were plotted against the diameters measured in the EAA, DB and TEM.

The CMD of electrically classified irregularly-shaped Y_2O_3 aggregate aerosols were measured with the EAA, DB and TEM. These CMD are shown in Figure 6 as the classifier diameter versus the diameters measured in the EAA, DB and TEM.

Table II summarizes the particle size parameters and the shape factors of three Y_2O_3 aerosols measured by both TEM and SAC techniques. The primary particle size distribution was measured from TEM micrographs. The number of primary particles per aggregate was determined from stereo TEM micrographs. From these data, the volume equivalent diameter (D_e) was calculated. The activity median aerodynamic diameters (D_{ae}) were determined in the SAC. From these data, the aerodynamic shape factor κ was calculated by using the equation,

$$\kappa = \frac{D_e^2 \, C_{D_e} \, \rho}{D_{ae}^2 \, C_{D_{ae}} \, \rho_o}$$

where C_{De} and C_{Dae} are the Cunningham slip corrections associated with D_e and D_{ae}, respectively, ρ is the density of the material and ρ_o is unit density.

Discussion

The stereo electron micrographs revealed that the aggregate aerosols were three-dimensional structures, a feature not revealed in the routine two-dimensional micrographs. The number of primary particles per aggregate can be determined more accurately from the stereo TEM micrographs than from the conventional two-dimentional TEM micrographs. Stereo viewing allows one to see the three-dimentional aspects of the irregular chains in addition to resolving two or more closely associated particles. Particle counting from stereo micrographs seems quite reproducable since counts made on the same sample by two different people were within 5% of each other.

The aerodynamically monodisperse aerosols (Fig. 2B) appear to have different shapes and sizes. The differences in the number of primary particles, primary particle sizes and the shapes of the aggregate aerosols are likely to be factors for such physically different aggregate aerosols having the same aerodynamic diameters. The data in Table II show the large differences in the number of primary particles per aggregate, which are of the same aerodynamic diameter.

The 'monodisperse' Y_2O_3 aggregate aerosols obtained with the electrical classifier (Fig. 2C) appeared to have two population of particles in the same size range. This is attributed to the presence of significant fractions of doubly charged particles. Since the electrical aerosol classifier separates aerosols under Boltzman charge equilibrium, it is expected that only a very small fraction of the aerosol will be doubly charged (14). The present experimental observation suggests that the aggregate Y_2O_3 aerosols acquire more doubly charged fraction than relatively spherical particles. This charging characteristics of the aggregate aerosols may be a factor in the correct determination of their size measurements with electrical instruments which are calibrated with spherical particles.

The CMD of a polydisperse Y_2O_3 aggregate aerosol measured with the EAA and TEM technique (Fig. 3) are in close agreement. However, the CMD calculated from the MMD measured with the DB was about 67% higher than that of CMD measured by the TEM method. The calculation of the CMD from MMD and σ_g required the assumption that the aerosol size distribution was log normal. Since the shape factor, slip correction and density are unknown, a direct comparison of the AMAD measured in the SAC cannot be made with the diameters measured in the other method. Another observation is the rather large σ_g measured in the EAA. Similar observations were noted even when the particles were spheres (8).

An electrically classified Y_2O_3 aggregate aerosol (Fig. 4) also showed substantially smaller particle size and larger σ_g in the EAA. The CMD of this aerosol measured in the DB was about 10% less than the classifier CMD. As noted earlier, the AMAD determined in the SAC cannot be compared with the CMD. Although the particles were electrically classified and were expected to be monodisperse, the σ_g were relatively large, especially in the EAA.

Very good correlations of all the size measurements were found for spherical silver chloride and fused clay aerosols (Fig. 5). However, when similar measurements were made on electrically classified Y_2O_3 aggregate aerosols the nominal diameters of the electrical classifier appear to be significantly larger than those measured with the EAA, DB and TEM (Fig. 6). This divergence increased with particle size. As shown by the duplicate measurements some experimental variabilities exist. However the divergence from the nominal electrical classifier diameter appears to be real. At present, it is not clear why this divergence exists in the sizes measured with the different instruments.

The aerodynamic shape factors calculated from the SAC and TEM data (Table II) were about 2. These values are comparable to the aerodynamic shape factors determined on aggregate aerosols of (U-Pu) O_2 (15) but are substantially different from that reported on Fe_2O_3 aggregate aerosols (16). The dynamic shape factor of UO_2 aggregate aerosols determined in a Milliken cell was about 3 (17). A recent publication reports the dynamic shape factors of aggregate aerosols of U_3O_8 and copper oxide determined from TEM and SAC data as well as from the decay curve of mass and number concentrations (18). These shape factors increased with the size and ranged from 4.3 for 0.39 μm AMAD particles to 8.5 for particles with AMAD of 0.57 μm. It is evident from these data that significant differences exist on these measured shape factors of aggregate aerosols.

Conclusions

The present study shows that differences exist in the Y_2O_3 aggregate aerosol sizes measured with the different instruments. The nominal diameters of the electrically classified Y_2O_3 aggregate aerosols were different from the diameters measured with the EAA, the DB, the SAC and by the TEM methods. This difference was more pronounced as the aggregate aerosol particle size increased. It appears that the aggregate aerosols have a larger fraction of doubly charged particles than similar size spherical particles.

In this study of aggregate aerosols, the use of stereo-electron micrographs was very valuable for determining the number of primary particles per aggregate and the different particle shapes. The different sized particles exhibiting the same aerodynamic diameter in the aerosol centrifuge may be partly related to the different shapes of the aggregates. Since substantial differences in the shape factors of these aggregate aerosols are reported in the literature, an extensive study using the stereo-electron micrographic techniques and other appropriate aerosol sizing methods on different shaped aggregate aerosols will be useful.

The sizes of 'monodisperse' aerosols measured with the EAA, DB, and TEM generally agreed with each other. However, the σ_g of the aerosol size distribution was larger than expected and the σ_g determined with the EAA was always the largest. Polydisperse aerosols showed the smallest size when measured with the EAA. Several size parameters such as the shape factor, density of the material and the slip correction were unknown; therefore, direct comparison of the aggregate aerosol size measured in the SAC cannot be made with the sizes measured with the other instruments. In this respect, it is suggested that all measured size parameters be reported and calculated sizes be provided only as a secondary size parameter. It is also advisable that the size measurement of aggregate aerosols be done using more than one method or as many methods as possible. The calibrations of aerosol instruments used in determining the sizes of irregularly-shaped aggregate aerosols require further study.

Acknowledgements: We would like to thank Dr. B. V. Mokler, Dr. M. D. Hoover, Dr. R. K. Wolff, Dr. R. F. Henderson, Dr. J. A. Pickrell and Mr. G. J. Newton for their critical review of the manuscript. We are especially thankful to Dr. R. O. McClellan for encouraging this study and to Mr. R. D. Brodbeck for his valuable technical assistance.

Literature

[1] Silberberg, M. Ed., "Nuclear Aerosols in Reactor Safety," OECD, Paris, (1979).

[2] Castleman, A. W. Jr., F. L. Horn and G. C. Lindauer, "On the Behavior of Aerosols under Fast Reactor Accident Conditions," BNL-14070, (1969).

[3] Chatfield, E. J., "Some Studies of the Aerosols Produced by the Combustion or Vaporization of Plutonium-Alkali Metal Mixtures," J. Nuclear Materials 32, p. 228, (1969).

[4] Kennedy, M. F., "Primary Aerosol Particle Size Distribution from Homogeneous Nucleation, Condensation and Particle Growth," NUREG-0391, (1971).

[5] Fuchs, N. A., and A. G. Sutugin, Highly Dispersed Aerosols, Ann Arbor Science Publishers, Ann Arbor, Michigan, (1970).

[6] Kanapilly, G. M., K. W. Tu, T. B. Larson, G. R. Fogel, and R. J. Luna, "Controlled Production of Ultrafine Metallic Aerosols by Vaporization of an Organic Chelate of the Metal," J. Colloid Interface, Sc. 65, p. 533, (1978).

[7] Liu, B. Y. H. and D. Y. H. Pui, "On the Performance of the Electrical Aerosol Analyzer," J. Aerosol Sci. 6, p. 249, (1975).

[8] Yeh, H. C., Y. S. Cheng, and G. M. Kanapilly, "Electrical Aerosol Analyzer: Date Reduction at High Altitudes or Low Pressure," Atmos. Environ. (Submitted).

[9] Sinclair, D. and G. S. Hoopes, "A Novel Form of Diffusion Battery," Amer. Ind. Hyg. Assoc. J. 36, p. 39, (1975).

[10] Cheng, Y. S., J. A. Keating, and G. M. Kanapilly, "Theory and Calibration of a Screen-Type Diffusion Battery," J. Aerosol Sci. (In Press).

[11] Stöber, W., and H. Flachsbart, "Size-Separating Precipitation of Aerosols in a Spinning Spiral Duct," Environ. Sci. Tech. 3, p. 1280, (1969).

[12] Raabe, O. G., G. M. Kanapilly and G. J. Newton, "New Methods for the Generation of Aerosols of Insoluble Particle for Use in Inhalation Studies," Inhaled Particles and Vapors III, p. 3 (1970).

[13] Morrow, P. E., and T. T. Mercer, "A Point-to-Plane Electrostatic Precipitator for Particle Size Sampling," Amer. Ind. Hyg. Ass. J. 25, p. 8, (1964).

[14] Liu, B. Y. H., and D. Y. H. Pui, "A Submicron Aerosol Standard and the Primary, Absolute Calibration of the Condensation Nuclei Counter," J. Colloid Interface Sci. 47, p. 155, (1974).

[15] Allen, M. D., O. R. Moss, and J. K. Briant, "Dynamic Shape Factors for LMFBR Mixed-Oxide Fuel Aggregates," J. Aerosol Sci. 10, p. 43, (1978).

[16] Kops, J., G. Dibbets, L. Hermans, and J. F. Van De Vate, "The Aerodynamic Diameter of Branched Chain-Like Aggregates," J. Aerosol Sc. 6, p. 329, (1975).

[17] Gordon, H., and J. A. Gieseke, "A Characterization of Agglomerates of UO_2 Aerosols Particles," NUREG/CR-0489, BMI-2009, (1978).

[18] Van De Vate, J. F., W. F. Van Leeuwen, A. Plomp, and H. C. D. Smit, "Dynamic Shape Factors: Measurement Techniques and Results on Aggregates of Solid Primaries," J. Aerosol Sci. 11, p. 67, (1980).

Table I Instruments Used for Size Characterization and Relevant Information

Instrument	Principle of Operation	Size Range Applicability (μm)	Size Parameter Measured
Electrical Aerosol Analyzer (EAA)	Electrical Mobility	0.003 to 1	CMD[a]
Diffusion Battery (DB)	Browian Diffusion	0.001 to 0.1	CMD or MMD[b]
Transmission Electron Microscope (TEM)	Electron Opacity and Micrography	0.01 to 10	CMD
Stöber Aerosol Centrifuge (SAC)	Mobility under Centrifugal Force	0.08 to 5	AMAD[c] or MMAD[d]

[a]Count median diameter.

[b]Mass median diameter.

[c]Activity median aerodynamic diameter.

[d]Mass median aerodynamic diameter.

Table II Particle Size Parameters and Shape Factors of Aerodynamically Monodisperse Aerosols Determined by Using TEM and SAC

Primary Particle Size					
CMD (nm)	σ_g	n	D_e (nm)	D_{ae} (nm)	κ
9	1.26	69 ± 66	41	110	1.9
10	1.20	125 ± 96	53	120	2.0
9	1.67	110 ± 79	64	100	2.9

CMD - Count median diameter, σ_g = geometric standard deviation, n = number of primary particles per aggregate, De = volume equivalent diameter, D_{ae} = Activity median aerodynamic diameter, and κ = shape factor.

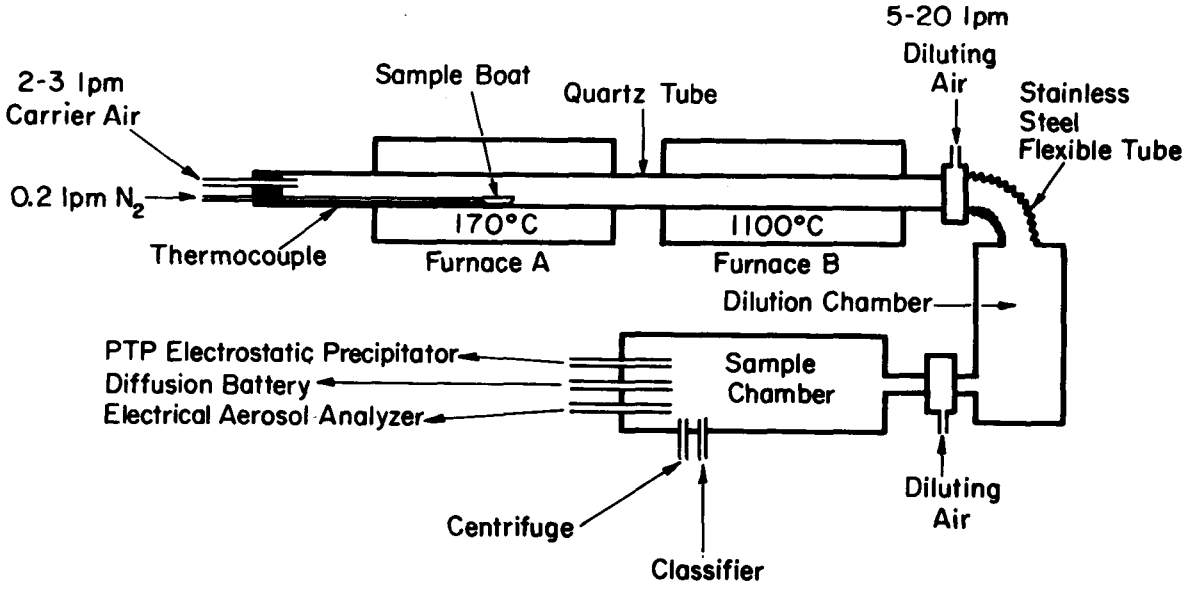

Figure 1. Schematics of the aerosol generation and sampling system.

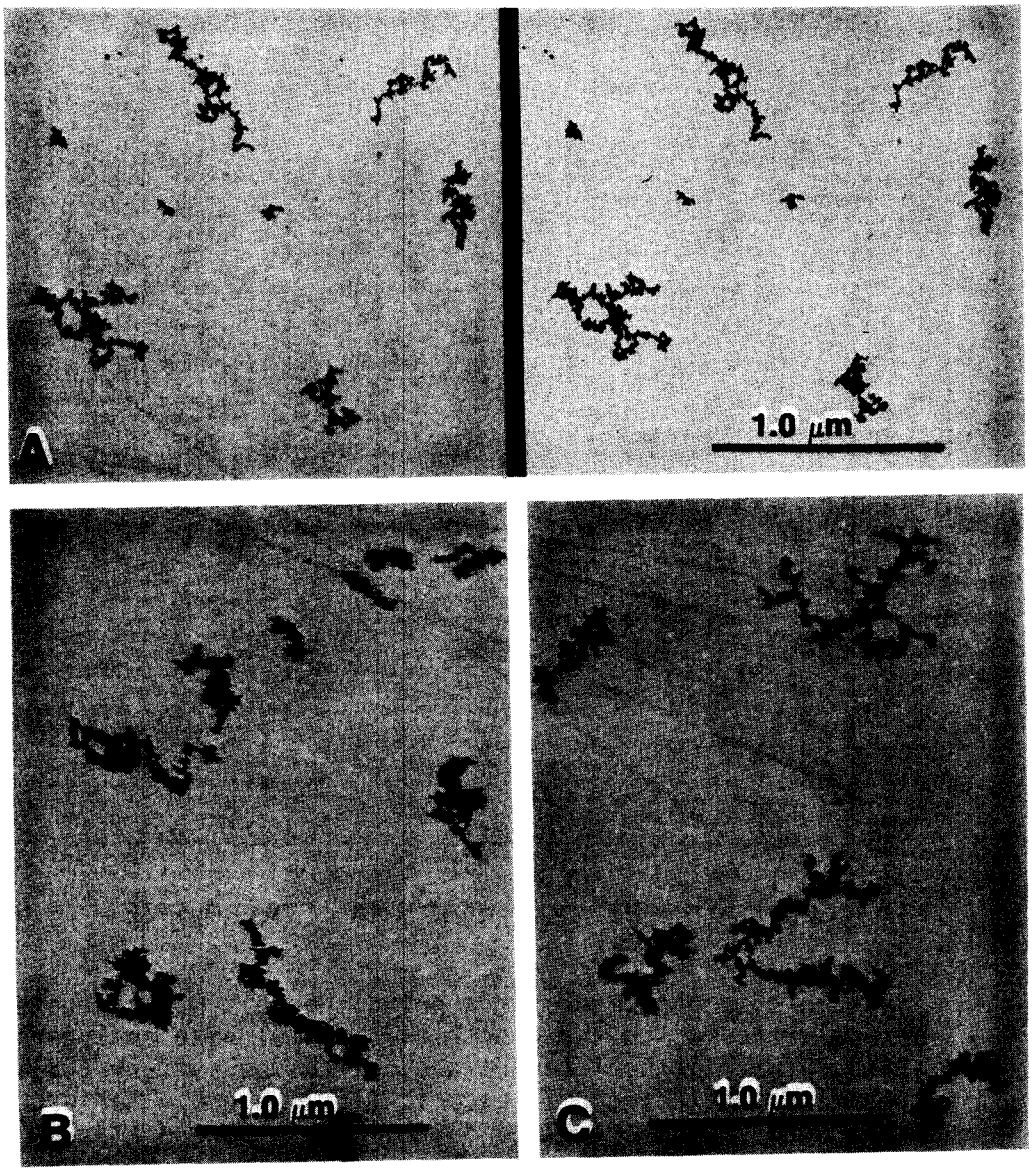

Figure 2. Transmission electron micrographs of Y_2O_3 aggregate aerosols. (A) Stereo pairs of a typical polydisperse aerosol, (B) Aerodynamically 'monodisperse' 0.1 μm aerosols and (C) electrically classified 0.21 μm aerosols.

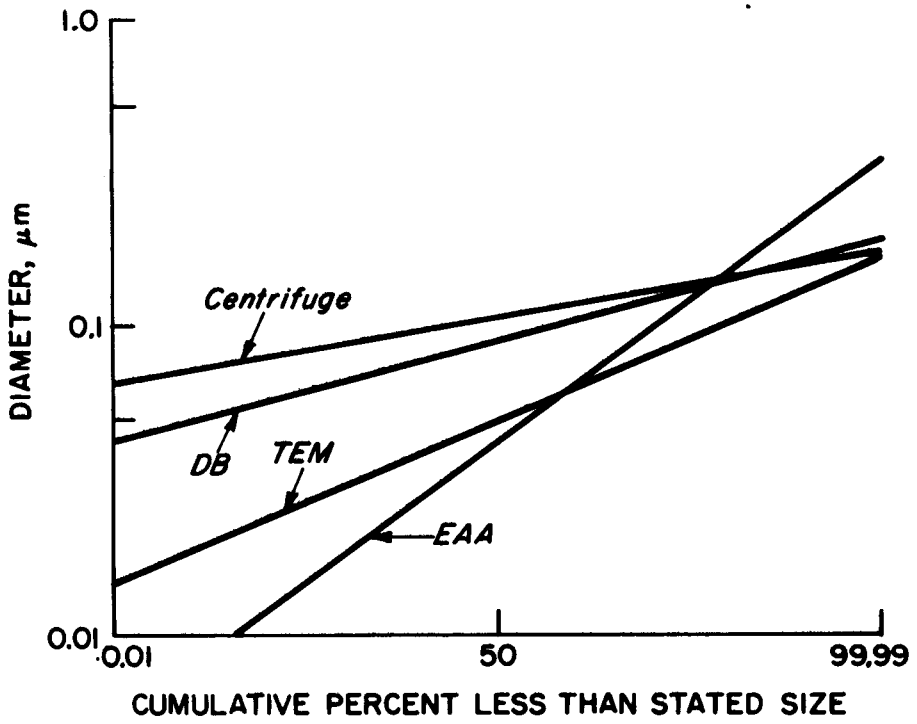

Figure 3. Particle size parameters of a polydisperse Y_2O_3 aggregate aerosol measured in the electrical aerosol size analyzer (EAA), Stöber aerosol centrifuge, diffusion battery (DB) and transmission electron microscopic (TEM) method. Measured particle sizes were CMD in the EAA and TEM, MMD in DB and AMAD in the centrifuge.

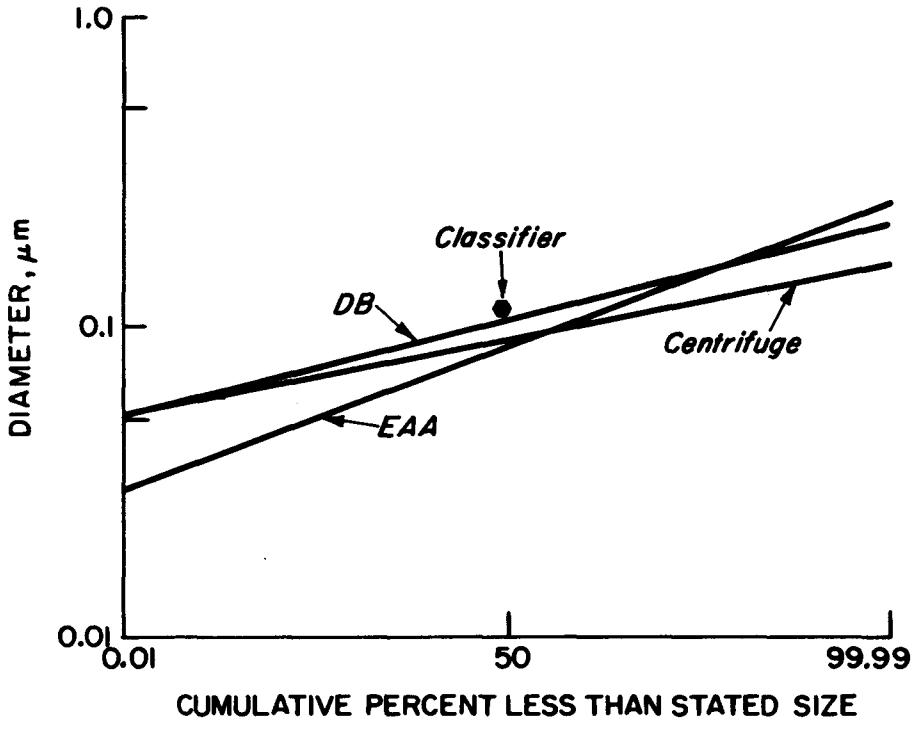

Figure 4. Particle size parameters of an electrically classified Y_2O_3 aerosol measured in the EAA, DB and the Aerosol centrifuge. Measured particle sizes were CMD in the EAA and TEM, MMD in DB and AMAD in the centrifuge.

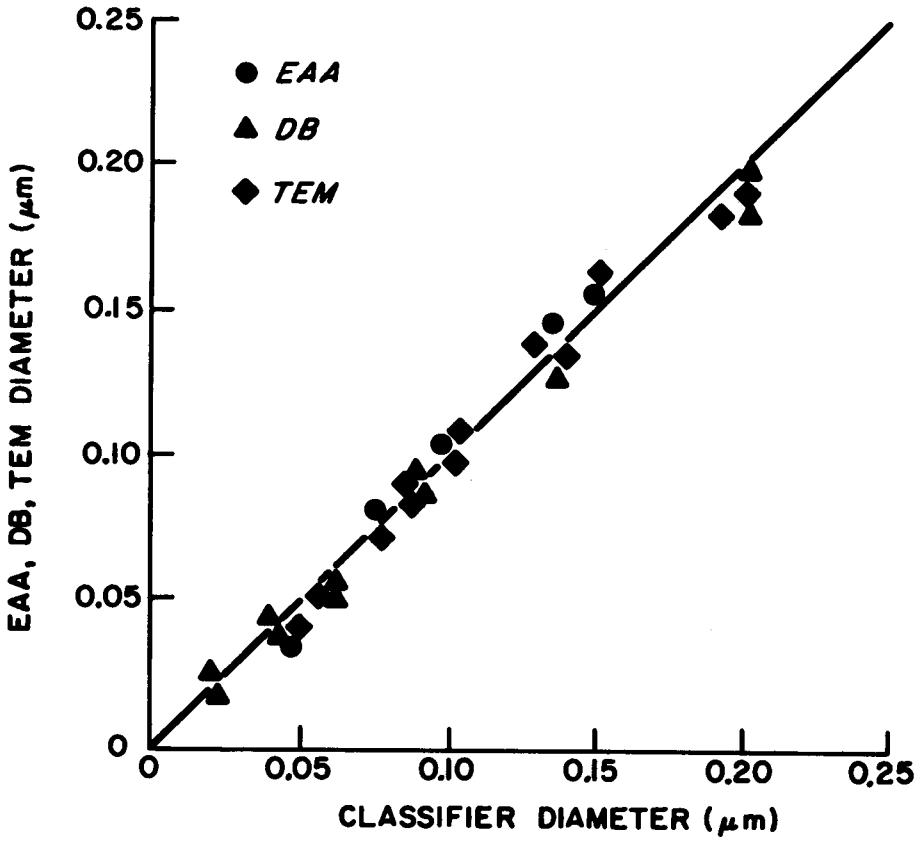

Figure 5. Comparison of CMD of electrically classified spherical particles with those measured in the EAA, DB and TEM.

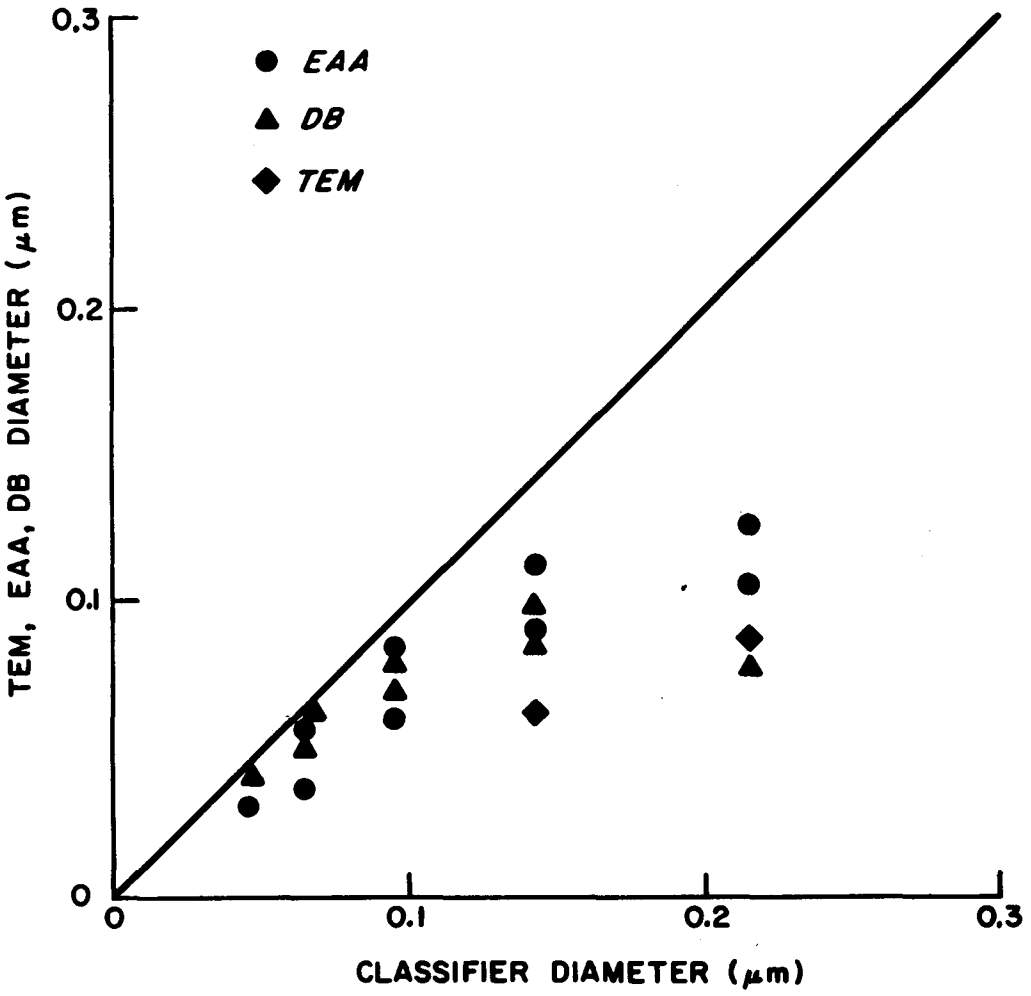

Figure 6. A comparison of CMD of electrically classified Y_2O_3 aggregate aerosols measured in the EAA, DB and TEM versus the nominal diameters of the electrical aerosol classifier.

STUDY OF MULTI-STAGES CASCADE IMPACTORS

D. Boulaud, G. Madelaine and J. Vendel
Commissariat à l'Energie Atomique
IPSN/DPr/STEP/SPT
Centre d'Etudes Nucléaires de Fontenay-aux-Roses
B.P. n° 6, 92260 FONTENAY AUX ROSES, France

ABSTRACT

This work is included in the general study of the behavior of aerosols produced from sodium-pool fire (Study : DSN/SESTR, DSN/SERS and DPr/STEP/SPT). The aim of this work is the calibration of the aerosol measurement device used in general experiments.

I. In the first part the calibration of the eight-stages ANDERSEN cascade impactor with monodispersed solid particles (polystyrene latex, fluorescein ammonium salt) will be described. The collection efficiency of the stages in relation to the nature of the different surfaces (glass plates, steel plates, oil-coated or uncoated, glass fiber filter) will be determined.

With coated plates the collection efficiency varies monotonically from 0% to 100% as the diameter of the particles increases, whereas with uncoated surfaces the efficiency rises up to values between 50% and 75% and then drops. Under optimal conditions the comparison between experimental efficiency curves and theoretical predictions shows a cut-off which is not as sharp as expected.

The results obtained with monodispersed aerosols will be compared to those obtained with aerosols generated by sodium fire.

II. The set-up of an aerosol size distribution from the results collected on a cascade impactor implies that each stage is characterized by one size. In fact some of these characteristic sizes depend on the distribution of the aerosol tested. This necessitates an exact knowledge of the interdependance.

The definition of the different characteristic diameters (cut-off diameter, mass median diameter, effective drop size) and the calculation methods which make it possible to find the value of these diameters from the collection efficiency curves obtained experimentally are recalled.

The Picknett numerical method which allows a direct calculation of the aerosol size distribution is also discussed.

Finally, after having determined the different characteristic diameters for the eight-stage ANDERSEN impactor, these various methods for setting up an aerosol size distribution will be compared in order to define their field of use.

A. CALIBRATION AND PARAMETERS INFLUENCING THE COLLECTION EFFICIENCY OF SOLID AEROSOLS

I. INTRODUCTION

Multi-stage cascade impactors are widely used instruments which measure the size distribution of aerosols whose diameters are between 0.5 and 10 µm. In spite of this wide use, their behavior in relation to a certain number of parameters which will be pointed out is rarely well known.

The different stage cut points are generally obtained from theoretical calculations rather than from experimental calibrations. The calculation procedures usually assume that all the stages have identical collection characteristics and that a multi-jet impactor is similar to a single-jet impactor. The effect of factors such as the jet velocity or jet Reynolds number, inlet conditions, as well as the state of the collection surfaces are ignored. One of the most complete theories available is that developed by Marple et al. (1) in the case of a simple impaction system with ideal flow conditions. This theory makes it possible to correctly predict the cut-point diameters of impactors which satisfy these assumptions. Nevertheless, for more complex impactor systems, it can lead to errors.

The important parameters affecting the theoretical data are wall loss, bounce and blow-off, deagglomeration and particle break-up, electrostatic attraction, and the nature of the collection surface. Because of the complexity of these factors, a theoretical treatment is not possible and only an experimental approach makes it possible to understand their importance and to minimize these effects if need be.

Much work has been done along these lines. More recently, Rao and Whitby (2) thoroughly examined the influence of the nature of collection surface on the collection efficiency.

The present study concerns the calibration of the Mark II ANDERSEN cascade impactor when used with solid aerosols, a special application being the size distribution measurement of aerosols resulting from sodium fire.

II. EXPERIMENTAL METHOD

The ultimate goal of an impactor calibration is to obtain collection efficiency (E) and wall loss of each stage as a function of the particle aerodynamic diameter (Dae).

The aerodynamic diameter of spherical particles is approximately

$$Dae = Dp\ (Cp/Cae)^{1/2}$$

where C and Cae represent the Cunningham factors, ρ the particle density and Dp the particle diameter. For non-spherical particles, the preceding equation should include a shape factor. However, to avoid uncertainties in Dae, it is preferable to use spherical particles for calibration.

II.1. Description of the impactor

The impactor used is the ANDERSEN Mark II. It has eight stages each consisting of a plate with circular holes and followed by a stainless-steel or glass collection plates. The operating parameters of the different impactor stages are given in Table I for a recommended flow rate of 28.3 l/mn. A filter whose purpose is to capture the fine fraction of the measured aerosol is placed downstream of the eight stages.

Table I

ANDERSEN Impactor (Q = 28.3 l/mn)

Stage	D (cm)	Number of holes	S/D	Surface (cm^2)	U (cm/s)	Re
1	2.55 (-1)	96	0.98	4.92	95.9	156.06
2	1.887 (-1)	96	1.38	2.68	176	211.5
3	9.14 (-2)	400	2,73	2.62	180	104.8
4	7.11 (-2)	400	3.51	1.58	298.5	135.2
5	5.33 (-2)	400	4.7	0.892	528.75	179.5
6	3.43 (-2)	400	7.3	0.370	1274.75	278.5
7	2.54 (-2)	400	9.8	0.202	2335	377.75
8	2.54 (-2)	201	9.8	0.101	4670	755.5

II.2. Monodispersed aerosol

As the study mainly concerns the ANDERSEN impactor response in relation to solid aerosols, the following were used :

- from 1 to 20 µm, fluorescein ammonium salt (FAS) whose volumic mass is 1.35 g/cm^3, furnished by the vibrating orifice monodispersec aerosol generator (Berglund ans Liu (3)) ;

- from 0.2 to 2 µm, polystirene latex (PSL) particles whose volumic mass is 1.05 g/cm^3.

II.3. General device

Figure 1 schematically represents the device used for this study. A rotameter with an accuracy of 2% measures the flow rate of air circulating in the impactor.

A typical experiment begins by washing and drying all the parts of the impactor. When FAS particles are used (4), they are accumulated during periods lasting from between 2 to 10 minutes, then the different parts of the impactor are washed. This method makes it possible to isolate wall loss. When PSL particles are used ; especially for the last two stages of the impactor, the collection efficiency is determined by measuring the concentrations upstream and downstream of the impactor with a particle optical counter. In this case plate collection and wall loss can be confused ; therefore, this method should only be used when wall loss is low.

III. SOLID PARTICLE BOUNCE AND BLOW-OFF

Rao and Whitby (2) have already treated this problem. Here, the problem is to bring to light the nature of the best-adapted collection surfaces for the Mark II ANDERSEN impactor. Three types of collection surfaces were tried out : grease-coated glass plates, non-coated glass plates, and glass-fiber filters (Gelman).

III.1. Experimental procedure

The general device used is represented on Fig. 1. The impactor was assembled with all the stages except those that are below the test stage, since the performance of a given stage should not be affected by the presence or absence of another downstream stages. One can observe that collection efficiency is not modified if tests are carried out on lonely stage.

A few glass plates were coated with grease by spreading drops of solution containing grease and trichloromethan, and then, drying in clean air. Evaporation of the trichloromethan leaves the plates with a thin coat of grease.

III.2. Results

Figure 2 shows for instance the results obtained with one stage of the ANDERSEN impactor for the different types of collection surfaces.

For the grease-coated glass plates, the collection efficiency varies monotonically from 0 to 100%. For glass plates the collection efficiency increases to around 75% and then drops rapidly. The same phenomena occurs for glass fiber filters but in a less-pronounced way.

IV. CALIBRATION WITH SOLID PARTICLES

IV.1. Experimental procedure

It is about the same as that used for studying blow-off. When FAS particles are used it is possible to obtain impactor wall loss.

This calibration was carried out using grease-coated glass plates as the collection surface.

IV.2. Results

Figure 3 shows the experimental variations of the collection efficiency for the different stages as a function of the aerodynamic diameter (Dae). For all stages the cut-off is sharp thus showing that the phenomena of bounce and blow-off are correctly taken care of. Collection efficiency

variations can be plotted from these curves as a function of the square root of Stokes number (Figure 4). This same figure shows the theoretical curve deducted from calculations by Marple and al. (1). The comparison of the theoretical and experimental results shows that they are in good agreement even though the slope of the experimental curves is less steeped and the trail towards the small Stokes numbers is greater for the experiments.

These slight differences can be explained by the fact that the theory is set up for a single jet flow with a Reynolds number of 3000 and a distance between the jet and the plate of between 2 and 5 times the diameter of the jet.

Figure 5 shows the impactor wall loss for solid particles, which becomes significant above 10 µm but remains low under 5 µm.

V. EXPERIMENTS WITH AEROSOLS ARISING FROM SODIUM COMBUSTION

Because this apparatus was used in experiments with sodium fires (5), tests were made on sodium combustion aerosols in a dry atmosphere (HR < 1% to 25°C).

In these tests, electronic microscope grids were placed on stages 7 and 8 and the size distribution of sodium aerosols deposited on these stages was determined. These particles were approximately spherical and their characteristics are shown in Table II.

Table II

Stage	nmd (µm)	mmd (µm)
8	0.35	0.56
7	0.56	0.80

nmd : number mediam diameter
mmd : mass median diameter.

The tested sodium aerosol had a mass mediam diameter MMD) between 1 and 2 µm and a standard deviation (σg) of around 1.75 and 2. The second part of this paper will show that under these conditions and knowing the collection efficiencies of the different stages, the effective mass median aerodynamic diameter (emmd) for stages 7 and 8 can be predicted.

The emmd values for stages 7 and 8 are shown in Table III along with the mmd values determined with an electron microscope.

The mmd determined with an electron microscope is very close to the emmd values predicted by calculation and relates to the aerodynamic diameters of particles whose density is 1. The closeness of these results indicates an apparent density of between 0.926 and 1.07 for sodium fire aerosols (values deducted from the extreme values of the Table). It should be noted that these comparisons do not represent an exact method for determining the apparent density of the particles but can be considered to be first approximations.

Table III

Stage	mmd (µm)	emmd			
		MMD = 1 µm		MMD = 2 µm	
		σg (1.75)	σg (2)	σg (1.75)	σg (2)
8	0.56	0.502	0.480	0.572	0.532
7	0.80	0.804	0.790	0.913	0.86

CONCLUSION

The calibration of the Mark II ANDERSEN impactor brought out the parasitic effects of solid particle bounce and blow-off when the nature of the collection surface is not well chosen.

By chosing grease-coated glass plates, sharp cut-off was obtained for all stages. Glass fiber filters could also be used but this would alter the collection efficiency curves which would make a new calibration necessary, as would any use under conditions different from those described in this paper.

B. DATA INTERPRETATION FOR SETTING UP SIZE DISTRIBUTIONS

I. INTRODUCTION

Determining mass distribution of an aerosol from data collected by a cascade impactor implies the characterization of each stage of the impactor by a size.

In fact some of these characteristic sizes depend on the measured aerosol distribution making a precise knowledge of this dependance necessary.

The first paragraph will define the different characteristic sizes for an impactor having perfect separation or not. The second paragraph describes the calculation method for characteristic sizes. A numeric method for determining size distributions will be described in the third paragraph. Finally, the last paragraph will deal with the comparison of the different methods.

The mass median diameter of each stage is generally written mmd and that of the complete distribution by MMD.

II. IMPACTOR CHARACTERISTIC DIAMETERS

A detailed study of characteristic diameters can be found in an article by Soole (6).

II.1. Ideal impactor

II.1.1. Cut-off size

It is convenient to consider first an ideal impactor in which the separation into two classes of particles at each stage is complete. The size at which the separation takes place is called the cut-off size (C-S). Thus in Figure 6 where a log-normal distribution (MMD = 10 µm, σg = 2) represents ingoing particles, a perfect separation at four stages for particle diameters of 15 µm, 10 µm, 5 µm and 2 µm is shown as an example, so that the masses deposited on each collection stage are represented by areas I, II, III, IV. The last area corresponds to particles which pass the last stage and are collected on the filter. Area I extends theoretically to an infinite size ; in practice it stops at the largest size occuring in the distribution.

It is clear from the figure that the cumulative undersize mass fraction can be obtained by plotting the percentage of the total mass passing a given stage against the cut-off size. This is true for all types of distribution.

II.1.2. Mass median diameter (mmd)

This diameter corresponds to the one which divides area I, II, III, and IV into two equal parts. The cumulative curve will be obtained by plotting the total mass fraction passing a given stage to which is added half the mass deposited on the stage in question as a function of the mmd of the stage.

II.1.3. EDS effective drop sizes

May's definition indicates that EDS are the particle diameters which, when plotted as a function of the total mass percentage collected by stage and those of succeeding stages give the curve describing the cumulative mass undersize to the size considered. An equivalent definition can be stated as follows : particle diameters when plotted as a function of the percentage of the total mass collected by stage and those preceeding give a curve describing the cumulative mass "greater than" the considered size. It is clear from Figure 6 that for an ideal impactor the EDS for a given stage (second defintion) are identical to the cut-off sizes.

Thus for an ideal impactor, any cumulative distribution can be obtained whitout error by using the preceeding methods. The cut-off size method is equivalent to the EDS method. The mmd method presents no additional advantage given the work involved to determine the mmd. Moreover, whereas the CS and EDS values are independant of the sample distribution, the mmd values are not. Thus, for an ideal impactor the CS and EDS values are preferable.

II.2. Real impactor

In practice separation never appears so suddenly and completely. To the contrary, for each stage there is a fine area of particle size where partial separation exists, so that these particles can appear on two or more adjacent stages. This overlapping therefore modifies the preceeding conclusions.

The characteristics of each stage are defined by a penetration curve $P_i(r)$ where i is the stage number and r the particle radius. The boundaries defining areas I, II, III, and IV are now seen as the product of the mass sample distribution and the function $P_i(r)$ (Figure 7). As a consequence the deposit, for example on stage three, will be increased by particles over 10 µm which escape from stage two and particles under 5 µm which do not reach stage four (area represented by g:). Nevertheless, other particles represented by area p will be lost on adjacent stages.

II.2.1. ECS Effective cut-off size

This is defined as the diameters of particles which have a 50% probability of penetrating a given stage. This characteristic diameter is by definition independant of the sample distribution. The cumulative mass curve plotted as a function of the ECS will be in error when associated with the existence of areas g and p.

II.2.2. Mass median diameter

It is necessary to define the effective mass median diameters (emmd's) for each stage and a series of known distribution which, when plotted as a function of the total percentage mass corresponding to half the deposit on a given stage to which is added the mass deposited on successive stages, must in fact reproduce the true cumulative curve. With an ideal impactor the mmd and the emmd are identical.

II.2.3. EDS Effective drop sizes

The definition is the same as the one used for perfect impactors but here the EDS values depend at the same time on the sample mass distribution and on the penetration functions $P_i(r)$. The cumulative mass curve is then plotted as a function of the EDS whitout error. It is seen that when real impactors are used, the curves for the sample distribution mass can be plotted whitout error only by using the EDS or the emmd's method. To the contrary, the ECS method is inevitably in error. Nevertheless, the EDS or the emmd's values to be used depend at the same time on the impactor's characteristics and on the sample distribution necessitating a successive approximation method.

III. CALCULATION OF CHARACTERISTIC SIZES

III.1. If in the sample distribution the total mass fraction in the interval r and r + dr is ydr and if $P_i(r)$ is the fraction of particles of radius r passing the ith stage, then the fraction of the particle in this interval which passes stage n is :

$$y\ dr \prod_{i=1}^{r} P_i(r) \qquad \text{or} \qquad y\ dr \prod_{i=1}^{r} [1 - E_i(r)]$$

$E_i(r)$ being the stage i collection efficiency for the particle radius r. Thus, the total fraction passing stage n is :

$$F_n = \int_0^{\infty} \prod_{i=1}^{n} [1 - E_i(r)]\ y\ dr$$

The total fraction passing stage (n-1) is :

$$F_{n-1} = \int_0^{\infty} \prod_{i=1}^{n-1} [1 - E_i(r)]\ y\ dr$$

Thus, there are as many integrals as stages.

By definition

$$y\ dr = \frac{f(r)\ r^3\ dr}{\int_0^{\infty} f(r)\ r^3\ dr}$$

If it is assumed that the particle distribution follows a log-normal law with a number median diameter 2 RN and a standard deviation σg

$$f(r)\ dr = [\exp(-X^2)\ dX]/\Pi^{1/2}$$

with

$$X = [\text{Log}(2r) - \text{Log}(2RN)]/(2)^{1/2}\ \text{Log}\ \sigma g$$

Integrals containing the collection efficiencies are obtained by carrying out the integration one step at a time as the $E_i(r)$ values are found experimentally and have no known analytical form.

Thus, for a given distribution the aerosol cumulative mass fraction passing the different stages F_n, F_{n-1}, F_i, F_1 can be calculated.

By knowing the cumulative mass fractions, the different stages can be characterized by EDS values such as

$$F_i = [1 + \text{erf}(XD_i)]/2$$

with

$$XD_i = [\text{Log}(2RD_i) - \text{Log}(2RM)]/(2)^{1/2}\ \text{Log}\ \sigma g,$$

and

$$2RD_i = (EDS)_i$$

The emmd's values are deduced in a similar way. In this case F_i values should include in addition half the mass deposited on the considered stage.

III.2. Application to the Mark II ANDERSEN impactor

Using experimentally determined collection efficiencies, the different characteristic sizes can be calculated.

III.2.1. Effective cut-off aerodynamic diameters (ECAD)

Stage	1	2	3	4	5	6	7	8
ECAD (µm)	7.5	5.8	4.5	3.1	1.75	1	0.62	0.35

III.2.2. Effective drop sizes (EDS) and effective mass median diameters (emmd)

The diameters were calculated for different aerosol log-normal distributions, for mass median diameters (MMD), and for variable standard deviations (σg). Table IV shows several types of results which are possible to obtain.

The MMD values are (0.5, 4, 15 µm) and the σg values are (1.5, 2.5, 5).

These calculations imply that the distribution maximum size corresponds to a maximum diameter of 50 µm.

For EDS and emmd, the cumulative distribution will be set up by successive approximations taking different diameter values from a table of the same type but more complete than Table IV.

IV. PICKNETT METHOD (7)

For an aerosol of a given distribution size, if the fraction of the mass retained by the impactor is A, according to Figure 8 a diameter D is obtained representing a monodispersed aerosol diameter having the same mass fraction collected by the impactor. This abrupt way of representing an aerosol leads to fixing an "apparent diameter".

While still examining only one stage of the impactor, the original aerosol can be represented by another made up of two monodispersed aerosols mixed in such proportions that the mass fraction collected by the impactor will be identical. The two particle diameters should be over and under the value D ; except for this condition, no restriction on the chosen values exists. d' and d" are these two diameters and E' and E" the collection efficiencies corresponding to the impactor. In order to calculate the fraction relative to each aerosol (f' and f") in the resulting aerosol,

the contribution of each size to the deposit captured by the impactor is examined.

$$f'E' + f''E'' = A$$

Since $f' + f'' = 1$, the composition of the resulting aerosol is determined completely as follows :

$$f' = (A - E'')/(E' - E'')$$

$$f'' = (E' - A)/(E' - E'')$$

This result can be of great importance when examining a multi-stages impactor. This paper deals with cascade impactors.

The procedure for multi-stages impactors is similar to the one used for single-stage impactors except that the definition of A is somewhat modified as A_1, A_2, etc. now represent the fractions deposited on stage 1, 2, etc. of the aerosol mass reaching the given stage.

The corresponding values for D are obtained as before. For an impactor having N stages, there will be N values for D and N + 1 particle sizes which can be used to represent the original aerosol.

These sizes are subjected to the following restrictions :

$$d_1 > D_1 > d_2 > D_2 \ldots d_i > D_i \ldots > d_N > D_N > d_N + 1$$

It should be well noted that the aerosol is represented as a combination of N + 1 different monodispersed aerosols, that is the particle diameters d are discrete values.

In the combined aerosol, the relative part of these particle sizes can be found by examining the contribution of each particle size to deposit M_1, M_2 ... on each stage.

$$1\begin{cases} \text{Stage 1: } f_1E_{11}+f_2E_{12}+ \ldots + f_iE_{1i}+ \ldots f_{N+1}E_{1N+1} = & M_1/\Sigma M_i \\ \text{Stage 2: } f_1E_{21}(1-E_{11})+f_2E_{22}(1-E_{12})+\ldots f_iE_{2i}(1-E_{1i})+\ldots f_{N+1}E_{2N+1}(1-E_{1N+1}) = & M_2/\Sigma M_i \\ \text{Stage N: } \sum_{i=1}^{N+1}\left(f_iE_{Ni}\prod_{k=1}^{N-1}(1-E_{ki})\right) = & M_N/\Sigma M_i \end{cases}$$

In these equations E_{ij} corresponds to the collection efficiency of stage i in relation to the particle diameter d_j.

The linear equation system associated with the relation

$$\sum_{i=1}^{N+1} f_i = 1$$

can be solved and gives the values for f_1 ; f_2 ... f_i ... and f_{N+1}.

These attached values and the aerosols having discrete values must be combined in order to obtain an aerosol representing a continuous distribution.

Wells' (8) method makes it possible to achieve this by writting the following equation of the cumulative mass fraction :

$$F_i = \frac{1}{2} f_i + \sum_{k=0}^{i-1} f_k$$

The final result of these operations is the cumulative mass distribution curve of an aerosol whose deposits on each stage are similar to those of the originally sampled aerosol. A curve corresponds to a series of N + 1 diameters chosen arbitrarily. The operation can thus be done again with a new series and the construction of the resulting cumulative curve can be improved each time.

V. COMPARISON OF THE DIFFERENT METHODS (ECAD, EDS, PICKNETT)

A theoretical simulation was carried out in order to compare the different methods for setting up a distribution size from the masses collected on the different stages of a Mark II ANDERSEN impactor.

Several cumulative mass distributions are used for this, first replacing this distribution by a large number of monodispersed aerosols whose frequence f is determined using the Wells equation. This being done ; the masses deposited on the various stages are calculated from equations (1). The last step consists of constructing with the help of the three methods described in the preceeding paragraphe the cumulative distribution from the masses restituted by the impactor. The different cumulative distributions chosen are described below. The original distribution is represented by the heavy line, the ECAD by squares, the EDS/triangle, and the values given by the Picknett method by circles.

a) Two log-normal functions (MMD = 2 µm, σg = 2 ; MMD = 5 µm, σg = 2.5) are shown in Figures 9 and 10. These distributions can be considered as typical of aerosols correctly analyzes by the ANDERSEN impactor. Under these conditions the three methods are about equal in restituting the original distribution.

b) A bimodal distribution is shown in Figure 11, containing two log-normal distributions of MMD 1 µm and 7 µm mixed in equal proportions. The Picknett method seems to be the best adapted for describing this bimodal distribution except in areas of small diameters.

c) Figure 12 shows a weakly dispersed (σg = 1.5) log-normal distribution having a small MMD (0.3 µm). The EDS method is the best in this case because the restitution is practically perfect.

d) Also tested (Figure 13) is a weakly dispersed (σg = 1.5) log-normal distribution but whose MMD (15 µm) represents a limit for the use of the

ANDERSEN impactor (93% of the mass is stopped on the first stage). In this case the EDS provide the most precise information but only for a small range of diameters. The Picknett method also properly restitutes the distribution.

The comparison of the different methods, making it possible to set up the cumulative mass distribution from the results obtained by the impactor, shows that the EDS and the Picknett methods are the best adapted to restituting a distribution with an uncertainty not exceeding 5% for the MMD and 10% for the standard deviation. Moreover, the EDS method is easier to use if the general shape of the distribution is known and if it has a simple analytical form (log-normal, for example).

CONCLUSION

Without underestimating the importance of a method for setting up distributions, it should be noted that the main sources of incertitude in using impactors come essentially from the parameters which can alter the collection efficiency curves of the various stages.

The most influencial parameters are wall loss, blow-off, and bounce, the importance of which depends on the maximum mass admissible by the impactor and on the nature of the collection surface. Moreover, as the procedures are complex, a purely theoretical treatment is not possible, and only an experimental approach makes it possible to understand how an impactor really operates and how to minimize its shortcomings.

BIBLIOGRAPHY

(1) MARPLE, V.A. and KLAUS WILLEKE
"Inertial impactors : Theory, design and use" Fine particles p. 411, Edited by B.Y.H. LIU, Academic Press, Inc. (1975)

(2) RAO, A.K. and WHITBY, K.T.
"Non-ideal collection characteristics of inertial impactors I and II" J. Aerosol Sci., Vol 9, p. 77 (1978)

(3) BERGLUND, R.N. and LIU, B.Y.H.
"Generation of monodisperse aerosol standards", Env. Sci. Technol., Vol 7, p. 147 (1973)

(4) STÖBER, W. and FLACHSBART, H.
"An evaluation of nebulized ammonium fluorescein as a laboratory aerosol", Atm. Env., Vol 7, p. 737 (1973)

(5) FERMANDJIAN, J., MALET, J.C., CASSELMAN, C, DUVERGER, G., BOULAUD, D., MADELAINE, G.
"Interpretation of the behavior of aerosols generated by a sodium pool fire", Paper presented to this meeting (1980)

(6) SOOLE, B.W.
"Concerning the calibration constants of cascade impactors, with special reference to the Casella", J. Aerosol Sci., Vol 2, p. 1 (1971)

(7) PICKNETT, R.G.
"A new method of determining aerosol size distributions from multi-stages sampler data", J. Aerosol Sci., Vol 3, p; 185 (1972)

(8) WELLS, B.J.
"An evaluation of the MAY type of cascade impactor", Health Physics, Vol 13, p. 1001 (1967)

TABLE IV

MMD (µm)		0.5		4		15	
σg	stage	EDS	emmd	EDS	emmd	EDS	emmd
	1	1.77	1.77	6.57	7.6	8.88	15.75
	2	1.77	1.77	5.05	5.66	6.5	8.0
	3	1.77	1.77	4.18	4.6	5.3	6.05
1,5	4	1.77	1.77	3.06	3.6	4.23	4.95
	5	1.1	1.21	1.8	2.6	4.23	4.23
	6	0.86	0.94	1.3	1.65	4.23	4.23
	7	0.57	0.67	1.13	1.23	4.23	4.23
	8	0.35	0.45	1.13	1.13	4.23	4.23
	1	7.6	8.74	7.82	11.85	11.09	23.33
	2	4.35	5.15	5.44	6.46	7.35	9.14
	3	3.4	3.76	4.27	4.81	5.61	6.48
2.5	4	2.42	2.78	2.98	3.57	3.82	4.75
	5	1.46	1.8	1.66	2.3	2.1	3.08
	6	0.97	1.17	1.1	1.39	1.41	1.82
	7	0.56	0.73	0.64	0.90	0.85	1.21
	8	0.33	0.43	0.38	0.54	0.85	0.86
	1	7.96	12.57	12.9	26.78	21	-
	2	5.26	6.33	8.01	10.07	12.27	16.04
	3	4.07	4.6	5.93	6.88	8.77	10.4
5	4	2.82	3.34	3.87	4.8	5.47	7.0
	5	1.58	2.064	2.0	2.80	2.7	3.96
	6	1.02	1.26	1.25	1.6	1.64	2.15
	7	0.58	0.76	0.685	0.95	0.90	1.27
	8	0.33	0.43	0.383	0.53	0.49	0.70

These values have been corrected for the absence of particles > 50 µm on stage 1.

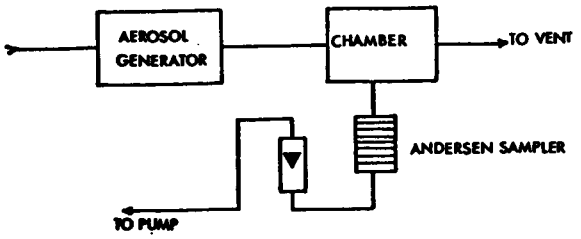

Fig. 1 : Schematic diagram of the experimental set up

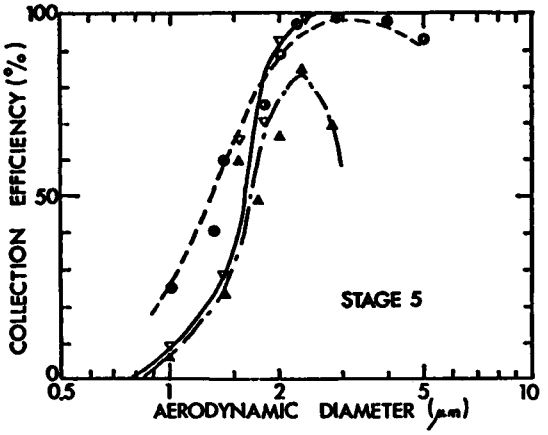

Fig. 2 : Stage 5 collection characteristics of the ANDERSEN sampler (white triangle : coated glass plates ; black triangle uncoated glass plates ; black circle : glass fiber filter)

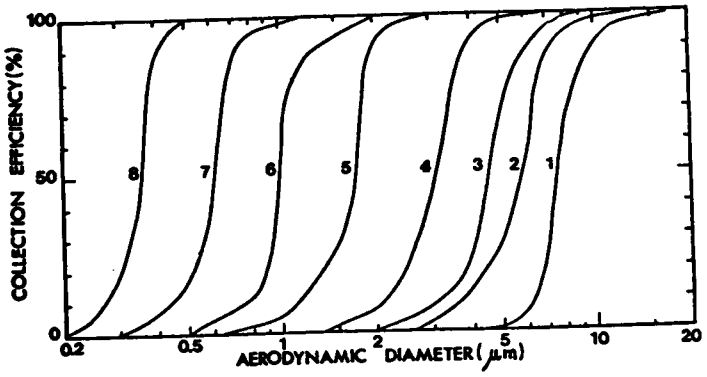

Fig. 3 : ANDERSEN Mark II collection characteristics

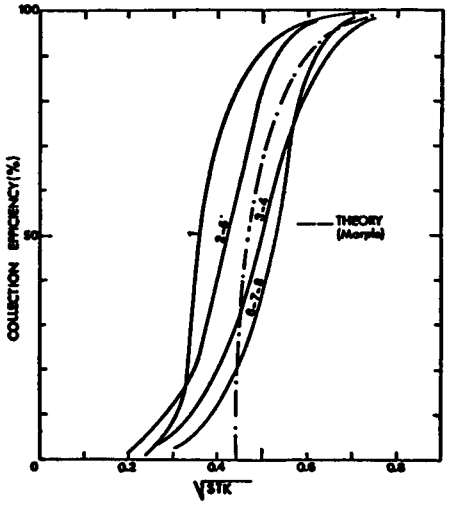

Fig. 4 : Collection efficiency as a function of square root of Stokes number

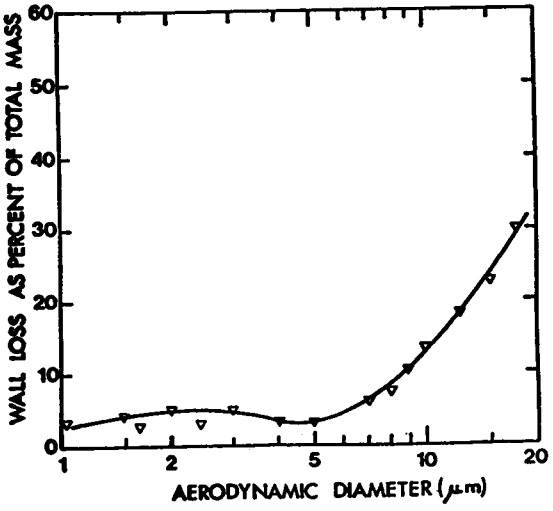

Fig. 5 : Wall losses of the ANDERSEN sampler

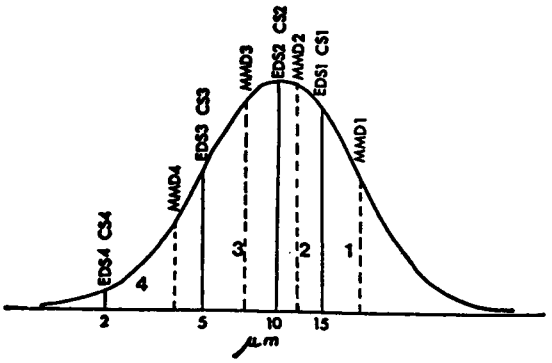

Fig. 6 : Log normal mass distribution (MMD = 10 µm, σ_g = 2) showing calibration diameters for an ideal impactor

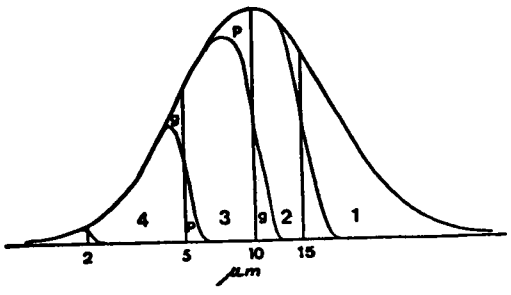

Fig. 7 : As Fig. 6 for a real impactor (g areas indicate gain of mass, p areas indicate loss of mass compared with an ideal impactor)

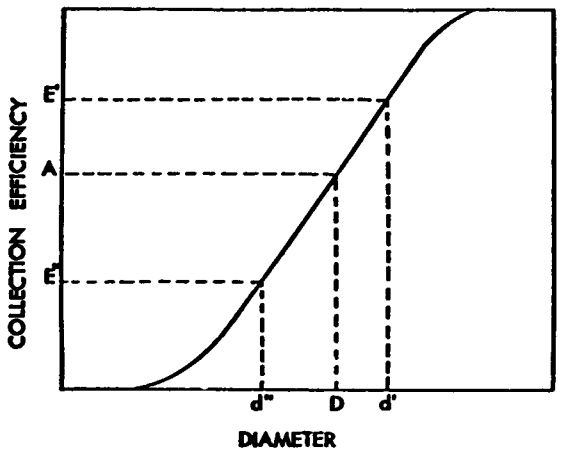

Fig. 8 : Collection efficiency curve for a single impaction stage

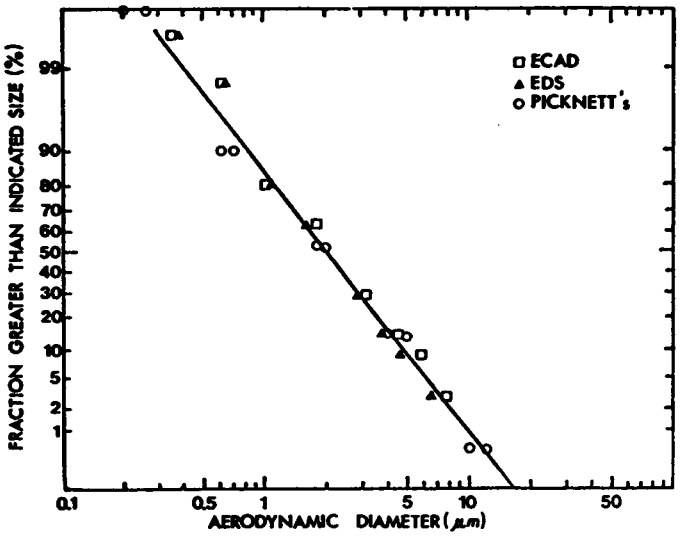

Fig. 9 : Log normal distribution (MMD = 2 μm, σg = 2). (⟶) original distribution

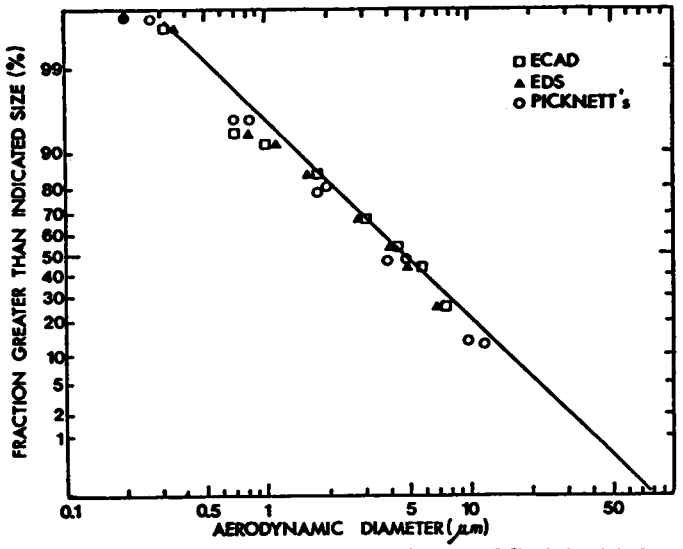

Fig. 10 : Log normal distribution (MMD = 5 μm, σg = 2.5). (⟶) original distribution

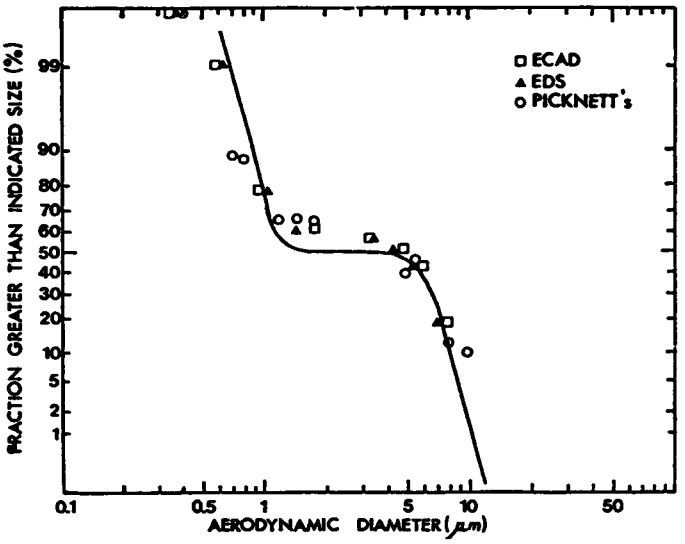

Fig. 11 : Bimodal size distribution (MMD_1 = 1 μm ; MMD_2 = 7 μm). (⟶) original distribution

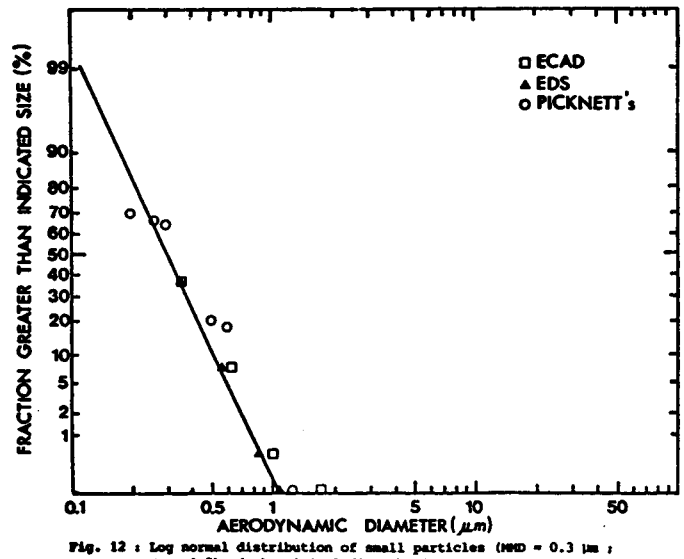

Fig. 12 : Log normal distribution of small particles (MMD = 0.3 μm ; σg = 1.5). (⟶) original distribution

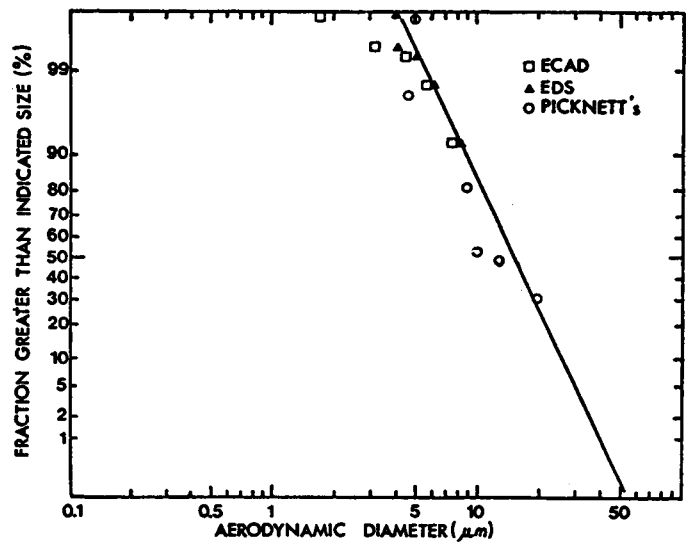

Fig. 13 : Log normal distribution of large particles (MMD = 15 μm ; σg = 1.5). (⟶) original distribution

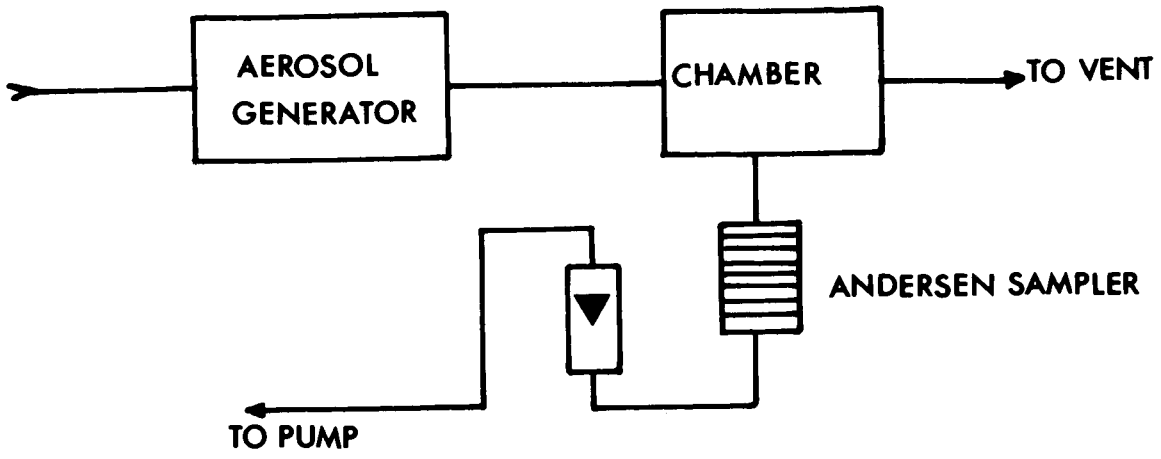

Fig. 1 : Schematic diagram of the experimental set up

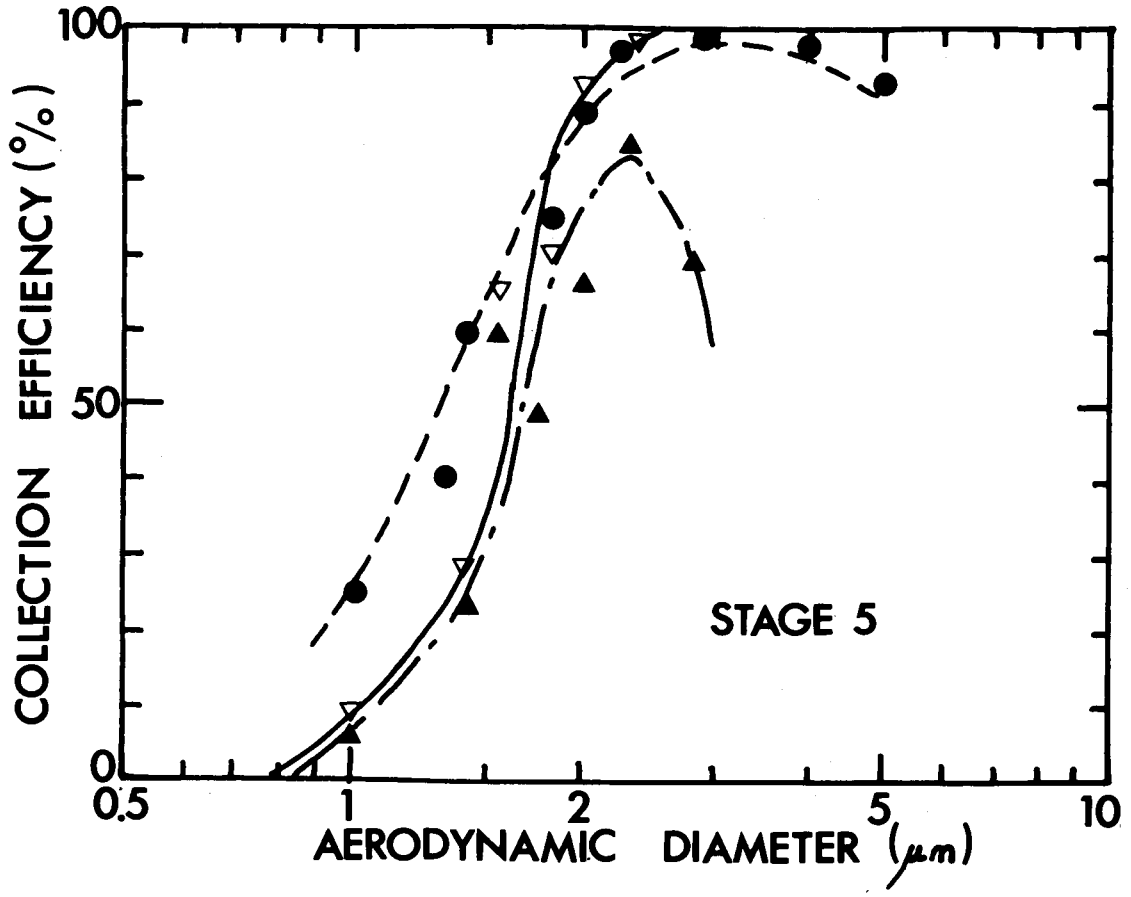

Fig. 2 : Stage 5 collection characteristics of the ANDERSEN sampler (white triangle : coated glass plates ; black triangle uncoated glass plates ; black circle : glass fiber filter)

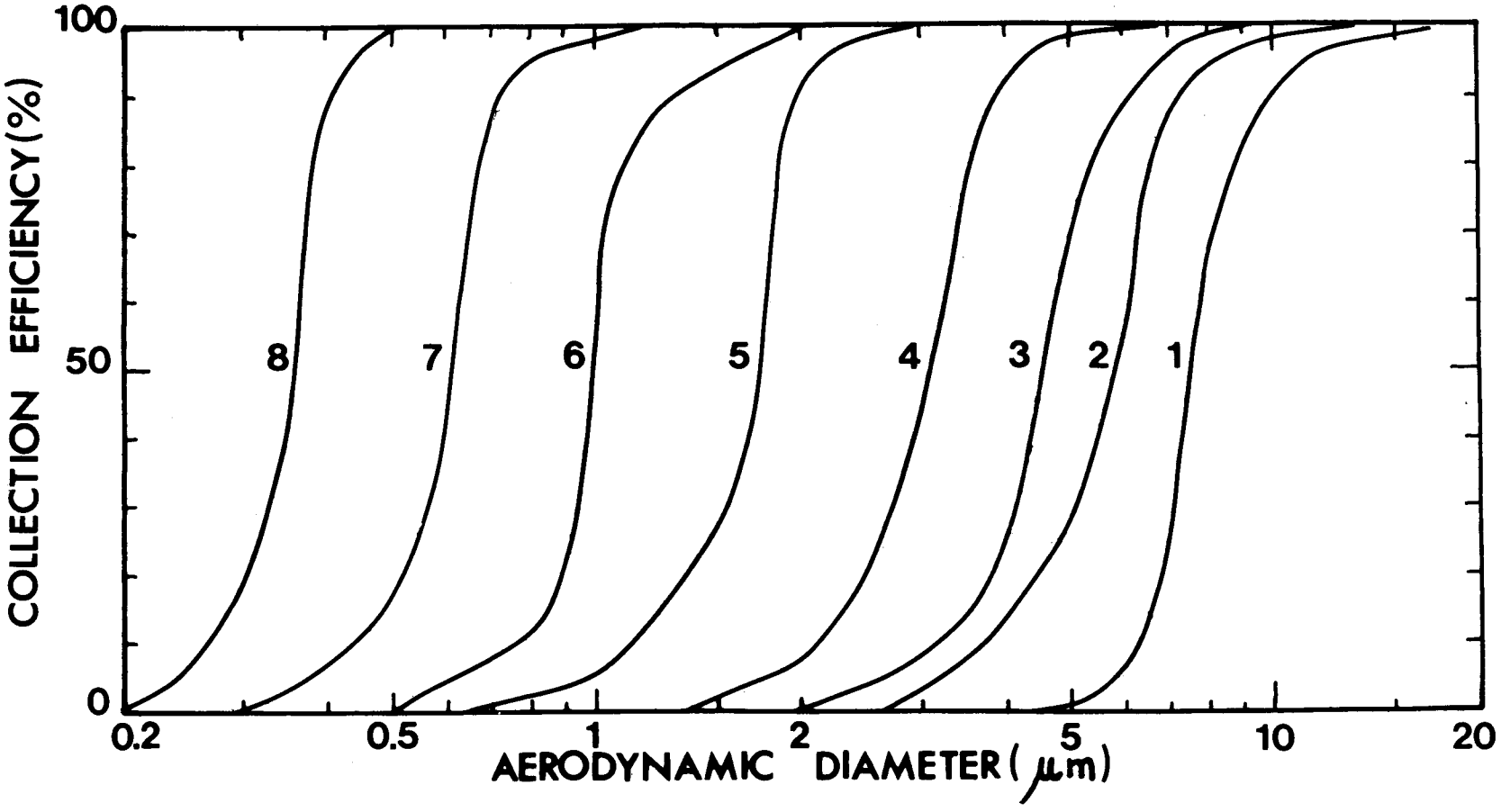

Fig. 3 : ANDERSEN Mark II collection characteristics

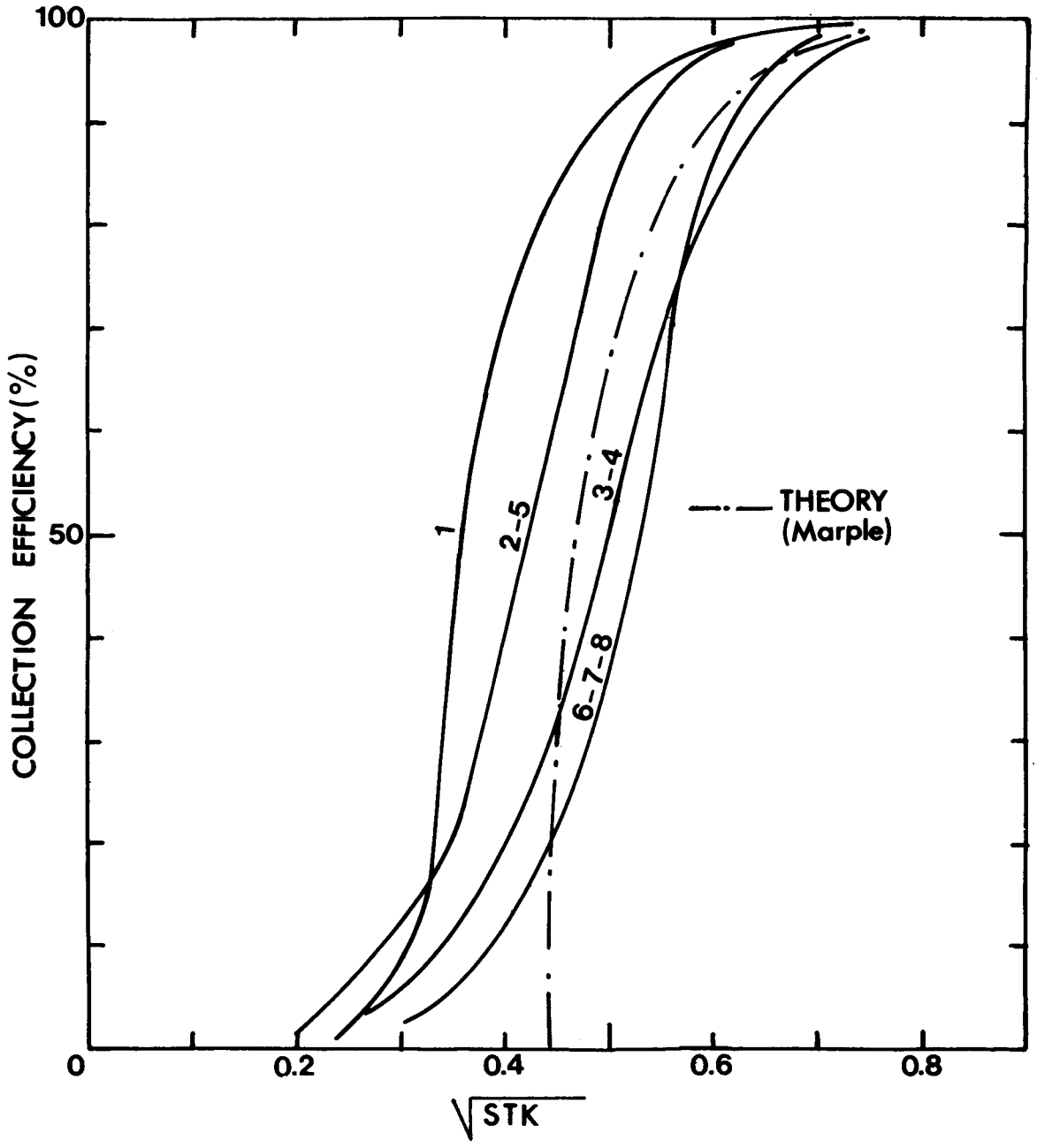

Fig. 4 : Collection efficiency as a function of square root of Stokes number

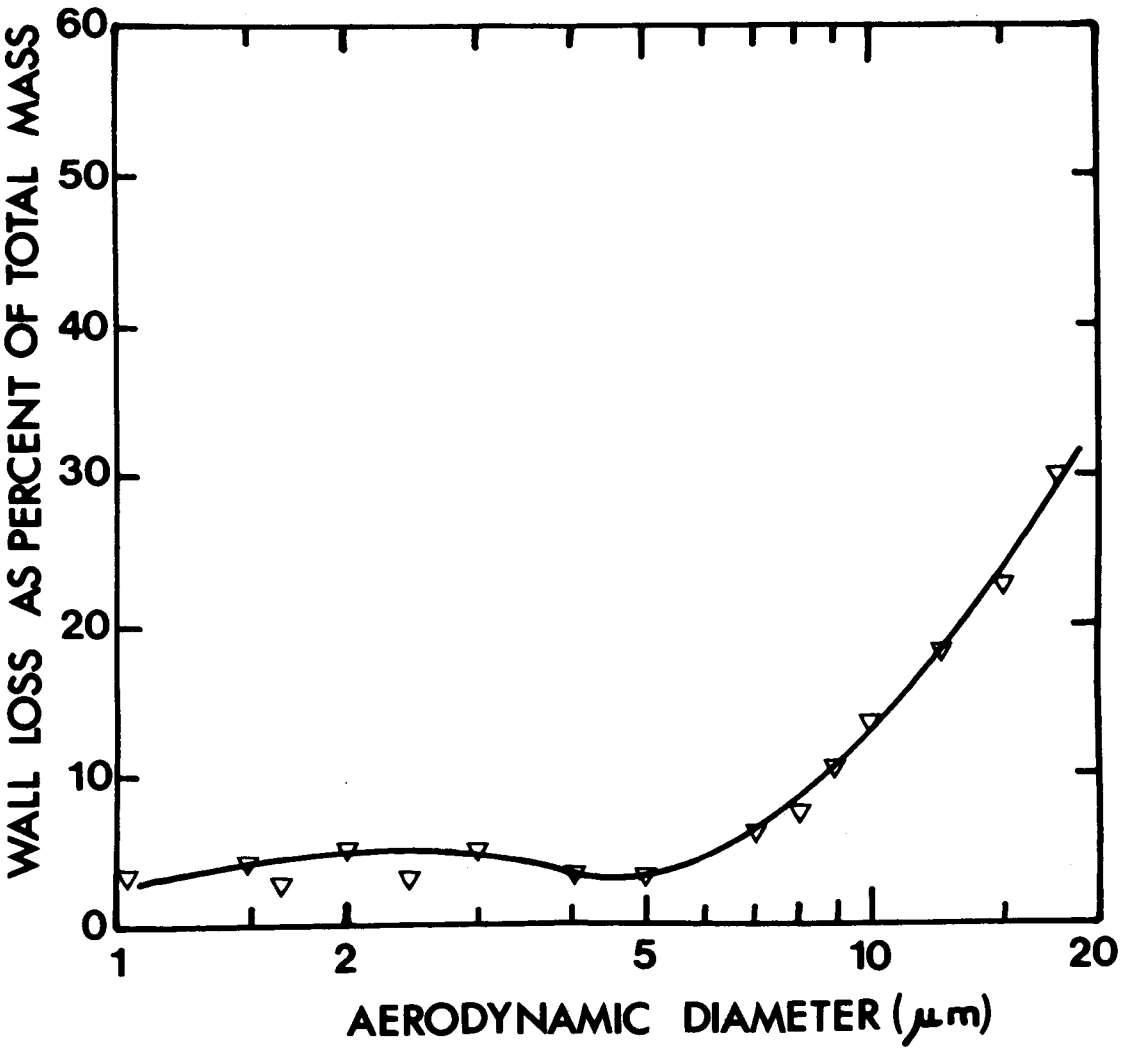

Fig. 5 : Wall losses of the ANDERSEN sampler

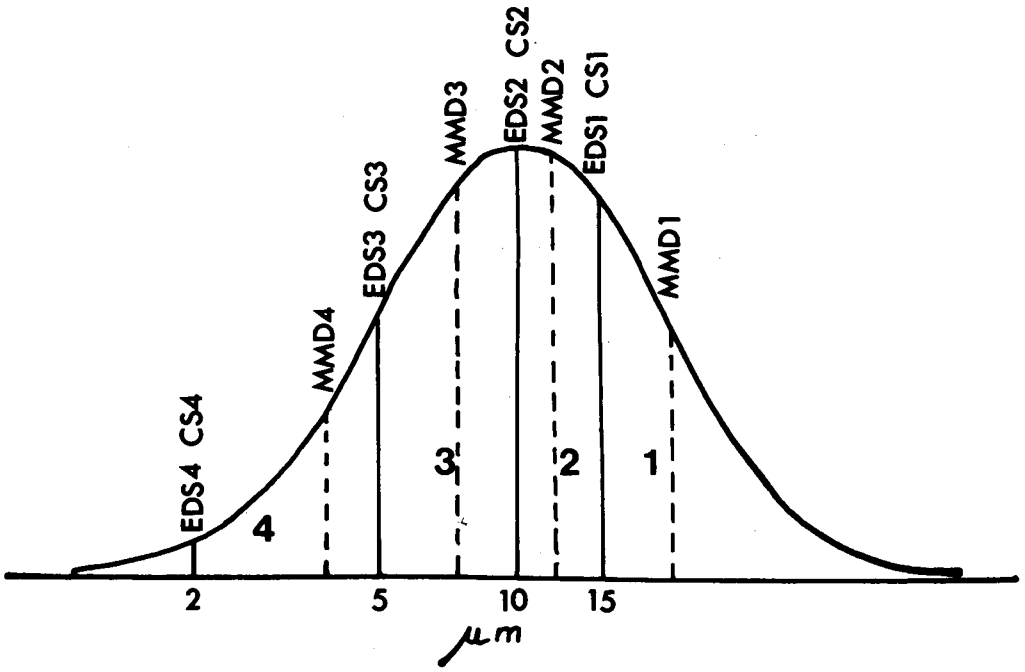

Fig. 6 : Log normal mass distribution (MMD = 10 µm, σg = 2) showing calibration diameters for an ideal impactor

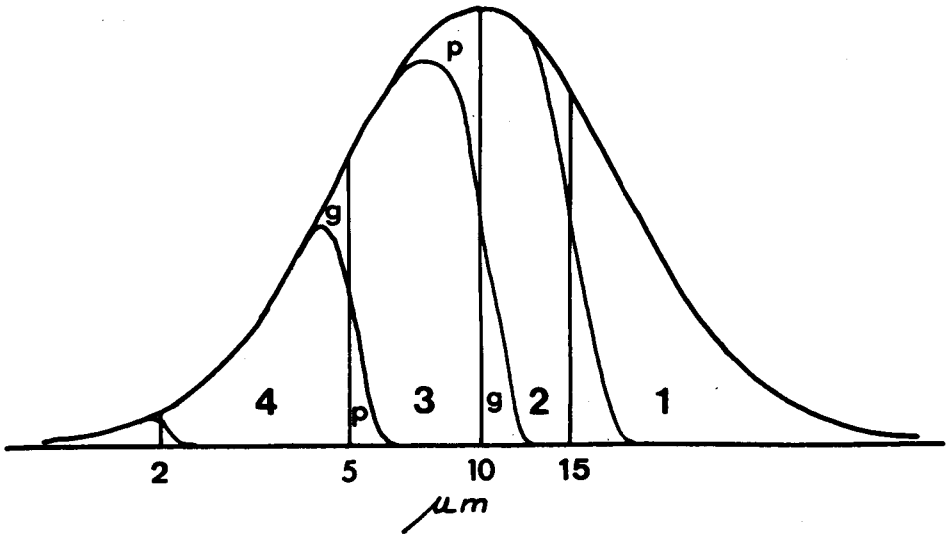

Fig. 7 : As Fig. 6 for a real impactor (g areas indicate gain of mass, p areas indicate loss of mass compared with an ideal impactor)

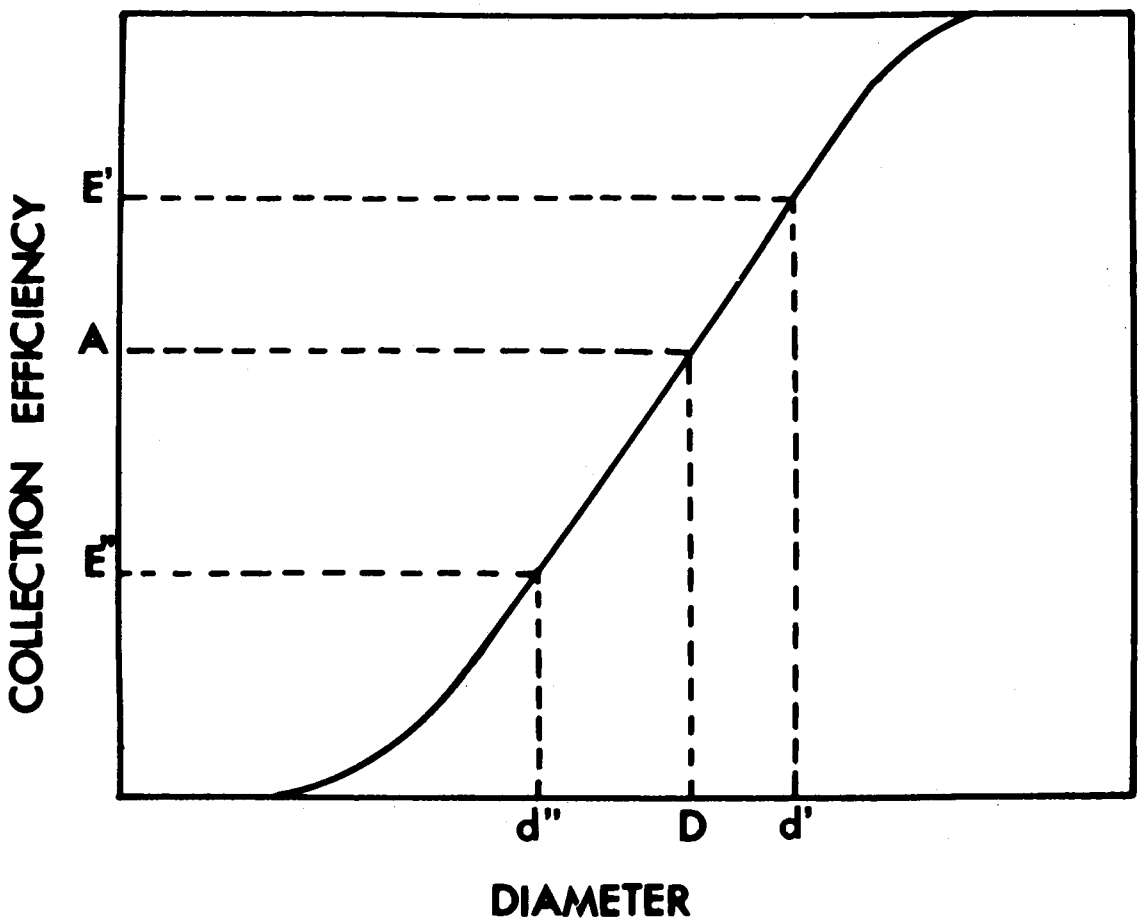

Fig. 8 : Collection efficiency curve for a single impaction stage

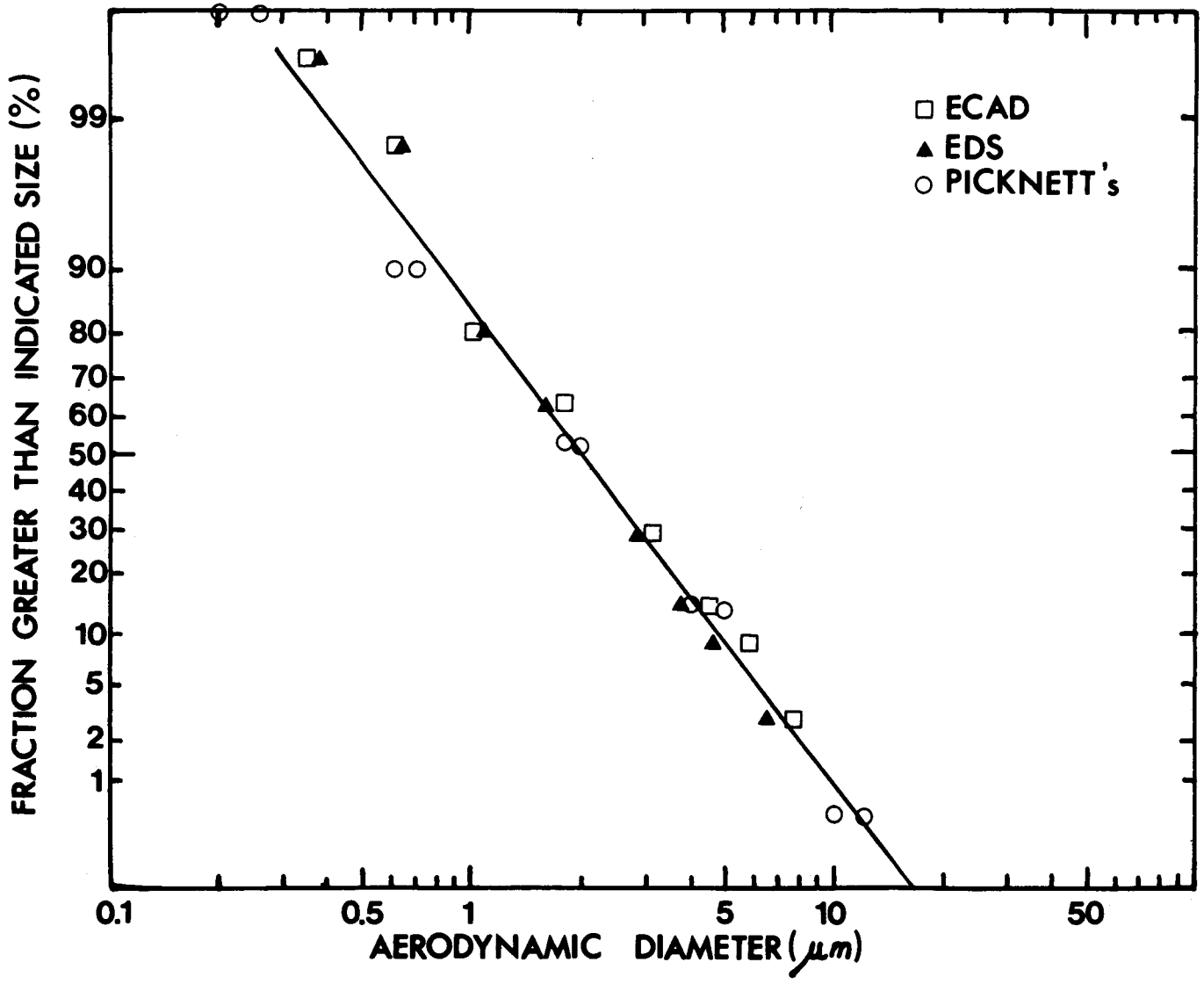

Fig. 9 : Log normal distribution (MMD = 2 μm, σg = 2). (—) original distribution

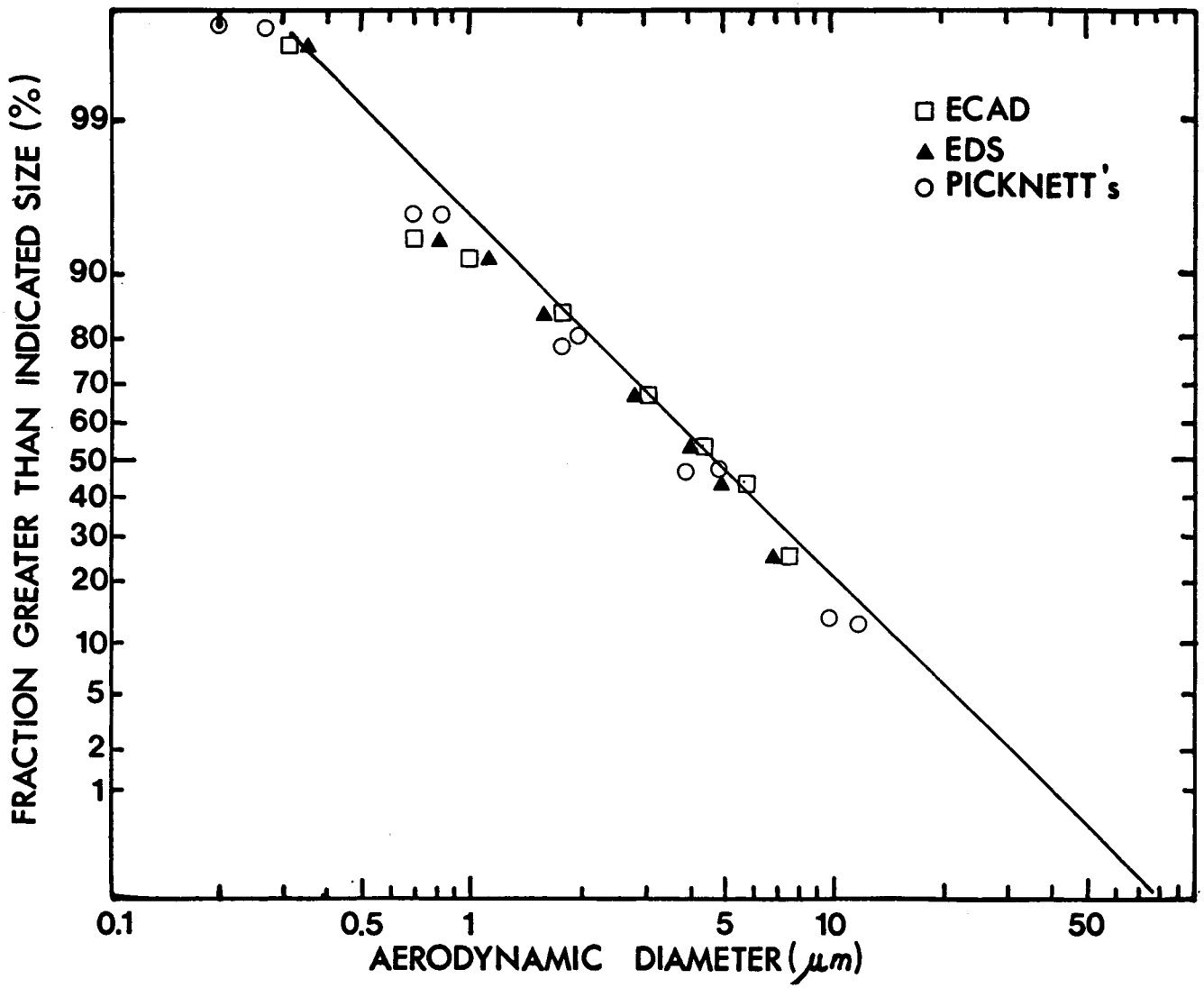

Fig. 10 : Log normal distribution (MMD = 5 μm, σg = 2.5). (—) original distribution

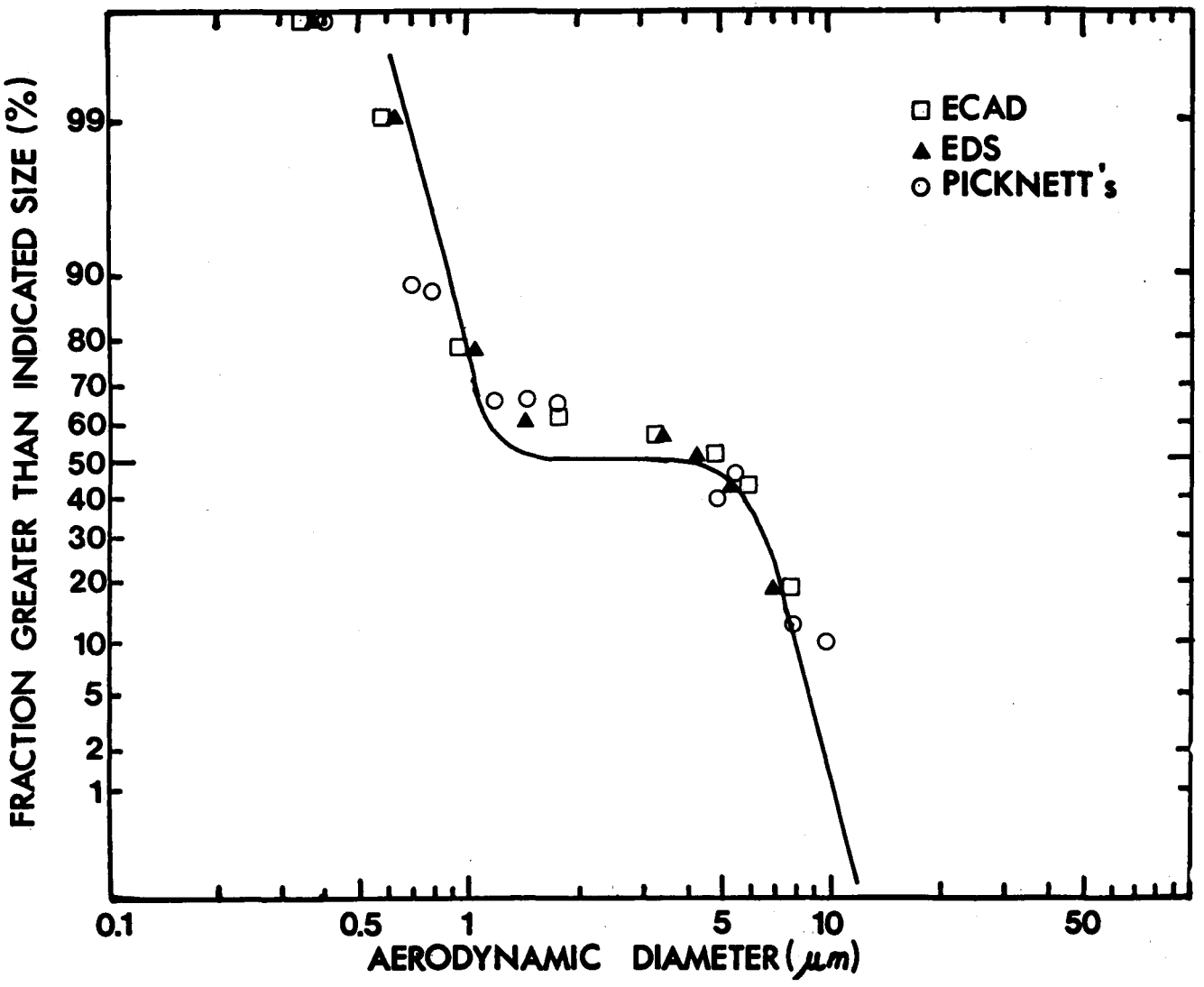

Fig. 11 : Bimodal size distribution (MMD_1 = 1 μm ; MMD_2 = 7 μm).
(—) original distribution

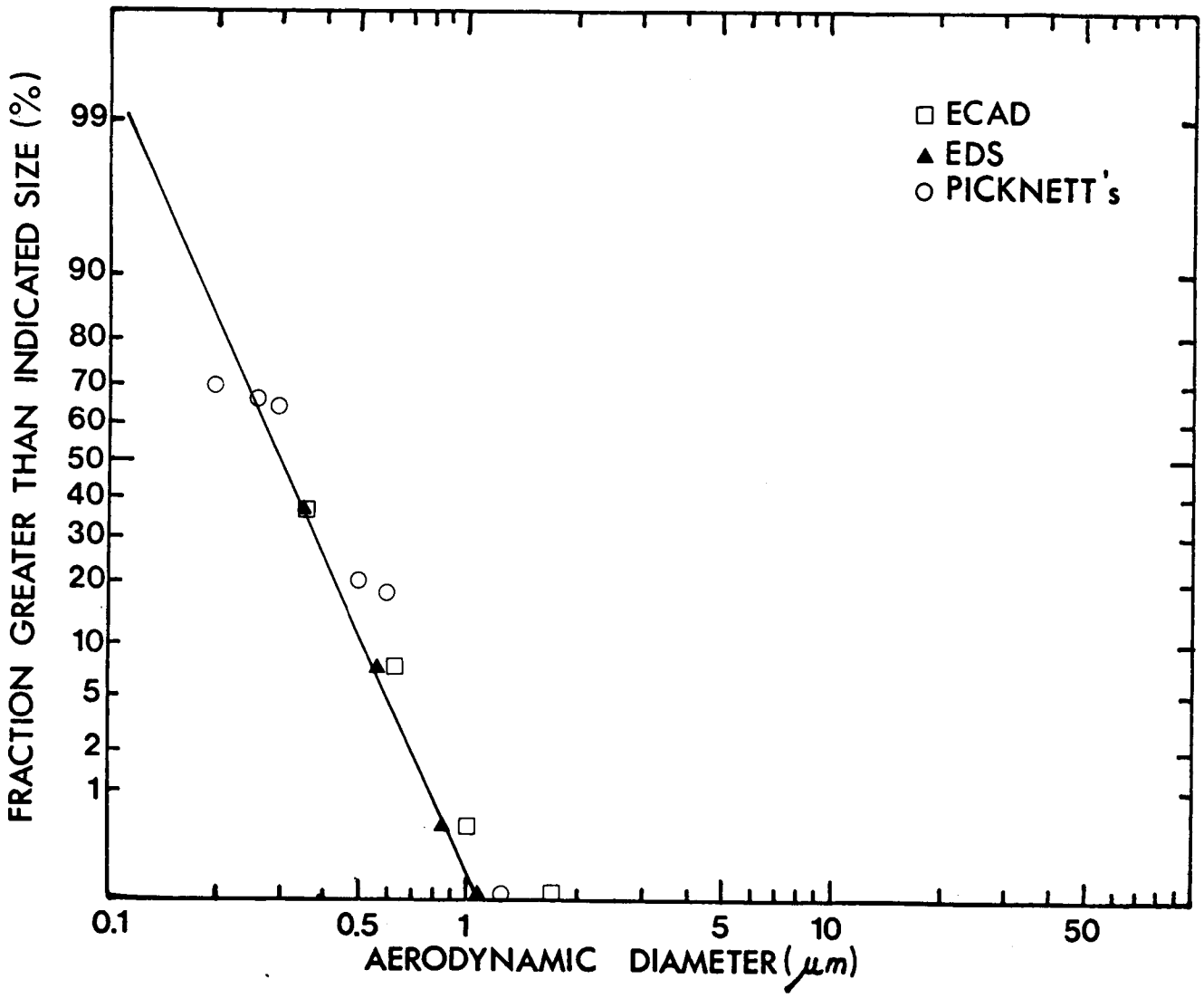

Fig. 12 : Log normal distribution of small particles (MMD = 0.3 μm ; σg = 1.5). (—) original distribution

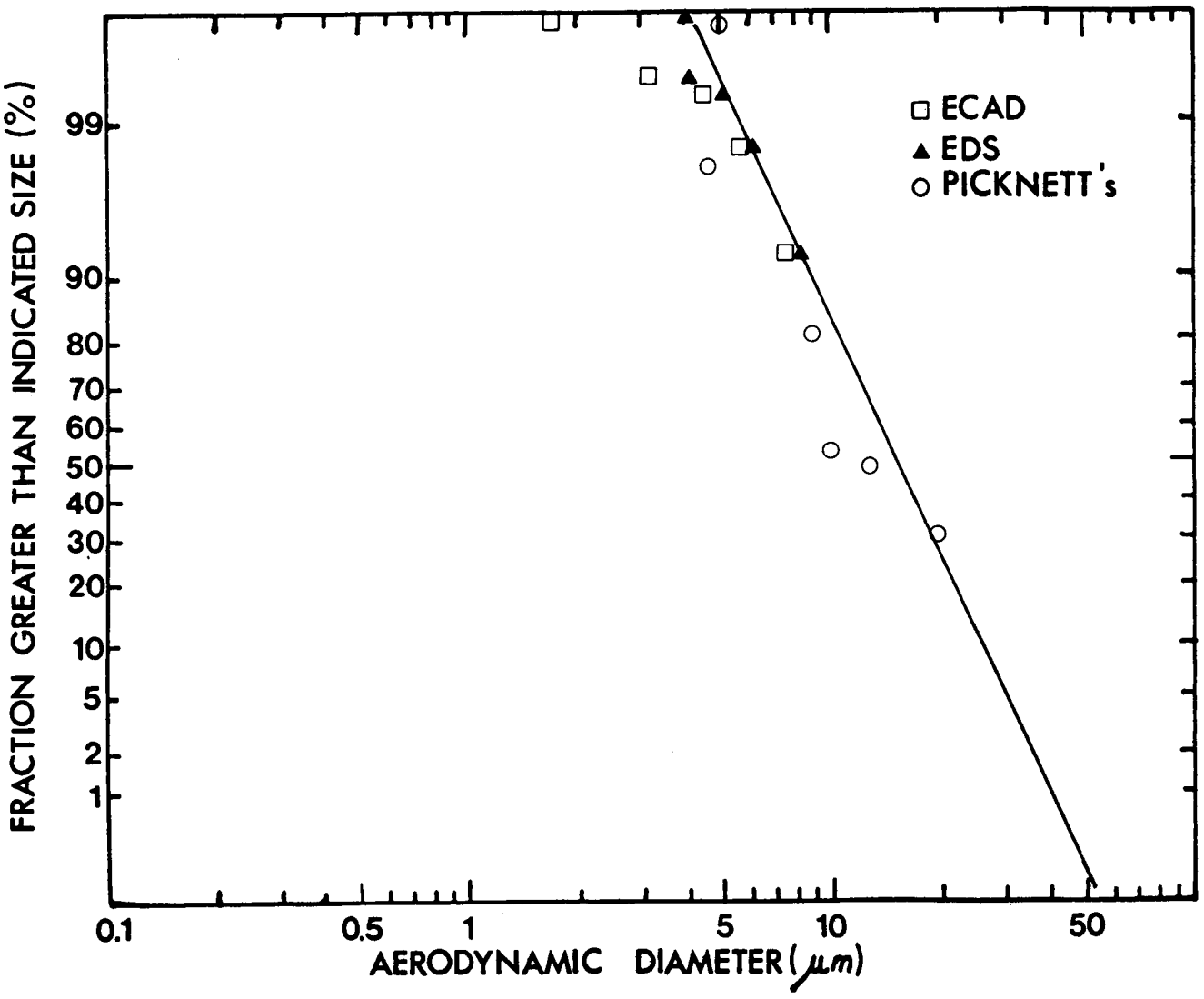

Fig. 13 : Log normal distribution of large particles (MMD = 15 μm ; σg = 1.5). (—) original distribution

WINFRITH STUDIES RELATED TO NUCLEAR AEROSOLS AND THE FAST REACTOR SAFETY PROGRAMME

J V Boyd, T R Holland, A L Nichols
AEE Winfrith
Dorchester, Dorset, UK

ABSTRACT

A laboratory devoted to fast reactor aerosol studies has been established at AEE Winfrith. The prime aim is to develop the necessary practical expertise to understand and evaluate nuclear aerosol data associated with hazardous emissions and clean-up plant. Our preliminary studies have been associated with two major problems involving sodium fires:

(1) representative sampling and physical analysis of sodium oxide aerosols,

(2) the determination of the sodium hydroxide-carbonate aerosol conversion rate.

The aerodynamic equivalent diameter and shape factors for a nuclear aerosol are very important in aerosol physics modelling codes. In situ analysis of sodium fire aerosols is not feasible with present techniques and the transfer of aerosol samples between the burn chamber and analytical equipment is important. Our aim is to study and develop sampling techniques that minimize such adverse effects as particle break up and/or agglomeration in the sampling lines and body of the analysis equipment prior to analysis. In association with these sampling studies, various forms of impactor design are being compared to determine their suitability for the measurement of aerodynamic equivalent diameters. Attempts are also being made to evaluate specific nuclear aerosol analysis equipment with a standard sodium oxide aerosol generated in well defined conditions. The movement of this standard sodium oxide aerosol by means of an air ejector system is being studied.

Preliminary studies have also been made with respect to the suitability of differential thermal analysis techniques to probe the chemical reaction between sodium hydroxide aerosol and carbon dioxide. The initial data will be presented in terms of the advantages, feasibility and limitation of this technique coupled to thermogravimetric analysis (DTA/TG).

1. INTRODUCTION

The release and transport of nuclear aerosols following a hypothetical core disruptive accident in a sodium-cooled fast reactor can be predicted by a number of aerosol modelling codes [1-5]. These computer codes require the introduction of a number of important input parameters or source terms before they can produce reasonable predictions of aerosol movement into the secondary containment and beyond. A recent critical review [6] emphasised the need to estimate the uncertainties associated with these input data and to assess their consequences with respect to radiological effects.

Included in these input data are source terms for aerosol formation/agglomeration which can be affected by chemical interaction. Uncertainties for these parameters can only be assessed by detailed practical studies and careful evaluation of the various experimental techniques. In April 1979 a NEA CSNI (Nuclear Energy Agency Committee on the Safety of Nuclear Installations) meeting [7] was unable to achieve a common consensus of opinion on the uncertainties arising from the measurement of nuclear aerosols. As a contribution to the resolution of this unsatisfactory situation, we have undertaken a detailed study of the uncertainties associated with the Andersen cascade impactor technique for the measurement of the aerodynamic equivalent diameter and particle size distribution of sodium fire aerosols. We also report our preliminary studies to monitor the concomitant effects of the chemical reactions between sodium oxide particles and water vapour/carbon dioxide in ambient air.

2. THE ANDERSEN CASCADE IMPACTOR

The Andersen impactor is a multi-stage round jet cascade impactor normally used in environmental studies to measure the size distribution (aerodynamic equivalent diameter) and total concentration of liquid and solid particulate matter [8,9]. The commercially available aluminium model [10] has been calibrated with unit density spherical particles, but is unsuitable to handle corrosive sodium oxide/hydroxide aerosols. We have manufactured a stainless steel version comprising eight stages held together with three spring clamps and O-ring seals. This stainless steel impactor has been compared with the commercial model and shows good agreement when operating at the recommended flow rate of 4.7×10^{-4} m^3 s^{-1} (1 ft^3 min^{-1}). Each stage contains precision drilled holes as detailed in Figure 1. The size of these jets is constant for each stage and decreases in each succeeding stage. Impaction on a particular collecting plate is dependent upon the aerodynamic equivalent diameter of the particle in the air flow through these jets.

Cascade impactors have been used regularly to monitor the particle size distributions of ageing sodium fire aerosols [11-13]. A major criticism of the technique is that the majority of impactors have been designed to analyse environmental/atmospheric aerosols (10^2 - 10^4 particles cm^{-3}) rather than high density (10^7 particles cm^{-3}) sodium fire aerosols. Great care needs to be taken to prevent overloading of impactor stages, and the time taken to collect samples has to be carefully controlled.

2.1 PARTICLE SIZE DISTRIBUTIONS

Small pool fires of sodium lasting 2-3 min were generated in a burn chamber of 0.74 m^3 with a floor area of 0.57 m^2. Accurately weighed quantities of (10.0 ± 0.1) g of sodium metal were ignited by means of a hot plate in a static atmosphere in which the relative humidity could not be controlled. The temperature within the burn chamber rose from 35 to 40°C during the fire and approximately 5% of the burning sodium formed an aerosol of sodium oxide. Two identical Andersen impactors placed inside the burn chamber and equidistant from the aerosol source were used to monitor aerosol particle size distributions at fixed periods of time after the start of the sodium fire. During sampling the flow rate through the impactors was maintained at 4.7 x 10^{-4} m^3 s^{-1} and the time taken to obtain a sample was varied to prevent stage overloading. Immediately before sampling the aerosol Perspex covers placed over the top of the impactors were removed. When the impactors were dismantled the stainless steel collecting plates were washed with a fixed volume of dilute hydrochloric acid for analysis by atomic absorption spectroscopy.

These experiments were repeated to determine experimental reproducibility and the relative humidity was noted prior to each experiment. Table I summarizes these initial experiments and Figures 2-4 illustrate three methods [14] of presenting the aerodynamic equivalent diameter-cumulative mass frequency data arising from these studies. The mean data represent the quantities of sodium deposited on the eight impactor stages when plotted against the upper limit of the defined particle size range of these stages. The most satisfactory linear relation is given by the logarithmic-probability presentation of Figure 4. However, the data show a distinct curvature for the samples taken after 1 min, which becomes even more pronounced and distorted beyond 10 min as the aerosol ages. Similar effects have been observed in other laboratories [12,13]. This makes the definition of sodium oxide aerosols in terms of d_{50} (particle diameter at 50% cumulative mass frequency) and σ_g (standard deviation) questionable when obtained from the assumption of a log normal distribution. Table II lists the values obtained from Figure 4 and their random error uncertainties. The standard deviation can be estimated using two formulae

$$\sigma_g = \frac{d_{50}}{d_{15.87}} \quad \text{or} \quad \frac{d_{84.13}}{d_{50}}$$

and both calculations are included in Table II to illustrate the deviation of the data from linearity. This has been defined in terms of an asymmetry parameter in Table II. This parameter is constant as the aerosol ages over the cumulative mass frequency range 15-85% and therefore is not affected by the more dramatic deviation from log normal distribution at the two extremes in particle size for the 20-30 min aerosols. The general consensus [15] is that log normal distributions are appropriate in the definition of primary aerosol particles, but their application to suspended aerosol agglomerates is more contentious.

Arguably, it is preferable to plot the curves (Figure 4) and use them to produce equal increment histograms (Figure 5) and distribution curves rather than distort the data to achieve log normality. The resultant

histograms clearly show the gradual change in the aerosol particle size distribution with time. As the sodium oxide aerosol is being generated (1 min) the modal value of particle size is between 0.4 - 0.8 μm; as the aerosol agglomerates and plates out, not only does the aerosol concentration decline but the modal value increases to 1.2 - 1.6 μm within 30 min.

The AEROSIM computer program [5] has been developed in the UK to predict the behaviour of non-vaporizing particles in a non-condensing stirred containment. The evolution of this program is linked to safety studies of the sodium-cooled fast breeder reactor and includes a number of limitations [1]. The results of our experiments with relatively low density sodium fire aerosols have been compared with the predictions of AEROSIM. This comparison has been undertaken by B C Walker and the results are presented in the appendix.

2.2 CHANGES IN RELATIVE HUMIDITY

The presence of water vapour in the atmosphere has been shown to increase the measured particle size distribution of sodium fire aerosols [16]. Sodium hydroxide droplets are formed at relative humidities above 40% [17] and may significantly affect the reproducibility of the experiments listed in Table I. Examples of the effects of the uncontrollable variations in relative humidity upon the sodium fire aerosol cumulative mass frequency data are shown in Figures 6 and 7. The changes that occur in the particle size distribution with a change from $(40 \pm 1)\%$ to $(50 \pm 1)\%$ in the relative humidity fall within the statistical errors of the data as defined in section 2.3. However, even for such a small change in the relative humidity, there is sufficient indication of an increase in the percentage frequency of larger particles with increase in relative humidity. Arguably these changes may be attributed to the chemical changes (see section 4) that will occur more rapidly at the higher humidity.

2.3 RANDOM ERRORS

The precision of the Andersen impactor technique has been estimated using the replicated results of the experiments listed in Table I. The mean values of the data and the 95% confidence limits are shown in Figures 8 and 9. These limits have been derived using Student's t-test. Even allowing for these random errors, the data show pronounced curvature and the comments and conclusions of section 2.1 still apply.

2.4 SYSTEMATIC ERRORS

Recent experiments by Parker et al [18] have thrown doubt on impactor studies of nuclear aerosols, suggesting that particles may break up or agglomerate within the body of the instrument either prior to impaction or as a result of the impaction process. This question of systematic errors throws doubt upon the validity of any nuclear aerosol impactor data.

The use of characterized and monodispersed aerosols (low density liquid aerosols such as di-octyl phthalate or olive oil) will accurately determine the particle size collecting efficiency of individual impactor stages [9, 19,20]. This calibration of individual impactors is very important.

However, it is questionable whether such experiments will aid in the identification of any problems associated with nuclear aerosol sampling and impaction within the instrument, if such problems really exist. A standard sodium oxide aerosol which can be characterized by means of optical and electron microscopy should be generated for sodium fire aerosol studies. This requires the burning of a fixed quantity of sodium in a sufficiently large controlled atmosphere environment. We hope to achieve this objective with the construction of a 6 m^3 controlled atmosphere burn chamber directly attached to a 3 m^3 controlled atmosphere analysis chamber.

3. REPRESENTATIVE SAMPLING OF SODIUM FIRE AEROSOLS

Ideally aerosol measurements should be undertaken in situ in conditions that do not disturb the physical form of the aerosol. This approach can be achieved with relatively low density aerosols containing particles above a critical size of approximately 5 μm [21,22]. However, because of their high particle concentration, current experiments to study sodium fire aerosols involve sucking a sample of the particles into a measuring region resulting in the following problems:

(i) disturbance of the sample,

(ii) delayed analysis of the sample after it passes along the sampling line,

(iii) lack of detailed positional information on individual particles.

Apart from aerosol movement caused by convection currents, sodium fires produce relatively motionless aerosols. Inappropriate sampling techniques may cause distortions in the measured particle size distribution arising from sample losses (agglomeration and plate-out) and gains (particle break-up and resuspension) along the sample line [7].

We have undertaken studies to determine the effects of varying sample flow rates along an extended sampling line shown in Figure 10. Sodium oxide aerosols with a maximum concentration of approximately 1.2 $\mu g\ cm^{-3}$ were generated in the burn chamber as described previously in section 2.1. At a specified time during or after the fire, the aerosol was analysed by means of two identical Andersen impactors. One of these was placed inside the burn chamber as shown in Figure 10; the other analysed a sample of the same aerosol via copper and flexible polythene tubing and a vented polythene chamber. In this way differences between the two sets of aerosol particle size data will reflect differences in the sampling procedures and should be independent of any systematic errors associated with the impactors. The sample line had a diameter of 2.5 cm and was 120 cm long with a right angle bend inside the burn chamber. When taking aerosol samples the flow rate through both impactors was maintained at the recommended value of $4.7 \times 10^{-4}\ m^3\ s^{-1}$. Only the flow rate of aerosol between the burn chamber and the plenum chamber was varied by means of a simple air ejector system. Compressed air was fed in mid-way along the sample line and directed towards the plenum chamber: this created a venturi effect and accelerated the flow of aerosol from the burn chamber to the vented plenum chamber. This

compressed air sampling system was only switched on when the impactors were operating. Details of the sampling aerosol flow rates are given in Table III and show that the inflow of compressed air diluted the plenum chamber aerosol by 25%.

Table IV lists the extent of our preliminary experiments and Figures 11-13 are examples of equivalent sets of data from the two impactors plotted on logarithmic-probability scales. Initial experiments, without the air ejector operating and with flow rates of 4.7×10^{-4} m^3 s^{-1}, showed remarkably good agreement (Figure 11) between the two impactors despite the extensive 120 cm journey of one of the aerosol samples. This agreement was excellent for all samples taken 30 sec - 30 min after sodium ignition. At higher flow rates to the plenum chamber (Figures 12 and 13) differences in equivalent impactor data depended upon the time at which sampling occurred and the flow rate induced by the air ejector. Figure 14 shows equal increment histograms of particle size for three different air ejector flow rates, all at 5 min after sodium ignition. The most significant differences occur at the higher aerosol flow rates ($>1.5 \times 10^{-2}$ m^3 s^{-1}) when all the relevant data show a break-up of particles in the 1.2 - 3.6 μm size range with a concomitant increase in the particles in the 0.4 - 0.8 μm size range. Agreement between equivalent impactor data at specific aerosol ageing times does occur below a flow rate of 1.5×10^{-2} m^3 s^{-1}, but this seems to be a transient effect and a complex function of the aerosol sampling flow rate and size distribution.

Somewhat surprisingly, these preliminary experiments indicate that, provided the recommended impactor flow rate of 4.7×10^{-4} m^3 s^{-1} is maintained, sodium fire aerosols with a concentration of 1.2 μg cm^{-3} can be satisfactorily sampled along relatively long sample lines. More rapid sampling flow rates into a secondary chamber prior to analysis resulted in significant distortions in the aerodynamic equivalent diameter particle size distribution. Earlier studies [23] have shown that the length and diameter of a sampling line are important in obtaining representative samples. Further experiments will be undertaken in which these two parameters will be varied to determine the extent to which sodium fire aerosols can be transported without causing agglomeration and plate-out. Studies will also be extended to higher concentration aerosols in which particle interaction along sampling lines might be expected to produce some distortion in the resultant particle size distribution.

4. CHEMICAL TRANSFORMATIONS OF SODIUM FIRE AEROSOLS

In an oxygen deficient atmosphere hot sodium burns to form sodium oxide:

$$4Na + O_2 \longrightarrow 2Na_2O \qquad \text{(sodium oxide)}$$

However, in an excess of air, the following reactions occur:

$$2Na + O_2 \longrightarrow Na_2O_2 \qquad \text{(sodium peroxide)}$$

$$Na + O_2 \longrightarrow NaO_2 \qquad \text{(sodium superoxide)}$$

These oxides will react with water vapour and carbon dioxide in the air to

form sodium hydroxide, carbonate and bicarbonate:

$$Na_2O + H_2O \longrightarrow 2NaOH$$

$$2Na_2O_2 + 2H_2O \longrightarrow 4NaOH + O_2$$

$$4NaO_2 + 2H_2O \longrightarrow 4NaOH + 3O_2$$

$$2NaOH + CO_2 \longrightarrow Na_2CO_3 + H_2O$$

$$Na_2CO_3 + H_2O + CO_2 \longrightarrow 2NaHCO_3$$

Physical constants for these sodium compounds are listed in Table V. These chemical aspects of sodium fire aerosols are important in two respects:

(i) the formation of sodium hydroxide and carbonate will alter the aerosol particle size distribution;

(ii) following a secondary circuit sodium fire, the inhalation of a sodium oxide/hydroxide aerosol is more harmful than an equivalent sodium carbonate aerosol.

The Threshold Limit Value-Ceiling (TLV-C), defined as the concentration to which workers should not be exposed instantaneously [24], is 2 mg m^{-3} for sodium hydroxide. Sodium carbonate is classed as a nuisance dust and is not included in the list of TLVs, and a five-fold increase in the tolerance level to 10 mg m^{-3} would appear to be a reasonable compromise. However, it should be noted that the TLV-C for sodium hydroxide is of questionable origin [17], and at present it is arguable whether there is sufficient information on which to base a TLV-C. Despite this uncertainty, it is evident that the conversion of sodium oxides/hydroxide to carbonate will reduce the hazard of an aerosol release.

Clough et al [25] have calculated the rate of transformation of sodium oxide aerosol to hydroxide and carbonate when released into the atmosphere. They estimate that both conversion rates will be of the order of a few minutes, depending upon the relative humidity and the degree of intermixing between the aerosol plume and ambient air. We are undertaking a programme of work to check and quantify the assumptions and calculations of Clough et al, concentrating our initial attention on the sodium hydroxide to carbonate conversion rate. Thermal analysis techniques show promise for the quantitative analysis of the chemical constituents of this mixed aerosol system. Outlined below are our trial experiments with standard sodium hydroxide/carbonate mixtures, aimed at determining the feasibility of these techniques.

4.1 THERMOGRAVIMETRIC ANALYSIS (TG)

Thermogravimetric analysis measures weight changes when a substance undergoes a programmed heat cycle, and was used to check the validity of the differential thermal analysis (DTA) studies described in section 4.2. Any chemical interaction between the TG nickel crucible and sodium hydroxide/

carbonate samples can be detected using this technique.

Known mixtures of powdered sodium hydroxide and anhydrous sodium carbonate were prepared in a dry nitrogen atmosphere glove box. Some of these samples were mixed with possible DTA diluents to eliminate thermal conductivity imbalances and to determine the suitability of these diluents in the elimination of sample creep problems. The TG analysis heat cycles up to 650°C were undertaken in a nitrogen atmosphere. The sodium hydroxide/carbonate mixtures showed weight losses of 2-5%, and titrimetric analysis of the samples before and after the heat cycle indicated no change in the hydroxyl to carbonate ratio; no interaction between the constituents of the mixture had occurred. Visual inspection showed that small quantities of molten salt had crept out of the crucible and that slight chemical attack on the crucible had occurred.

Samples containing the proposed diluents (zirconium and nickel oxides) gave large weight changes at temperatures in excess of 500°C (zirconium oxide) and 630°C (nickel oxide). Early experiments using a nickel metal powder diluent showed a small reaction at 320°C. However, for DTA studies below 500°C, nickel oxide or nickel powder could act as suitable creep prevention diluents when determining the sodium hydroxide constituent (see below).

4.2 DIFFERENTIAL THERMAL ANALYSIS (DTA)

This technique compares the temperature changes of a substance during a programmed heat cycle with an inert material (aluminium oxide) undergoing identical treatment. Standard homogeneous mixtures of powdered sodium hydroxide and anhydrous sodium carbonate were loaded into nickel crucibles (Figure 15a) and heat cycled up to 450°C in a nitrogen atmosphere. A single melting point peak was obtained at 318°C for sodium hydroxide.

At present, movement of the sample (molten sodium hydroxide creep) limits the majority of our studies to below 450°C with a heating rate of 10 deg C min^{-1}. Satisfactory sodium hydroxide melting profiles (Figure 16) are obtained and the data for these DTA curves are listed in Table VI. As shown in Figure 17 the melting point peak height for sodium hydroxide is directly proportional to the quantity of hydroxide in the homogeneous mixture. A similar effect should be observed with the melting point peak (851°C) of sodium carbonate. Hence, if the creep problem can be overcome, it should be possible to determine the quantities of hydroxide and carbonate in an aerosol mixture collected and analysed by DTA. The resulting peak heights (or areas) of the melting hydroxide/carbonate represent a specific amount of hydroxide/carbonate which can be determined from calibration data.

The small shoulder on the higher temperature side of the sodium hydroxide melting point peak is produced by the molten sodium hydroxide reacting with the nickel crucible. This effect was reduced by sandwiching microspheres of sodium hydroxide (mean diameter 1.3 mm) between two layers of sodium carbonate. The results of these experiments are shown in Table VII and differ from the data for the homogeneous mixtures as shown in Figure 17. The use of microspheres delays attack on the nickel crucible, reduces the endothermic contribution of this reaction to the melting point curve and improves the precision of the data.

Some preliminary DTA studies have also been made of sodium carbonate/bicarbonate mixtures. Satisfactory thermal peaks for quantitative analysis have been obtained which represent the decomposition of sodium bicarbonate and the melting of sodium carbonate.

For the DTA technique to be successful it is important that samples can be analysed for hydroxide and carbonate. We hope to overcome the mobility of molten sodium hydroxide by careful design of the crucible (Figure 15b) to trap the molten salt by surface tension capillary forces. These crucibles will be made from Inconel metal with an improved thermocouple geometry for increased sensitivity. If these modifications prove to be successful, a combined DTA-TG microgram facility is envisaged with careful consideration given to methods of sampling sufficient sodium fire aerosol for analysis. The aerosols will be generated in the controlled atmosphere facility described in section 2.4.

5. CONCLUDING REMARKS

Selected techniques have been explored to sample and analyse the physical properties and chemical constituents of sodium fire aerosols. The initial aim has been to evaluate the validity of specific analytical equipment when applied to a study of sodium oxide aerosols.

In general the cascade impactor has been accepted as the most suitable inertial device to measure the concentration and aerodynamic equivalent diameter size distribution of nuclear aerosols. Different types of impactor have been redesigned and operated at lower flow rates with varying degrees of success [11,12,18]. The most popular system is the Andersen impactor[10] nominally consisting of eight stages and constructed in stainless steel. Sodium oxide aerosol analyses have been made by means of this standard design of Andersen impactor, the aerosol passing through the impactor for a carefully controlled time interval to avoid overloading of the stages. Low concentration sodium fire aerosols were studied for ½ - 30 min after 10 g sodium fires in a 0.74 m^3 burn chamber. Random errors were relatively small and the resultant size distribution data showed a marked deviation from log normality as the aerosol aged. The problem of systematic errors is more difficult to quantify; we plan to extend our impactor studies to other systems including the May [26] and AI-Lovelace impactors, and a Stöber spiral-duct centrifuge [27]. An intercomparison of these different measuring techniques might prove more useful in ascertaining the extent of systematic errors.

The sampling of sodium oxide/hydroxide aerosols down extensive sample lines to analytical equipment needs to be carefully controlled. Too high a flow rate nullifies the significance of the data, destroying the physical characteristics of the aerosol prior to sampling. If possible, sampling lines should be avoided and robust analytical equipment should be placed inside the burn chamber.

Our feasibility studies of the use of DTA/TG to determine the chemical constituents of a sodium fire aerosol show initial promise. The quantity of sodium hydroxide can be determined in a homogeneous mixture of sodium hydroxide and sodium carbonate. We hope to refine this technique to deter-

mine the amounts of sodium carbonate and bicarbonate in aerosol samples. In this way, using a single combined technique, it should be possible to verify the calculations of Clough et al [25] with respect to the rate of conversion of sodium hydroxide aerosol to the less hazardous sodium carbonate.

ACKNOWLEDGEMENTS

The authors would like to acknowledge the experimental assistance of P R Jacobs and N A Rowe. Aid in the analysis of the impactor data was gratefully received from K W Snelling and B C Walker.

REFERENCES

1 Nuclear Aerosols in Reactor Safety, CSNI Report June 1979, NEA OECD.

2 Hubner, R.S., Vaughan, E.U., Baurmash, L., A1-AEC-13038, 1973.

3 Jordan, H., Sack, C., KFK 2151, 1975.

4 Gieseke, J.A., Lee, K.W., Reed, L.D., BMI-NUREG-1991, 1978.

5 Walker, B.C., Kirby, C.R., Williams, R.J., SRD R98, 1978.

6 Nuclear Aerosols in Reactor Safety, CSNI Report June 1979, Chapter 7, NEA OECD.

7 Critical Review of Aerosol Measurement Techniques, SINDOC(79)77.

8 IAEA Technical Reports Series No 179, Particle Size Analysis in Estimating the Significance of Airborne Contamination, Vienna, 1978.

9 Fuchs, N.A. in Fundamentals of Aerosol Science, Editor: D.T. Shaw, John Wiley and Sons, New York, 1978.

10 Andersen 2000 Inc., Atlanta, Georgia, USA.

11 Kawahara, S., Murata, T., Yusa, H., Sagawa, N., J. Nucl. Science Tech. 14, 343, 1977.

12 Cushing, K.M., Lacey, G.E., McCain, J.D., Smith, W.B., EAP-600/2-76-280, 1976.

13 Adams, R.E., Kress, T.S., Parsly, L.F., ORNL/NUREG/TM-179, 1978.
Parker, G.W., Creek, G.E. in ORNL/NUREG/TM-142.
Editors: M.H. Fontana, T.S. Kress.

14 Herdan, G., Small Particle Statistics, Butterworths, London, 1960.

15 Williams, R.J., SRD R82, 1978.

16 Murata, M., Naritomi, M., Yoshida, Y., Kokubu, M., J. Nucl. Science Tech 11, 65, 1974.

17 Cooper, D.W., Underhill, D.W., Ellenbecker, M.J., private communication, 1977.

18 Parker, G.W., Creek, G.E., Sutton, A.L. in NUREG/CR-0752, 1979.
Editors: T.S. Kress, M.L. Tobias.
Parker, G.W., Sutton, A.L. in NUREG/CR-0844, 1979,
Editors: T.S. Kress, J.T. Han.
Parker, G.W., Sutton, A.L. in NUREG/CR-1062, 1979,
Editors: T.S. Kress, A.L. Wright.

19 Andersen, A.A., Am. Ind. Hyg. Assoc. J., 27, 160, 1966.

20 Flesh, J.P., Norris, C.H., Nugent, A.E., Am. Ind. Hyg. Assoc. J., 28, 507, 1967.

21 Swithenbank, J., Beer, J.M., Taylor, D.S., Abbot, D., McCreath, G.C., Prog. Astro and Aero, 53, 421, 1977.

22 Bexon, R., Dalzell, M.G., Stainer, M.C., Optics and Laser Tech., 161, 1976.

23 Holland, T.R., Macintyre, A.C., AEEW - R 1317, 1980.

24 Threshold Limit Values for 1978, HSE Guidance Note EH 15/78.

25 Clough, W.S., Garland, J.A., J. Nucl. Energy 25, 425, 1971.

26 May, K.R., J. Sci. Inst., 22, 187, 1945.

27 Stöber, W., Flachsbart, H., Environ. Sci. Tech. 3, 1280, 1969.

APPENDIX

B C Walker
SRD Culcheth, Warrington, UK

Figures 18 and 19 show comparisons carried out between AEROSIM [1] and some of the experimental data described in section 2.1. The agglomeration processes included in the calculations were Brownian motion and gravitational settling; the deposition processes were defined in terms of diffusion and sedimentation, and thermophoresis effects were not included. Data used in AEROSIM included the following:

Volume of chamber	= 0.74 m^3
Area for deposition due to diffusion	= 4.36 m^2
Area for gravitational deposition	= 0.57 m^2
Boundary layer thickness for diffusion to the walls	= 100 μm
Particle density	= 1.124 g cm^{-3}
Total airborne mass	= 0.2 g

The initial particle size distribution was taken to be that given by the data from the first impactor sample (30 sec or 1 min). The particles were assumed to be spherical and a reduced density was used to account for voids. The collision efficiency was taken from data by Loyalka [2]. The computations were repeated using the Fuchs' formula for the collision efficiency and there was little effect on the results as expected for this low mass concentration.

The predictions are in good agreement with the experimental results for particle sizes greater than about 2 μm. AEROSIM overestimates the proportions of smaller particles and this suggests that the plate-out or Brownian agglomeration rates are too low since these are the processes most likely to affect the small particles. The discrepancies could be due to errors in the following:

(i) deposition area,

(ii) boundary layer thickness,

(iii) chamber temperature,

(iv) inhomogeneities which affect the mass concentration,

(v) particle density and shape.

REFERENCES

1 Walker, B.C., Kirby, C.R., Williams, R.J., SRD R98, 1978.

2 Loyalka, S.K., NUREG/CR-0780, 1979.

Table I

10 g sodium fires in ambient air, using 2 Andersen cascade impactors per experiment.

Number of Experiments	Time at which sample was taken after Na ignition (min)	Length of sampling time (sec)	Relative Humidity (%)
3	½	30	49,49,49
3	½	60	33,42,43
6	1	60	43,46,46,50,52,52
3	1	120	39,45,45
3	5	30	49,50,52
3	5	180	38,40,43
3	10	20	45,46,52
3	10	180	34,38,43
3	20	30	46,50,50
2	20	240	36,48
1	20	360	38
3	30	240	46,52,57

Table II

Variation in (d_{50}) and (σ_g) for ageing sodium fire aerosols, initial equilibrium concentration ~ 1.2 μg cm^{-3}

Time sample was taken after Na ignition (min)	d_{50} (μm)	σ_g		Asymmetry parameter*
		$\frac{d_{50}}{d_{15.87}}$	$\frac{d_{84.13}}{d_{50}}$	
½	$1.0^{+0.3}_{-0.1}$	$1.8^{+0.7}_{-0.5}$	$2.4^{+1.0}_{-1.1}$	1.3
1	$1.2^{+0.2}_{-0.2}$	$1.9^{+0.6}_{-0.5}$	$2.3^{+1.4}_{-0.8}$	1.2
5	$1.4^{+0.2}_{-0.3}$	$1.9^{+0.5}_{-0.7}$	$2.1^{+0.9}_{-0.6}$	1.1
10	$1.4^{+0.3}_{-0.2}$	$1.5^{+0.5}_{-0.3}$	$1.9^{+0.6}_{-0.7}$	1.3
20	$1.4^{+0.3}_{-0.1}$	$1.4^{+0.8}_{-0.2}$	$1.7^{+0.8}_{-0.5}$	1.2
30	$1.4^{+0.4}_{-0.2}$	$1.3^{+0.5}_{-0.3}$	$1.6^{+0.4}_{-0.5}$	1.2

*Asymmetry parameter $= \left(\frac{d_{84.13}}{d_{50}}\right) \cdot \left(\frac{d_{15.87}}{d_{50}}\right)$

Table III

Air Ejector Sampling Flow Rates

Air Ejector			Aerosol Flow Rate ($m^3\ s^{-1}$)	Total Flow into Plenum Chamber ($m^3\ s^{-1}$)
Air Pressure (psi)	(Pa)	Flow Rate ($m^3\ s^{-1}$)		
5	3.4×10^4	8.0×10^{-4}	2.0×10^{-3}	2.8×10^{-3}
10	6.9×10^4	1.87×10^{-3}	6.5×10^{-3}	8.4×10^{-3}
15	10.3×10^4	3.20×10^{-3}	1.05×10^{-2}	1.37×10^{-2}
20	13.8×10^4	4.89×10^{-3}	1.52×10^{-2}	2.01×10^{-2}
25	17.2×10^4	5.40×10^{-3}	1.85×10^{-2}	2.40×10^{-2}
30	20.7×10^4	6.50×10^{-3}	2.18×10^{-2}	2.83×10^{-2}
Error		$\pm$ 10%		$\pm$ 10%

Table IV

Aerosol Sampling Studies: 10 g sodium fires in ambient air

Aerosol Flow Rate ($m^3\ s^{-1}$)	Time at which sample was taken after Na ignition (min)*
4.7×10^{-4}	½, 1, 5, 10, 20, 30
2.0×10^{-3}	½, 1, 5, 10, 20, 30
6.5×10^{-3}	½, 5, 10, 20, 30
1.05×10^{-2}	½, 1, 5, 10, 20, 30
1.52×10^{-2}	½, 1, 5, 10
1.85×10^{-2}	½, 1, 5, 10, 20, 30
2.18×10^{-2}	½, 1, 5, 10, 20, 30

*Each experiment was repeated at least three times at the specified sampling times.

Table V

Physical Constants of Sodium Fire Compounds

Compound	M Pt ^{o}C	Density g ml^{-1}	Mol. Wt.
Na_2CO_3	851	2.532	105.99
$Na_2CO_3.H_2O$	$-H_2O$, 100	2.25	124.00
$Na_2CO_3.7H_2O$	$-H_2O$, 32	1.51	232.10
$Na_2CO_3.10H_2O$	32.5-34.5	1.44	286.14
$NaHCO_3$	$-CO_2$, 270	2.159	84.00
NaOH	318.4	2.130	40.00
Na_2O	920	2.27	61.98
Na_2O_2	d 460	2.61	77.98
$Na_2O_2.8H_2O$	d 30	-	222.10
NaO_2	-	2.21	54.99

(d....decomposes)

Table VI

Homogeneous Mixtures of Sodium Hydroxide and Anhydrous Sodium Carbonate

Weight Ratios		Weights (mg)		Relative Peak Height (mm)	Peak Height / Wt NaOH	Mean	σ_g
NaOH	Na_2CO_3	NaOH	Na_2CO_3				
10	90	7.02 7.43	63.2 66.9	13 16	1.85 2.15	2.00	0.21
30	70	13.2 17.6	30.7 42.1	26 32.5	1.97 1.84	1.90	0.09
50	50	32.7 48.1	32.7 48.0	63 76.5	1.93 1.59	1.76	0.24
90	10	94.6 65.4	10.5 7.3	160 120	1.69 1.97	1.83	0.20

Mean $\frac{\text{Peak Height}}{\text{Wt NaOH}} = 1.87$

Standard Deviation (σ_g) = 0.17

Coefficient of Variation $\pm$ 9%

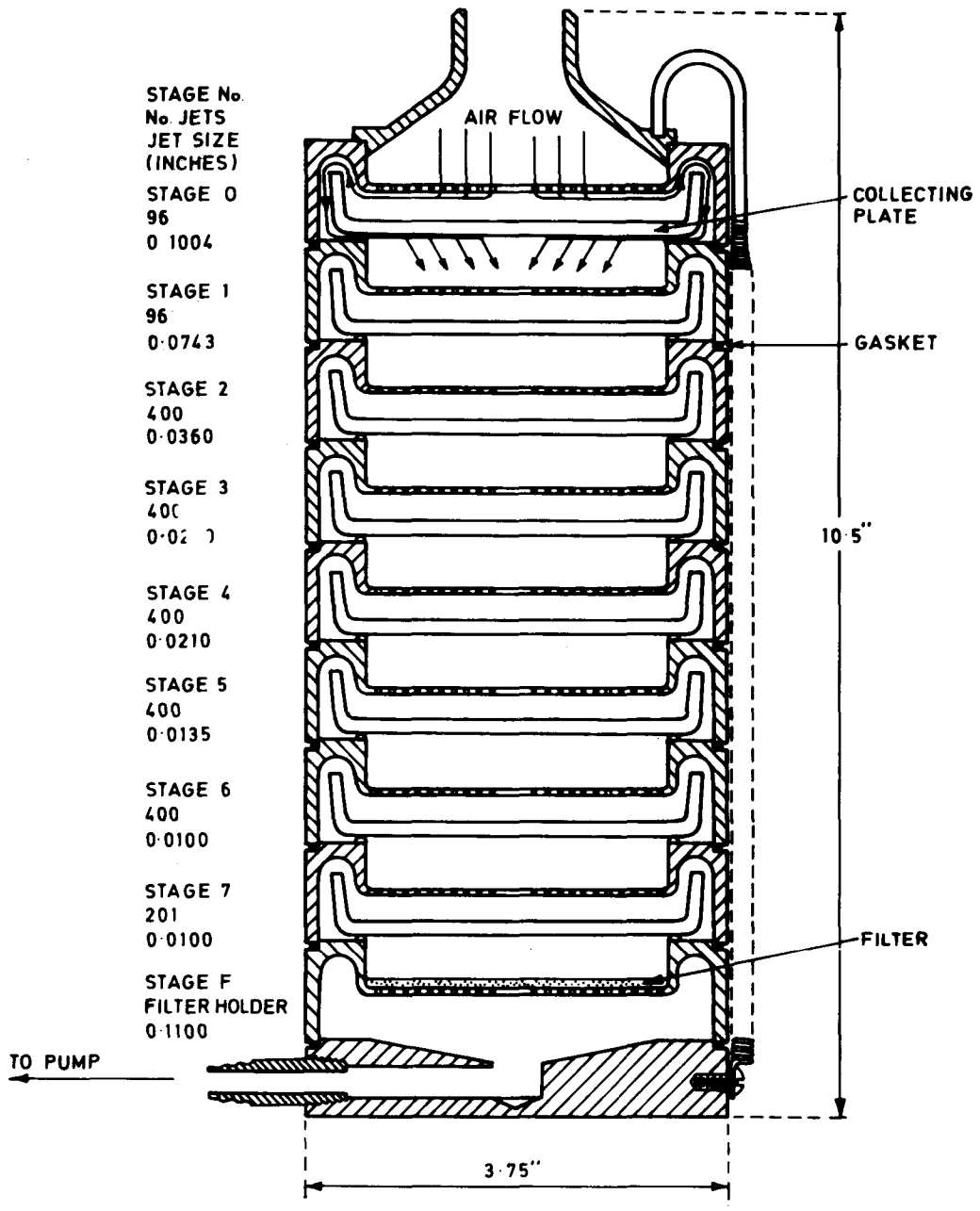

FIG.1 ANDERSEN CASCADE IMPACTOR

Table VII

Sodium Hydroxide Microspheres in Anhydrous Sodium Carbonate

Weight NaOH (mg)	Relative Peak Height (mm)	$\frac{\text{Peak Height}}{\text{Wt NaOH}}$
12.1	17	1.405
19.4	31	1.598
32.5	47.5	1.462
48.3	76	1.573
48.9	69	1.411
74.6	102.5	1.374
79.8	109	1.366
99.5	133	1.337

Mean $\frac{\text{Peak Height}}{\text{Wt NaOH}} = 1.44$

Standard Deviation (σ g) = 0.10

Coefficient of Variation $\pm$ 7%

FIG 2 ANDERSEN IMPACTOR DATA FOR SODIUM FIRE AEROSOLS: CUMULATIVE FREQUENCY — ATTEMPTED NORMAL PRESENTATION

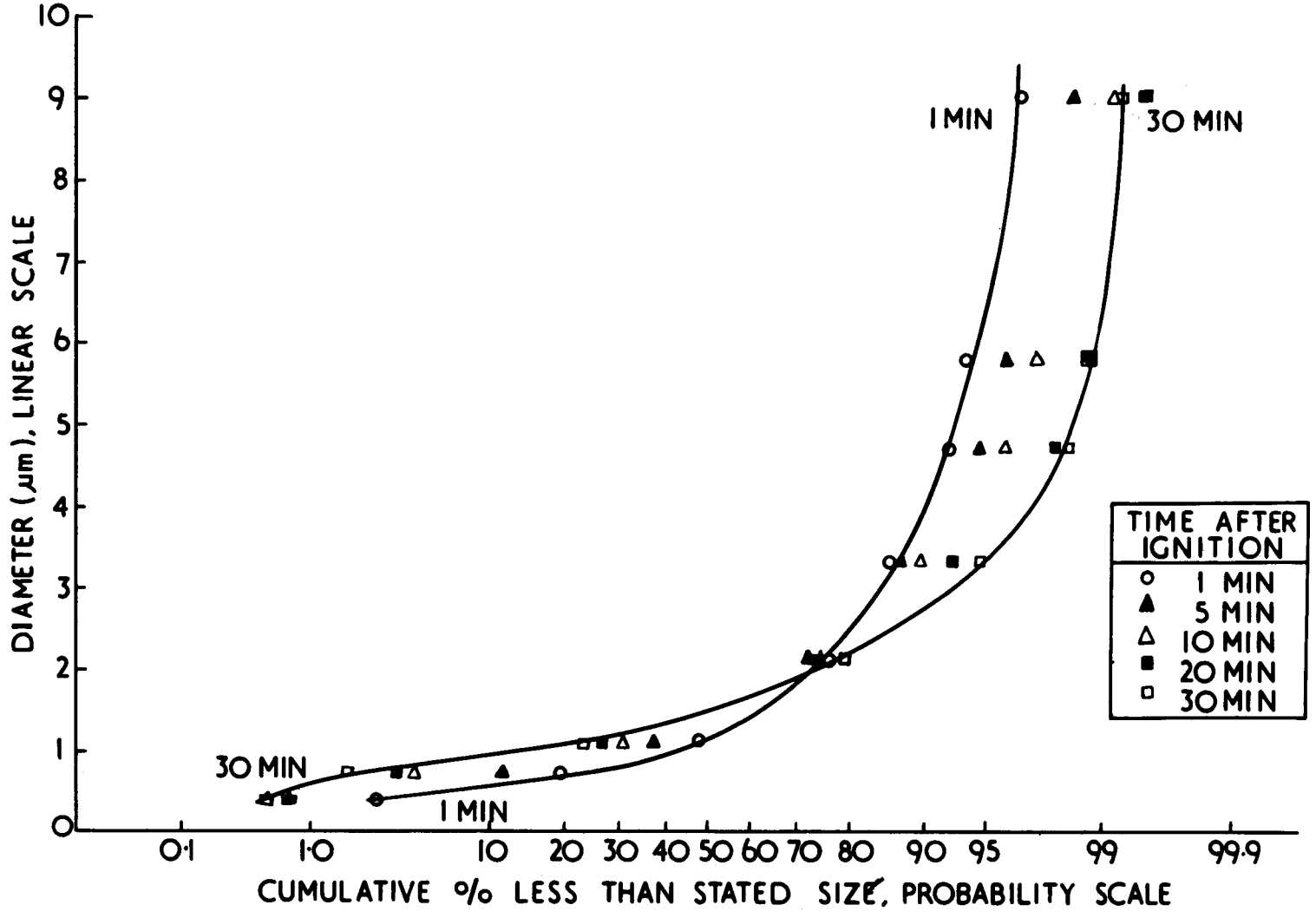

FIG 3 ANDERSEN IMPACTOR DATA FOR SODIUM FIRE AEROSOLS: CUMULATIVE FREQUENCY—ATTEMPTED ROSIN-RAMMLER PRESENTATION

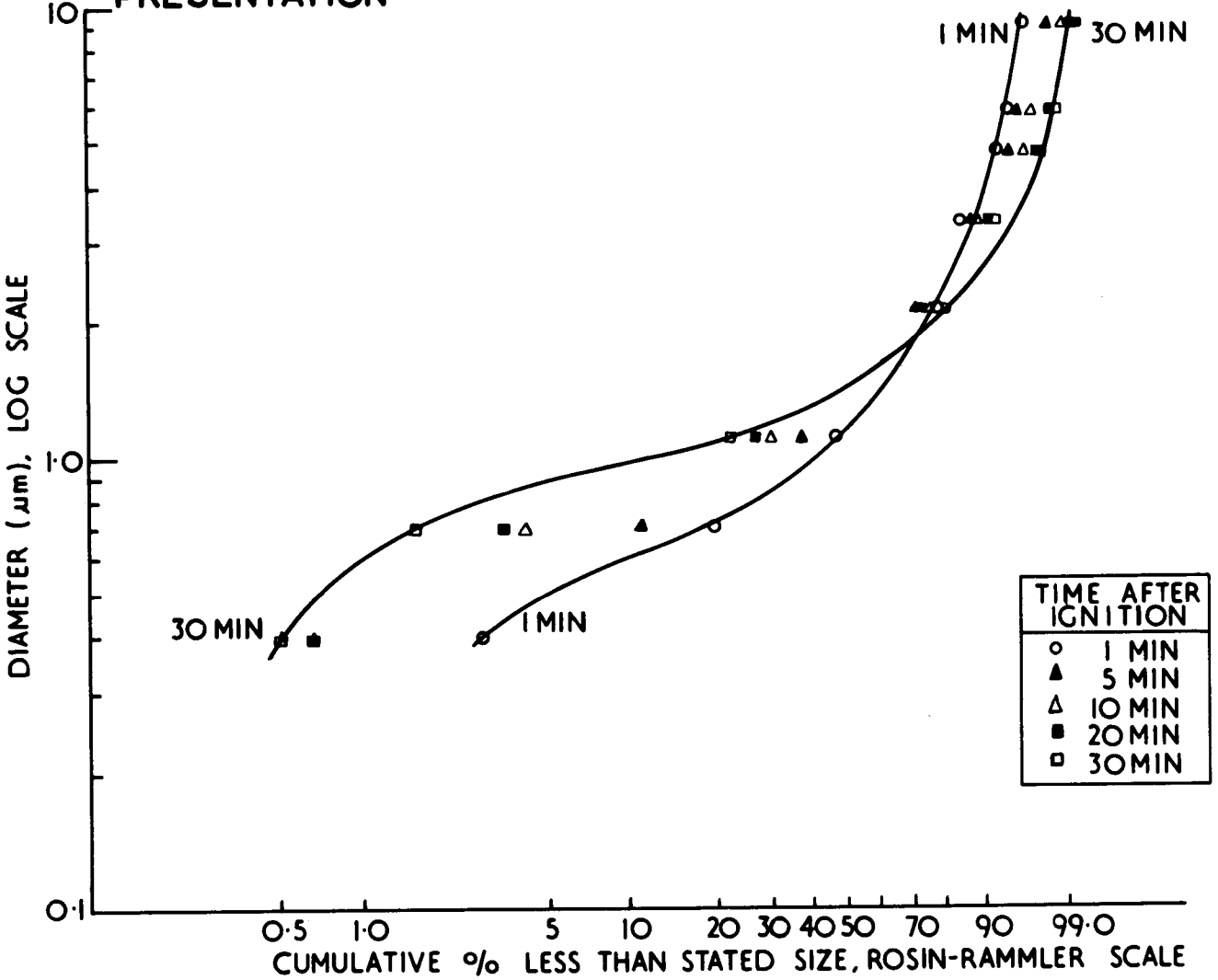

FIG 4 ANDERSEN IMPACTOR DATA FOR SODIUM FIRE AEROSOLS: CUMULATIVE FREQUENCY—ATTEMPTED LOGNORMAL PRESENTATION

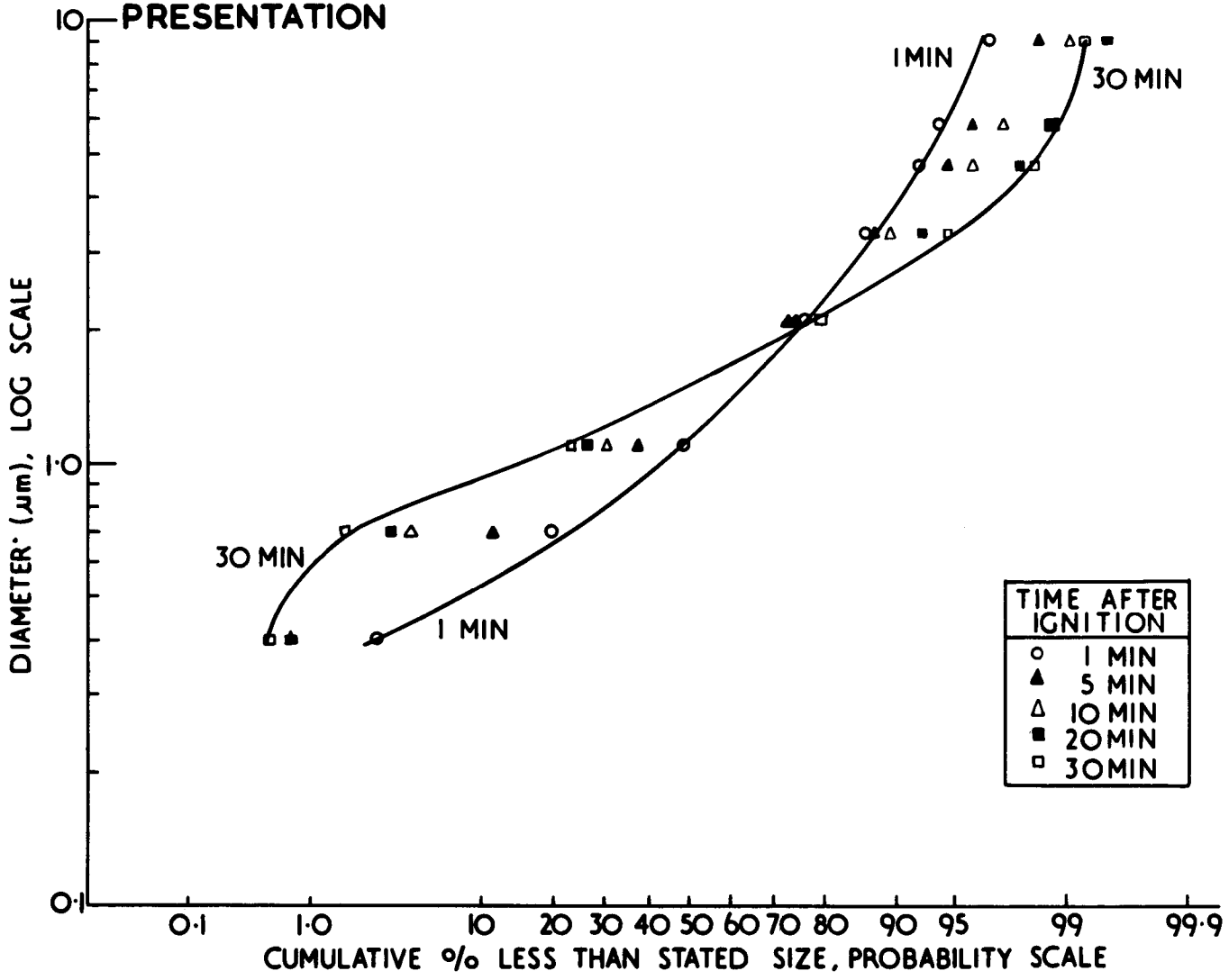

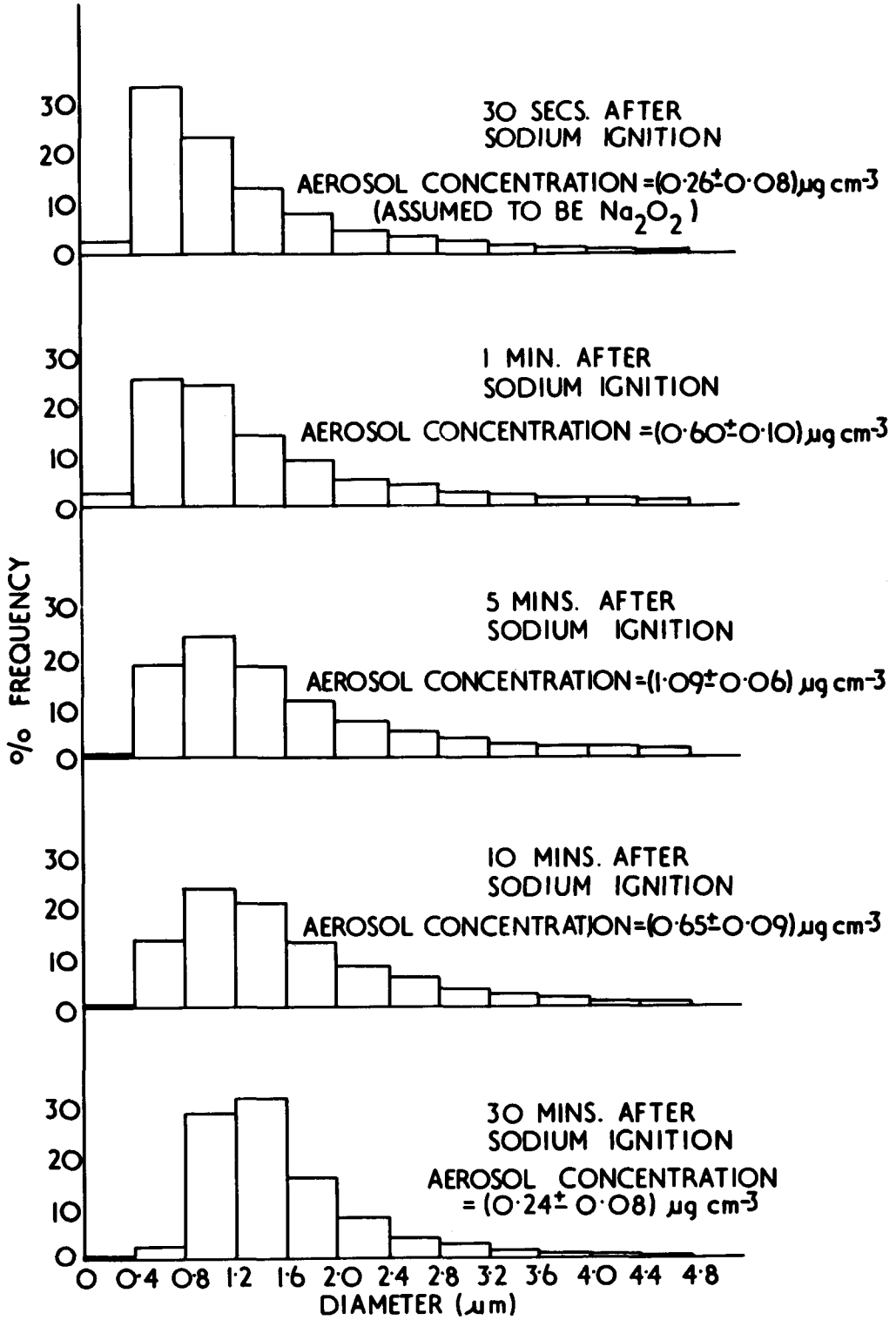

FIG 5 PARTICLE DIAMETER v % FREQUENCY HISTOGRAMS OF SODIUM FIRE ANDERSEN IMPACTOR DATA

FIG 6 ANDERSEN IMPACTOR DATA FOR SODIUM FIRE AEROSOLS: EFFECT OF RELATIVE HUMIDITY 5min AFTER SODIUM IGNITION

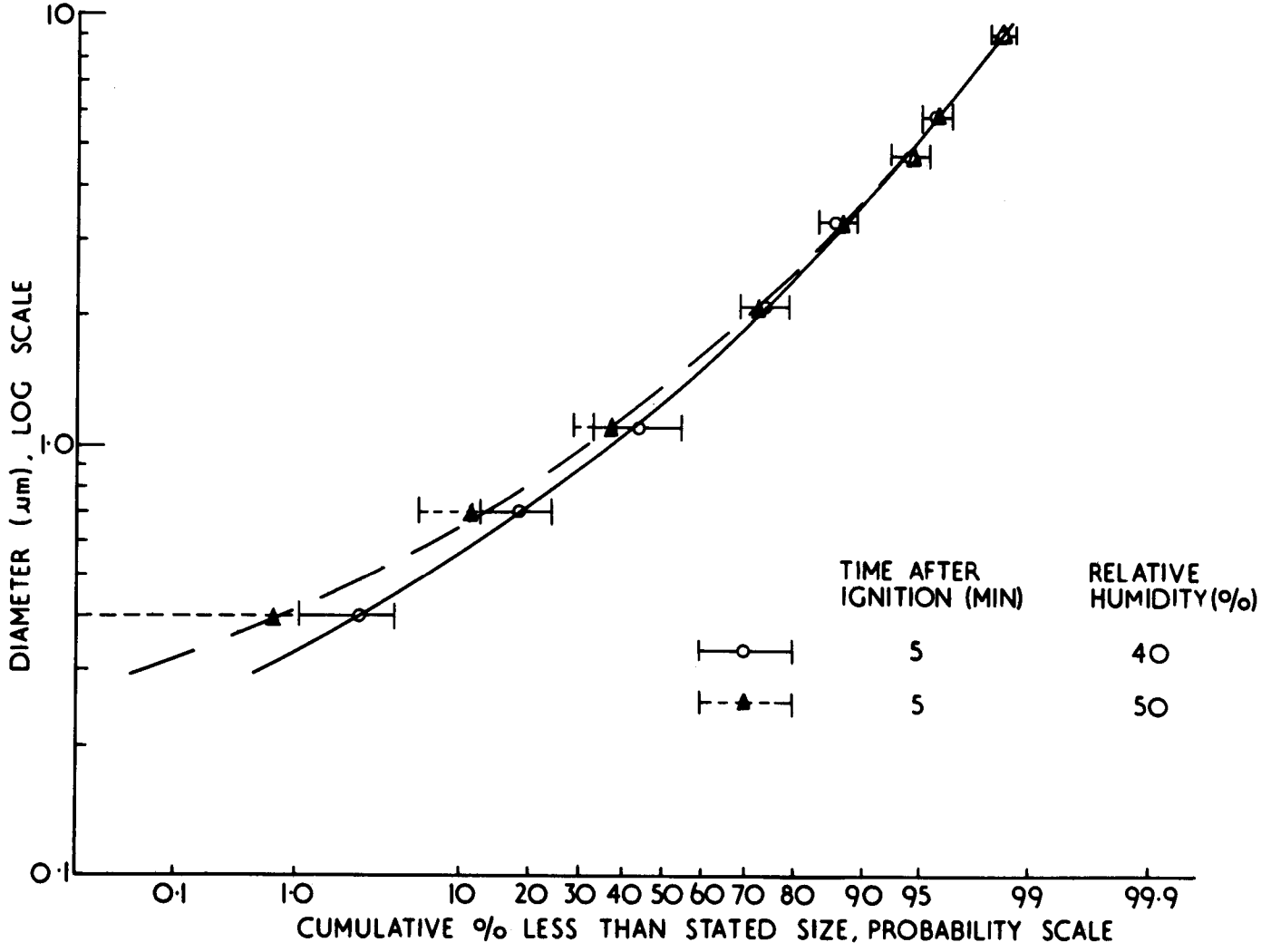

FIG 7 ANDERSEN IMPACTOR DATA FOR SODIUM FIRE AEROSOLS : EFFECT OF RELATIVE HUMIDITY 20 min AFTER SODIUM IGNITION

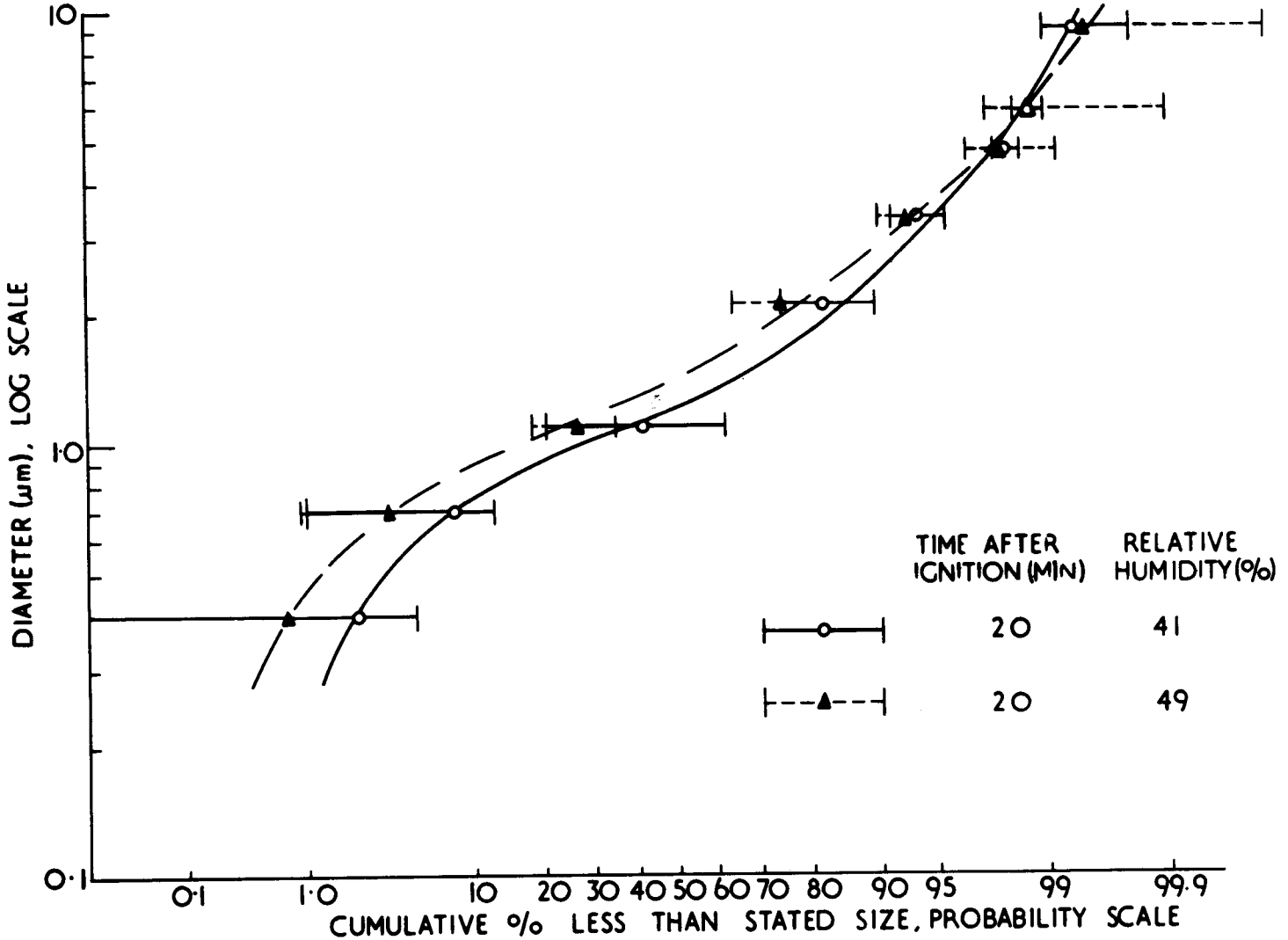

FIG 8 RANDOM ERRORS: ANDERSEN IMPACTOR DATA FOR A SODIUM FIRE AEROSOL SAMPLED 30SECS. AFTER SODIUM IGNITION

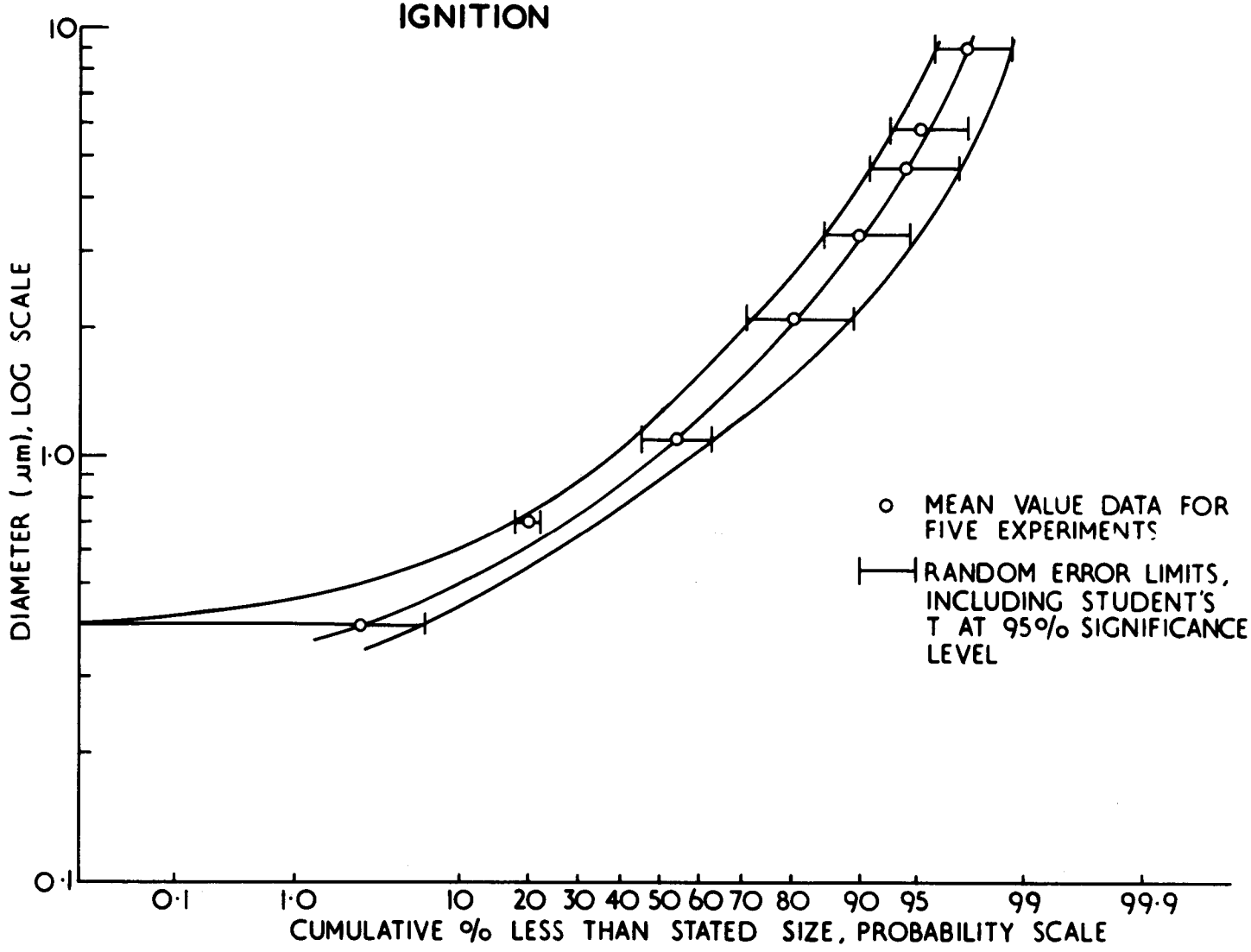

FIG 9 RANDOM ERRORS: ANDERSEN IMPACTOR DATA FOR A SODIUM FIRE AEROSOL SAMPLED 30MINS. AFTER SODIUM IGNITION

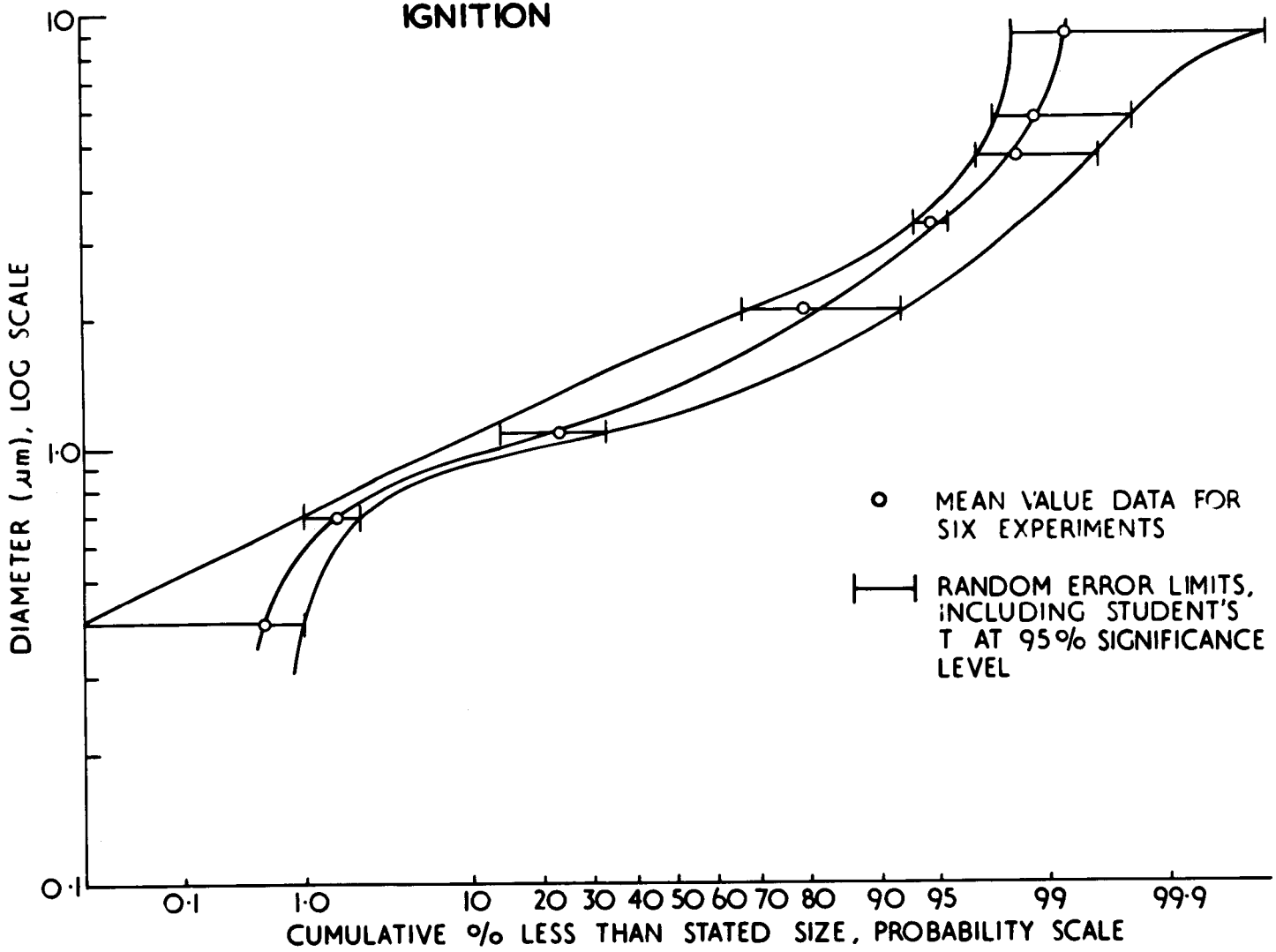

FIG 10 SODIUM BURN CHAMBER AND AIR EJECTOR SAMPLING SYSTEM

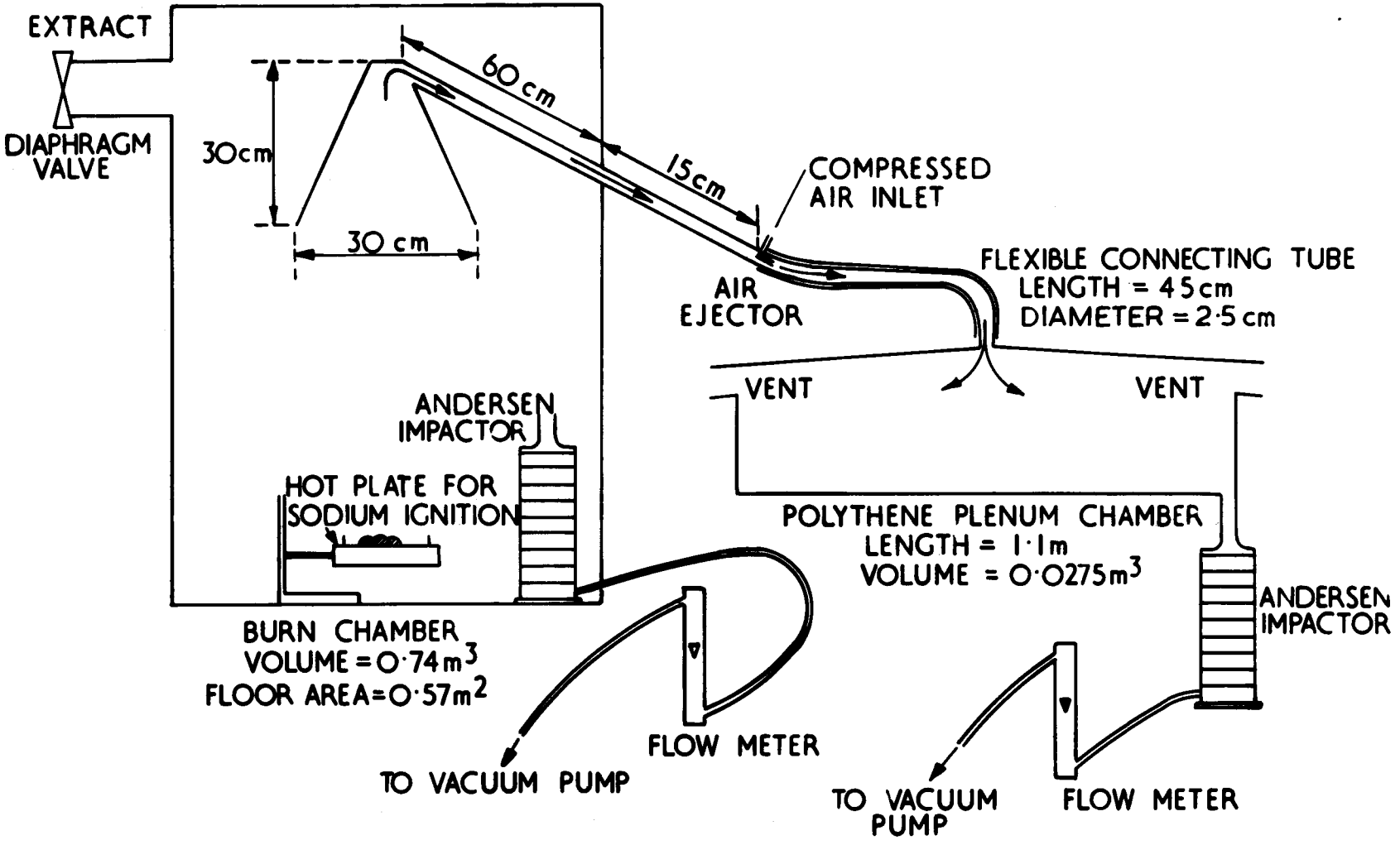

FIG. 11 ANDERSEN IMPACTOR DATA SAMPLED 5 MINS AFTER SODIUM IGNITION AT A FLOW RATE OF $4.7 \times 10^{-4} m^3 s^{-1}$

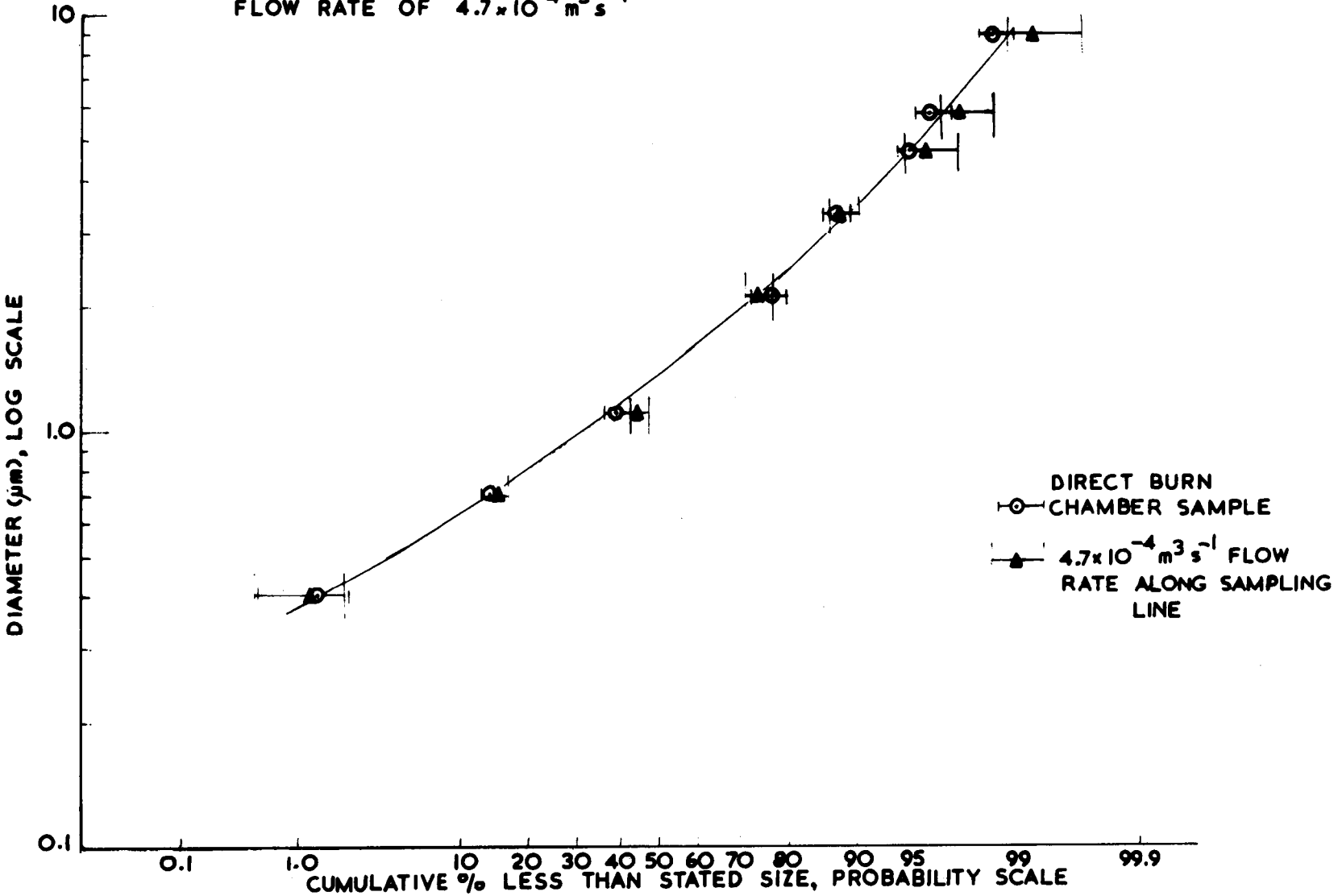

FIG 12 ANDERSEN IMPACTOR DATA SAMPLED 5 MINS. AFTER SODIUM IGNITION USING AIR EJECTOR AT A FLOW RATE OF $2{\cdot}0 \times 10^{-3} m^3 s^{-1}$

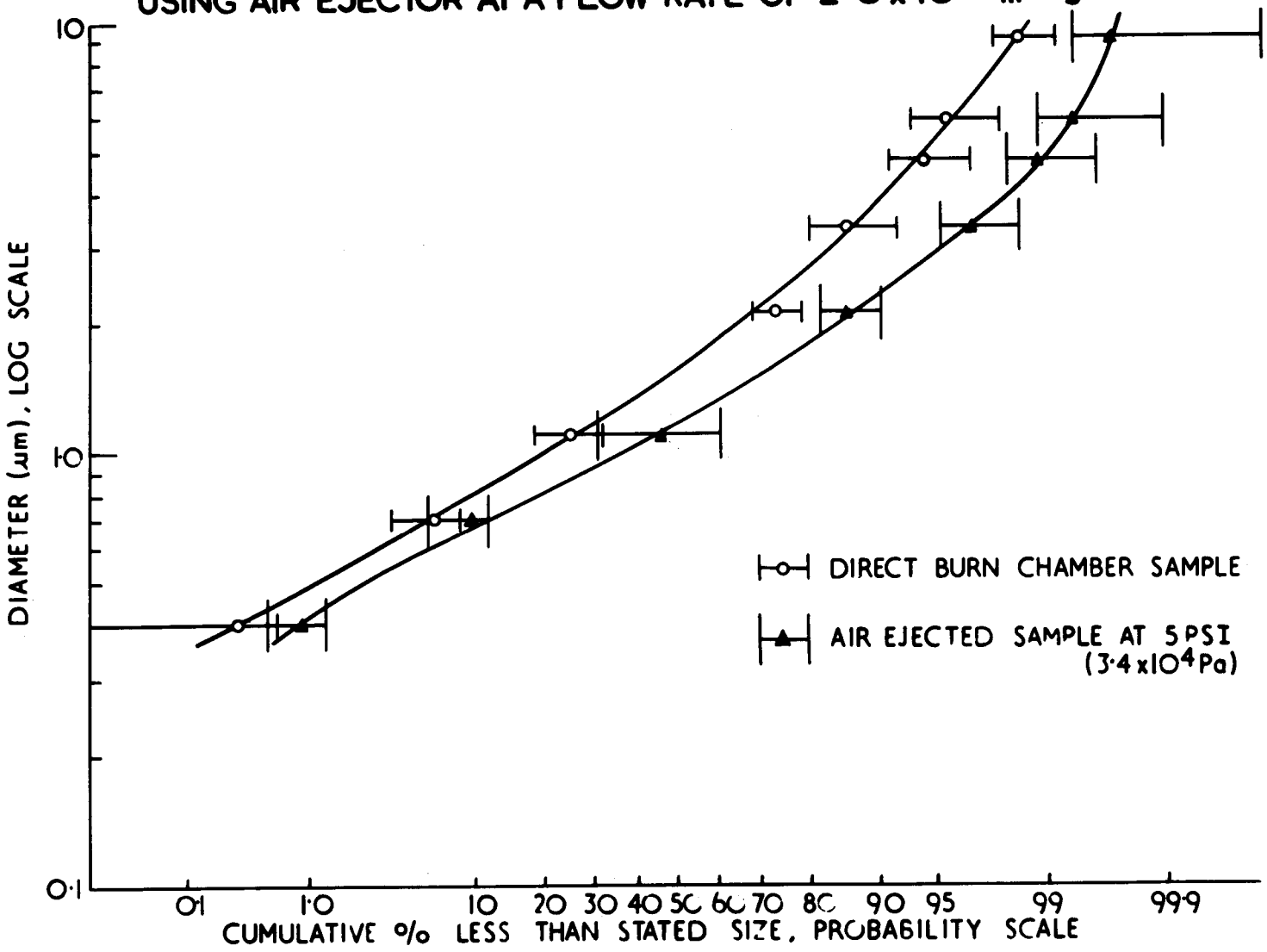

FIG 13 ANDERSEN IMPACTOR DATA SAMPLED 5 MINS. AFTER SODIUM IGNITION USING AIR EJECTOR AT A FLOW RATE OF $2{\cdot}18 \times 10^{-2} m^3 s^{-1}$

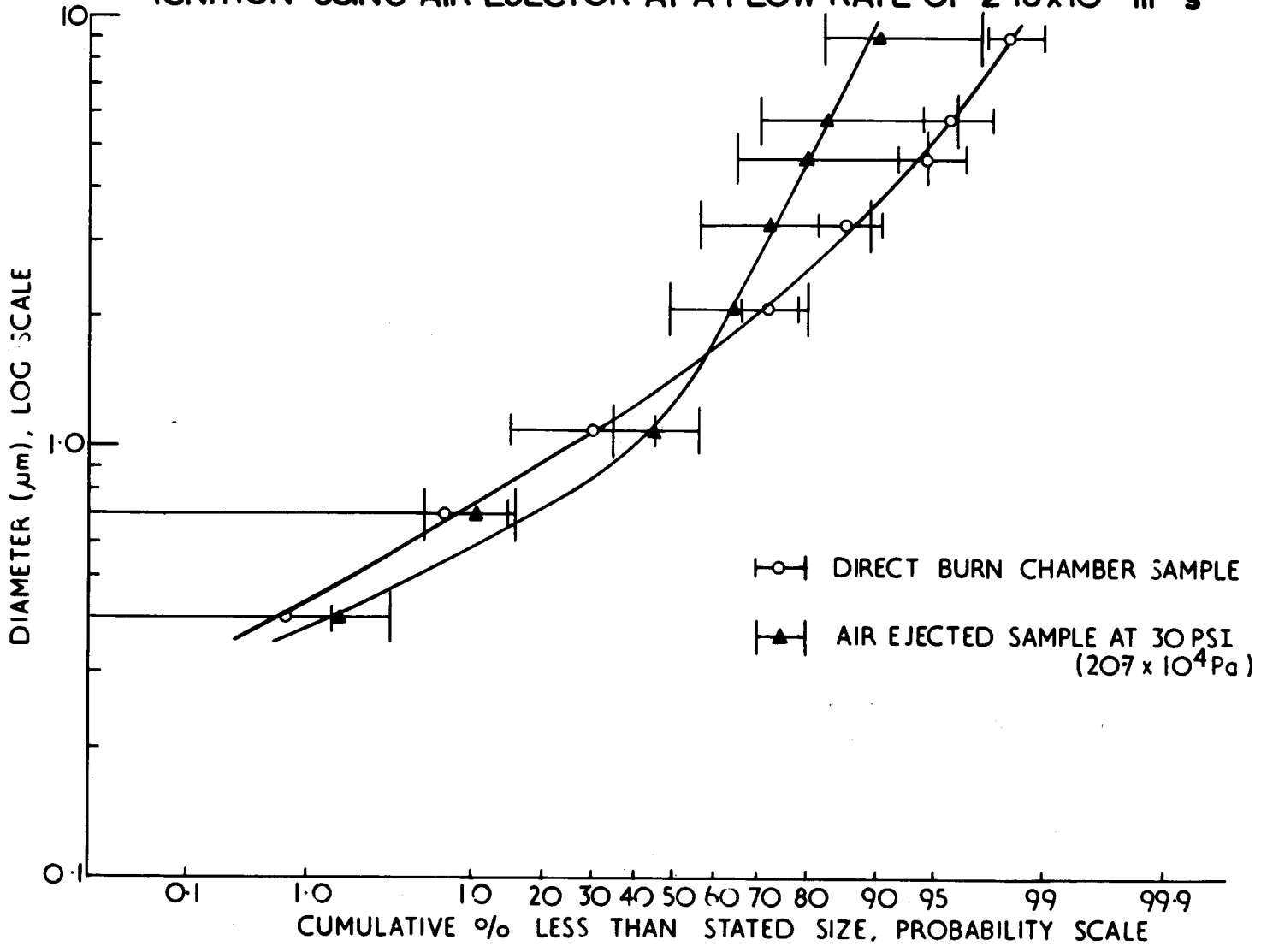

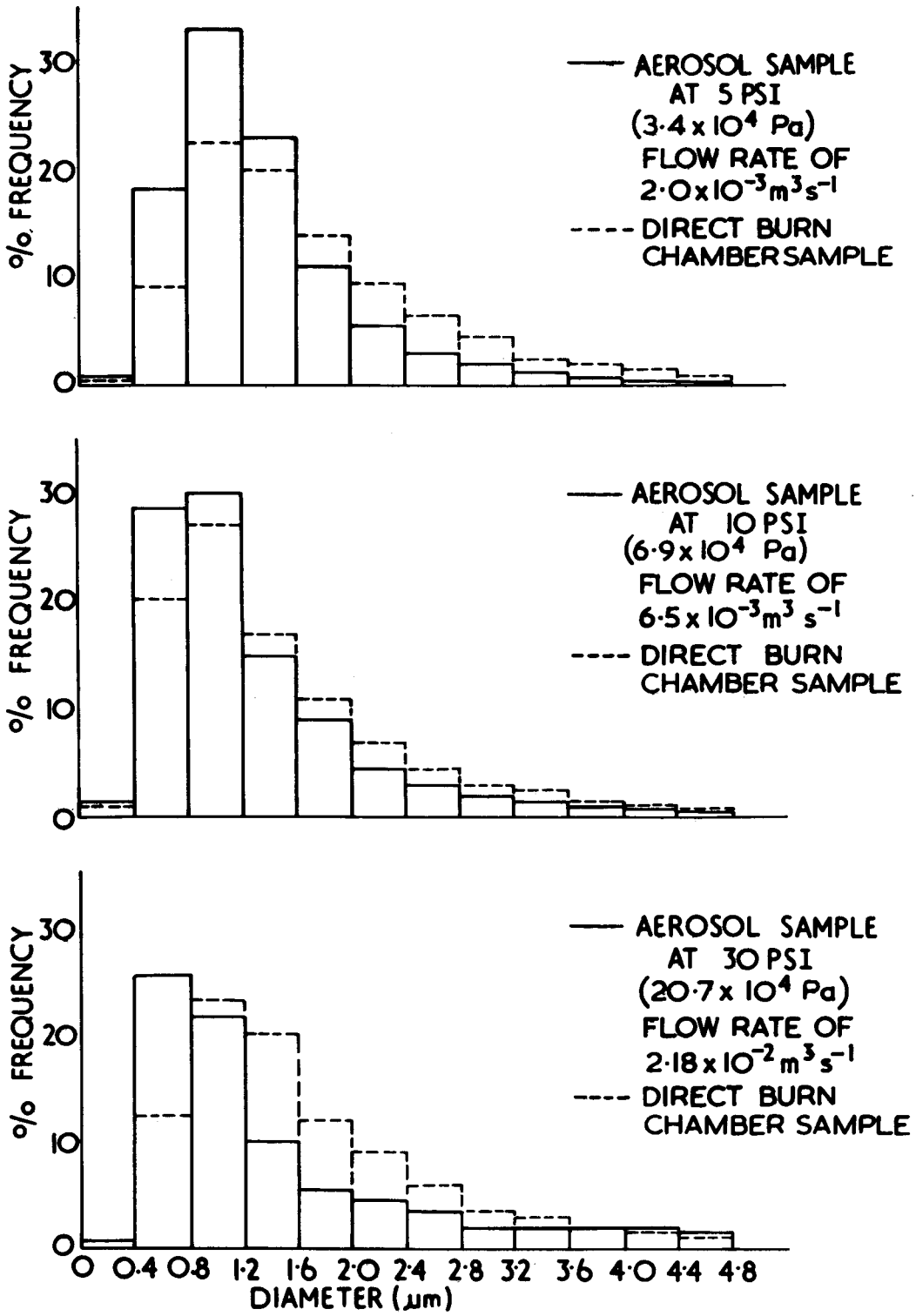

FIG 14 HISTOGRAMS SHOWING ANDERSEN IMPACTOR DATA : AEROSOL SAMPLED 5 MINS AFTER SODIUM IGNITION

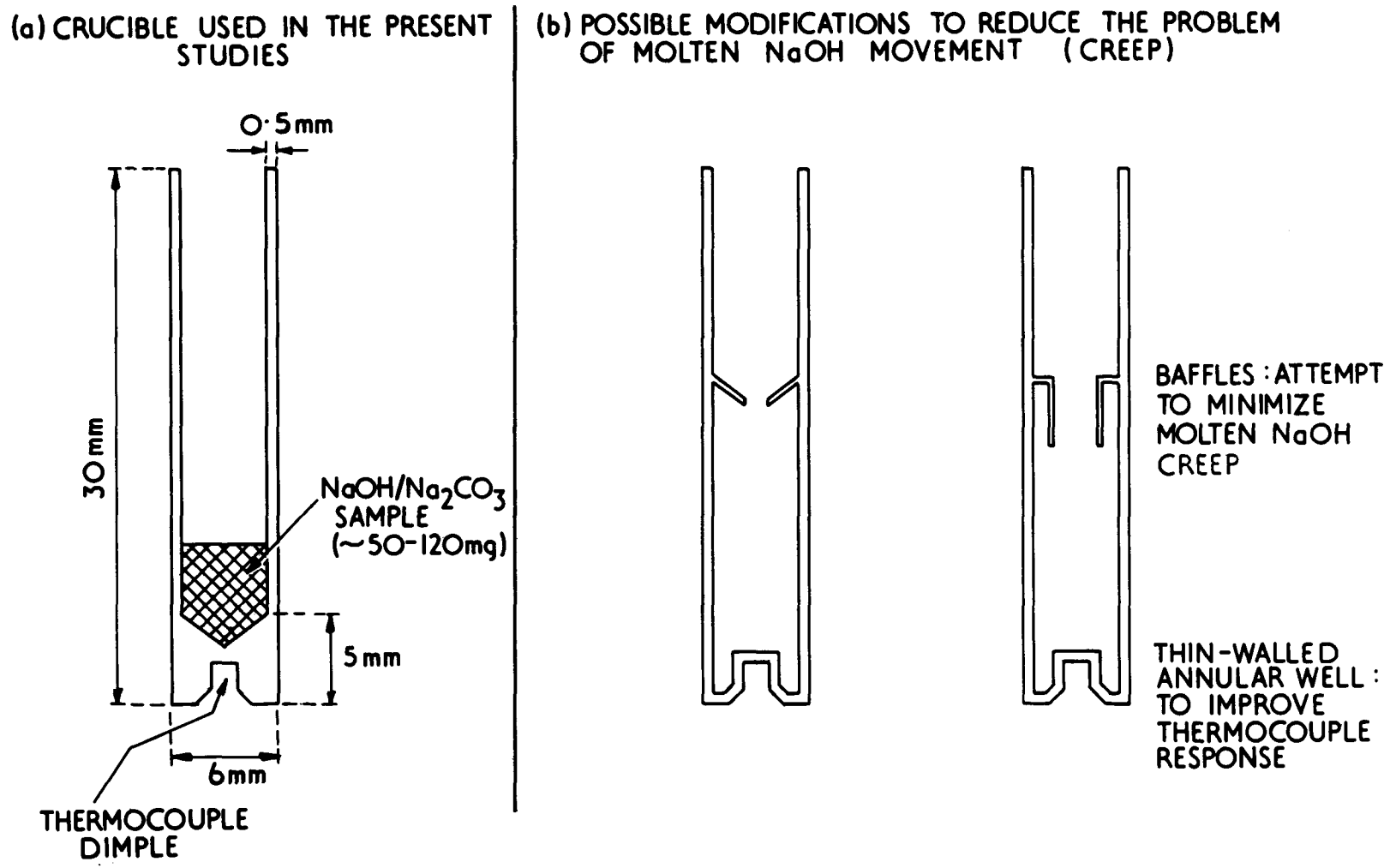

FIG 15 NICKEL CRUCIBLES FOR DIFFERENTIAL THERMAL ANALYSIS STUDIES

FIG 16 DTA CURVES FOR $NaOH/Na_2CO_3$ MIXTURES WITH CHANGE IN NaOH CONTENT

10°C PER MIN IN A NITROGEN ATMOSPHERE

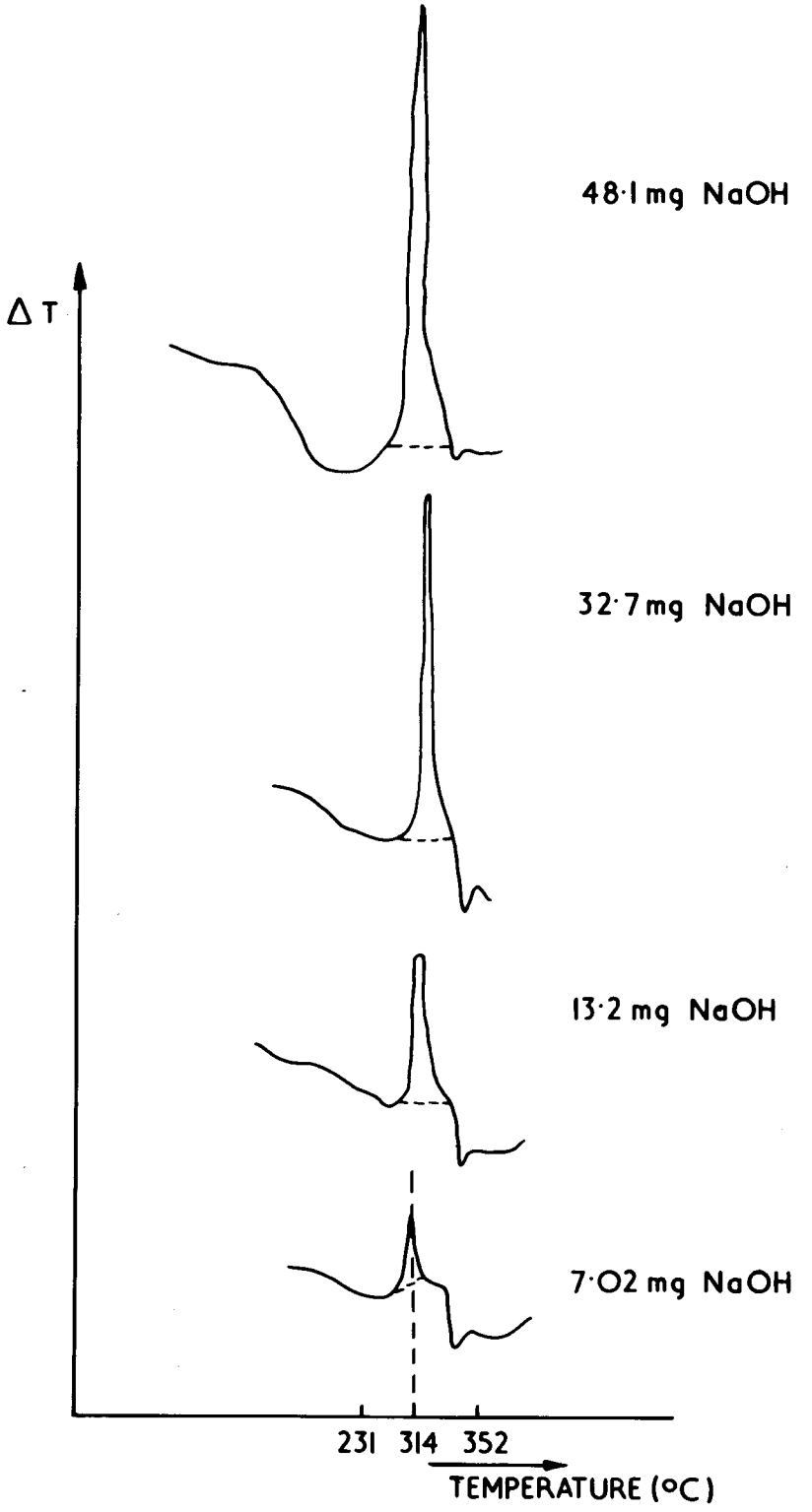

FIG 17. DTA DATA : VARIATION OF NaOH MELTING POINT PEAK HEIGHT WITH CHANGE IN WEIGHT OF Na OH COMPONENT OF Na OH / Na_2CO_3 MIXTURES

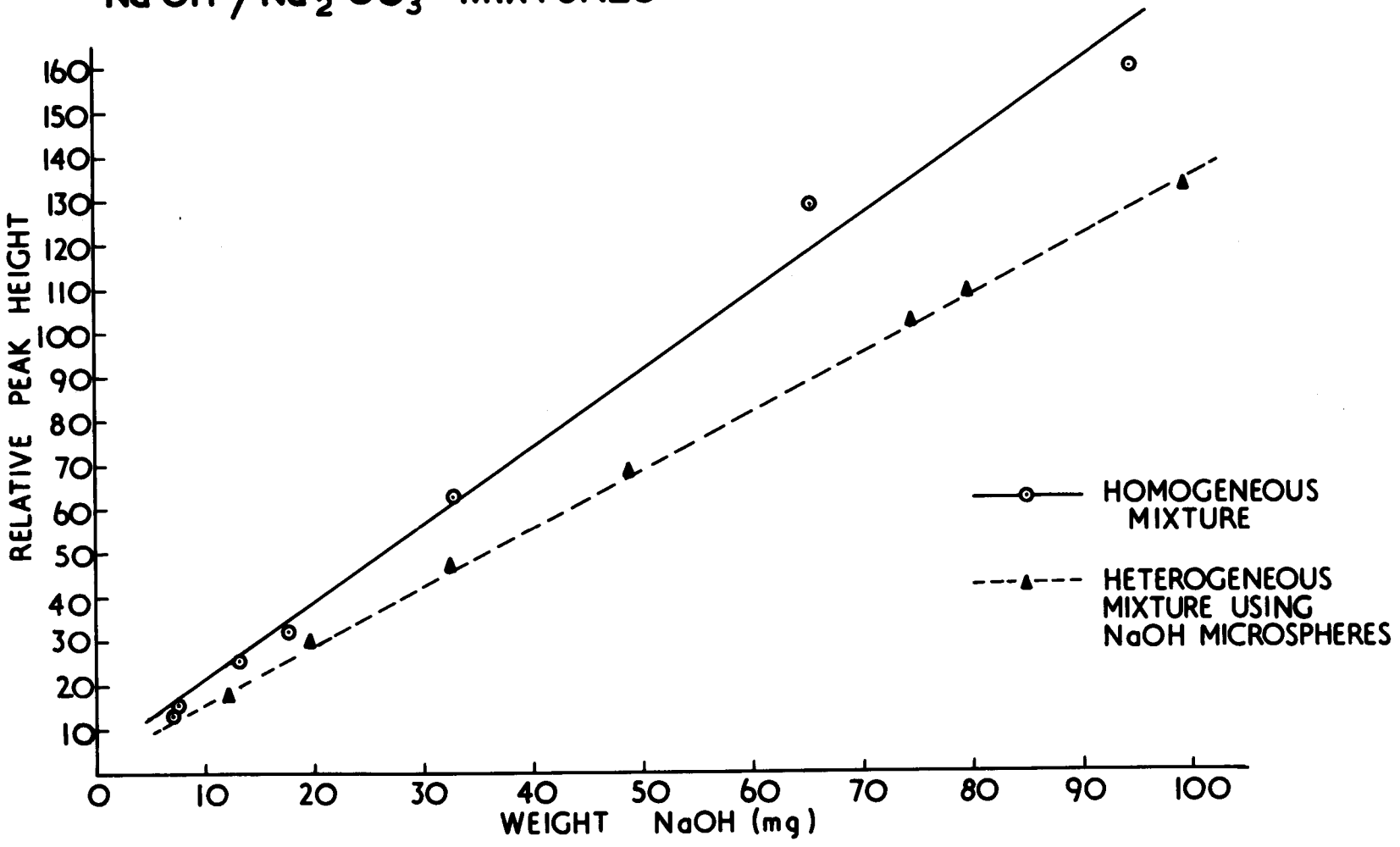

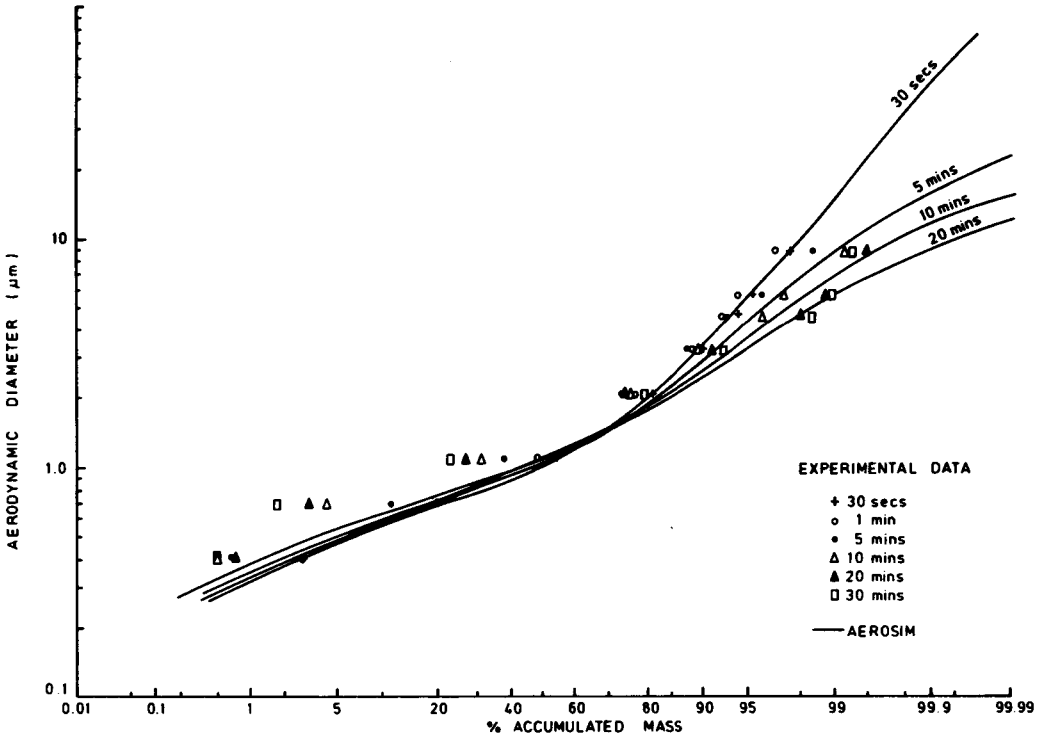

FIG. 18 COMPARISON OF AEROSIM WITH EXPERIMENTAL DATA - CASE 1

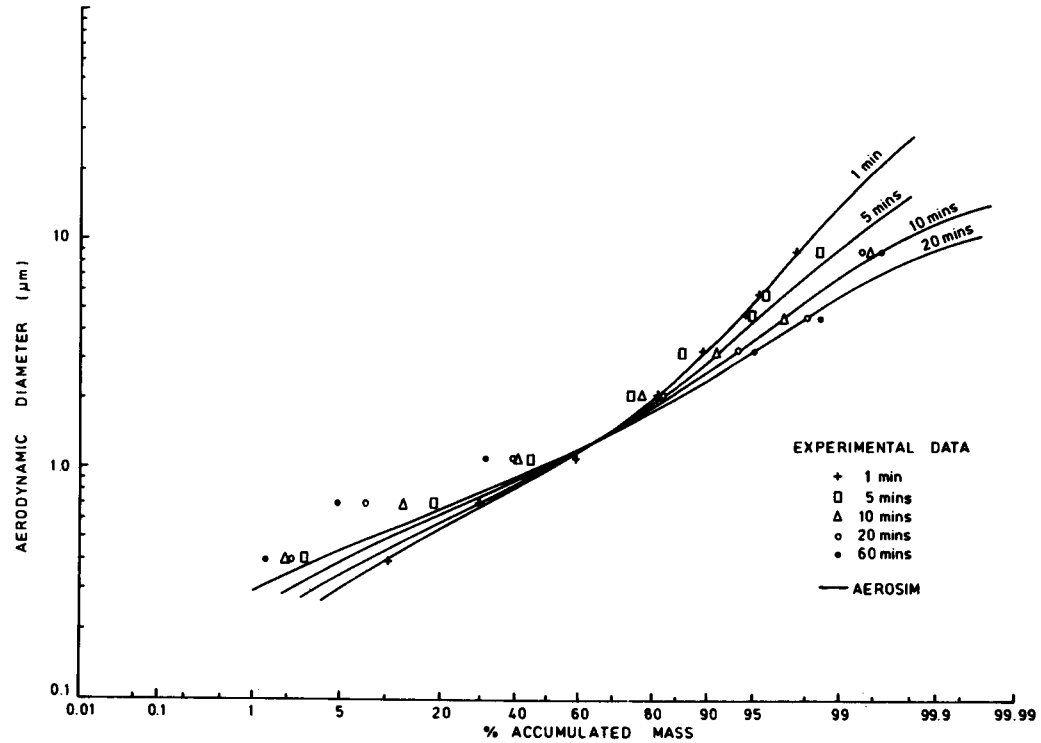

FIG. 19 COMPARISON OF AEROSIM WITH EXPERIMENTAL DATA - CASE 2

Measurement of High Concentration DOP Aerosols by a Laser Dust Counter

S. Kitani and Y. Ikezawa
Japan Atomic Energy Research Institute
Tokai-mura, Ibraki-ken, 319-11 Japan
M. Kozuka
Japan Air Cleaning Association
Iwamoto-cho 2-6-12, Chiyoda-ku,Tokyo
101 Japan

Abstract

Light-scattering technique is widely used in industries to measure the particle size distribution and the particle number concentration of aerosols. The number concentration of aerosol is limmited in dilute samples less than 100 particles per cm^3. A laser dust counter was applied to measure DOP aerosols with high concentration and polydispersed particle-size distribution. The results showed that the measurement of particle number concentration can be made to 10^5 particles per cm^3 of the particle size range 0.1 - 0.5 μm. These results were compared with those obtained by electric aerosol size analyzer and cascade impactor.

I. Introduction

In nuclear facilities, there are required to develop instruments to measure aerosol properties in-situ, especially in severe circumstances. The main properties of aerosols are chemical composition and their physical properties such as particle size distribution, number density, particle density and particle shape factor.

Light scattering technique has been widely used for characterization of aerosols, because of its theoretical background by Mie theory. Commercially available photo-counters, for example Royco photo-counter, using white light of tungsten lamp as the light source, can measure the aerosol particles in the range of 0.3 - 10 μm, and the particle number density 0 -100 particles/cm^3. Laser light has been applied to the light source. Marshall et al.[1]studied the characterization of polymer latex aerosols by measuring 360° light scattering patterns. The particle sizes, however, could be measured from 0.3 to 11 μm and the particle number density was 400 particle/cm^3. The restriction of both instruments in their capability of particle size measurement arises from S/N by interference from Rayleigh scattering of air molecules.

A newly developed Laser dust counter,Hitachi Laser Dust Monitor TSI-500, was applied to the characterization of polydisperse DOP aerosols in its size distribution and number density. The results are compared with those measured by an electric aerosol analyzer and a cascade impactor.

II. Experimental

II.1 Apparatus

Fig. 1 shows the fundamental construction of the Laser dust counter (LDC) The laser beam of 0.6328 μm in wave length(He-Ne laser, 8mW,

multimode) passes in the aerosol stream co-axilly. The aerosol surrounded with clean air is introduced into the photocell with the flow rate of 2.8 l/min.

Since the scattered light over 90°±21° is collected with respect to 100 μm of the incident beam, the volume available for photo-counting in the cell is 100 μm or 1000 μm in diameter and 100 μm in length. The summary of the counter's specification is shown in Table 1.

Polystylene latex particles (PSL) of each size (m=1.592, D=0.109 ~ 2.02 μm) were dispersed by injecting the solution with a nebrizer and the respective particles were measured by LDC. Table 2 shows one of the test results. The 80~90 % of PSL primary particles consiting of 0.109 or 0.176 μm were counted in the size range of 0.1~0.2 μm. This result shows that the resolution of 0.1 μm is established by LDC. Fig.2 shows the integrated light scattering cross section of PSL and DOP spheres, respectively, as a function of particle size [3]. Experimental results of scattered light intensities by PSL are plotted in relative values.

II.2 Measurement of polydisperse DOP aerosol

Polydisperse DOP aerosols of 0.5 μm in MMD were generated by mechanical dispersion of DOP liquid by Laskin nozzle. The DOP aerosols of a given concentration were made by diluting them with filtered air and the aerosols were homogenized with a motor-driven mixing fan as shown in Fig.3.

A test was intended to see how the LDC can follow higher number concentration of aerosol. The mass concentration of the DOP aerosol was measured by a Low-volume Air Sampler* and the particle size distribution by Andersen aerosol sampler (AAS)**. Fig.4 shows the experimental results of the total number concentration including the counts in respective size range of the Range 1 and Range 2. The change between ranges can be made automatically. In this test the time of measurement in one range was taken for 10 seconds.

* Shibata Filter Holder 8005-255

** Andersen Particle Fractionating Sampler Model-5600

If the particle size distribution is log-normal, a relation between mass concentration C_m(g/cm^3) and number concentration C_n(particles/cm^3) is shown as

$$C_m = \frac{\rho\pi}{6} C_n \cdot D_g^3 \cdot \exp\,(4.5\ \ln^2\sigma_g)\,, \qquad (1)$$

where ρ (g/cm^3) is the particle density, D_g is CMD(μm) and σ_g is the geometric standard deviation. Fig. 4 shows the relationship up to about 10^5particles/cm^3. Above the mass concentration of 10 mg/m^3, the counting decreases suddenly.

The counting-loss L due to the coincidence of particles in the sensing volume v (cm^3) is given as [4]

$$L = 1 - \exp\,(-\,C_n \cdot v)\,. \qquad (2)$$

Table 3 shows the counting-loss as a function of sensing volume of the LDC. Since the sensing volume in Range 1 is 7.8×10^{-7}cm^3, the coincidence -loss of 10 % corresponds to 1.3×10^5 particles/cm^3 and the volume in Range 2 7.8×10^{-5} cm^3 to 1.3×10^3 particles/cm^3.

The particle size distribution of the same DOP aerosols were measured by LDC and electric aerosol analyzer (EAA) and found to be log-normal as shown in Fig.5. Although EAA is suitable for measuring aerosol particles ranged in 0.003 - 1 μm and LDC for particles in 0.1 - 10 μm, there is a good fit between the results . This means that they check the technique each other and as far as the particle range measured by both methods are reliable.

A cumulative mass percentage by AAS is plotted against particle size together with the results measured by LDC in Fig. 6. Although AAS can measure particles larger than 0.4 μm, there is a small discrepancy between both data with a same value of σ_g.

III summary

A particle counter with a small sensing volume has been developed by applying laser beam as the light source. The counter was used to investigate the measurement of polydisperse DOP aerosols for particle size and number concentration. The data were compared with those obtained by EAA and AAS. It was found that all instruments used in the test show reliable. LDC can be applicable to measure the particle size down to

0.1 μm and the number concentration up to 10^5 particles/cm^3 for particles smaller than 0.5 μm and 10^3 particles/cm^3 for particles larger than 0.5 μm.

Another performance of LDC to point out is to sample aerosols with a high flowrate. AAS and EAA are reliable instrument to characterize aerosol, however,data analysis in-situ are not profitable comparing to LDC.

References

[1]T.R.Marshall, C.S.Parmenter and M.Seaver, J. Colloid and Interface Sci., Vol. 55,p. 64, (1976)

[2]K. Suda, Rev. Sci. Instrum. to be published.

[3]K. Suda, Private communication.

[4] R. Jaenike, J. Aerosol Sci. Vol. 30, p.95 (1972)

TABLE 1 SUMMARY OF SPECIFICATION OF HITACHI LASER DUSTMONITOR TSI-500

LIGHT SOURCE	HE-NE LASER 8 mW WAVE LENGTH 0.6328 μM
OPTICS	COLLECTING SOLID ANGLE 90±21° STERADIANS 0.5 CONVERGED LASER BEAM WIDTH 100 μM 100 μM
SAMPLE AIRFLOW SHEATH AIRFLOW	2.8 1/MIN 3.2 1/MIN
NUMBER OF SIZE RANGE	RANGE 1 0.1 - 0.2 μM 0.2 - 0.3 0.3 - 0.4 0.4 - 0.5 RANGE 2 0.5 - 1.0 μM 1 - 2 2 - 4 4 - 6 6 - 10
DISPLAY	PARTICLE COUNTS IN FOUR DIGIT DECIMAL
COUNTING TIME	MANUAL SETTING 1 - 36000 SEC

TABLE 2 PARTICLE SIZE DISTRIBUTION OF PSL AEROSOLS MEASURED BY A LASER DUST COUNTER

AESOSOL PARITICLE SIZE	PRIMARY PARTICLE SIZE	
	0.109±0.0027μM	0.176±0.026μM
0.1 ~ 0.2 μM	89.0 %	84.6 %
0.2 ~ 0.3	10.6	14.7
0.3 ~ 0.4	0.4	0.7
0.4 ~ 0.5	0	0
>0.5	0	0

TABLE 3 COINCIDENCE-LOSS AND AEROSOL NUMBER CONCENTRATION AS A FUNCTION OF SENSING VOLUME

COINCIDENCE-LOSS (%)	NUMBER CONC. (PARTICLES/CM^3)	
	RANGE 1	RANGE 2
1	1.28×10^4	1.28×10^2
3	3.88×10^4	3.88×10^2
5	6.53×10^4	6.53×10^2
10	1.34×10^5	1.34×10^3
30	4.54×10^5	4.54×10^3

SENSING VOLUME
RANGE 1 : 7.85×10^{-7} CM^3
RANGE 2 : 7.85×10^{-5} CM^3

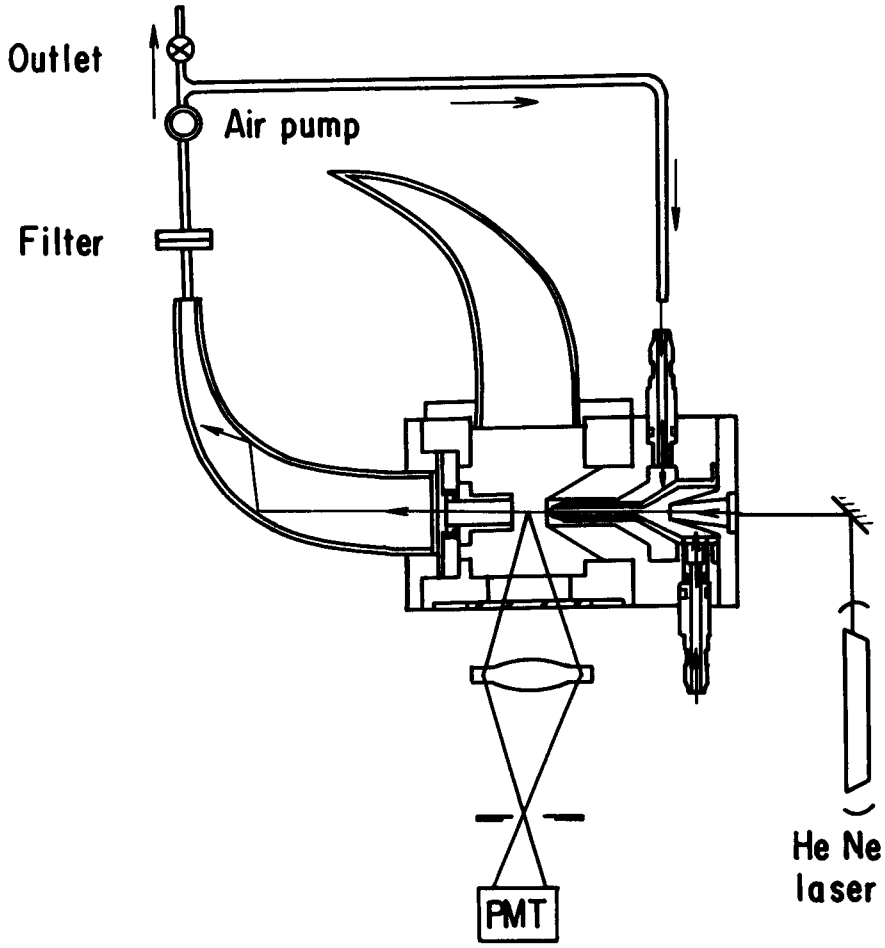

Fig. 1 Fundamental construction of light scattering cell in Hitachi laser dustmonitor

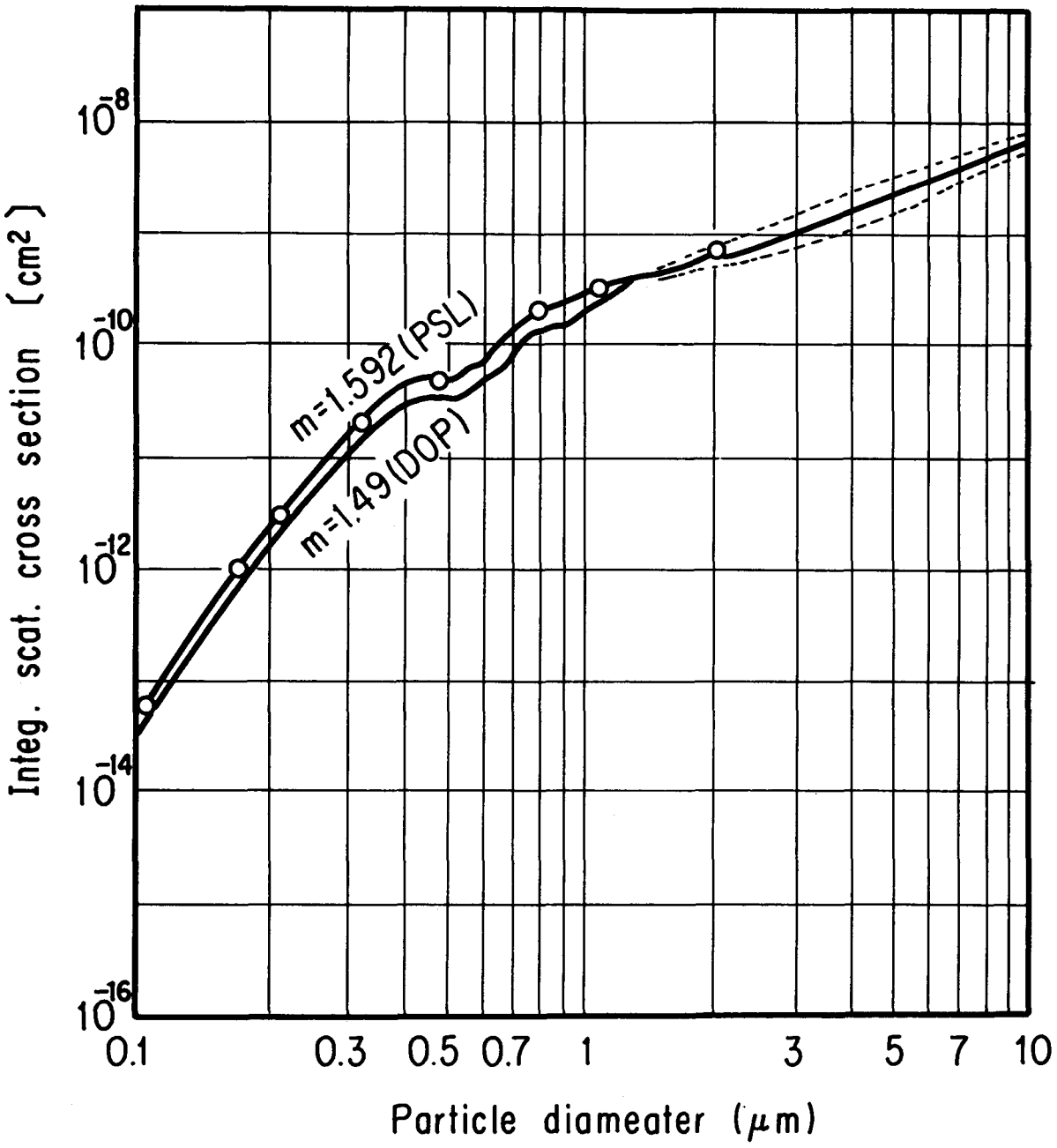

Fig. 2 Integrated light scattering cross section for polystylene latex and DOP spheres
(Collecting angle 90 ± 21 deg.)

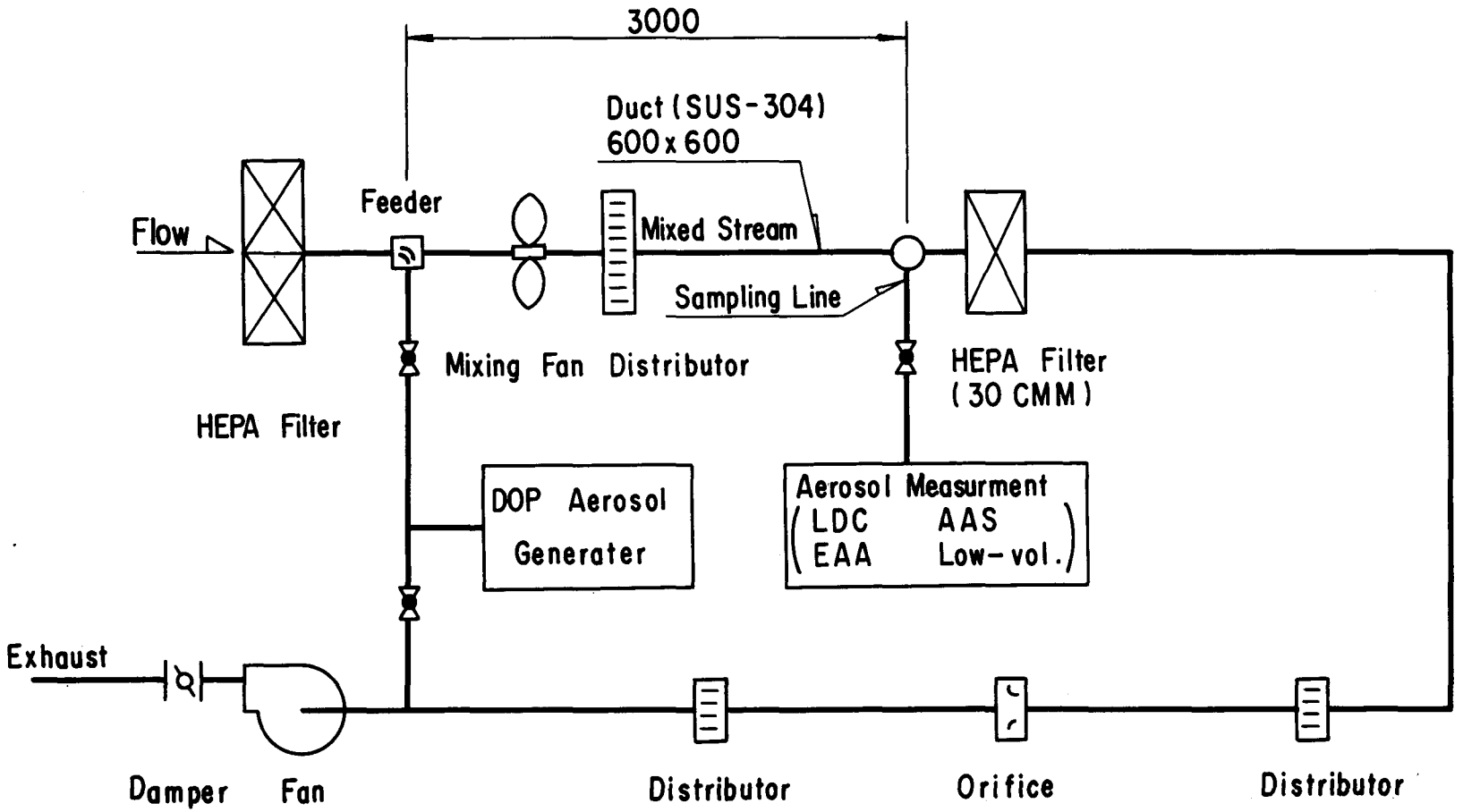

Fig. 3 Polydisperse DOP Aerosol Test

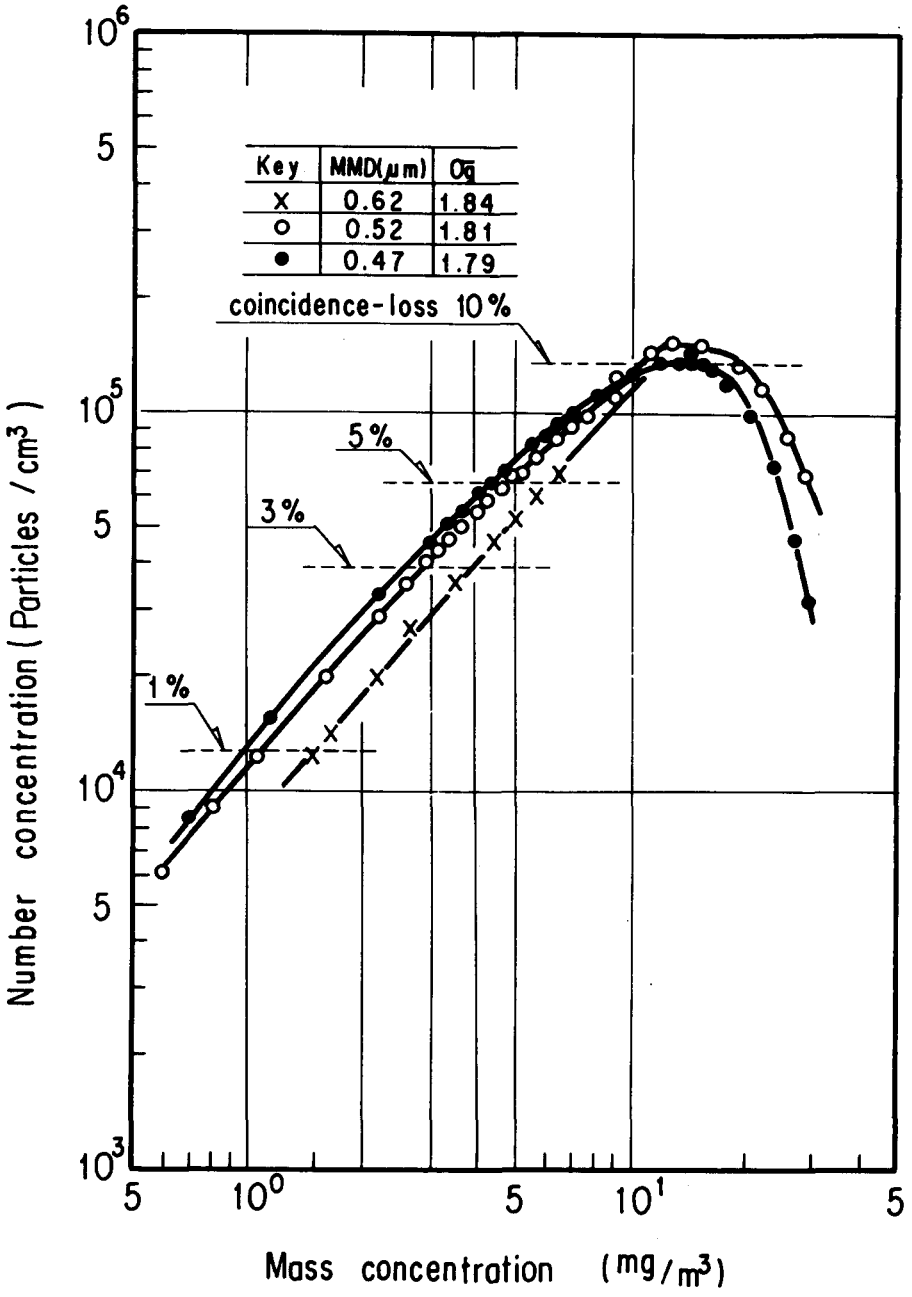

Fig. 4 Number concentratiom vs. coincidence loss for DOP aerosol

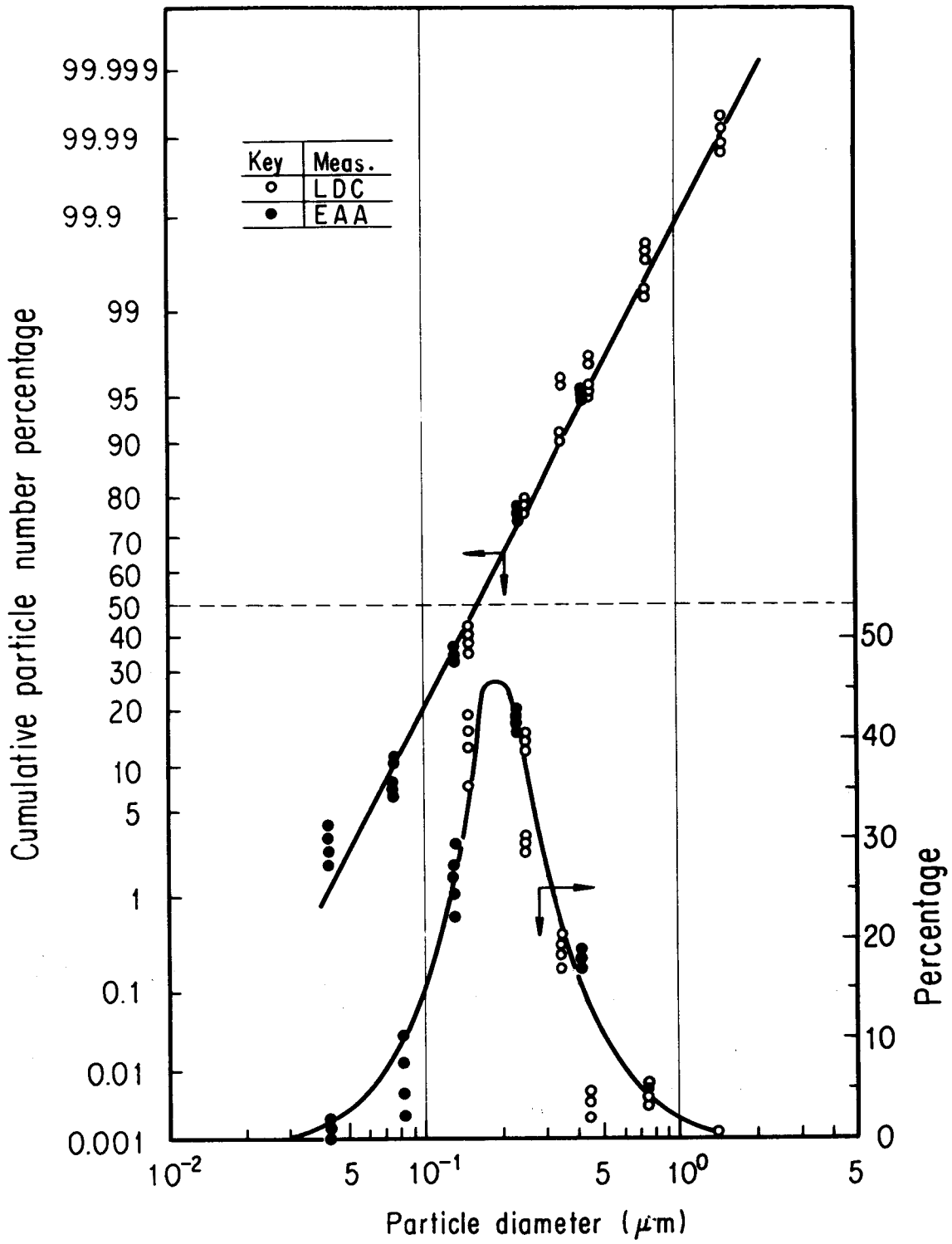

Fig. 5 Particle size distribution of a DOP aerosol sample measured by an electric aerosol analyzer and a laser dust counter

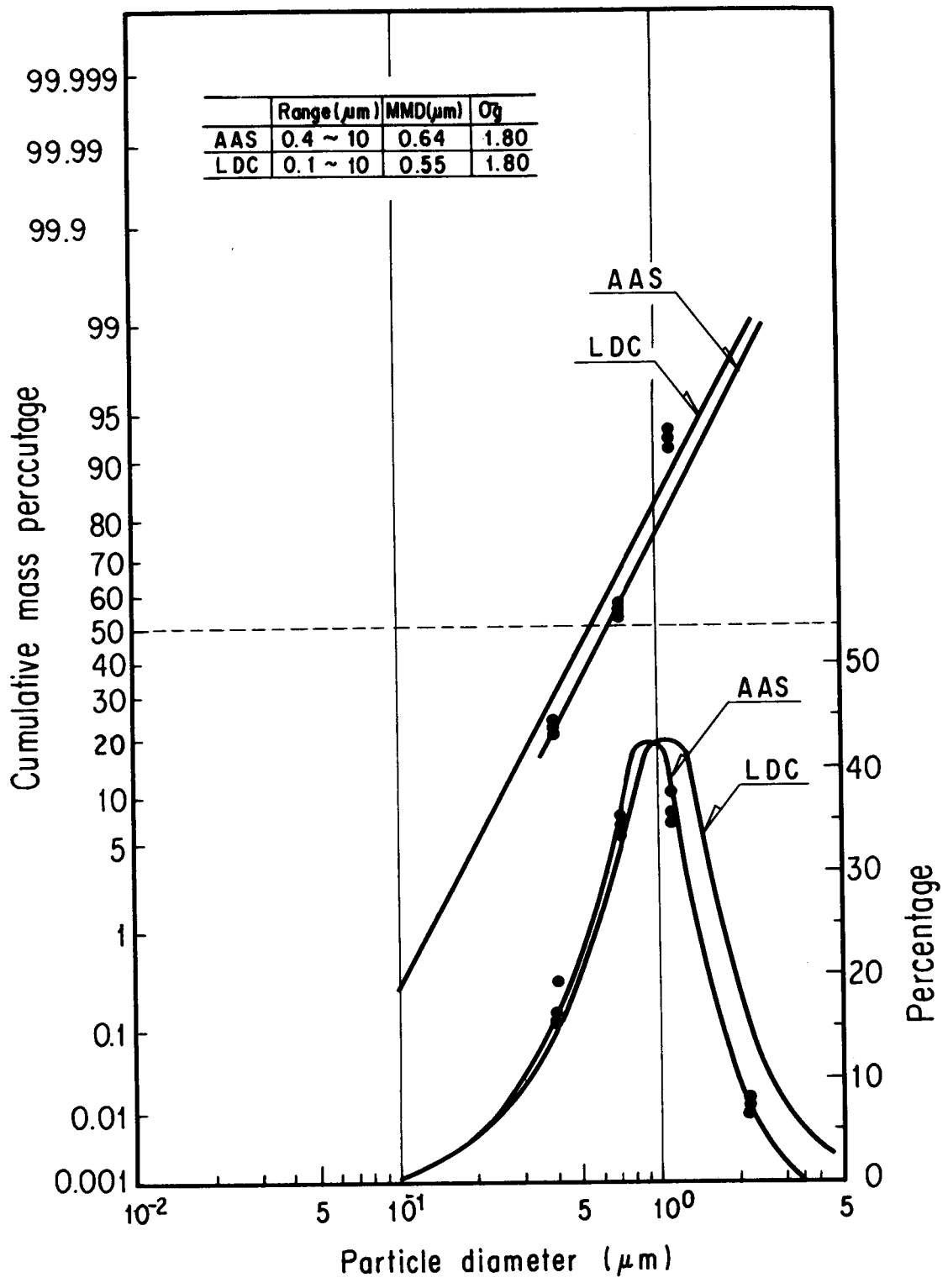

Fig. 6 Particle size distribution of a DOP aerosol sample measured by a cascade impactor (AAS) and a laser dust counter

SUMMARY - PANEL DISCUSSION ON NUCLEAR AEROSOL MEASUREMENTS

Moderator: J. F. van de Vate

Members: V. Prodi, Italy
G. W. Parker, USA
S. Kitani, Japan
D. C. Torgerson, Canada

The purpose of the discussion was defined as being the assessment of measuring ranges of acceptable accuracy of the various aerosol measurement methods available for validation of nuclear aerosol codes. Plus or minus 25% was indicated as an acceptable accuracy, provided systematic errors (mainly due to non-representative sampling) do not play an important role. Nuclear aerosols have the following features which to a great extent complicate the measurements. They have high mass and number concentrations changing very fast in the early life. The particle size ranges from a few 0.01 μm at birth up to several 10 μm later on. There can exist extreme conditions of high temperature, reactive materials and condensation.

In view of this and the general output of computer codes, the measurement methods can be grouped into three categories - mass concentration measurement, - number concentration measurements, - size measurement.

1. Mass concentration (also see Table 1)

Filtration is the most suitable and widely used sampling technique. Electrostatic sampling is also very useful. Inertial sampling, however, is subject to various losses of particles in the size extremes. The intake velocity of thermal precipitators is unacceptably low, making these samplers unsuitable for particles larger than a few μm. Both inertial and thermophoretic sampling are not recommended. The techniques for sample analysis are: chemical or radio analytical analysis, β-ray attenuation, piezo-electric microbalance and gravimetry. With the exception of weighing, the combinations of the various sampling methods with these analytical methods lead to practical measuring ranges with a lower limit of 1 - 10 $\mu g.m^{-3}$ which make them all suitable for yielding data for code validation. Though weighing is less precise, this

technique still is very useful for high mass concentrations. The piezo-electric microbalance is not recommended for solid aggregate aerosols.

It is felt that the main problems with the accuracy of the above given methods for mass concentration measurement are in the entering of and transport in the sampling lines. Calculation and measurement of sampling line losses must be standard procedures in each experiment. Assessment of the effect of non-representative sampling of larger particles (> 5 μm) from the containment atmospheres which are in random movement, is not possible at this time.

2. Number concentration measurement (also see Table II)

The measurement methods can be grouped into two parts according to the analytical techniques of particle counting: optical methods and (electron) microscopical. Optical methods are highly recommended over the second group in view of the high response rates. Laser light scattering counters have measuring ranges up to 10^5 cm^{-3} due to the small sensing volumes. Though short sampling lines are possible, the entrance of the counters can give rise to significant losses of larger particles.

Condensation nuclei counters are very well suited for the measurement of number concentrations of nuclear aerosol in view of their high response rate and their high upper limit of the measuring range: 10^6 - 10^7 cm^{-3}. However, it is reported that these counters can fail to measure sodium fire aerosols correctly.

Filtration and electrostatic (point-to-plane) precipitation can yield samples of solid particles useful for microscopic or electron microscopic counting. The low response rate and tedious counting procedures make them less attractive. Probably, these techniques are useful as reference techniques.

Reference concerning the sampling problems should be made to the previous section on mass concentration measurement.

3. Size measurement (also see Table III)

With the exception of a few cases (particles smaller than 0.1 μm; condensation processes) the aerodynamic diameter is the aerosol size parameter relevant to aerosol rate processes. The aerodynamic diameter can be converted into the mass equivalent diameter (which is in codes the only computer output concerning particle size) by means of the dynamic shape factor and the particle's bulk density. A number of instruments for measuring aerodynamic diameter distributions have been discussed. The spiral centrifuge appears to be the most precise, accurate and reliable instrument in the size range of 0.1 - several μm. For particles larger than several μm, sampling problems limit its use. Impactors which are very popular and relatively easy to use, are subject to considerable errors like overloading, bounce, reentrainment, wall losses, and disaggregation in case of aggregates. The acceptable measuring range is from 0.1 μm to 10 μm though this upper limit can be lower under turbulent conditions. Electrical mobility analysers have their application mainly in the less interesting range of fine particles (0.01 - 0.5 μm). There are problems with the analysis of non-spherical particles and the cross-sensitivity is rather high. Optical particle counters are proposed for size measurement of nuclear aerosols in view of the fast response and on-line analysis. However, the relevance of the sizes measured with this technique for characterizing the aerodynamic aerosol behavior is suspected. Settling chambers have been used for size measurement. Their limitations are in the fields of difficult flow control, limited size resolution and long residence times (particle growth). Cyclones, though finding limited application, have similar size fractionation properties as impactors.

TABLE I. MEASUREMENT METHODS FOR AEROSOL MASS CONCENTRATION

Sampling	Analysis	Practical measuring range	Limitations
filtration	chemical/ radioanalytical	$\geq 1\ \mu g.m^{-3}$	filter blanks, sample contamination, s.l.l.*
electrostatic	chemical/ radioanalytical	$\geq 1\ \mu g.m^{-3}$	s.l.l.*, anal. detection limit
impaction	chemical/ radioanalytical	$\geq 0.1\ \mu g.m^{-3}$	losses of coarse and fine particles
thermophoretic	chemical/ radioanalytical	$\geq 10\ \mu g.m^{-3}$	s.l.l.*
filtration	β-ray absorption	$\geq 1\ \mu g.m^{-3}$	s.l.l.*
electrostatic	piezo-electric	$\geq 1\ \mu g.m^{-3}$	not for aggregates
filtration	weighing	$\geq 0.01\ g.m^{-3}$	hygroscopicness of filter, weighing interferences

*s.l.l. = sampling line losses

TABLE II. MEASUREMENT METHODS FOR AEROSOL NUMBER CONCENTRATION

Sampling	Analysis	Practical measuring range	Limitations
suction	light scatt.	10^{-2}-10^{5}cm^{-3}	>0.3 μm, coincidence
suction	condensation + light scatt. or absorption	10^{-2} / 10^{2})-10^{6}cm^{-3}	s.l.l.*
filtration	(electron) microscopy	10^{2}-10^{5}cm^{-3}	overlap coincidence
electro-static	(electron) microscopy	10^{-2}-10^{6}cm^{-3}	s.l.l.*

*s.l.l. = sampling line losses

TABLE III. MEASUREMENT METHODS FOR PARTICLE SIZE (AERODYNAMIC DIAMETER)

Size fractionation by	Practical measuring range	Limitations
centrifuge	0.1 - several μm	inlet losses
impactor	0.1 - (10) μm	various losses, disaggregation
electric mobility analyzer	0.01 - 0.5 μm	only spherical particles, bad size resolution
optical particle spectrometer	> 0.3 μm	only spherical particles, bad resolution 0.5 - 1.5 μm
cyclone	> few μm	size resolution comparable to impactors
settling chamber	> few μm	bad size resolution

ASPECTS OF THE MOMENTS METHOD FOR AEROSOL CALCULATIONS

E. U. Vaughan
Rockwell International, Energy Systems Group
Canoga Park, California 91304, USA

ABSTRACT

The basis of the aerosol codes HAA-3 and HAARM is the assumption that the particle-size distribution remains log-normal as long as agglomeration processes remain significant. The three parameters of the distribution (airborne concentration, median particle size, and logarithmic variance) are followed in time by means of rate equations for the distribution moments of orders zero, one, and two. Presented here are improvements in the representation by such equations of the thermophoresis process and of the effects of the decrease in effective particle density with increasing particle size. Explicit analytic consequences of special cases of the equations are also presented, both for use in checking the codes and for the sake of possible added insight into aerosol behavior.

I. INTRODUCTION

The evolution of the concentration and size distribution of the particles constituting an aerosol under the influence of sources and of agglomeration and removal processes is described by an integro-differential equation that is not very simple. Analytic solution is possible, with some trouble, only in a few unrealistic cases and reliable numerical solutions that are not impractically slow and expensive have been difficult to discover. A third alternative is represented by the aerosol codes HAA-3 [1], and HAARM [2], which assume that the particle-size distribution remains log-normal as long as agglomeration processes remain significant. The three parameters of the distribution (airborne concentration, median particle size, and logarithmic variance) are followed in time by means of three differential equations derived as rate equations for the distribution moments of orders zero, one, and two.

The contributions to this moments method that are presented below are of two types. The first is to improve the accuracy of the moment equations representing recent additions to or modifications of the physical processes modeled by the codes. The second is to derive explicit analytic consequences of the moment equations, in special cases where this is possible, both for use in checking the codes and for the sake of possible added insight into aerosol behavior.

II. IMPROVEMENT OF MOMENT RATE EQUATIONS

Because of the conservation of mass during aerosol coagulation, the mass, m, of the aerosol particle is the size parameter most readily available for aerosol calculations. It is used in aerosol codes as the basic particle size variable. The present exposition will follow the "HAA-3 User Report" [1] in using as the independent variable the cube, V, of the radius, r, of the sphere of ideal density, ρ_I, having the same mass as the actual particle, where

$$V = r^3 = 3m/(4\pi\rho_I) \quad . \tag{1}$$

An actual aerosol particle is quite different from a sphere of ideal density in both appearance and behavior. In particular, the settling velocity, U_s, differs from that given by Stokes for an ideal sphere by a correction factor, here designated α and introduced in the form

$$U_s = \alpha mg/(6\pi\eta V^{1/3}) \quad , \tag{2}$$

where η is the dynamic viscosity of the suspending air, and the Cunningham correction has been omitted. Since the factor m, the particle mass, is not subject to correction, the factor α is interpreted as dividing $r = V^{1/3}$ to produce the effective particle radius corresponding to an effective density different from the ideal density.

The original practice of taking α as a constant is now sometimes varied [2] by taking α as a function of particle size. The functional form suggested by Stöber, et al. [3][4] is

$$\alpha = \alpha_0 (V_0/V)^{1/3} , \tag{3}$$

where V_0 is a convenient reference value of V and α_0 is the corresponding value of α. Since corrections to this form suggested by experiments of Kops, et al. [5] are not supported by later experiments of van de Vate, et al. [6], and the subject is still under investigation, it seems best for the present to restrict attention to the relatively simple form of Equation 3.

The change from constant α to this form of varying α is the principal model modification whose corresponding moment rate equations have now been improved. The other is the introduction of thermophoresis as a deposition mechanism. The method used hitherto [2] to treat these effects is to replace V, either in $\alpha(V)$ or in the thermophoretic removal-rate coefficient, by an average value, $\bar{V}$. The average used is the ratio of the moments of orders one and zero. This method has the advantage of applicability to any functional dependence on V, including the Kops form [5] of $\alpha(V)$ and the Brock form [7] of thermophoretic deposition rate. The significance of the loss of accuracy due to this approximation is reduced by the uncertainties already present in the models and by any inaccuracy that may result from the log-normal assumption.

For the relatively simple form of $\alpha(V)$ of Equation 3, however, there is no obstacle to the derivation of the exact moment rate equations. The same is true of Brock's thermophoretic velocity, provided certain intractable but relatively small terms in the denominator, representing higher order effects of the nonvanishing mean free path of air molecules, are omitted. These terms can then be restored by the previous method [2] of using in them an average value for V, but the original choice of the average used for this purpose can be reconsidered and, in fact, has been improved. The new moment rate equations obtained by these improved derivations are now being incorporated in the current developmental version of HAA-3, called HAA-3C.

The effect of the new treatment of thermophoresis, prior to the restoration of the correction terms previously mentioned, is to make this process depend on particle size in exactly the same way as diffusive wall deposition with the Cunningham correction omitted. Since the boundary layer thickness for Brownian diffusion has commonly been treated as an empirically adjustable parameter in applying the codes, it appears that a fairly good approximation to thermophoresis was present implicitly even in the early version that had no explicit thermophoresis model, empirical adjustment naturally being made to fit the total wall deposition.

The fallout rate coefficient is simply the ratio of the settling velocity U_S of Equation 2 to a suitable mean containment height. Consequently, the older method of introducing $\alpha(V)$ from Equation 3 by using $\alpha(\bar{V})$ produces a

factor $(\bar{V}V)^{-1/3}$ which, when corrected, becomes $V^{-2/3}$ instead. Integration with respect to V to get moment equations then leads to results for the two cases that differ as follows. The contribution to the k^{th} moment equation (where k = 0, 1, or 2) acquires from the correction a new factor

$$\exp(-ku/3) , \tag{4}$$

where u, the logarithmic variance of the log-normal distribution, is related to the customary width parameter, σ, by the equation

$$u = (3\ell n\sigma)^2 . \tag{5}$$

The effect of the new analysis on gravitational agglomeration is considerably more complex, despite the fact that this process does not contribute to the rate equation for the first moment. One important effect, however, can be stated simply. The ratio of the contributions to the rate equations for the moments of orders two and zero acquires in the corrected treatment a factor

$$\exp(u/3) \tag{6}$$

that is not present in the treatment using $\bar{V}$. This is the same factor by which successive moments differ in Equation 4.

The above summary of the effects of size dependence of α on gravitational processes (fallout and agglomeration) does not include the Cunningham correction. This omission does not affect the orders of magnitude of the various contributions, however. The main effect of improving the treatment using $\bar{V}$ can thus be seen to be changes in the relative sizes of various rate contributions by factors of exp(u/3) or its square. When the usual width-parameter σ has the value 2, which is not unreasonable, the value of u from Equation 5 is about 4.5, and so is the value of exp(u/3). This appears to be a substantial effect.

III. EXPLICIT ANALYTIC RESULTS

The original exposition [8] of the moments method based on a log-normal size distribution included a partial analytic solution of the resulting differential equation system for the case of Brownian agglomeration without the Cunningham correction. Despite its limitations, this work was of considerable interest because of its conclusion that Brownian agglomeration, in the absence of other processes, would cause the width, σ, of the size distribution to evolve toward a "self-preserving" value near 1.32. Partly because of this encouraging precedent, and partly because of the need for explicit analytic results with which to compare numerical solutions as a check of the codes being developed, the differential equation system produced by the moments method has been examined in search of analytically tractable special cases.

If agglomeration processes only are considered, sources and removal processes being omitted, the system is simplified because of the resulting conservation of suspended mass concentration. This conserved quantity being the moment of order one, only the two moments of orders zero and two can vary, and the order of the system is reduced from third to second. The fact that the coagulation kernel is independent of the time permits a further reduction of order by elimination of the time, leading to a first-order differential equation relating the two moments that vary. The principal question is then whether or not that equation is tractable. The result found is that the equation is tractable for any particular agglomeration process considered by itself, provided the Cunningham correction is omitted.

These considerations are exemplified by the case of gravitational agglomeration with constant collision efficiency and size-independent Stokes correction factor α. In the absence of the Cunningham correction, the rate equations for the moments, X_k, are [1]

$$\dot{X}_0 = -G_1 X_0 X_1 \exp(\mu/3) f(u) \ , \tag{7}$$

$$\dot{X}_1 = 0 \ , \tag{8}$$

$$\dot{X}_2 = 2G_1 X_1 X_2 \exp(\mu/3 + u/3) f(u) \ , \tag{9}$$

where

$$f(u) = \exp(u/18)\left[\exp(u/3)\operatorname{erf}(2\sqrt{u/3}) + 2\ \operatorname{erf}(\sqrt{u/3})\right] \ , \tag{10}$$

and the log-normal parameters, μ and u, are expressed in terms of the moments by the relations

$$\exp(-2\mu) = X_0{}^3 X_2 / X_1{}^4 \ , \tag{11}$$

$$\exp(u) = X_0 X_2 / X_1{}^2 \ , \tag{12}$$

while G_1 is a constant.

The constant value of X_1 implied by Equation 8 being denoted by x, the result of eliminating the time by taking the ratio of Equations 7 and 9 is written, with help from Equation 12, as

$$dX_2/dX_0 = -2X_2{}^{4/3}/(X_0 x)^{2/3} \ . \tag{13}$$

This equation is readily solved by separation of variables, with the result

$$(x/X_2)^{1/3} = 2(X_0/x)^{1/3} - D \ , \tag{14}$$

where D is a constant of integration. According to Equation 12, the necessity that u be positive requires that D be positive.

Use of Equations 11, 12, and 14 reduces Equation 9 to an equation for X_2 as a function of the time. Because of the complexity of the function f(u) given by Equation 10, this equation cannot be solved explicitly. For large values of X_2, however, it simplifies approximately to

$$\dot{X}_2 \approx 2G_1(2/D)^{7/9}x^{32/27}X_2^{29/27} . \tag{15}$$

The solution of this equation can be written

$$2G_1x^{32/27}(2/D)^{7/9}(t^* - t) \approx (27/2)/X_2^{2/27} , \tag{16}$$

where the constant of integration, t*, is a finite time value at which the second moment, X_2, becomes infinite. This constant cannot be evaluated explicitly in terms of the initial conditions unless the approximate Equation 15 is already valid for those conditions. Equation 14 then gives the value approached by X_0 as t approaches t* and x/X_2 approaches zero.

The value of these results is limited by the unrealism of omitting all removal processes, the localization of Equation 16 to times approaching the undetermined t*, the incompleteness of Equation 14 by itself, and the availability of numerical solutions. Nevertheless, the partial result at Equation 14 does provide a means of checking numerical solutions and the codes that produce them. Also, the divergence of the second moment at a finite time in the absence of removal mechanisms shows that gravitational agglomeration has a far greater potential than Brownian agglomeration, which does not lead to such behavior, for producing large agglomerates.

Similar results, in the form of a single explicit integral of the system (in addition to the conservation law for X_1) together with divergence of X_2 at an undetermined finite time, have also been derived for gravitational agglomeration when the collision efficiency or the Stokes correction factor α is a function of particle size. Thus, all these cases admit analytic tests of numerical results and show a strong tendency to produce large agglomerates rapidly.

If removal processes are considered in the absence of agglomeration, the loss of the conservation law for airborne concentration is compensated by the total lack of physical interaction between the aerosol particles. This property is expressed mathematically as "homogeneity" of the differential equation system, in the sense that the system is unchanged if all moments X_k are multipled by the same constant. It follows that a closed system of lower order (second instead of third) can be obtained by using ratios of the moments instead of the moments themselves. This system can be reduced to a first-order equation by elimination of the time because the removal rates, like the coagulation rates, do not contain the time explicitly. The resulting equation can be solved if the original system

is sufficiently simple, which happens if no more than a single removal process is considered with omission of such complicating details as the Cunningham correction.

The special case of fallout with size-independent Stokes correction factor α gives an example of these generalities. The ratios of the moments are

$$p = X_1/X_0 \ , \ q = X_2/X_1 \ , \tag{17}$$

and it is convenient to introduce also a function

$$y = \exp(2u/3) - 1 = (q/p)^{2/3} - 1 \ , \tag{18}$$

the equivalence of the two forms following from Equations 12 and 17. The first integral of the system of rate equations [1] without the Cunningham correction is

$$y = Hq^{2/3} \ , \tag{19}$$

where H, the constant of integration, is positive because u of Equation 18 must be positive. A second integral can be obtained explicitly in the form

$$X_1 = X_{10}\exp\left[(3/2)(1/y_0 - 1/y)\right], \tag{20}$$

where X_{10} and y_0 are the values of X_1 and y at t = 0. The rate equation for y then has the form

$$\dot{y} = -(2/3)(G_R/H)y^3(1 + y)^{-1/6} \ , \tag{21}$$

which is a little too complex for practical explicit solution. Nevertheless, it has two simple features worth noting.

The first is that the time enters only in the combination

$$G_R t/H \ , \tag{22}$$

so the solution must give y as a function of this combination, after which Equation 20 gives the airborne concentration X_1 (as a function of time) also in terms of this combination. Both t and G_R are prevented by dimensional considerations from appearing otherwise than in the combination $G_R t$, but the inclusion of H in the combination is a further restriction on the solution.

The second feature of Equation 21 is that y, which decreases with increasing time, ultimately becomes small enough to justify its neglect relative to unity. The equation is then

$$\dot{y} \approx -2G_R y^3/(3H) \ , \tag{23}$$

and has the simple solution

$$(4/3)(G_R/H)(t - t_o) \approx 1/y^2 - 1/y_o^2 , \qquad (24)$$

where t_o is the value of t at which y would have the value y_o if the approximate Equation 23, rather than the exact Equation 21, were followed backward to times before the approximation is valid. From Equations 24 and 20, it follows that the logarithm of the airborne concentration $X_1(t)$ ultimately decreases like the square root of a linear function of the time. This statement is subject to experimental testing, since agglomeration is insignificant compared to fallout in the late stages of aerosol evolution. Ignorance of the constant t_o makes it difficult, however, to exploit this result to simplify experimental plotting of $X_1(t)$.

These analyses of greatly simplified special cases of the aerosol moment equations do not exhaust the possibilities for arriving at explicit results. Another idea that has been tried is to look for steady states, in which the time derivatives of all the moments vanish. The situation thus envisaged has a source of fine aerosol particles that agglomerate to large sizes at which they fall out. Because of the wide range of particle sizes created in this way, the width parameter u is large and the equations may be simplified by retaining only the terms that increase most rapidly with increasing u.

In the rate equation for the moment of order zero [1] the contribution from the source, S_o, must be balanced by an agglomeration process. Since Brownian agglomeration increases rather slowly with increasing u, it appears probable that gravitational agglomeration is the dominant process. The equation then takes the simplified form

$$S_o = G_1 X_0 X_1 \exp(\mu/3 + 7u/18) . \qquad (25)$$

In the rate equation for the first moment [1] there is no contribution from agglomeration and the source contribution, S_1, must be balanced by removal. Neglecting all removal other than fallout, as is appropriate for large containments, the equation between the dominant terms is

$$S_1 = G_R X_1 \exp(2\mu/3 + 8u/9) . \qquad (26)$$

The second moment and its rate equation [1] are dominated by large particles. The source particles being small, the source contribution to the equation can be neglected. The dominant terms of the resulting balance between fallout and agglomeration then constitute the equation

$$G_R \exp(\mu/3 + 5u/6) = 2G_1 X_1 . \qquad (27)$$

Equations 25, 26, and 27, together with Equations 11 and 12, constitute a system of five equations for the five quantities X_0, X_1, X_2, μ, and u. The simplifying approximations that have been made have reduced them to

binomial equations. By taking logarithms of both sides, they are transformed into linear equations in μ, u, and the logarithms of the moments. Since this happens only for binomial equations, the tractability of the system depends on the approximations. The linear system has a unique solution that determines the airborne concentration, the average particle size, and the width of the particle-size distribution to be:

$$X_1 = (S_o/4S_1)^{1/6}(S_1/G_1)^{1/2} , \tag{28}$$

$$\exp(\mu) = (S_1/2S_o)^{31/28}(G_R{}^2/2S_1G_1)^{3/28} , \tag{29}$$

$$u = \frac{9}{14} \ell n \left[4S_oG_1/G_R{}^2\right] . \tag{30}$$

The independence of X_1 of Equation 28 from the fallout constant G_R is an aspect of a phenomenon that has already been observed [1] [9] in calculations with HAA-3B. This is that X_1 is fairly sensitive to the product, $\alpha\epsilon$, of the Stokes correction factor and the collision efficiency, but is quite insensitive to variations of these parameters that do not change their product. Since $\alpha\epsilon$ is a factor of G_1 and α is a factor of G_R, this means that X_1 is sensitive to G_1 but not to G_R. This situation is now confirmed analytically for the steady state.

The extension of the insensitivity to G_R to conditions other than the steady state may come about as follows. During the approach to the steady state, fallout is not very important until the late stages when the departure from the steady state has become too small for G_R to have much effect. When the steady state is lost at the termination of the source, the evolution of the system cannot at first be followed except numerically, but becomes analytically tractable again when the concentration is reduced to a value so low that agglomeration effectively ceases ("SSM condition"), as in Equations 19 through 21. At this stage, G_R enters only in the combination at Equation 22 containing H. Apparently this constant of integration, H, whose value is established during the intractable transition regime, adjusts itself to compensate for changes in G_R, leaving the ratio H/G_R quite stable.

IV. CONCLUDING COMMENTS

While the explicit analytic results that have been obtained for special cases of the aerosol moment equations are expected to be useful in checking computer programming, the extension of such results to obtain approximations to complete solutions has limited value because of the special and frequently unrealistic character of the tractable cases, the inability to express the constant of integration associated with the approximation in terms of the initial conditions, and the intention of relying on the numerical solutions provided by computer codes. Nevertheless, it is believed that the light thrown on the previously observed insensitivity of airborne concentration histories to the fallout coefficient G_R, as well as the suggestiveness of the divergence of the second moment at a finite time if growth by gravitational agglomeration is not

checked by fallout, are interesting and significant results of these partial or approximate analyses.

The improved representation of new mechanisms, or of corrected models of old ones, as exemplified in the treatments above of thermophoresis and of size-dependence of the Stokes correction factor α, is expected to be a recurring process as progress continues in experimental investigation of aerosol behavior. The factor α is still under investigation, as well as the gravitational collision efficiency, and effects of humidity, evaporation and condensation, and mixed composition of the aerosols are beginning to be reported. New problems for the moments method will arise from such work. These problems can be attacked with increased confidence in view of the successes represented by the new formulations presented herein.

REFERENCES

1. Hubner, R. S., et al., "HAA-3 User Report," AI-AEC-13038 (March 30, 1973)

2. Gieseke, J. A., et al., "HAARM-3 Users Manual," BMI-NUREG-1991 (January 5, 1978)

3. Stöber, W., et al., "The Aerodynamic Diameter of Aggregates of Uniform Spheres," J. Colloid Interf. Sci, 29, 710 (1969)

4. Stöber, W., et al., "Der Aerodynamische Durchmesser von Latex-aggregaten und Asbestfassern," Staub-Reinhalt. Luft 30, 277 (1970)

5. Kops, J., et al., "The Aerodynamic Diameter of Branched Chain-Like Aggregates," J. Aerosol Sci. 6, 329 (1975)

6. van de Vate, J. F. et al., "Aerodynamic Properties of Aerosols and Their Leakage Through Concrete Containment Structures," to appear in the Proceedings of the ANS/ENS International Meeting on Fast Reactor Safety Technology, Seattle, Washington, USA, August 19-23, 1979

7. Reed, L. D., and Gieseke, J. A., "HAARM-2 Users Manual," BMI-X-665 (October 1975)

8. Cohen, E. R., and Vaughan, E. U., "Approximate Solution of the Equations for Aerosol Agglomeration," J. Colloid Interf. Sci. 35, 612 (1971)

9. Hilliard, R. K., et al., "Aerosol Behavior During Sodium Pool Fires in a Large Vessel - CSTF Tests AB1 and AB2," HEDL-TME 79-28 (June 1979)

THE RELATIVE IMPORTANCE OF VARIOUS COAGULATION AND REMOVAL MECHANISMS FOR AEROSOLS IN FINITE CONTAINERS

M.M.R. Williams
Nuclear Engineering Department
Queen Mary College
University of London

T.M. Fry
Associated Nuclear Services
Epsom, UK

S.A. Harbison
Nuclear Installations Inspectorate
Health and Safety Executive
London, UK

ABSTRACT

Seven distinct processes of aerosol particle coagulation and removal are studied and assessed quantitatively. These are Brownian coagulation, sedimentation coagulation, laminar and turbulent shear coagulation, turbulent inertial coagulation, diffusion to surfaces and gravitational settling. From the basic kinetic balance equation for the particle volume distribution function, n(v,t), we obtain coupled equations for the aerosol number density and volume fraction. The magnitudes of the removal rates for the seven mechanisms described above are given in a concise form. The results show the dominance of Brownian coagulation at early stages in the aerosol life, with the progressive increase in importance of gravitational settling as the aerosol ages. Other mechanisms, such as turbulent and laminar shear coagulation, are seen to be only of secondary importance, unless some artificial method is introduced to promote their action.

1. INTRODUCTION

An understanding of the behaviour of radioactive aerosols is of importance in predicting the consequences of hypothetical reactor accidents. Qualitative considerations indicate that a number of natural processes should cause dispersoids to be removed from the gas phase and so reduce the amount of radioactive material that is available for release to the environment. However, in the past, many of these processes have been so poorly quantified that they have tended to be discounted in safety analyses; this has undoubtedly led to extremely pessimistic estimates of the radiological consequences of some large reactor accidents. More recently, a number of important experimental and analytical advances have been made and it is now possible to attempt to include aerosol coagulation and removal processes in safety analyses. The CSNI state-of-the-art report [1] on Nuclear Aerosols in Reactor Safety concluded that analysis methods, supported by a substantial data base, were at an advanced state of development for predicting nuclear aerosol transport in LMFBR containment following postulated severe accidents. The report also found an encouraging level of agreement between the predictions of the various aerosol codes for the LMFBR "postulated generalised working accident".

The present paper describes part of a general quantitative study [2] of the behaviour of aerosols under conditions representative of those that might be encountered in a hypothetical whole-core accident in a commercial fast reactor. The problem of the behaviour of an aerosol in a containment has been studied analytically, with the object of obtaining estimates of the relative importance of different coagulation and removal processes. A further purpose of the work has been to obtain estimates of aerosol density and particle mean radius as functions of time. The overall intention of these studies has been to provide the safety assessor with a series of analytical expressions which can be used to explore the regions of importance for the various aerosol processes and so judge the likely impact of alternative design options on the safety case. Seven coagulation and removal processes are considered and their relative importance is assessed by comparing the corresponding rates of reduction of particle number density, using the similarity transform technique. The method is easy to use and, for general comparative surveys, is unlikely to be a source of large errors.

In order to assess quantitatively the time dependence of aerosol density and particle size, only the two most important mechanisms are considered, namely Brownian coagulation and gravitational settling. Using the similarity transform, a complete solution of the kinetic equation in the absence of source terms, valid over a useful range of particle size, is obtained. The analytical expressions enable the aerosol density, volume fraction of suspended matter and mean particle volume to be obtained quickly without the need to employ the full kinetic equation. Comparison of these results with numerical solutions of the kinetic equation show excellent agreement.

2. THE COAGULATION AND REMOVAL MECHANISMS

In this section we give mathematical expressions for the coagulation and removal mechanisms and cast them into a form convenient for study. The basic kinetic equation for the particle volume distribution function takes the following form:

$$\frac{\partial n(v,t)}{\partial t} + \left\{\frac{1}{\tau_s(v)} + \frac{1}{\tau_p(v)}\right\} n(v,t) = \tfrac{1}{2}\int_0^v du\, f(u,v-u)\, n(u,t)\, n(v-u,t) - n(v,t)\int_0^\infty du\, f(u,v)\, n(u,t) + S(v,t) \qquad (1)$$

In (1), τ_s is the time constant for removal by settling under gravity, and τ_p is the time constant for removal by diffusion to surfaces. As usual, $f(u,v)$ denotes the coagulation kernel. $S(v,t)$ is a source term due to continuously produced aerosol. In principle, we should also include a removal term due to evaporation, but generally this may be ignored.

We proceed by taking moments of (1), i.e. multiplying by v^n and integrating over all v, $0<v<\infty$. The results for n=0 and n=1 give the two basic conservation equations upon which our work will rest. Thus we find:

$$\frac{dN(t)}{dt} = -\tfrac{1}{2}\int_0^\infty du \int_0^\infty dv\, f(u,v)\, n(u,t)\, n(v,t) - \int_0^\infty dv \left\{\frac{1}{\tau_s(v)} + \frac{1}{\tau_p(v)}\right\} n(v,t) + S(t) \quad (2)$$

where the total particle number density, N(t), is given by:

$$N(t) = \int dv\, n(v,t) \quad (3)$$

Similarly, conservation of volume gives:

$$\frac{d}{dt}\int_0^\infty dv\, v\, n(v,t) = -\int_0^\infty dv\, v \left\{\frac{1}{\tau_s(v)} + \frac{1}{\tau_p(v)}\right\} n(v,t) + S_v(t) \quad (4)$$

The integral on the left hand side of (4) we call $\phi(t)$ and note that it corresponds to the total volume of particulate matter per unit volume of space, i.e. the volume fraction. In the absence of both sources and deposition, $\phi(t)$ is a constant.

Let us now outline the forms taken by the various parameters appearing above.

(a) Brownian coagulation with first order Cunningham correction

$$f(u,v) = \frac{2kT}{3\eta}\left\{\frac{1}{u^{1/3}} + \frac{1}{v^{1/3}}\right\}(u^{1/3} + v^{1/3}) + \alpha\frac{2kT}{3\eta}\left\{\frac{4\pi}{3}\right\}^{1/3}\left\{\frac{1}{u^{2/3}} + \frac{1}{v^{2/3}}\right\}(u^{1/3} + v^{1/3}) \quad (5)$$

where $\alpha = 1.125\lambda_G$, λ_G being the mean free path of gas atoms in the host gas.

(b) Differential sedimentation coagulation

$$f(u,v) = \frac{\rho_p g}{6\eta}\left\{\frac{3}{4\pi}\right\}^{1/3} E_S(u,v)\,(u^{1/3} + v^{1/3})^3\,|u^{1/3} - v^{1/3}| \quad (6)$$

where $E_S(u,v)$ is the collision efficiency appropriate to this mechanism.

(c) Coagulation due to laminar shear flow

$$f(u,v) = \frac{\Gamma}{\pi} E_L(u,v)\,(u^{1/3} + v^{1/3})^3 \quad (7)$$

where Γ is the velocity gradient and E_L the appropriate collision efficiency.

(d) Coagulation due to turbulent shear flow

$$f(u,v) = 0.975\left(\frac{E_T\rho_G}{\eta}\right)^{1/2}\frac{\hat{E}(u,v)}{\pi}(u^{1/3} + v^{1/3})^3 \quad (8)$$

where E_T is the rate of energy dissipation in turbulence per unit mass of gas and $\hat{E}$ the appropriate collision efficiency.

(e) Coagulation due to turbulent inertial flow

$$f(u,v) = \frac{2}{9}\frac{E_T^{3/4}}{\eta^{5/4}}\rho_G^{1/4}\rho_p\left\{\frac{3}{4\pi}\right\}^{1/3}\tilde{E}(u,v)\,(u^{1/3}+v^{1/3})^3\,|u^{1/3}-v^{1/3}| \quad (9)$$

According to Saffman and Turner [3], the factor 2/9 should be replaced by 1.28.

(f) Removal by diffusion to surfaces

In a well mixed aerosol which is continuously stirred, deposition takes place onto surfaces by diffusion through a sub-layer of thickness δ. The time constant for this process is given by:

$$\frac{1}{\tau_p(v)} = \frac{D(v)S}{V\delta} \tag{10}$$

where S is the surface area of the vessel, V its volume and D(v) is the Brownian diffusion coefficient, viz:

$$D(v) = \frac{kT}{6\pi\eta}\left\{\frac{4\pi}{3}\right\}^{1/3} \frac{1}{v^{1/3}}\left\{1 + \frac{1.813\lambda_G}{v^{1/3}}\right\} \tag{11}$$

where we have used the first order Cunningham correction.

(g) Removal by settling under gravity

The rate of removal due to settling can be approximated by a time constant for residence, viz:

$$\frac{1}{\tau_s(v)} = \frac{V_s(v)}{h} \tag{12}$$

where h is the height of the containment chamber and $V_s(v)$ is the Stokes settling velocity given by:

$$V_s(v) = \frac{2\rho_p g}{9\eta}\left\{\frac{3}{4\pi}\right\}^{2/3} v^{2/3} \tag{13}$$

In principle, a Cunningham correction should be included here, but in practice the settling term is only important when particles have become sufficiently large for this correction to be small.

3. USE OF THE SIMILARITY TRANSFORM METHOD

It is well known that a consistent solution of the kinetic equation may be obtained by using a similarity transform, in which the solution is represented in the form:

$$n(v,t) = \frac{N^2(t)}{\phi(t)}\,\psi\left\{\frac{vN(t)}{\phi(t)}\right\} \tag{14}$$

where $\psi(x)$ is a universal function for a particular process. In this section, we use this method to evaluate each coagulation and removal mechanism and then compare them as functions of particle number density. It is useful to note that Lindauer and Castleman [4] have found experimentally that the log-normal distribution is a good approximation to $\psi(\eta)$. However, we use $\psi(\eta)=e^{-\eta}$ for simplicity.

3.1 Transformation of the coagulation and removal rate equations

The coagulation or removal rate, R_i, for each of the seven processes discussed above is transformed into a function of N and ϕ by substitution of (14) into the right-hand sides of (2) and (4). Then we find:

(a) Brownian coagulation

$$R_1 = \frac{4.4183kT}{3\eta} N^2 + \frac{4.4183kT}{3\eta}(3.0753\,\lambda_G)\,\phi^{-1/3} N^{7/3} \tag{15}$$

(b) Differential sedimentation coagulation

$$R_2 = \frac{\rho_p g}{12\eta}\left(\frac{3}{4\pi}\right)^{1/3} K_S\, \phi^{5/3} N^{2/3} \qquad (K_S \simeq 0.4) \tag{16}$$

(c) Coagulation due to laminar shear flow

$$R_3 = \frac{\Gamma}{2\pi} K_L \phi N \qquad (K_L \simeq 0.8) \tag{17}$$

(d) Coagulation due to turbulent shear flow

$$R_4 = 0.975 \left(\frac{E_T \rho_G}{\eta}\right)^{\frac{1}{2}} \frac{\hat{K}_T}{2\pi} \phi N \tag{18}$$

(e) Coagulation due to turbulent inertial flow

$$R_5 = \frac{2}{9} \frac{E_T^{3/4}}{\eta^{5/4}} \rho_G^{1/4} \rho_p \left(\frac{3}{4\pi}\right)^{5/3} \tilde{K}_T \phi^{5/3} N^{2/3} \tag{19}$$

where $\tilde{K}_T$ involves the collision efficiency in inertial collisions. We shall take $\tilde{K}_T = K_S$, but there is some uncertainty here.

(f) Diffusion to surfaces

$$R_6 = \Gamma(2/3) \left(\frac{4\pi}{3}\right)^{1/3} \frac{SkT}{V\delta 6\pi\eta} \phi^{-1/3} N^{1/3} + \Gamma(1/3) \left(\frac{4\pi}{3}\right)^{1/3} \frac{SkT}{V\delta 6\pi\eta} 1.813 \lambda_G \phi^{-2/3} N^{5/3} \tag{20}$$

(20) contains a first order Cunningham correction.

(g) Settling under gravity

$$R_7 = \frac{2}{9} \frac{\rho_p g}{h\eta} \Gamma(5/3) \left(\frac{3}{4\pi}\right)^{2/3} \phi^{2/3} N^{1/3} \tag{21}$$

In order to complete the loss rates, we require from (4) the volume removal rate. The contribution to this from coagulation is of course zero, but there is a continuous loss through diffusion and settling. Thus we have:

$$\frac{d\phi(t)}{dt} = -\int_0^\infty dv\, v \frac{V_s(v)}{h} n(v,t) - \int_0^\infty dv\, v \frac{D(v)S}{V\delta} n(v,t) \tag{22}$$

Using the similarity transform, we find:

$$\frac{d\phi(t)}{dt} = -R_8 - R_9 \tag{23}$$

where the settling term:

$$R_8 = \frac{2\rho_p g}{9h\eta} \left(\frac{3}{4\pi}\right)^{2/3} \Gamma(5/3) \phi^{5/3} N^{-2/3} \tag{24}$$

The diffusion term is:

$$R_9 = \frac{SkT}{V\delta 6\pi\eta} \left(\frac{4\pi}{3}\right)^{1/3} \Gamma(5/3) \phi^{2/3} N^{1/3} + \frac{SkT}{V\delta 6\pi\eta} \left(\frac{4\pi}{3}\right)^{1/3} \Gamma(4/3)\, 1.813 \lambda_G \phi^{1/3} N^{2/3} \tag{25}$$

We are now in a position to compare the coagulation and removal rates for different situations.

3.2 Comparison of coagulation and removal rates

In order to examine the relative importance of the individual coagulation and removal mechanisms, each of the terms denoted by R_i is renormalized such that

$$\tilde{R}_i = R_i / \Sigma_i R_i \tag{26}$$

is the relative coagulation or removal rate. For any given case, the $\tilde{R}_i$ can easily be calculated as functions of N, so long as ϕ may be treated as

constant. This assumption of a constant value of ϕ is correct when coagulation is the dominant process, but is less satisfactory when diffusion to surfaces or gravitational settling are important, for these would reduce ϕ progressively.

Examples of the application of the method are shown in Fig. 1 and 2. The case illustrated in these figures uses the following data. The host medium is air at NTP and the aerosol is assumed to be contained in a vessel of height 2 m and radius 1 m. The initial concentration of matter in the vessel, c_o, is 10^{-3} kg m^{-3}. With ρ_p=6000 kg m^{-3}, the initial volume fraction, ϕ_o, is 1.67×10^{-7}. The thickness of the boundary layer, δ, through which diffusion to the walls takes place, is assumed to be 10 μm. Some authors suggest that the diffusion layer thickness, δ, should be 10^{-4} m (indeed there is wide disagreement on this figure). Further data are: velocity gradient for laminar shear flow, $\Gamma = 10\ s^{-1}$ and rate of energy dissipation in turbulence, $E_T = 0.1\ m^2\ s^{-3}$.

In Fig. 1, only coagulation is considered, the rates of removal by diffusion to surfaces and by gravitational settling being negligible, as would be the case for a very large container. The figure shows that, in the case illustrated, Brownian motion is the predominant coagulation mechanism until the particle diameter approaches 2 μm. Thereafter, coagulation due to differential sedimentation becomes more important. It is interesting to note how the curves for the laminar shear and turbulent shear mechanisms, which are mutually parallel, pass through maxima. The curves for differential sedimentation and turbulent inertia are also mutually parallel. The relative importance of the mechanisms is, of course, sensitive to the values of the relevant parameters. These are, for laminar shear, Γ, the velocity gradient, and, for turbulent shear and turbulent inertia, E_T, the rate of energy dissipation in turbulence. We have chosen the largest values of Γ and E_T cited in the literature, but note that both could be increased artificially. It should be noted that the relative importance of the different coagulation mechanisms is determined by particle diameter, but is independent of the particle number density.

In Fig. 2, removal by diffusion to surfaces and by gravitational settling is introduced, with rates corresponding to a right cylindrical container of height 2 m and radius 1 m. However, the volume fraction, ϕ, is kept fixed at its initial value, which means that no account is taken of the effects of these two removal mechanisms on particle number density. The figure shows that, in this case, Brownian coagulation predominates until the particle number density has fallen to about 0.1% of its initial value, when removal by gravitational settling overtakes it in importance. At this stage, the mean particle diameter is about 1 μm. With such a small container, coagulation by mechanisms other than Brownian motion never becomes of great importance, but it is interesting to note the positions of the maxima in the curves. The relative importance of the two removal mechanisms in relation to the five coagulation mechanisms is not only dependent on particle diameter, but also on particle number density. For a given particle diameter, the rates of removal are directly proportional to particle number density, whereas the rates of coagulation are proportional to its square. Thus Fig. 2 is representative only of a particular value of volume fraction, here 1.67×10^{-7}.

4. TIME-DEPENDENT SOLUTION

Fig. 1 gives both a static picture of the relative importance of each coagulation mechanism at any given particle diameter, and a dynamic picture of the change in relative importance of the different coagulation

mechanisms as particle size increases. Unfortunately, Fig. 2 can only be used for the static picture, as it is plotted for constant volume fraction, whereas the removal mechanisms would progressively reduce the volume fraction in a dynamic situation.

To obtain a time-dependent solution of the general case, with five coagulation and two removal mechanisms in operation, is beyond the scope of this paper, but a simpler case can be solved, the results being expressed in non-dimensional form. This is the case where only Brownian coagulation and gravitational settling are effective, as for example in Fig. 2. The basic equation for the number density can be written from (15) and (21) as (neglecting Cunningham corrections):

$$\frac{dN}{dt} = -\frac{4.4183kT}{3\eta} N^2 - \frac{2}{9}\frac{\rho_p g}{h\eta}\,\Gamma(5/3)\,\left(\frac{3}{4\pi}\right)^{2/3}\phi^{2/3}N^{1/3} \tag{27}$$

and that for the volume fraction from (24) as:

$$\frac{d\phi}{dt} = -\frac{2\rho_p g}{9h\eta}\left(\frac{3}{4\pi}\right)^{2/3}\Gamma(8/3)\,\phi^{5/3}N^{-2/3} \tag{28}$$

Now we define the following non-dimensional quantities:

- a non-dimensional time variable

$$\tilde{t} = \frac{2r_o^2\rho_p g t}{9h\eta} \tag{29}$$

- a non-dimensional parameter determined by the amount of material initially released and the initial particle size

$$L = \frac{9B_o h\eta N_o}{4\rho_p g r_o^2} \equiv \frac{3.3137\ kThN_o}{\rho_p g r_o^2} \tag{30}$$

- a non-dimensional number density variable

$$\tilde{N}(t) = L\,\frac{N(t)}{N_o} \tag{31}$$

- a non-dimensional volume fraction variable

$$\tilde{\phi}(t) = \phi/\phi_o \tag{32}$$

In terms of these new variables (27) and (28) now become:

$$\frac{d\tilde{N}}{d\tilde{t}} = -2\tilde{N}^2 - \Gamma(5/3)\,L^{2/3}\,\tilde{\phi}^{2/3}\,\tilde{N}^{1/3} \tag{33}$$

and

$$\frac{d\tilde{\phi}}{d\tilde{t}} = \Gamma(8/3)\,L^{2/3}\,\frac{\tilde{\phi}^{5/3}}{\tilde{N}^{2/3}} \tag{34}$$

Dividing (33) by (34) and rearranging we obtain:

$$\frac{d\tilde{N}}{d\tilde{\phi}} = \frac{2}{\alpha_2 L^{2/3}}\,\frac{\tilde{N}^{8/3}}{\tilde{\phi}^{5/3}} + \frac{\alpha_1}{\alpha_2}\,\frac{\tilde{N}}{\tilde{\phi}} \tag{35}$$

where $2/\alpha_2 = 1.3293$ and $\alpha_1/\alpha_2 = 0.6$.

By simple transformations, (35) may be solved analytically and we find:

$$\frac{1}{\tilde{N}} = \left[\left(L^{-5/3} + \frac{10}{\alpha_2}L^{-2/3}\right)\frac{1}{\tilde{\phi}} - \frac{10L^{-2/3}}{\alpha_2\tilde{\phi}^{2/3}}\right]^{3/5} \tag{36}$$

Knowing $\tilde{N}$ as a function of $\tilde{\phi}$ we may solve (34) for $\tilde{t}$ as a function of $\tilde{\phi}$. This is written as:

$$\tilde{t} = \frac{1.9938\ (1+\alpha)^{2/5}}{L^{2/3}\ A^{2/5}} \int_0^{1-\tilde{\phi}^{1/3}} \frac{dw}{(\alpha+w)^{2/5}\ (1-w)^{3/5}} \qquad (37)$$

where $1/\alpha = 6.6463\ L$ and $A = L^{-5/3} + 6.6463\ L^{-2/3}$.

From (37) we can obtain $\tilde{\phi}(t)$, $\tilde{N}(t)$ and the non-dimensional mean particle volume:

$$\tilde{v}(t) = \frac{\tilde{\phi}}{\tilde{N}} = \frac{v(t)}{Lv_o} \qquad (38)$$

where v_o is the mean initial volume of a particle.

The only parameter to vary in the calculations is L, which depends on the amount of material initially released and the initial particle size. Fig. 3 shows $\tilde{N}$ and $\tilde{\phi}$ explicitly as functions of $\tilde{t}$ for three values of L. It is to be noted that, initially, $\tilde{\phi}$ remains very close to unity. The reason for this is the dominance of Brownian coagulation, which does not remove material from the system. Later, as gravitational settling becomes more important, $\tilde{\phi}$ decreases rapidly due to material accumulating on the floor. Fig. 4 shows the behaviour of $\tilde{v}$, the non-dimensional average particle volume, as a function of time. We note that, in each case, this value passes through a maximum.

To illustrate their significance, the curves marked $L=3\times10^3$ apply where the initial particle diameter is 0.1 μm and the initial particle number density 1.6×10^{13} m^{-3}. They also apply where the initial particle diameter is 1 μm and the initial number density 1.6×10^{15} m^{-3}. To convert to time, the value of $\tilde{t}$ must be multiplied by 1.13×10^6 in the first example, or by 1.13×10^4 in the second example. In the first example, $\tilde{\phi}$ has fallen to 0.5, i.e. half the material has settled on the floor, when $\tilde{t}=0.029$, i.e. $t = 3.3\times10^4$s = 9 hours. At that time, the number density has fallen to 0.44% of its initial value and the mean particle volume is approaching its maximal value. At the maximum, $\tilde{v}=0.04$, so $\bar{v}=120\ v_o$ and the mean particle diameter is about 0.49 μm. In the second example, half the material has settled on the floor when t = 330s = 5.5 minutes. As before, the number density has fallen to 0.44% of its initial value and the mean particle volume is approaching its maximal value, in this example 4.9 μm.

The curves marked $L=3\times10^5$ would apply to the case with an initial particle diameter of 0.1 μm, if the initial particle number density were 1.6×10^{15} m^{-3}. With the higher number density, coagulation is more rapid, leading to earlier deposition. Half the material has settled at $\tilde{t}=0.0044$, i.e. $t = 5.0\times10^3$s = 1.4 hours. At that time, the number density has fallen to 0.028% of its initial value. The mean particle volume is, as before, approaching its maximal value, $\tilde{v}=0.0062$, so $\bar{v}=1860\ v_o$ and the maximum particle diameter is about 1.23 μm.

We also remark that our results are in reasonable agreement with those of Lindauer and Castleman [5], who solved the kinetic equation for n(v,t). This gives confidence in the use of similarity methods for initial survey studies.

5. DISCUSSION

In the initial part of our study seven distinct mechanisms for coagulation and removal are considered and, by means of a similarity transform, are reduced to depend on the number density and volume fraction only

(aside from the basic parameters of density, viscosity, etc.). The relative effects are assessed by calculating the relative reaction rates as functions of particle number density. Since decreasing number density is related to increasing time, we can obtain useful ideas about the functioning of each removal mechanism as the aerosol ages. It is clear that Brownian coagulation dominates during the early stages and that removal by diffusion to surfaces and gravitational settling become significant later, depending strongly on the initial average particle size. Other mechanisms, such as turbulent and laminar shear, do not appear to be important removal processes early in the aerosol life and, although their significance increases as the aerosol ages, it seems unlikely that they would ever become of great importance, unless some artificial method of promoting them were introduced.

In order to obtain time-dependent results for the relative importance of gravitational settling and Brownian coagulation, without introducing the full scale calculation of $n(v,t)$ used by Lindauer and Castleman, we have derived an exact solution using similarity transforms. This enables N and ϕ to be obtained in a convenient non-dimensional form, in terms of a single floating parameter, L, which is determined by the magnitude of the amount of material initially released and the initial particle size. Numerical results are obtained and illustrated graphically, showing clearly how Brownian coagulation gives way to gravitational settling. A range of situations can be studied using these curves. An interesting feature is the way in which the mean particle volume changes with time; this goes through a maximum at a certain time after the initial release, due to the competing effects of coagulation and settling. Such behaviour is in general agreement with the results of Lindauer and Castleman and provides a convenient and reliable method for studying aerosol behaviour in enclosed vessels.

REFERENCES

Nuclear Aerosols in Reactor Safety. Pub. Nuclear Energy Agency, OECD, 1979.

Fry, T.M. Quantitative assessment of the magnitudes of aerosol processes, ANS Report No.183, Associated Nuclear Services, 1980.

Saffman, P. and Turner, J. J. Fluid Mech., Vol.1, p.16, 1956.

Lindauer, G.C. and Castleman, A.W. Jr. Aerosol Sci., Vol.2, p.85, 1971.

Lindauer, G.C. and Castleman, A.W. Jr. Nucl.Sci.& Eng., Vol.43, p.212, 1971.

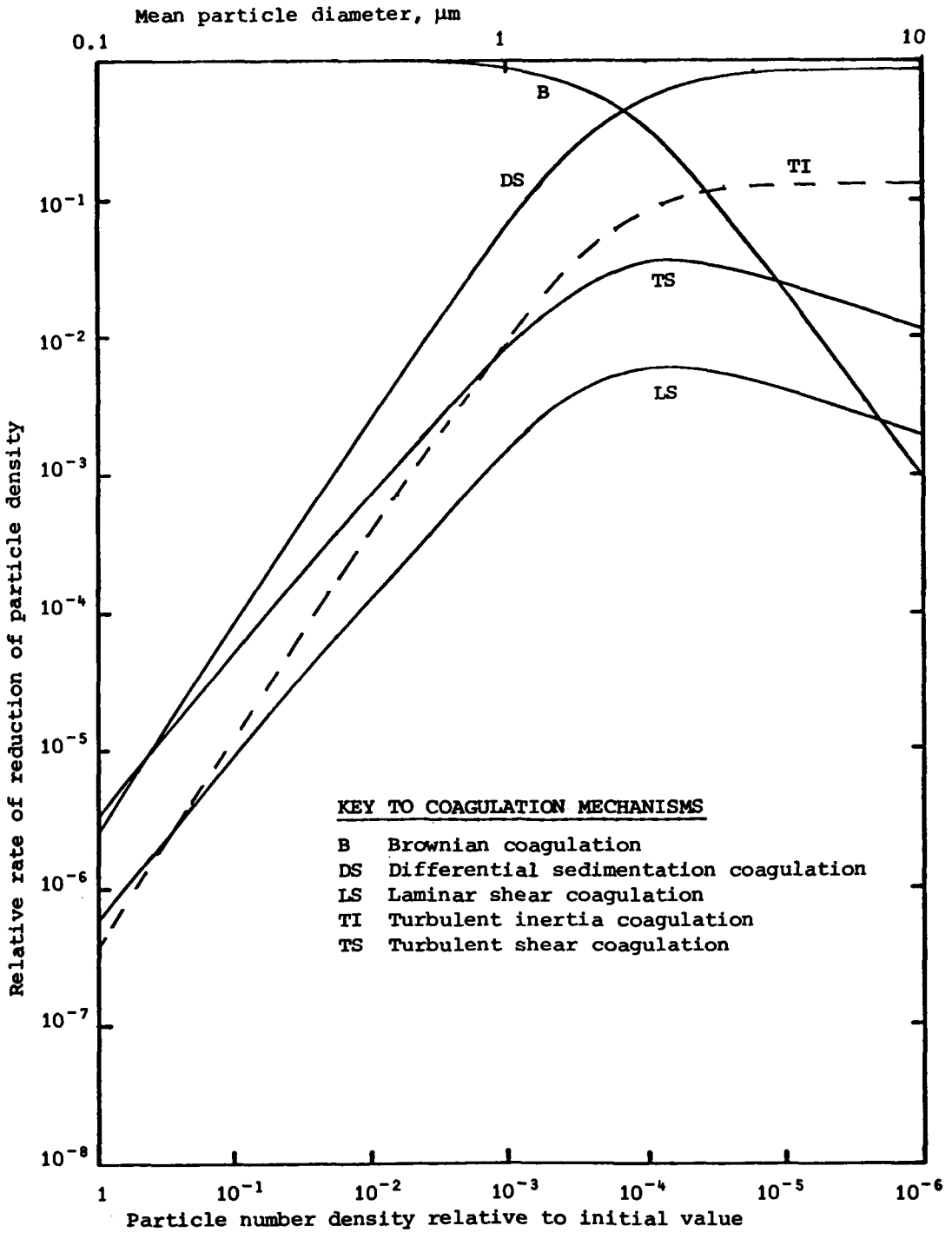

Note: Particle material density: 6000 kg m^{-3}

FIGURE 1 CHANGES IN RELATIVE IMPORTANCE OF COAGULATION MECHANISMS WITH PARTICLE SIZE

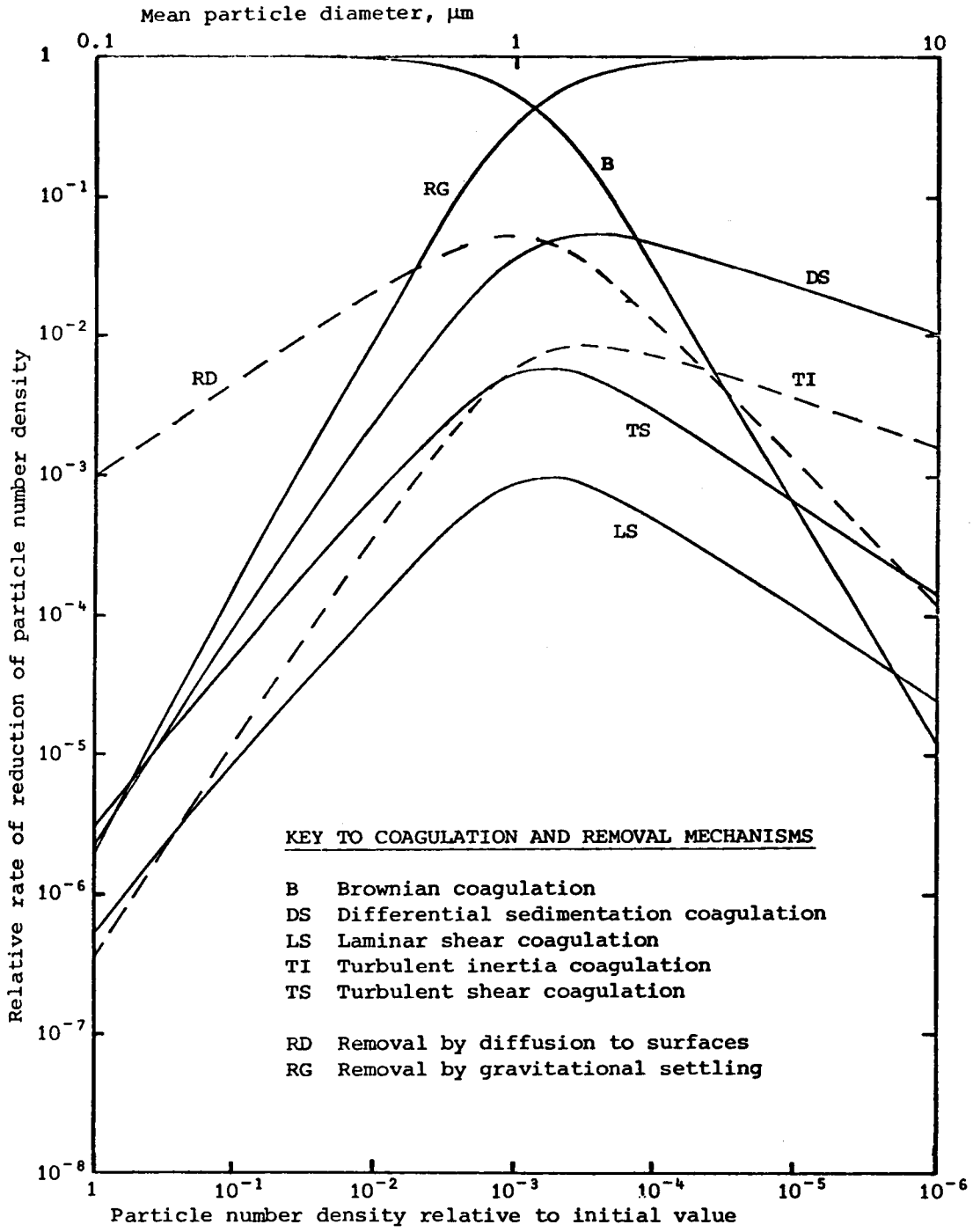

Notes: Mass concentration of particulate: 1×10^{-3} kg m^{-3}
Volume fraction (fixed): 1.67×10^{-7}

FIGURE 2 CHANGES IN RELATIVE IMPORTANCE OF COAGULATION AND REMOVAL MECHANISMS WITH PARTICLE SIZE AT FIXED VOLUME FRACTION

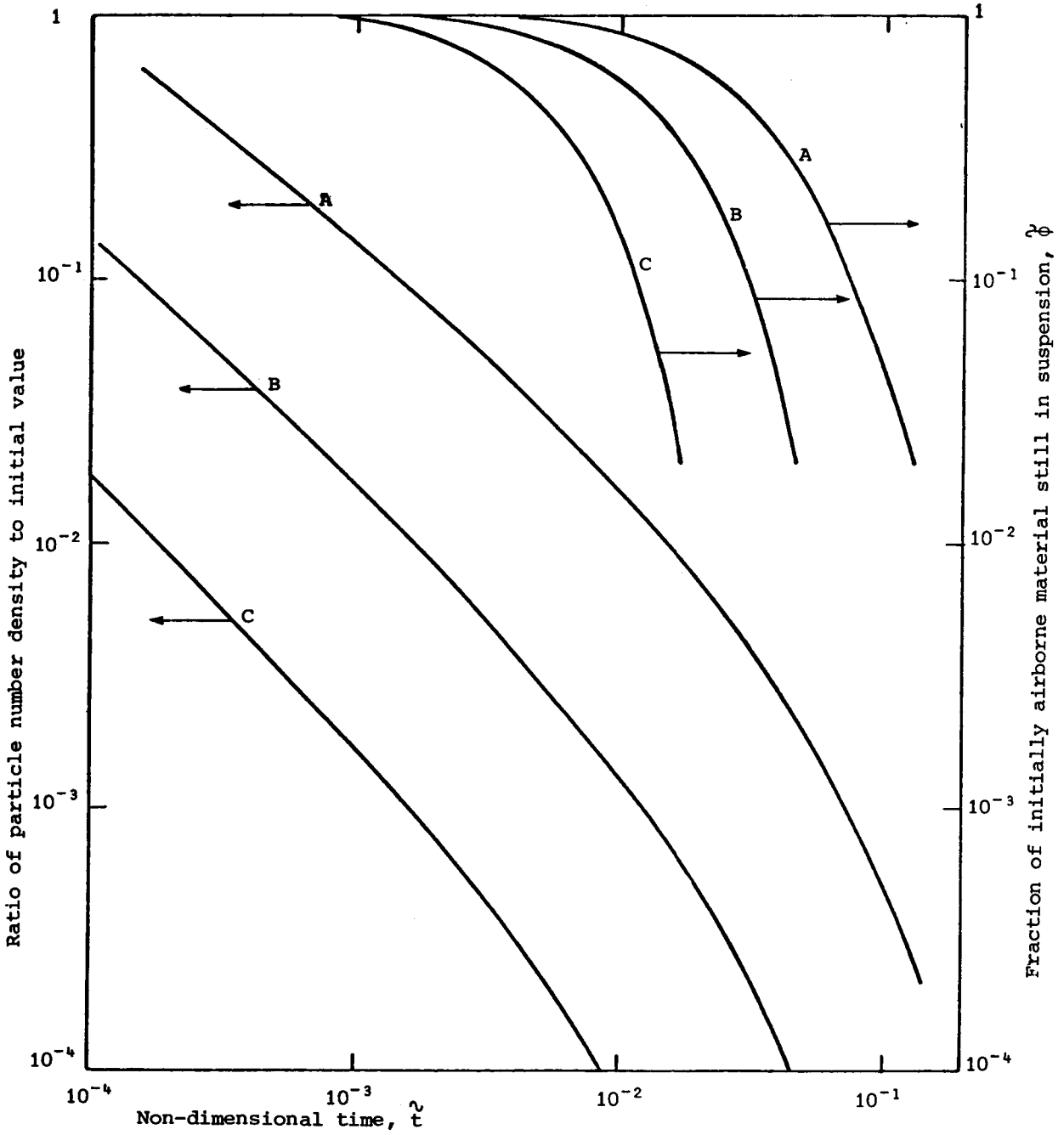

KEY: A $L = 3 \times 10^3$
B $L = 3 \times 10^4$
C $L = 3 \times 10^5$

FIGURE 3 NON-DIMENSIONAL REPRESENTATION OF THE TIME-DEPENDENT BEHAVIOUR OF AN AEROSOL UNDERGOING BROWNIAN COAGULATION AND GRAVITATIONAL SETTLING.

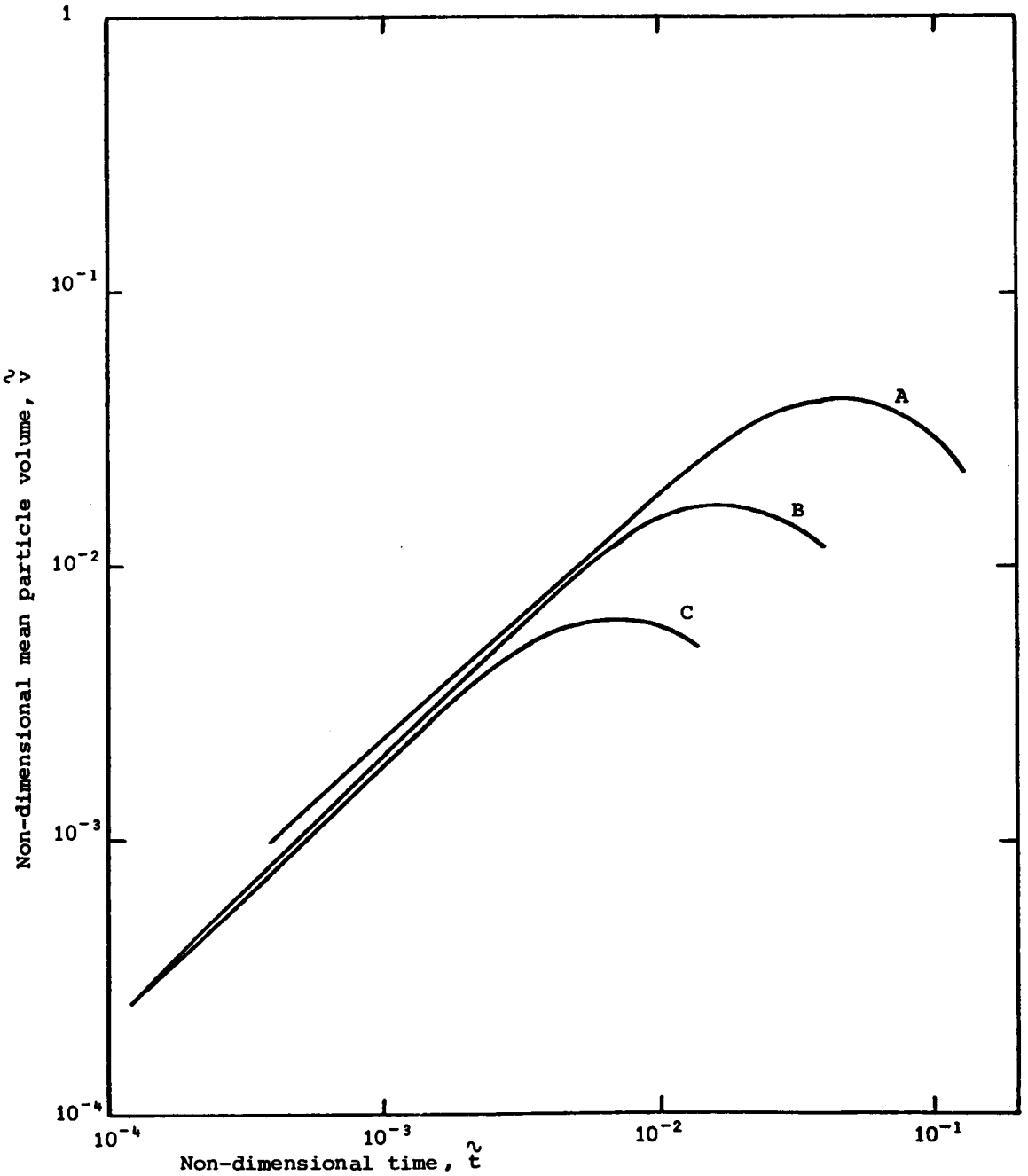

FIGURE 4 NON-DIMENSIONAL REPRESENTATION OF THE CHANGE OF PARTICLE VOLUME WITH TIME IN AN AEROSOL UNDERGOING BROWNIAN COAGULATION AND GRAVITATIONAL SETTLING.

AEROSOL BEHAVIOR MODELING

H. Jordan, P. M. Schumacher, J. A. Gieseke
and K. W. Lee
Battelle Columbus Laboratories
Columbus, Ohio

ABSTRACT

There are two aspects to aerosol behavior modeling. One concerns the mathematical modeling of individual behavior mechanisms, the other the technique employed in solving the model. The latter is of interest because the high concentrations of particulate matter expected in large nuclear reactor containments present problems of scale that are not readily mastered numerically. Thus numerical schemes that agree on the laboratory scale sometimes diverge on the large scale. It is therefore important to validate a code's solution approach as well as its mechanistic models.

This paper addresses the simplifying assumptions of the HAARM-3 solution technique by comparing HAARM-3 with a reference code, QUICK, that minimizes simplifying assumptions at the expense, however, of computer storage space and running time. The accuracy of the QUICK code has been successfully tested against alternate methods. The comparison shows remarkable agreement between the two codes for many accident scenarios of interest. It also shows order of magnitude divergence in some cases. As a possible explanation it is suggested that, in a sense, HAARM-3 represents a first order correction to a monodisperse model and that some divergence of its predictions relative to those of a more accurate model must be expected when particle size distributions are, or become, very disperse.

The second part of this paper addresses the assumption of uniform aerosol mixing that is fundamental to most existing nuclear aerosol behavior models. To quantify the significance of this assumption, a computer code, the ZONE code, has been developed at Battelle. This code accounts for spatial inhomogeneities using a cell model approach. Predictions of the ZONE code for severe sodium fire accidents are presented and compared with corresponding predictions using the QUICK code. The comparison shows the generally conservative prediction of complete mixing models during the sodium burn period. Complete mixing is predicted by the ZONE code immediately after the fire ceases and for the following period, the predictions of the ZONE code coincide with those of QUICK.

INTRODUCTION

The function of aerosol behavior codes in nuclear safety research is twofold. First, they represent a vehicle for aiding in the understanding of the various mechanisms that play a role in the behavior of aerosols in simulation experiments. Second, and more crucially, they provide the means of extrapolating experimental results from the necessarily small scale to actual reactor accident situations.

Our confidence in the ability of a code to fulfill the latter role rests chiefly on its "verification" by simulation experiments. This, to date, has principally consisted of comparing experimentally observed aerosol particle mass concentrations to those predicted by the code. A more critical "verification" test would be a comparison of particle size distributions as a function of time. These reflect the effects of the various mechanisms more sensitivity than their second moments. They represent, in any case, the code prediction necessary for coupling to release calculations that must consider particle size discrimination in active filter systems or by leak paths through containment breaches. While good agreement between predicted and measured particle mass concentration is suggestive of code validity, it is by no means clear that it conclusively demonstrates the correctness of all the mechanistic models that play a role. Insufficient model assumptions and inaccuracies of model solution techniques can conceivably lead to agreement on the small, but divergence on the large, scale. Thus, it is important to realize that "verification" by comparison with small scale experiments is in large measure tuning of undetermined model parameters. This does not in itself invalidate the verification, provided the solution technique of the overall aerosol behavior model is adequate and adjusting parameters against experimental results does not in part simply compensate an incorrect solution. Fortunately, solution techniques are amenable to purely theoretical verification and can therefore be largely decoupled from experimental model validation.

In this paper we address two of the points raised above. We first present results of an extensive verification of the solution technique of the widely used HAARM-3 code. For this analysis the HAARM-3 code was compared to a reference solution method (the QUICK code) that was itself successfully tested against a number of other solution schemes. We then present results of a zeroth order analysis of the fundamental model assumption of all present day aerosol behavior codes - that of uniform mixing of the aerosol. For this latter analysis, a new code (ZONE), based on QUICK, was created that accounts for inhomogeneities by compartmentalizing the containment volume into zones connected by fluid flow.

COMPARISON OF THE HAARM-3 AND QUICK CODES

The mathematical model underlying all present day nuclear aerosol behavior codes can be case into the following familiar form:

$$\frac{\partial n(x,t)}{\partial t} = \frac{1}{2}\int_0^x K(x',x-x')\, n(x',t)\, n(x-x',t)\, dx' - n(x,t)\int_0^\infty K(x,x')n(x',t)dx' - R(x)n(x,t) + S(x)\ . \quad (1)$$

Here, per unit volume,

$n(x,t)dx$ = number of particles of mass x in dx at time t

$K(x,x')n(x)n(x')dxdx'$ = rate of collision between particles of mass x in dx and x' in dx'

$R(x)n(x,t)dx$ = rate of removal of particles of mass x in dx from the aerosol system

$S(x)dx$ = rate of introduction of particles of mass x in dx into the aerosol system.

Note that uniform mixing of the aerosol is implicit in this formulation.

All codes approach the solution of Equation (1) by discretizing the mass dependence of the distribution density, n(x,t). This results in a set of coupled ordinary differential equations in t that can be solved by standard solution techniques, though, in extreme cases, with difficulty. In HAARM-3, discretion is achieved by taking the moments of Equation (1). The resulting infinite set of differential equations for the moments can be closed by assuming a fixed functional form of the distribution density for all time. Thus, in HAARM-3, the distribution density is assumed to remain lognormal. This permits closure on just three equations and for many coagulation kernels, K(x,x'), of interest, analytic evaluation of the mass integrals. Details of this technique can be found in Reference 1.

A general distribution density, n(x,t), that can be approximated by a power series of k terms in x for all time in general requires k moments to uniquely determine it. It thus seems reasonable to expect closure on just three moments to present a severe restriction on the general validity of the HAARM-3 code. For this reason, we undertook an extensive analysis of the validity of the lognormal assumption in HAARM-3 by comparing results of calculations with it and the QUICK code. QUICK is presently the most efficient yet accurate aerosol behavior code available to us. It makes no prior assumptions about the form of the size distribution function and has been tested successfully against analytic solutions and higher order solution techniques [2].

Code Comparison Basis

In comparing the codes, an attempt was made to encompass as much of the range of presently postulated and simulated accident conditions as possible. To do so, the vessels considered ranged from typical prototype LMFBR containments to the NSPP simulation vessel. Accident conditions were extracted from the report to the CSNI on aerosol behavior [3] and the range of remaining parameters taken from the HAARM-3 sensitivity study [4]. Based on this study, only those aerosol behavior mechanisms were considered that play a dominant role in large vessels. These are: Brownian coagulation,

gravitational coagulation, diffusional deposition and gravitational deposition. sition. To make the results as transparent as possible variation of parameters such as temperature, pressure and particle density were not considered and the source rate was taken as constant to source cut-off. These restrictions are secondary in nature and should not significantly affect the outcome of the comparison.

For numerical reasons, QUICK solves the aerosol model, Equation (1), in nondimensional form. Nondimensionalization is, however, also expedient for code comparison purposes. Thus the set of 16 dimensional parameters of the restricted model we analyzed reduces to just 6 nondimensional groups. Equally as important, 4 of these nondimensional groups are directly related to the aerosol behavior mechanisms considered and give a measure of the relative importance of a given mechanism. Since all mechanisms are modeled as independent of one another, the dimensional groups are independent. Their relevance to the model is transparent, whereas that of the dimensional parameters is generally difficult to discern.

Details of the nondimensionalization scheme are given in Reference 2. For understanding the results presented here, it is sufficient to point out the following. Nondimensionalization was achieved by scaling time with the characteristic time for Brownian coagulation at maximum particle concentration; particle mass with the average initial particle mass; and number concentration with the maximum number concentration. It was found useful to treat long term sources and instantaneous sources separately and to characterize the former by pure UO_2 aerosols, the latter by pure Na fire aerosols. For long term sources, the maximum particle number concentration was taken to be the integral of the source output.

The nondimensional groups of this comparison are then

- SRBC - rate of source rate to initial Brownian coagulation rate
- GDBC - proportional to the ratio of the initial gravitational deposition rate to the initial Brownian coagulation rate
- DDGD - ratio of the initial diffusive deposition rate to the initial gravitational deposition rate
- GKBC - proportional to the ratio of the initial gravitational coagulation rate ot the initial Brownian coagulation rate
- KN - nondimensional Knudsen number
- σ - logrithmic standard deviation of the initial (source) particle size distribution
- ε - collision efficiency (constant)

Note that ε and GCBC only occur as the product ε*GCBC and thus really only constitute one nondimensional group. They are treated separately here because of the large uncertainty in ε which is assumed constant in this comparison but is in reality a function of the size of the collision partners and their densitities.

The set of comparison runs was picked as follows. First, the nondimensional groups were calculated for all possible combinations of the extreme values of the dimensional parameters. A matrix of the extreme values of the nondimensional groups could then be set up. Ideally, the comparison should have been made for all combinations of these extreme values. However, while the dimensionless groups are mechanistically independent, they have a common implicit dependence on the physical systems on which they are based. Arbitrary combination of the extremes of the dimensionless groups in fact leads to physical systems that are totally outside the region of interest. To show possible divergence of code predictions outside the region of interest, however, would serve no useful purpose. The comparison runs were therefore determined by picking extremes of each nondimensional group one at a time, with the remaining groups assuming values as close as possible to their geometric mean values, commensurate with an aerosol system of physical interest.

Results of Code Comparison

It was hoped that this comparison would result in the definition, in nondimensional group space, of a region of adequate code agreement. This has not been possible, basically because of the inordinate effort required. Such a region would in any case be sensitive to the criteria chosen to define agreement. It has been possible, however, to identify trends in those cases where some disagreement exists and to interpret the probable cause for such disagreement.

For lack of space, only those cases illustrative of disagreement are presented in the accompanying figures. Figure 1 is representative of the relative behavior of the mass concentration curves predicted by the two codes for instantaneous UO_2 releases for which significant disagreement exists. Invariably, in these cases, HAARM-3 overpredicts the suspended aerosol mass concentration early in its evolution, then underpredicts it, relative to QUICK. These cases are associated with large (>1) values of GCBC, and, significantly, broad initial size distribution (σ = 2.7). The fact that the curve cross-over point occurs earlier for larger values of GCBC indicates the causative effect of GCBC. It is, however, not possible to completely isolate the individual contributions of σ, GCBC and GDBC since, for the cases considered, these groups are loosely correlated. That is, a large σ implies a broad particle size distribution and therefore large initial particles. These in turn cause gravitational coagulation (GCBC) and settling (GDBC) to be relatively large.

This observation, and those to be made below lead us to the following interpretation of why HAARM-3 results sometimes diverge from those of QUICK. A narrow particle size distribution is esentially a Dirac delta function. Since the latter collapses the infinite set of differential equations for the moments into just two equations, it is easy to see that three such equations, as in HAARM-3, may suffice to describe a system whose particle size distribution deviates but little from a delta function. If the particle size distribution is broad, or has a chance to become broad by coagulation, however, just three moments equations are less adequate. In this context

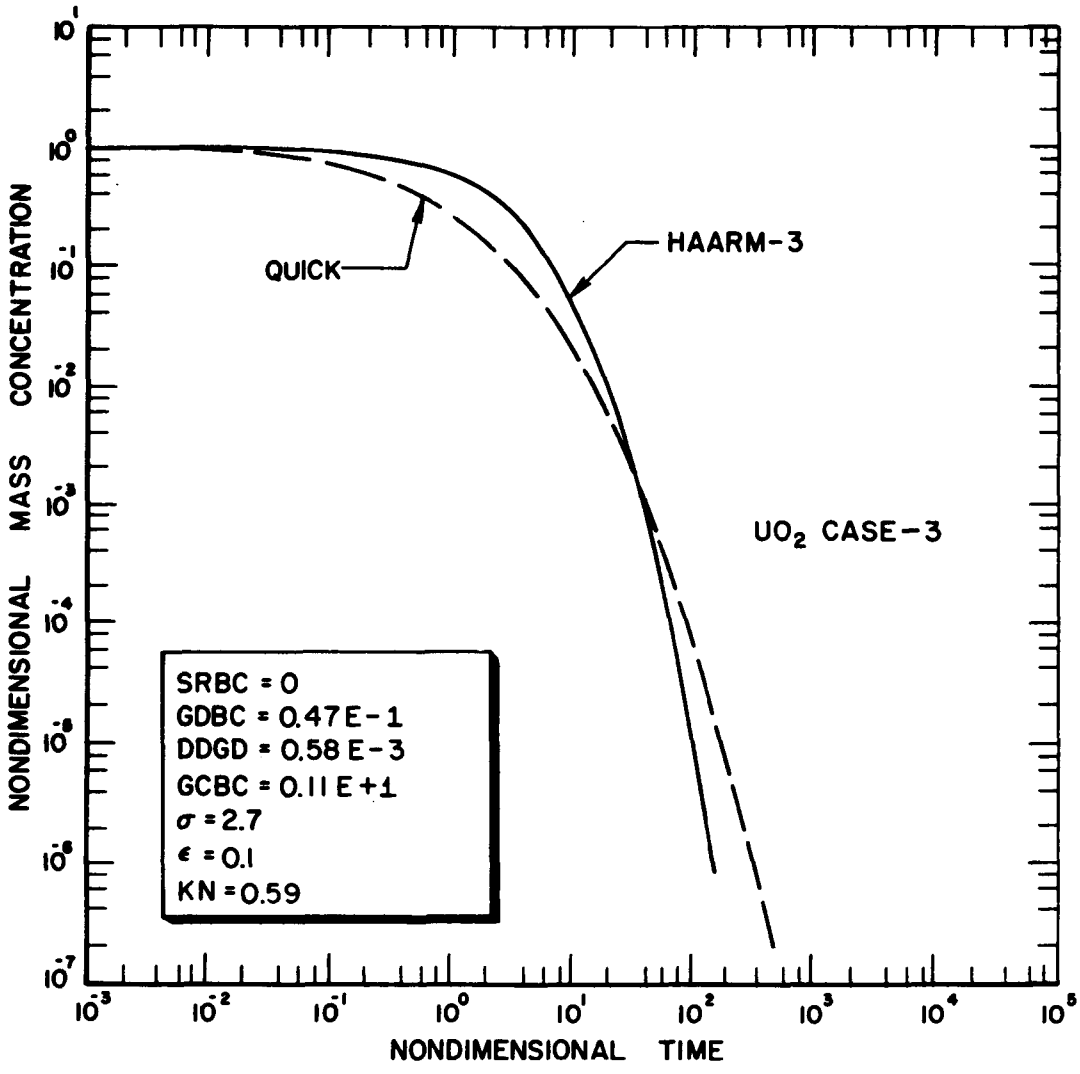

Figure 1. Comparison of HAARM-3 with QUICK: Instantaneous Source. Mass Concentration.

it is interesting to note that while Brownian coagulation tends to stabilize a particle size distribution, gravitational coagulation rapidly broadens it.

Figure 2 is representative of the relative behavior of the predicted mass concentrations in the case of a sodium fire, again when significant disagreement obtains. Note that here, too, the initial (source) particle size distribution is broad. It is interesting that after source cut-off the curves mirror the behavior of those for the instantaneous source,

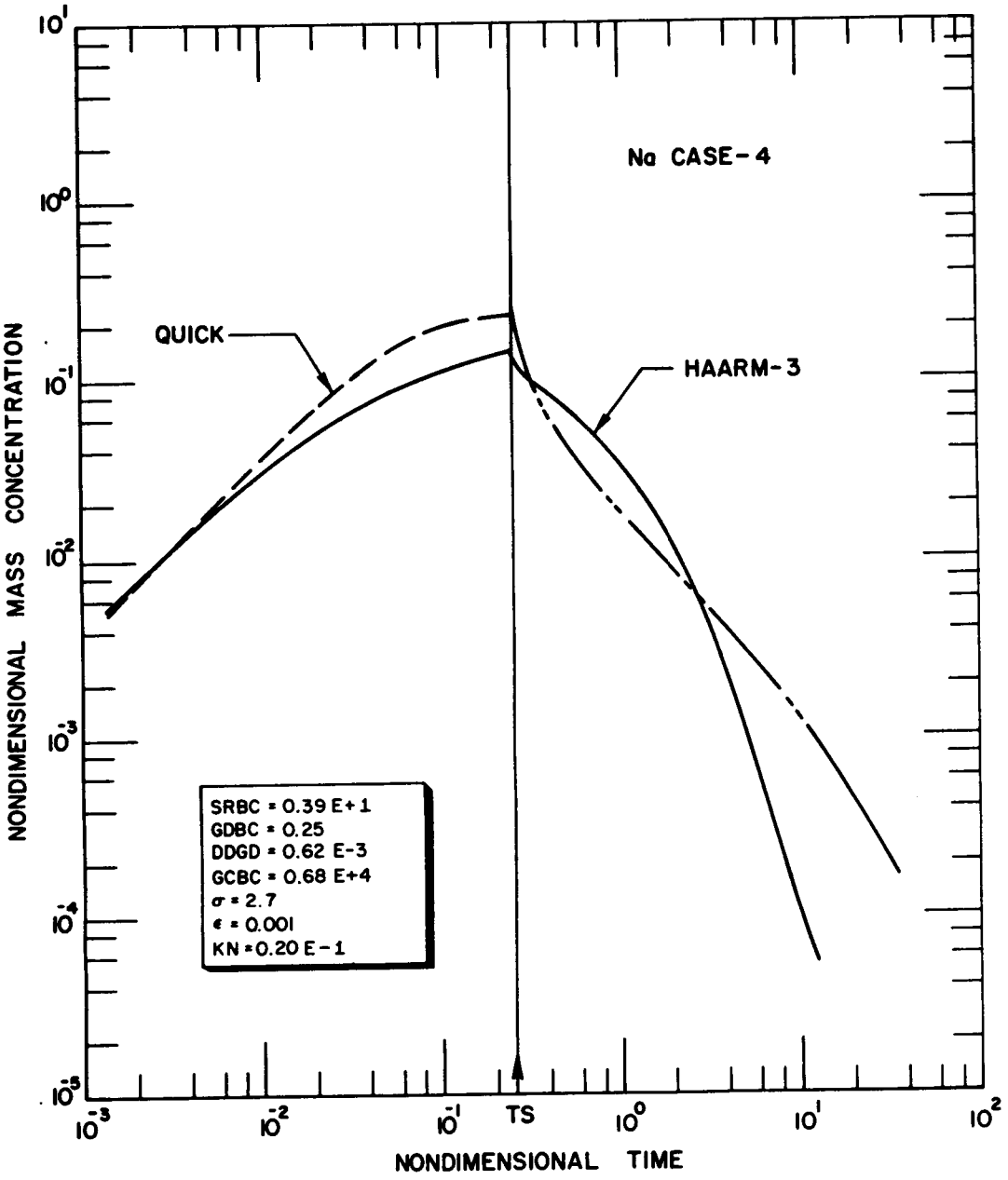

Figure 2. Comparison of HAARM-3 with QUICK: Long Term Source. Mass Concentration.

Figure 1. That is, an initially conservative HAARM-3 prediction becomes unconservative at later times.

Figure 3 gives the mass distribution density corresponding to the maximum time considered for the case shown in Figure 1. It is drawn as $\frac{d[xn(x,t)]}{d\ \ln x}$ vs $\ln x$ so that equal areas on the graph represent equal contributions to the total mass concentration. It is clear that QUICK predicts about half the suspended particle mass to be due to smaller particles than those predicted by HAARM-3.

Figure 4 gives the mass distribution density at source cut-off time corresponding to the case shown in Figure 2. Note that at this time HAARM-3 underpredicts particle size relative to QUICK. From the behavior of the corresponding mass concentration curves, however, it is clear that this relationship reverses and becomes similar to that of Figure 3 at later times.

It is interesting to note that for all Na cases with narrow particle source distributions, the predicted steady state source cut-off distributions, whether narrow or broad, agree well with each other. For those of these cases for which the steady state distributions are narrow, the mass concentrations predicted by the two codes agree for all time. For those cases, however, for which the steady state distributions are broad, the predicted mass concentrations diverge with increasing time beyond cut-off, and they do so in the same sense as those of Figures 1 and 2.

These observations tend to confirm our interpretation of the basic cause for divergence between the two codes. A further corroboration comes from an analysis in which we investigated the limiting case of an aerosol undergoing diffusional deposition and gravitational settling only. This case pertains to aerosols of sufficiently low density that coagulation plays a minor role. It has the obvious advantage of permitting an analytic solution.

When the initial size distribution is narrow, the HAARM-3 predicted mass concentrations and size distributions agree precisely with the analytic results. When the initial size distributions are broad ($\sigma = 2.0$), the predicted mass concentrations, Figure 5, and size distributions, Figure 6, diverge from the analytic results. Furthermore, they do so in precisely the sense already observed in Figures 1 and 2. Other results from that analysis, which cannot be shown here for lack of space, show that the divergence between the code predictions increases with increasing σ and increasing dominance of sedimentation relative to diffusive deposition.

One can conclude, therefore, that for those situations which either start with a broad distribution or develop one in the evolution of the aerosol system, HAARM-3 predictions must be viewed cautiously. Broad distributions are not necessarily developed by long term sources only. Thus Figure 7 shows a broad distribution obtainable in a full size LMFBR containment from an initial UO_2 concentration of 30 g/m^3. It is important to note, however,

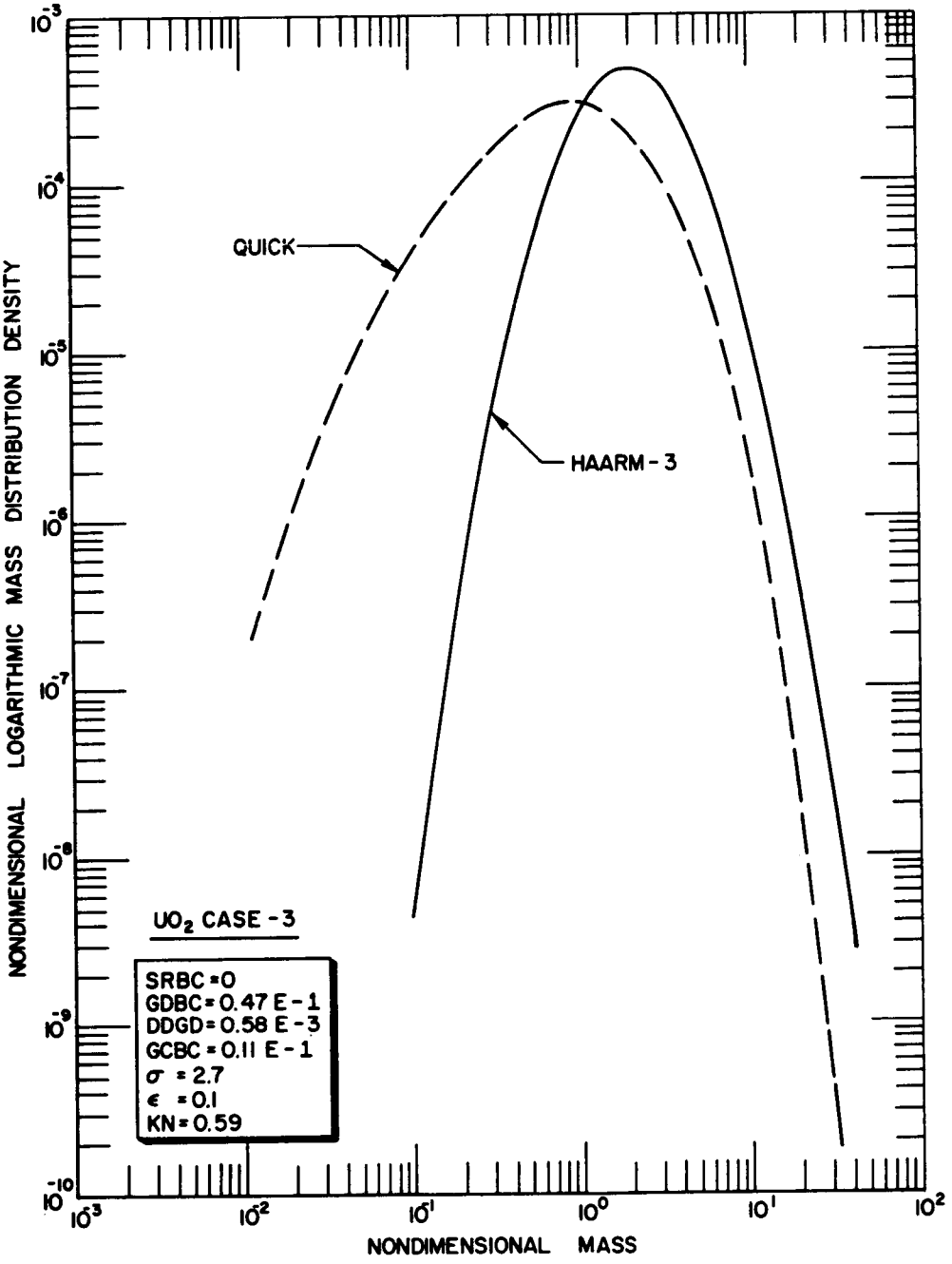

Figure 3. Comparison of HAARM-3 with QUICK: Instantaneous Source. Size Distribution.

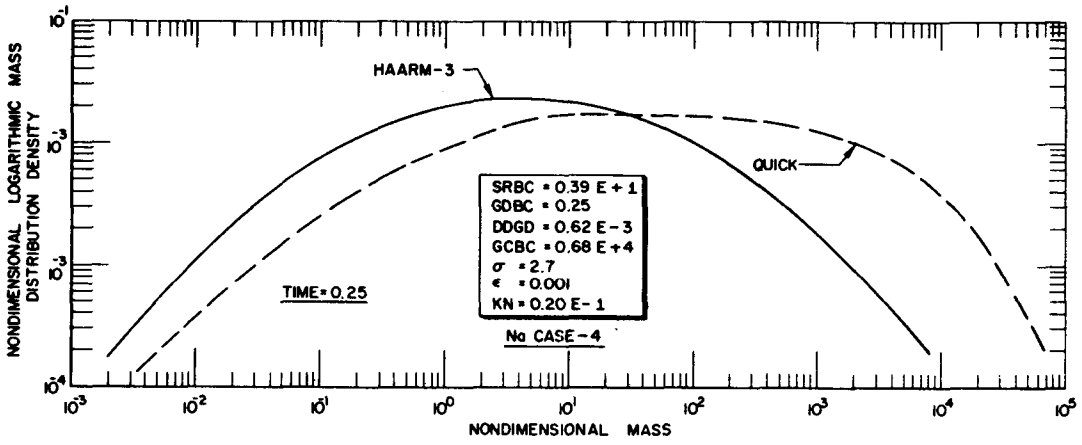

Figure 4. Comparison of HAARM-3 with QUICK: Long Term Source. Size Distribution at Source Cut-Off.

that maximum divergence never exceeds about an order of magnitude and does not reach this size until the suspended mass concentration has diminished from its maximum value by orders of magnitude.

If one looks at a comparison of the cumulative mass leaked from the containment as a quantitative measure of agreement, the two codes never diverge by more than a factor of two or three. This is illustrated for selected worst cases in Figure 8 which shows a plot of the ratio of the predicted leaked masses as a function of time.

COMPARISON OF THE ZONE AND QUICK CODES

Present nuclear aerosol behavior codes invariably invoke the assumption of a homogeneously mixed containment. This assumption is thought to be conservative in terms of mass leaked to the environment and has the advantage of permitting calculations without detailed knowledge of containment internal structure or location of the burning sodium pool, for example.

It is, however, apparent that, for a long term sodium fire in particular, convective loops are likely to be set up. These will mix the containment atmosphere, but in a regular fashion. That is, aerosol particles created immediately above the flame zone of the fire will rise vertically in a "chimney" and not see the containment walls until they reach the return loop. During this transport period, which is characterized by high aerosol concentrations, rapid particle growth can be expected, so that a particle may be significantly larger when it sees the containment walls than when immediately above the fire zone. Such a picture contradicts the homogeneously mixed concept and indicates, instead, a delay time for mixing or a characteristic mixing time.

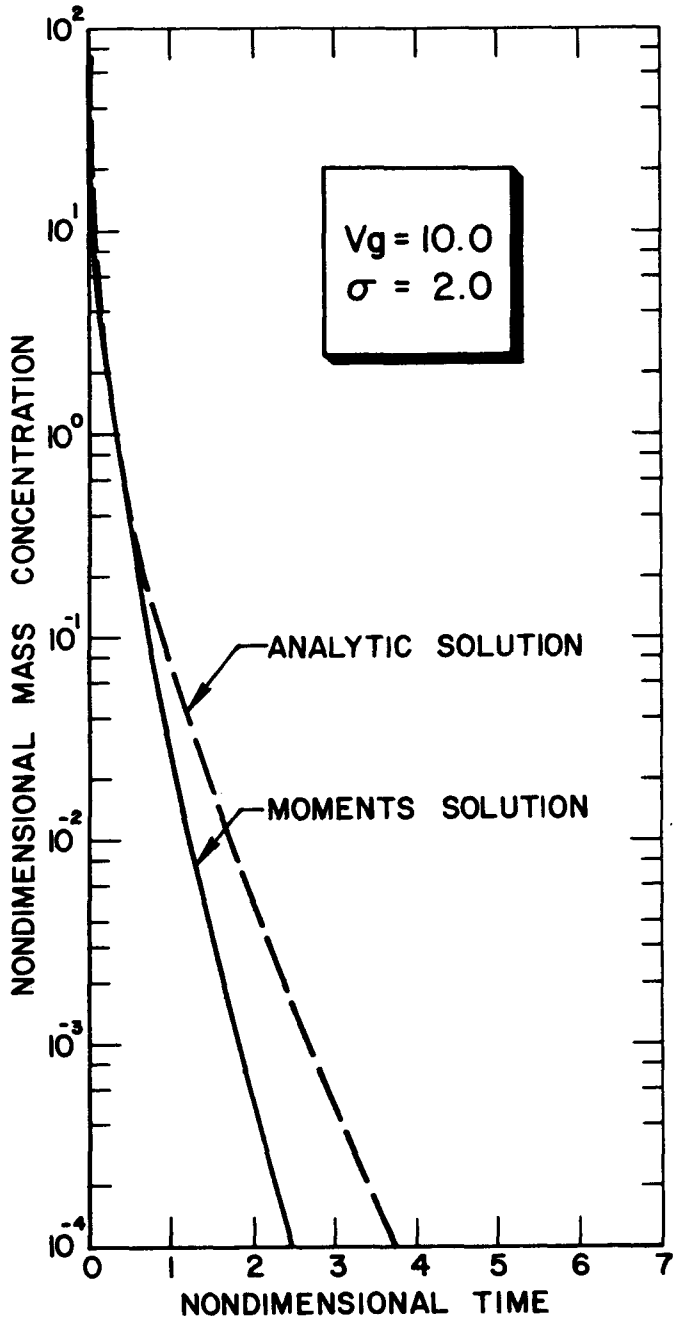

Figure 5. Comparison of Moments Solution with Analytic Solution: Instantaneous Source. No Coagulation. Mass Concentration.

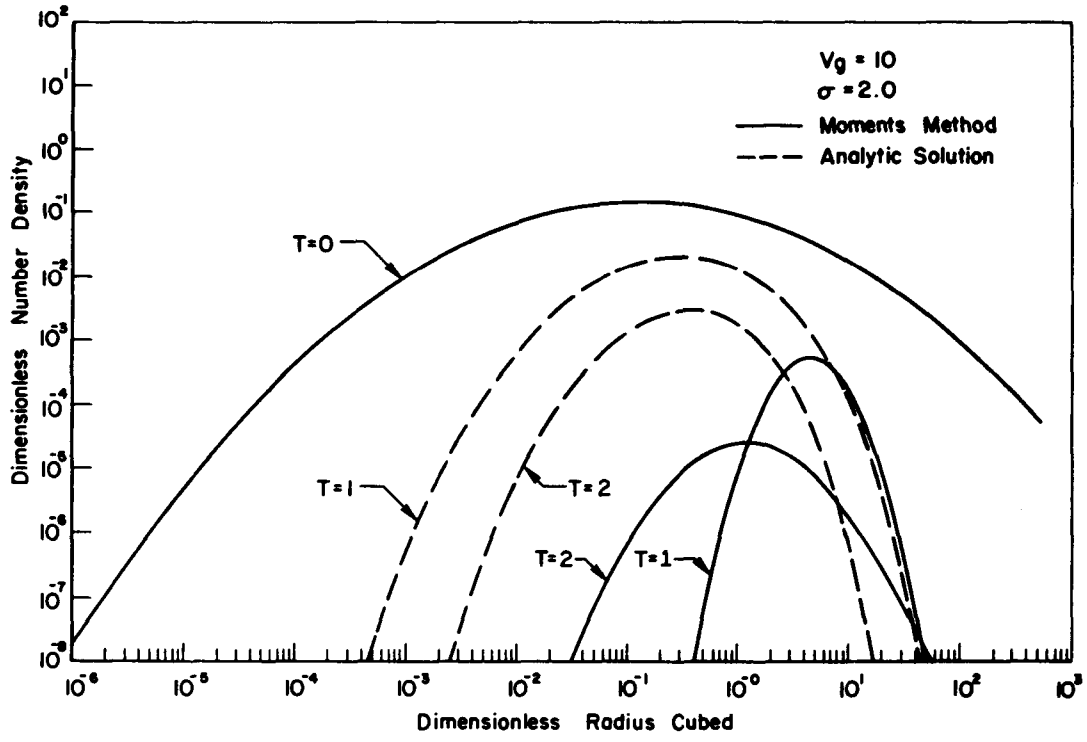

Figure 6. Comparison of Moments Solution with Analytic Solution: Instantaneous Source. No Coagulation. Size Distribution.

Intuitively, one would expect the homogeneously mixed model to begin to break down when the characteristic coagulation time is much smaller than the characteristic mixing time. Thus, for an intense fire, the concentration of particles in a relatively small chimney volume should lead to larger particles than the immediate dispersal to the whole containment of the same particle source, provided their residence time in the chimney is long enough.

In order to assess, quantitatively, the significance of a localized aerosol source relative to a completely dispersed one, an aerosol behavior code (ZONE) [5] was created that accounts for localization in a zeroth-order approach by compartmentalizing the containment volume into three zones that are connected by convective flow. Calculations with ZONE for extreme full scale reactor accident were then compared with corresponding calculations using the QUICK code.

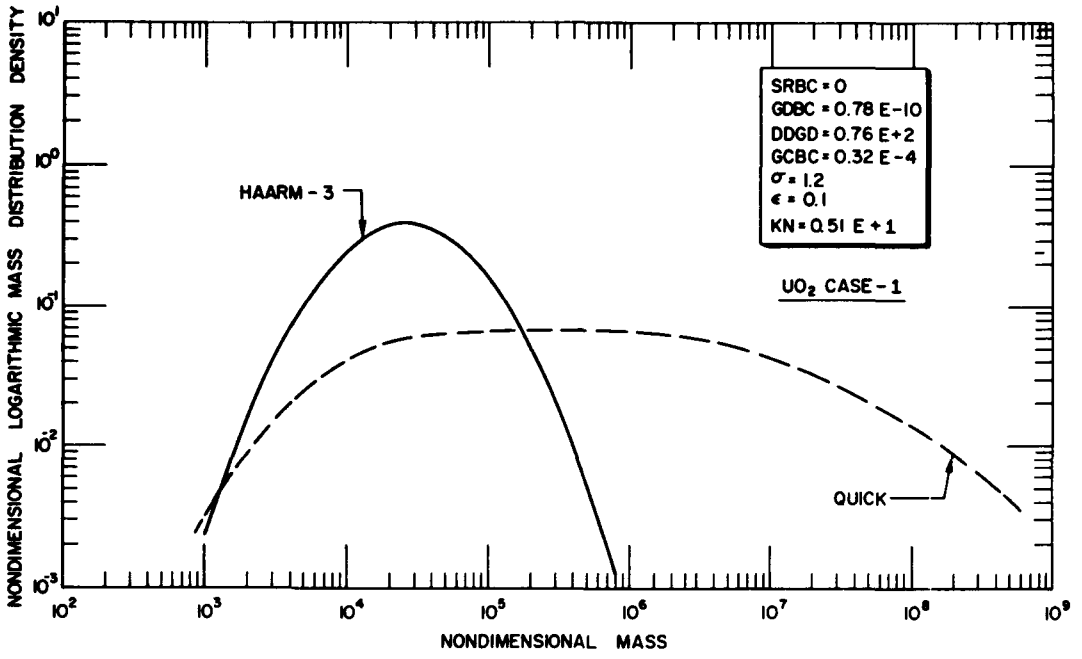

Figure 7. Comparison of HAARM-3 with QUICK: Instantaneous Source. Size Distribution.

ZONE Model

It was recognized early in the development of the ZONE code that the addition of a continuous spatial dependence to the aerosol behavior problem would be very involved if not beyond present day computation capacities and that, indeed, the effort might very well not be justified. Instead, in order to bracket the problem, a simpler approach was envisioned, the results of which could be used to judge the advisability of more involved analyses.

In this approach, the containment is subdivided into three zones as depicted in Figure 9. It is assumed that, to a first approximation, the expected convective behavior of the containment atmosphere above a pool fire can be simulated by considering each zone homogeneously mixed within itself, but connected by fluid flow equivalent to the expected convective flow as indicated by the arrows in the figure. This flow can be taken from existing codes [5], but because of the elementary nature of the present approach, little detail of the flow is required, so that rough estimates can be used to bracket expected conditions.

A full description of aerosol behavior in the containment is then provided by coupling three separate QUICK models, one for each zone. Details of the ZONE model can be found in Reference 5.

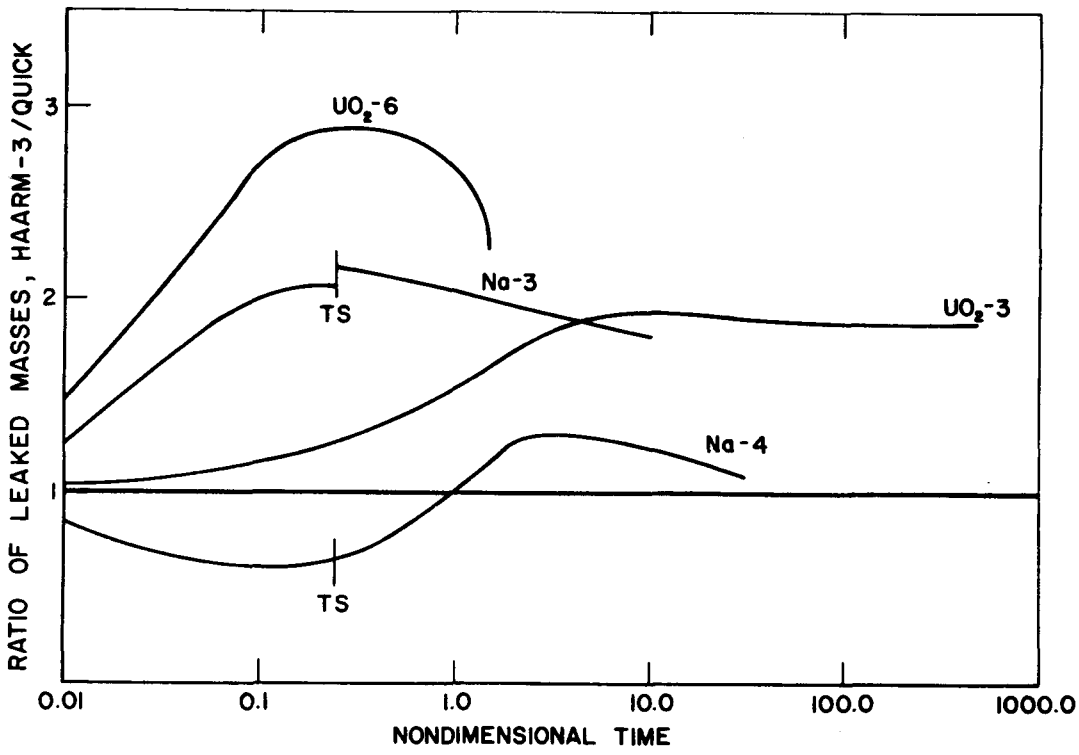

Figure 8. Comparison of HAARM-3 with QUICK: Worst Case Cumulative Release Ratios HAARM-3/QUICK.

Choice of Accident Conditions Considered

Unlike the general comparison of HAARM-3 and QUICK presented above, a comparison of ZONE and QUICK need not encompass all possible accident and simulation conditions. For one, only long term sodium fires need be considered since only these will produce the convective effect under study, and for another, it is intuitively obvious that only slow convection is likely to result in inhomogeneity. It is also clear that greatest divergence is likely for full scale containments.

For comparison purposes, therefore, the source duration time was taken to be the largest considered reasonable for LMFBR accidents, 50 hrs [3]. The source rate was then determined by assuming that all the sodium that can stoichiometrically burn to Na_2O_2 is burned during this time at a constant rate. This is less than the total sodium primary system inventory. Note that for simplicity, the probable production of Na_2O in the later stages of the fire has been ignored by this assumption. This simplification is not expected to affect the results significantly.

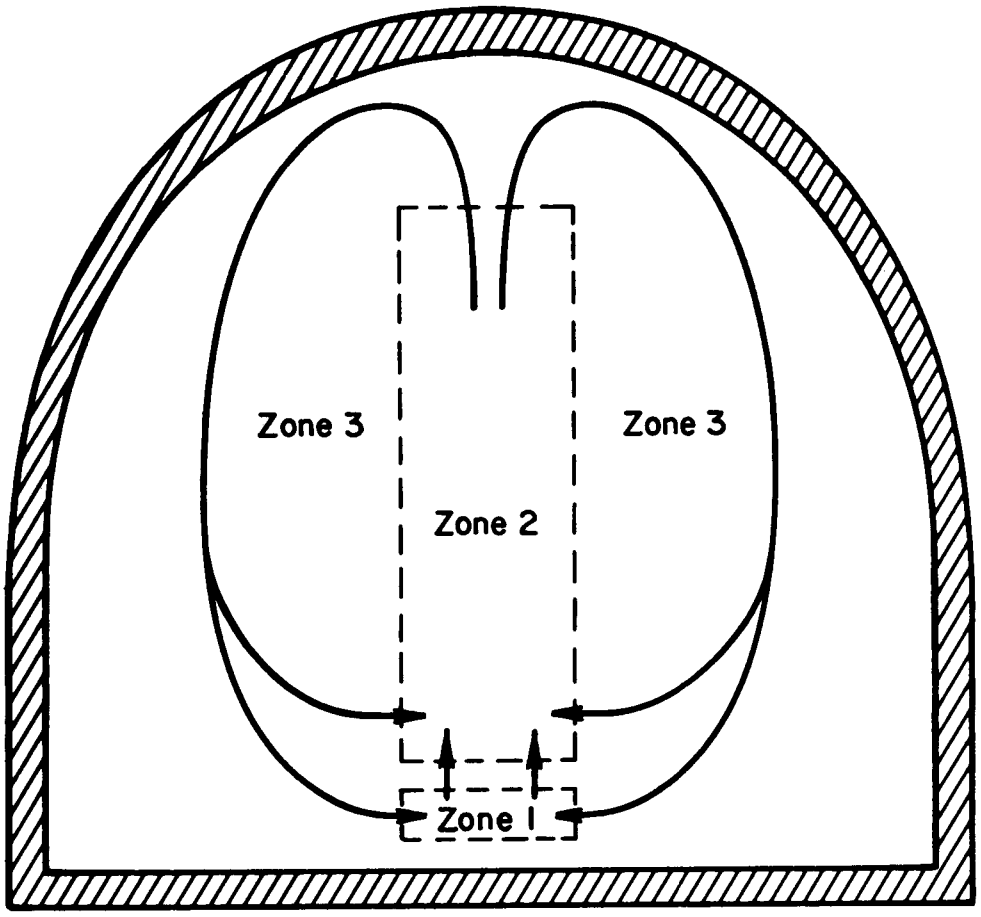

Figure 9. Zonal Scheme for a Sodium Pool Fire in a Reactor Containment.

Flow rates were parametrically varied, starting with the lowest reasonable values. Thus, the minimal flow rate into the fire zone was chosen as twice the stoichiometric flow rate. This is a typical combustion requirement. The entrained convective flow was chosen so as to yield lowest likely flow velocities in the chimney.

Geometric dimensions of the three zones were chosen in loose analogy with calculated results of the CONVEC code [6]. These are not expected to sensitively influence the results, and were kept the same for all runs performed. Finally, source particle size was assumed constant and taken from typical simulation experiment results.

As base case we chose the physical extremium of minimum combustion air flow into and out of the fire zone (0.4 cm/sec for a fire zone radius of 9 m) and a flow velocity of 3.4 cm flow up the chimney.

To test our choice of base case as that most likely to show divergence between the cellular and homogeneous models, a case was run for which the source was assumed to consume all oxygen in the containment in just one hour, thus yielding a high intensity, short source. Such a source must yield very large chimney velocities. Again to yield most divergent results, the lowest physically reasonable velocities were assumed: 100 cm/sec from the fire zone with a chimney velocity of 500 cm/sec.

Discussion of Results

Figure 10 shows the nondimensional mass concentrations as a function of nondimensional time for the base case discussed above. It illustrates the expected high concentration of Zone 1 relative to Zone 3; within a factor of 50 of the maximum concentration possible. All three zones have essentially reached steady state after a very short time relative to source cutoff ($\sim 10^{-2} \cdot TS$). This steady state also holds for the mass in each particle size class (the size distribution) so that from a dimensionless time of 10^2 to 7.1×10^3 small particles released by the source in effect spill off the large particle end of the distribution and deposit on horizontal surfaces without affecting the size distribution of suspended material.

Note that the mass concentration calculated by the QUICK code (dashed curve) falls higher (factor of about 2) than that of Zone 3 for the ZONE code. This can be interepreted as a conservatism of the homogeneous mixing approach since containment leaks are likely to be fed by Zone 3. The FRBC are the additional nondimensional groups required by the ZONE model. They can be interpreted as follows

$$FRBC1 = \tau_B/\tau_{11} , \qquad FRBC3 = \tau_B/\tau_{22} ,$$

$$FRBC2 = \tau_B/\tau_{12} , \qquad FRBC4 = \tau_B/\tau_{32} ,$$

$$FRBC5 = \tau_B/\tau_{33} ,$$

where τ_B = characteristic time for maximum Brownian coagulation,

τ_{11} = residence time of combustion air flow in the fire zone, Zone (1)

τ_{12} = residence time of combustion air flow in the chimney, Zone (2)

τ_{22} = residence time of entrained air flow in the chimney, Zone (2)

τ_{33} = residence time of outer convection loop flow in the outer containment, Zone 3.

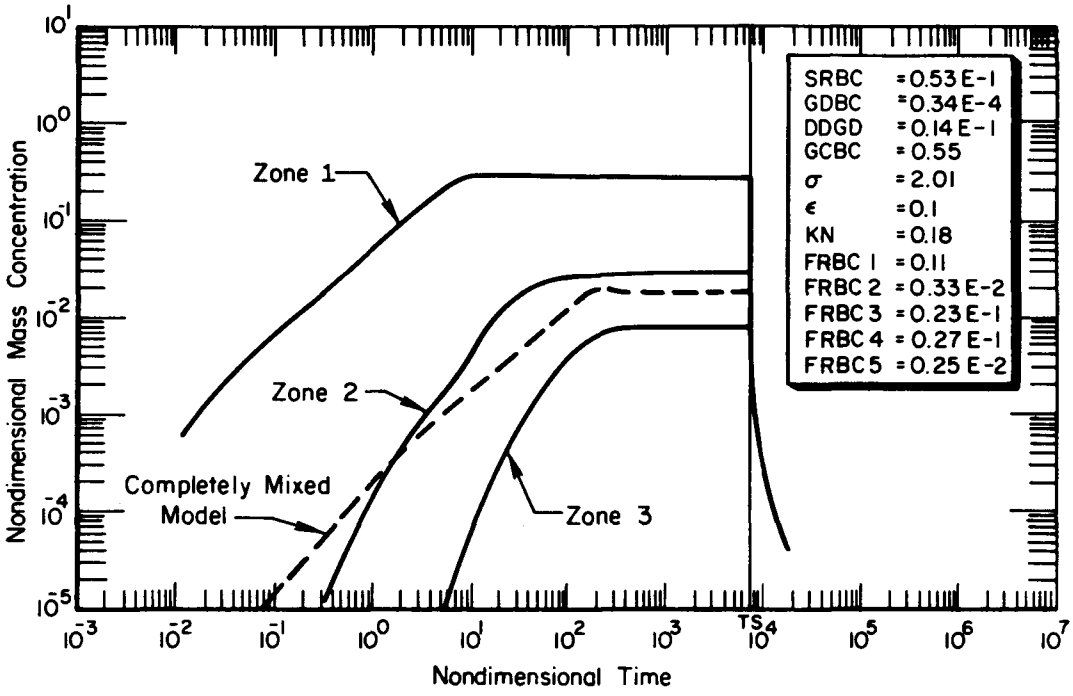

Figure 10. Comparison of ZONE with QUICK: Sodium Pool Fire. Long Term Source. Mass Concentration.

Figure 11 shows the results for the short, intense source case. As expected the inhomogeneity of the aerosol is reduced relative to the base case. Again, instantaneous mixing occurs after source cut-off and both codes predict the same mass concentration decay from the steady state.

It is interesting to note that the particle size distributions for the three zones are, except for a normalizing constant, practically identical. This is shown for the base case by Figure 12. It explains the agreement between ZONE and QUICK results once the source ceases and can be understood from the values of the flow groups (FRBC) that show, even for extreme cases, that coagulation is not much faster than the mixing rate.

Finally, Figure 13 shows the negligible influence of convective flow on the particle size distribution at a time 2.4 times the source cut-off time.

CONCLUSION

In the broadly based verification effort on the HAARM-3 solution technique, we attempted to encompass all geometries and accident conditions of interest in reactor safety research and analysis. It was found that HAARM-3

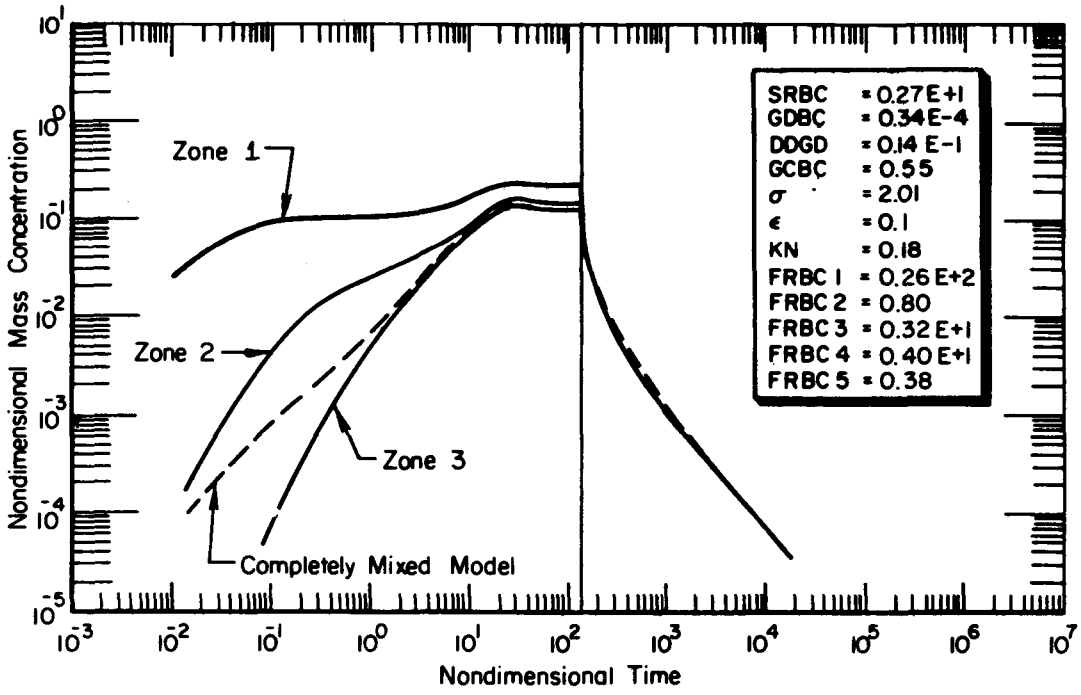

Figure 11. Comparison of ZONE with QUICK: Sodium Pool Fire. Short Term Source. Mass Concentration.

predictions of mass concentration were in excellent agreement with those of the reference code in many instances. When the two codes disagree, they do so by more than an order of magnitude in mass concentration only after the bulk of the originally suspended particle mass has deposited on available surfaces. This fact is reflected by a comparison of the cumulative leaked masses predicted by HAARM-3 and the reference code. These never differ by more than a factor of three. In this sense, therefore, it seems reasonable to claim HAARM-3 capable of its principle function, that of extrapolating experimental results to full scale accident situations. If in the future, however, accident analysis should receive a more critical assessment of suspended mass by particle size, this claim needs to be reevaluated.

In the analysis of the comparison results we attempted to show that, in a sense, the HAARM-3 solution technique represents a first order improvement on a purely monodisperse treatment of the aerosol behavior problem. The more polydisperse the aerosol to be analyzed, the further the divergence between HAARM-3 predictions and those of the reference model.

The fundamental assumption of all aerosol behavior models, that the aerosol can be treated as uniformally mixed, was shown in the second part

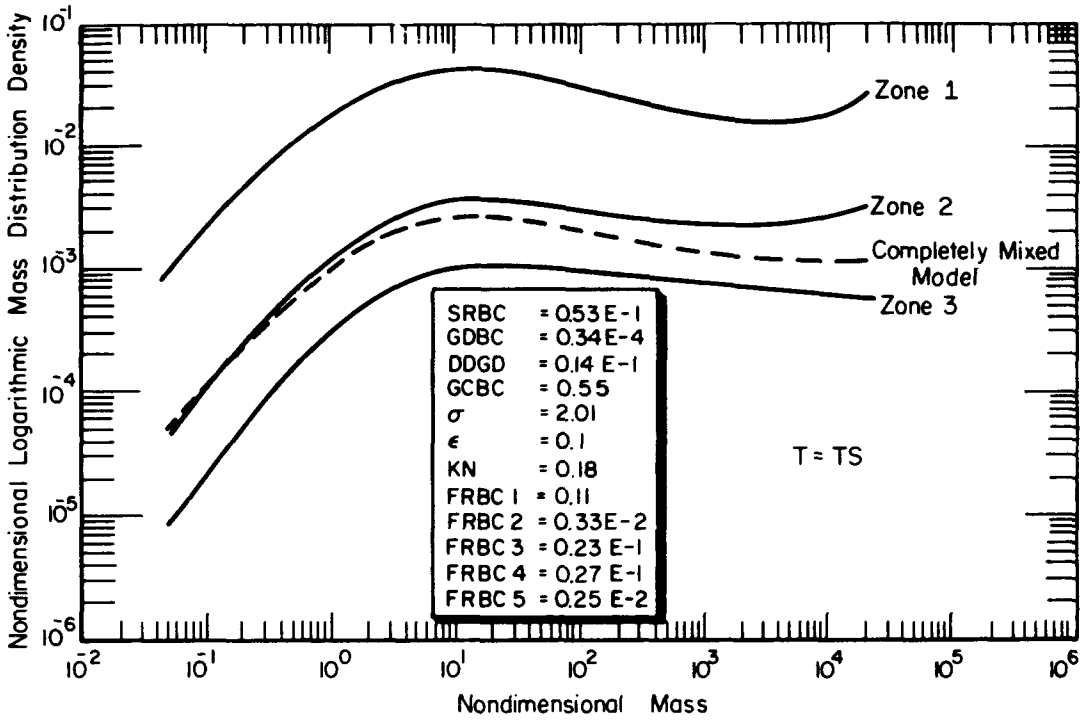

Figure 12. Comparison of ZONE with QUICK: Sodium Pool Fire. Long Term Source. Size Distribution at Source Cut-Off.

of this paper to be conservative by perhaps a factor of two in mass concentration during the steady state phase of source fed aerosol behavior. After this phase, homogeneity is rapidly established and the aerosol behavior indistinguishable from one treated as homogeneous throughout the accident sequence.

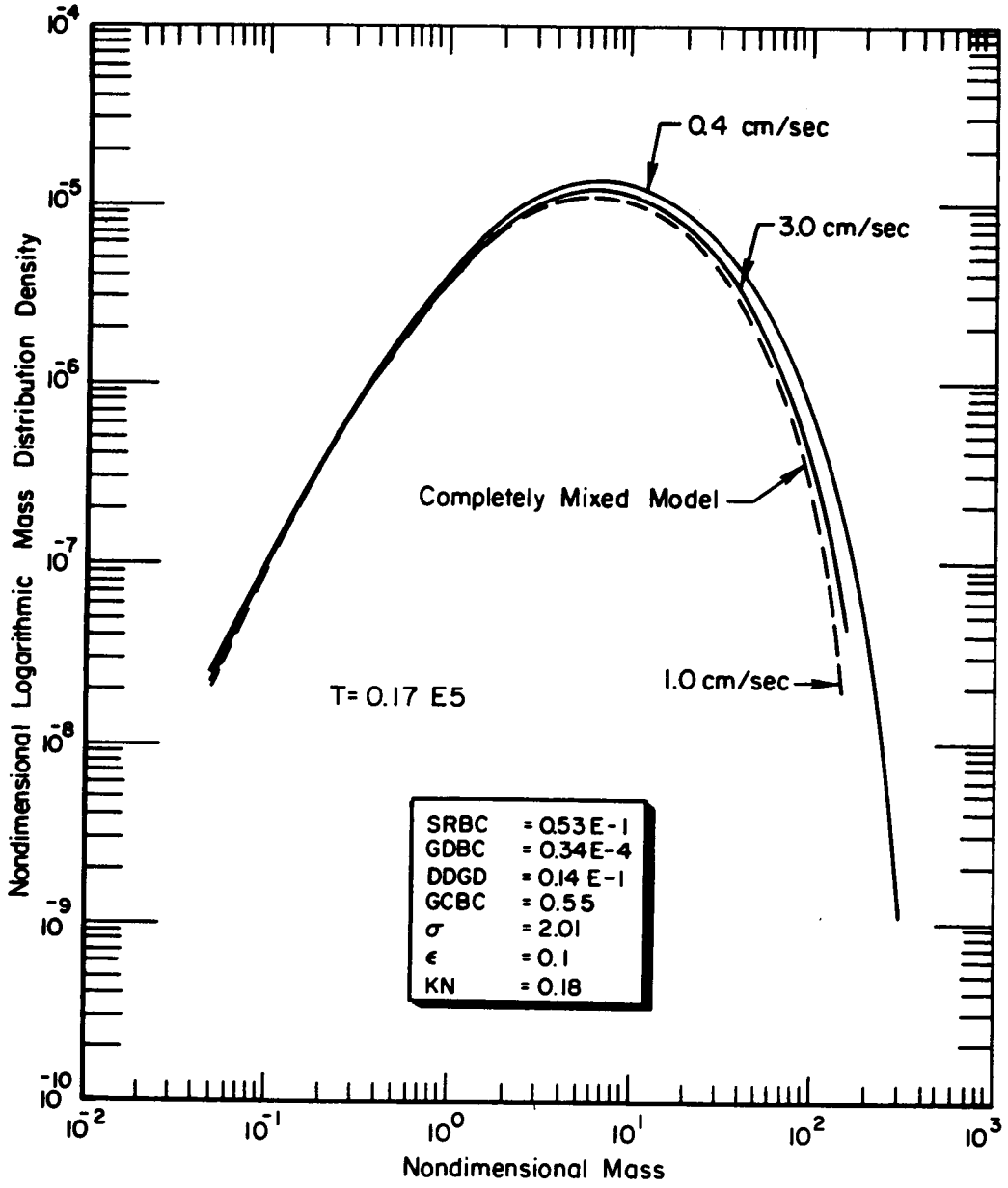

Figure 13. Comparison of ZONE with QUICK: Sodium Pool Fire. Long Term Source. Size Distribution at 2.4 × Source Cut-Off.

REFERENCES

1. Gieseke, J. A., et al., "HAARM-3 User's Manual," BMI-NUREG-1991 (1978).

2. Jordan, H., et al., "Recent Results of Nuclear Aerosol Behavior Code Development," Proceedings of the International Meeting on Fast Reactor Safety Technology, Seattle, Washington, August 19-23, 1979.

3. "Nuclear Aerosols in Reactor Safety," CSNI Report to the OECD (June 1979).

4. Lee, K. W., et al., "Sensitivity Analysis of the HAARM-3 Code," NUREG/CR-0527, BMI-2027 (1978).

5. Jordan, H., et al., "Multiple Zone Aerosol Behavior Model," NUREG/CR-1294, BMI-2042 (1980).

6. Cooke, R. L., Jr., et al., "A Parametric Study of Temperature, Pressure and Burning Rate Resulting from Large Sodium Fires in the CSE Containment Vessel," BNWL-B-391 (1974).

DEVELOPMENT OF INTERPOLATION FORMULAE FOR RAPID EVALUATION OF THE ATTENUATION DUE TO AEROSOL PROCESSES OF RADIOACTIVE RELEASE FOLLOWING HYPOTHETICAL FAST REACTOR ACCIDENTS

B Y Underwood, B C Walker and R J Williams
Safety and Reliability Directorate, UKAEA
Culcheth, Warrington, U.K.

ABSTRACT

This study investigates via a parametric survey the essential factors determining the magnitude of the release mitigation to be obtained from aerosol deposition and thereby develops analytical and graphical representations which enable a rapid estimation of these attenuations over a range of source magnitudes, leak rates and containment geometries.

The benefits obtained from aerosol deposition are conveniently exhibited by expressing airborne mass concentration and cumulative leaked mass in terms of non-dimensional attenuation factors which relate the quantities arising with deposition to those arising without deposition. Agglomeration is seen to play a crucial role in promoting deposition, and the reduction in release can amount to orders of magnitude on the time scale of a day for accidents involving high initial concentrations of airborne particulate.

In the context of source magnitude variation for instantaneous releases the appearance of an envelope decay curve for the airborne mass concentration enables simple representations of airborne mass and leaked mass to be developed. The leaked mass for constant fractional leak rate reaches an asymptotic limit at long times, a limit which varies only weakly with injected mass concentration.

With regard to variation in containment size, the domination of deposition processes by gravitational settling results in attenuation factors for a given injected mass concentration - for containments of given height- being virtually independent of the area of walls (and roof). In addition, although the process coefficient for gravitational settling is inversely proportional to height, the net effect of a change in height on the attenuation factors for a given initial concentration is remarkably small where the attenuations are significantly different from unity on the time scale of a day. Thus, within the range of interest, attenuation factors for instantaneous releases are only a function of time and initial concentration to fair approximation.

Sensitivity studies indicate that uncertainties in the form and magnitude of the collision efficiency for gravitational agglomeration can have substantial effect on attenuation factors, with the simple Fuchs formula giving optimistic results.

1. INTRODUCTION

Computer calculations of aerosol behaviour in the regime of particle concentration for which agglomeration is important can be time-consuming and expensive. Yet there are situations in which the magnitude of the mitigation in consequences claimable from aerosol deposition is required throughout a range of its dependent variables. For example, in a quantitative risk assessment using the event tree/fault tree method a large number of possible sequences follow any initiator. The need to evaluate ultimate consequences for each sequence points to the usefulness of techniques which would enable a rapid evaluation of the various physical phenomena influencing them.

In the LMFBR attention has been focussed on low frequency/potentially high consequence sequences in the belief that aerosol processes in the secondary containment can play an important part in consequence mitigation. A full event-tree description of the potential containment response to a hypothetical core disruptive accident (HCDA) would need to take into account, inter alia, the performance of containment isolation systems and aircleaning systems. In this study attention is focussed on the mitigation in consequences claimable from natural deposition processes alone, both for the situation in which the containment is successfully isolated and maintains integrity but leaks to the environment at a low rate, and for the situation in which it is isolated initially but loses integrity after some time. Within this framework one can envisage a variety of source magnitudes, release rates and release durations, together with a range of leak rates and containment endurance times.

Another context in which it is useful to know how the release reduction factor varies throughout a parameter range is in assessing the relative merits of different design specifications for the secondary containment. Clearly the effect of the size/shape of the containment on aerosol deposition is only one of the many considerations figuring in containment assessment, but it is of interest to be able to identify the important features of the dependence and readily quantify the influence.

2. MODELLING

The modelling assumptions behind this study are discussed in [1], but in summary some of the major ones are:

2.1. The processes included are Brownian and gravitational agglomeration, gravitational settling and diffusive deposition. Among the processes excluded are turbulent agglomeration, turbulent impaction and thermophoresis which require more detailed modelling of the fluid flow and thermal conditions in the containment.

2.2. Aerosol homogeneity and co-agglomeration are assumed.

2.3. It is assumed that mixed sodium peroxide/core particles contain insufficient core material to influence their aerosol behaviour. This study considers the radioactive aerosol to be released at the same time as the sodium peroxide so that the airborne radioactive mass is subject to the same attenuations as the airborne sodium peroxide mass and the particle-size distribution associated with the radioactivity will be that of the sodium peroxide particulate.

Details of the method of solution used by the computer programme Aerosim are given in [2].

3. DATA

The data are divided into 2 groups: those assumed not to vary from situation to situation, and parameters which are varied throughout a range to determine their functional influence on attenuation factors. A decision on the best choice of data was aided by the recommendations of the state-of-the-art report [3]. Table I shows the values and ranges; detailed discussion is given in [1] but some highlights are as follows: The sodium oxide particulate is assumed to form approximately spherical cluster agglomerates and the "effective density" [3] formulation of particle correction factors is used. The density correction factor is taken to be independent of the number of primaries in an agglomerate; the best numerical value is uncertain but was based on measurements in [4] and [5].

In this paper attention is restricted to instantaneous releases; results for prolonged sources will be reported separately. The study assumes that the fractional leak rate is constant up to the instant of loss of containment integrity. No credit is taken for deposition processes along the leakage route. The analysis exploits the simplification resulting from the assumption of small leak rates (say, $\lesssim 10^{v}$/o per day) in that the shape of the cumulative leaked mass versus time curves are independent of leak rate.

4. RESULTS

4.1. DEPENDENCE ON SOURCE MASS

Figure 1 shows the airborne mass concentration as a function of time for various quantities of sodium peroxide instantaneously suspended at t = 0 with uniform concentration throughout a 50m x 50m containment (containment A). The shape of each of these curves can be understood in terms of an initial period during which deposition rates are low but during which particles grow by agglomeration to a size range where gravitational settling becomes appreciable, and this is borne out by the variation of mass median radius with time - Figure 2. This airborne concentration distribution results in curves of cumulative leaked mass (for constant leak rate) as a function of time shown in Figure 3. Clearly the time at which the deposition rate becomes appreciable decreases as initial airborne mass increases due to the more rapid agglomeration at higher concentrations; this can be quantified by evaluating the time at which the airborne mass falls by a factor of 2 as a function of initial mass - Table II - which shows approximately an inverse proportionality for masses > 1Te.

A remarkable feature of the curves in figure 1 is that, to good approximation, the decay of the airborne concentration is governed by a single "envelope" curve. This feature enables a simplified representation of the airborne mass concentration curve to be devised (ignoring the finite time required to make the transition onto the envelope curve): if for the envelope curve the airborne mass concentration as a function of time has the functional form E(t), then for an injected mass concentration

C_i, the airborne mass concentration at any time t, C(t) can be taken as

$$C(t) = C_i \text{ for } t \leq t(C_i); \quad C(t) = E(t) \text{ for } t > t(C_i)$$

where $E(t(C_i)) = C_i$

Within this simple representation the cumulative leaked mass (CLM) for small constant fractional leak rate L and total injected mass M

$$= M\,tL \quad \text{for } t \leq t(C_i),$$

and for containment volume V

$$= L\left[Mt(C_i) + V\int_{t(C_i)}^{t} E(t')dt'\right] \quad \text{for } t > t(C_i)$$

Further implications of the "envelope-curve" feature can be obtained by making the (not too drastic) approximation that its form is a straight line in log-log space

$$\text{i.e. } E(t) = At^{-B}$$

Then $t(Ci) = (A/C_i)^{1/B}$ and the cumulative leaked mass for $t > t(C_i)$ becomes

$$CLM(t) = LV\left[\frac{B}{B-1} A^{1/B} C_i^{(B-1)/B} - \frac{A}{B-1} t^{1-B}\right]$$

In general one can distinguish two cases: for $B > 1$ the time-dependent term diminishes with increasing time, implying that for each initial concentration the leaked mass reaches an asymptote. Also, the asymptotic leaked mass increased monotonically with initial concentration. On the other hand, for $B < 1$, the cumulative leaked mass approaches a power-law increase with time, with a convergence of the curves corresponding to different initial concentrations.

For the conditions of this study, the best fit for A and B are

$$A = 157.8, \quad B = 1.21 \text{ (with t in seconds and E in kg.m}^{-3}\text{)}$$

and the first of the above possibilities applies. However, it is noteworthy that since B is not much different from unity the dependence of the asymptotic leaked mass on initial concentration is weak, ie to the power $B-1/B$. Note also that for $B \approx 1$, $t(C_i) \simeq 1/C_i$ as already indicated.

4.2. DEFINITION OF ATTENUATION FACTORS

It is convenient to define non-dimensional attenuation factors which are normalized representations of airborne mass concentration and cumulative leaked mass:

The <u>leakage attenuation factor</u> (LAF) at time t

= cumulative mass which would have leaked up to time t in the absence of deposition/actual cumulative leaked mass up to time t

For instantaneous sources, assuming constant fractional leak rate L the numerator is simply $M(1 - e^{-Lt})$ which, for the small values of Lt considered here $\sim$ MLt.

<u>The airborne attenuation factor</u> (AAF) at time t

= total mass injected into containment before time t/mass remaining airborne at time t.

These parameters have a direct practical relevance: for the situation in which the containment maintains its integrity indefinitely and releases mass to the environment only via its standing (small) leak rate, the leakage attenuation factor is a measure of the benefit which can be claimed from aerosol deposition. For the situation in which the containment survives for a time before losing integrity, the airborne attenuation factor is a measure of the benefit to be claimed from the reduction - via aerosol deposition - in the amount of mass available for release upon loss of integrity (assuming no resuspension).

Figures 4 and 5 show the conversion of figures 1 and 3 into these non-dimensional factors. Also shown on the figures is the attenuation factor which would have been obtained in the absence of agglomeration - ie purely from deposition of primaries - illustrating the vital role of agglomeration. The relationship between LAF and AAF for instantaneous sources is

$$1/LAF(t) = (1/t) \int_0^t (1/AAF(t')) \, dt'$$

In the small leak rate approximation, both AFs are independent of leak rate.

4.3. ESSENTIAL DEPENDENCIES

The functional dependencies of the attenuation factors on the parameters chosen for variation are now considered. For agglomeration processes, the effect of differing initial masses suspended in different containments is dependent on total mass concentration. For deposition processes, the rates at a given concentration depend on the ratio of wall area to volume (through the diffusive deposition term) and height (through the gravitational settling term). Thus for instantaneous sources the attenuation factors can be taken as

$$AF = AF(t, C_i, h, A_w/V) \text{ where}$$

t = time measured from instant of mass suspension
C_i = injected mass concentration
h = height
A_w/V = ratio of wall area to volume

For the conditions prevailing in these calculations diffusive deposition can be expected to make a small contribution to the total deposition (except perhaps at early and late times when the airborne particulate is dominantly $\lesssim 1 \mu m$). This implies little dependence of attenuation factors on A_w/V, and this is demonstrated by the results in Table III which shows the attenuation factors after 24 hours for 3 containments of the same height but different A_w/V with the initial mass concentration adjusted to be the same (1.02×10^{-2} kg/m^3, equivalent to 1 Te in the 50m x 50m containment) in each case. The degree to which attenuations are independent of A_w/V will depend on the initial concentration, but for the range of concentrations at which attenuation factors significantly greater than unity are attained in a reasonable time ($\lesssim$ few days), the agglomeration which this implies ensures that gravitational deposition dominates. Therefore, for the region of interest one need only consider

$$AF = AF\ (t,\ C_i,\ h)$$

The variation with height of the attenuation factor at a given time for given initial concentration arises through the gravitational settling process, the coefficient of which scales inversely with height. The net effect of a change in height is illustrated in figures 6 and 7 which show the attenuation factors as a function of time for containment heights of 30m, 50m, and 100m (initial concentration fixed at 1.02×10^{-2} kg/m^3). As expected, the higher containment has a slower fall-off in airborne mass concentration and hence consistently smaller attenuation factors at any given time. However, the magnitude of the difference in attenuation factors is remarkably small even for times of the order of a day. This is especially true for the leakage attenuation factor (since it involves integration over earlier parts of the airborne concentration curve): for a factor of over x3 difference in height the leakage attenuation factor even at 24 hours differs by only a factor of 15%. This feature is explicable in terms of a partial compensation via agglomeration: a reduced deposition coefficient for particles of a given size preserves a higher concentration, leading to greater agglomeration; the increase in size leads to an increased deposition rate. This explanation is borne out by an examination of the variation of mass median radius with time as shown in figure 8; for the higher containment particles are consistently larger. Clearly for very low initial concentrations this partial compensation is less effective, but in this regime the attenuation factors approach unity on the time scale of a day. Thus, for the ranges of parameters of interest, the dependence of the attenuation factors on height can be ignored to a fair approximation. This is convincingly demonstrated in figure 9, showing the leakage attenuation factor at 24 hours for a number of containments and a range of initial concentrations: data points arising from containments of different height in principle lie on separate curves, but because of the proximity of these curves it is possible to reduce all the data to a single curve.

Since the attenuation factors are thus effectively only a function of time and initial concentration

$$\text{ie } AF = AF(t,\ C_i)$$

it is possible to graphically represent all the information as a set of generic curves, giving AF versus t for various C_i or alternatively AF versus C_i for various t. The latter curves, based on the data obtained in this study are shown in figures 10, 11 and enable a rapid estimation of potential attenuations from aerosol deposition in a wide range of circumstances.

The implication of the above results concerning the dependence of attenuation factor on containment geometry is that the envelope decay curve is virtually the same for all containments within the range of dimensions under consideration: it can be taken to have the functional form of the envelope curve for the 50m high containment, referred to above as E(t). On this basis each of the generic curves of AF versus C_i for given t can be represented by 2 straight-line sections:

$$AAF\ (t,\ C_i) = 1 \quad \text{for } t \leq t\ (C_i)$$
$$AAF\ (t,\ C_i) = \frac{C_i}{E(t)} \quad \text{for } t > t\ (C_i)$$

where $E\ (t\ (C_i)) = C_i$

and on this model

$$LAF\ (t, C_i) = 1 \quad \text{for} \quad t \leq t(C_i)$$

$$LAF\ (t, C_i) = \frac{C_i t}{C_i\, t(C_i) + \int_{t(C_i)}^{t} E(t')\, dt'} \qquad t > t(C_i)$$

Using the power-law approximation to E (t) gives

$$AAF\ (t, C_i) = \frac{C_i t^B}{A} \text{ and}$$

$$t > t(C_i)$$

$$LAF\ (t, C_i) = \frac{C_i t}{\left[\frac{B}{B-1} \cdot A^{1/B} \cdot C_i^{\frac{B-1}{B}} - \frac{A}{B-1}\, t^{1-B}\right]}$$

which at long time (B>1) becomes

$$LAF\ (t, C_i) \rightarrow \frac{(B-1)}{BA^{1/B}}\, C_i^{1/B}\, t \quad , \quad \text{or} \frac{(B-1)}{B}\, \frac{t}{t(C_i)}$$

5.4. SENSITIVITY

The slope and intercept of the envelope curve will be a function of the various fixed input parameters, and it is instructive to examine the influence of uncertainties in these data on the attenuation factors. The data listed in Table IV were changed one at a time from their base values by an amount considered to be representative of the uncertainty in them; the effect on the attenuation factor at various times is shown in Table IV:

5.4.1. Initial particle size distribution.

Studies in the past have noted the insensitivity of leaked mass to initial particle size distribution [6] as borne out by the present study. A factor of 2 increase in r_g gives ~ 12% increase in leakage attenuation at times beyond a few hours, which arises from the earlier fall-off in airborne mass concentration as a result of the size distribution being initially closer to the regime of rapid gravitational settling. A decrease in the geometric standard deviation of the initial distribution results in a lowering of the attenuation factor since the wings of the distribution do not now extend so far into the size range of rapid deposition, but a change in σ_g from 2 to 1.5 leads to only 5% decrease in leakage attenuation at 24 hours.

5.4.2. Density correction factor.

The table shows the effect of reducing α from 0.4 to 0.2, a change considered representative of the level of its uncertainty. The change in attenuation factors which this produces is remarkably small at all times considered. This must arise from a compensation: at the lower density a given initial size distribution corresponds to particles of smaller mass which would settle under gravity more slowly. However, the initial number concentration for a given total mass is higher so agglomeration is more rapid, and the resulting net effect is small.

5.4.3. Collision efficiency

Recent work [7] has indicated that the simple Fuchs formula [8] used here may overestimate the collision efficiency in some size ranges, and neglect a dependence on the absolute size of r_1 and r_2 in addition to their relative size. As a preliminary check on sensitivity to ϵ, the Fuchs formula was simply scaled down by a factor of 2. The results in Table IV show a significant effect at all times much beyond $t(C_i)$ amounting to $\sim$30% decrease in the leakage attenuation factor at 24 hours. A further test was made using an approximate representation of the results tabulated by Loyalka for sodium oxide particles (obtained, however, for a different particle density to that used here; the results are known to be strongly density dependent). The shape of ϵ from this work is quite idiosyncratic in the range 1 - 20 μm, and often lies below the Fuchs formula. Figure 12 shows that the airborne mass concentration falls off much more slowly for the Loyalka values; Table IV shows that the decrease in leakage attenuation factor at 24 hours amounts to almost a factor of 3, demonstrating that the Fuchs formula may give very optimistic estimates of mitigation. This degree of sensitivity suggests that the omission of turbulent agglomeration could have an important, though conservative, influence.

REFERENCES

1. Underwood B.Y., et al., "Study of Phenomena Determining the Radiological Consequences of a Severe Fast Reactor Accident", UKAEA/SRD Report (to be published) (1980)
2. Walker B.C., et al., "Discretization and Integration of Equation Governing Aerosol Behaviour" UKAEA/SRD Report SRD R98 (1978)
3. OEDC, "Nuclear Aerosols in Reactor Safety". CSNI/SOAR No. 1. NEA, OECD (1979)
4. Gieseke J A, et al., "Aerosol Measurements and Modelling for Fast Reactor Safety" BMI-NUREG-1975 Battelle Columbus Laboratories (1977)
5. Hinds W., et al., "Density and Shape Factor of Sodium Aerosol" COO-2803-4. Harvard University School of Public Health (1977)
6. Lee K W., et al., "Sensitivity Analysis of the HAARM-3 Code" NUREG/CR-0527 BMI-2008 (1978)
7. Loyalka S K., "Analysis of Aerosol Particles Undergoing Gravitational Agglomeration" NUREG/CR-0780 College of Engineering, University of Missouri - Columbia (1979)
8. Fuchs N.A., "The Mechanics of Aerosols" Pergamon Press (1964)

Table I Input data: fixed and parametric ranges.

Fixed	
Temperature	423K
Pressure	0.15 MPa
Density of carrier gas	1.23 kg m^{-3}
Viscosity " "	2.4×10^{-5} $kgm^{-1}s^{-1}$
Mean free path "	7.2×10^{-8} m
Initial size distribution	lognormal
r_g	0.25μ m
σ_g	2
Chemical form of particulate	$Na_2 O_2$
Bulk density	2805 kg m^{-3}
Density correction factor	0.4
Collision efficiency	$\frac{3}{2}\left(\frac{r_1}{r_1+r_2}\right)^2$; $r_2 > r_1$
Diffusion boundary layer thickness	100μ m
Parametric ranges	
Source mass - instantaneous	0.1, 1, 5, 20 Te
Containment height	30, 50, 100 m
Containment diameter	44, 50, 60, 100, 200 m
Leak rate	any constant leak rate ($\lesssim 10^{\%}$/o per day)
Times of interest	up to several days

TABLE II Time for the airborne mass to fall by a factor of two versus total injected mass (containment A)

Source Mass, M (Te)	$t_{\frac{1}{2}}$ (Sec)	M $t_{\frac{1}{2}}$
0.1	3.6×10^4	3.6×10^3
1	5.4×10^3	5.4×10^3
5	1.2×10^3	6.0×10^3
10	6.5×10^2	6.5×10^3
20	3.3×10^2	6.6×10^3

TABLE III Attenuation factors after 24 hours for same injected mass concentration in containments of different $A_w/_V$, height = 50m.

$A_w/_V$ m	Volume m^3	AAF(24hr)	LAF(24hr)
10^{-1}	9.82×10^4	71.8	8.69
6×10^{-2}	3.93×10^5	71.7	8.69
4×10^{-2}	1.57×10^6	71.7	8.69

Table IV 5 Te injected into Containment A: attenuation factors at several times for a change in selected input data

	Leakage Attenuation Factor			Airborne Attenuation Factor		
	1 hr	10 hr	24 hr	1 hr	10 hr	24 hr
Base case	2.3	13.8	30.1	6.7	102	345
$r_g \rightarrow 0.5$	2.7	15.4	33.3	7.4	102	343
$\sigma_g \rightarrow 1.5$	2.1	13.0	28.4	6.5	101	339
$\alpha \rightarrow 0.2$	2.3	14.6	31.7	7.4	108	343
$dT/dx \rightarrow 50$ K/cm	2.3	14.0	30.8	6.8	111	435
$\epsilon \rightarrow \epsilon/2$	1.7	9.4	20.5	4.0	66	239
$\epsilon \rightarrow$ Loyalka	1.3	5.6	11.4	2.2	24	85

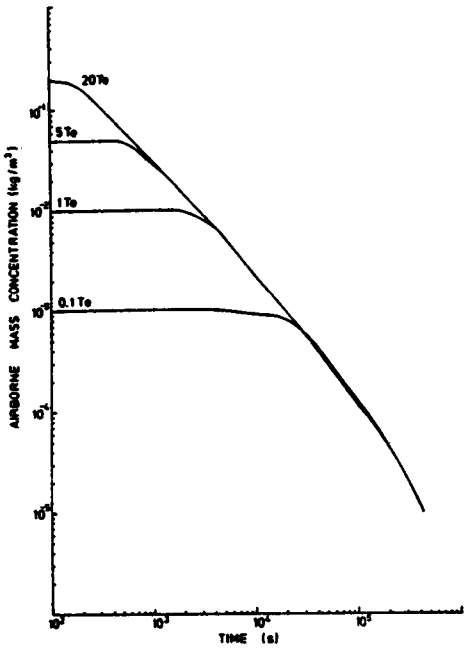

FIG. 1 AIRBORNE MASS CONCENTRATION / TIME - INSTANTANEOUS SOURCE - CONTAINMENT A

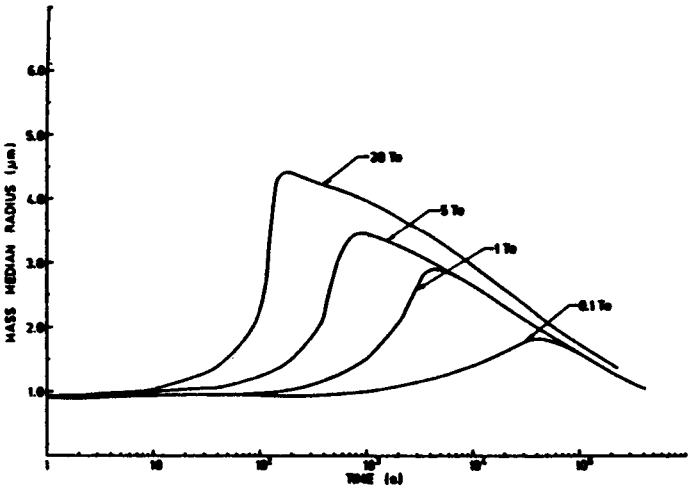

FIG. 2 VARIATION OF MASS MEDIAN RADIUS WITH TIME - INSTANTANEOUS SOURCE - CONTAINMENT A

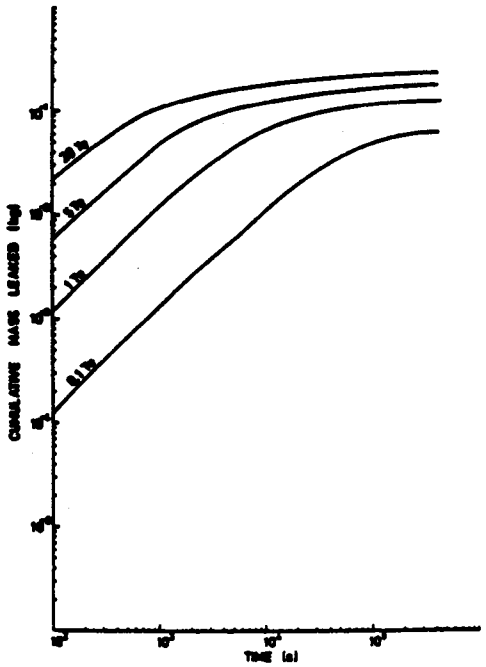

FIG. 3 CUMULATIVE MASS LEAKED/ TIME - INSTANTANEOUS SOURCE - CONTAINMENT A LEAK RATE 0.1 % PER DAY

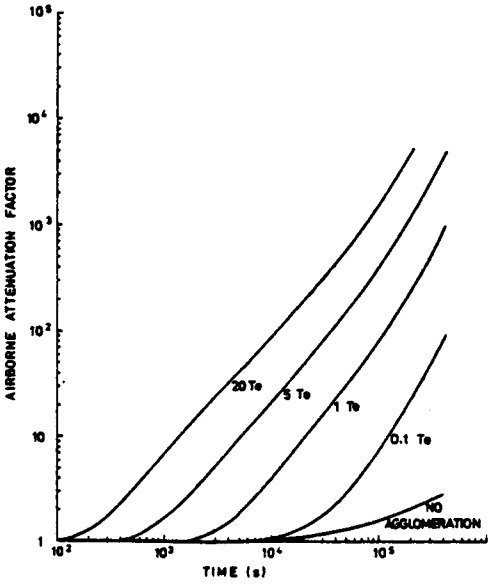

FIG. 4 AIRBORNE ATTENUATION FACTOR / TIME - INSTANTANEOUS SOURCE - CONTAINMENT A

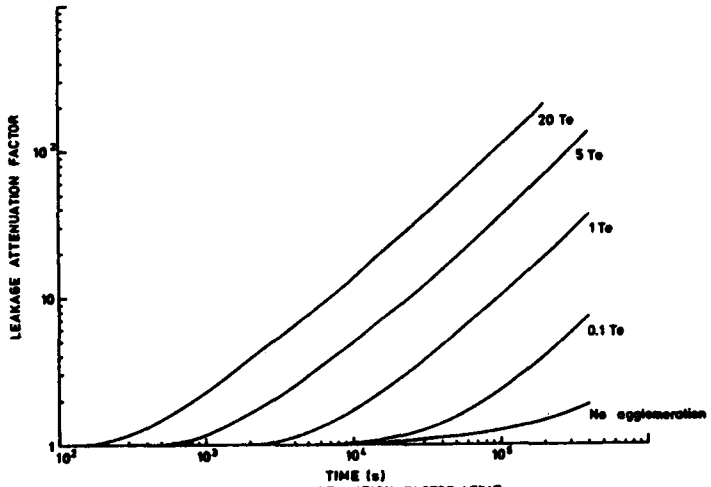

FIG.5 LEAKAGE ATTENUATION FACTOR / TIME – INSTANTANEOUS SOURCE-CONTAINMENT A

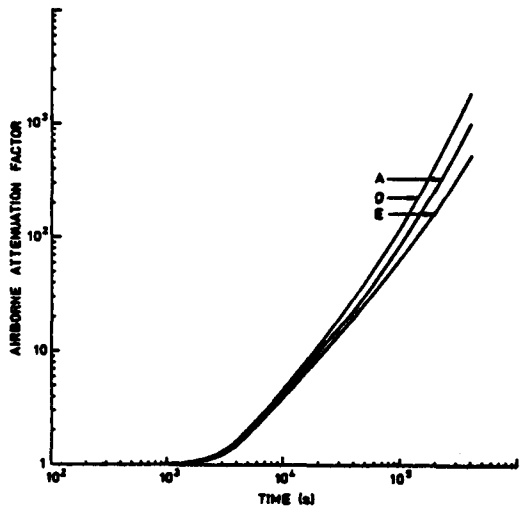

FIG. 6 AIRBORNE ATTENUATION FACTOR / TIME – EFFECT OF CONTAINMENT HEIGHT.

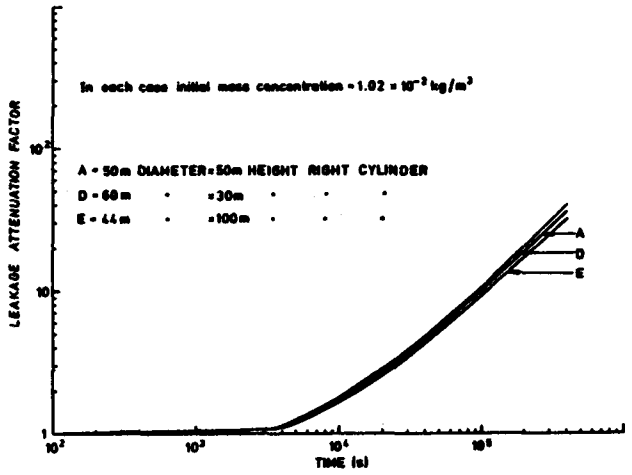

FIG. 7 LEAKAGE ATTENUATION FACTOR / TIME - EFFECT OF CONTAINMENT HEIGHT

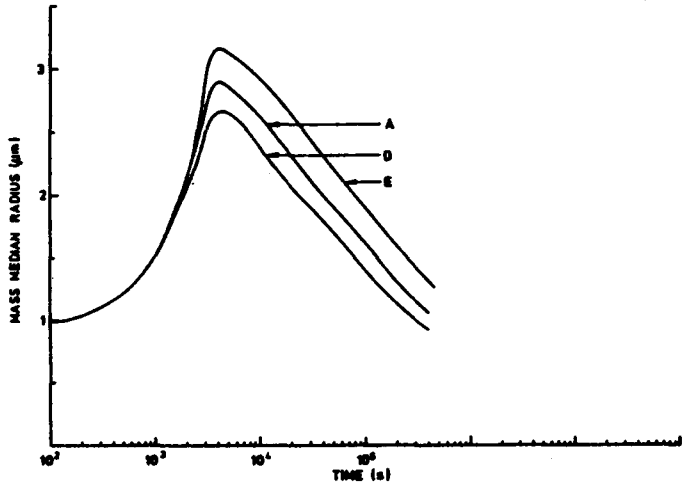

FIG. 8 MASS MEDIAN RADIUS / TIME - EFFECT OF CONTAINMENT HEIGHT

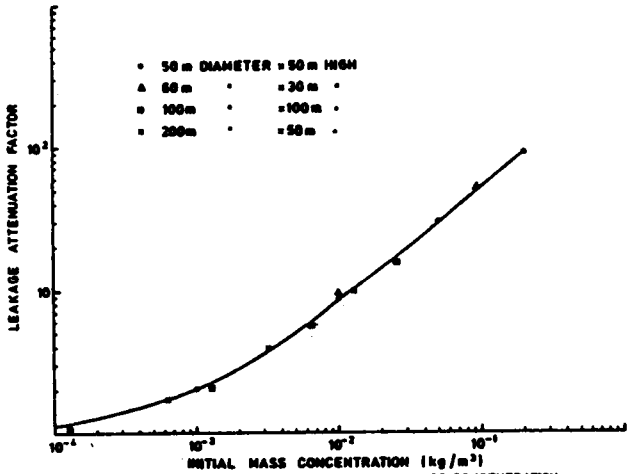

FIG. 9 LEAKAGE ATTENUATION FACTOR / INITIAL MASS CONCENTRATION - 24 HOURS AFTER INJECTION OF MASS

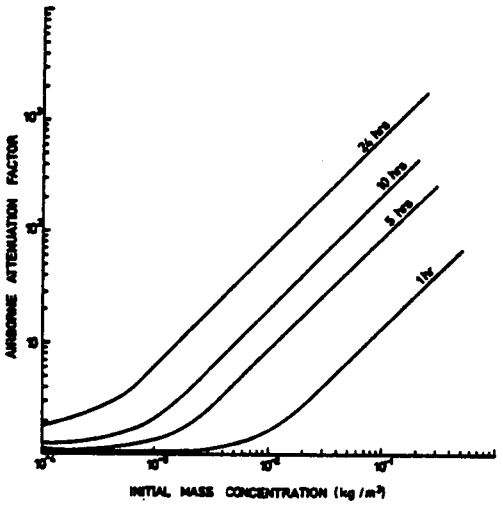

FIG. 11 AIRBORNE ATTENUATION FACTOR / INITIAL AIRBORNE MASS CONCENTRATION

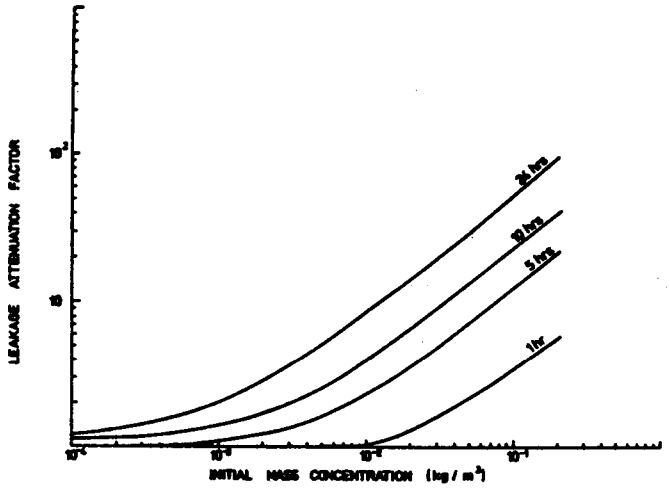

FIG. 10 LEAKAGE ATTENUATION FACTOR / INITIAL MASS CONCENTRATION

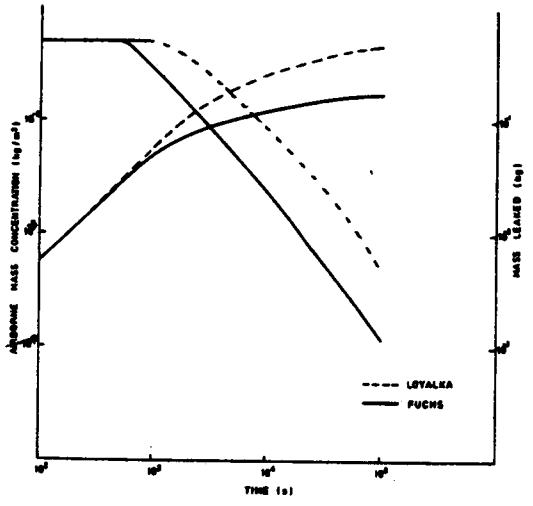

FIG. 12 AIRBORNE MASS CONCENTRATION AND LEAKED MASS Vs. TIME FOR TWO C REPRESENTATIONS

INFLUENCE OF THE SOURCE TERM PARAMETERS ON AEROSOL BEHAVIOR IN CORE MELT DOWN ACCIDENTS IN LWRS

H. Bunz, M. Koyro, W. Schöck
Laboratory for Aerosol Physics and Filter Technology
Project Nuclear Safety
Kernforschungszentrum Karlsruhe, FRG

ABSTRACT

A study dealing with the influence of the different source term parameters is presented for the case of an assumed core melt down accident. Calculations with the NAUA-code were carried out using a variety of different values for the aerosol size parameters as well as for the total release airborne mass over a realistic range. The values of the latter indicate a far greater influence on the aerosol behavior than those of the size parameters. An attempt is made to explain these results in qualitative terms. Whilst assessing the radiological consequences of the accident a number of other parameters were also discovered to be of great importance.

INTRODUCTION

As it is commonly known, the purpose of the NAUA-code is to calculate the behavior of radioactive aerosols in a LWR-containment as they are assumed to be released in a core melt down accident [1] . Since the accident sequences,which have to be considered, are very different, the model equations taken as a basis of the code should be strictly physical. In particular it seems impossible to use empirical integral depletion coefficients measured in one or two experiments. Therefore, the NAUA-code calculates each aerosolphysical process recognized as being important. The model equations for these processes were checked by means of experiments and improved when necessary. Only as final verification is an integral experiment planned for the future.

At the moment the code is in the status that all aerosolphysical processes involved are correctly formulated, only bearing in mind the well known problems in the Knudsen transition region and for non-spherical particles. It takes into account the Brownian coagulation, the sedimentation, the diffusion and the condensation of water onto the particles. The aqueous and the solid fractions of the particles are calculated as functions of particle size and time. The principle scheme of the code can be seen in Fig. 1, showing the input and output as well as the processes involved. It should be mentioned that, as regards the problems of non-spherical particles, in the meantime measurements are available for the dynamical shape factor, the water condensation on real particles and to a certain extent even for the coagulation shape factor [2] .

To clarify the relative importance of the different input parameters a study was carried out where especially the parameters of the aerosol source term were varied over a wide range. The source term was recognized as being very important whilst an assessment was made of the radiological consequences of the accident [3] . The reason for this is that measuring of source term data under real accident conditions is impossible and the extrapolation of the data yielded in simulation experiments is difficult since the thermodynamics of the gas in the reactor pressure vessel (RPV) is not sufficiently known for a description of the mutual cooling and heating of the gas. But the formation and the growth of the recondensation aerosol particles are strongly influenced by the temperatures and their space and time gradients. Therefore, the question remains open whether the size of the particles in the accident is the same or similar as revealed in the experiments. In order to analyse the influence of the assumed error in the aerosol size measurements, a number of calculations with the NAUA-code were carried out where the aerosol size parameters were varied over the whole range which can be expected during an accident.

THE ACCIDENT TAKEN AS A BASIS OF THE STUDY

As a basis a core melt down accident was assumed in a typical German 1300 MW_e PWR. The containment was considered as a single volume of 72000 m^3 with a total surface of 31000 m^2 and a floor area of 2500 m^2. The temperature functions and steam release rates were taken from [4] . The time dependence was assumed as shown in Fig. 2. The first significant release occurs during the evaporation of the residual water in the RPV. The release rate is taken as linearly increasing in the period when the core heats up and starts to melt. The flow of evaporating steam through the broken primary system acts as a driving force.After drying out of the RPV no further release into the containment takes place. When the RPV melts through and the molten core falls into the concrete basement, a second part of the aerosols is assumed to be released at a constant rate and to be composed of fuel with fission products and of concrete. This second release period contains 20% of the airborne fuel material. The vapour and the gases from the decomposing concrete carry the aerosol particles into the containment. After about 8200 sec the melt is cooled down from about 2500°C to about 1800°C and no further aerosol release takes place. It should be mentioned that the duration of the aerosol source and its exact time function is not very important as long as it is smaller than the average time the aerosol particles spend in the volume. This time is in the range of several hours.

The water condensation onto the particles was not taken into account as the calculations were in general performed for the fourth phase of the accident with the melt on the concrete. For this period it can be assumed that the temperature of the steam released from the concrete is so high that condensation is only possible on the relatively cold walls and not on the particles.

RESULTS OF THE STUDY

As basic values for the aerosol size distribution a mean geometric radius (r_g) of 0.1 µm and a logarithm of the geometric standard deviation (σ) of 0.3 were used assuming only for convenience a log-normal distribution. These values are in the range given in [1] . But firstly the total initial released mass was varied from the best estimate value 1000 kg (this is about 1% of the core) down to 72 kg and up to 2500 kg. The last value can be estimated by experimental results yielded in the German fission product release program [5] . The result can be seen in Fig. 3. It shows the typical behavior that in the long range the mass concentration is lower in the cases with higher initial release [6] . The reason for this behavior is the coagulation effecting larger faster settling particles in these cases.

After that the size parameters were varied for each release value in a range which can be considered as realistic. Except for the pair of values mentioned above, in all three cases two other combinations were used; these are r_g = o.1 μm, ln σ = 0.7 and r_g = 0.3, ln σ = 0.4. The effect can be seen in the Figures 4 to 9. They show the mass and number concentration and the average radius for the release of 72 kg and 1000 kg as a function of time. The interesting and at first sight surprising result is the independence of all three functions on the initial aerosol size distribution of the source particles. This fact can be at least qualitatively explained by the following consideration. If, with a fixed initial released mass, the primary particles are small, then the number concentration and the correlated coagulation rate are high. Therefore, as a result the particles grow and the number concentration decreases. In contrast to this the coagulation rate is low if the particles are large and the number concentration is small. This behavior can be imagined especially for such large volumes as a containment of a LWR, where the time the particles spend in it is long enough to enable the aerosol system to reach an equilibrium state in most cases.

To confirm these results and to exclude special effects of the code only, which can be possibly assumed, calculations were also performed with different upper and lower limits for the size distribution as well as with the PARDISEKO IIIb code [7] which uses a log(r)-equidistant scale instead of the r-equidistant scale in the NAUA-code. But always the same results were obtained.

To find out the limits of these statements another set of calculations were performed with a - for core melt down accident of course unrealistically low - release of only 72 g or 1 mg/m³ respectively. In this case the effect of the coagulation should be weakened due to the low number concentration. This can be clearly seen in Fig. 10. This figure shows the average radius as a function of time for three combinations of size parameters. For the fairly large particles (r_g = 0.3 μ, ln σ = 0.4) there is obviously nearly no effect of the coagulation, as the average radius does not increase at the beginning but slightly decreases over the whole time due to settling of the larger particles of the size distribution. In the other cases the average radius increases with a slope depending on the particle size but obviously approximating to the same steady state value. It can be assumed that all three curves will come together in the infinity. This would mean that even in this very unrealistic case the aerosol behavior is quite similar compared to the others with the only difference that the time is much longer the aerosol system needs to reach a steady state independent of the initial values.

Therefore, as a general result it can be stated that the variation of the aerosol removal rate is quite weak when the aerosol size parameters are changed. This is valid at least for the fourth phase of the core melt down accident when no condensation on the particles takes place.

EFFECTS ON THE FUTURE R & D WORK

As shown the decay of the aerosols under core melt down conditions depends only weakly on the size parameters of the initial aerosol particles. Therefore, the exact measurement of the size of the primary particles is not so essential as believed formerly. This result is also useful in view of the facts reported above namely the impossibility to measure the aerosol formation under the real thermodynamic conditions.

But while estimating the radiological consequences of the accident a number of other important parameters can be discovered. These are the total released mass, the thermodynamics of the containment atmosphere, the steam sources, the build-up of the pressure, the failure time of the containment and the containment leak rates. The last points are of course strongly correlated and depend on the interaction between the melt and the concrete and the release of steam and non-condensable gases from the concrete. As far as the released mass is concerned the chemical composition of the aerosol particles and their content of the different fission products is of great interest in addition to their total amount.

To evaluate the effect of the steam condensation on the particles it is necessary to know the process of the removal of the latent heat arising in the atmosphere due to this condensation and, in connection with this removal, the distribution of the steam between the particles and the walls. This will be examined in a theorectical and experimental program to be started this year.

SUMMARY

A study to evaluate the importance of the different source term parameters was carried out for an assumed core melt down accident in a LWR.

The aerosol size parameters were found to be of relative insignificance in comparison with the influence of the other parameters such as total released mass, composition of the aerosol particles (only for the radiological consequences), and the general thermodynamics of the containment. Therefore, the exact measurement of the particle sizes is not so essential and a greater effort should be made to examine the other open problems.

REFERENCES

[1] Nuclear Aerosols in Reactor Safety, OECD-NEA, SOAR 1, CSNI 34 (1979)

[2] B. Rehn: Direct Measurements of the Coagulation Shape Factor of Aerosol Particles; This conference

[3] L.W. Lee, J.A. Gieseke, L.D. Reed: Sensitivity Analysis of the HAARM 3-code
BMI-2008, NUREG / CR-0527 (1978)

[4] K. Hassmann, X. Jacobsen, M. Peeks, J.P. Hosemann, A. Skokan, M. Reimann, S. Dorner: Abschätzung der H_2-Entwicklung aus der mit dem Beton-wechselwirkenden Kernschmelze
BMFT RS 237 Abschlußbericht (KWU, KfK/PNS) (1978)

[5] H. Wild, H. Albrecht, V. Matschoß: Untersuchung zur Aktivitätsfreisetzung beim LWR-Kernschmelzen
Jahrestagung Kerntechnik, Berlin (1980)

[6] H. Bunz, W. Schöck: Abbau freigesetzter Spaltprodukte in DWR-Sicherheitsbehältern (NAUA-Programm)
PNS-Jahreskolloquium (1978)

[7] H. Bunz: PARDISEKO IIIb Ein Computerprogramm zur Berechnung des Aerosolverhaltens in geschlossenen Behältern
KfK - 2903 (1980)

predict the removal of radioactive aerosols from the atmosphere of an LWR-containment during hypothetical core meltdown accidents. The model is based on microscale physical aerosol processes in a condensing atmosphere. The relevant parameters are determined experimentally.

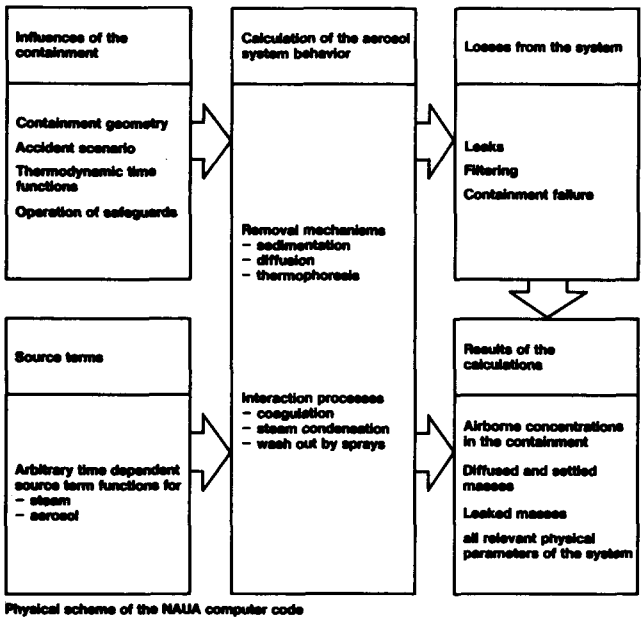

Physical scheme of the NAUA computer code

Fig. 1

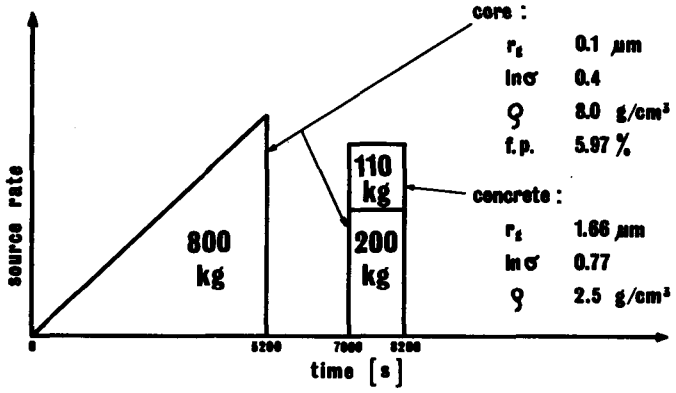

KfK LAF 1

Aerosol source term in the meltdown calculations

Fig. 2

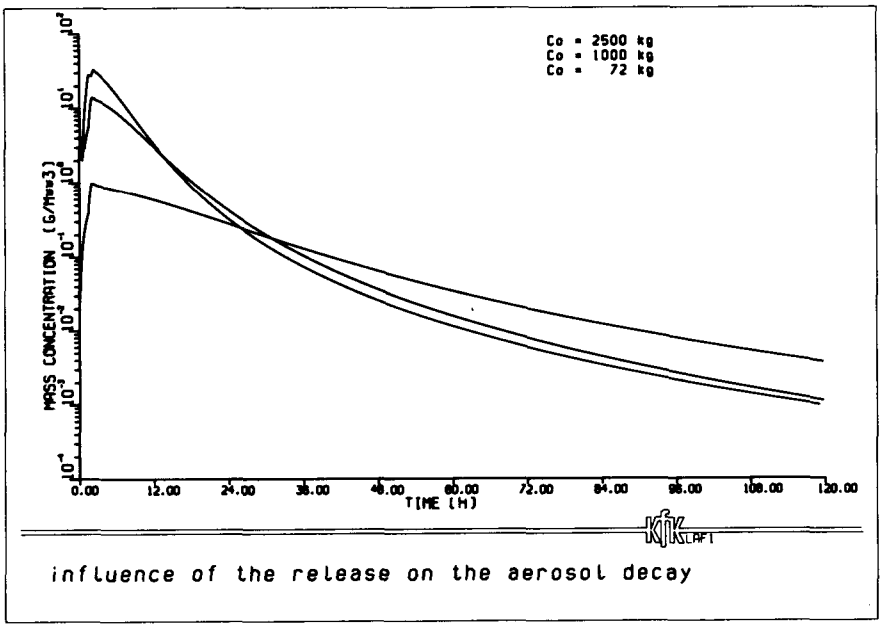

influence of the release on the aerosol decay

Fig. 3

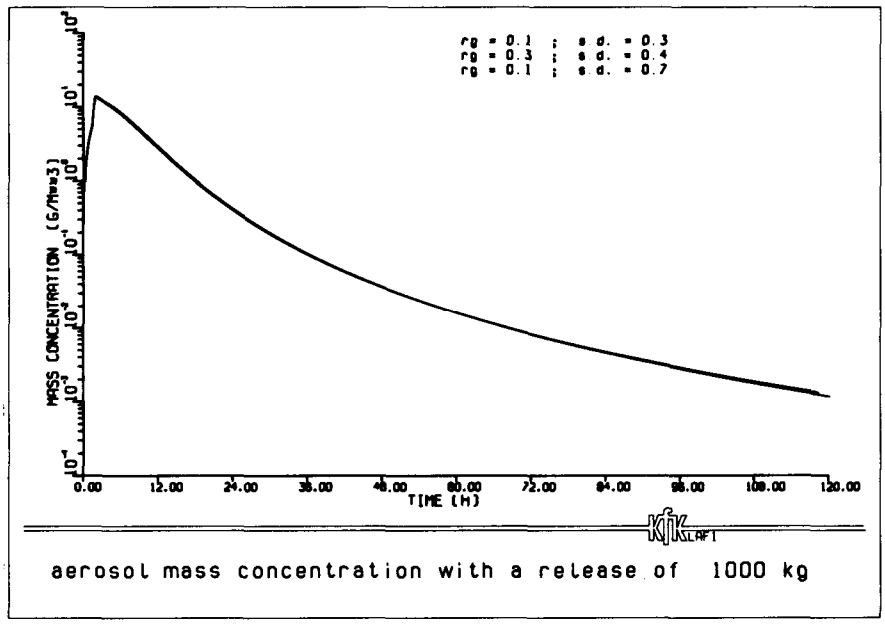

aerosol mass concentration with a release of 1000 kg

Fig. 4

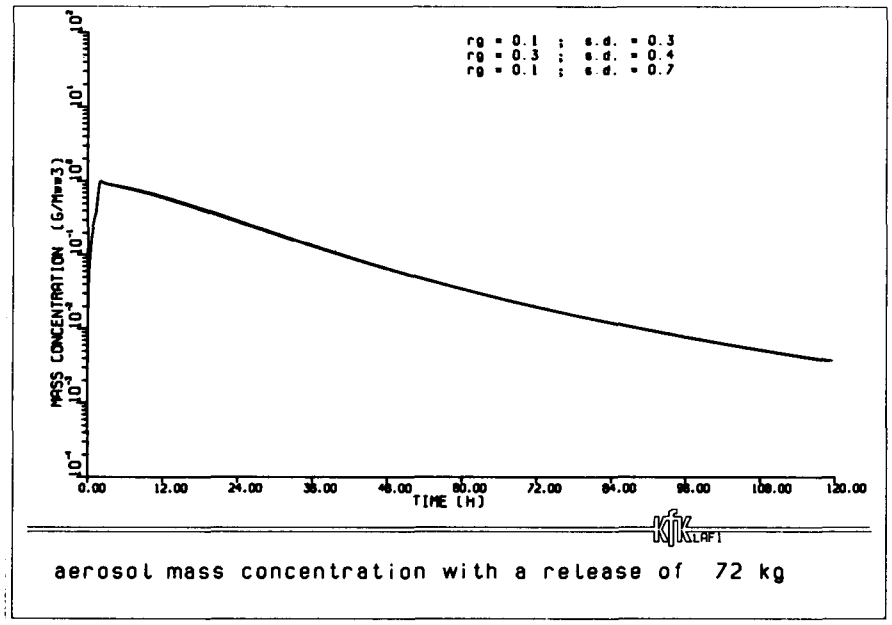
rg = 0.1 ; s.d. = 0.3
rg = 0.3 ; s.d. = 0.4
rg = 0.1 ; s.d. = 0.7
MASS CONCENTRATION (G/Mm3)
TIME (H)
0.00
12.00
24.00
36.00
48.00
60.00
72.00
84.00
96.00
108.00
120.00
KfK
LAFI
aerosol mass concentration with a release of 72 kg

Fig. 5

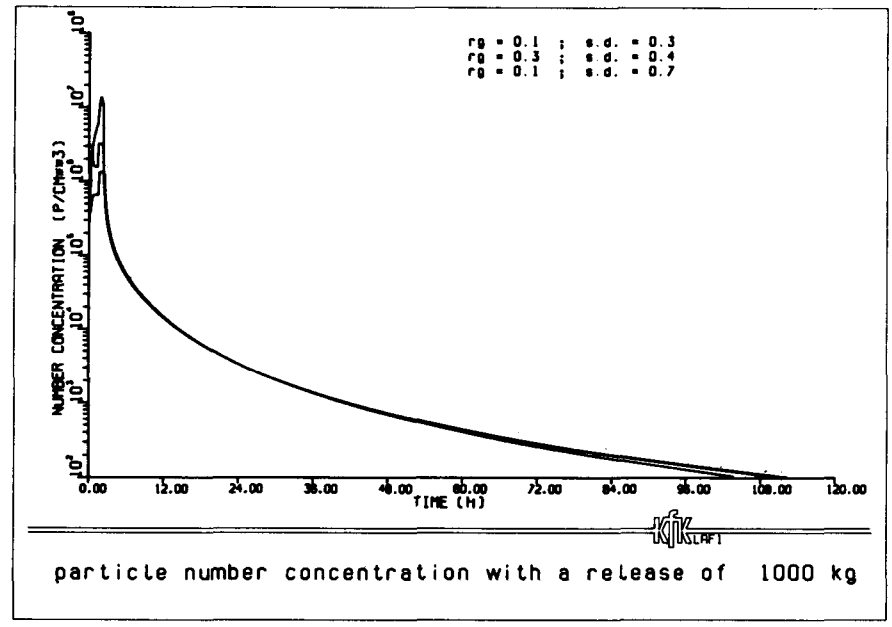
rg = 0.1 ; s.d. = 0.3
rg = 0.3 ; s.d. = 0.4
rg = 0.1 ; s.d. = 0.7
NUMBER CONCENTRATION (P/CMm3)
TIME (H)
0.00
12.00
24.00
36.00
48.00
60.00
72.00
84.00
96.00
108.00
120.00
KfK
LAFI
particle number concentration with a release of 1000 kg

Fig. 6

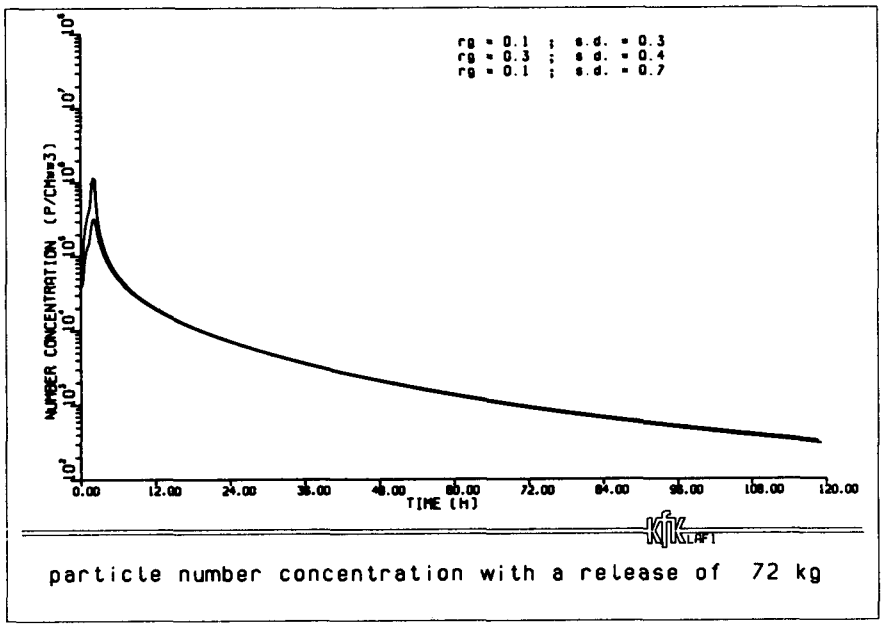

particle number concentration with a release of 72 kg

Fig. 7

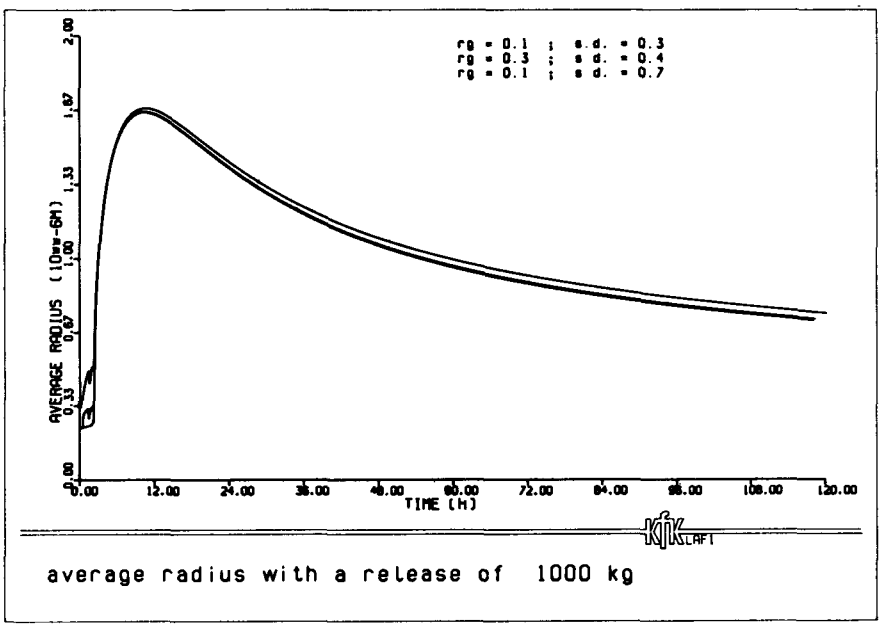

average radius with a release of 1000 kg

Fig. 8

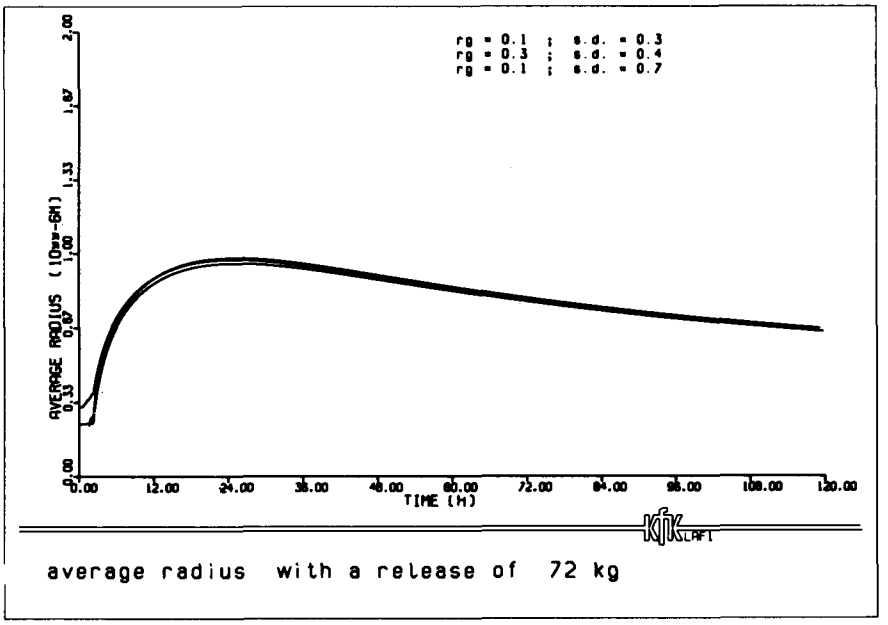

average radius with a release of 72 kg

Fig. 9

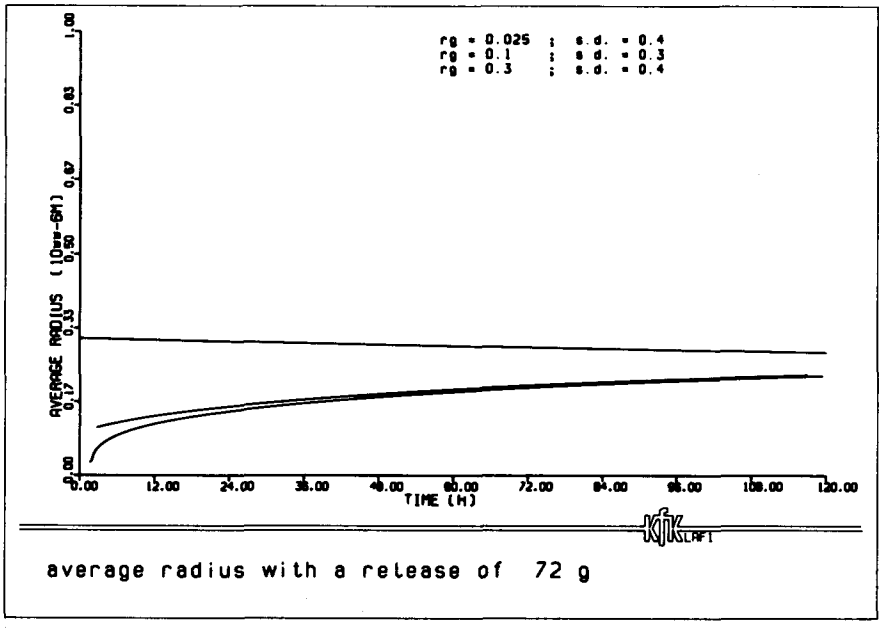

average radius with a release of 72 g

Fig. 10

AEROSOL BEHAVIOR MODEL VALIDATION PROCEDURE

J. A. Gieseke, K. W. Lee and H. Jordan
Battelle Columbus Laboratories
Columbus, Ohio

ABSTRACT

A systematic and logical procedure has been developed for validating computer models that calculate aerosol behavior within LMFBR containments through comparisons with experimental measurements. By defining various dimensionless parameters which represent the importance of one aerosol behavior mechanism relative to another, domains of predominant individual mechanisms and their interactions were determined. Six different aerosol behavior mechanisms were considered including agglomeration due to Brownian diffusion, gravitational settling and turbulence, and depositions due to sedimentation, Brownian diffusion and thermophoresis. Expected accident conditions for full scale reactor designs were then mapped into the formulated domains of mechanism predominance. The results show that the three coagulation mechanisms can be important individually or in combination depending on the assumed accident conditions. Among the three deposition mechanisms considered, Brownian diffusion was found to be of least significance for all geometries and conditions considered.

A selected number of existing experiments have been used to illustrate the correspondence of these ranges. In addition to experiments for mechanism validation, several additional experiments are recommended for validating specific assumptions employed in the current models such spatial homogeneity of aerosol concentration within the containment vessel and interaction rates among aerosols formed from different materials. Finally, criteria to be used for assessing agreements between predictions and experiments are suggested.

INTRODUCTION

Currently, radiological consequences of assumed accidents for liquid metal fast breeder reactors (LMFBR) are assessed largely on results of analyses which give the time dependent concentration of radioactive species released within the reactor containment. Since many such species are initially suspended in aerosol form or adsorbed onto particles within the containment, calculation of aerosol behavior is of critical importance for predicting the amount of radioactive species released from the reactor containment. In calculating aerosol behavior, the current aerosol behavior models [1-4] employ various rate processes including diffusional, gravitational and turbulent agglomeration, and deposition due to Brownian diffusion, sedimentation and thermophoresis. Both explicit and implicit assumptions employed in most of the current models are that aerosol concentration and gas temperature are spatially homogeneous except across the boundary layers near the walls.

In order to validate the developed models, many experiments have been conducted in the past and generally good agreement with model calculations have been obtained. However, many of these experiments have been conducted in small scale vessels. Therefore, the agreement obtained with model predictions may not guarantee that the models will also yield adequate calculations for full-scale reactor situations since the question of scaling must be considered. Another consideration for validating the model is to ensure that in validation experiments all the important variables are studied over the entire range defined by postulated accident conditions.

In the present study, a systematic and logical procedure has been developed for validating aerosol behavior codes through comparisons with experimental measurements. Various dimensionless terms which represent importance of one aerosol behavior mechanism relative to another have been first defined and domains of predominance for the individual mechanisms and their interactions are identified. The predominant aerosol behavior mechanisms in the full-scale reactor situation are then identified for use in determining the conditions for validation experiments. In addition, several special experiments that are necessary to justify the assumptions employed in the models are recommended.

AEROSOL BEHAVIOR MODEL FEATURES

The governing integro-differential equation describing the rate of change of particle concentration within an enclosed space is written as

$$\frac{\partial}{\partial t} n(x,t) = [1/2 \int_0^x \Phi(\xi, x-\xi)\, n(\xi,t)\, n(x-\xi,t)\, d\xi - n(x,t) \int_0^\infty \Phi(x,\xi)\, n(\xi,t)\, d\xi] - n(x,t)\, R(x) + S(x,t) , \quad (1)$$

where Φ is the collision kernel predicting the probability of collision between two particles of volume x and ξ. n, aerosol number density, t,

time, R, the removal rate of particles due to various depositon mechanisms of particles, and S is the aerosol source rate of particles.

Although the validation procedure described in this paper can, in principle, apply to any aerosol behavior model, discussions will be limited to the HAARM-3 model [5] for which the present procedure has specifically been prepared. The HAARM-3 code uses the method of moments to solve the integro-differential equation shown in Equation (1) to calculate the rate of collisions among airborne particles having a heterogeneous size distribution as well as the rate of particle deposition on the floor of an enclosed vessel, the rate of deposition of particles on the walls, and the leakage of airborne particles. In calculating the aerosol agglomeration and deposition rates which are dependent on the morphological properties of agglomerates, the results of a recent experimental study [6] have been utilized. The effects of nonspherical shape of the agglomerates on settling velocity and collision rate are also accounted for in the code. Details of the solution technique are described elsewhere [1,2,5].

The assumptions, both explicit and implicit, as employed in the HAARM-3 code include the following:

(1) The aerosol in the containment vessel is well-mixed and there are no spatial inhomogeneities for the aerosol.

(2) The size distribution for the aerosol is always lognormal, although the distribution parameters are allowed to vary.

(3) Wall deposition occurs by diffusion or thermophoresis across "boundary layers" in the gas at the surfaces. Both the concentration and the temperature gradients across these boundary layers are describable in terms of an average value for all deposition surfaces.

(4) Agglomerates of sodium oxides are nearly spherical and by assuming a spherical shape, the size of the agglomerates can be corrected by using a single factor, α, that accounts for the reduced density of the porous structure. This correction factor is size dependent.

(5) Agglomerates of UO_2 particles are "chain-like". Such chain-like agglomerates fall at a rate corrected by a size independent parameter, χ, and have a projected or collision area for agglomeration corrected by a second size independent parameter, γ.

(6) Aerosol particles calculated to deposit on wall or floor surfaces remain deposited and are not resuspended.

(7) There are so few particles of large sizes that inertial effects in the gravitational agglomeration process can be neglected for the entire aerosol size distribution.

(8) Agglomeration and deposition rates are describable in terms of linear sums of the individual rate constants or deposition velocities, respectively.

APPROACH TO VERIFICATION PROCEDURE

Because the HAARM-3 code is mechanistic in nature, it must be demonstrated in the validation procedure that the code adequately describes the physical processes or mechanisms which occur and that the code is applicable to the expected or assumed accident situations. These considerations suggest that an important step in code verification is the identification of possible boundaries or ranges for variables and conditions. In addition, the requirements for verification become more explicit. Experimental verification should demonstrate that the individual mechanisms or processes affecting behavior are described analytically, that all significant mechanisms are included, and that interactions among individual mechanisms or processes are properly described.

The verification process should first identify by sensitivity analysis the most important variables affecting code output, then specify experiments which will investigate the ability of the code to predict the effects of changes in these variables, and finally analyze the results to determine if the code predictions are suitably in agreement with the experimental results.

Specification of Important Variables

A methodology to perform a sensitivity analysis of the HAARM-3 computer code was developed and used to study the effects on aerosol behavior of various independent variables of the code, such as initial aerosol properties and containment geometry [7]. By varying these independent variables and observing the change in results calculated with the computer code, it is possible to analyze the sensitiveness of the aerosol behavior to various variables. Thus, the sensitivity of a computer model may be defined as a measure of change in output variables to variation in input variables.

In that study, first order sensitivities of leaked mass to changes in individual variables were calculated by running the HAARM-3 computer code based on the one-at-a-time design. Depending on the results of these first order sensitivity calculations, higher order sensitivities of significant value were also obtained. By assuming that the range of each variable used in the analysis was established with the same confidence interval, the importance of each individual input variable and model parameter was ranked.

The sensitivity analysis results have shown that the leakage rate, source duration time, the mean size of source aerosol, and source rate are found to increase the leaked mass most effectively. It is also found that increasing particle collision efficiency, collision shape factor, or turbulent energy dissipation rate are most effective in reducing the leaked mass. It is interesting to note that all these highly ranked input variables are those which control the rate of aerosol agglomeration. Diffusion boundary layer thickness, wall temperature gradient, slip correction factor, and wall temperature gradient, slip correction factor, and wall area to volume ratio were found to be among the variables which affect the aerosol behavior the least.

Specification of Important Mechanisms

The next consideration in the procedure is to provide proper accounting for the effects of scaling of various aerosol behavior mechanisms. Although the HAARM-3 computer code is to be used ultimately for predicting aerosol behavior in full scale vessels, experiments for validating the code are performed in various smaller-scaled facilities. Similitude between the small-scale and full-scale situations must be properly satisfied. The most convenient and simplest approach is to seek various dimensionless terms which govern aerosol behavior. Since one of the objectives of the planned code validation experiments is to verify the soundness of important aerosol mechanisms, the corresponding dimensionless terms representing these mechanism were obtained. This approach is useful for evaluating the adequacy of individual and combined basic mechanisms.

The approach taken here is similar to that reported by Okuyama, et al. [8], however, their procedure has been expanded to consider aerosol behavior mechanisms taken in three groups of three each. The first group considers the relative importance of coagulation, sedimentation and diffusion to walls. The second group concerns the three major agglomeration mechanisms, and the final group concerns the relative importance among the mechanisms for removing aerosols.

Okuyama, et al. originally suggested the following three dimensionless terms:

$$\text{Brownian Coagulation vs Sedimentation:} \quad CG = [K_o n_o C_m (r_{go}) H]/[v_t(r_{go})] \tag{2}$$

$$\text{Diffusion vs Sedimentation:} \quad DG = [D(r_{go}) AH]/[v_t(r_{go}) V\Delta] \tag{3}$$

$$\text{Brownian Coagulation vs Diffusion:} \quad CD = [K_o n_o C_m(r_{go}) V\Delta]/[D(r_{go})A]; \tag{4}$$

where K_o ($= 4kT/3\mu$) is the collision constant, k the Boltzmann constant, T the temperature, μ the gas viscosity, n_o the initial aerosol number concentration, C_m the Cunningham slip correction factor, r_{go} the initial geometric number median radius, v_t the terminal settling velocity, H the vessel height, V the vessel volume, D the diffusion coefficient, A the vessel wall area and Δ the wall plating parameter (diffusion layer thickness).

In order to represent relative importance among the three agglomeration mechanisms (Brownian, gravitational and turbulent agglomeration), the following three dimensional parameters may be defined by comparing the respective agglomeration rate kernels:

$$\text{Brownian vs Gravitational:} \quad BG = \bar{K}_B/\bar{K}_G \tag{5}$$

$$\text{Turbulent vs Gravitational:} \quad TG = \bar{K}_T/\bar{K}_G \tag{6}$$

$$\text{Brownian vs Turbulent:} \quad BT = \bar{K}_B/\bar{K}_T \ , \tag{7}$$

where $\bar{K}_B$, $\bar{K}_G$ and $\bar{K}_T$ are the average values of the kernel over the initial size distribution for Brownian, gravitational and turbulent agglomeration, respectively. Detailed expressions for the above kernels in terms of the mean particle size and the geometric standard deviation can be found elsewhere [9].

The final group of mechanisms concerns the relative importance among three deposition mechanisms: Brownian wall diffusion, gravitational sedimentation and wall deposition due to thermophoretic forces. Two additional terms involving the deposition velocity due to thermophoretic forces may be defined as

$$\text{Thermophoresis vs Sedimentation:} \quad ThG = [Av_{th}H]/[v_tV] \tag{8}$$

$$\text{Diffusion vs Thermophoresis:} \quad DTh = D/[v_{th}\Delta] \tag{9}$$

where v_{th} is the thermophoretic velocity and ThG and DTh are the dimensionless terms showing relative importance of thermophoresis to sedimentation and that of diffusion to sedimentation, respectively. The third dimensionless group in this set was previously defined as DG in Equation (3).

The dimensionless groups defined above have been evaluated for regions of predominance and the results are shown in Figure 1, 2 and 3. The curves shown bounding the individual mechanisms represent a magnitude of 9 times that of neighboring groups. Details on the procedure to obtain these curves are reported elsewhere [9]. The plots, given in terms of dimensionless groups, allow for convenient identification or selection of accident or experimental conditions in terms of aerosol behavior mechanisms of importance.

Since experimental conditions must be selected on the basis of individual mechanism verification over the range of expected accident conditions and must account for some special considerations to be noted, the selection process must proceed first with an analysis of the estimated accident conditions to identify ranges for dimensionless groups and individual parameters that must be considered.

Estimated accident conditions have been defined in terms of FFTF, Super Phenix, CRBR, and a full scale conceptual design, and have employed the coolant and fuel releases to containment used in assessing radiological consequences of accidents for these designs. Further, mean initial aerosol particle radii of 0.25 μm (A Cases) and 5.0 μm (B Cases) have been employed. A range from maximum release rates down to 10^{-4} times the maximum value, parameters for diffusional wall deposition over a range of 10 times, and turbulent energy dissipation rate over a range of 100 times were used to construct regions of interest. The resulting regions are shown as the shaded areas in Figures 1 to 3.

The regions mapped by the expected conditions for postulated accidents are shown to lead to some generalizations regarding experimental verification

needs. The experiments need cover only those regions found to be predominant but should also cover conditions where individual mechanisms can be isolated and the model adequacy evaluated. It is seen from Figure 1 that the overall aerosol behavior is controlled by agglomeration and sedimentation for the expected conditions. From Figure 2 it is then seen that the three agglomeration mechanisms are each expected to contribute significantly. From Figure 3 it follows that deposition is controlled more strongly by sedimentation and thermophoretic wall deposition than by Brownian diffusional deposition.

These general observations are consistent with the results of the sensitivity analysis which emphasized individual variables. However, the approach using dimensionless groups allows selection of experimental conditions such that individual mechanisms can be studied and expected accident conditions can be covered.

Other Experimental Considerations

In addition to the validation of correctness for individual and interacting mechanisms using results from experiments selected by the procedures described in the previous section, there are also special effects that must be considered. Such effects result from consideration of the assumptions on which the HAARM-3 code is based. Additional factors likely to be of most importance are the following:

(1) Spatial inhomogeneity of aerosol concentration within the vessel

(2) Interaction rates among aerosols formed from different materials (e.g. fuel materials, structural materials, sodium oxides)

(3) Characteristics of agglomerates formed from more than one material

(4) Localized thermal effects that might alter deposition or sedimentation rates

(5) Heating or electrical charging of particles that affects agglomeration or deposition rates or that leads to resuspension

(6) Air flow patterns from changing thermal conditions or containment venting that could lead to resuspension.

The effects listed above are to a large extent associated with accident definitions. Experiments to validate the code for application to accident analyses must therefore be selected to include those effects believed to be significant for the various accident scenarios or conditions. The experiments must be selected to determine if these effects are significant or if mechanisms currently excluded should be added to the code.

EXPERIMENTAL DESIGN PROCEDURES

The important variables for experimental study in the verification process are those identified by the sensitivity analysis. Values selected for these variables must be consistent with the expected range under accident

conditions and must be taken in combinations to provide proper values for the dimensionless groups. The crucial variables, exclusive of experiment geometry, and the suggested ranges for consideration are: (1) particle size (0.02 - 0 μm); (2) aerosol mass concentration (0.2-200 g/m^3); (3) aerosol material density (2-12 g/cm^3); (4) turbulent energy dissipation rate (10^{-2} to 1.0 m^2/sec^3); and (5) wall temperature gradient (1000-10,000 C/m).

Other important parameters affecting agglomeration and sedimentation are those factors which correct for non-ideal behavior. These factors include the collision efficiency between particles, the mobility correction factor, and the collision area factor resulting from chain-like or fluffy agglomerates. Since these factors cannot be controlled independently, they should be studied at least initially in separate effects experiments designed specifically for their determination. In addition, the factors noted previously as special considerations should also be addressed in separate experiments.

The remaining factors of importance are those representing vessel geometry. Vessel geometry is, of course, fixed by the various experimental facilities that have been used in the past or that are now available. By considering the specific sizes and configurations of these, the combinations of experimental variables and vessel dimensions must be used to choose values for DG and CG, BG and TG, and DG and ThG that cover the regimes representative of estimated accident conditions, and that isolate the predominant mechanisms individually.

The recommended experimental conditions noted as ranges for variables, values for dimensionless groups, and special or separate considerations are intended to provide guidelines for experimental validation needs. Not all experiments are still to be performed and it is of interest to evaluate past experiments to determine the extent to which results fall within the dimensionless group ranges for expected reactor accident conditions as determined by the HAARM-3 code. This procedure is illustrated by considering experimental data from three test facilities which were selected to encompass a wide range of airborne concentrations and geometries. The facilities included CSTF and NSPP, two facilities which are currently performing aerosol experiments, and LTC, from which two runs, Nos. 3 and 5, were selected.

Figures 1 to 3 include the ranges of conditions for expected accidents and also include the resulting dimensionless parameters determined from experimental data taken during CSTF, NSPP and LTC tests. Results clearly show that these experiments were performed such that the conditions fall approximately within the limits of the dimensionless terms determined for large scale reactor accident conditions. These examples illustrate the selection of experimental measurements in terms of dimensionless groups. The validation process will continue by comparing code predictions with experimental data after uncertainties in the data have been evaluated.

CRITERIA FOR CODE COMPARISON

A critical and final feature of the code verification process is the establishing of criteria by which to assess whether the code predictions are adequately accurate. These criteria relate to both the need for accuracy in the code prediction and the accuracy of the experimental data. The use of the HAARM-3 code in evaluating radiological consequences will probably be adequate if it can predict within a factor of two or three the actual mass leakage from a containment vessel assuming no attenuation in the leak path. Since the leakage rate and time may be arbitrary, this means that airborne concentration predictions within a factor of about two are adequate.

Such a comparison, of course, is complicated by uncertainties in the data and the need for the code predictions to be conservative. Some allowance for experimental data spread must be made and restrictions must be placed on the comparison to assure conservatisms. It is therefore selected as a criterion for determining code adequacy that the airborne concentration prediction fall within a factor of two above the mean value of the experimental concentration data and that the 95 percent confidence limit for the data should not exceed 2 times the mean. These conditions must apply for the time regime specified as the time at which the mass airborne concentration is maximum to the time at which the concentration is below 1/1000 of the maximum. At this latter time the mass airborne concentration is negligible in terms of its total contribution to actual mass leakage from the containment vessel.

In a similar fashion, it is desirable to compare code predicted particle sizes with experimental measurements. Particle sizes are important because aerosol behavior mechanisms are size dependent. Comparisons should be based on mean aerodynamic particle size since this size is the one most often measured experimentally (using size analyzers such as cascade impactors or spiral centrifuges) and the HAARM-3 code provides output directly as aerodynamic size. In this case, an acceptable prediction will be taken as one that falls between plus or minus 1.5 times the measured value for the mean aerodynamic size, with the condition that the 95 percent confidence limits for the data are within the range of ±1.5 times the average value and that the time regime be as identified previously.

ACKNOWLEDGMENT

This work was carried out as a part of a contract for Aerosol Measurements and Modeling for Fast Reactor Safety under Contract No. NRC-04-76-293-07, sponsored by the U.S. Nuclear Regulatory Commission.

REFERENCES

1. Gieseke, J. A., K. W. Lee and L. D. Reed, "HAARM-3 Users Manual," BMI-NUREG-1991, Battelle-Columbus (January 1978).

2. Hubner, R. S., E. U. Vaughan and L. Baurmash, "HAA-3 User Report," AI-AEC-13038, Atomics International (1973).

3. Bunz, H., W. Muhr and W. Schikarski, "Untersuchungen zum Verhalten von Rekondensationsaerosolen in geshlossen Behältern," Proc. GAF Meeting, Aerosole in Naturwissenschaft, Medizin und Tecknik -- Messtechnik und technische Anwendung, Karlsruhe (October 1977).

4. Walker, B. C., C. R. Kirby and R. J. Williams, "Discretization and Integration of the Equation Governing Aerosol Behaviour," SRD R 98, United Kingdom Atomic Energy Authority (1978).

5. Reed, L. D., K. W. Lee and J. A. Gieseke, "The Behavior of Contained Radioactive Suspensions," accepted for publication in Nucl. Sci. Engng.

6. Gieseke, J. A., et al., "Characteristics of Agglomerates of Sodium Oxide Aerosol Particulates," BMI-NUREG-1977, Battelle-Columbus (January 1978).

7. Lee, K. W., J. A. Gieseke and L. D. Reed, "Sensitivity Analysis of the HAARM-3 Code," NUREG/CR-0527 and BMI-2008, Battelle-Columbus (October 1978).

8. Okuyama, K., Y. Kousaka and T. Yoshida, "Behavior of Aerosols Undergoing Brownian Coagulation, Brownian Diffusion and Gravitational Settling in a Closed Chamber," J. Chem. Engr. Jpn., Vol. 9, No. 2, pp. 140-146 (1976).

9. Gieseke, J. A., et al., "HAARM-3 Code Validation Plan," Report to NRC, Battelle-Columbus, in preparation (1980).

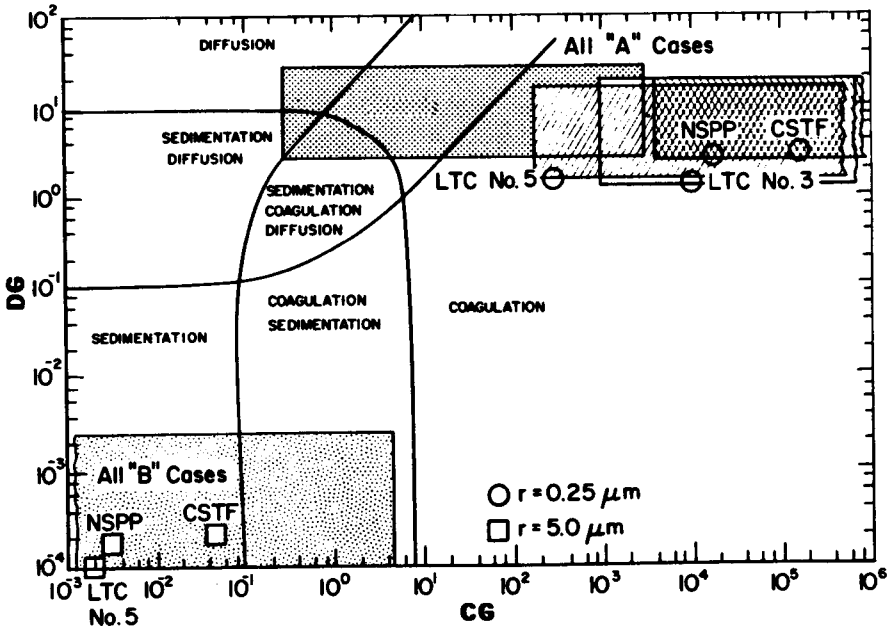

FIGURE 1. CONTROLLING MECHANISMS FOR SELECTED EXPERIMENTS

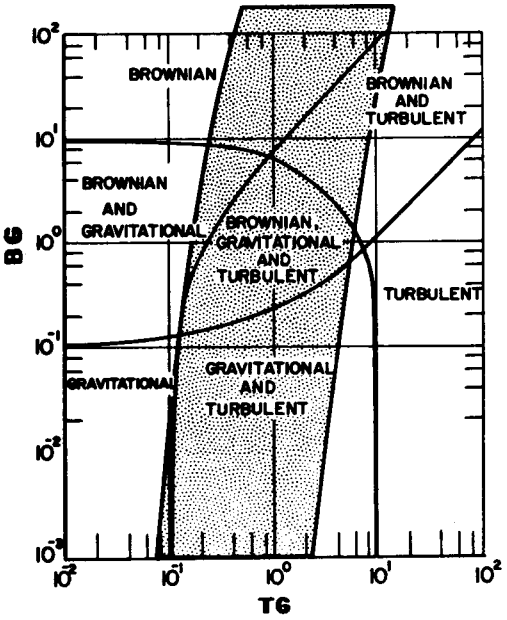

FIGURE 2. CONTROLLING AGGLOMERATION MECHANISMS UNDER ESTIMATED ACCIDENT CONDITIONS

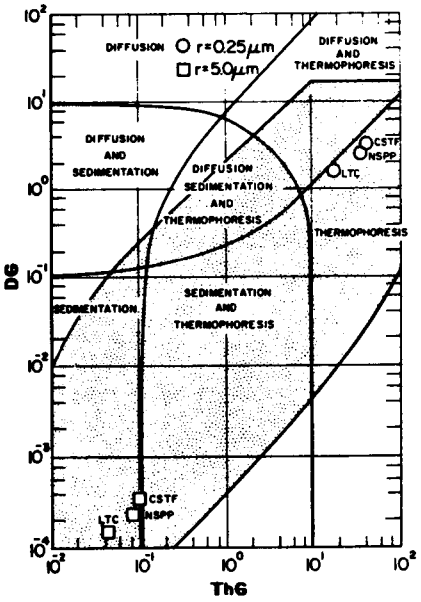

FIGURE 3. DEPOSITION MECHANISM IMPORTANCE FOR EXPERIMENTAL AND POSTULATED CONDITIONS

INTERPRETATION OF THE BEHAVIOR OF AEROSOLS GENERATED BY A SODIUM POOL FIRE

J. Fermandjian*, J.C. Malet**, C. Casselman**
G. Duverger de Cuy**, D. Boulaud*, G. Madelaine*
Commissariat à l'Energie Atomique
Institut de Protection et de Sûreté Nucléaire
* Fontenay-aux-Roses, France
** Cadarache, France

ABSTRACT

For computer model validation, an experimental program on sodium pool fire tests (sodium mass = 10 kg - combustion area = 0.125 m^2 - initial sodium temperature = 450°C) is underway in a 4.4 m^3 steel vessel (diameter = 1.6 m - height = 2.2 m - wall area/volume = 3.4 m^{-1} - floor area/volume = 0.46 m^{-1}) with aerosol mass concentrations superior to 10 g Na_2O_2/m^3.

These tests made it possible to obtain :

- the mass concentration evolution and the size distribution of the suspended particles, particularly by means of cascade impactors - ANDERSEN, 8 stages - with dilution system,

- the emission rate of the source particles (fire subdivided into a series of sequences from the reference test (total combustion) : fire of predetermined duration by lid setting on the pan),

- the kinetics of the aerosol removal on the vessel floor (0.24 g $Na_2O_2/m^2.s$).

The application of the computer models (HAARM 3 and PARDISEKO 3B) to these tests showed an agreement between experiments and calculations (factor less than 5 for the mass concentration) by using adequate values for the adjustable parameters (dynamic shape factor - $1 < \kappa < 1.5$ -, coagulation shape factor - $1 < f < 1.5$ -, efficiency collision for gravitational agglomeration- $0.1 < \varepsilon < 0.3$ - , boundary layer thicknesses for brownian diffusion - 0.01 mm $< \delta_D <$ 0.1 mm - and for thermophoresis - 1 mm $< \delta_T <$ 3 mm -, correction factor density - $0.2 < \alpha < 0.6$ -).

I - INTRODUCTION

A program is being carried out at the French Atomic Energy Commission (CEA) to study the behavior of sodium oxide aerosols in a 4.4 m^3 containment vessel at Cadarache.

The purposes of this program are :

- to provide the experimental qualification to the HAARM 3 and PARDISEKO 3B aerosol behavioral codes,

- to demonstrate the influence of thermal currents on the aerosol behavior, (validation of the computer code ESBI [1] making it possible to determine the gas flowrates between the different zones in the future model for multiple aerosol behavior zones).

This paper concerns only the first part (four tests performed) ; the second one will be performed in the near future.

EMIS tests are conducted to determine accurately the emission rate of the source particles during a sodium pool fire. This is done in order to check the validity of the hypothesis most frequently used, that is, a constant emission rate, during the application of computer codes. The fire is subdivided into a series of sequences from the reference test (total combustion) : fire of predetermined duration by the setting of the lid on the pan.

II - EXPERIMENTAL ARRANGEMENT

II-1. Experimental equipment

A diagram of the experimental arrangement is shown in Figure 1. Table I gives the dimensions of the containment vessel (design pressure = 0.56 MPa). The 4.4 m^3 vessel is a carbon steel cylinder with dished ends having a diameter of 1.6 m and a total height of 2.2 m. The floor area is 2 m^2 and the wall area (including top and bottom) is 15 m^2. All interior surfaces are coated with an epoxy-Na paint.

A 0.01 m^3 sodium tank was located outside of the containment vessel. The carbon steel burning pan was centered near the bottom of the containment vessel and it was equipped with a gasketed lid which permits the departure and termination of the aerosol source on command. The burning pan was heat insulated (mineral wool : 5 cm thick ; λ = 0.078 W/m.°C).

II-2. Test conditions

The four tests were performed with essentially the same initial conditions. The initial containment atmosphere was air at normal temperature and relative humidity. Test conditions are listed in Table I.

II-3. Test procedure

II-3.1. General procedure

The procedure used in each of the four tests was to heat the sodium up to

600°C in the auxiliary sodium tank. Then a valve was opened and nitrogen pressure forced the sodium through a heated delivery line into the burning pan. At a time defined as the "zero time" of the test, the pan lid was lifted (at this time, the sodium temperature was 450°C). After a predetermined duration, the replacing of the pan lid stopped the combustion process. Each fire corresponded to a subdivision of the reference test (total combustion).

Temperature measurements were made continuously by 29 thermocouples (12 for the gas, 14 for the vessel walls, 3 for the sodium pool - Figure 2). Containment atmosphere overpressure measurement was also continuous.

The oxygen fraction was kept constant (21 %) by feeding from bottles : oxygen consumed by sodium combustion was removed by oxygen injection with flowrate measurement.

Data acquisition instrumentation was provided.

II-3.2. Aerosol measurements

Four locations throughout the atmosphere could be utilized for sampling filters (mass concentration) or cascade impactor (mass concentration and particle size distribution) - See Figure 3.

Measurements were made of the kinetics of aerosol removal on the vessel floor by means of a sequential sampling device (coupon samplers for aerosol fallout measurement) which was located on the vessel floor.

The aerosol samples were subjected to a quantitative analysis by atomic absorption spectrometry so as to determine the mass of sodium.

One day after the fire, selective water washing (floor, then walls) and alkalimetry analysis yielded the masses of aerosols settled on the floor and diffused on the walls.

The fractions of each oxide (sodium monoxide and sodium peroxide) in the combustion residue were determined by sampling and quantitative analysis (gas phase chromatography and alkalimetry).

These analyses and the number of oxygen moles consumed in the combustion process made it possible to determine :

- the sodium burning rate,
- the mass of burnt sodium,
- the fraction of oxide ejection (ratio of the sodium mass released in the form of aerosols to the mass of burnt sodium).

Remark about the cascade impactor [2]

For aerosol measurements, we chose the multi-stage cascade impactor ANDERSEN 2000, type MARK II (eight-stage multi-circular jet type) with nominal flowrate equal to 28.3 l/min associated with dilution system (Figure 4) to allow sampling times longer than 15 seconds without overloading the impactor stages.

The mass loading capacity of the cascade impactor (which is about 150 mg) and the sampling time determine the value of the flowrate Q_1 to be used. The flowrate Q_2 is fixed automatically in order to respect the nominal flowrate Q_3 of the cascade impactor.

The collection stages are glass plates coated with grease in order to limit the bouncing and re-entrainment.

The effective cut-off diameters of the stages have been evaluated by means of a monodisperse aerosol generator (type Berglund-Liu) :

- solid aerosols of fluorescein ammonium salt (density = 1.35 g/cm^3) for diameters varying from 1 to 20 µm.
- solid aerosols of latex polystirene (density = 1.05 g/cm^3) for diameters varying between 0.3 to 1.5 µm.

The weight of the aerosol removed on the impactor stages made it possible to evaluate the total mass concentration of the suspended particles. Then a quantitative analysis by atomic absorption spectrometry yielded the sodium content of the suspended particles.

In the case of our tests the dilution system works efficaciously since it makes it possible to obtain a reasonable load for the cascade impactor with sampling time greater than 30 seconds. Furthermore, the amounts lost in the pipes, in the dilution system and in the cascade impactor are acceptable (about 10 % for a particle diameter of 5 µm and 50 % for a particle diameter of 15 µm).

II-3.3. Convection current velocity measurements

The description of thermal gaseous flow inside the containment vessel during the fire will be made by means of two kinds of devices (figure 5):

- three special double hot wire probes located in the rising column above the pool to determine gas velocity (cross correlation) and to account for the turbulence (auto correlation) by statistical averaging of the data ;

- four tridimensional non linear PITOT probes located outside the rising column to determine direction, sense and amplitude of flow velocity.

These two devices will be equipped with an aerosol cleaning system (mechanical for hot wire probes and pneumatic for PITOT probes).

At present, these probes have only been tested and they seem to work properly. They will be used in the next tests.

III - EXPERIMENTAL RESULTS

III-1. Containment response

The atmosphere within the containment vessel was fairly homogeneous, excluding, of course, the region near the surface of the sodium pool. This conclusion was reached by noting that the standard deviation from the mean bulk gas temperature was about 20 % of the mean and that the

suspended mass concentration at three locations varied in the course of the tests.

The containment pressure and temperatures (gas and wall) for the EMIS 03 test are plotted in figures 6 and 7.

III-2. Sodium fire and aerosol generation

Figure 8 shows the sodium temperature versus time for the EMIS 01 test (total combustion). We also noted on this figure the duration of the tests.

The sodium combustion rate was nearly identical for three tests, averaging 33.5 kg $Na/h.m^2$; a higher value was found for the EMIS 02 test (Table II).

The fraction of released aerosol was nearly the same for three tests, averaging 0.24 ; a higher value was found for the EMIS 03 test (Table II).

The values given in Table II (total aerosol mass released and source duration) seem to indicate three areas relative to the rate of emission of particles from the source : warm up, regular combustion and progressive extinction (results to be confirmed by the next tests).

Sodium recovery by selective post-test washing of the vessel surfaces showed that approximately 25 % of the aerosol was deposited on the vessel walls, while 75 % settled on vessel floor (Table III).

The chemical reaction mechanism of the sodium combustion differed according to the test. It varied between 23.5 to 44.6 % Na/Na_2O_2.

III-3. Suspended mass concentration

The concentrations of suspended mass (as sodium peroxide) are plotted in Figure 9 for the EMIS 02, 03 and 04 tests : mean values of samples (filter and cascade impactor) taken concurrently at three locations in the containment atmosphere. The maximum concentrations of suspended particles were 28, 40 and 28 g Na_2O_2/m^3 for EMIS 02, 03 and 04 tests respectively.

The results show a rapid increase of the mass concentration during the first minutes ; then, a smaller increase until the sodium fire end. Besides, for the EMIS 02 test, the results show an equilibrium between source particles and particles removed. As soon as the burning pan lid was set down stopping the aerosol release, the concentrations decrease rapidly.

The results given by the cascade impactors in different locations in the containment vessel display discrepancies (of about a factor of 2) with each other during the tests ; these results differ from those obtained in the CSTF vessel of 850 m^3, for which a relatively good homogeneity had been observed [3] .

III-4. Suspended particle size distribution

Most of the cascade impactor samples taken in these tests yielded good approximations to a straight line (log normal distribution). A typical

example of the data is shown in Figure 10 (cumulative particle mass more than stated diameter versus particle aerodynamic diameter - EMIS 03 test at t = 108 minutes).

During the sodium pool fire period, the aerodynamic mass median diameter varies between 1 to 3 µm ; immediately after the end of the fire, first it increases rapidly and a few minutes after it decreases slowly.

At the beginning of the sodium fire, the standard geometric deviation is equal to 1.5 ; it increases up to 2 by the end of the fire and then varies between 1.9 and 2.

The results given by cascade impactors in different locations in the containment vessel show small discrepancies (factor 1.2 for the AMMD) between them during the tests.

III-5. Kinetics of the aerosol removed on the vessel floor

Figure 11 shows the settled mass on the vessel floor versus time for the EMIS 02, 03 and 04 tests. During the sodium fire period (except the first ten minutes) the removal rate is nearly identical for these tests : 0.48 g Na_2O_2/s or 0.24 g Na_2O_2/m^2.s.

IV - COMPARISON OF EXPERIMENTAL RESULTS WITH HAARM 3 and PARDISEKO 3B COMPUTER CALCULATIONS

The HAARM 3 [4] and PARDISEKO 3B [5] codes were applied to the interpretation of the EMIS 03 and 04 tests using the data mentioned in Table II (source duration, sodium mass released as aerosol).

These computer codes take into account the aerosol processes coagulation, sedimentation, thermophoresis and brownian diffusion.

The essential difference between the two computer codes is related to the solution method of the integro-differential equation governing the behavior of the aerosol :

- In the PARDISEKO 3B code, the integro-differential equation is solved numerically without assumption on the type of size distribution for the suspended particles ;
- In the HAARM 3 code, the integro-differential is replaced by three first order differential equations using the method of moments, which is implemented by assuming the size distribution of the emitted and suspended particles to be log-normal at all times. Then, these three first order differential equations are solved numerically.

IV-1. Input parameters for the HAARM 3 and PARDISEKO 3B codes

We mention below the assumptions adopted during this study.

a) Properties of the carrier gas :

- The containment atmosphere is assumed to have the properties of dry air at 100°C and at 0.110 MPa, average values during sodium pool fire tests (PARDISEKO 3B code).
- The pressure and the temperature of the air in the vessel were allowed to vary with time according to the experimental measurements (HAARM 3 code).

b) Source particle size distribution :

The source particle size distribution was taken to be of log-normal form with mass median radius R_{50} = 0.5 µm and geometric standard deviation σ_g = 2, values suggested by the CSNI Group of Experts [6] .

c) Aerosol chemical composition :

The chemical form of the aerosol is taken into account relatively to the physical properties of the particulates. In excess oxygen the main reaction product of sodium burning is sodium peroxide Na_2O_2. The experimental results confirm this fact ; in the present study the above fact is used to relate the airborne mass of aerosol to its sodium content.

d) Particle shape and density :

The CSNI report [6] implies that it is reasonable to assume that sodium oxide particles form approximately spherical cluster agglomerates rather than the long chain-like structure of dry fuel-oxide agglomerates. In this study, all agglomerates were assumed to be spherical throughout their airborne life.

This simplification leads to the use of a single "correction factor" to relate the radius of a particle to its mass, namely a factor α which allows for the presence of voids within the agglomerate.

For this study, the value of the density correction factor α has been deduced from the calibration of the cascade impactor : sodium oxide aerosol behavior identical to that of particles of about 1 g/cm^3 density (this value is close to that obtained by Battelle Columbus Laboratories [7] and to that obtained by Harvard University [8]).

e) Collision efficiency (gravitational coagulation)

The collision efficiency ε was taken in order to obtain the smallest deviations between the calculated and experimental mass concentration curves.
We tried to use the theoretical solution $\varepsilon(t)$ but these attempts failed to give satisfactory results for the EMIS tests.

f) Diffusion boundary layer thickness :

Quite widely varying estimates of the diffusion boundary layer thickness have been deduced by research scientists in different groups. For this study, a value δ_D of 100 µm was considered realistic. It must be remarked, however, that the results of EMIS calculations are insensitive to this parameter (Table IV).

g) Thermophoresis boundary layer thickness :

The thickness of the thermophoresis boundary layer δ_T used for this study corresponds to a thermal gradient of about 200°K/cm near the walls of the vessel for the EMIS tests. This value was chosen as providing the best experiment-calculation agreement for masses deposited by diffusion.

The temperatures of the gas and of the walls of the vessel, necessary for the calculation of the thermal gradient, were deduced from the experimental measurements.

IV-2. Suspended mass concentration

Figures 12 and 13 show aerosol mass concentration versus time : experimental results (mean values) and calculated results by HAARM 3 and PARDISEKO 3B codes for the EMIS 03 and 04 tests.

Test EMIS 03 (Figure 12)

During the sodium fire period, the code results are conservative related to the mean values of the experimental results (on figure 12 the upper and lower values of the mass concentration, measured in different locations within the vessel atmosphere, at every sampling time, are plotted) and PARDISEKO 3B shows a peak which does not appear in those of HAARM 3.

After the end of the fire, PARDISEKO 3B remains conservative as compared with the mean values of the experimental results while the results calculated by HAARM 3 become smaller than the experimental values.

Test EMIS 04 (Figure 13)

During the test period, the code results are conservative as compared with the mean values of the experimental results (on Figure 13 the upper and lower values of the mass concentration, measured in different locations within the vessel atmosphere, at every sampling time, are plotted) and the shapes of the experimental and calculated (HAARM 3) curves are identical.

In these two cases (EMIS 03 and 04 tests), we noticed that the slopes of the calculated curves (after the fire end) are steeper with HAARM 3 than with PARDISEKO 3B.

IV-3. Suspended size distribution

Figures 14 and 15 show aerodynamic mass median diameter and standard geometric deviation versus time (experimental results and calculated results by HAARM 3 and PARDISEKO 3B) for the EMIS 03 and 04 tests.

Aerodynamic mass median diameter

The evolution of the AMMD given by cascade impactors (see paragraph III.4) is similar to that obtained by the codes except at the beginning of the fire where the shapes of the curves obtained by HAARM 3 and PARDISEKO 3B are very different from that of the experiment and from each other (presence of a peak with PARDISEKO 3B).

We noticed that the experimental value of AMMD at the beginning of the fire is nearly identical to that suggested by the CSNI Group of Experts [6].

Furthermore, the experimental AMMD are, in general, smaller than the calculated AMMD (Figure 10).

Standard geometric deviation

The experimental and calculated values are different but the variations in time are similar. These discrepancies are due, in particular, to the fact that the initial value of σ_g, used by the codes, was 2 (value suggested by the CSNI Group of Experts [6]) while the initial value of σ_g measured was 1.5.

IV-4. Kinetics of the aerosol removed on the vessel floor

Figures 16 and 17 show settled mass versus time (experimental results obtained by means of a sequential sampling device and calculated results by HAARM 3 and PARDISEKO 3B) for the EMIS 03 and 04 tests.

In these two cases, the shapes of the experimental and calculated curves are similar with the same slope in the middle region (see paragraph III.5: removal rate = 0.48 g Na_2O_2/s or 0.24 g $Na_2O_2/m^2.s$).

The difference between the experimental and calculated "total settled mass" are of about 10 % (Table III).

V - DISCUSSION and CONCLUSION

HAARM 3 and PARDISEKO 3B calculations gave the best fit of the mass concentration curve (for the EMIS 03 and 04 tests) using the following data for the input parameters :

- collision efficiency for gravitational coagulation $0.1 < \varepsilon < 0.3$,
- thermal boundary layer thickness $1 \text{ mm} < \delta_T < 3 \text{ mm}$,
- dynamic shape factor $1 < \kappa < 1.5$,
- coagulation shape factor $1 < f < 1.5$,
- correction factor density $0.2 < \alpha < 0.6$.

Up to now, we have been using constant values for the above parameters and it would be necessary to know their analytical expression versus time, mainly for ε and δ_T.

For the suspended mass concentration, the results obtained using the above values of the input parameters indicate a discrepancy between the calculation and the experiment (mean value) of :

- less than a factor 5 during the sodium fire period,
- a factor between 1 and 5 after the end of the fire.

For the aerodynamic mass median diameter, PARDISEKO 3B is closer to the experiment than HAARM 3, except for the peak at the beginning of the fire. This peak is not observed in the impactor data. Besides, immediately after the end of the fire, the experimental values are smaller than the values given by HAARM 3.

Initial particle size diameter was determined experimentally to be about 1.2 µm (AMMD), value close to that suggested by the CSNI Group of Experts [6] .

For the standard geometric deviation σ_g, the initial experimental value is determined to be about 1.5, which differs from the value 2 suggested by the CSNI Group of Experts [4] . It will be interesting to confirm this result.

For the settled mass, the calculations and the experiments agree within an error margin of 10 %.

Figures 12, 13, 16 and 17 are not coherent with each other ; the experimental values for the mass concentration and the settled mass are both smaller than the calculated values. The explanations could be :

- First, that the experimental results have been obtained by two different devices (mass concentration by filters and cascade impactor - settled mass by one sequential sampling device) ;

- Secondly, that the experimental value of the removal kinetics on the vessel walls is greater than the value calculated by the codes during the sodium fire period.

The future EMIS tests will make it possible to assess the gas velocity and temperature fields inside the containment vessel, which will be used for the validation of the computer model ESBI [1] . This code calculates, mainly :

- the temperature and velocity fields in the vessel atmosphere,
- the rate of energy dissipation in turbulence (used in the formulation of the turbulent coagulation included in the HAARM 3 code).

The code results make it possible to assess the gas flowrates between the different zones in the future model for multiple aerosol behavior zones.

The knowledge of the fluid flow and the thermal gradient near the vessel walls (given by the ESBI code) will make it easier to determine :

- the analytical expression versus time of the thermal boundary layer thickness δ_T. Up to now, we have been using adjustable constant values in the codes,
- the deposition by turbulent impaction.

The future EMIS tests will also give further information about the evolution of the emission rate of the source particles during the sodium pool fire.

The application of the codes to the reactor case will be performed after validation of these codes with the EMIS tests (4.4 m^3), with the ESMERALDA tests (3600 m^3), and with the tests carried out in the German FAUNA Vessel (220 m^3) in Karlsruhe. The scale effect will be evaluated on this occasion.

VI - REFERENCES

[1] MAGNAUD, J.P., et al., "Programme ESBI - Notice d'utilisation". Private communication.

[2] BOULAUD, D., "Study of multi-stage impactors", Paper presented to this meeting (Session III - Measurement techniques).

[3] HILLIARD, R.K., "Summary of HEDL sodium fire tests", HEDL-SA-1669, (1978).

[4] GIESEKE, J.A., "HAARM 3 users manual", BMI-NUREG-1991, (1978).

[5] BUNZ, H., "Ein Computerprogramm zur Berechnung des Aerosolverhaltens in geschlossenen Behältern", Report to be published.

[6] "Nuclear aerosols in reactor safety. A state-of-the art report by a group of experts of the NEA Committee on the Safety of Nuclear Installations", CSNI/SOAR n°1, (1979).

[7] GIESEKE, J.A., et al., "Characteristics of agglomerates of sodium oxide particles", BMI-NUREG-1977, (1977).

[8] HINDS, W., et al. "Density and shape factor of sodium aerosol", COO-2803-04, (1977).

TABLE I - SUMMARY OF CONDITIONS FOR SODIUM POOL FIRE TESTS.

	EMIS 01	EMIS 02	EMIS 03	EMIS 04
Containment vessel				
Diameter, m	1.6	1.6	1.6	1.6
Overall height, m	2.2	2.2	2.2	2.2
Volume, m^3	4.4	4.4	4.4	4.4
Floor area, m^2	2	2	2	2
Wall area, m^2	15	15	15	15
Vessel steel mass, kg	450	450	450	450
Burning pan material	Carbon steel	Carbon steel	Carbon steel	Carbon steel
Sodium spill				
Mass sodium spilled, kg	9.4	9.7	9.8	9.9
Sodium burn pan surface, m^2	0.125	0.125	0.125	0.125
Initial sodium temperature, °C	450	450	450	450
Pool depth, m	0.09	0.09	0.09	0.09
Initial containment atmosphere				
Oxygen, vol. %	21	21	21	21
Temperature, °C	33	36	38	25
Pressure, MPa	0.0961	0.0996	0.0984	0.0980

TABLE II - SUMMARY OF RESULTS FOR SODIUM POOL FIRE TESTS.

	EMIS 01	EMIS 02	EMIS 03	EMIS 04
Sodium combustion - Aerosol source				
Total sodium oxidized, kg	8.24	8.01	2.3	1.1
Fraction of oxidized sodium released	0.25	0.22	0.40	0.25
Source duration, s	7200	4800	1980	900
Average source rate (as sodium), g/s	0.28	0.37	0.47	0.31
Total aerosol mass released (as sodium), kg	2.02	1.79	0.93	0.28
Total aerosol mass released (as Na_2O_2), kg	3.43	3.03	1.57	0.47
Chemical reaction mechanism, % Na/Na_2O_2	39.0	23.5	44.6	30.2
Average sodium combustion rate, kg/ $h.m^2$	33.5	47.8	33.1	33.7
Containment atmosphere during test				
Maximum temperature, °C	196	169	138	84
Maximum pressure, MPa	0.127	0.138	0.120	0.111
Final oxygen, vol. %	21	21	21	21
Consumed oxygen, moles	127	116	38	15

TABLE III - COMPARISON EXPERIMENT-CALCULATION
- SETTLED AND DIFFUSED AEROSOL MASSES (MASS FRACTION)

TEST NAME	SETTLED MASS , %			DIFFUSED MASS , %		
	EXPERIMENT	HAARM 3	PARDISEKO 3B	EXPERIMENT	HAARM 3	PARDISEKO 3B
EMIS 01	70.5	65	-	29.5	35	-
EMIS 02	70.5	65.5	-	29.5	34.5	-
EMIS 03	77.5	78.5	78	22.5	21.5	22
EMIS 04	75	87	83	25	13	17

TABLE IV - DIFFUSED AEROSOL MASSES BY BROWNIAN AND THERMOPHORESIS DIFFUSION
(PARDISEKO 3B RESULTS)

TEST NAME	Removal by brownian diffusion, g/m^2	Removal by thermophoresis, g/m^2	Removal by thermophoresis / Removal by brownian diffusion
EMIS 03	0.016	23.3	1456
EMIS 04	0.008	5.25	656

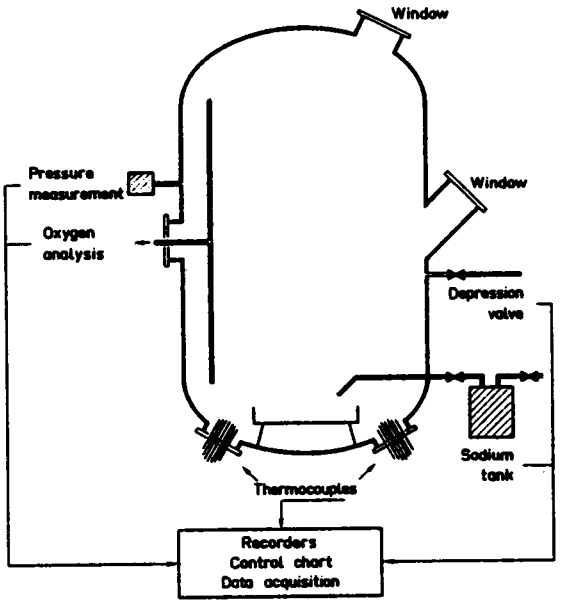

Figure 1 _ Diagram of the 4.4 m^3 vessel.

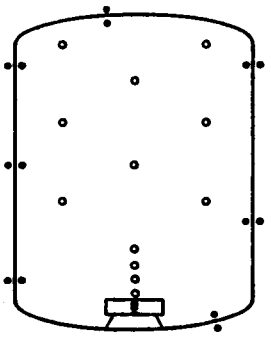

Figure 2 _ Locations of thermocouples within the vessel atmosphere.

o gas
• wall
× sodium

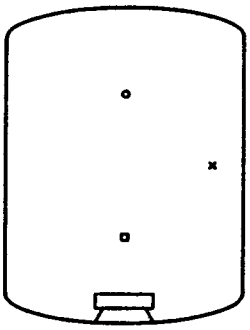

Figure 3 _ Locations of aerosol samplings within the vessel atmosphere.

EMIS 03 test { × impactor, o filter
EMIS 04 test { □ impactor, o filter

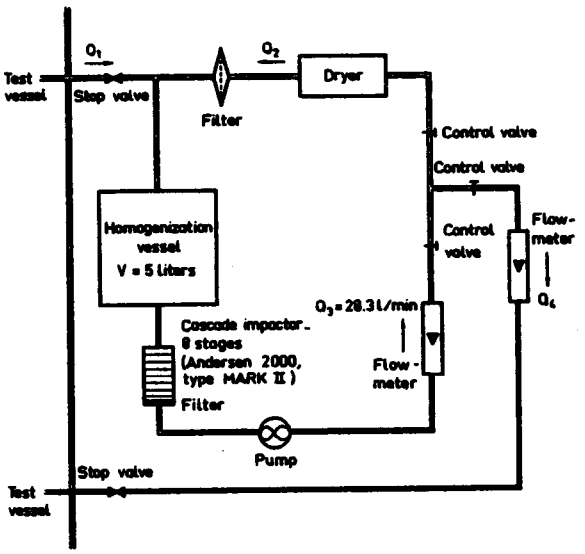

Figure 4 _ Aerosol sampling _ Dilution system.

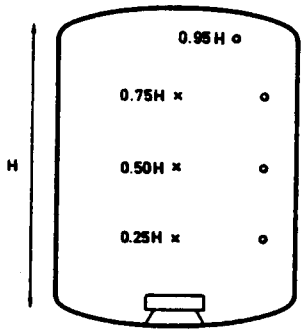

Figure 5 _ Locations of convection current velocity detectors within the vessel atmosphere.

× double hot wire probes
o Pitot probes

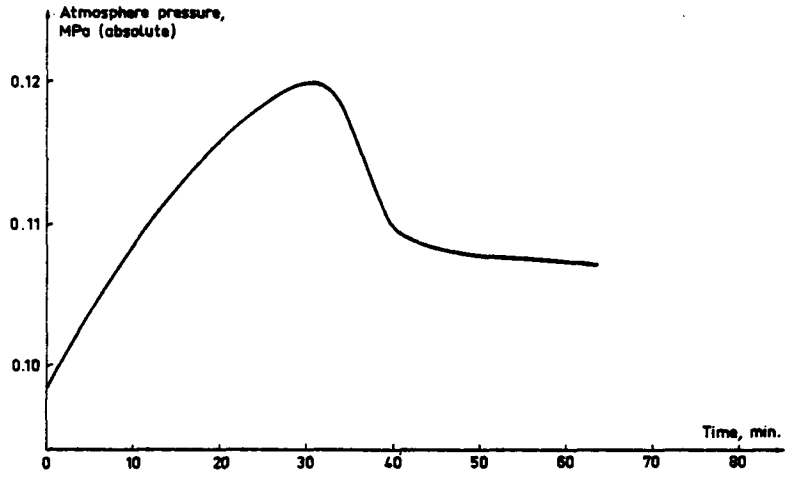

Figure 6 _ Containment pressure versus time, EMIS 03 test.

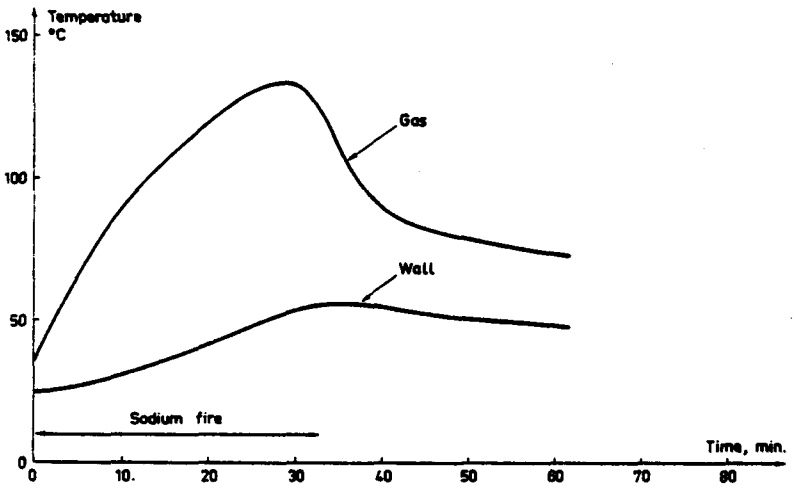

Figure 7 _ Mean gas temperature and mean wall temperature versus time, EMIS 03 test.

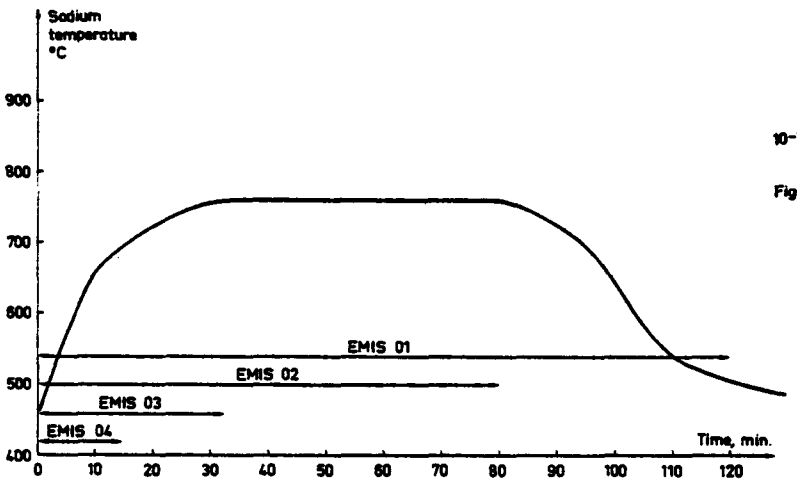

Figure 8 _ Sodium temperature versus time, EMIS 01 test.

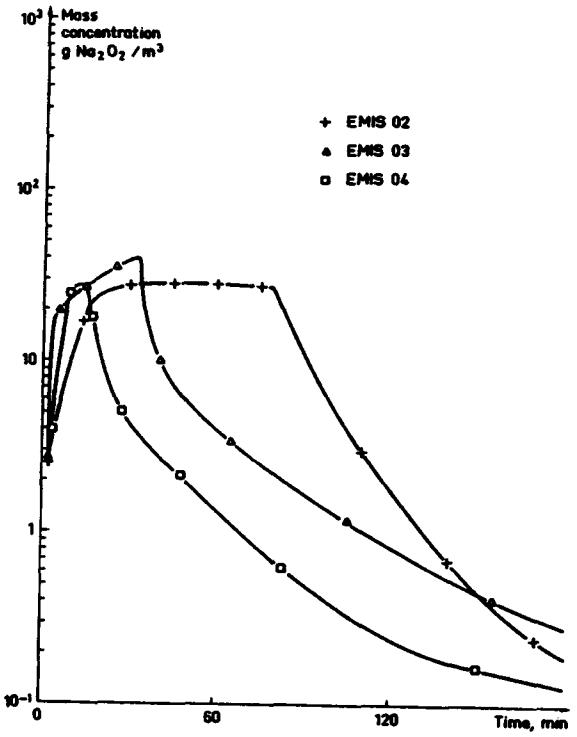

Figure 9 _ Mass concentration versus time for EMIS 02, 03 and 04 tests (experimental results – mean values).

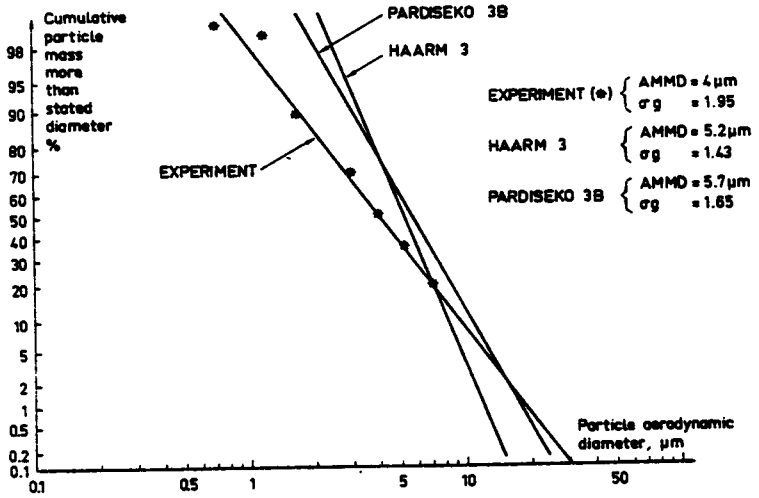

Figure 10 - Comparison of code results with impactor data (cumulative particle size distribution), EMIS 03 test at t = 108 minutes.

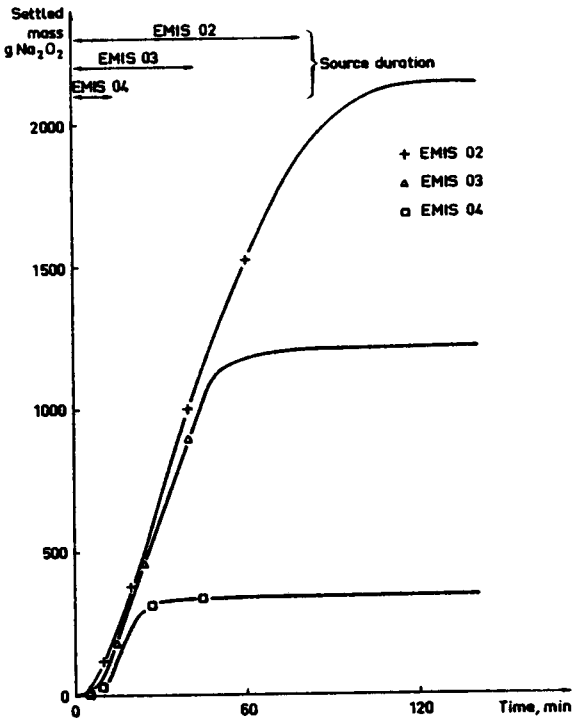

Figure 11 - Settled mass versus time, for EMIS 02, 03 and 04 tests (experimental results).

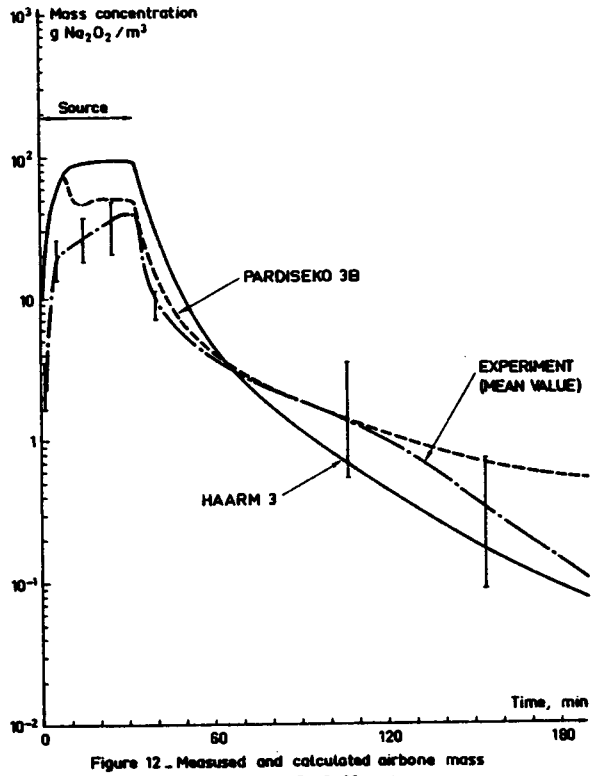

Figure 12 - Measured and calculated airborne mass concentration, EMIS 03 test.

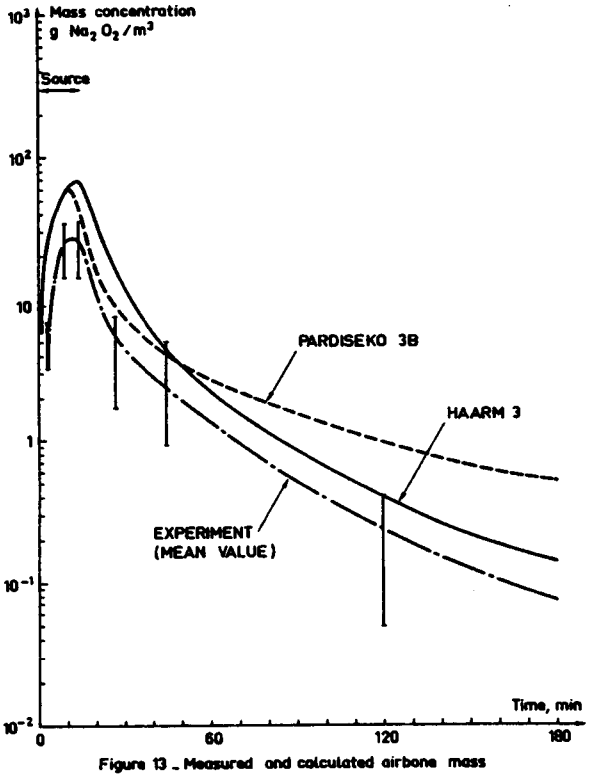

Figure 13 - Measured and calculated airborne mass concentration, EMIS 04 test.

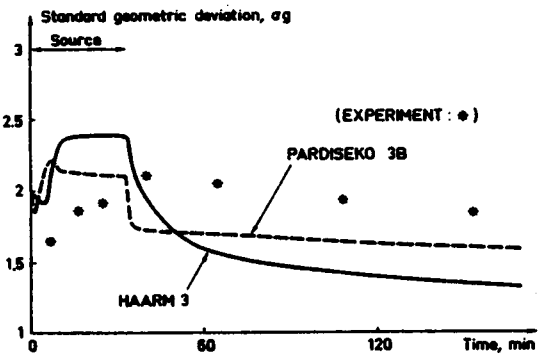

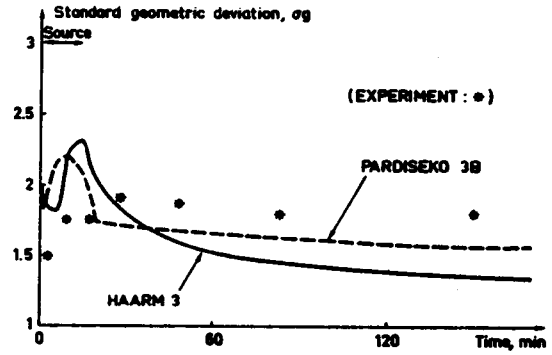

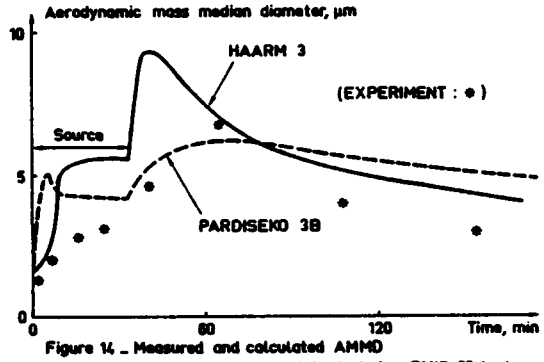

Figure 14 - Measured and calculated AMMD and standard geometric deviation, EMIS 03 test.

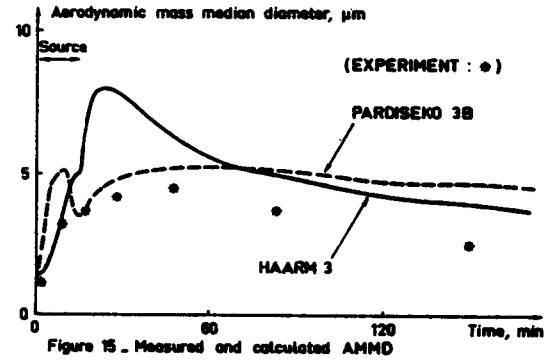

Figure 15 - Measured and calculated AMMD and standard geometric deviation, EMIS 04 test.

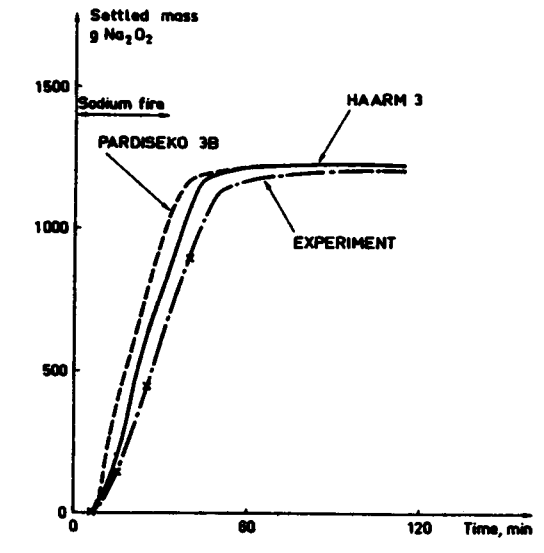

Figure 16 - Measured and calculated settled mass, EMIS 03 test.

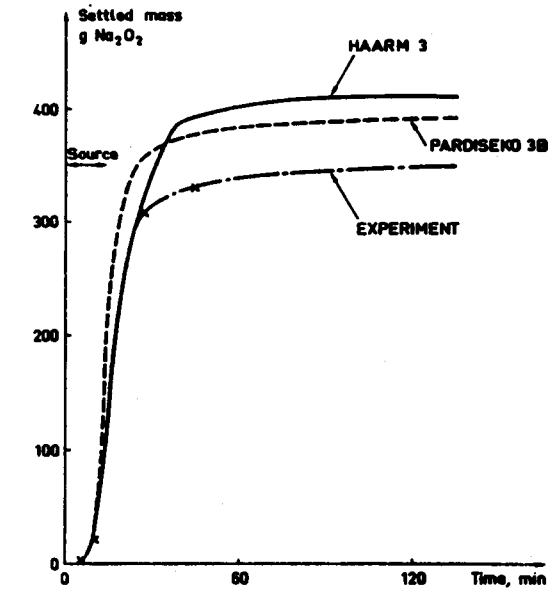

Figure 17 - Measured and calculated settled mass, EMIS 04 test.

BEHAVIOR OF SODIUM OXIDE, URANIUM OXIDE AND MIXED SODIUM OXIDE-URANIUM OXIDE AEROSOLS IN A LARGE VESSEL

R. E. Adams T. S. Kress
J. T. Han M. Silberberg*

Oak Ridge National Laboratory
Oak Ridge, Tennessee 37830, USA

ABSTRACT

Results are reported for experiments on the behavior of sodium oxide aerosols, uranium oxide aerosols, and various mixtures of these in the Nuclear Safety Pilot Plant (NSPP) vessel at Oak Ridge National Laboratory. The NSPP program, sponsored by the Nuclear Regulatory Commission, is to provide experimental qualification of the HAARM-3 aerosol behavioral code being independently developed at Battelle-Columbus Laboratories. The results of fourteen single-component and six mixed-component aerosol experiments are presented along with selected comparisons with code predictions.

---

* Experimental Fast Reactor Safety Research Branch, Nuclear Regulatory Commission

INTRODUCTION

A program is being conducted at the Oak Ridge National Laboratory (ORNL) to study the behavior of sodium oxide aerosols, uranium oxide aerosols, and mixtures of these in the 38.3-m^3 containment vessel of the Nuclear Safety Pilot Plant (NSPP). The purpose of the program, sponsored by the Nuclear Regulatory Commission (NRC), is to provide the experimental qualification to the HAARM-3 aerosol behavioral code,[1] which is under independent development for NRC at Battelle-Columbus Laboratories (BCL).

Experiments are conducted to explore the behavior of various mixtures of the two major liquid-metal fast breeder reactor (LMFBR) nuclear aerosol species under conditions appropriate for speculated releases into the secondary containment caused by hypothetical LMFBR accidents. The program plan provides for studies of single-component aerosols of both sodium and uranium oxides to establish their individual characteristics and for studies to evaluate the behavior of mixtures of these aerosols at varying mass ratios and sequences of generation.

The NSPP facility includes a test containment vessel, aerosol generating equipment, analytical sampling and system parameter measuring equipment, and an in-vessel liquid spray decontamination system. The NSPP vessel is a stainless steel cylinder with dished ends having a diameter of 3.05 m, a total height of 5.49 m, and a volume of 38.3 m^3. The floor area is 7.7 m^2, and the internal surface area (including top, bottom, and structural items) is 68.9 m^2. The equipment for the measurement of aerosol parameters includes filter samplers for measuring the aerosol mass concentrations, coupon samplers for aerosol fallout and plateout measurements, cascade impactors, for determining the aerodynamic particle size distributions of the aerosol, and electrostatic precipitators for collecting samples for electron microscopy. Other system parameters measured are vessel atmosphere temperatures, wall temperature gradients, and vessel pressure.

EXPERIMENTAL

Sodium Oxide Aerosol Experiments

Fourteen single-component aerosol experiments have been conducted. In four of these experiments, sodium oxide aerosol was produced by sodium pool fires of 1, 5, 5, and 10 kg of heated sodium with maximum observed aerosol concentrations of 6, 11, 11, and 25 $\mu g/cm^3$, respectively. (The two runs at 5 kg illustrate reproducibility of the data.) The observed mass concentration transients for these are given in Fig. 1. Aerodynamic diameters of the agglomerating aerosols increased from the source size up to as large as 4 μ. The burning sodium produced temperatures in the vessel atmosphere ranging from 323 to 358 K and pressures ranging from 0.110 to 0.112 MPa.

Three sodium oxide aerosol experiments were performed by injecting 5 or 10 kg of heated sodium into the vessel through a single spray nozzle. Estimated maximum aerosol concentrations at the time of termination of the sodium spray were in the 40- to 60-$\mu g/cm^3$ range. The aerodynamic mass median diameter of the agglomerating aerosols increased rapidly from the source size to as large as $\sim$7 μ and then decreased over 10 hr to about 1.5 to 2.0 μ. The fractional disappearance of this aerosol from the vessel atmosphere was consistent with those in the sodium pool fire experiments. The vessel atmosphere temperatures, as expected, were larger than those produced by sodium pool fires, and a gradient was produced from the bottom to the top of the vessel; maximum temperatures near the top of the vessel ranged from 0.139 to 0.145 MPa. Both the temperature and pressure transients were of short duration, however.

Uranium Oxide Aerosol Experiments

Seven single-component uranium oxide aerosol experiments were also conducted. In three of these experiments, the aerosol was generated by vaporizing a uranium metal electrode in a dc-arc and allowing it to combine with the oxygen in the vessel atmosphere.[2] Four additional experiments were conducted using an aerosol generator adapted from a commercial plasma metallizing torch[3] in which powdered uranium metal and oxygen gas are introduced into an argon plasma by means of a special adapter/combustion chamber. Figure 2 presents the measured mass concentration transient for all seven of these tests.

When using the dc-arc generator, the duration of generation was long (compared with that in the sodium oxide experiments), and the maximum aerosol concentrations were small. For the three experiments, maximum aerosol concentrations of only 0.05, 0.13, and 0.22 $\mu g/cm^3$ were produced. The aerodynamic mass median diameter of the agglomerating aerosol grew to a maximum of 1.8 μ. Temperature and pressure changes in the vessel atmosphere were small.

Larger uranium oxide aerosol concentrations were achieved with the plasma torch aerosol generator. The four experiments reported produced maximum aerosol concentrations ranging from 0.7 to 5. $\mu g/cm^3$ at termination of generation. At these higher concentrations, the fractional disappearance of the aerosol was larger than at the lower concentrations, and the aerodynamic mass median diameter of the agglomerating aerosol became larger. During one of the larger concentration experiments, (run 205), agglomerated particle diameters in the 4- to 5-μ range were measured.

Mixed Sodium Oxide-Uranium Oxide Aerosol Experiments

A series of experiments is underway to investigate the aerodynamic behavior of an admixture of sodium oxide and uranium oxide aerosols. It is of interest to study the influence of each aerosol on the other, and determine if the two aerosols act independently in a closed vessel, or if the two aerosols mix and act as a "new" single-component aerosol with properties different from those of the individual aerosol components. This series of experiments was designed to investigate (1) the influence of particle size on the agglomeration process wherein one aerosol is generated first, allowed to increase from source-size to larger sizes by agglomeration, then mixed with a freshly-generated aerosol of source-size particles, and (2) the influence of relative mass ratio of the two aerosols wherein the two are generated and mixed simultaneously and allowed to agglomerate from source-size particles. The experiments performed to date are listed in Table I, below.

Table I

Mixed Sodium Oxide-Uranium Oxide Aerosol Experiments

Experiment (Run) No.	Sequence of Mixing	Mass Ratio at Mixing (Na_2O/U_3O_8)
301	Uranium Oxide First Followed by Sodium Oxide at 102 min	30/1
302	Uranium Oxide First Followed by Sodium Oxide at 93 min	4/1
306	Sodium Oxide First Followed by Uranium Oxide at 44 min	1/1
303	Simultaneous Generation	1/1.2
304	Simultaneous Generation	1/10
305	Simultaneous Generation	3.5/1

In all of these experiments, the initial atmosphere was air at a relative humidity of less than 20%. Temperature and pressure generated in the vessel by the experiments were similar to those produced by comparable single-component sodium pool fire experiments.

Influence of aerosol size - The first mixed-oxide aerosol experiment (No. 301) was performed by generating uranium oxide (with the DC-Arc generator) for a 20 min period, allowing a period of 82 min for agglomeration to proceed, and then introducing sodium oxide aerosol by means of a pool fire of

3 min duration. Figure 3 displays the results from this experiment. The uranium oxide aerosol concentration decreased over the 82 min period of agglomeration, until, at the time of initiation of the sodium pool fire, the concentration was an estimated 0.1 $\mu g/cm^3$. Upon introduction of the sodium oxide aerosol, the concentration of uranium oxide dropped singificantly, and the rate of removal from the vessel atmosphere was similar to that of the sodium oxide component. This behavior, supported by the fallout data, suggested that the two aerosols were co-agglomerating and, for the most part, acting as a single aerosol. Figure 3 also contains, for comparison, the results from single component aerosol experiments with sodium oxide or uranium oxide. Run 203 illustrates the behavior that would be expected from a comparable single-component uranium oxide aerosol experiment; Run 101 illustrates the behavior of a comparable sodium oxide aerosol experiment. It is observed that the newly-generated sodium oxide aerosol has a large influence on the aerodynamic behavior of an agglomerated uranium oxide aerosol.

A similar experiment (No. 302), performed at a different aerosol mass ratio, produced results comparable to those observed in Run 301.

The influence of a newly-generated uranium oxide aerosol on the agglomerated sodium oxide aerosol was studied in Experiment (Run) 306. The sodium oxide aerosol was produced by a sodium pool fire of 26 min duration and then allowed to agglomerate for an additional period of 18 min, at which time the concentration was estimated to be 4.5 $\mu g/cm^3$. Uranium oxide aerosol generation (by the plasma torch generator) was initiated at the end of the agglomeration period and continued for 13 min. The results of this experiment are illustrated in Fig. 4. Upon introduction of the uranium oxide aerosol, the concentration of the sodium oxide aerosol decreased significantly. Over the period of 16 min after start of the uranium oxide aerosol generation, the sodium oxide aerosol concentration dropped about 92%. This behavior, supported by the fallout data, suggested that the two aerosols were co-agglomerating. Figure 4 also contains, for comparison, the results from single-component experiments with sodium oxide or uranium oxide aerosols.

Influence of aerosol mass ratio - Three experiments have been conducted to investigate the influence of the mass ratio of the two components of a mixed-oxide aerosol on its aerodynamic behavior. In the first experiment, Run 303, the target mass ratio of the two aerosols was 1 to 1. Uranium oxide aerosol generation (with the plasma torch generator) was initiated first and followed by sodium oxide aerosol generation (by a sodium pool fire) 1.5 min later. The uranium oxide aerosol generation period was about 25 min and the sodium oxide aerosol generation period was about 12 min. Measured aerosol mass concentration for each component of this mixed-oxide aerosol as a function of time are given in Fig. 5. Over the first nine hours of the run, the measured mass ratio of uranium oxide to sodium oxide ranged over the interval from 1.2 to 2.5. The concentration values for sodium oxide, at times greater than 500 min, are probably slightly greater than actual values; the reagents used in dissolving the mixed-oxide samples were found to contain a low-level sodium impurity, and large uncertainty is associated with the corrections made to the measured values to compensate for this. The observed behavior of this mixed-oxide aerosol, supported by fallout data and other measurements, suggests that the two aerosols were co-agglomerating and the composite behavior was somewhat

different from that of a single-component aerosol. At the termination of the experiment at 119 hrs, the approximate distribution of the aerosol components was indicated to be 88% of the sodium oxide and 82% of the uranium oxide on the floor of the vessel and 12% of the sodium oxide and 18% of the uranium oxide plated onto internal surfaces.

The second experiment (Run 304) was to investigate the behavior of a mixed-oxide aerosol having a mass ratio of about 10 to 1 (uranium oxide to sodium oxide). Sodium oxide generation was initiated first and then followed by the start of uranium oxide aerosol generation 2 min later. The sodium oxide generation period was 3 min and the uranium oxide aerosol generation period was 19 min. At the termination of the uranium oxide aerosol generation period, the mass ratio of uranium oxide to sodium oxide was about 10 to 1. Over the first 8 hrs, the measured mass ratio decreased from about 10 to 1 to about 1 to 1. The behavior of this mixed-oxide aerosol was very similar to that produced in Run 303, with all measurements indicating co-agglomeration. The test was terminated at 48 hrs and the aerosol distribution indicated that 73% of the uranium oxide and 50% of the sodium oxide had deposited on the floor, and 27% of the uranium oxide and 50% of the sodium oxide had deposited on the internal surfaces of the vessel.

The third experiment (Run 305) was to investigate the behavior of a mixed-oxide aerosol at a 10 to 1 mass ratio of sodium oxide to uranium oxide. The uranium oxide aerosol was generated for 5.7 min and 1 min later, the sodium oxide aerosol generation was initiated by a sodium pool fire which lasted for about 17 min. Because of the delay in starting the sodium pool fire, this experiment was not exactly comparable to Runs 303 and 304; in some respects, it was similar to the delayed mixing experiments (Runs 301, 302 and 306). The first aerosol mass sample was taken at 5 min into the sodium oxide generation period, and the mass ratio of sodium oxide to uranium oxide was 3.4 to 1. The second aerosol sample was taken 15.5 min into the sodium oxide generation period, and the mass ratio of sodium oxide to uranium oxide had increased to about 275 to 1. Early fallout of the sodium oxide aerosol removed a major fraction of the uranium oxide aerosol from the vessel atmosphere. The airborne uranium oxide content of the vessel atmosphere was reduced about 97% during the interval between the first and second aerosol sample. This observation was substantiated by the aerosol fallout rate measurements. At the termination of the experiment (48 hrs), the distribution of aerosol indicated that 84% of the sodium oxide and 80% of the uranium oxide had deposited on the floor of the vessel, and 16% of the sodium oxide and 20% of the uranium oxide had deposited on internal surfaces of the vessel.

Comments - Based upon the results from these six experiments, some general observations may be made. The airborne concentration of an agglomerated (aged) aerosol is reduced significantly when mixed with a newly-generated aerosol of source-size particles. For a given aerosol, either sodium oxide or uranium oxide, less material is made airborne when generated simultaneously with a second aerosol, than when generated alone. In both types of experiments on mixed-oxide aerosols, enhanced fallout is noted during, and shortly following, the generation or mixing periods. The aerodynamic behavior of a mixed-oxide aerosol seems to be similar even though the mass ratio of the two aerosols may differ at the time of mixing. In Fig. 6, all six of the experiments are compared. For this figure, time is measured from the start of mixing of the two aerosols so that the three delayed mixing experiments can be compared

with the three experiments where mixing was more or less simultaneous. The rate of disappearance of these mixed-oxide aerosols from the vessel atmosphere is similar even though the mass ratio and size of particles at mixing vary singificantly. All experimental evidence seems to indicate that the two aerosols co-agglomerate and the material remaining airborne acts in a manner similar to sodium oxide or uranium oxide aerosols, but not entirely like either.

COMPARISON OF EXPERIMENTAL RESULTS WITH HAARM-3 CODE PREDICTIONS

The HAARM-3 aerosol code, being independently developed for NRC by Battelle-Columbus Laboratories, is utilized in the NSPP program for pretest predictions and posttest comparisons of the aerosol experiments. Comparisons between the code predictions and experimental results for sodium oxide aerosols and low-concentration uranium oxide aerosols have been generally favorable.[4,5]

The code predictions for recently-performed higher-concentration uranium oxide aerosol experiments (NSPP Runs 204-207) have also been favorable. For example, Fig. 7 illustrates the agreement for Run 207; the code prediction agrees with the experimental results within a factor of 2. Parameters used in the code input were: α = density correction factor = 1, χ = dynamic shape factor = 3, and γ = collision shape factor = 10.

Use of the HAARM-3 code to predict the behavior of a mixed-oxide aerosol is in an early state of application at ORNL. Since the code was developed for a single-component aerosol, application in describing the behavior of a mixed-oxide aerosol requires appropriate averaging of the aerosol properties of the individual components for use as code input. As a first attempt, the mixed-oxide aerosols were treated as if they were a single-component aerosol with a mass-averaged material density:

$$\bar{\rho} = (C_1\rho_1 + C_2\rho_2)/(C_1 + C_2)$$

where

$\bar{\rho}$ = assumed average material density for the two-component aerosol,

C_1 = initial mass concentration of U_3O_8 aerosol in the NSPP vessel $\mu g/cm^3$,

ρ_1 = U_3O_8 material density = 8.3 g/cm^3,

C_2 = initial mass concentration of Na_2O aerosol, $\mu g/cm^3$, and

ρ_2 = Na_2O material density = 2.27 g/cm^3.

The calculations were initiated at a time when the aerosol particle size distribution had been measured after the aerosol generation was terminated. A summary of the input data used in the calculations is presented in Table II.

Table II

A Summary of Input Data Used in HAARM-3 Calculations For NSPP Runs 207 and 303-305

Run No.	207	303	304	305
Aerosol	U_3O_8	U_3O_8 + Na_2O	U_3O_8 + Na_2O	U_3O_8 + Na_2O
Initial time, min	25.8	28.5	25.3	36.0
Initial aerosol concentration,* 10^6 particles/cm^3	3670.	7.77	25.0	5.23
Initial mass concentration, $\mu g/cm^3$	3.43	2.51	2.85	6.20
Initial aerosol mass median radius, μm	0.434	0.843	0.429	1.76
Initial aerosol geometric standard deviation based on radius	3.80	2.50	2.30	2.50
Mass-averaged aerosol material density, g/cm^3	8.30	5.63	7.81	2.27
Average vessel temperature, K	294	323	323	323
Temperature gradient at vessel wall, K/cm	negligible	negligible	negligible	negligible

*Estimated from the measurements of aerosol mass concentration and particle size distributions.

Figures 8 and 9 show the comparisons between the code predictions and the measured mixed-oxide aerosol concentrations for NSPP Runs 303 and 304 in which the uranium oxide mass was either nearly equal to or much higher than

that of the sodium oxide. Two calculations were performed for each run - one assuming that the behavior of the mixed-oxide aerosol would be like that of uranium oxide (with chain-agglomerate particles) and the other assuming that the behavior would be like that of sodium oxide (with nearly spherical particles). The code calculations based upon chain-agglomerate particle behavior compare more favorably with experimental measurements than those based upon spherical particle behavior.

Figure 10 contains the comparison for NSPP Run 305 in which the uranium oxide mass in the mixed-oxide aerosol was lower than that of the sodium oxide. The code calculation based upon chain-agglomerate particle behavior generally underpredicts, and the calculation based upon spherical particle behavior overpredicts the measured concentrations.

Based upon this initial application at ORNL of the HAARM-3 code for predicting the behavior of mixed-oxide aerosols, it appears that the mixed-oxide aerosol behaves more like an aerosol composed of chain-agglomerate particles, than spherical ones, when the uranium oxide mass is nearly equal to or higher than that of the sodium oxide. However, for a mixed-oxide aerosol in which the uranium oxide mass is much lower than that of sodium oxide, the behavior is neither like that of chain-agglomerate particles nor of spherical particles. Further investigation of this code application is underway.

ACKNOWLEDGEMENTS

Research is sponsored by the Office of Nuclear Regulatory Research, Nuclear Regulatory Commission, under Interagency Agreement DOE 40-551-75 with the U. S. Department of Energy under Contract No. W-7405-eng-26 with Union Carbide Corporation Nuclear Division.

The authors wish to acknowledge the excellent technical support of R. F. Benson, M. T. Hurst, and L. J. Shersky (Retired) in the performance of these aerosol experiments.

REFERENCES

1. J. A. Gieseke, K. W. Lee, and L. D. Reed, "HAARM-3 User's Manual," BMI-NUREG-1991, Battelle-Columbus Laboratories (1978).
2. R. E. Adams et al., "Uranium and Sodium Oxide Aerosol Experiments: NSPP Tests 201-203 and Tests 301-302, Data Record Report," ORNL/NUREG/TM-343, Oak Ridge National Laboratory (1979).
3. T. S. Kress, "LMFBR Aerosol Release and Transport Program Quarterly Progress Report for January-March 1978," ORNL/NUREG/TM-213, Oak Ridge National Laboratory (1978).
4. R. E. Adams et al., "Behavior of Sodium Oxide and Uranium Oxide Aerosols in a Large Vessel," Proceedings of the International Meeting on Fast Reactor Safety Technology, Seattle, Washington, August 19-23, 1979.
5. M. Silberberg, Editor, "Nuclear Aerosols in Reactor Safety," Nuclear Energy Agency, Organization for Economic Cooperation and Development, CSNI/SOAR No. 1, June 1979.

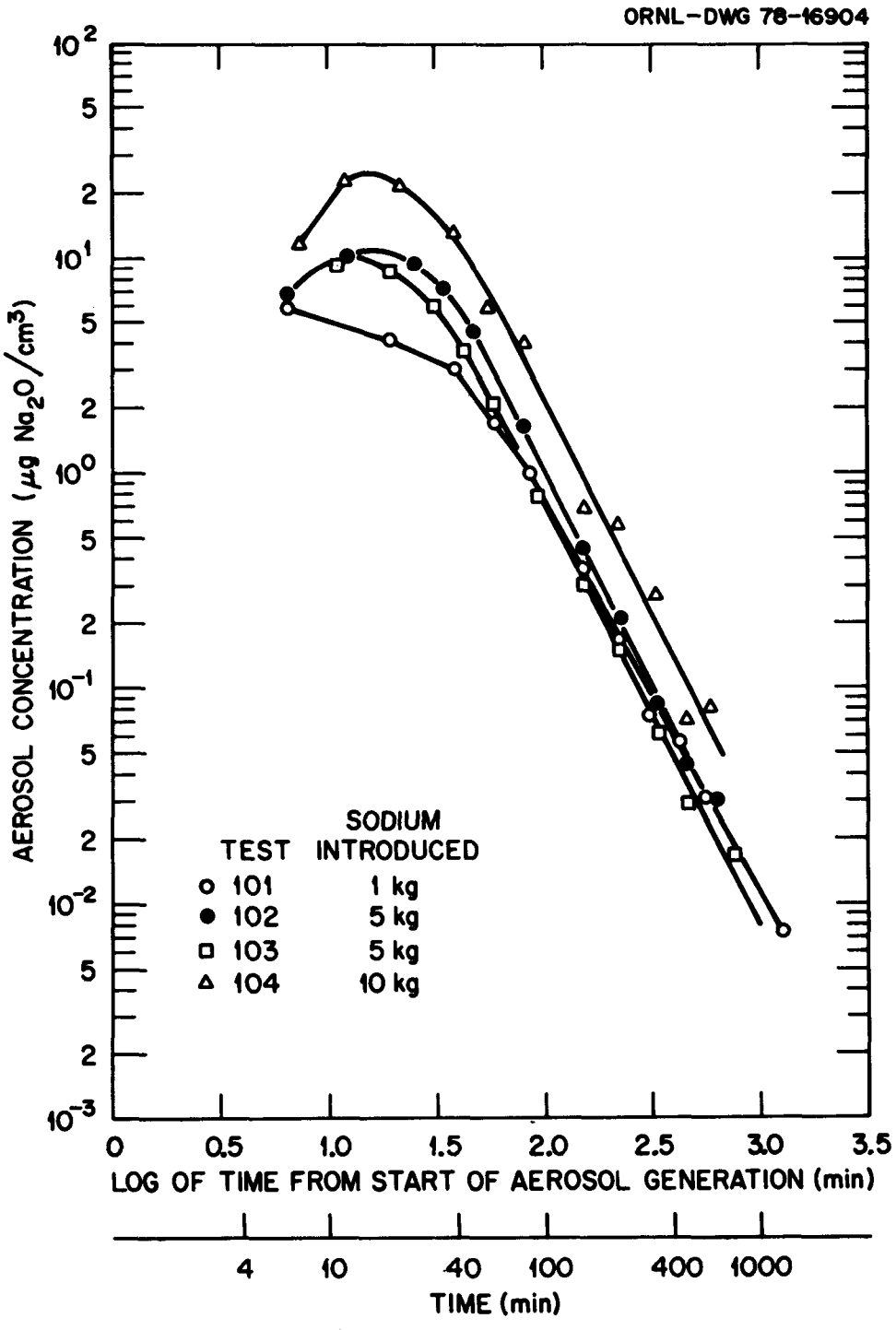

Fig. 1. Behavior of Sodium Oxide Aerosols Produced by Sodium Pool Fires

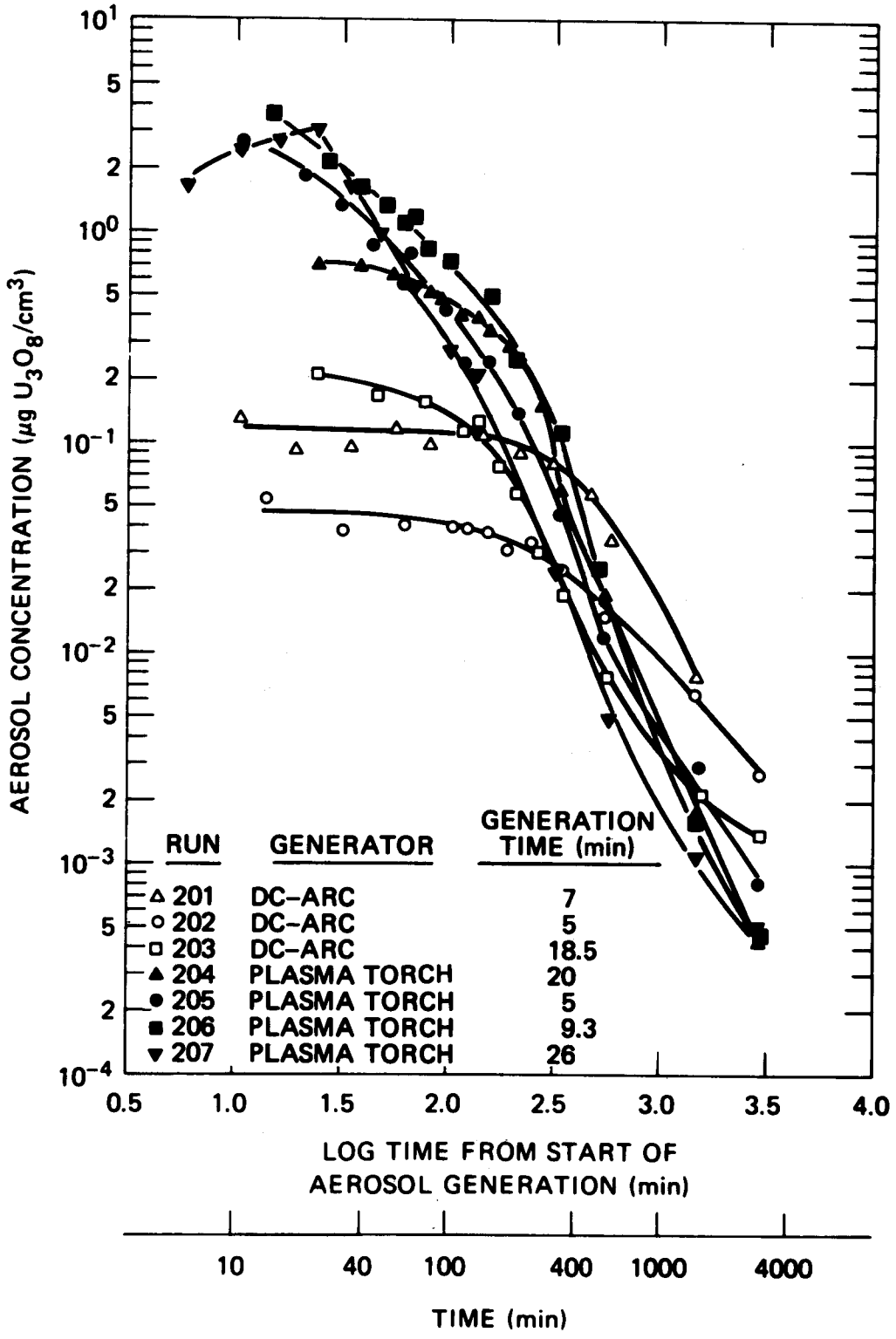

Fig. 2. Behavior of Uranium Oxide Aerosols (Runs 201-207)

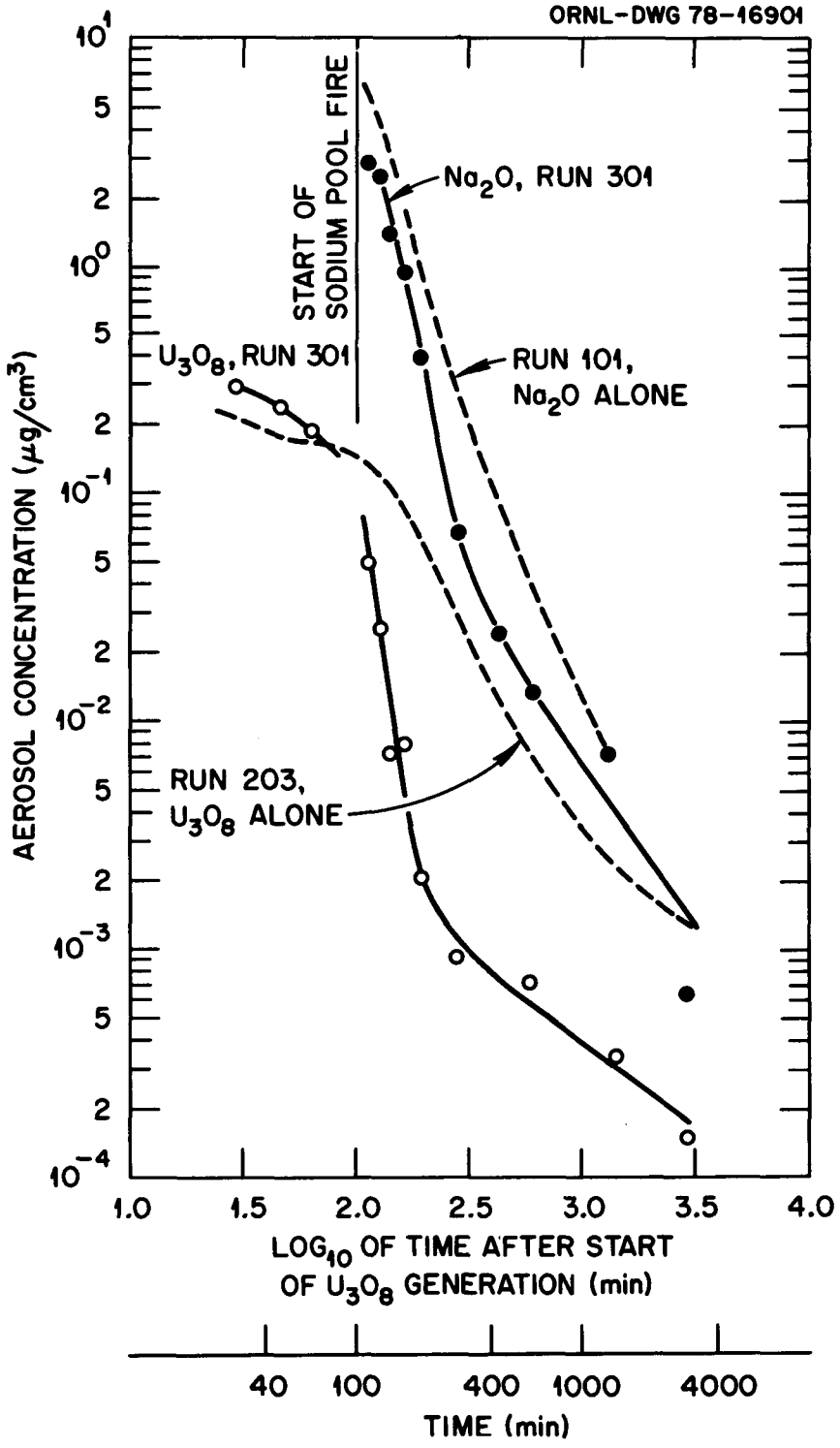

Fig. 3. Comparison of Mixed Oxide Aerosol Behavior (Run 301) With Single-Component Aerosol Behavior (Runs 101 and 203)

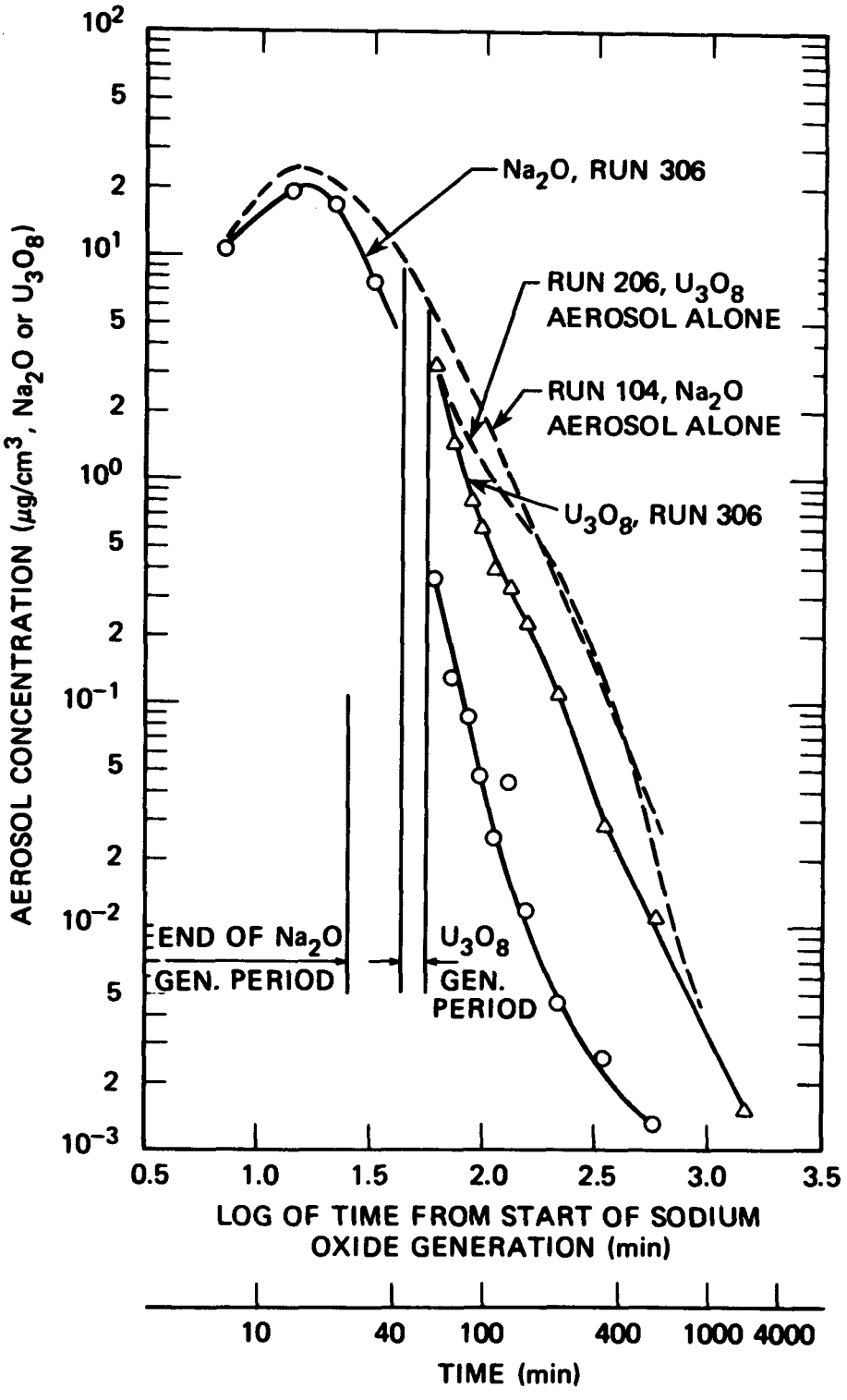

Fig. 4. Comparison of Mixed Oxide Aerosol Behavior (Run 306) With Single Component Aerosol Behavior

(Runs 104 and 206)

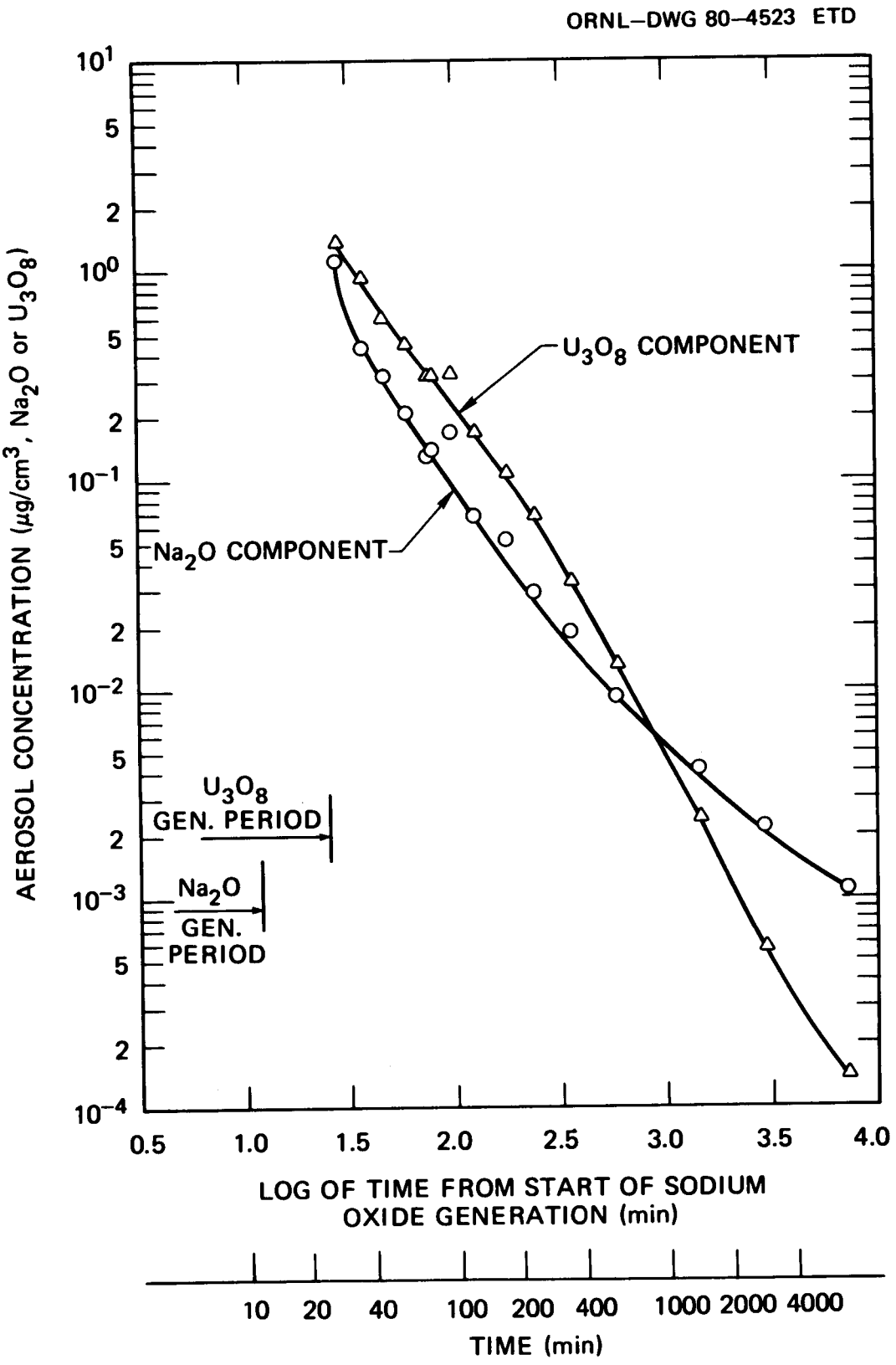

Fig. 5. Behavior of Each Component of a Mixed Oxide Aerosol (Run 303)

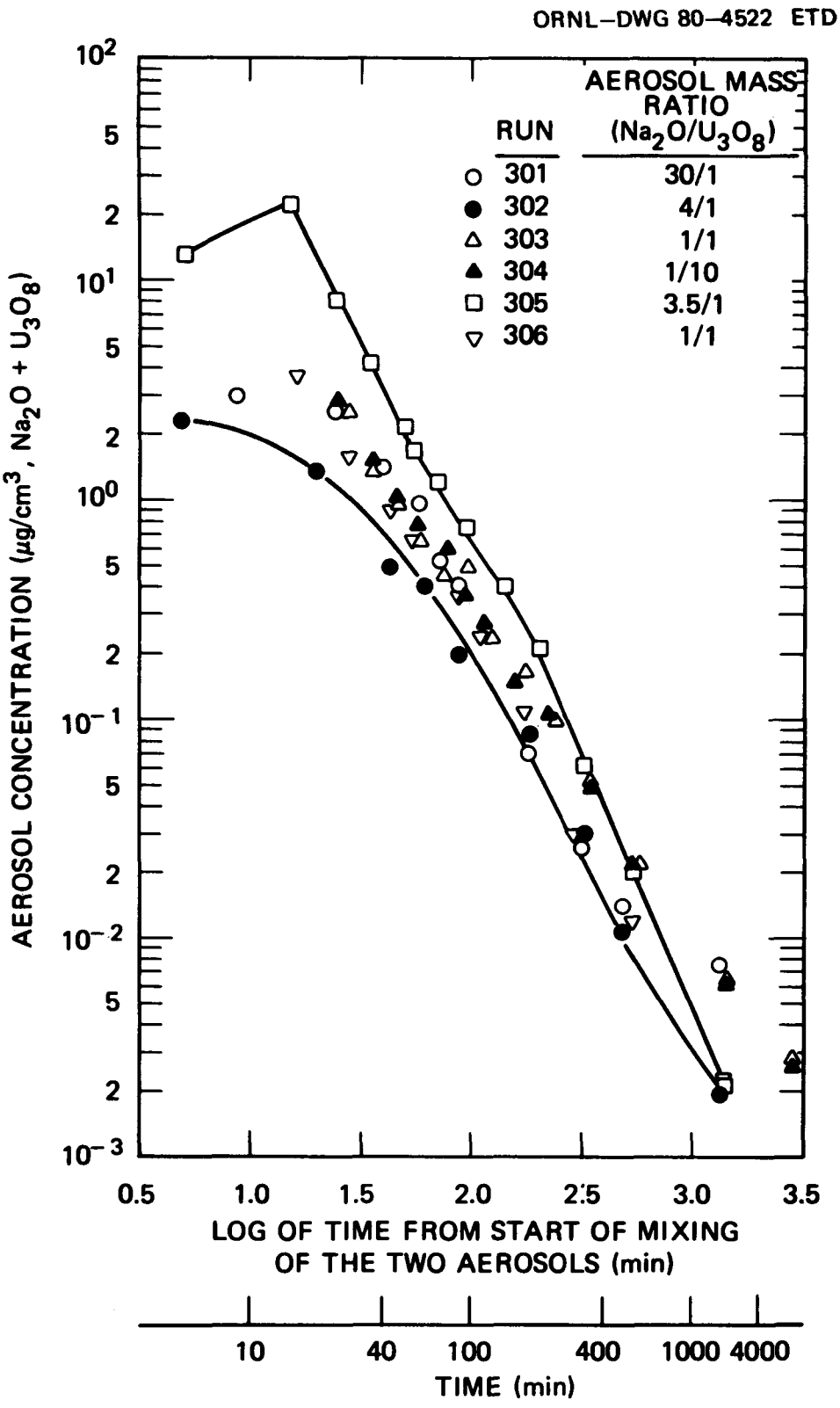

Fig. 6. Behavior of the Mixed Oxide Aerosol Remaining Airborne After Mixing of the Two Components

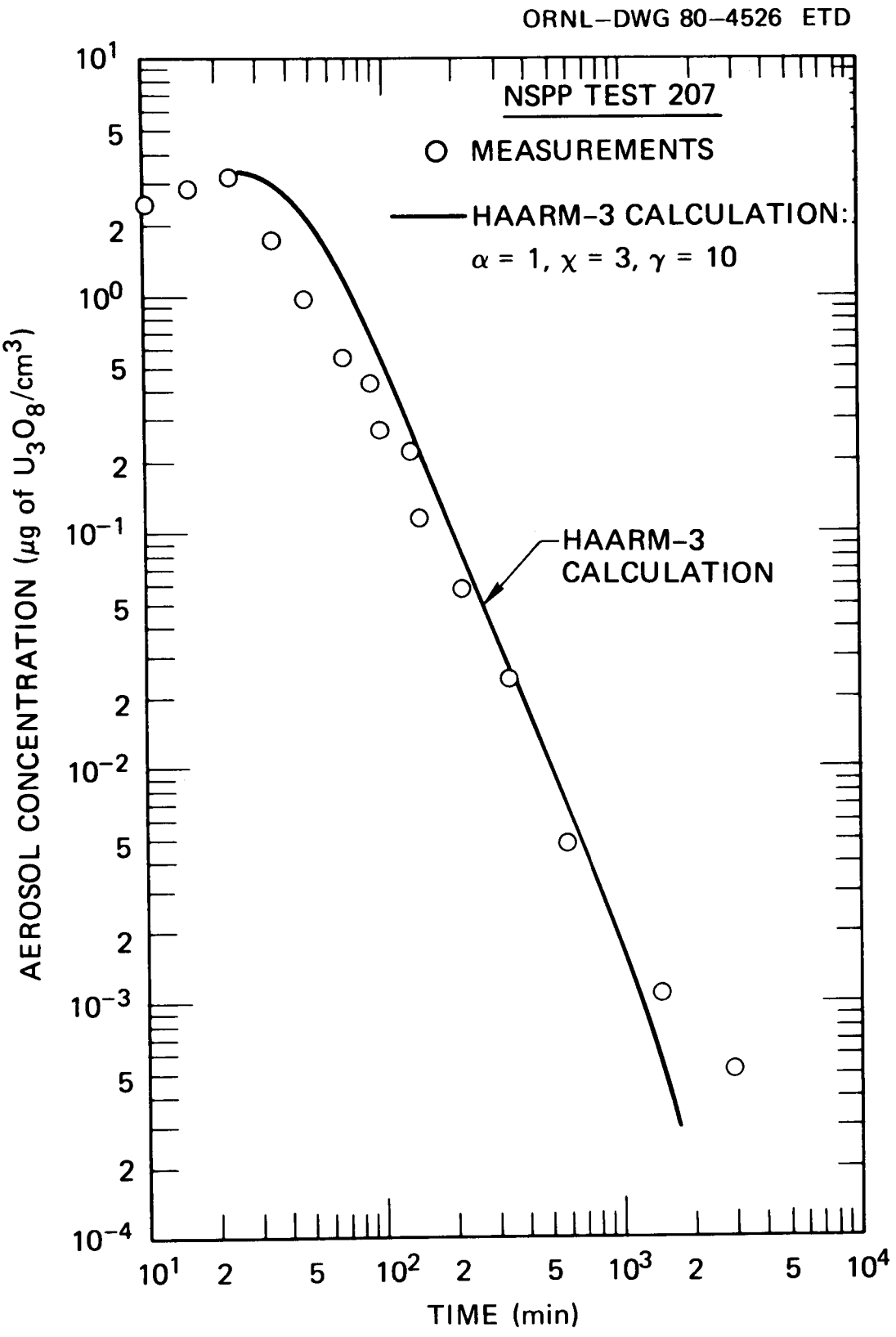

Fig. 7. Comparison of HAARM-3 Calculation With Experimental Results From Uranium Oxide Aerosol Run 207

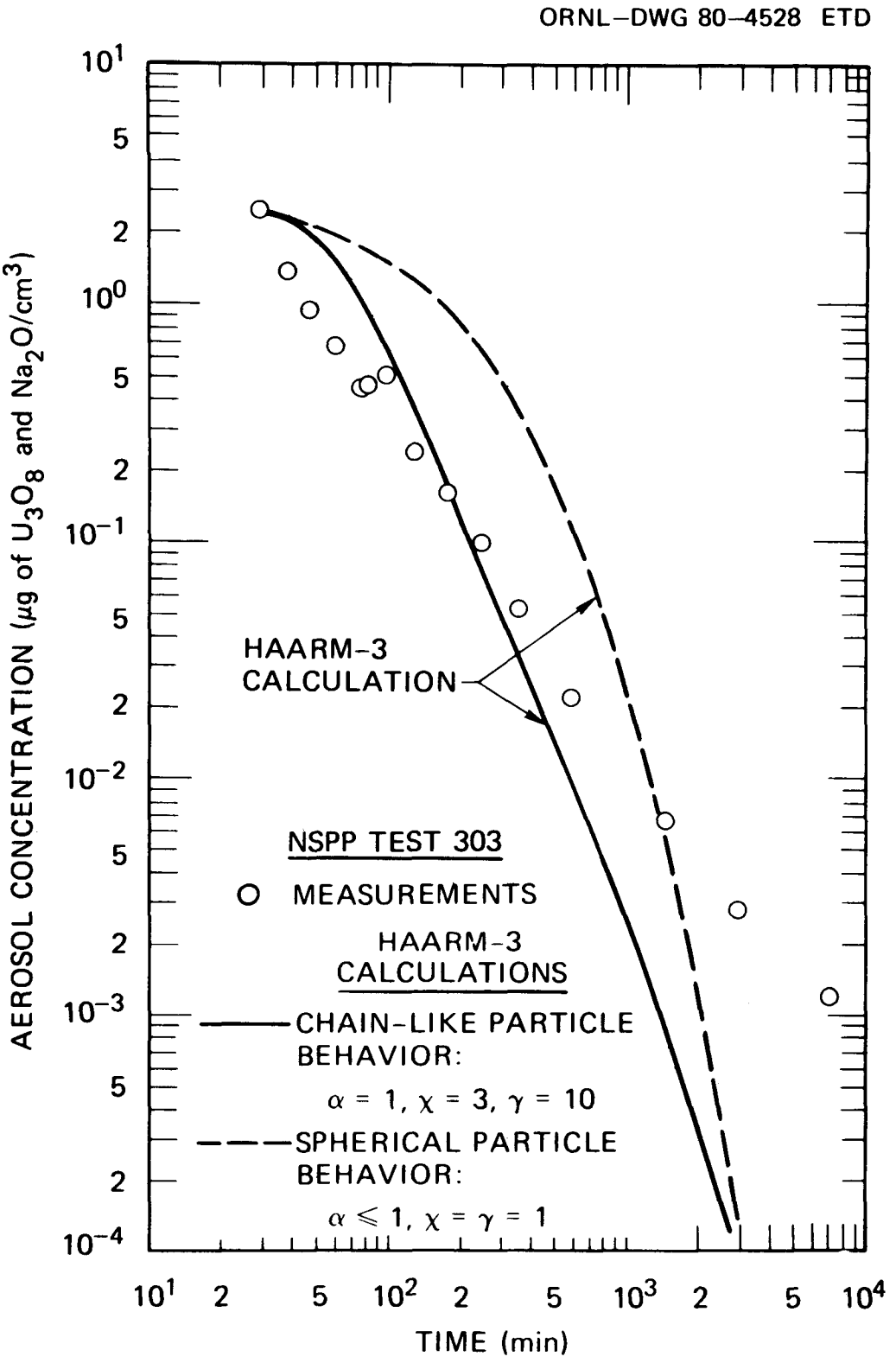

Fig. 8. Comparison of HAARM-3 Calculations With Experimental Results From Mixed Oxide Aerosol Run 303

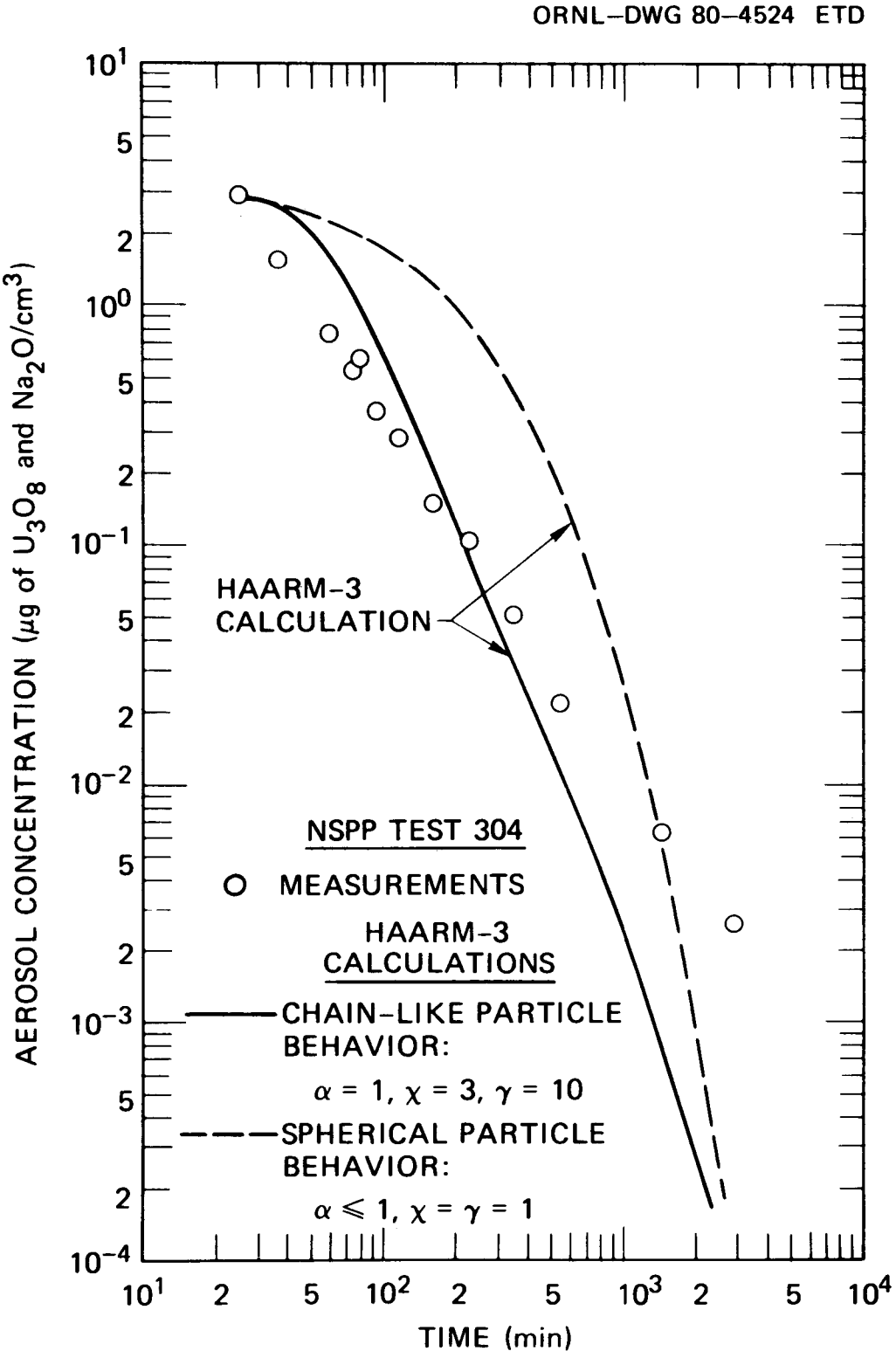

Fig. 9. Comparison of HAARM-3 Calculations With Experimental Results From Mixed Oxide Aerosol Run 304

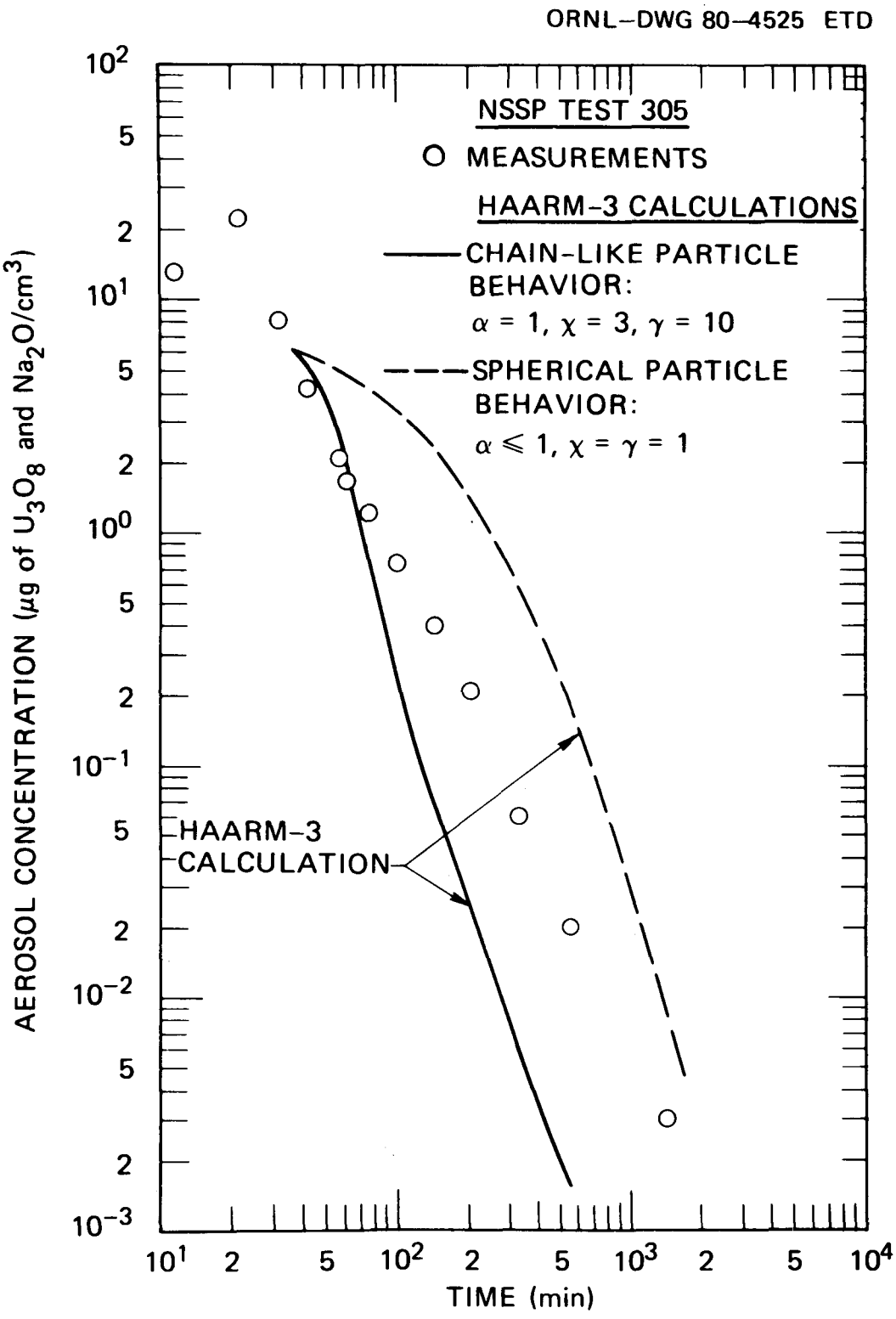

Fig. 10. Comparison of HAARM-3 Calculations With Experimental Results From Mixed Oxide Aerosol Run 305

COMPARISON OF AEROSOL BEHAVIOR DURING SODIUM FIRES IN CSTF WITH THE HAA-3B CODE

A. K. Postma
R. K. Owen
Hanford Engineering Development Laboratory
Operated by Westinghouse Hanford Company for
The U. S. Department of Energy under Contract EY-76-C-14-2170
Richland, Washington, U. S. A.

ABSTRACT

Four large-scale tests using sodium fire aerosol sources have been carried out in the Containment Systems Test Facility (CSTF). Two of the tests employed pool fires and two used spray fires as the aerosol source. Because the CSTF containment vessel is approximately half-scale (20.3 m in height) of a typical reactor building, the CSTF results have provided a large-scale proof test of the HAA-3B Code.

For the two pool fire tests, the measured and predicted airborne concentrations were in good agreement when the aerosol source term was based on post-test measurements of aerosol formation, accounting for water vapor uptake. When viewed on the basis of leaked mass, predicted and measured concentrations agreed within a factor of 2.

Particle sizes measured in the pool fires attained a peak value of approximately 8 μm AMMD shortly after the fire was extinguished and then decreased with time to 1.5 μm at 10^5 sec. Measured size agreed with the sizes predicted by the HAA-3B Code within ±30 except during the burn period; during which time the predicted sizes were smaller than observed.

INTRODUCTION

A sodium fire within an enclosed space can generate sizable quantities of airborne oxide particles as an aerosol. The aerosol mass concentration of these particles can be high and represents a potential source of leakage from containment when coupled with the thermally produced over-pressure.

To assist in the understanding of the consequences of such fires, a series of tests is in progress in the Containment Systems Test Facility (CSTF) at the Hanford Engineering Development Laboratory (HEDL) under the sponsorship of the U. S. Department of Energy. These tests have included studies of aerosol behavior and containment response for both pool fires [1] and

spray fires [2]. These tests are designed to provide characterized sodium fire aerosols for comparison with aerosol code predictions, and to provide test data of pressure and temperature transients during the fires.

The objective of the present paper is to show the degree to which the observed aerosol behavior agrees with predictions made by the HAA-3B Code.

EXPERIMENTAL FACILITY AND PROCEDURE

The CSTF is shown schematically in Figure 1. The chief feature is the 850-m^3, 20-m high model containment vessel. It is a carbon steel vessel designed for 0.517 MPa pressure and 0.1%/day leakage. The inner surfaces are coated with a modified phenolic paint and the outer shell is covered with 25.4 mm thick fiberglass insulation. Two windows are provided for visual and camera observations.

Sodium at up to 650°C can be supplied to the vessel from two supply tanks of 1700 and 115-liter capacity. Aerosol samples can be taken through four airlock penetrations at various elevations and by ten remote cluster samplers located throughout the vessel atmosphere. Extensive thermocouple, gas analysis, aerosol characterization and data acquisition instrumentation is provided.

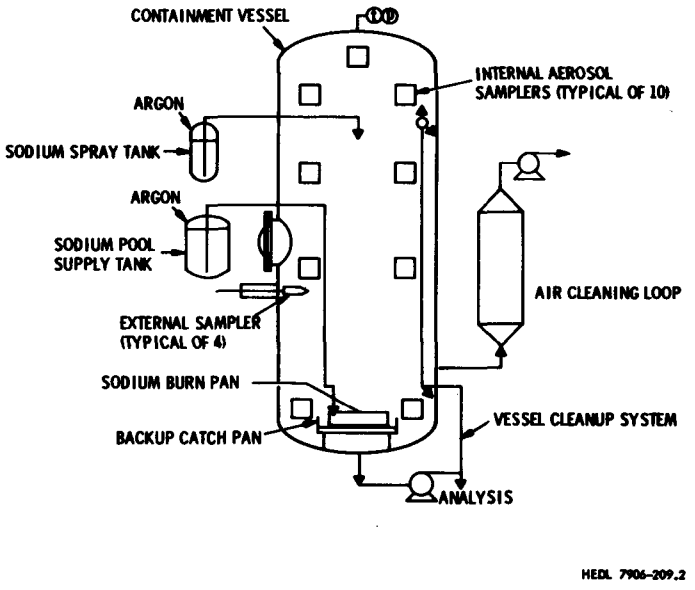

Fig. 1 Containment System Test Facility Schematic

Pool Fire Aerosol Source

The test arrangement used in the pool-fire tests is shown schematically in Figure 1. As indicated, the vessel was equipped to contain a sodium pool fire of definite duration and provided various instrumentation and sampling equipment required to characterize the aerosol.

Prior to the test, sodium was heated to 600°C in a 1.7-m^3 vessel constructed of Type 304 stainless steel (SS). At time zero (t_o) a valve was opened and argon pressure forced sodium through a 2-in. schedule 40 pipe 52.5-mm ID) into a carbon steel pan centered near the bottom of the containment vessel. The burn pan, which was 0.36-m deep and had a rectangular cross section 1.81 m x 2.42 m, rested on insulating firebrick and its sides were insulated. The pan's hinged, gasketed lid permitted termination of the aerosol source on command.

Conditions for the two pool fire tests are summarized in Table 1.

TABLE I

TEST CONDITIONS FOR CSTF TESTS AB1 AND AB2

SODIUM SPILL	AB1	AB2
Mass sodium spilled (kg)	410	472
Sodium burn pan surface (m^2)	4.4	4.4
Initial sodium temperature (°C)	600	600
Sodium fire duration (s)	3600	3600
Total sodium oxidized (kg)	157	175
STEAM ADDITION		
Flow started (seconds after t_o)	-	960
Flow stopped (seconds after t_o)	-	4560
Flow rate (kg/s)	0	0.019
INITIAL CONTAINMENT ATMOSPHERE		
Oxygen (Vol%)	19.8	20.9
Dew Point (°C)	10.0	7.6
Temperature (°C)	26.5	20.5
Pressure (MPa, absolute)	0.125	0.128

Spray Fire Source

Two sodium spray tests were performed in the CSTF as part of a continuing test series. The test conditions are listed in Table II. Test AB3 was a short duration spray (140 s), while test NT1 lasted 4.7 hrs. Both tests used commercial spray nozzles which sprayed downward from a height of 16 m above the floor of the CSTF vessel. With this fall distance most of the drops were expected to burn before contacting the catch pan so that aerosol would result primarily from the spray and not from a pool fire in the catch pan.

Sodium flow to the nozzles was controlled by keeping a constant argon cover gas pressure on sodium in the supply tank. The amount of sodium delivered to the system was determined by the tank weight change and confirmed by determining the sodium recovered from the vessel washes at the test conclusion.

TABLE II

SUMMARY OF CONDITIONS FOR SPRAY FIRE TESTS AB3 AND NT1

Spray Parameters	AB3	NT1
Number of nozzles	2	1
Nozzle manufacturer	Spraying Systems Co.	Spray. Sys. Co.
Catalogue number	3/8 BA15	1/4 B1
Nozzle orientation	Downward	Downward
Pressure drop across nozzle, psid (MPa)	40 (0.276)	10/40 (0.068/0.276)
Total Na flow rate, kg/s	0.34	0.0034 for $1x10^4$s 0.0058 for $6.7x10^3$s
Na Temperature °F (°C)	1110 (600)	1011 (545)
Spray drop size, μm, MMD	670	380/320
Drop size standard deviation σ_g	1.5	1.5
Spray duration, seconds	140	1.7×10^4
Total Na sprayed, kg	48	82
Nozzle height above floor, ft (m)	54 (16)	54 (16)
Initial CV Atmospheric Conditions		
Composition	Normal Air	Normal Air
Temperature, °F (°C)	66.0 (19)	72 (22)
Pressure, psia (MPa)	18.1 (0.125)	18 (0.124)
Dew Point, °F (°C)	42 (5.6)	50 (10.1)

Aerosol Characterization Methods

The aerosol was characterized by withdrawing samples through various instruments. The aerosol characterization methods used are summarized in Table III.

TABLE III

AEROSOL CHARACTERIZATION METHODS USED

Parameter	Measurement Method
Mass Concentration	Filter Samples
Particle Size	Cascade Impactors Concentration Decay Horizontal Elutriator Deposition Coupons
Wall Deposition Fraction	Post-Test Water Wash Swipes
Fraction Aerosolized	Post-Test Water Wash

COMPARISON OF AEROSOL BEHAVIOR WITH PREDICTION

Airborne Mass Concentration

Airborne mass concentration predicted by the HAA-3B code [3] prior to test completion for the pool fire tests is exhibited in Figure 2. As indicated, the fraction of burned sodium emitted as an aerosol was treated as a parameter and was varied from 10 to 40%. Sodium burning rates calculated from the SOFIRE-II Code [4], multiplied by an aerosolization factor were used to obtain the particle source rate.

Based on data from earlier sodium fire tests, [5] it was anticipated that somewhere between 20 and 30% of burned sodium would be released from the pool as an aerosol.

From the comparison of predicted and measured concentrations shown in Figure 2, generally good agreement is apparent. At early times (<1000 s) the code underpredicted the concentration. This discrepancy can be attributed mainly to uptake of water vapor by particles of Na_2O_2. Test AB2 results fall above the predictions after the aerosol source was terminated. Water vapor uptake caused a more rapid fallout during the fire period and, based on sodium released as an aerosol, a slightly higher attenuation factor was achieved by settling in AB2 than in AB1.

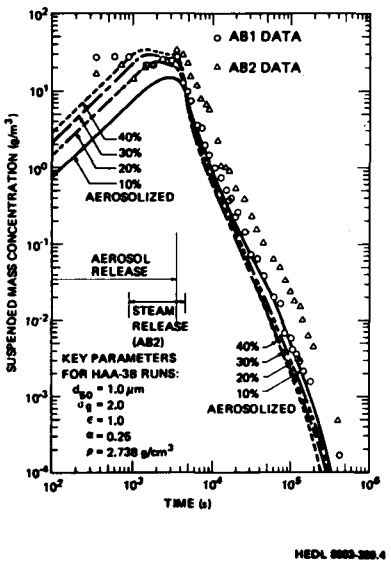

FIGURE 2. Pretest Predictions Made by the HAA-3B Code.

Post-test predictions were made on the basis of an experimentally derived source rate, and the value of the density modification factor which appeared to best fit the experimental data. The following plausible assumptions were used to compute the source rate:

- The mass of sodium aerosolized was obtained from test results,
- Sodium aerosol production rate was assumed to be proportional to oxygen concentration,
- Aerosol particles were assumed to be in equilibrium with available water vapor, [6] and
- Water vapor uptake was counted as an aerosol source.

Comparisons between experiment and theory for AB1 are made in Figure 3. A very good fit is obtained when $\alpha\varepsilon$ is assigned a value of 0.20. Predictions based on an $\alpha\varepsilon$ product of 0.20 agrees best with the measured concentrations near the maximum. When $\alpha\varepsilon$ is assigned a value of 0.10, the maximum concentration is overpredicted.

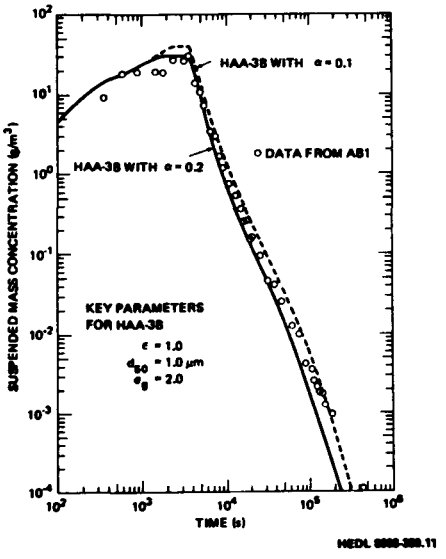

FIGURE 3. Comparison of Measured and Predicted Aerosol Concentrations for Test AB1.

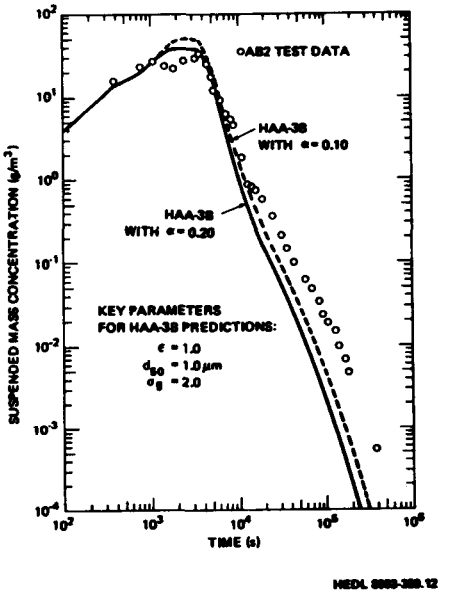

FIGURE 4. Comparison of Measured and Predicted Airborne Concentrations in Test AB2.

Predicted and measured airborne mass concentrations for Test AB2 are compared in Figure 4. The prediction based on an $\alpha\varepsilon$ product of 0.20 agrees best with the measured concentrations near the maximum. When $\alpha\varepsilon$ is assigned a value of 0.10, the maximum concentration is overpredicted.

The aerosol mass concentration in AB3 is shown as a log-log plot in Figure 5. The experimental points are the mean values of 12 filter samples for test AB3 taken at various locations from high to low in the vessel. The concentration is plotted as total mass. The post-test predictions made by the HAA-3B code are also shown in Figure 5 for two aerosol release fractions. The code overpredicted concentration for the first few minutes, but underpredicted at longer times.

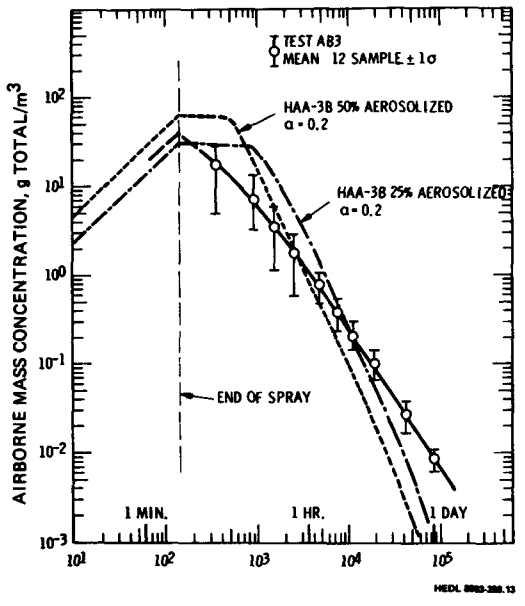

FIGURE 5. Measured and Predicted Airborne Concentration Test AB3.

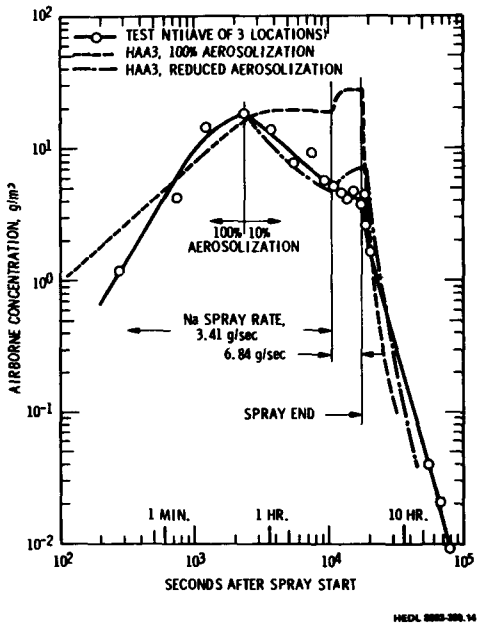

FIGURE 6. Measured and Predicted Airborne Mass Concentration, Test NT1.

Similar information is shown in Figure 6 for the low spray rate test NT1. In both tests the code predicted higher concentrations than were measured. These results can be explained by a high rate removal process operating during the spray which would reduce the airborne concentrations and, hence, also reduce the particle size. The smaller particle size would then remain airborne longer because of reduced settling and deposition rates. We do not know what the removal process may be, but at the conclusion of these tests heavy deposits on the top dome and gratings in the CV were noted. A second possibility for the low concentrations is a lower than expected aerosolization. The apparent reduction in aerosol generation during the

NT1 spray may be related to crust formation around the nozzle which distributed the spray pattern. Such crusts have been observed in subsequent tests in the CSTF to reduce the fractions aerosolized. To estimate the possible effects of the nozzle crusting, Figure 6 also gives concentration for a spray which releases 100% of the spray as aerosol until 2.3×10^3 seconds. The fraction aerosolized is then decreased to 10% until the end of the spray. An improved fit to the experimental data was obtained, thus suggesting that the source rate may not have been constant during the tests.

Aerosol Mass Leaked

The most important function of an aerosol behavior model is the prediction of the mass of material that could leak from a vessel over a specified time period; therefore, the most sensitive test of code adequacy is its ability to correctly predict leaked mass. Leaked mass was computed from the measured concentrations in both tests using

$$\text{Mass Leaked} = \int_0^t QC_g dt \qquad (1)$$

Where:

Q = Leak flow rate (m^3/s),
C_g = Airborne mass concentration (g/m^3), and
t = Time (s).

Leak flow rate Q was assigned a value of 0.1% of contained gas volume per day, and decontamination within the leak path was neglected in the calculations of leaked mass presented herein. Equation (1) was numerically evaluated from smoothed concentration data and by the HAA-3B Code.

Calculated values of mass leaked are presented in Figure 7 for Test AB1. Predictions based on an $\alpha\varepsilon$ product of 0.2 and the time-dependent source rate which accounted for water vapor uptake are in near-perfect agreement with test results. When $\alpha\varepsilon$ is assigned a value of 0.1, test results are overpredicted for times longer than 30 seconds.

Leaked masses for Test AB2 are shown in Figure 8. As was the case for Test AB1, predictions agree with experiment when $\alpha\varepsilon$ is assigned a value of 0.20 and the source rate is computed to account for water vapor sorption. The goodness of fit between predictions and experiment is better for leaked mass than for the suspended concentrations because deviations evident in Figure 4 occur at low mass concentrations and, therefore, contribute little to leaked mass.

HAA-3B code calculations of the integrated mass leaked (at an assumed contant 0.1%/day leak rate) are shown in Figure 9 for two aerosol releases for test AB3. Leakage calculated from the test data is also given. The code provides a conservative estimate. Note also that most all of the leakage occurs during early times, and that the fraction aerosolized has only a minor effect on the total mass leaked.

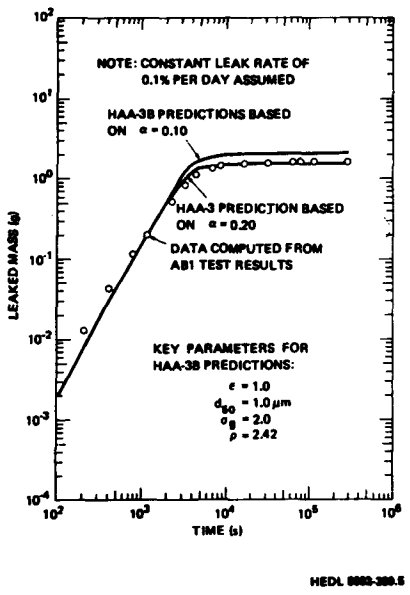

FIGURE 7. Comparison of Predicted and Measured Aerosol Mass Leaked for Test AB1 When Water Vapor Uptake is Accounted For.

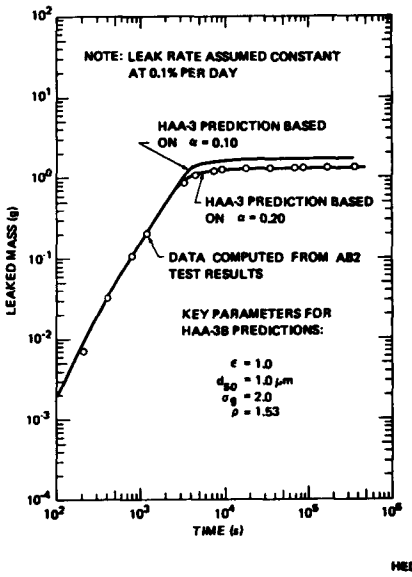

FIGURE 8. Comparison of Predicted and Measured Aerosol Mass Leaked for Test AB2 When Water Vapor Uptake is Accounted For.

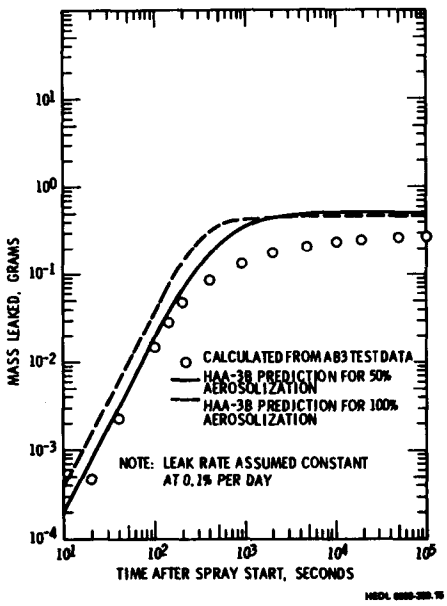

FIGURE 9. Measured and Predicted Aerosol Leakage from Containment.

Aerosol Particle Size

The effective settling diameter, which characterizes the mass settling rate, is related to the mass median particle diameter by equation (2).

$$(d_s)_a = AMMD \exp(\ln^2 \sigma_g) \quad (2)$$

Where:

$(d_s)_a$ = Aerodynamic settling mean diameter,

AMMD = Aerodynamic mass median diameter, and

σ_g = Geometric standard deviation.

Settling mean diameters computed from cascade impactor data and settling measurements are compared with HAA-3B code predictions for Test AB1 in Figure 10. Very good agreement is apparent except for the earliest sample. Agglomeration in the sodium burning zone and in the plume apparently caused significant particle growth.

A settling mean particle diameter was computed from the concentration decay curve measured after the aerosol source was terminated. The variation in settling mean diameter calculated in this way is shown in Figure 10 as a dashed line. Very good agreement with the line calculated from the HAA-3B code is apparent.

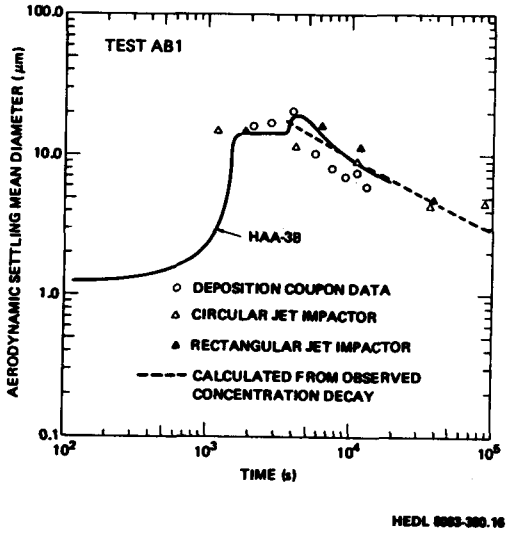

FIGURE 10. Comparison of Measured and Predicted Settling Mean Particle Diameters in Test AB1.

Aerodynamic settling diameters that were computed from AB2 test results are shown in Figure 11. Particle diameters computed from cascade impactor data agree quite well with HAA-3B predictions except for the early sample. The circular jet impactor sample withdrawn at 1080 seconds indicated a particle diameter of 27.6 μm. The large diameter calculated from the first impactor sample reflected an unusually large standard deviation (3.8) obtained from a graphic plot of stage mass accumulations. This large standard deviation was singularly high and may be erroneous. On the other hand, the deposition coupon data agreed quite well with the cascade impactor for this early sample.

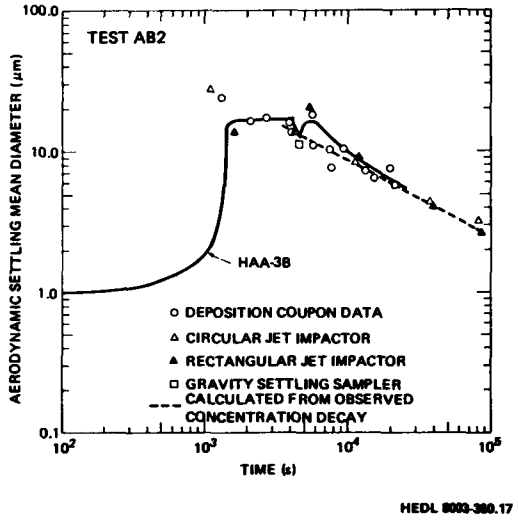

FIGURE 11. Comparison of Measured and Predicted Settling Mean Particle Diameters in Test AB2.

Figure 12 presents the particle sizes measured for test AB3 using two types of cascade impactors. The sizes calculated by HAA-3B for the 50% aerosolization case show a good agreement to the measured sizes. Figure 12 also plots the size derived from the mass concentration changes within containment, assuming that gravity settling was the only removal mechanism. Again, good agreement is obtained.

Plated Mass

Wall deposition of particles is computed in HAA-3B as though the plateout rate were contolled by diffusion across a boundary layer of thickenss Δ:

$$\text{Plateout Rate} = \frac{(C_g - C_w)DA_w}{\Delta} \qquad (3)$$

Where:

C_g = Particle concentration in bulk gas,
C_w = Particle concentration in gas at surface, assumed to be zero,
D = Particle diffusivity,
A_w = Wall area for plateout, and
Δ = Thickness of boundary layer.

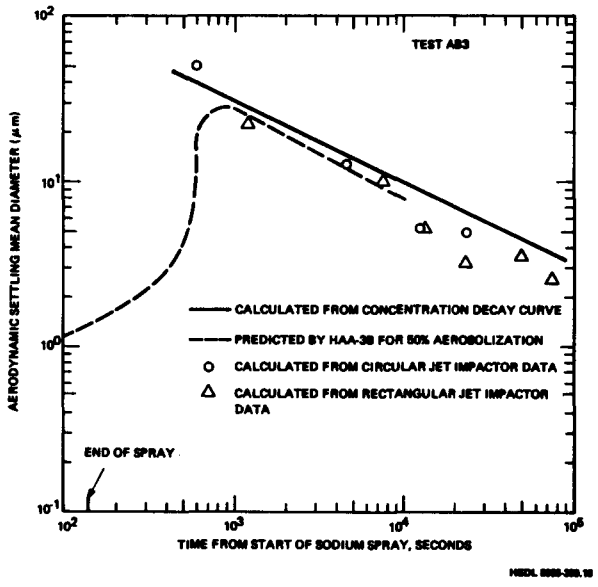

FIGURE 12. Measured and Predicted Particle Sizes, Test AB3.

In the HAA-3B runs made for Tests AB1 and AB2, the boundary layer thickness was assigned a value of 1.6×10^{-5} cm and the wall area, accounting for internal structures, was assigned a value of 1000 m^2. This area is 1.92 times the area of the outer vessel wall (520 m^2). Plateout fractions measured in Tests AB1 and AB2 are compared to HAA-3B predictions in Table IV.

Visual observations of the wall deposit suggested that most deposition occurred by a process other than diffusion. Vertical walls were covered with a very thin layer of fine oxide particles plus larger spotty deposits of oxide several millimeters in diameter, which protruded outward by as

TABLE IV

COMPARISON OF MEASURED AND PREDICTED PLATEOUT IN CSTF POOL-FIRE TESTS

Test Number	Fraction of Aerosol Mass Plated	
	Predicted[(a)]	Measured
AB1	0.094	0.084
AB2	0.063	0.069

(a) Using $A_w/V = 1.176\ (-2)\ cm^{-1}$, $\Delta = 0.16\ \mu m$

much as several millimeters and were spaced about 10 mm apart. Some larger spots, 10 to 20 mm in diameter, protruding as much as 6 mm from the wall, were also present. The density of the wall deposit was strongly affected by outward projections and wall roughness. These observations suggested that wall deposits formed mainly by two processes: 1) small roughness projections captured moving particles by impaction, and 2) particles were deposited by turbulent deposition when the boundary layer was disturbed by a surface irregularity.

CONCLUSIONS

The comparisons between the large-scale pool and spray fire aerosol tests and HAA-3B predictions have shown the code to be a good predictor of the most important aspects of aerosol behavior. The following conclusions and summary statements are supported by the work completed.

- Airborne mass concentration and leaked mass were accurately predicted by the code when the correct aerosol source was employed.
- Optimum agreement between theory and experiment was obtained when the $\alpha\varepsilon$ product was assigned a value of 0.20. This value is close to values obtained from smaller-scale experiments at Atomics International [3] and from single-particle measurements made at Battelle, Columbus Laboratory [7].
- Predicted values of airborne mass concentration and leaked mass were quite insensitive to input parameters such as source particle size distribution and floor area.
- For times longer than $\sim$1000 s, the predicted and measured particle size distributions agreed very well; at shorter times, the code underpredicted particle size. This discrepancy is thought to have resulted from agglomeration of particles in the burning zone and in the plume above the source, which is not fully accounted for by the model.

- Plated mass agreed with the predicted value when a Δ of $\sim$1.6 x 10^{-5} cm was used. This boundary layer thickness appears to be unrealistically small. Visual observations of the spotty wall deposit suggested that mechanisms other than diffusion controlled wall deposition; however wall deposition is a minor removal mechanism in large containment vessels, so imprecise predictions of this quantity have little impact on controlling aspects of aerosol behavior for full-scale reactor plants.

- The discrepancies which were identified introduce conservatism into the model and if model improvements were made, only small changes in predicted accident consequences would be expected.

REFERENCES

1. R. K. Hilliard, J. D. McCormack and A. K. Postma, "Aerosol Behavior During Sodium Pool Fires in a Large Vessel -- CSTF Tests AB1 and AB2," HEDL-TM 79-28, Hanford Engineering Development Laboratory, Richland, Washington (1979).

2. J. D. McCormack, R. K. Hilliard, A. K. Postma, and R. K. Owen. "Aerosol Behavior During Sodium Spray Fires," Proceedings of ANS-ENS International Meeting on Fast Reactor Safety Technology, Seattle, Washington, August 19-23, 1979 (pp 823-831).

3. R. S. Hubner et al. "HAA-3 User Report," AI-AEC-13088, Atomics International, March 30, 1973.

4. P. Beiriger et al. "SOFIRE-II User Report," AI-AEC-13055, Atomics International, March 30, 1973.

5. R. K. Hilliard, "Summary of HEDL Sodium Fire Tests," HEDL-SA 1669, Hanford Engineering Development Laboratory, November 1978. Paper presented at IAEA/IWGFR Specialists' Meeting on Sodium Fires and Prevention, Cadarache, France, November 20-24, 1978.

6. Chemical Engineer's Handbook, J. H. Perry (ed.), 3rd ed., McGraw-Hill Book Co., NY, 1950, p. 173.

7. J. A. Gieseke et al. "Characteristics of Agglomerates of Sodium Oxide Aerosol Particles, BMI-NUREG-1977, Battelle, Columbus Laboratories, August 1977.

ANALYTICAL STUDIES ON URANIUM OXIDE, SODIUM OXIDE AND THEIR MIXED AEROSOLS BY USING ABC-3B

N. Mitsutsuka
Power Reactor and Nuclear Fuel Development Corp.
Tokyo, Japan

H. Obata
Century Research Center Corp.
Tokyo, Japan

ABSTRACT

The behavior of uranium oxide, sodium oxide and their mixed aerosols was studied using ABC-3B code. The code was partly revised to treat aerosol size distribution more reasonably and to account for shape factors. Comparison of code prediction by using apparent density value of 0.4 to 1.0 g/cm^3 with former JAERI experiment results on uranium oxide aerosol showed better agreement compared with the former calculations by using ABC-2. The best matched result was obtained at 3.42 dynamic shape factor and 1.14 collision shape factor. Sodium oxide aerosols can be predicted tolerably well by using 0.3 g/cm^3 apparent density, as have been reported previously. They are better predicted by using 2.1 dynamic shape factor and 2.3 collision shape factor. Only limited case was studied on mixed aerosols, their shape factors found to be an intermediate value between uranium oxide and sodium oxide values.

INTRODUCTION

Analysis of nuclear aerosol behavior, associated with postulated reactor accidents, is of particular importance for the assessment of their radiological consequences. In liquid metal fast breeder reactors, aerosols include sodium oxide and plutonium oxide and uranium oxide fuels. In Japan, research on sodium oxide and fuel aerosols started for the licensing of Japanese experimental fast breeder "JOYO". A series of aerosol experiments were performed at JAERI using a 1 m^3 closed vessel [1], [4]. A code for the analysis of Aerosol Behavior in Containment, "ABC", was also developed by JAERI [2], [3].

Comparison of the ABC prediction with test data and its revision have been conducted by PNC. The analysis of the test data from the JAERI vessel and from the LTV of AI gave good agreement concerning the sodium aerosol [6]. Regarding uranium oxide and mixed aerosols, however, a discrepancy exists between the test data and the code prediction.

In the present work, the JAERI test data on uranium oxide and mixed aerosols [5] were analyzed by the ABC-3B code. During the course of the study, the code was revised to allow a wider range radii analysis and to account for shape factors, for better prediction of the test data.

ANALYTICAL PROCEDURE

ABC-3B Description

Detailed ABC code descriptions have been presented elswhere [2], [3]. The code features treating aerosol particle size distribution with a finite set of descrete size particle classes. Such aerosol processes as agglomeration, gravitational sedimentation, diffusion plate out and leakage to the secondary containment are calculated by solving a finite set of ordinary simultaneous differential equations by the Runge-Kutta method. ABC-3B is the newest version and includes all the aerosol processes which were used in the former ABC versions and gravitational agglomeration [7]. The numerical algorithm is also improved to treat the mass conservation more strictly and to afford long time range calculations.

Numerical Treatment of Aerosol Particle Size Distriubtion

Aerosol particles are known to have a log-normal distribution. Two methods are applied in ABC-3B to treat the aerosol distribution numerically. One is to divide it into constant radius increment classes, which was originally used in ABC-1. The other is to divide it into constant volume increment classes, which was orignally used in ABC-2. The former method can treat the aerosol distribution over a wider particle radii range than the latter, under a limited number of classes. However, particle radii range to be treated is limited by the number of classes, even if the ABC-1 method is used. For example, to cover up to 5 μm particle radius in 100 classes, the smallest particle size is limited to 0.05μm. Moreover, the classing method inevitably supplys rough particle size meshes for smaller

particles. To supply reasonable particle size meshes over a wide particle size range, another classing method, geometric classing, was developed. In geometric classing, aerosol particle volume between the smallest (V_{min}) and the largest volume (V_{max}) are divided into n classes. The volume of the ith class particle, V_i, is expressed as follows:

$$V_i = V_{min} x^{i-1}, \tag{1}$$

where
$$x = \sqrt[n]{\frac{V_{max}}{V_{min}}} . \tag{2}$$

Figure 1 gives examples of each classing method for a log-normal distribution. In the geometric classing, the differences in logarithmic particle volume and radius between ith and (i+1)th classes are constant as $\ell n\ x$ and $\ell n(1/3x)$, respectively. Therefore, count median radius can be obtained directly from the distribution.

Shape Factor

ABC code was made as to use actual particle radii and to correct the aerodynamic nature by apparent density [7]. Recently, two other shape factors, dynamic shape factor χ and collision shape factor γ, are being used in several codes [9], [10]. The following revision was made to ABC-3B to account for the above shape factors.

The diffusivity of ith class particle due to Brownian motion is given as follows by using X,

$$D_i = \frac{\kappa T}{6\pi X \mu R_i} \left(1 + \frac{A_i}{R_i}\right) , \tag{3}$$

where κ is Boltzman's constant, T is absolute temperature, μ is the viscosity, R_i is radius of ith class particle and A_i is the Stokes-Cunningham correction factor.

The settling velocity of the ith class particle V_i is given as follows,

$$V_i = \frac{2\ \rho\ g}{9\ X\ \mu} R_i^2 \left(1 + \frac{A_i}{R_i}\right), \tag{4}$$

where ρ is the density of the particle and g is the gravitational constant.

Assuming collision shape factor Γ is constant, agglomeration rate constants K_B, resulting from Brownian diffusion, and K_G, resulting from gravitational settling, are given as follows:

$$K_B = 4\pi\ (D_i + D_j)\ (R_i + R_j)\Gamma, \tag{5}$$

$$K_G = \pi(R_i + R_j)^2\ |\ V_i - V_j\ |\ \Gamma^2 . \tag{6}$$

RESULTS AND COMPARISON WITH EXPRIMENTS

In the previous JAERI experiments, airborne mass concentration, settling flux and particle size distribution were measured by using the 1 m^3 vessel [5]. Apparent density of the aerosols was estimated by using the above mentioned experimental data, assuming that airborne particles have the same distribution as the settled particles and follow Stokes' law of gravitational sedimentation. Hereafter, ABC code predictions will be compared with the experimental data, by changing such input parameters as apparent density and shape factors.

Apparent Density Effect

In order to study apparent density correction effectiveness for uranium oxide aerosol behavior prediction, airborne mass concentration changes were calculated by ABC-3B, changing the apparent density values. The results are given in Fig. 2, together with the experimental data. Solid lines in the figure show the code predictions at apparent density values of 0.4, 0.6 and 1.0 g/cm^3, respectively. Initial airborne mass concentration was assumed to be 2×10^{-7} g/cm^3 and initial particle size distribution was assumed to be a log-normal distribution of 0.3 μm in count median diameter and 1.90 in geometric standard deviation.

The broken line in the figure shows the former prediction by using ABC-2 [6]. In the former prediction, airborne particle gravitational sedimentation rate was evaluated to be 10 times higher due to inadequate selection of the experimental condition data input, which resulted in a quicker decrease in airborne mass concentration.

By using the proper sedimentation rate, code predictions give better agreement. However, a tendancy exists to give lower concentrations in the early stage (up to 700 minutes) and higher ones in the later stage (after 1000 minutes). Such a discrepancy cannot be overcome by simply selecting the apparent densities.

Figure 3 gives the predicted aerosol particle size distributions with lapse of time at 0.6 g/cm^3 apparent density value. The count median radius increases from 0.3 μm at the beginning to 0.7 μm at 255 minutes, whereas the measured aerosol radii were less than 0.34 in count median radii. The above discrepancies suggest the necessity to account for such shape factors to correct both aerodynamic nature and collision efficiency for aerosol particles.

Shape Factors Effect

Generally speaking, terminal settling velocities for non-spherical aerosol particles are slower than those calculated by using Stokes' equation. A factor κ is used to correlate Stokes' terminal velocity v_s to the accutual settling velocity v_c, as follows,

$$v_c = \kappa\, v_s = \frac{2\kappa\rho g R^2}{9\mu}\left(1 + \frac{A}{R}\right), \qquad (7)$$

where ρ is aerosol particle density. As was mentioned in the previous section, apparent density ρ_o was estimated from the settling flux and includes a correction to the non-spherical effect:

$$\rho_o = \kappa \rho . \tag{8}$$

Pettyjohn reported the following emperical formula for correction factor κ for non-spherical particles in laminar flow water [8],

$$\kappa = 0.843 \log \frac{\psi_w}{0.065} , \tag{9}$$

where ψ_w is degree of sphericity for the particle according to Wadell and is defined as follows:

$$\psi_w = \frac{\text{Volume equivalent sphere surface}}{\text{actual particle surface}}$$

$$\simeq \frac{\text{Particle projection area equivalent circle radius}}{\text{particle projection circumscribed circle radius.}} \tag{10}$$

JAERI measured ψ_w valuse for uranium oxide, sodium oxide and mixed aerosols[5]. Table I lists ψ_w and κ values calculated using Eq. (9).

Correction factor κ corresponds to a reciprocal of the previously mentioned dynamic shape factor X. A parametric survey was accomplished by changing shape factors X and Γ. When dynamic shape factor X is used, aerosol density ρ ($\rho=\rho_o X$) was used to put the initial settling flux equal to the measured values.

Table I Apparent density, degree of sphericity and correction factor for aerosols

	100% U_3O_8	85% U_3O_8+Na_2O	100% Na_2O
ρ_o (g/cm^3) (Initial)	0.57	2.17	-
ρ_o (g/cm^3) (Average)	0.62±0.08	2.70±0.4	0.35±0.05
ψ_w	0.659	0.810	0.833
κ	0.848	0.924	0.934

(a) Uranium oxide

Table II summarizes input parameters for 100% U_3O_8 aerosol analyses. Figure 4 gives code predictions for airborne mass concentration. In order to show the difference in each prediction more clearly, a linear abscissa was used. The above calculations were started at the first measuring point, i.e., 50 minutes after the beginning of the experiment. As was mentioned previously, the prediction by using apparent density

(case 1) gives higher concentrations than the experiment in the later stage. Case 2 ($X=\kappa^{-1}=1.18$, $\Gamma=1.0$) and case 5 ($X=1.5\kappa^{-1}=1.77$, $\Gamma=1/3\kappa=0.59$) show better agreement with the experimental data, among all the cases.

Figure 5 gives the changes in count median radius (r_g) with lapse of time. The predicted r_g values show considerable increases, especially in case 1, whereas the measured r_g values did not show a marked increase. Case 5 shows the smallest increase among the above predictions. Figure 6 gives a log-log plot of the airborne mass concentration for case 5. As was shown in the figure, the code prediction was considerably improved by using shape factors X and Γ.

Table II Input parameters for 100% U_3O_8 analysis

	Case 1	Case 2	Case 3	Case 4	Case 5
ρ (g/cm)	0.57	0.67	0.67	1.01	1.01
X	1.0	1.18	1.18	1.77	1.77
Γ	1.0	1.0	0.59	1.0	0.59

(b) Mixed aerosols

Figure 7 shows code predictions for 85 wt % U_3O_8 and 15 wt % Na_2O mixed aerosols. Input parameters are summarized in Table III. Calculations were started at first measuring point, i.e., 25 minutes after the beginning of the experiment. Case 2 (X = 1.08, Γ = 1.0) and case 6 (X=1.62, Γ=1.0, ρ=2.35) showed better agreement.

Figure 7 shows r_g value changes with lapse of time. Case 4 and case 5 agree well with the experiment.

Table III Input parameters for 85% U_3O_8 analysis

	Case 1	Case 2	Case 3	Case 4	Case 5	Case 6
ρ (g/cm^2)	2.17	2.35	2.35	3.52	3.52	2.35
X	1.0	1.08	1.08	1.62	1.62	1.62
Γ	1.0	1.00	0.54	1.00	0.54	1.00

(c) Sodium aerosol

It has been reported that the ABC code can predict sodium oxide aerosol behavior satisfactorily by using aerosol source distribution of 0.5 μm in r_g and 1.7 in σ_g and 0.3 g/cm^3 apparent density [6].

Broken lines in Fig. 9 give ABC code predictions on the JAERI experiments of 100% Na_2O, by using the above mentioned conditions. As a whole, the predictions show tolerable agreement with the experiments. The solide lines in the figure give predictions using X=1.1 and Γ=1.2. The code predictions are also improved fairly well by using the shape factors in the case of 100% Na_2O aerosols.

DISCUSSIONS

In the present study, projected area equivalent radius (Heywood radius) was used as particle radius, which closely comparable to the actual radius. In some computer codes, shape factors χ and γ are defined as correction factors for the mass equivalent radius [9], [10]. Therefore, some conversions of the currently used shape factors are needed to compare with reported values.

Mass equivalent radius based shape factors χ and γ are given as follows by neglecting the slip correction effect,

$$\chi = X \left(\frac{\rho}{\rho_m}\right)^{-1/3} , \tag{11}$$

$$\gamma = \Gamma \left(\frac{\rho}{\rho_m}\right)^{-1/3} , \tag{12}$$

where ρ_m is material density. Table IV gives χ and γ values for the principal cases, together with other data. The use of apparent density means to use χ and γ, both equal to $\left(\frac{\rho_o}{\rho_m}\right)^{-1/3}$.

Allen et al. reported the dynamic shape factor for mixed oxide fuel aggregates to be 2.85 at 0.5 μm aerodynamic diameter and 1.96 at 1.5μm[11]. Gordon and Gieseke reported 3 or 3.25 χ value for UO_2 aerosol particles[12]. In the PARDISEKO-IIIb code, 3.5 dynamic shape factor is used for UO_2 condensation aerosols [10]. The dynamic shape factor for uranium oxide aerosol in the present study is about 2.6 to 3.4 and shows reasonable agreement with the previous studies.

Particle radii for uranium oxide aerosol did not show a marked increase in the JAERI experiment. The closest matched collision shape factor value of 1.14 is very small, compared with previously reported value of 8.2 by KfK[10].

The χ value for sodium aerosol is much smaller than that for uranium oxide. On the other hand, the γ value is expected to be larger than that for uranium oxide. Only the 85% U_3O_8 mixed aerosol case was analyzed in the present study, the results show intermediate characteristics between uranium oxide and sodium oxide, showing the best matched result at χ=2.28 and γ=1.41.

Table IV Aerosol density and shape factors

	100% U_3O_8			85% U_3O_8			100% Na_2O	
	Case 1	Case 5	Case 2	Case 1	Case 6	Case 2	Caee 1	Case 2
ρ_m (g/cm^3)	7.31	7.31	7.31	6.55	6.55	6.55	2.27	2.27
ρ (g/cm^3)	0.57	1.01	0.67	2.17	2.35	2.35	0.30	0.33
X	1.0	1.77	1.18	1.0	1.62	1.08	1.0	1.1
χ	2.34	3.42	2.61	1.45	2.28	1.41	1.96	2.1
Γ	1.0	0.59	1.0	1.0	1.00	1.00	1.0	1.2
γ	2.34	1.14	2.22	1.45	1.41	1.41	1.96	2.3

CONCLUSIONS

The behavior of uranium oxide, sodium oxide and their mixed aerosols was studied by using ABC-3B code. The code was partly revised to account for the shape factors and to treat aerosol size distribution more reasonably. Comparison of code prediction with former JAERI experiment results gave the best match at 3.42 dynamic shape factor and 1.14 collision shape factor, in case of 100% U_3O_8 aerosol. Sodium oxide aerosols can be predicted tolerably well by using 0.3 g/cm^3 apparent density. They are better predicted by using 2.1 χ value and 2.3 γ value. The shape factors for mixed aerosols are found to be an intermediate value between uranium oxide and sodium oxide values.

ACKNOWLEDGEMENT

The authors gratefully acknowledge useful suggestions of Mr. K. Akagane of FBR Engineering Office and encouragement accorded by Dr. K. Mochizuki of PNC.

REFERENCES

[1] Kitani, S., et al., "Behavior of Sodium Oxide Aerosol in a Closed Chamber," J. Nucl. Sci. Technol., Vol. 10, No.9, p.556 (1973)

[2] Nishio, G., Kitani, S., "A Hazard Analysis of Plutonium Aersol Released in an LMFBR Hypothetical Accident [ABC-Code]," PNC J250 74-25 (1974)
[3] Nishio, G., et al., "Evaluation of Pultonium Oxide Aerosol Release from an LMFBR in a Hypothetical Accident," Nucl. Eng. Design, Vol. 34, No.3, p.417 (1975)
[4] Nishio, G., et al., "Behavior of Sodium Oxide Aerosol in Closed Chamber under Thermal Convection Flow," J. Nucl. Sci. Technol., Vol. 14, No.1, p.12 (1977)
[5] Nishio, G., et al, "Measurement of Aerosol Density of sodium Oxide, Uranium Oxide and Their Mixed Aerosols," JAERI-M-8798 (1980)
[6] Akagane, K., et al., "Analysis of Aerosol Behavior for Fast Reactor Safety," PNC N241 78-06 (1978)
[7] Akagane, K., et al., "Development of a Code for Analysis of Nuclear Aerosol Behavior in Reactor Containment under Fast Reactor Accident Conditions," PNC N241 79-13 (1979) (in Japanese)
[8] Pettyjohn, E. S., et al., Chem. Eng. Prog., Vol. 44, No.2 p.157 (1948)
[9] Gieseke, J.A., et al., "HAARM-3 Users Manual," BMI-NUREG-1991 (1978)
[10] Alexas, A., et al., "Sodium Fire Aerosol Experimental and Analytical Result - Large Scale Tests in FAUNA," Proc. Int. meeting on Fast Reactor Safety Technology, Vol. 2, pp. 874-883, ANS (1979)
[11] Allen, M.D., et al., "Dynamic Shape Factors for LMFBR Mixed-Oxide Fuel Aggregates," J. Aerosol Sci., Vol. 10, p.43 (1978)
[12] Gordon, H., Gieseke, J.A., "Characterization of Agglomerates of UO_2 Aerosol Particles," NUREG/CR-0489, BMI-2009 (1978)

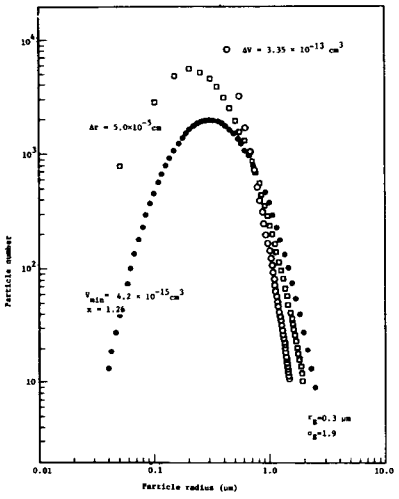

Figure 1 Log-normal particle size distribution by different classing methods

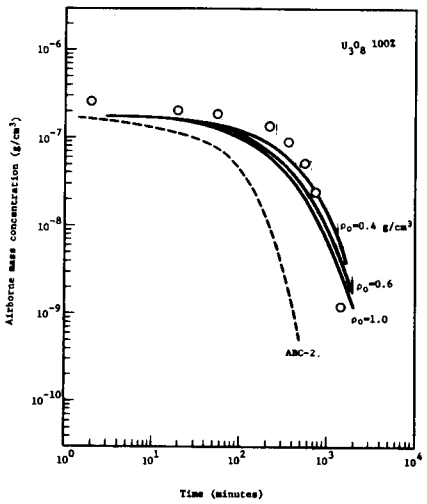

Figure 2 Apparent density effect on uranium oxide airborne mass concentration change

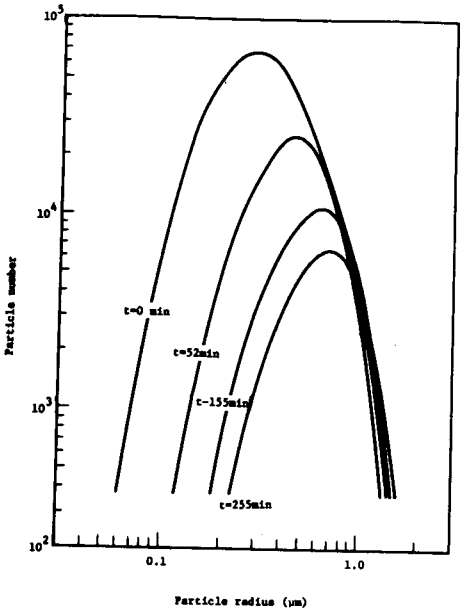

Figure 3 Calculated changes in uranium oxide particle size distribution

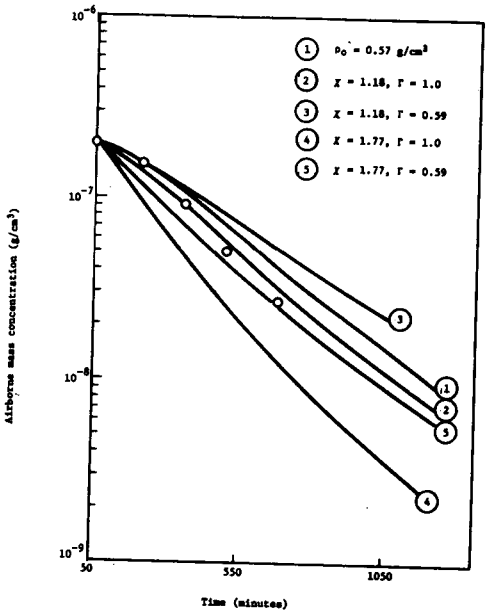

Figure 4 Shape factor effect on uranium oxide airborne mass concentration change

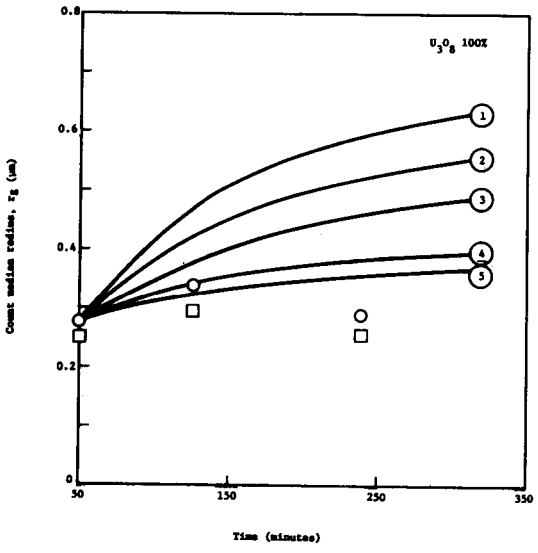

Figure 5 Changes in count median radius of uranium oxide aerosol

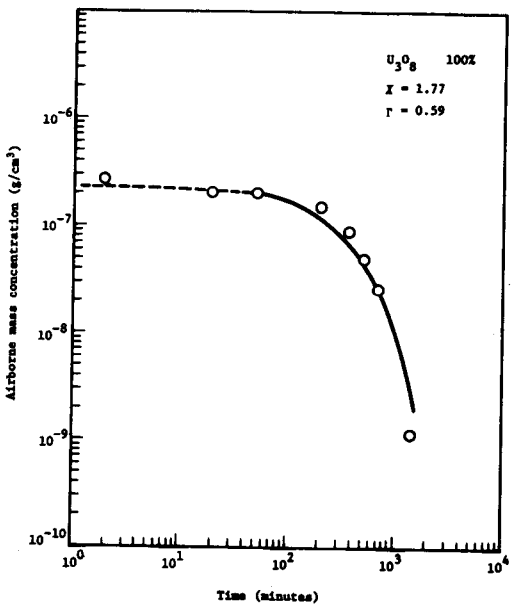

Figure 6 Change in uranium oxide airborne mass concentration

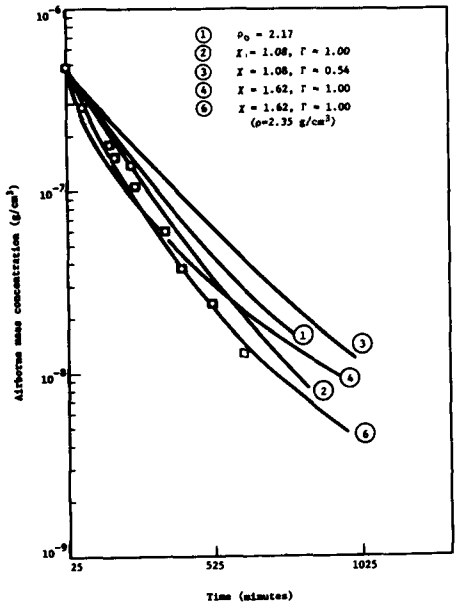

Figure 7 Shape factor effect on mixed aerosol airborne mass concentration

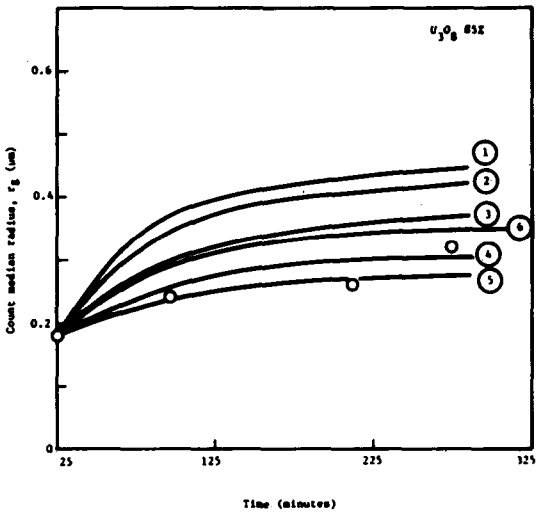

Figure 8 Changes in count median radius of mixed aerosols

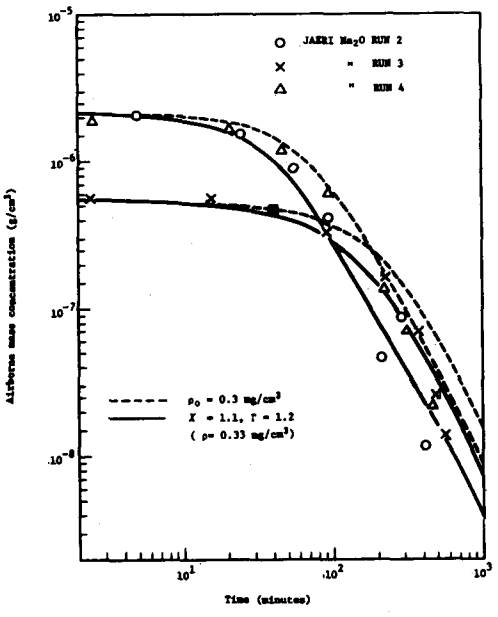

Figure 9 Changes in sodium oxide aerosol airborne mass concentration

APPLICATION OF AEROSOL TECHNOLOGY IN LMFBR DESIGN*

L. E. Strawbridge and E. H. Hemmerle

Westinghouse Advanced Reactors Division
Madison, Pennsylvania 15663
United States of America

CSNI Specialist Meeting on Nuclear Aerosols in Reactor Safety
Gatlinburg, Tennessee
April 15-17, 1980

ABSTRACT

Aerosol technology is applied in several areas in the safety assessment of liquid metal fast breeder reactors. This paper discusses the application of this technology in the assessment of the Clinch River Breeder Reactor Plant. The importance of considering aerosol effects is discussed for sodium fires, the assessment of site suitability and the assessment of the consequences of accidents beyond the design base such as hypothetical core disruptive accidents. Areas in which further development work could have the most impact are indicated.

*This work was performed under U.S. DOE Contract EW-76-C-15-2395.

APPLICATION OF AEROSOL TECHNOLOGY IN LMFBR DESIGN

1.0 INTRODUCTION

This paper focuses on the application of aerosol technology in the design and safety assessment of a Liquid Metal Fast Breeder Reactor, specifically the Clinch River Breeder Reactor Plant (CRBRP). By focusing on the actual application of this technology in a specific plant, guidance can be provided on the range of parameter values of practical interest. Furthermore, the importance of considering aerosol effects in the various safety assessments will be evident. This will permit areas to be identified where future development work could have the largest benefits in terms of reducing uncertainties in aerosol phenomenology.

The areas in which aerosol effects are considered in CRBRP safety assessments include sodium spills in inert and air-filled cells, the assessment of site suitability (based on a containment source term defined by the Nuclear Regulatory Commission), the environmental qualification of equipment, and the assessment of the consequences of accidents beyond the design base such as hypothetical core disruptive accidents (HCDAs). This paper specifically considers a large sodium spill in a deinerted cell, site suitability assessment and HCDA consequences.

The aerosol analyses reported here have used the HAA-3B computer code[1], available from the Argonne Code Center. The analytical model accounts for particle production (source term); Brownian and gravitational agglomeration; and settling, plating and leakage removal mechanisms. The source-term particles are assumed to be evenly and instantaneously distributed throughout the chamber and the particle size distribution is log-normal. The calculation of radiological doses typically uses the COMRADEX-III computer code[2], available from the Argonne Code Center. The input to COMRADEX includes the rate of aerosol depletion as a function of time predicted by the HAA-3B computer code.

2.0 ACCIDENTS WITHIN THE DESIGN BASE

Aerosol phenomenology is applied to assess the consequences of several of the design base accidents that have been postulated for CRBRP. This phenomenology includes both the production and attenuation of sodium and fuel material aerosols. These aerosols with their associated radioactivity control the resultant doses to off-site areas, provide hostile environments for operating equipment in the adjacent areas and impact the operation of on-site equipment following release to the air through mechanisms such as their ingestion by safety related equipment (for example, the emergency diesel generators and the shutdown heat removal system). The Project is considering the effects of aerosols on the design of safety related equipment. The discussion here will be limited to the Site Suitability Source Term and events associated with systems containing primary sodium coolant. These systems are contained within the Reactor Containment Building (RCB) or the Reactor Service Building and aerosol release from these buildings is controlled by confinement and/or filtration.

2.1 SITE SUITABILITY ASSESSMENT

In assessing the suitability of a specific site for the construction of a nuclear power plant, one of the factors considered is the predicted radiological doses resulting from a postulated major core release which has consequences that conservatively envelop all accidents postulated for evaluation during the design. For CRBRP, the source terms for this postulated release have been defined by NRC on a non-mechanistic basis. They consist of the instantaneous release to the RCB atmosphere of 100% of the noble gases, 25% of the halogens, 1% of the fuel material, and 1% of the remaining fission products. The total quantity of aerosol material is 90 Kg of plutonium and uranium-oxide and 5 Kg of fission products. Subsequent to its release from the core, the aerosol material agglomerates and settles to the floor or plates out on the walls of the RCB; the radioactivity decays and a fraction of the suspended material leaks from the building.

The depletion of the airborne aerosol and the amount plated on the walls and settled to the floor are predicted with the HAA-3B code[1]. The aerosol source particle distribution is assumed to be log-normal with a count mean particle radius of 0.1 microns and a geometric mean deviation of 2 microns. The particle density is 10.7 Kg/m^3. The RCB design leakage rate of 0.1% per day is used for the accident duration. The aerosol mass concentration in the RCB as a function of time is shown in Figure 1. The initial concentration is 0.9 gm/m^3.

Of the total leakage from the RCB, 99% is to the confinement annulus which encloses the RCB steel shell. This volume is maintained at a negative pressure with respect to ambient atmosphere. Following RCB isolation in the event of an accident, the air within this volume is recirculated through filters and a fraction (less than 30%) of the filtered air is discharged to compensate for inleakage and to maintain the negative pressure. Of the remaining 1% leakage from the RCB, 0.6 is leaked directly to the outside atmosphere and 0.4 is leaked to the RSB. The latter is filtered before release to the atmosphere.

The off-site exposure from this postulated release is given in Table I. The dose with the least margin to the established limits is the 2 hour bone dose at the site boundary. Aerosol depletion has reduced this dose by about 6 percent. Considerable aerosol attenuation occurs in the longer term. As indicated on Figure 1, less than 1 percent of the initial concentration remains after 10 days. When the radiological releases are weighted by the dispersion factors, the 30 day bone and lung doses are reduced by more than a factor of two as a result of aerosol depletion.

2.2 SODIUM FIRES

A major source of aerosols for CRBRP is the leaking of sodium from equipment and its subsequent burning. Equipment containing primary sodium coolant is normally housed in steel lined cells inerted with nitrogen in which the oxygen concentration is maintained below two volume percent. The small size of these cells, the limited leakage and the low oxygen concentration significantly limit the amount of sodium burning and aerosol generation in the event of a sodium spill.

A major sodium spill from a sodium storage vessel (1.1×10^5 Kg) when the cell containing it is de-inerted for maintenance operations has been postulated to evaluate the adequacy of the RCB design. Normal operating procedures would not permit this large quantity of sodium to be in the storage vessel when the cell is deinerted. In addition, access hatches between the cell and the operating floor of the RCB are assumed open thus making all air above the operating floor available for sodium burning. (The RCB volume above the operating floor is 1.0×10^5 m^3). The rate of sodium burning is predicted with the two cell version of the SOFIRE Code[3] which includes provisions for natural circulation of the atmosphere between the cell and the upper portions of the RCB. It has been conservatively assumed that 27 percent of the sodium monoxide produced is introduced uniformly throughout the upper region of the RCB. The HAA-3B Code is then used to predict the aerosol concentration and the COMRADEX-III Code is used to evaluate the off-site doses. The significant aerosol characteristics for these predictions are a source particle radius of 0.3 microns, a mean deviation of 2 microns and a density of 2.27 Kg/m^3.

Figure 2 shows the aerosol production rate. The total aerosol produced is 28,300 Kg. The oxygen concentration in the RCB atmosphere decreases from 23 percent to 0.7 percent during the 400 hours considered. The aerosol concentration is shown on Figure 3. The peak concentration is 11.5 gm/m^3 at 3 hours and remains above 1.5 gm/m^3 at 400 hours. At this time, the aerosol deposition on the floor of the RCB is 10.8 Kg/m^2 and plateout on the walls amounts to 0.13 Kg/m^2.

The off-site exposure resulting from this postulated event is shown on Table II. The values are low relative to the limits established for judging acceptability. In developing these doses, it has been assumed that the radioactivity contained in the aerosol is equivalent to that contained in the sodium prior to burning and that ten days have elapsed between the initiation of the accident and full power operation of the reactor. The sodium considered is the primary coolant drained from the system to the storage vessel following shutdown.

Aerosol settling has a significant effect on the concentrations within the RCB. This can be seen from Figure 3. The maximum amount of aerosol airborne at any time is less than 1150 Kg, as compared to 28,300 Kg of aerosol introduced into the RCB atmosphere. Significant reduction in the off-site doses results from this depletion. However, the predicted off-site doses would still be small compared to the limits even if no aerosol effects were considered.

The amounts of sodium burning and aerosol production are significantly lower in the equipment cells when the atmosphere is inerted. The largest inerted cell within CRBRP has a free volume of 3230 m^3. Consumption of all the contained oxygen would produce less than 300 Kg of sodium monoxide. While the inerted cells are not specifically designed to retain sodium aerosols, leakage must be very low (0.36% per day at 2.5 inches of water pressure differential) to maintain the required cell atmosphere purity during normal operation. Very little of the aerosol is expected to leak from such steel lined cells.

2.3 ENVIRONMENTAL QUALIFICATION OF EQUIPMENT

Radiation doses and chemical environments resulting from both the site suitability assessment and the large sodium fire are being considered in the development of requirements for the environmental qualification of Class 1E equipment within the RCB. Similar requirements are being developed for mechanical equipment. For safety related equipment outside the RCB, such as emergency diesel generators and the shutdown heat removal system, limiting aerosol conditions arise from consideration of non-radioactive sodium fires in air environments. These accidents are outside the scope of the present paper but are being considered in the design of all safety related equipment.

3.0 ACCIDENTS BEYOND THE DESIGN BASE

The study of consequences of accidents beyond the design base in CRBRP has focused on hypothetical core disruptive accidents. The Project and the Nuclear Regulatory Commission have agreed that the initiators of HCDAs can and must be reduced to a probability low enough to justify their exclusion from the spectrum of design basis accidents. Nevertheless, prudence dictates that additional measures be taken to reduce residual risks from potential accidents having a lower probability than design basis accidents. Accordingly, margins beyond the design base have been included to mitigate the consequences of such low probability accidents.

The overall approach used in providing margins beyond the design base has been described in previous papers [4,5] and will not be repeated here, except where information is required to understand the radiological analyses (including aerosol effects) described herein.

The important features that provide margin beyond the design base and thereby mitigate radiolgoical consequences include:

1. A system that prevents overpressure in the reactor cavity by venting to the upper part of the reactor containment building.

2. A system to permit venting and purging of the reactor containment building to prevent overpressure or excessive hydrogen concentrations.

3. A containment cleanup system that processes all vented or purged materials. This cleanup system is designed to have a minimum efficiency of 99% for vented materials in the solid or liquid state and 97% for vapors (NaI, SeO_2 and Sb_2O_3) subject to condensation in the cleanup system. No credit is taken for removal of noble gases in the cleanup system.

3.1 SOURCE TERMS

The calculation of radiological consequences of an HCDA considers the release to the reactor containment building to occur in phases:

1. An initial release phase that considers potential releases through the reactor vessel head seals and releases through the reactor cavity vent within a few hours after reactor vessel and guard vessel penetration (assumed to occur at 1000 seconds).

2. A sodium boil-up phase that considers releases during the time that sodium in the reactor cavity is boiling (typically 100 to 200 hours).

3. A post sodium boil-dry phase that considers the long term releases from a molten pool of fuel, fission products and concrete.

Table III presents source terms for four cases which involve different initial releases. The initial release depends on the leakage through the head which, in turn, may depend on the energetics assumed to be associated with the HCDA. The best estimate of the consequences of an HCDA in CRBRP is that it would be non-energetic; i.e., no substantial dynamic loads would be imposed on the reactor coolant boundary. Case 1 in Table III is intended to represent this best estimate case. Cases 2, 3 and 4 are intended to represent more pessimistic assumptions on energy release and leak paths through the head. Discussion of the bases for the source terms used in the four cases is provided below.

3.1.1 NON-ENERGETIC CORE MELTDOWN

Initial Release Phase

The initial release phase includes materials that, because of their physical state or high volatility, are not expected to be retained to an appreciable extent in the liquid sodium. For a non-energetic meltdown, 100% of the noble gases (Kr, Xe) and 100% of the more volatile elements (Cs, Rb) are assumed to be released immediately from the molten fuel. Although no appreciable release of these nuclides to the reactor containment building would be expected until after the penetration of the reactor vessel and guard vessel and subsequent release through the reactor cavity vent (beyond 1000 seconds), the radiological analyses conservatively are based on the release at time zero.

Boil-Up Phase

During the sodium boil-up phase the non-gaseous radioactivity trapped in the sodium pool enters the reactor containment building atmosphere as the sodium pool boils.

One hundred percent of the halogens (principally I) and the remaining volatile elements (Se, Sb, Te) are assumed to have been released from the molten fuel, uniformly distributed in the sodium pool, and then released to the reactor containment building atmosphere in proportion to the sodium vaporization (i.e., no credit for partitioning).

It was assumed that after release from the sodium pool 100% of the volatiles will co-agglomerate with sodium based particulates. That assumption is based on two premises. First, the volatiles are in a non-gaseous state (i.e., they are either a liquid or solid aerosol) and as such are capable of agglomerating. Second, an aerosol composed of different chemical species will coagulate into single aggregates and settle as one material.

An evaluation of the first premise, based on the physical conditions associated with the release of volatile fission products from the sodium pool, residence in the reactor containment building and release from the building has been made. The volatiles are assumed to be released from the sodium pool as a gas at a temperature corresponding to the temperature of burning sodium. The time required for these volatile fission products to reach thermal equilibrium with the reactor containment building atmosphere (minutes) is short compared to the average residence time in the building (hours). The reactor containment building atmosphere temperature (peak ∿900°F, average <750°F over the release period) is well below the boiling points of the volatile fission products and their oxides so they would condense to liquids or solids very quickly and have ample time to agglomerate before being vented. Experimental evidence supporting the second premise is reported in Reference 6.

The non-volatile fission products would be quenched in the sodium and form particulates. Based on measurements of particle size distributions in the ANL M-series tests, approximately 15% of the fuel could exist in particles small enough to remain suspended in the sodium pool[7]. These suspended fuel particles would contain a proportionate amount of solid fission products.

Based on a survey[8] of experimental data on liquid carry-over from commercial evaporators and entrainment of solid particles in the vapor stream from an evaporating liquid pool, it was concluded that the decontamination factor (partitioning factor) for plutonium particles would be at least a factor of 1000.

Partitioning of solid fission products in the sodium as it vaporizes is based on the method summarized in Reference 9. The combined partitioning of the fuel and sodium results in a release of 1% of the total non-volatile solid fission product inventory.

The fuel release during the sodium boilup phase is estimated by considering the two attenuating mechanisms discussed above, i.e., 15% of the fuel particulate remaining in suspension following meltdown and reparticulation, and a partition factor of 1000. This would result in approximately 300 grams of plutonium being carried into the RCB atmosphere with the boiling sodium.

Post Boil-Dry Phase

After the sodium pool in the reactor cavity has evaporated, a dry fuel/steel debris bed is left which may then melt into the underlying concrete. Most of the fission product release is expected to occur prior to this time[10]. Potential mechanisms for further release of fission products and plutonium from the dry debris bed are: (1) surface vaporization; (2) particle levitation; and (3) gas sparging. Evaluations of the first two mechanisms indicate that they would result in a negligible contribution to the plutonium release associated with the boiling sodium pool. The volatile fission products are assumed to have been completely released earlier. The non-volatile fission products have vapor pressures similar to or lower than the vapor pressure of fuel[7]. Thus, like the fuel, no significant fraction of the remaining fission products would be released from the molten surface due to the first two mechanisms.

The evaluation of the release of fission products and plutonium due to gas sparging indicates that those products whose releases are enhanced the most by sparging are the more volatile products which the analysis already considers to be totally released. The release of the other less volatile products by sparging is accounted for by the 1% release fraction assigned to the non-volatile fission products in the boil-up phase source term. Plutonium release from the molten pool by sparging could be on the order of 13 Kg over a several month period and this has been assumed to be released to the reactor containment building during the post sodium boil-dry phase. Based on the 99% filter efficiency and taking credit for aerosol fallout and plate-out in the reactor containment building (but not in the reactor cavity), about 45 grams of plutonium could be released to the atmosphere over a several month period beginning at sodium boildry (∿5 days) after the start of the accident.

3.1.2 ENERGETIC HCDA

Initial Release Phase

The case described in Section 3.1.1 is based on the expected consequence of a hypothetical core disruptive accident; namely a non-energetic condition and consequently, no significant immediate release of sodium or non-volatile fission products through the reactor vessel head. Several variations of the expected case were analyzed using successively more pessimistic assumptions on the initial releases through the reactor vessel head.

The second case in Table III is similar to the expected case (Case 1) except that an energetic hypothetical core disruptive accident is assumed. The available work energy, if the fuel vapor were expanded to one atmosphere, is 661 MJ. The fraction of the core inventory of fuel which is vaporized and transported to the cover gas region as a vapor is based on a single hemispherical bubble model which takes no credit for heat losses from the bubble while rising through the sodium pool and core structure[11]. The results of this analysis indicate that 7.3% of the core fuel inventory could reach the cover gas space in the form of vapor. Since the reactor vessel, head and primary system are designed to retain their structural integrity for the dynamic loadings corresponding to the 661 MJ condition, the immediate releases would still be limited. To represent this condition, an immediate release of 1000 pounds of sodium and gas leak rate of 1000 standard cubic centimeters per second for the first 1000 seconds are used.

The combination of the 1000 scc/sec leak rate and aerosol depletion in the cover gas region (which results in very low concentration within 100 seconds) would limit the amount of fuel and fission products in the initial release phase to 0.026% of the core inventory. This fraction was assumed to be released at time zero in Case 2 described in Table III.

The two additional cases evaluated (Cases 3 and 4) arbitrarily employed progressively larger initial releases of fuel, sodium, and the less volatile fission products. These cases were useful to examine the sensitivity of the consequences to releases that are much larger than expected.

Boil-Up Phase

The release associated with the sodium vapor phase for Case 2 is similar to that of Case 1. As Cases 3 and 4 were considered more severe and released more fuel and fission products in the initial phase, correspondingly lesser amounts of these products would be present in the sodium boil-up phase. The source terms for these four hypothetical accident scenarios are summarized in Table III.

Post Boil-Dry Phase

The same considerations apply as discussed for Case 1.

3.2 RADIOLOGICAL DOSE CALCULATIONS

3.2.1 METHODS AND DATA BASE

The radiological release from the reactor containment building to the environment depends on the concentration of suspended radioactivity in the reactor containment building, the pressure, the vent rate from the building (including the effects of purging), and the effectiveness of the containment cleanup system.

The suspended concentration of radionuclides is a function of the source generation rate, the containment vent rate and the aerosol deposition rate. These interacting effects are taken into account using the HAA-3B computer code.

The COMRADEX computer code is used to calculate the release of radioactivity from the reactor containment building, including the effects of radioactive decay, aerosol depletion (from HAA-3B) and the containment cleanup system. COMRADEX calculates, as a function of time and downwind location, doses resulting from direct gamma shine, inhalation of radioactive material, and cloud submersion taking into account atmospheric dispersion. The atmospheric dispersion factors for these margin beyond the design base analyses are based on the "50% cumulative frequency" (atmospheric dispersion more favorable 50% of the time) values applicable to the CRBRP site.

Dose conversion factors (rem/ci) used in the COMRADEX code to calculate specific organ doses were taken from References 12 and 13 where possible. Factors for isotopes not given in these References are from Reference 14.

The radiological analyses consider that the reactor containment building leaks at a low rate (based on the design leak rate of 0.1%/day at 10 psig) during the first 36 hours, during which time the normal containment safety systems are effective. This includes a filter system that filters the containment building leakage, except for 1% which is assumed to bypass the filter system. Starting at 36 hours, the containment is vented to atmospheric pressure and subsequently purged to maintain hydrogen concentrations at acceptable levels. The vented materials enter the containment cleanup system, which has the efficiencies defined previously.

3.2.2 RESULTS OF DOSE CALCULATIONS

Using the methods described in Section 3.2.1 the radiological doses at the Exclusion Boundary (0.42 miles) and the Low Population Zone (2.5 miles) were calculated for the four different source terms described in Section 3.1. These doses are summarized in Table IV. The 30 day LPZ doses include the plutonium released after boil-dry to 30 days. Plutonium release beyond 30 days could result in an additional 10 rem to the LPZ bone dose.

The dose consequences of the four cases that assumed varying degrees of severity of the hypothetical accident are all quite low for accidents beyond the design base. For example, the maximum whole body dose is predicted to be about 3 rem and the maximum thyroid dose would be about 100 rem. Bone doses are about 30 rem. The 30 day LPZ doses are generally more limiting than the two hour exclusion boundary doses.

3.2.3 IMPORTANCE OF AEROSOL DEPLETION MECHANISMS

The results in Table IV show that the 30 day LPZ doses are not strongly sensitive to the degree of severity of the initial release source term. As the initial release to the reactor containment building increases, the rate of aerosol depletion increases which acts as an inverse feedback to limit the release from the reactor containment building. Consequently, so long as the initial release does not result in failure of the containment barrier, the radiological consequences are relatively insensitive to the magnitude of the release. For the full range of releases considered in Cases 1 through 4, the reactor containment building pressure and temperatures would not result in failure of the containment barrier.

The dose reduction factors attributed to aerosol depletion mechanisms are provided in Table V. This shows that the aerosol effects are much more important when the initial releases are high and this results in a relative insensitivity of the doses to the initial release.

In addition to the dose reduction provided by aerosol attenuation, another important aspect of aerosol attenuation is the reduction in the quantity of material that the containment cleanup system must handle. The vaporization of the sodium and subsequent chemical reactions in the containment building result in the production of massive quantities of aerosols. Considering aerosol attenuation, up to 140,000 kg (300,000 lbs.) may enter the cleanup system. Without aerosol attenuation, the quantity could be nearly six times as much and this would have a substantial impact on the design of the containment cleanup system.

During the post sodium boil-dry phase, the aerosol concentration in the reactor containment building due to sparged materials from the molten pool are low and aerosol attenuation processes are less effective than during earlier times. However, the long term release of plutonium is still reduced by about a factor of three by aerosol attenuation in the reactor containment building. Scoping analyses of the effectiveness of aerosol attenuation within the reactor cavity during the post sodium boil-dry phase indicate that attenuations of about a factor of three could result. This has not been included in the current analyses but could be an important area for future work.

4.0 SUMMARY AND CONCLUSIONS

A reasonable understanding of aerosol phenomenology exists and tools are available to predict the effect of the principal attenuating mechanisms. Sufficient comparisons have been made with experimental data to support the acceptability of the analytic models for most conditions of interest.

The radiological analyses for CRBRP include aerosol effects in a number of areas. Based on those assessments, the following conclusions and recommendations are made:

1. For the site suitability assessment, the two hour bone dose at the site boundary is most limiting and is not sensitive to aerosol depletion. With the non-mechanistic definition of the radiological source by NRC for this assessment, little can be gained by refining the applicable aerosol technology. However, aerosol attenuation reduces the predicted 30 day lung and bone doses at the low population zone boundary by more than a factor of two. Current technology appears adequate for predicting the attenuation of these low density aerosols.

2. For the major sodium spill in the de-inerted cell within the RCB, significant reductions in the off-site doses result from the depletion of aerosols. Considerable margins exist, however, between the predicted doses and the established limits. Present technology appears adequate for predicting the consequences of this event.

3. The aerosol attentuation within the reactor containment building is important in assessing the consequences of HCDAs. Non-gaseous releases are reduced by about a factor of six, which reduces both radiological consequences and the requirements imposed on the containment cleanup system. A reasonable data base exists to support these analyses.

4. A large aerosol attenuation within the cover gas space following an HCDA is predicted. Because of the high density, temperature and nature of the aerosols, the prediction of attenuation is uncertain. However, based on comparing Cases 3 and 4 to Case 2 in Tables IV and V, the radiological consequences are not very sensitive to the initial releases through the head. Therefore, the reduction of uncertainties in this area is not considered to have high priority.

5. In the post sodium boil-dry phase, the principal mechanisms for release is gas sparging from the pool of molten materials. Current assessments do not consider the aerosol attenuation in the reactor cavity for these sparged materials and the resulting dose contribution from these materials is significant. Scoping calculations indicate aerosol attenuations of about a factor of three. Further assessments of this area are recommended. Contributors to the uncertainty in this part of the calculation include:

A. Uncertainty in the quantity of fuel and fission products released by sparging and the amount of other materials (e.g., from molten concrete) that could contribute to the aerosol. Potential for crust formation and its effect are also uncertain.

B. Uncertainty in leak paths and surfaces available for plateout (recognizing that some internal structures may have failed by this time).

C. Uncertainty in temperature of the reactor cavity atmosphere and the plateout surfaces, also uncertainty in the condition of the surfaces (coated with oxides, etc.).

A combination of analytic and experimental work may be required to reduce these uncertainties so that credit for aerosol attenuation in this area can be taken.

6. Attenuation of aerosols as they pass through potential leak paths has been observed but credit for reduced leakage has not been taken in the current analyses. This could be important in risk assessments although the leak paths may not be well defined. This is considered to be an area for future refinement of the realistic assessment of highly improbable events.

5.0 REFERENCES

1. R. S. Hubner, E. V. Vaughan, L. Baurmash, "HAA-3 User Report", AI-AEC-13038, March 1973.

2. J. M. Otter and P. A. Conners, "Description of the COMRADEX-III Code", TI-001-130-053, June 30, 1975, Rockwell International, Atomics International Div., Canoga Park, CA.

3. P. Beiriger, et al, "SOFIRE II User Report", AI-AEC-13055, March 30, 1973.

4. J. R. Schornhorst, L. E. Strawbridge and P. Bradbury, "Evaluations of CRBRP Thermal Margin Beyond the Design Base", in Proceedings of the Third Post-Accident Heat Removal Information Exchange, ANL-78-10, (1977), p. 317.

5. L. E. Strawbridge, "CRBRP Structural and Thermal Margin Beyond the Design Base", in Proceedings of the International Meeting on Fast Reactor Safety Technology, Seattle, Washington, August 19-23, 1979, p. 1230.

6. "FFTF Site Safety Analysis: Meteorology and Climatology, Appendix D - Aerosol Behavior Analysis", BNWL-1350, April 1, 1970.

7. L. Baker, Jr., et al, "Post Accident Heat Removal Technology", ANL/RAS 74-12, July 1974. (Availability: U.S. DOE Technical Information Center)

8. "Radiological Assessment Models, Tenth Quarterly Report, December 1976-February 1977", GEFR-14034-10, March 1977. (Availability: U.S. DOE Technical Information Center)

9. "Radiological Assessment Models, Ninth Quarterly Report, September - November 1976", GEAP-14034-9, December 1976. (Availability: U.S. DOE Technical Information Center)

10. "Reactor Safety Study - An Assessment of Accident Risks in U.S. Commercial Nuclear Power Plants, Appendix VII, Release of Radioactivity in Reactor Accidents", WASH-1400, October 1975.

11. "Radiological Assessment Models, Fifth Quarterly Report September - November 1975", GEAP-14034-5, December 1975 (Availability: U.S. DOE Technical Information Center).

12. U.S. Nuclear Regulatory Commission, "Calculation of Annual Doses to Man from Routine Releases of Reactor Effluents for the Purpose of Evaluating Compliance with 10CFR Part 50, Appendix I", Regulatory Guide 1.109, Revision 1, October 1977.

13. G. R. Hoenes and J. K. Soldat, "Age-Specific Radiation Dose Commitment Factors for a One-Year Chronic Intake", NUREG-0172, November 1977.

14. E. R. Specht, "Internal Dose Factors for COMRADEX-II", TI-001-130-051, February 24, 1975, Rockwell International, Atomics International Div., Canoga Park, California.

TABLE I

OFF-SITE EXPOSURE FOR SITE SUITABILITY SOURCE TERM

Organ	Dose (Rem) Dose Limits For CP* Evaluation	2-Hour Site Boundary (0.42 Miles)	30-Day Low Population Zone (2.5 Miles)
Bone	15	9.3	5.3
Lung	7.5	4.1	2.3
Thyroid	150	17.7	9.6
Whole Body**	20	3.5	1.5

TABLE II

OFF-SITE EXPOSURE FOR RCB SODIUM FIRE ACCIDENT

Organ	Dose (Rem) Dose Limits For CP* Evaluation	2-Hour Site Boundary (0.42 Miles)	30-Day Low Population Zone (2.5 Miles)
Bone	15	3.3×10^{-5}	6.1×10^{-5}
Lung	7.5	1.4×10^{-4}	2.5×10^{-4}
Thyroid	150	4.9×10^{-4}	9.0×10^{-4}
Whole Body**	20	1.6×10^{-5}	2.9×10^{-5}

*Construction Permit limits are specified by NRC at lower values than Operating License limits (10CFR100).

**Includes inhalation, external gamma cloud, and direct gamma shine exposures.

TABLE III

CORE SOURCE TERMS RELEASED TO THE REACTOR CONTAINMENT BUILDING FOR HYPOTHETICAL ACCIDENT SCENARIOS CONSIDERED

	Initial Release Phase	Sodium Boil-Up Phase
Case 1	100% Noble Gases	100% Halogens
	100% Cs and Rb	100% Other Volatile F.P. 1% Solid F.P. 0.015% Fuel 0.5×10^6 kg of Na
Case 2	100% Noble Gases	100% Halogens
	100% Cs and Rb	100% Other Volatile F.P.
	454 kg (1000 lb.) of Na with 100 PPB Pu	1% Solid F.P.
	0.026% Fuel*, Solid F.P., Halogens	0.015% Fuel 0.5×10^6 kg of Na
Case 3	100% Noble Gases	1% of Remaining 99% of Solid F.P.
	100% Halogens	0.015% Fuel
	100% All Volatiles	0.5×10^6 kg of Na
	1% Fuel*	
	1% Solid F.P.	
	454 kg (1000 lb.) of Na	
Case 4	100% Noble Gases	1% of Remaining 95% of Solid F.P.
	100% Halogens	0.015% Fuel
	100% All Volatiles	0.5×10^6 kg of Na
	5% Fuel*	
	5% Solid F.P.	
	1500 kg (3300 lb.) of Na	

Note: After boil-dry the only significant contribution to the source term is plutonium release due to gas sparging. This additional source amounts to about 13 kg of plutonium released from the molten pool, which has been assumed to be freely transmitted to the RCB over a several month period and is considered the same for all four cases.

*Includes plutonium in blankets and core.

TABLE IV

DOSE SUMMARY FOR HYPOTHETICAL ACCIDENT SCENARIOS CONSIDERED

		Doses in Rem			
	Organ	Case 1	Case 2	Case 3	Case 4
2 Hour Exclusion Boundary	Bone	0.0043	0.028	0.93	3.83
	Lung	0.0035	0.0055	0.15	0.39
	Thyroid	0.0067	0.0096	11.3	9.51
	Whole Body	0.16	0.16	0.24	0.32
30 Day Low Population Zone	Bone	32.1	32.1	32.7	33.2
	Lung	3.08	3.09	2.15	2.15
	Thyroid	99.2	99.2	5.31	1.72
	Whole Body	2.98	2.97	2.54	2.41

TABLE V

DOSE REDUCTION FACTORS DUE TO AEROSOL EFFECTS WITHIN THE REACTOR CONTAINMENT BUILDING IN HYPOTHETICAL ACCIDENT SCENARIOS CONSIDERED

		Dose Without Aerosol Effects / Dose With Aerosol Effects			
	Organ	Case 1	Case 2	Case 3	Case 4
2 Hour Exclusion Boundary	Bone	1.05	1.03	1.03	1.22
	Lung	1.01	1.01	1.03	1.23
	Thyroid	1.03	1.03	1.03	1.22
	Whole Body	1.00	1.01	1.01	1.11
30 Day Low Population Zone	Bone	3.0	3.1	6.3	19.4
	Lung	4.1	4.2	10.5	28.1
	Thyroid	4.8	4.8	93	286
	Whole Body	2.1	2.2	3.8	8.5

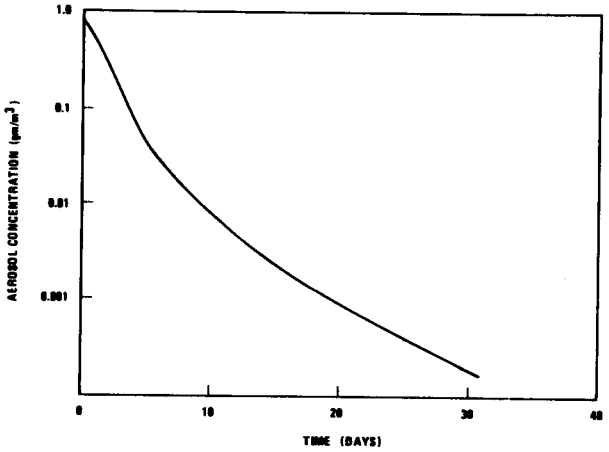

Figure 1. Aerosol Concentration in the RCB for Site Suitability Assessment

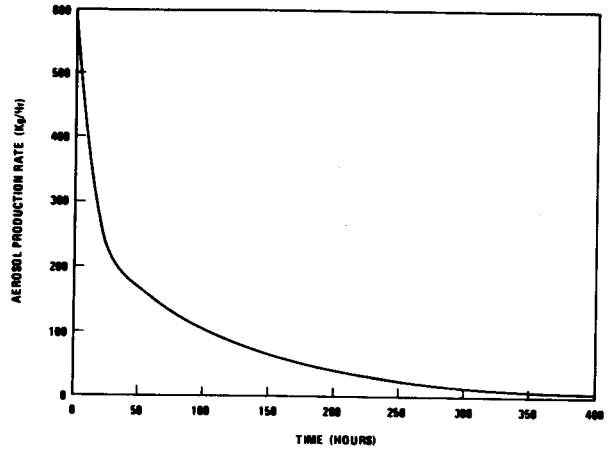

Figure 2. Aerosol Production Rate During the RCB Sodium Fire Accident

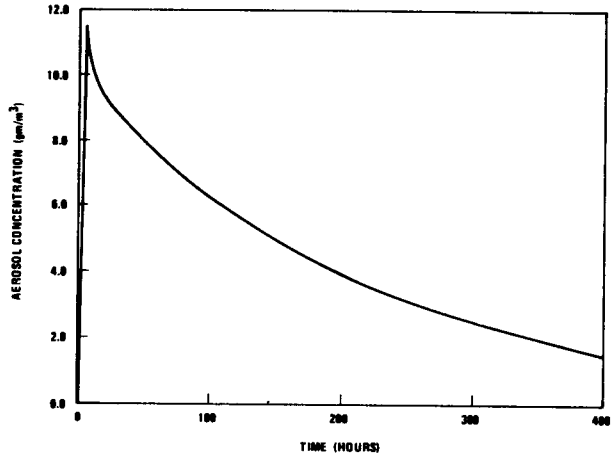

Figure 3. RCB Aerosol Concentration During the RCB Sodium Fire Accident

SENSITIVITY ANALYSIS OF AEROSOL BEHAVIOR MODEL

K. W. Lee, J. A. Gieseke and L. D. Reed
Battelle Columbus Laboratories
Columbus, Ohio

ABSTRACT

A methodology to perform the sensitivity analysis of a fast running computer code was developed. Based on this methodology, the sensitiveness of various independent input variables and model parameters such as initial aerosol properties and containment geometry to the code output has subsequently been studied using the latest version of the aerosol behavior code, designated HAARM-3. The amount of aerosol leaked from the containment was used as the reference code output. The analysis results showed that (1) leak flow rate, (2) particle collision efficiency, (3) aerosol source duration time, (4) mean particle size, (5) source rate and (6) particle collision shape factor are those which significantly influence the code output in that order. It is further found that these important variables are directly related to reactor accident conditions implying the importance of accident postulations. Among the model parameters, those which govern the aerosol agglomeration mechanism are also found to be important. However, the input variables and parameters that govern the rate of aerosol deposition on walls do not greatly influence the amount of aerosol leaked.

INTRODUCTION

Aerosol behavior within nuclear reactor containments is of vital importance in the overall safety analysis of Liquid Metal Fast Breeder Reactors (LMFBR) since the concentration of radiological species eventually reaching the atmosphere following a postulated accident is directly related to airborne concentrations within the containment of the reactor. Mathematical models describing the behavior of aerosols in closed environments, besides providing a direct means of assessing the importance of specific assumptions regarding accident sequences, will also serve as the basic tool with which to predict the consequences of various postulated accident situations. Consequently, considerable efforts have been recently directed toward the development of accurate and physically realistic theoretical aerosol behavior models.[1-4].

These models have accounted for various mechanisms affecting agglomeration rates of airborne particulate matter as well as particle removal rates from closed systems. Because of its short computation times, the HAARM-3 code [1] is being extensively used in analyzing the radiological consequences of assumed accidents. In general, the time-dependent aerosol concentration, particle size and release of airborne particles calculated by the HAARM-3 model are functions of assumed containment geometry and assumed particle properties. Therefore it is of natural interest in both analytical and experimental nuclear reactor safety studies to obtain information on the sensitiveness of the model to changes in these variables.

The sensitivity of a computer model may be defined as a measure of change in output variables to variation in input variables. It should be noted that results or conclusions drawn out of the sensitivity study of a computer model do not warrant the actual sensitivity of aerosol behavior itself. However, when the computer model is assumed sufficiently accurate, the analysis results can be useful in estimating the effects of various parameters on the actual aerosol behavior. In addition, results of such a sensitivity study will play a significant role in guiding future experimental programs intended to validate and improve the computer model and in studying optimal containment design features. As a result of the present analysis, the importance of each input variable and model parameter has been ranked. In addition, a response surface has been obtained to fit the HAARM-3 calculations empirically.

The HAARM-3 computer code calculates the rate of collisions among airborne particles having a heterogeneous size distribution, the rate of particle deposition on the floor of an enclosed vessel, the rate of deposition of particles on the walls, the leakage of airborne particles, and the injection of particles from a source. The agglomeration growth of particles resulting from particle-particle collisions is considered to be the result of Brownian motion, differential settling velocities, and gas turbulence effects. One of the assumptions employed in the model is that the aerosol size distributions remain lognormal throughout time. However, the three size distribution parameters of the mean aerosol size, the geometric standard deviation, and the total

concentration are allowed to vary. In addition, the aerosol particles are assumed to be uniformly distributed within the containment. In calculating the aerosol agglomeration and deposition rates which are dependent on the morphological properties of agglomerates, the results of a recent experimental study [5] have been utilized. The effects of nonspherical shape of the agglomerates on settling velocity and collision rate are also accounted for in the code.

MATERIAL AND METHODOLOGY

As mentioned previously, one of the immediate objectives of performing a sensitivity analysis is to identify all the important input variables and different model parameters involved in the HAARM-3 code. These important variables and parameters may be regarded as those affecting, to a significant extent, the aerosol size distribution, and the mass released from the containment. Airborne mass concentration and released mass are easily interchanged since released mass is the product of airborne concentration, leakage rate, and elapsed time. Two basic but similar approaches could be considered for sensitivity analyses.

The rate of change of airborne concentration or of leaked mass with respect to any variable can be determined by direct analytical procedures. For instance, the effect of vessel surface on airborne number concentration could be evaluated by calculating the corresponding derivative. However, in most cases the derivatives are not analytically obtainable and computer-estimated derivatives are necessary. Even then the derivative values are applicable only for a single set of values for other variables, and the magnitude of the derivative for various sets of conditions can be determined only by repeated calculations.

A second approach is to select a baseline set of conditions and vary the parameters or variables individually to assess their effects on airborne concentration or leaked mass over a range of limiting values for each variable. This approach then allows estimations of the first order sensitivity of predicted airborne concentrations or leaked mass to select changes in individual variables to be determined. Information on higher order sensitivites can also be obtained by allowing more than one variable or parameter to vary around the baseline, although it is possible to do the same employing other methods such as those similar to the conventional design of experiments. In the present study, the second approach has been adopted.

It is desirable to obtain the sensitivity of the code output not only to the code input variables but also to the uncertainties of different model parameters involved in the HAARM-3 codes. Therefore, both input variables and model parameters have been indiscriminately treated since this presents no analytical or procedural problems. The resulting sensitivity of the code output to both code inputs and model parameters can also be evaluated in a similar manner.

A total of 17 input variables and model parameters have been chosen for the present sensitivity analysis. Table 1 is the list of the selected variables, their baseline values, and ranges of the variables. The baseline values have been obtained using a combination of available experimental data and engineering judgment. More specifically, the base case appearing in the table has been chosen for the case of sodium oxide aerosol suspended in a containment of approximately CRBR dimensions. For the range of variables, the available experimental data were compiled and then the 95 percent confidence interval for each variable was sought. Although the mean free path of gas molecules, gas viscosity, and gas density could additionally be included, it is assumed that they are well defined by the vessel temperature and pressure, and uncertainties in their calculation are not significant.

Since one of the objectives of the present sensitivity analysis was to extend the variable range wide enough to cover as many applications as possible, the range of each variable has been set such that most of the established ranges exceed the corresponding 95 percent confidence interval. For the limits of some model parameters such as particle collision efficiency (ε), there is not enough information available. The range for these parameters is therefore set by using engineering judgment to supplement the available information. For example, the range for particle collision efficiency, ε, was set to vary between 1.0 and 0.01 since ε cannot theoretically exceed 1.0 and the practical lower limit of the collision efficiency would be about 0.01 as most results predict. One advantage of extending the variable range is that results of sensitivity analysis can be applied to this extended range. However, the inherent disadvantage of this practice is that accuracy of the results would deteriorate accordingly. For example, derivatives obtained using two levels which are far apart would be less accurate than those obtained using levels which are located very close to the base point. Therefore, it is necessary to compromise between these two contradicting characteristics of the analysis. It is believed, however, that the established ranges will cover most of the expected values encountered in future applications.

Although there are many output variables from the HAARM-3 on which the sensitivity analysis could be based, all of these outputs are computed by the HAARM-3 code as functions of time. These include the mass concentration of suspended aerosol, the number concentration of aerosol, the standard deviation of aerosol, the settled mass, the plated mass, the leaked mass, etc. For the quantitative analysis, the accumulated mass of leaked aerosol has been chosen as a reference output, since this quantity is considered to be the primary and ultimate concern for the purpose of the nuclear reactor safety analysis.

Sensitivities

In order to obtain the first order sensitivity to a particular variable, two runs of the computer code are made with the selected variable at each a high and low extreme value while all the other variables are held at their baseline values. In other words, the first order sensitivity at the baseline

TABLE 1. BASELINE AND THE RANGE OF VARIABLES USED IN SENSITIVITY ANALYSIS OF THE HAARM-3 CODE

	Symbol	Variables/Parameters	Base Case	Range
1.	SO	Source rate, #/cc sec	5×10^{5}	5×10^{8} - 5×10^{3}
2.	RSOR	Mass median particle radium, μm	0.5	1.0 - 0.05
3.	SIGSOR	Geometric standard deviation, σ_g	1.5	2.5 - 1.2
4.	TAUIN	Source cutoff time, sec	100	1000 - 10
5.	RHO	Aerosol density, g/cm^3	2.27	10 - 1
6.	AWOV	Area ratio of wall to vessel volume cm^{-1}	1.1×10^{-3}	8.8×10^{-2} - 5.5×10^{-4}
7.	AFOV	Area ratio of floor to vessel volume, cm^{-1}	2.4×10^{-4}	2.1×10^{-2} - 1.2×10^{-4}
8.	TEMP	Temperature, K	320	500 - 273
9.	DELTA	Diffusion boundary layer, cm	1×10^{-3}	1×10^{-2} - 5×10^{-5}
10.	TGRADW	Temperature gradient, K/cm	40	200 - 0
11.	RVL	Leak rate, percent/day	0.1	0.5 - 0
12.	P	Pressure, $dynes/cm^2$	1.012×10^{6}	2.024×10^{6} - 1.012×10^{6}
13.	EPST	Turbulent energy dissp. rate, cm^2/sec^3	0	3000 - 0
14.	EFF	Particle collision efficiency, ε	Variable	1 - 0.001
15.	ALPHA	Density correction factor, α	Variable	1 - 0.01
16.	GAMMA	Collision shape factor, γ	1	10 - 1
17.	CM	Coefficient for Cunningham slip, C_m	1.37	1.8 - 1

is assumed to be equal to a partial derivative of the output y with respect to variable x_i and is obtained as

$$\frac{\partial y}{\partial x_i} = \frac{y_{max} - y_{min}}{\Delta x_i} \tag{1}$$

Here i designates the variable of interest, Δx_i is an increment of x_i between the two extreme cases, and y_{max} and y_{min} represent the code outputs with x_i set at the two extreme cases. This procedure is called the one-at-a-time (OAT) design.

Although calculated results for the first order sensitivities should provide much information about the computer code, these sensitivities do not provide a complete analysis of sensitivity of the computer code or necessarily a thorough identification of important variables. In general, a combination of more than one variable can have significant effects on the code output and this is called interaction of variables. For example, the sensitivity of the code to one variable i with another variable j held at a level different from the baseline is also of interest. These interactions can be represented by the second order derivatives, $\partial^2 y/\partial x_i \partial x_j$, with $i \neq j$, and can be obtained similarly as

$$\frac{\partial^2 y}{\partial x_i \partial x_j} = \frac{(y_{max,max} - y_{min,max}) - (y_{max,min} - y_{min,min})}{\Delta x_i \Delta x_j} \tag{2}$$

where i,j represent two input variables of interest, $y_{a,b}$ is the code output with x_i and x_j set at a and b, respectively. The third order sensitivity is computed,

$$\frac{\partial^3 y}{\partial x_i \partial x_j \partial x_k} = \frac{1}{\Delta x_i \Delta x_j \Delta x_k} \tag{3}$$

$$\cdot \; [(y_{max,max,max} - y_{min,max,max}) - (y_{max,min,max} - y_{min,min,max})]$$

$$- \; [(y_{max,max,min} - y_{min,max,min}) - (y_{max,min,min} - y_{min,min,min})]$$

and so on, where i, j, and k designate the variables whose interactions are of interest.

The expansion of any function with the Taylor series contains additional quadratic and higher terms such as $\partial^2 y/\partial x_i^2$, $\partial^3 y/\partial x_i^3$, etc., serving as a measure of the change in first order derivatives and so on. Unless the output of a computer code forms a nearly straight line with respect to the variable of interest, these may also be significant. Since these effects may be useful for constructing a response surface as will be discussed later, the quadratic effects have been added in the present study. The computation of these terms requires a set of code runs with more than two levels as shown:

$$\frac{\partial^2 y}{\partial x_i^2} = \frac{y_{max} - 2y_{base} + y_{min}}{\Delta x_{i1} \Delta x_{i2}} \tag{4}$$

and so on. Where y_{base} is the computer output for base case and Δx_{i1} and Δx_{i2} are increments of the input variable between the maximum point and the base case and between the base case and the minimum point, respectively. It can also be pointed out that there are other terms such as $\partial^3 y/\partial x_i^2 \partial x_j$, $\partial^4 y/\partial x_i^3 \partial x_j$, $\partial^4 y/\partial x_i^2 \partial x_j^2$, etc. However, these derivatives are assumed to be insignificant for all practical purposes.

In general, the total number of all the high order sensitivities is prohibitively large when many variables are involved, such as in the present case. As mentioned previously, the number of variables to be studied in the present analysis is as many as 17. Since the purpose of the present sensitivity analysis is to identify all the important sensitivities of input variables including interactions, the following stragey for calculating high order sensitivities has been taken to achieve the goal at an affordable minimum number of computer runs.

By selecting the variables whose first order sensitivity is found to be relatively large, all the important variable interactions can be identified adequately. For example, if the first order derivatives with respect to any two input variables are small, it can be assumed that the code output is essentially independent of these two particular input variables and that their higher order interactions are negligible. This can be stated mathematically as

$$\text{if} \qquad \frac{\partial y}{\partial x_g} \simeq 0 \quad \text{and} \quad \frac{\partial y}{\partial x_h} \simeq 0, \tag{5}$$

then we write

$$y = f(\{x_i\}), \text{ where } i \neq g \text{ and } i \neq h. \tag{6}$$

We then have,

$$\frac{\partial^2 y}{\partial x_g \partial x_h} \simeq 0 \ . \tag{7}$$

In this way, a number of insignificant two-way interactions can be identified and only important second order sensitivities can be sought. Since a similar procedure can be taken for the interactions higher than two factors, all the important interactions can be obtained.

Although the number of high order sensitivites of interest could be reduced by the strategy just discussed, the required number of computer runs may still remain too high. For example, Equation (2) shows that four computer runs are required to calculate one third order derivative. If we are interested in calculating ten of these alone, a total of 40 runs is necessary.

Since a large number of required computer runs would eventually limit the number of sensitivities which can be evaluated in this study, an additional strategy has been sought as follows. Let us rewrite Equations (1) and (4) involving two variables.

$$\frac{\partial y}{\partial x_i} = \frac{y_{max,base} - y_{min,base}}{\Delta x_i}$$
$$\frac{\partial y}{\partial x_j} = \frac{y_{base,max} - y_{base,min}}{\Delta x_j} \tag{8}$$

$$\frac{\partial^2 y}{\partial x_i^2} = \frac{y_{max,base} - 2y_{base,base} + y_{min,base}}{\Delta x_{i1}\Delta x_{i2}} \tag{9}$$

Instead of using Equation (2) in which computer runs are made with two variables, i and j set at their extreme values, an alternative procedure is to approximate the derivative using the maximum values and the base case such that

$$\frac{\partial^2 y}{\partial x_i \partial x_j} = \frac{(y_{max,max} - y_{base,max}) - (y_{max,base} - y_{base,base})}{\Delta x_i \Delta x_j} \tag{10}$$

where Δx_i and Δx_j are the increments of x_i and x_j, respectively, between their maximum value and the base case. It can now be noted that all the y values except $y_{max,max}$ in Equation (10) are already available from the previous OAT design as shown in Equations (8) and (9). Therefore, the number of computer runs required to calculate the second order sensitivity is only one compared to the four runs needed if Equation (2) is used. Since higher order sensitivities of importance are to be identified and calculated depending on he calculation results of lower order sensitivities, it always remains true in the present method that only one additional computer run is needed for a calculation of each high order sensitivities.

In summary, the present method starts by constructing the OAT design by which all the $\partial y/\partial x_i$ and $\partial^2 y/\partial x_i^2$ are first calculated and then depending upon results of each preceding step, the method marches further to calculate the values of $\partial^2 y/\partial x_i \partial x_j$, $\partial^3 y/\partial x_i \partial x_j \partial x_k$, etc. Unlike many sensitivity analyses where code computation time is limited and it is often assumed that all the interactions involving certain factors are inherently small, the present method can identify and calculate all the higher interactions of significant value. It is possible to pursue this rather comprehensive analysis since the HAARM-3 code takes very little computing time. Nevertheless, the number of necessary computer runs can still be adequately reduced.

Response Surface

Response surfaces can serve to provide a visualized geometry that represents the contour of an output variable for a given set of the input variables. The term "response surface" is directly originated from the so-called response function which gives the relation between the output variables and any given combination of the input variables at various levels. A response surface is often utilized advantageously to find the best experimental conditions in various industrial applications [6-7].

In the present study, the exact relation between output and input is, of course, given by the computer code. However, an approximation to this relation can also be obtained by the response surface work which is available as an immediate product of the sensitivity analysis. The resulting response surface can then be used as an empirical approximation to the true computer calculation. Provided that the relation between the response and input variables is complicated but smooth, it is possible and common to represent this relation by a polynomial equation.

In general, the representation of the relation becomes closer to the true response surface as many terms of higher degree are included. For example. the polynomial equation can be written

$$
\begin{aligned}
y = {} & b_o \\
& + b_1 x_1 + b_2 x_2 + b_3 x_3 + \cdots\cdots\cdots \\
& + b_{11} x_1^2 + b_{22} x_2^2 + \cdots\cdots + b_{12} x_1 x_2 + b_{23} x_2 x_3 + \cdots\cdots \\
& + b_{111} x_1^3 + b_{222} x_2^3 + \cdots\cdots + b_{112} x_1^2 x_2 + b_{113} x_1^2 x_2 \cdots \\
& + \cdots\cdots\cdots\cdots
\end{aligned}
\tag{11}
$$

where all the coefficients are unknown. The degree of a term is defined by the number of variables multiplied together.[7] The form of polynomial equation to be used is somewhat arbitrary depending upon the number of factors involved, the required accuracy and the available number of code runs that can be afforded. Using a suitably chosen set of computer runs, the response surface work determines the coefficients. When the polynomial equation includes nonlinear terms, a so-called nonlinear regression analysis can be used to determine the coefficients. This analysis which has been adopted in this study may be briefly described here.

If y is the true response of a set of input variables and $\hat{y}$ is the value that could be obtained by the response surface work, we write

$$
\begin{aligned}
y &= \hat{y} + e \\
&= f(\bar{b}_m : \bar{v}_m) + e
\end{aligned}
\tag{12}
$$

where

f is the assumed nonlinear function

m is the number of terms in the function

$\bar{b}$ is the coefficients to be determined

$\bar{v}$ is the combined terms of input variables

e is the residual error.

Then the nonlinear regression analysis is a procedure to seek the values of b_m that minimize the RSS (residual sum of squares) using the available experimental cases. Here, RSS is defined as

$$RSS = \sum_{i=1}^{k} e_i^2 = \sum_{i=1}^{k} (y_i - \hat{y}_i)^2 \qquad (13)$$

where $y_i = f(\bar{b}_m, \bar{v}_m)$, represents the value predicted by the regression equation for the i-th case, y_i is the true value for the same case, and k is the number of available cases based on which the regression analysis is to be performed. In minimizing RSS in the nonlinear regression analysis, the coefficients b_i cannot generally be solved in a straightforward manner. The methods used are, in general, iterative. One of the widely used interation methods for the RSS minimization is called the simplex method [8].

RESULTS AND DISCUSSIONS

The calculated results of the sensitivity analysis employing the described strategy are given here in the order of first order sensitivity, second order sensitivities with and without interactions, higher order sensitivities and finally results of the response surface work.

First Order Sensitivities

The first order effects were investigated using the standard OAT design where each variable is set at an extreme value with all other sixteen variables held fixed at a base case. The base case used in the present analysis is given in Table 1.

Based on this OAT design, the first order effects have first been calculated using Equation (1). For the purpose of ranking the resulting sensitivities, the values of Δy ($= y_{max} - y_{min}$) have been compared with each other. This procedure has been taken based on the assumption that the range of each variable has been established with the same confidence level. In other words, if each variable is normalized around the mean value such that $\tilde{x}_i = (x_i - \bar{x})/n_i\sigma_i$, the sensitivity can be defined as $S_i = (y_{max} - y_{min})/2n_i$, where y_{max} and y_{min} are the outputs at x_{max} ($= \bar{x} + n_i\sigma_i$) and x_{min} ($= \bar{x} - n_i\sigma_i$). Since it is assumed that the range of each variable covers the same confidence interval, n_i becomes identical for each variable. Therefore, Δy_i ($= y_{max} - y_{min}$) is then a direct measure of first order sensitivities [9].

The calculated and ranked sensitivites are listed in decending order in Table 2. The symbols used in the table are as defined in Table 1. It is seen that the leakage rate, source duration time, the mean size of source aerosol, and source rate are found to increase the leaked mass most effectively. Since the leaked mass is linearly related to the leakage flow rate and suspended aerosol concentration, it is not surprising to find that the cited input variables directly related to these factors were found to be ranked very highly. Since source duration time, mean size of source aerosol, and source rate are all related to a postulated accident situation, it can be said that the amount of aerosols leaked into the environment is strongly dependent upon the accident conditions. It is also found that increasing particle collision efficiency, collision shape factor, or turbulent energy dissipation rate are most effective in reducing the leaked mass. It is interesting to note that all these highly ranked input variables are those which control the rate of aerosol agglomeration. However, ALPHA and AFOV tend to cause the leaked mass to increase to an only moderate extent. Diffusion boundary layer thickness, the wall temperature gradient, slip correction factor, and AWOV are shown to be among those which affect the aerosol behavior the least. With the exception of CM, these are the parameters which affect the various aerosol wall deposition mechanisms. Therefore, it can be concluded that deposition rates on walls such as those due to diffusion and thermophoresis are not significant for the vessel size comparable to that as established by the present base case. More discussion of these results will be provided as other results are subsequently presented. Calculated values of leaked mass for selected runs as a function of time showing the effects of various input values are given in Figures 1 through 4.

Second Order Effects -- Quadratic Effects

The quadratic effects based on this procedure as calculated by Equation (4) are listed in Table 3. Based on the values of Δy_i, the input variables and model parameters have been ranked in a similar fashion as before. It is interesting to note that the variables are found to be ranked in an approximately similar order as those in Table 2.

Second and Higher Order Sensitivities

For the second order sensitivities allowing interactions, the top 10 variables out of 17 from Table 2 were chosen and the sensitivities of a total 45 possible combinations using those were all calculated. As discussed previously, calculation of the second order sensitivities requires four additional computer runs for each sensitivity of Equation (2) is to be utilized. Instead, Equation (10) has been used where only the maximum and the base case values are used. In this case, the required number of additional computer runs is only one.

Table 4 gives the results of these calculations showing only the ten most important interactions after being ranked according to their Δy_i values. Figure 5 shows one example of the second order effects. According to Table 4, pairs of SO-TAUIN, RVL-TAUIN, RSOR-TAUIN, RVL-GAMMA and RVL-EFF are among the most significant interactions in enhancing the leaked mass.

TABLE 2. CALCULATION RESULTS OF FIRST ORDER SENSITIVITIES

Rank	Variable/ Parameter	Δy, μg	$\frac{\partial y}{\partial x_i}$
1	RVL	6.928×10^{8}	1.197×10^{16}
2	EFF	-4.988×10^{8}	-5.038×10^{8}
3	TAUIN	2.187×10^{8}	2.209×10^{5}
4	RSOR	1.771×10^{8}	1.807×10^{8}
5	SO	1.532×10^{8}	3.067×10^{1}
6	GAMMA	-1.338×10^{8}	-1.487×10^{7}
7	EPST	-1.204×10^{8}	-4.013×10^{4}
8	ALPHA	1.122×10^{8}	1.123×10^{8}
9	APOV	-1.066×10^{8}	-5.105×10^{9}
10	RHO	9.96×10^{7}	1.107×10^{7}
11	SIGSOR	-8.232×10^{7}	-6.332×10^{7}
12	P	6.08×10^{7}	2.014×10^{1}
13	TEMP	-2.14×10^{7}	-9.427×10^{4}
14	AMOV	-1.7×10^{7}	-1.944×10^{8}
15	CM	-3.5×10^{6}	-4.375×10^{6}
16	TGRADW	-1.2×10^{6}	-6.000×10^{3}
17	DELTA	0.0	0.0

TABLE 3. CALCULATION RESULTS OF SECOND ORDER SENSITIVITY WITHOUT INTERACTION

Rank	Variable/ Parameter	Δy, μg	$\frac{\partial^2 y}{\partial x_i^2}$
1	RVL	4.158×10^{8}	7.762×10^{23}
2	EFF	2.467×10^{8}	1.007×10^{9}
3	EPST	1.150×10^{8}	5.751×10^{1}
4	TAUIN	1.139×10^{8}	1.406×10^{3}
5	RSOR	-9.909×10^{7}	-4.129×10^{8}
6	GAMMA	9.032×10^{7}	6.451×10^{6}
7	APOV	-8.315×10^{7}	-3.338×10^{13}
8	SIGSOR	-8.252×10^{7}	-2.084×10^{8}
9	SO	-5.838×10^{7}	-2.620×10^{-5}
10	ALPHA	-5.08×10^{7}	-2.105×10^{8}
11	RHO	4.24×10^{7}	4.319×10^{6}
12	P	-2.8×10^{7}	-7.566×10^{-5}
13	AMOV	-1.66×10^{7}	-3.473×10^{13}
14	TEMP	-9.4×10^{6}	-1.111×10^{3}
15	TGRADW	-6.0×10^{5}	-9.375×10^{1}
16	CM	-1.0×10^{5}	-6.285×10^{5}
17	DELTA	0.0	0.0

TABLE 4. CALCULATION RESULTS OF SECOND ORDER SENSITIVITY WITH INTERACTION

Rank	Variables i	Variables j	Δy, μg	$\frac{\partial^2 y}{\partial x_i \partial x_j}$
1	SO	TAUIN	9.318×10^{8}	2.301×10^{-1}
2	TAUIN	RVL	6.649×10^{8}	1.596×10^{13}
3	RSOR	TAUIN	5.987×10^{8}	1.330×10^{6}
4	RVL	GAMMA	-5.356×10^{8}	-1.285×10^{15}
5	RVL	EFF	-5.045×10^{8}	-2.179×10^{16}
6	RVL	EPST	-4.817×10^{8}	-3.468×10^{12}
7	APOV	RVL	-3.797×10^{8}	-3.950×10^{17}
8	TAUIN	RHO	3.580×10^{8}	5.146×10^{4}
9	RHO	RVL	2.842×10^{8}	7.941×10^{14}
10	SO	RVL	1.895×10^{8}	9.096×10^{8}

The third and higher order sensitivities with interactions could also be calculated and examined in a smiliar way. Although it is not generally common in the sensitivity analysis of a computer code or experimental design to study such higher order sensitivities, primarily due to progressively increasing number of code runs or experiments, calculations were made as follows for the third order sensitivities. The five variables which have been ranked most highly from the first order sensitivity results have been chosen. Among the possible ten combinations of these variables, seven interactions were calculated. The results showed that among the calculated sensitivities, RVL-TAUIN-SO, RVL-TAUIN-RSOR, EFF-TAUIN-SO and RVL-EFF-TAUIN have significant interactions [10]. Depending upon the required information and the extent to which the analysis is to be performed, one can calculate as many interactions as needed this way. For the present analysis, however, no further sensitivites have been determined.

So far, discussions have been limited to ranking of same-order sensitivities for the various variables. It may be pointed out that except for the values listed in Table 3, the various Δy's already calculated can be used directly for comparisons between the first and higher order sensitivites. This reasoning can be justified if a function having more than one variable is expanded into a Taylor series expansion. However, the values for Δy's as shown in Table 3 should be divided by 2 for the same reason. It can be noted from Tables 2 and 3, that the results for both first order sensitivities and those of second order without interactions are of the same order and hence, comparable. For example, the second order sensitivity for RVL without interaction as listed in Table 3 may be computed 205 g which is half of the original value and ranked fourth if inserted into Table 2. It is also noted that some of the higher order sensitivities as shown in Tables 3 and 4 are much larger than those listed in Table 2 indicating the significant of various interaction effects.

Response Surface

Using the results of the present sensitivity analysis, a nonlinear regression analysis has been performed to obtain the response surface for the HAARM-3 code. As previously discussed, the first step to the response surface development is to determine an assumed functional relation. If all the sensitivities obtained so far are to be included for the purpose, the coefficients of the response surface can be readily replaced by the various effects already obtained. As an alternative means, a response surface with a reduced number of terms has been sought. Instead of substituting the derivatives to the coefficient of each term, those coefficients have been obtained using a nonlinear regression analysis [11]. As an assumed form of the response surface, the terms whose Δy values are larger than 1×10^8 μg from the calculated results have been included. As a result, the response surface has the form of

$$y = \sum_{i=1}^{10} b_i x_i + b_{11}x_1x_3 + b_{12}x_1x_6 + b_{13}x_2x_3 + b_{14}x_2x_6 + b_{15}x_3x_4 + b_{16}x_3x_6 + b_{17}x_3x_{10} + b_{18}x_4x_6 + b_{19}x_5x_6 + b_{20}x_5x_{10} + b_{21}x_6x_7 + b_{22}x_6x_8 + b_{23}x_6x_9 + b_{24}x_6x_{10} + b_{25}x_7x_8 + b_{26}x_7x_{10} + b_{27}x_8x_{10} + b_{28}x_1x_6x_{10} + b_{29}x_1x_3x_6 + b_{30}x_2x_3x_6 + b_{31}x_1x_2x_6 + b_{32}x_1x_6x_7 + b_{33}x_1x_3x_{10} + b_{34}x_3x_6x_{10} + b_{35}x_3^2 + b_{36}x_6^2 + b_{37}x_7^2 + b_{38}x_{10}^2 + b_{39}x_1x_3x_6x_{10} + b_{40} \quad (14)$$

where

$x_1 = (SO - 5 \times 10^5)/4.995 \times 10^6$

$x_2 = (RSOR - 0.5)/0.98$

$x_3 = (TAUIN - 100)/990$

$x_4 = (RHO - 2.27)/9.0$

$x_5 = (AFOV - 2.4 \times 10^{-4})/2.088 \times 10^{-2}$

$x_6 = (RVL - 1.157 \times 10^{-8})/5.787 \times 10^{-8}$

$x_7 = (EPST)/3000$

$x_8 = (GAMMA - 1.0)/9$

$x_9 = (ALPHA - 0.59)/0.41$

$x_{10} = (EFF - 0.5)/0.5.$

The regression analysis using the results of a total 72 cases gave the values of coefficients and these are reported elsewhere [10].

Using the response surface just obtained, the leak mass for each case has been calculated and compared with the original output in Figure 6. It is shown that the response surface can closely approximate the computer output, especially for high values of leaked mass. However, the agreement between the response surface and the actual output is seen to be less satisfactory for low values of leaked mass. The reason for this discrepancy can be explained as follows. As discussed previously, the nonlinear regression analysis calculates a set of the coefficients which minimize the residual sum of squares. Since the leaked mass dealt within the present analysis ranges over several orders of magnitude, it is obvious that the residual sums of squares for low

values of leaked mass are dominated by those for higher values in the minimization process. To obtain a better correlation in the log-log scale, one may seek to minimize the quantity, RSS = $\Sigma(\ell n\ y - \ell n\ \hat{y})^2$ as an alternative.

CONCLUSIONS

Based on results of the present sensitivity analysis, the following conclusions can be made:

(1) The results of the first order sensitivities show that (1) leak rate, (2) collision efficiency, (3) source duration time, (4) particle size, (5) source rate, (6) collision shape factor, (7) turbulent energy dissipation rate, (8) density correction factor, and (9) the area ratio of floor to wall can significantly affect the code output in that order. Considering that the calculated sensitivities of the above variables are all of the same order of magnitude, and since the sensitivities can vary somewhat depending on the choice of range for the variables, the exact order established in the given list might alter to a certain extent.

(2) Among the various input variables, leakage rate, source particle size and source rate have been found to influence most the output of HAARM-3 computer code. These input variables are directly related to accident conditions, and therefore, the importance of accident situation postulations has been shown.

(3) Among the various model parameters, those which govern the rate of aerosol agglomeration are found to be important. Particle collision efficiency, collision shape factor and turbulent energy dissipation rate have been identified to belong to this category. Further, it can be said that high values of these parameters cause the amount of leaked material to be reduced.

(4) The input variables and model parameters that are related to the aerosol deposition mechanisms do not greatly influence the amount of aerosol leaked from the containment.

(5) Calculation results of two-way interactions show that the pairs: source rate and source duration time, leak rate and source duration time, and mean particle size and source duration time, are among the most significant interactions in increasing the predicted leaked mass.

(6) The response surface equation found in the analysis has been found to be in good agreement with the HAARM-3 computer calculation for leaked mass.

ACKNOWLEDGMENT

This work was carried out as a part of a contract for Aerosol Measurements and Modeling for Fast Reactor Safety under Contract No. NRC-04-76-293-07, sponsored by the U.S. Nuclear Regulatory Commission.

REFERENCES

1. Gieseke, J. A., K. W. Lee and L. D. Reed, "HAARM-3 Users Manual," BMI-NUREG-1991, Battelle-Columbus (January 1978).

2. Hubner, R. S., E. U. Vaughan and L. Baurmash, "HAA-3 User Report," AI-AEC-13038, Atomics International (1973).

3. Bunz, H., W. Muhr and W. Schikarski, "Untersuchungen zum Verhalten von Rekondensationsaerosolen in geshlossen Behältern," Proc. GAF Meeting, Aerosole in Naturwissenschaft, Medizin und Technik -- Messtechnik und technische Anwendung, Karlsruhe (October 1977).

4. Walker, B. C., C. R. Kirby and R. J. Williams, "Discretization and Integration of the Equation Governing Aerosol Behaviour," SRD R 98, United Kingdom Atomic Energy Authority (1978).

5. Gieseke, J. A., L. D. Reed, H. Jordan and K. W. Lee, "Characteristics of Agglomerates of Sodium Oxide Aerosol Particles," BMI-NUREG-1977 (August 1, 1977).

6. Box, G.E.P. and N. R. Draper, Biometrika, Vol. 50, pp. 335-352 (1963).

7. Box, G.E.P., et al., The Design and Analysis of Industrial Experiments, Hafner Publishing Company, New York (1956).

8. Nelder, J.A. and R. Mead, "A Simplex Method for Function Minimization," Computer J., Vol. 7, pp. 308-313 (1965).

9. Baybutt, P., P. Cybulskis, R. S. Denning and R. E. Kurth, "Sensitivity Study of Reactor Accident Consequences," BCL Status Report to U.S. NRC (January 10, 1978).

10. Lee, K. W., J. A. Gieseke and L. D. Reed, "Sensitivity Analysis of the HAARM-3 Code," NUREG/CR-0527 and BMI-2008, Battelle-Columbus (October 1978).

11. Aird, T. J., "SPSS Subprogram NONLINEAR: Nonlinear Regression," Northwestern University, Vogelback Computer Center, Manual No. 313 (1972).

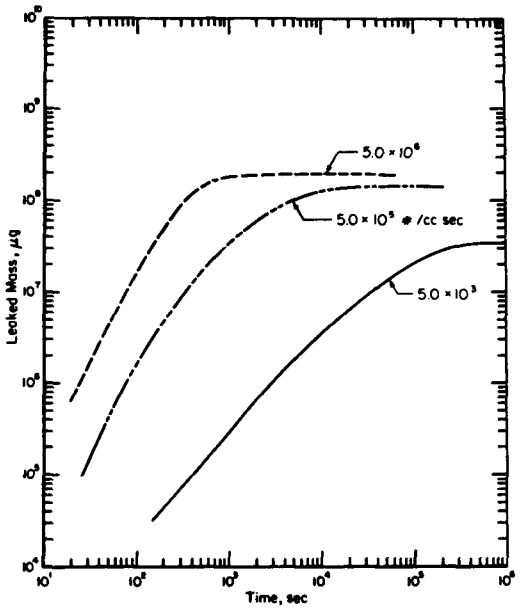

Figure 1. HAARM-3 Calculation Result for Leaked Aerosol Mass as a Function of Aerosol Source Rate

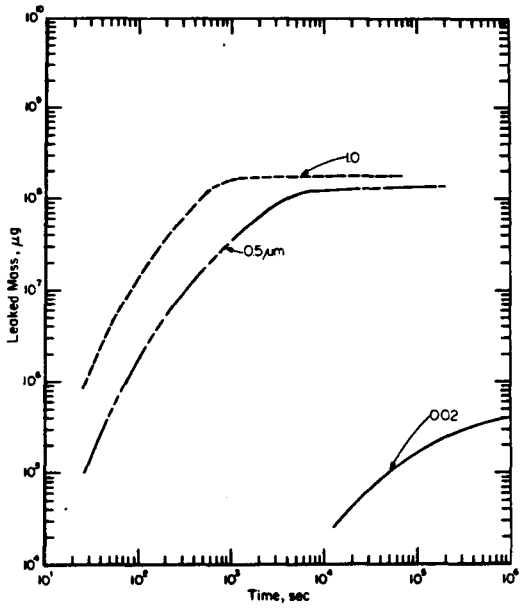

Figure 2. HAARM-3 Calculation Result for Leaked Aerosol Mass as a Function of Median Particle Radius

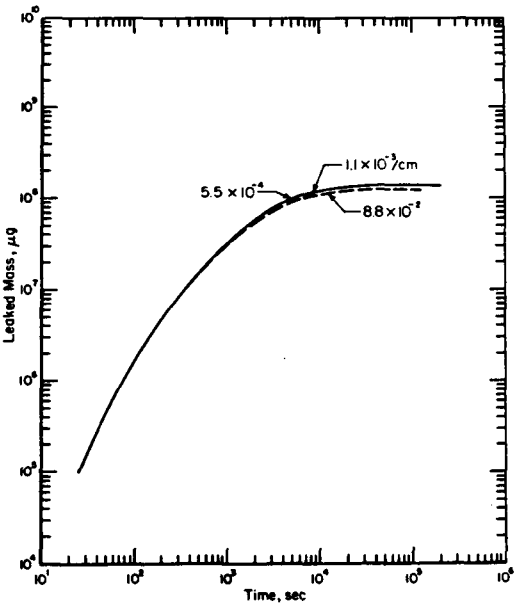

Figure 3. HAARM-3 Calculation Result for Leaked Aerosol Mass as a Function of Ratio of Wall Area to Vessel Volume

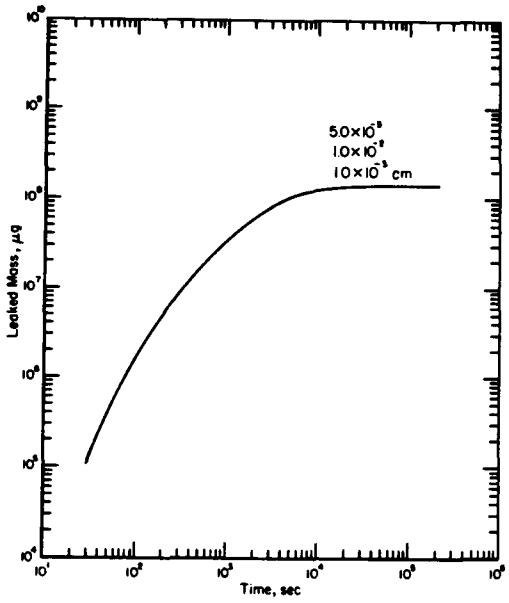

Figure 4. HAARM-3 Calculation Result for Leaked Aerosol Mass as a Function of Diffusion Boundary Layer Thickness

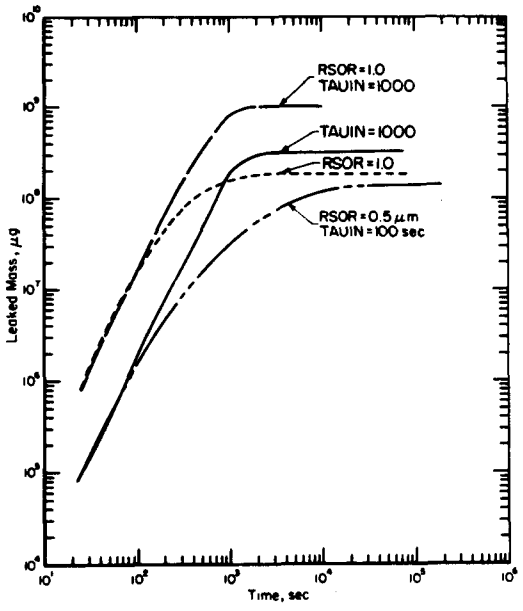

Figure 5. HAARM-3 Calculation Results Showing Interaction of Source Particle Size and Source Cut-off Time

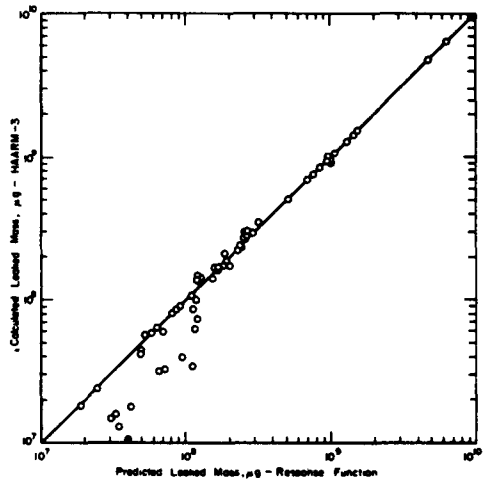

Figure 6. Comparison of the Leaked Masses Predicted by the Response Surface Function Calculated by HAARM-3 Computer Code

EVALUATION MODELS AND THEIR INFLUENCE ON RADIOLOGICAL CONSEQUENCES OF HYPOTHETICAL ACCIDENTS IN FFTF

D. D. Stepnewski, J. P. Hale,
H. C. Martin, R. D. Peak,
G. R. Franz

Hanford Engineering Development Laboratory

Richland, Washington 99352, U.S.A.

ABSTRACT

This paper examines the influence of radiological evaluation models and assumptions on the off-site consequences of hypothetical core disruptive accidents. The effects of initial source term, time of containment venting, meteorology, biological dose model, and aerosol fallout have been included in this investigation. The analyses were based on two postulated scenarios of a severe hypothetical reactor vessel melt-through accident for a 400 MW_t fast reactor. Within each accident scenario, the results show that, although other variables are significant, radiological consequences are strongly affected by the amount of aerosol fallout occurring in the incident.

INTRODUCTION

In a fast reactor hypothetical core disruptive accident (HCDA) in which failure of all emergency cooling provisions and the melt-through of the reactor vessel and guard vessel are assumed, it is postulated that radioactive materials will be released from the primary coolant boundary. Variations in the treatment of these hypothetical releases have a decided bearing on site boundary doses. This paper examines several calculational models and their influence on off-site radiological consequences. The extreme events upon which this study is based cannot be mechanistically justified, and are postulated solely for the purpose of evaluating containment margins inherent in the plant design. Nevertheless, the events are useful to demonstrate the impact of aerosol behavior and associated variables which are involved in the evaluation of site boundary doses.

Reactor containment building (RCB) transient conditions which constitute the basic scenario-dependent input into the radiological evaluation were computed by the CACECO code [1]. Design details for the RCB have been based upon the Fast Flux Test Facility and are described in a previous paper [2]. In summary, the FFTF reactor is housed in a steel lined concrete cavity 11 meters in diameter by 13 meters high. The RCB is a steel shell 42 meters in diameter and 58 meters in overall height. The foregoing arrangement is shown schematically in Figure 1.

Two cases were analyzed in this paper. Both cases postulate the release into the RCB of 450 kg of sodium, the entire core inventory of noble gases, 1% of the fuel, transuranics, and fission products at time zero in the HCDA scenario. This release, which is assumed to occur through non-mechanistically failed reactor vessel head seals, constitutes the initial aerosol source in the RCB. Subsequent aerosol input is a result of sodium vaporization in the reactor cavity and depends on the temporal details of the accident.

The first case, identified as Case 766, assumed that the HCDA core debris and sodium spilled into the reactor cavity three hours after the HCDA. It was further assumed that the steel liner failed, the sodium attacked the concrete under the failed liner, and that hydrogen, generated by the reaction of sodium with water from the concrete, would necessitate venting the building to avoid exceeding the lower flammability limit of hydrogen in air. The venting was computed to occur 11.6 hours after the HCDA (the possibility of hydrogen-oxygen recombination was discounted). From the time of venting, the building was purged with fresh air to maintain hydrogen concentration at or below the lower flammability limit of 4%. RCB transient conditions are shown in Figure 2.

The second case, identified as Case 768, was based on an assumed melting attack of the reactor cavity by the core debris. This case has been described in detail in an earlier paper [3]. Briefly, the melting

attack model leads to core debris penetration of the cavity floor in 30.5 hours. At that time, the core debris and sodium spill into a region beneath the reactor cavity where unlined concrete walls are exposed to sodium. These conditions would lead to very rapid sodium boil-up and pressurization of the RCB. To avoid exceeding the RCB design pressure of 69 kPa gauge, it was assumed that the building would be vented at approximately 31 hours. Transient conditions are shown in Figure 3.

The radiological consequence comparisons reported here are based on the two foregoing accident scenarios.

CODE DESCRIPTION AND MODELING TECHNIQUES

Major analytical codes used were RIBD [4], CACECO [1], SPRAY [5], HAA [6], and COMRADEX [7]. Figure 4 presents a "flow chart" showing the relationship of the codes employed in these analyses. The RIBD code was used to determine the decay heat and inventory of radionuclides in the core at the "End-of-Equilibrium-Cycle" condition. The table of time vs. decay heat for the noble gases and other fission product was used to input to the CACECO code. This fission product inventory data from RIBD and similar data on coolant, fuel and transuranics were combined into a library by the code NEWLYB. This library is used as input to the COMRADEX-H code.

A spray expulsion of sodium past the reactor head seals was assumed in the HCDA evaluation. The resultant sodium spray reaction with air in the reactor head compartment was modeled by the SPRAY code. The SPRAY analysis shows only a slight increase in RCB pressure. The CACECO analysis was performed concurrently with the SPRAY analysis and accounts for sodium pool burning in the head compartment, as well as subsequent events associated with the boil-up phase. CACECO provides a multicell thermodynamic analysis of the transient event. The code models the phenomena of the accident scenario, calculating cell temperature and pressure from mass and energy balances that involve chemical reactions, water vapor releases upon heating of concrete, decay heating, sodium transfers between cells, and leakage to the outside atmosphere. CACECO results are used in CCLST to prepare the input for HAA-3C and TRIMIT.

The HAA-3C code was used to calculate the fallout within the containment vessel. In addition to aerosols associated with the initial HCDA expulsion, the sodium boil-off rate from CACECO was used as the aerosol source rate. It was assumed that all sodium boiled off from the reactor cavity was converted into the sodium oxide even though some scenarios predict that oxygen is depleted and humidity levels indicate that sodium hydroxide would be formed. The hydroxide tends to agglomerate better than the oxide; therefore, agglomeration based upon oxide is conservative. Figure 5 shows the suspended concentration of sodium "oxide" in the RCB atmosphere.

The TRIMIT program was used to edit data from SPRAY, CACECO and HAA-3C into a series of input files for COMRADEX-H. The dissolved volatile

fission products (As, Se, Br, Rd, Cd, I, and Cs) were assumed to be fully dispersed within the sodium and were liberated as the sodium vaporized. The TRIMIT program is also used to predict the vaporization of cesium and sodium iodide from the sodium pool. Figure 6 shows the fraction of fission products vaporized as a function of sodium vaporization [8]. TRIMIT generates input files for COMRADEX-H. These data are shown in the next three figures. Figure 7 shows the sodium vapor leak rates from the reactor cavity to the RCB. The leak rates are expressed as instantaneous fractions of the quantities ultimately released from the cavity. Figure 8 shows the leak rates from the containment building to the environs expressed as fraction of the RCB free volume. Figure 9 shows the aerosol fallout rate in the RCB as fraction of the instantaneous amount suspended.

COMRADEX-H was applied to calculate the quantity of each radioactive isotope released from the containment as a function of time. For the initial release, the code calculates radioactive production and decay, fallout, and leakage from the RCB for each isotope in the library. For each of the volatiles, the code first considers radioactive production and decay in the reactor cavity, and leakage (boil-off) from the cavity to the RCB; within the RCB the code calculates the radioactive production and decay, the fallout, and the leakage from the RCB. These time dependent releases are summed with those from the initial release to yield the total release to the environs. Figure 10 shows the cumulative release of radionuclides, by physical class, from containment.

Following release from containment, each isotope was diminished by decay (but not by fallout) and the concentration was reduced by atmospheric dispersion enroute to the receptors. Finally, COMRADEX-H calculates the doses to receptors located at selected distances for various periods. During each execution of COMRADEX-H, a file called "outdat" is written. The program ADDEM sums the information on each file and generates a single "outdat" file. This file is then read by the plotting programs NUKARF and SLYDOSE. NUKARF plots releases and concentrations of radioactive isotopes or groups. SLYDOSE plots dose vs. distance curves.

PARAMETRIC COMPARISON

To demonstrate the sensitivity of the results of radiological analyses to the input models, parameters evaluated were: 1) Scenario, 2) Initial HCDA Expulsion, 3) Halogen State, 4) Aerosol Model, 5) Meteorological Model, and 6) Biological Dose Model. To delineate the effects, normalized doses, rather than explicit values, are presented in this paper. Doses calculated for comparison cases were divided by the doses calculated for the base cases.

Scenario

The accident scenario will, of course, influence radiological consequences. For the two cases used here, the most influential characteristics are vent time and sodium boil-up rate. For Case 768, venting occurred at 30.5 hours and total reactor sodium inventory of 280,000 kg was either boiled off or reacted by 360 hours. The vent rate was 1.9 m^3/sec maximum and decreased to about 0.05 m^3/sec at 360 hours.

For Case 766, venting of the RCB occurred at 11.6 hours and approximately 2/3 of the sodium remained in the reactor cavity at 720 hours. The purge rate was assumed at a nominally constant level of 1.3 m^3/sec for the remainder of the 30-day period of the analysis.

Table I shows normalized site boundary doses from the two scenarios, both computed with the same models. The increases in the bone, lung, and whole body doses are due to solids liberated by the early vent and purge in Case 766. Even though the thyroid dose is lower in Case 766, over half of it was due to halogens liberated by the early vent. By contrast, in Case 768 the thyroid dose due to the initial release was less than 0.2% of the total. The total thyroid dose for Case 768 exceeds that from Case 766 due to the far larger amount of sodium boiled out of the cavity in the former case.

TABLE I Scenario Comparison

Case	Normalized Site Boundary Doses			
	Bone	Thyroid	Lung	Whole Body
768B - Vent at 30.5 hr Rapid sodium boiling	1	1	1	1
766B - Vent at 11.6 hr, low sodium vaporization	24.6	0.4	24.0	12.5

Initial HCDA Expulsion

The mechanistic release for the FFTF HCDA was assumed to be 100% of the noble gases and 1% of the core materials. Assuming a different value will directly affect the doses which are dependent upon non-volatile solids. The effect of doubling the solids in the initial HCDA expulsion is shown in Table II. The bone dose is directly proportional to the solids in the initial release. In Case 768, the thyroid dose is essentially unaffected because the iodine release is controlled by the sodium boilup, which is independent of the initial expulsion. In Case 766, however, sodium vaporization is only about 10% of that occurring in Case 768. Thus, the thyroid dose is controlled by halogens in the initial HCDA expulsion.

TABLE II Parametric Comparison - Initial Expulsion

Description	Normalized Site Boundary Doses Bone	Thyroid	Lung	Whole Body
Case 768B-1% Solids in Initial Expulsion	1	1	1	1
Case 768P-2% Solids in Initial Expulsion	2.0	1.0	1.9	1.4
Case 766B-1% Solids in Initial Expulsion	1	1	1	1
Case 766P-2% Solids in Initial Expulsion	2.0	1.5	2.0	1.9

Halogen State

When free halogens; i.e., in the vapor state and therefore not subject to fallout, were assumed to be present in the initial HCDA release, the thyroid doses were increased. The effects are shown in Table III. The net increase was governed by decay time prior to venting; waiting from 12 to 31 hours to vent reduced the increase by a factor of three.

TABLE III Parametric Comparison - Halogen State

Description	Normalized Thyroid Dose
Case 768B - No Free Halogens	1
Case 768H - Free Halogens in Initial Release	2.1
Case 766B - No Free Halogens	1
Case 766H - Free Halogens in Initial Release	6.5

Aerosol Model

The aerosol fallout computed by HAA-3C was varied by applying a multiplier to the fallout rate. Site boundary normalized doses as a function of fallout rate multiplier are shown in Figure 11. In Case 768, RCB venting is delayed for over 24 hours providing time for substantial fallout before airborne material is carried out of the building. After that time, aerosol concentrations were calculated to reach very high levels of about 33 g/m^3 due to high sodium boilup. The aerosol input to the RCB terminated about halfway through the 30-day evaluation period. As a result of these scenario dependent factors, the dose is less sensitive to increases in fallout rate in excess of that predicted by the HAA-3C model. However, if no fallout occurred at all, doses could be one or two orders of magnitude higher.

For Case 766, venting was assumed at 11 hours; this time is insufficient for the initial HCDA release to fall out of the RCB atmosphere. A

relatively low, but steady aerosol input provides a suspended concentration of about 3 g/m^3, prevailing over much of the 30-day period. As a result, the normalized dose continues to vary as a function of fallout rate multiplier over the range investigated.

Meteorological Model

The meteorological model used in the analyses was a representation of the sequence given in Regulatory Guide 1.3. Another meteorological model was provided by NRC; this model was based on Washington Public Power Supply System (WPPSS) data taken over a one-year period at the Hanford Site; this second model is more conservative. Both meteorological sequences assume that, at the time of the accident initiation, there is very little meteorological dispersion. The dispersion becomes progressively greater as the time increases from the accident initiation. Results are shown in Table IV.

TABLE IV Parametric Comparison - Meteorology

	Normalized Site Boundary Doses			
Description	Bone	Thyroid	Lung	Whole Body
Case 768B - Reg. Guide 1.3 Meteorology	1	1	1	1
Case 768M - WPPSS Meteorology	1.6	3.6	1.6	2.3
Case 766B - Reg. Guide 1.3 Meteorology	1	1	1	1
Case 766M - WPPSS Meteorology	2.7	3.1	2.7	2.7

The result of the changing dispersion is that, for a given release of radioactivity, the dose to the receptor is higher when the dispersion is lower; i.e., the dose would be higher for an early release than for a later one. In the parametric cases the doses were increased, but since they largely accumulated during the first few hours following the vent, the increases simply reflect the ratio of the dispersions of the two models at the time of vent. The exceptions are the thyroid doses and the whole body dose of Case 768 which were strongly influenced by the boilup which occurred later in time.

Biological Dose Model

The models which were used in this comparison are the NUREG-0172 [9], ICRP-2 [10] and ICRP-2 modified with a new lung model. Results of the comparison are shown in Table V. The new lung model assumes that insoluble plutonium is retained in the lung rather than migrating to the bone. Consequently, bone doses from the new lung modified ICRP-2 model are almost a factor of ten lower than those computed with the NUREG-0172 model; conversely, the lung dose is a factor of two higher.

The ICRP-2 whole body internal dose is less than NUREG-0172 because the former fails to account for the whole body internal dose from plutonium

whereas the NUREG model does. Case 766 lung and whole body ICRP-2 doses are lower than Case 768 values because the ICRP-2 model accentuates (because of higher F values) the contribution of the volatile solids, particularly iodine and cesium. More of these isotopes are released in Case 768 than 766 owing to high sodium boilup rates computed in the former case.

TABLE V Parametric Comparison - Biological

	Normalized Site Boundary Doses			
Description	Bone	Thyroid	Lung	Whole Body
Case 768B - NUREG-0172	1	1	1	1
Case 768F - ICRP-2		1.0	1.7	0.4
Case 768L - New Lung	0.1		2.0	
Case 766B - NUREG-0172	1	1	1	1
Case 766F - ICRP-2		1.0	0.5	0.1
Case 766L - New Lung	0.1		2.0	

CONCLUSION

The content of the initial HCDA expulsion affects the consequences predictably. Likewise, the effect of halogen state is predictable, but it is not normally considered to be a variable since it is very difficult for halogens and sodium to coexist in a vapor state without combining.

The meteorological and biological dose models are normally fixed administratively for all analyses concerning a given facility. The treatment here only serves to illustrate the sensitivity of the results to some possible choices.

Of all the parameters investigated, aerosol fallout has the greatest effect on consequences. There is, of course, a large interaction with the scenario, most notably, time of venting. Thus a rapid fallout rate is important in early venting cases. It is judged important to have reliable models of fallout from relatively dilute concentrations, since low aerosol concentration may be characteristic of containment building purging. Implicit in the use of the aerosol models is the assumption that their experimental bases are consistent with the scenarios to which the models are being applied. Additional areas of interest include:

- Aerosol behavior in the presence of condensing vapors, both sodium and water.
- Fallout under conditions of convection currents within a RCB.
- Fallout while a building is being purged.
- Potential for re-suspension of aerosols during rapid blowdown of a containment building.
- Fallout during downwind transport.

References

1. R. D. Peak, "User's Guide to CACECO Containment Analysis Code," HEDL-TME-79-22, June 1979.

2. R. D. Peak, et al., "FFTF Containment of Hypothetical Accidents" Proceeding ANS/ENS International Meeting on Fast Reactor Safety Technology, Seattle, Washington (1979)

3. Ibid.

4. D. R. Marr, A User's Manual for Computer Code RIBD-II, A Fission Product Inventory Code, Hanford Engineering Development Laboratory, HEDL-TME-75-76, January 1975.

5. P. R. Shire, Spray Code User's Report, HEDL, HEDL-TME-76-94, March 1977.

6. L. Baurmash, et al., HAA-3 User Report, Atomics International, AI-AEC-13088, 1973. (HAA-3C denotes the current version in use at HEDL).

7. G. W. Spangler, et. al., Description of the COMRADEX Code, Atomics International, AI-67-TDR-108, 1967. (COMRADEX-H denotes the current version in use at HEDL)

8. A. W. Castleman, Jr., Review of Fission Product and Aerosol Behavior for LMFBR Systems, Brookhaven National Laboratory, November 1972. AICHE Paper No. 77E.

9. G. R. Hoenes and J. K. Soldat, Age-Specific Radiation Dose Commitment Factors for a One-Year Chronic Intake, Battelle Pacific Northwest Laboratories, NUREG-0172, November 1977.

10. Recommendations of the International Commission of Radiological Protection, ICRP Publication 2, Report of Committee II on Permissible Dose for Internal Radiation, 1959, published for ICRP by Pergamon Press.

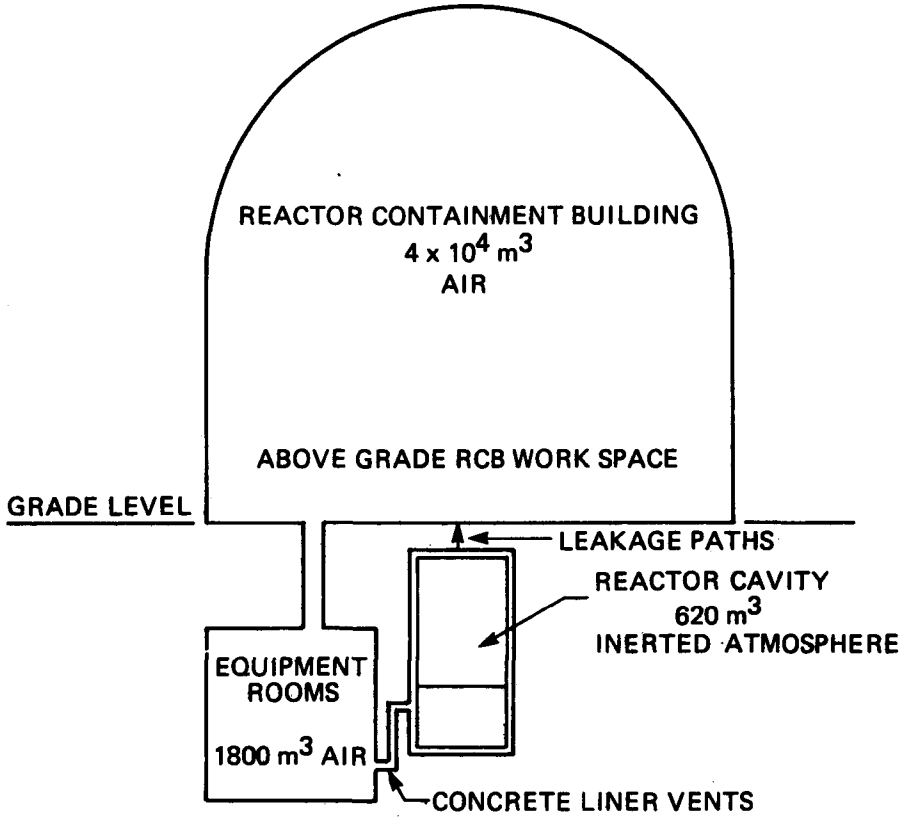

HEDL 8003-326-3

Figure 1 - Secondary Containment Model

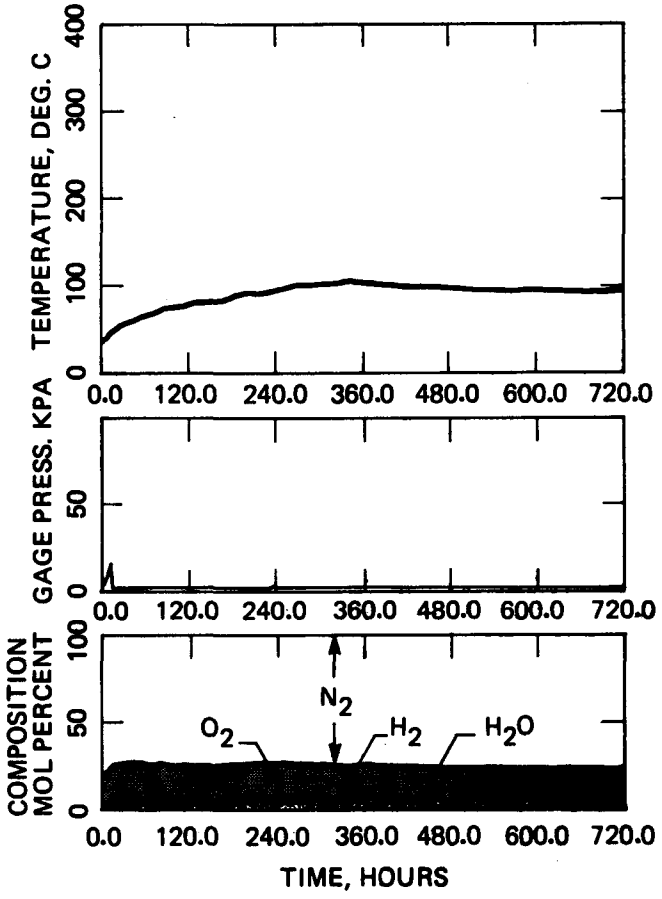

HEDL 8003-326-1

Figure 2 - RCB Transient Conditions for Case 766

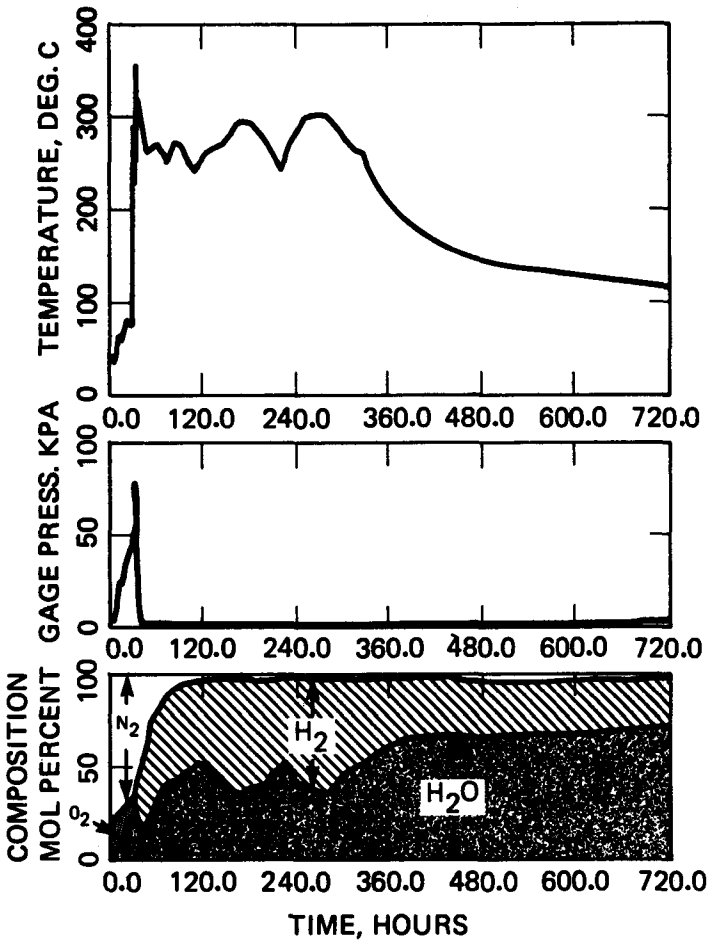

Figure 3 - RCB Transient Conditions for Case 768

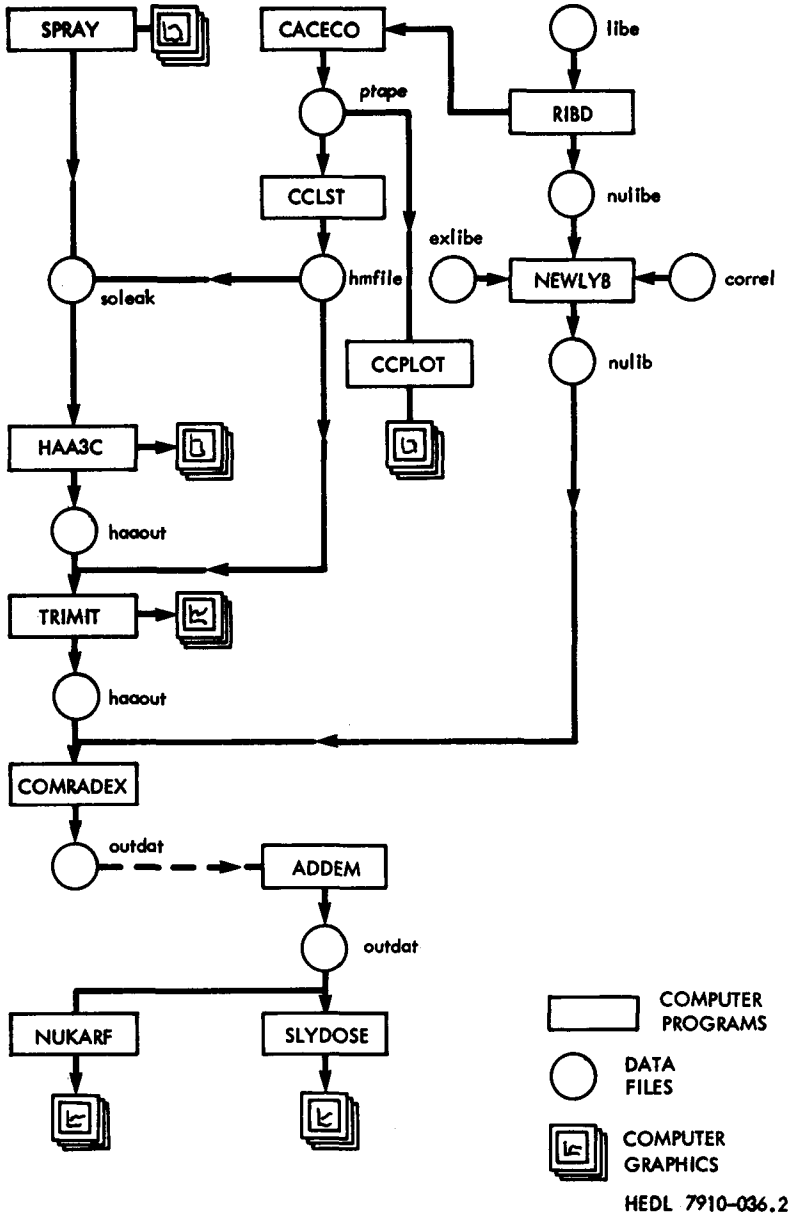

Figure 4 - Relationship of Codes & Files

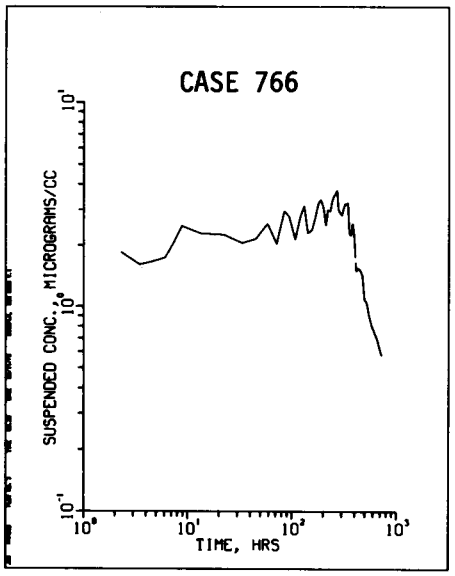

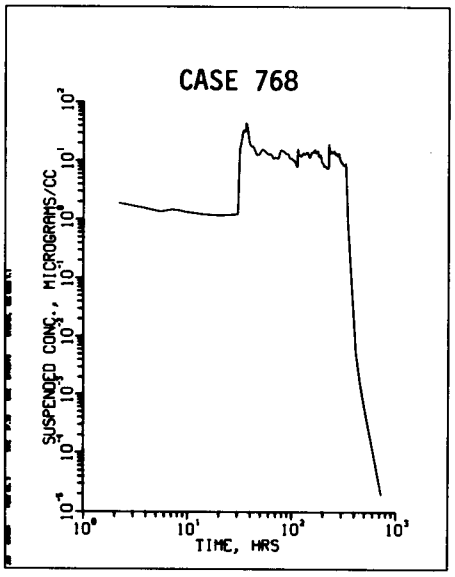

Suspended Aerosol Concentration
Figure 5

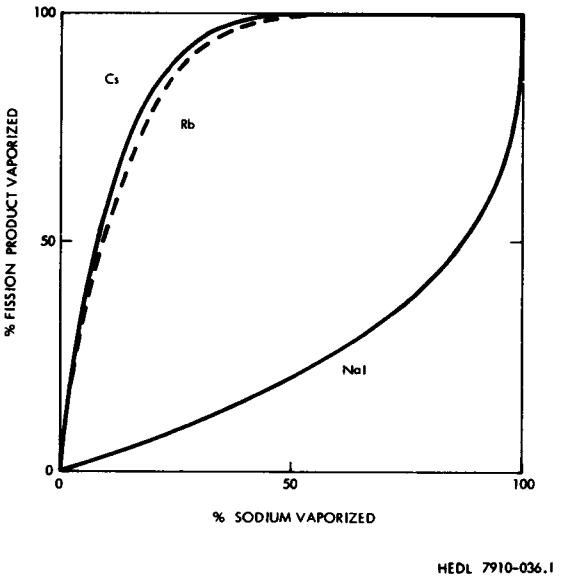

Figure 6 - Fission Product - Sodium Equilibrium Vaporization

HEDL 8004-044.3

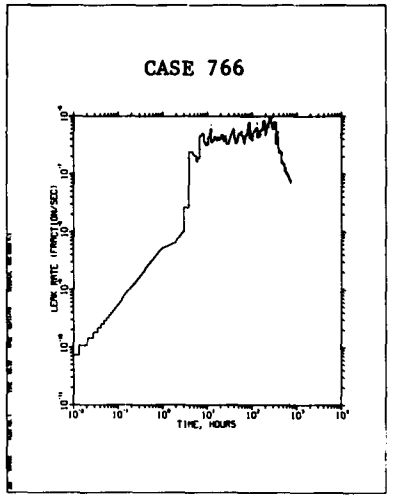

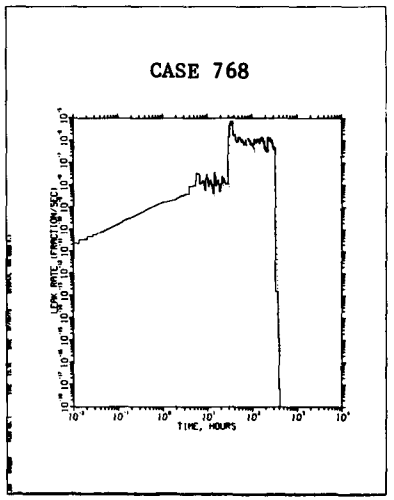

SOURCE RATE FROM BOILUP

Figure 7

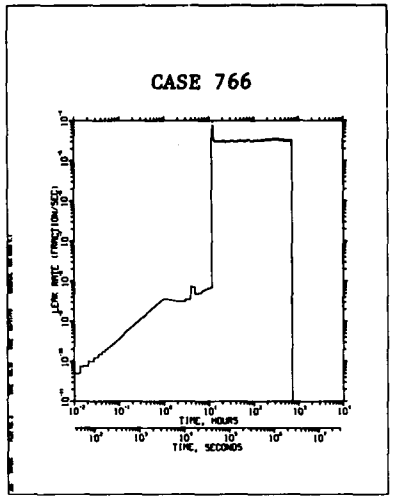

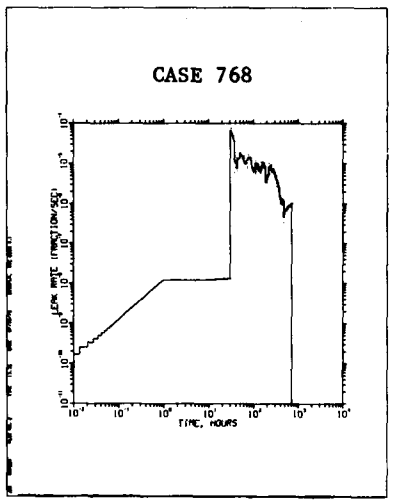

RCB DISCHARGE

Figure 8

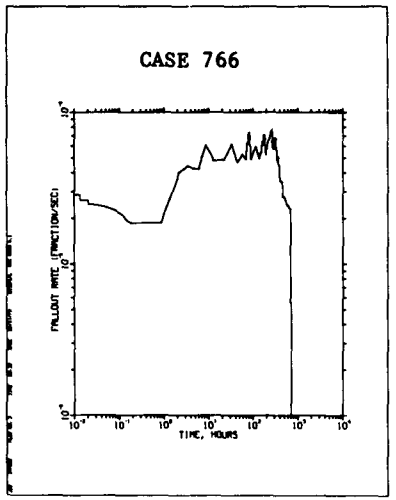

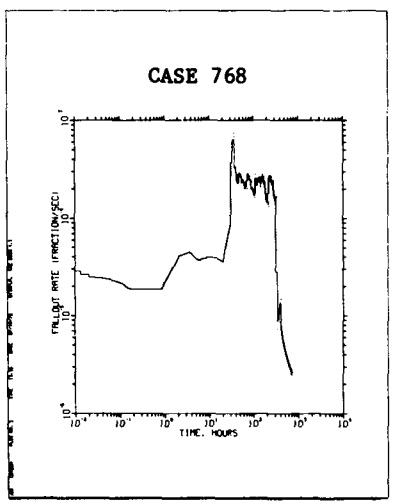

FALLOUT IN RCB

Figure 9

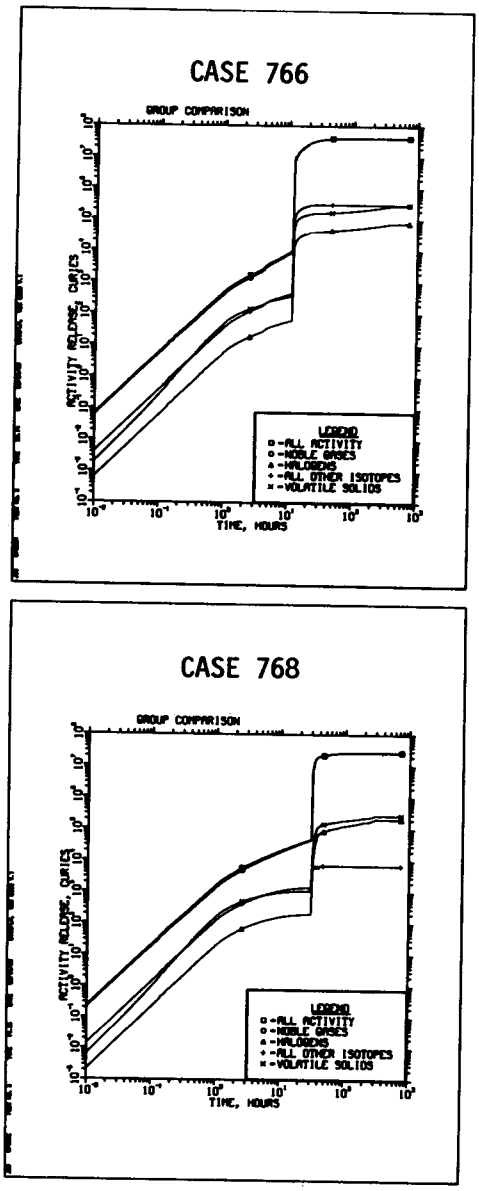

RELEASE FROM CONTAINMENT
FIGURE 10

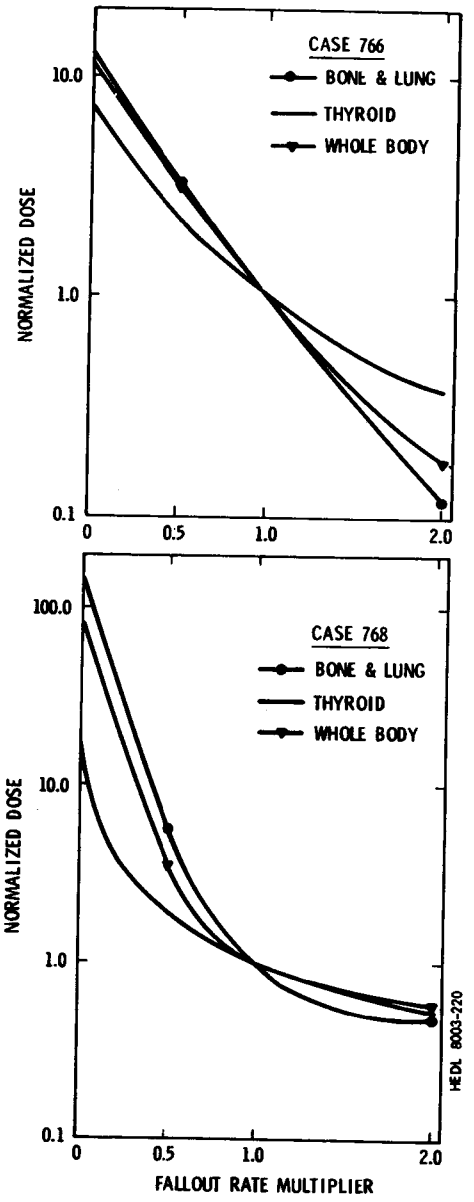

PARAMETRIC COMPARISON - AEROSOL MODEL
FIGURE 11

HEDL 8004-044.2

NUCLEAR AEROSOLS IN REACTOR SAFETY - WHAT REMAINS TO BE DONE?*

The following is a list of areas where additional useful work remains to be done in nuclear aerosol technology. This list was derived largely from an apparently good consensus developed among the nuclear aerosol specialists attending the meeting, as reflected in summaries prepared by the Session Chairmen, comments from Sessions I thru VI and the closing panel discussion.

Aerosol Source Terms

1. An improved understanding and quantification of source terms is needed:

   - LWR: release of non-radioactive materials, release into steam atmospheres, release during fuel melting, release during core-concrete interaction, and release of short-lived nuclides.

   - LMFBR: energetic HCDA head release; long-term core melt releases (core-coolant interaction, core-concrete interaction, and sodium-concrete reaction).

2. Experimental definition of the source term (radioactive and non-radioactive materials) should include the rate of release, size distribution of released particles, concentration in the transport medium at the release location, time duration of release, and chemical nature of the released aerosol material.

Aerosol Processes

Additional information on agglomerate properties (shape or form factors and correction factors) is needed for adequate description of aerosol behavior processes over a wide range of accident conditions for LWRs and LMFBRs. This information is needed for single and multi-specie aerosol agglomerates.

Mathematical and Computer Modelling

1. Technical coordination between code developers and experimental aerosol researchers needs to be improved.

2. Aerosol code development must be strongly focused on accident analysis applications and the needs of the various users.

3. Priorities of experimental investigations should be reevaluated as significant improvements are made to the codes.

4. Additional code improvements to describe chemical reactions of the aerosols and condensation of sodium vapor would be useful.

---

* Coordinated and edited by M. Silberberg

Comparison of Codes and Experiments

1. More work is needed to establish quantitative criteria for code validation goals to determine when the code validation is adequate.

2. Greater emphasis should be placed on pre-test predictions and the use of shape and correction factors independently measured or theoretically estimated, in order to avoid use of adjustable parameters *a posteriori* and the problems this could bring for use at fullscale accident conditions.

3. More work is needed on the quantification of turbulent agglomeration and the related measurements of gas convection in test vessels.

4. There is a need for greater uniformity (and standardization) among different groups in the definition and useage of various morphological correction factors.

CSNI SPECIALISTS MEETING ON NUCLEAR AEROSOLS IN REACTOR SAFETY

Gatlinburg, Tennessee, 15th-17th April 1980

PARTICIPANTS

Mr. R. E. Adams
Oak Ridge National Laboratory
USA

Mr. H. Alter
U. S. Department of Energy
USA

Dr. L. Baker, Jr.
Argonne National Laboratory
USA

Mr. D. Boulaud
Commissariat à l'Energie Atomique
FRANCE

Mr. S. L. Brown
Clinch River Breeder Reactor Project
USA

Mr. H. Bunz
Kernforschungszentrun Karlsruhe GmbH
F. R. of GERMANY

Mr. K. E. Buttrey
Rockwell International
USA

Dr. D. W. Cooper
Harvard School of Public Health
USA

Mr. J. E. Dick
Atomic Energy of Canada, Ltd.
CANADA

Mr. R. M. Elrick
Sandia Laboratories
USA

Dr. J. Fermandjian
Commissariat à l'Energie Atomique
FRANCE

Dr. J. A. Gieseke
Battelle-Columbus Laboratories
USA

Dr. S. A. Harbison
Nuclear Installations Inspectorate
UNITED KINGDOM

Mr. R. K. Hilliard
Hanford Engineering Development Laboratory
USA

Mr. P. Hosemann
PNS
F. R. of GERMANY

Dr. T. C. Huang
General Electric Company
USA

Mr. K. O. Johansson
Studsvik Energiteknik AB
SWEDEN

Mr. H. Jordan
Battelle-Columbus Laboratories
USA

Mr. G. M. Kanapilly
Lovelace ITRI
USA

Dr. Edward Keshock
University of Tennessee
USA

Dr. S. Kitani
JAERI
JAPAN

Mr. Heinz Kottowski
European Community (EURATOM)
ITALY

Dr. T. S. Kress
Oak Ridge National Laboratory
USA

Dr. K. Lee
Battelle-Columbus Laboratories
USA

Mr. A. L'Homme
Commissariat à l'Energie Atomique
FRANCE

Dr. J. K. Long
U. S. Nuclear Regulatory Commission
USA

Ms. J. P. Longworth
Berkeley Nuclear Laboratories
UNITED KINGDOM

Mr. S. K. Loyalka
University of Missouri-Columbia
USA

Mr. G. Madelaine
Commissariat à l'Energie Atomique
FRANCE

Mr. A. P. Malinauskas
Oak Ridge National Laboratory
USA

Mr. H. C. Martin
Westinghouse Hanford Company
USA

Mr. J. D. McCormack
Hanford Engineering Development Laboratory
USA

Mr. N. Mitsutsuka
Power Reactor and Nuclear Fuel Development Corporation
JAPAN

Dr. H. A. Morewitz
Rockwell International
USA

Mr. C. T. Nelson
Rockwell International
USA

Dr. A. L. Nichols
United Kingdom Atomic Energy Authority
UNITED KINGDOM

Mr. H. Obata
Century Research Center Corporation
JAPAN

Mr. J. P. Olivier
OECD Nuclear Energy Agency
FRANCE

Mrs. Piera Olivieri
Natl. Comm. Nuclear Energy Health Physics Laboratory
ITALY

Mr. G. W. Parker
Oak Ridge National Laboratory
USA

Dr. A. K. Postma
Hanford Engineering Development Laboratory
USA

Mr. Dana A. Powers
Sandia Laboratories
USA

Professor V. Prodi
Natl. Comm. Nuclear Energy Health Physics Laboratory
ITALY

Mr. B. Rehn
Kernforschungszentrun Karlsruhe GmbH
F. R. of GERMANY

Dr. A. B. Reynolds
University of Virginia
USA

Mr. M. Ruhbaum
Kraftwerk Union
F. R. of GERMANY

Dr. W. Schikarski
Kernforschungszentrun Karlsruhe GmbH
F. R. of GERMANY

Mr. W. Schuetz
Kernforschungszentrun Karlsruhe GmbH
F. R. of GERMANY

Dr. W. Schöck
Kernforschungszentrun Karlsruhe GmbH
F. R. of GERMANY

Mr. P. R. Shire
Hanford Engineering Development Laboratory
USA

Mr. M. Silberberg
U. S. Nuclear Regulatory Commission
USA

Mr. D. D. Stepnewski
Westinghouse Hanford Company
USA

Mr. W. Stöber
Fraunhofer-Institute für Toxikologie und Aerosolforschung
F. R. of GERMANY

Mr. L. E. Strawbridge
Westinghouse Electric Corporation
USA

Mr. T. Tachino
Mitsubishi Atomic Power Industries Inc.
JAPAN

Dr. M. L. Tobias
Oak Ridge National Laboratory
USA

Dr. D. C. Torgeson
Whiteshell Nuclear Research Est.
CANADA

Mr. R. F. Tuttle
University of Missouri
USA

Dr. B. Y. Underwood
United Kingdom Atomic Energy Authority
UNITED KINGDOM

Dr. J. F. Van de Vate
Netherlands Energy Research
Foundation ECN
NETHERLANDS

Dr. E. V. Vaughan
Rockwell International
USA

Dr. A. L. Wright
Oak Ridge National Laboratory
USA

NUREG/CR-1724
ORNL/NUREG/TM-404
CSNI-45
Category Dist. R7

Internal Distribution

1. R. E. Adams
2. T. D. Anderson
3. H. W. Bertini
4. J. R. Buchanan
5. N. Callaham
6. W. B. Cottrell
7. G. F. Flanagan
8. M. H. Fontana
9. H. W. Hoffman
10-14. T. S. Kress
15. R. E. MacPherson
16. A. P. Malinauskas
17. F. R. Mynatt
18. M. F. Osborne
19. G. W. Parker
20. P. Patriarca
21. J. L. Rich
22. A. M. Smith
23. I. Spiewak
24. J. A. Stevens
25. A. L. Sutton, Jr.
26. M. L. Tobias
27. H. E. Trammell
28. D. B. Trauger
29. J. L. Wantland
30. G. D. Whitman
31. R. P. Wichner
32. A. L. Wright
33. ORNL Patent Office
34. Central Research Library
35. Y-12 Document Reference Section
36-37. Laboratory Records Department
38. Laboratory Records (RC)

External Distribution

39. K. Aisaka, Agency of Natural Resources, JAPAN
40. A. Alonso, Director, Departmento de Seguridad Nuclear, Ministerio de Industria, SPAIN
41. H. Alter, DOE, UNITED STATES
42. Professor N. Aybers, Director, Nükleer Enerji Enstitüsü, Istanbul Teknik Universitusi, TURQUIE
43. Dr. L. Baker, Jr., Argonne National Laboratory, UNITED STATES
44. Dr. Banaschik, Gesellschaft für Reaktorsicherheit, R. F. d'ALLEMAGNE
45. W. Binner, Institutsleiter für Reaktortechnik und Koordinator für Reaktorsicherheit, Oesterreichische Studiengesellschaft für Atomenergie, AUTRICHE
46. Professor Dr. Adolf Birkhofer, Lehnstuhl für Reaktordynamik und Reaktorsicherheit der Technischen Universität Müchen, Gesellschaft für Reaktorsicherheit mbH, R. F. d'ALLEMAGNE
47. T. Bjoerlo, Institutt for Atomenergi, NORWAY
48. D. Boulaud, Commissariat à l'Energie Atomique, Centre d'Etudes Nucléaires, FRANCE
49. S. L. Brown, Clinch River Breeder Reactor Project, UNITED STATES
50. Dr. R. J. Budnitz, Director, Office of Nuclear Regulatory Research, NRC, UNITED STATES

51. Dr. Heinz Buechler, Ministerialrat, Bundesministerium des Innern, R. F. d'ALLEMAGNE
52. H. Bunz, Laboratorium für Aerosolphysik und Filtertechnik, F.R. of GERMANY
53. D. P. Burnham, Westinghouse Instrumentation Division, UNITED STATES
54. K. E. Buttrey, Rockwell International, UNITED STATES
55. R. G. Chenoweth, Jr., President, Engineering and Hydrocarbons Division, Union Carbide Corporation, UNITED STATES
56. Professor Nicholas G. Chrysochoides, Director, Reactor Department, Greek Atomic Energy Commission, GREECE
57. J. T. Cockburn, Manager of Manufacturing Planning, Celanese Chemical Co., Inc., UNITED STATES
58. F. Cogne, Chef du Département de Sûreté Nucléaire, CEA, FRANCE
59. Dr. D. W. Cooper, Harvard School of Public Health, UNITED STATES
60. Dr. Peter Courvoisier, Leiter, Abteilung für die Sicherheit der Kernanlagen, Eidgenössisches Amt für Energie-wirtschaft, SUISSE
61. Dr. D. W. Crancher, Director, Nuclear Plant Safety Unit, Regulatory and External Relations Branch, AAEC, AUSTRALIE
62. M. C. Cunningham, Irish Nuclear Energy Board, IRELAND
63. J. E. Dick, Atomic Energy of Canada, Ltd., CANADA
64. Director, Office of Nuclear Regulatory Research, Nuclear Regulatory Commission, Washington, D.C. 20555, UNITED STATES
65. Z. Domaratzki, Director, Reactor and Acceleration Branch, AECB, CANADA
66. Monsieur H. Dopchie, Association Vincotte ASBL, BELGIQUE
67. R. M. Elrick, Sandia Laboratories, UNITED STATES
68. Dr. Tapio Eurola, Deputy Director, Department of Reactor Safety, Institute of Radiation Protection, FINLANDE
69. J. Fermandjian, Départment de Sûretté Nucléaire, IPSN/DSN/SESRS, Centre d'Etudes Nucléaires, FRANCE
70. J. A. Firing, Institutt for Atomenergi, NORWAY
71. R. Gausden, Chief Inspector of Nuclear Installations, Health and Safety Executive, NII, ANGLETERRE
72. Dr. J. A. Gieseke, Battelle-Columbus Laboratories, UNITED STATES
73. E. V. Gilby, UKAEA/SRD, ANGLETERRE
74. P. Giuliani, Direzione Centrale della Sicurezza, Nucleare e della Protezione Sanitaria, CNEN, ITALY
75. E. L. Gluekler, Argonne National Laboratory, UNITED STATES
76. Dr. W.R.A. Goosens, Chemistry Service: C.I.T., Studiencentrum voor Kernenergie, BELGIQUE
77. J. D. Griffith, Deputy Director, Nuclear Power Development Division, DOE, UNITED STATES
78. W. S. Gronow, Deputy Chief Inspector of Nuclear Installations, Health and Safety Executive, NII, ANGLETERRE
79. T. Hanratty, Professor-Department of Chemical Engineering, University of Illinois, UNITED STATES
80. Dr. S. A. Harbison, Health and Safety Executive, Nuclear Installations Inspectorate, ANGLETERRE
81. M. Hayakawa, Director, Reactor Regulation Division, Science and Technology Agency, JAPAN
82. Dr. E. Hellstrand, Department of Safety and Waste Management, Studsvik Energiteknik AB, SUEDE

83. R. K. Hilliard, Hanford Engineering Development Laboratory, UNITED STATES
84. P. Hosemann, Kernforschungszentrum Karlsruhe GmbH, PNS, F. R. of GERMANY
85. Dr. T. C. Huang, General Electric Company, UNITED STATES
86. K. O. Johansson, Studsvik Energiteknik AB, SWEDEN
87. H. Jordan, Battelle-Columbus Laboratories, UNITED STATES
88. S. Jordan, Kernforschungszentrum Karlsruhe GmbH, Laboratorium für Aerosolphysik und Filtertechnik, F. R. of GERMANY
89. G. M. Kanapilly, Lovelace ITRI, UNITED STATES
90. Kumao Kaneko, Director, Nuclear Energy Division, United Nations Bureau, Ministry of Foreign Affairs, JAPAN
91. J. Karangelos, Head, Safety and Licensing Section, Public Power Office, GREECE
92. Dr. E. Keshock, University of Tennessee, UNITED STATES
93. G. H. Kinchin, Director, UKAEA/SRD, ANGLETERRE
94. Professor S. Kitani, JAERI, JAPAN
95. Mr. Klersy, Director des Projets, CCE-Euratom Centre Commun de Recherches, ITALY
96. H. Kottowski, EURATOM, COMMISSION OF EUROPEAN COMMUNITIES
97. K. H. Krewer, Regierungsdirektor, Bundesministerium für Forschung und Technologie, R. F. d'ALLEMAGNE
98. Y. Kurihara, Director, Technology Promotion Division, Science and Technology Agency, JAPAN
99. Dr. J. D. Lafleur, Jr., Deputy Director, Office of International Programs, NRC, UNITED STATES
100. Dr. S. Lanza, Assistant Professor, Istituto di Impianti Nucleari, Università di Pisa, ITALY
101. Dr. K. Lee, Battelle-Columbus Laboratories, UNITED STATES
102. F. Leonard, Chef du Département BR2, Centre d'Etude de l'Energie Nucléaire, BELGIQUE
103. A. L'Homme, Commissariat à l'Energie Atomique, FRANCE
104. Dr. Walter B. Loewenstein, Director, Nuclear Safety and Analysis Department, EPRI, UNITED STATES
105. Dr. J. K. Long, Nuclear Regulatory Commission, UNITED STATES
106. Ms. J. P. Longworth, Central Electricity Generating Board, Berkeley Nuclear Laboratories, UNITED KINGDOM
107. S. K. Loyalka, University of Missouri-Columbia, UNITED STATES
108. L. F. Lischer, Vice President, Engineering and Research (Retired), Commonwealth Edison Company, UNITED STATES
109. G. Madelaine, STEPAM/IPSN, Centre d'Etudes Nucléaires, FRANCE
110. D. Malnes, Institutt for Atomenergi, NORWAY
111. D. Manesse, Département de Sûreté Nucléaire, I.P.S.N., Centre d'Etudes Nucléaires, FRANCE
112. A. F. Marques De Carvalho, Nuclear Safety and Protection, Ministry of Industry, PORTUGAL
113. H. C. Martin, Westinghouse Hanford Company, UNITED STATES
114. F. G. May, Nuclear Science and Technology Branch, AAEC Research Establishment, AUSTRALIE
115. J. D. McCormack, Hanford Engineering Development Laboratory, Westinghouse Hanford Company, UNITED STATES
116. A. Merelli, RAD/Divisione Ricerche di Sicurezza, CNEN, ITALY
117. A. Messiah, Service Central de Sûreté des Installations Nucléaires, FRANCE

118. B. Micheelsen, Head, Department of Reactor Technology, Research Establishment Risø, DANEMARK
119. N. Mitsutsuka, PNC, JAPAN
120. K. Mochizuki, Head, Safety Research, PNC, JAPAN
121. M. Moelsaeter, Secretary, Norwegian Nuclear Energy Safety Authority, NORWAY
122. M. Moller-Madsen, Director, Inspectorate of Nuclear Installations, DANEMARK
123. Dr. H. A. Morewitz, Project Manager, LMFBR Physics and Safety, Atomics International, UNITED STATES
124. Dr. L. D. Muhlestein, Hanford Engineering Development Laboratory, Westinghouse Hanford Company, UNITED STATES
125. G. Naschi, Director, Safety and Health Protection Directorate, CNEN, ITALY
126. C. T. Nelson, Energy Systems Group, Rockwell International, UNITED STATES
127. Dr. A. L. Nichols, UKAEA, Atomic Energy Establishment, Winfrith, ANGLETERRE
128. Dr. L. Nordstrom, Director General, Swedish Nuclear Power Inspectorate, SUEDE
129. H. Obata, Century Research Center Corporation, JAPAN
130. Office of Assistant Manager for Energy Research and Development, DOE-ORO, UNITED STATES
131. J. P. Olivier, OECD, FRANCE
132. Mrs. P. Oliviera, Natl. Comm. Nuclear Energy, Health Physics Laboratory, ITALY
133. L. Pease, Manager, Reactor Performance Engineering, AECL-Power Projects, CANADA
134. G. Penelle, Chef de Service, Contrôle Radioprotection ASBL, BELGIQUE
135. M. Perello, Head of Standards Service, Departmento de Seguridad Nuclear, Ministerio de Industria, Junta de Energia Nuclear, SPAIN
136. Dr. A. K. Postma, Hanford Engineering Development Laboratory, Westinghouse Hanford Company, UNITED STATES
137. D. A. Powers, Sandia Laboratories, UNITED STATES
138. Professor V. Prodi, Natl. Comm. Nuclear Energy, Health Physics Laboratory, ITALY
139. B. Rehn, Kernforschungszentrum Karlsruhe GmbH, Laboratorium für Aerosolphysik und Filtertechnik, F.R. of GERMANY
140. Dr. A. B. Reynolds, University of Virginia, UNITED STATES
141. J. M. Rolland, Counseller (Atomic Energy) Australian Embassy, AUTRICHE
142. M. Rosen, Deputy Director, Division of Nuclear Safety and Environmental Protection, IAEA, AUTRICHE
143. Dr. D. Ross, Director, Division of Project Management, NRC, UNITED STATES
144. R. Rudman, Director of Planning, EPRI, UNITED STATES
145. M. Ruhbaum, Kernforschungszentrum Karlsruhe GmbH, Laboratorium für Aerosolphysik und Filtertechnik, F.R. of GERMANY
146. H. Satake, Director, Nuclear Material Regulation Division, Nuclear Safety Bureau, Science and Technology Agency, JAPAN
147. K. Sato, Chief, Reactor Safety Code, Development Laboratory, Division of Reactor Safety Evaluation, JAERI, JAPAN

148. Dr. W. Schikarski, Kernforschungszentrum Karlsruhe GmbH, Laboratorium für Aerosolphysik und Filtertechnik, F.R. of GERMANY
149. Dr. W. Schöck, Kernforschungszentrum Karlsruhe GmbH, Laboratorium für Aerosolphysik und Filtertechnik, F.R. of GERMANY
150. R. G. Scholvinck, Reactor Study and Design Division, Energieonderzoek Centrum, PAYS-BAS
151. W. Schuetz, Kernforschungszentrum Karlsruhe GmbH, Laboratorium für Aerosolphysik und Filtertechnik, F.R. of GERMANY
152. R. Sherry, Division of Reactor Safety Research, NRC, UNITED STATES
153. P. R. Shire, Hanford Engineering Development Laboratory, Westinghouse Hanford Company, UNITED STATES
154. M. Silberberg, Chief, Experimental Fast Reactor Safety Branch, Division of Reactor Safety Research, NRC, UNITED STATES
155. A. F. Spano, Special Assistant for International Research Programs to Director of Office of Nuclear Regulatory Research, NRC, UNITED STATES
156. D. D. Stepnewski, Westinghouse Hanford Company, UNITES STATES
157. W. Stöber, Fraunhofer-Institute für Toxikologie und Aerosolforschung, F.R. of GERMANY
158. L. E. Strawbridge, Westinghouse Electric Corporation, UNITES STATES
159. T. Tachino, Advanced Reactor Engineering Department, Mitsubishi Atomic Power Industries, Inc., Nuclear Development Centre, JAPAN
160. P. Tanguy, Directeur, IPSN-CEA, FRANCE
161-162. Technical Information Center, DOE, UNITED STATES
163. Dr. D. C. Torgeson, Atomic Energy of Canada Limited, Whiteshell Nuclear Establishment, CANADA
164. R. F. Tuttle, University of Missouri, UNITED STATES
165. Dr. B. Y. Underwood, UKAEA, Safety and Reliability Directorate, ANGLETERRE
166. C. John van Daatselaar, Head, Nuclear Development, Ministerie van Sociale Zaken, Directoraat-Generaal van de Arbeid, PAYS-BAS
167. Dr. J. F. van de Vate, Chemistry Division, Netherlands Energy Research Foundation ECN, PAYS-BAS
168. E. V. Vaughn, Energy Systems Group, Rockwell International, UNITED STATES
169. W. Vinck, Head, Division of Safety of Nuclear Installations, BELGIQUE
170. Dr. Antti P. U. Vuorinen, Director, Nuclear Safety Institute of Radiation Protection, FINLANDE
171. F. Weehuizen, Abteilung für die Sicherheit der Kernanlagen, Eidgenössisches Institut für Reaktorforschung, SUISSE
172. C. Zaffiro, Direzione Centrale della Sicurezza Nuclear e della Protezione Sanitari, CNEN, ITALY
173. Dr. H. Zikidis, Greek Atomic Energy Commission, Nuclear Research Center, GREECE
174-553. Given Distribution as shown in Category R7 (NTIS - 10 copies)

☆ U.S. GOVERNMENT PRINTING OFFICE: 1981-740-062/118